WOODHEAD PUBLISHING SERIES IN ELECTRONIC AND OPTICAL MATERIALS

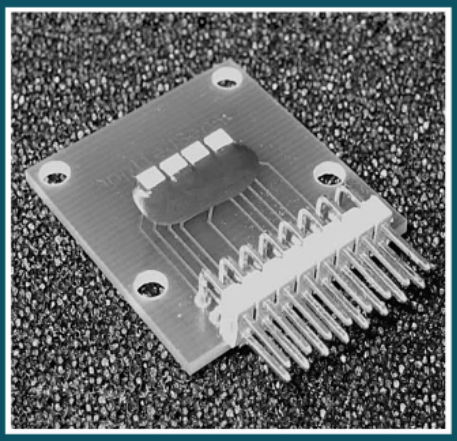

Semiconductor gas sensors

Edited by Raivo Jaaniso and Ooi Kiang Tan

WP
WOODHEAD PUBLISHING

VISIT…

Semiconductor gas sensors

© Woodhead Publishing Limited, 2013

Related titles:

Handbook of MEMS for wireless and mobile applications
(ISBN 978-0-85709-271-7)

MEMS for automotive and aerospace applications
(ISBN 978-0-85709-118-5)

Smart sensors and MEMS
(ISBN 978-0-85709-502-2)

Details of these books and a complete list of titles from Woodhead Publishing can be obtained by:

- visiting our web site at www.woodheadpublishing.com
- contacting Customer Services (e-mail: sales@woodheadpublishing.com; fax: +44 (0) 1223 832819; tel.: +44 (0) 1223 499140 ext. 130; address: Woodhead Publishing Limited, 80, High Street, Sawston, Cambridge CB22 3HJ, UK)
- in North America, contacting our US office (e-mail: usmarketing@woodheadpublishing.com; tel.: (215) 928 9112; address: Woodhead Publishing, 1518 Walnut Street, Suite 1100, Philadelphia, PA 19102-3406, USA)

If you would like e-versions of our content, please visit our online platform: www.woodheadpublishingonline.com. Please recommend it to your librarian so that everyone in your institution can benefit from the wealth of content on the site.

We are always happy to receive suggestions for new books from potential editors. To enquire about contributing to our Electronic and Optical series, please send your name, contact address and details of the topic/s you are interested in to laura.pugh@woodheadpublishing.com. We look forward to hearing from you.

The team responsible for publishing this book:

Commissioning Editor: Laura Pugh
Publications Coordinator: Adam Davies
Project Editor: Anneka Hess
Editorial and Production Manager: Mary Campbell
Production Editor: Mandy Kingsmill
Project Manager: Newgen Knowledge Works Pvt Ltd
Copyeditor: Newgen Knowledge Works Pvt Ltd
Proofreader: Newgen Knowledge Works Pvt Ltd
Cover Designer: Terry Callanan

© Woodhead Publishing Limited, 2013

Woodhead Publishing Series in Electronic and Optical Materials:
Number 38

Semiconductor gas sensors

Edited by
Raivo Jaaniso and
Ooi Kiang Tan

Oxford Cambridge Philadelphia New Delhi

© Woodhead Publishing Limited, 2013

Published by Woodhead Publishing Limited,
80 High Street, Sawston, Cambridge CB22 3HJ, UK
www.woodheadpublishing.com
www.woodheadpublishingonline.com

Woodhead Publishing, 1518 Walnut Street, Suite 1100, Philadelphia,
PA 19102-3406, USA

Woodhead Publishing India Private Limited, 303 Vardaan House, 7/28 Ansari Road,
Daryaganj, New Delhi - 110002, India
www.woodheadpublishingindia.com

First published 2013, Woodhead Publishing Limited
© Woodhead Publishing Limited, 2013. The publisher has made every effort to ensure that permission for copyright material has been obtained by authors wishing to use such material. The authors and the publisher will be glad to hear from any copyright holder it has not been possible to contact.
The authors have asserted their moral rights.

This book contains information obtained from authentic and highly regarded sources. Reprinted material is quoted with permission, and sources are indicated. Reasonable efforts have been made to publish reliable data and information, but the authors and the publisher cannot assume responsibility for the validity of all materials. Neither the authors nor the publisher, nor anyone else associated with this publication, shall be liable for any loss, damage or liability directly or indirectly caused or alleged to be caused by this book.

Neither this book nor any part may be reproduced or transmitted in any form or by any means, electronic or mechanical, including photocopying, microfilming and recording, or by any information storage or retrieval system, without permission in writing from Woodhead Publishing Limited.

The consent of Woodhead Publishing Limited does not extend to copying for general distribution, for promotion, for creating new works, or for resale. Specific permission must be obtained in writing from Woodhead Publishing Limited for such copying.

Trademark notice: Product or corporate names may be trademarks or registered trademarks, and are used only for identification and explanation, without intent to infringe.

British Library Cataloguing in Publication Data
A catalogue record for this book is available from the British Library.

Library of Congress Control Number: 2013942858

ISBN 978-0-85709-236-6 (print)
ISBN 978-0-85709-866-5 (online)
ISSN 2050-1501 Woodhead Publishing Series in Electronic and Optical Materials (print)
ISSN 2050-151X Woodhead Publishing Series in Electronic and Optical Materials (online)

The publisher's policy is to use permanent paper from mills that operate a sustainable forestry policy, and which has been manufactured from pulp which is processed using acid-free and elemental chlorine-free practices. Furthermore, the publisher ensures that the text paper and cover board used have met acceptable environmental accreditation standards.

Typeset by Newgen Knowledge Works Pvt Ltd, India
Printed by Lightning Source

© Woodhead Publishing Limited, 2013

Contents

Contributor contact details *xi*
Woodhead Publishing Series in Electronic and Optical Materials *xv*

Part I Introduction 1

1 Fundamentals of semiconductor gas sensors 3
N. Yamazoe and K. Shimanoe, Kyushu University, Japan

1.1 Introduction 3
1.2 Classification of semiconductor gas sensors 4
1.3 Resistor type sensors: empirical aspects 5
1.4 Resistor type sensors: theoretical aspects 13
1.5 Non-resistive sensors 23
1.6 Future trends 31
1.7 References 33

2 Conduction mechanism in semiconducting metal oxide sensing films: impact on transduction 35
N. Bârsan, M. Huebner and U. Weimar, University of Tübingen, Germany

2.1 Introduction 35
2.2 General discussion about sensing with semiconducting metal oxide gas sensors 36
2.3 Sensing and transduction for *p*- and *n*-type semiconducting metal oxides 42
2.4 Investigation of the conduction mechanism in semiconducting metal oxide sensing layers: studies in working conditions 51
2.5 Conclusion and future trends 61
2.6 References 61

© Woodhead Publishing Limited, 2013

3 Electrode materials and electrode-oxide interfaces in semiconductor gas sensors 64
S. P. Lee, Kyungnam University, Korea

3.1 Introduction 64
3.2 Electrode materials for semiconductor gas sensors 65
3.3 Electrode-oxide semiconductor interfaces 80
3.4 Charge carrier transport in the electrode-oxide semiconductor interfaces 89
3.5 Gas/solid interactions in the electrode-oxide semiconductor interfaces 103
3.6 Conclusion 109
3.7 References 109

Part II Advanced sensing methods and structures 115

4 Recent trends in silicon carbide (SiC) and graphene-based gas sensors 117
M. Andersson, A. Lloyd Spetz and R. Pearce, Linköping University, Sweden

4.1 Introduction 117
4.2 Background: transduction and sensing mechanisms 119
4.3 Recent material developments for improved selectivity of SiC gas sensors 130
4.4 Dynamic sensor operation 134
4.5 Novel SiC and graphene-based sensor devices 137
4.6 Conclusion 148
4.7 References 150

5 Recent advances in wide bandgap semiconductor-based gas sensors 159
F. Ren and S. J. Pearton, University of Florida, USA

5.1 Introduction 159
5.2 Gas sensing 160
5.3 Hydrogen sensing 167
5.4 GaN Schottky diode sensor 182
5.5 Nanostructured wide bandgap materials 188
5.6 Silicon carbide Schottky diode hydrogen sensor 199
5.7 Wireless sensor network development 201

© Woodhead Publishing Limited, 2013

5.8 Conclusion 205
5.9 Acknowledgments 206
5.10 References 207

6 Micromachined semiconductor gas sensors 220
D. Briand, Ecole Polytechnique Fédérale de Lausanne, Switzerland and J. Courbat, Innovative Sensor Technology IST AG, Switzerland

6.1 Introduction 220
6.2 A brief history of semiconductors as gas sensitive devices 221
6.3 Micro-hotplate concept and technologies 222
6.4 Micromachined metal-oxide gas sensors 230
6.5 Complementary metal-oxide semiconductor (CMOS)-compatible metal-oxide gas sensors 242
6.6 Micromachined field-effect gas sensors 247
6.7 Trends and perspectives 249
6.8 Conclusion 255
6.9 References 255

7 Semiconducting direct thermoelectric gas sensors 261
F. Rettig and R. Moos, University of Bayreuth, Germany

7.1 Introduction 261
7.2 Direct thermoelectric gas sensors 267
7.3 Conclusion and future trends 291
7.4 References 293

Part III Nanomaterials for gas sensing 297

8 One- and two-dimensional metal oxide nanostructures for chemical sensing 299
E. Comini, Brescia University, Italy

8.1 Introduction 299
8.2 Deposition techniques 300
8.3 Conductometric sensor 306
8.4 Transduction principles and related novel devices 307
8.5 Conclusion and future trends 310
8.6 References 310

© Woodhead Publishing Limited, 2013

9 Semiconductor quantum dots for photoluminescence-based gas sensing 316
Z. Zhao, M. A. Carpenter and M. A. Petrukhina, University at Albany-SUNY, USA

9.1 Introduction 316
9.2 Quantum dot synthesis, surface functionalization and polymer encapsulation 319
9.3 Quantum dots for sensing: dependence of detection limits and selectivity on surface-modifying ligands 329
9.4 Quantum dot–polymer system 338
9.5 Quantum dot–nanopore array system 343
9.6 Conclusion and future trends 348
9.7 Acknowledgments 349
9.8 References 349

10 Coated and functionalised single-walled carbon nanotubes (SWCNTs) as gas sensors 356
Y. Battie, Université de Lorraine, France and O. Ducloux, ONERA, France

10.1 Introduction 356
10.2 Gas sensor architecture 358
10.3 Gas sensing mechanisms 364
10.4 Routes towards sensor selectivity 370
10.5 Applications 377
10.6 Conclusion 380
10.7 References 381

11 Carbon nanotube and metal oxide hybrid materials for gas sensing 386
T. Kerdcharoen, Mahidol University, Thailand and C.Wongchoosuk, Kasetsart University, Thailand

11.1 Introduction 386
11.2 Fabrication and synthesis of carbon nanotube–metal oxide sensing devices 389
11.3 Preparation of carbon nanotube–metal oxide sensing films 390
11.4 Sensor assembly 395
11.5 Characterization of carbon nanotube–metal oxide materials 396
11.6 Sensing mechanism of carbon nanotube–metal oxide gas sensors 401

© Woodhead Publishing Limited, 2013

11.7 Conclusion 403
11.8 References 403

12 Porous silicon gas sensors 408
V. M. Aroutiounian, Yerevan State University, Armenia

12.1 Introduction 408
12.2 Conductivity and capacitance sensors 409
12.3 Luminescence from PSi 411
12.4 Optical and photo properties of PSi sensors 414
12.5 PSi noise sensors 417
12.6 Different PSi gas sensors 422
12.7 Conclusion 424
12.8 References 425

Part IV Applications of semiconductor gas sensors 431

13 Metal oxide semiconductor gas sensors in environmental monitoring 433
R. Binions, Queen Mary, University of London, UK and A. J. T. Naik, University College London, UK

13.1 Introduction 433
13.2 Sensor synthesis methods 436
13.3 Metal oxide semiconductors in detecting environmentally important gases 442
13.4 Advances in carbon monoxide sensors 446
13.5 Advances in carbon dioxide sensors 448
13.6 Advances in nitrogen oxides sensors 452
13.7 Future trends 456
13.8 Conclusion 460
13.9 Sources of further information and advice 460
13.10 References 461

14 Semiconductor gas sensors for chemical warfare agents 467
D.-D. Lee and J.-C. Kim, Kyungpook National University, Korea

14.1 Introduction 467
14.2 Chemical warfare agents 468
14.3 Chemical warfare agent detecting techniques 471

© Woodhead Publishing Limited, 2013

14.4 Device preparation 473
14.5 Sensing properties 479
14.6 Conclusion 488
14.7 References 488

15 Integrated complementary metal oxide semiconductor-based sensors for gas and odour detection 491
P. K. Guha and S. Santra, Indian Institute of Technology, Kharagpur, India and J. W. Gardner, University of Warwick, UK

15.1 Introduction 491
15.2 Micro-resistive complementary metal oxide semiconductor gas sensors 492
15.3 Micro-calorimetric complementary metal oxide semiconductor gas sensor 495
15.4 Sensing materials and their deposition on complementary metal oxide semiconductor gas sensors 496
15.5 Interface circuitry and its integration 499
15.6 Integrated multi-sensor and sensor array systems 504
15.7 Conclusion and future trends 506
15.8 Useful web addresses 507
15.9 References 507

16 Solid-state sensors for carbon dioxide detection 510
G. G. Mandayo, CEIT-IK4 and Tecnun, Spain and J. Herrán, CIDETEC-IK4, Spain

16.1 Introduction 510
16.2 Electrochemical sensors 513
16.3 Impedimetric, capacitive and resistive sensors 520
16.4 Field effect transistor sensors 527
16.5 New approaches to enhance sensor performance 528
16.6 Conclusion and future trends 531
16.7 References 531

Index *537*

© Woodhead Publishing Limited, 2013

Contributor contact details

(* = main contact)

Editors

R. Jaaniso
Institute of Physics
University of Tartu
Tartu 51014
Estonia

E-mail: raivo.jaaniso@ut.ee

O. K. Tan
School of Electrical & Electronic Engineering
Nanyang Technological University
S1-B1a-06, 50 Nanyang Avenue
Singapore 639798

E-mail: EOKTAN@ntu.edu.sg

Chapter 1

N. Yamazoe* and K. Shimanoe
Faculty of Engineering Sciences
Kyusyu University
Japan
6–1 Kasuga-koen
Kasuga
Fukuoka 816–8580
Japan

Email: noboru.yamazoe.510@m.kyushu-u.ac.jp; shimanoe.kengo.695@m.kyushu-u.ac.jp

Chapter 2

N. Bârsan*, M. Huebner and U. Weimar
Faculty of Science
Institute of Physical Chemistry
University of Tübingen
Auf der Morgenstelle 15
72076 Tuebingen
Germany

E-mail: nb@ipc.uni-tuebingen.de

Chapter 3

S. P. Lee
Department of Electronic Engineering
Kyungnam University
449 Wolyong dong
Masanhappogu
Changwon
Kyungnam 631–701
Republic of Korea

E-mail: sensors@kyungnam.ac.kr

Chapter 4

M. Andersson and A. Lloyd Spetz*
Division of Applied Sensor Science
Department of Physics, Chemistry and Biology
Linköping University
SE-581 83

© Woodhead Publishing Limited, 2013

Linköping
Sweden

E-mail: mikan@ifm.liu.se; spetz@ifm.liu.se

R. Pearce
National Physical Laboratory
Hampton Road
Teddington
Middlesex
TW11 0LW
United Kingdom

E-mail: ruth.pearce@npl.co.uk

Chapter 5

F. Ren and S. J. Pearton*
Department of Chemical Engineering
University of Florida
Gainesville
FL 32611
USA

Email: ren@che.ufl.edu; spear@mse.ufl.edu

Chapter 6

D. Briand*
Ecole Polytechnique Fédérale de Lausanne (EPFL)
Institute of Microengineering (IMT)
Sensors, Actuators and Microsystems Laboratory (SAMLAB)
Maladière 71b 2000 Neuchâtel
Switzerland

E-mail: danick.briand@epfl.ch

J. Courbat
Innovative Sensor Technology IST AG
Stegrütistrasse 14
CH-9642 Ebnat-Kappel
Switzerland

E-mail: jerome.courbat@ist-ag.com

Chapter 7

F. Rettig and R. Moos*
University of Bayreuth
Department of Functional Materials
95440 Bayreuth
Germany

E-mail: Functional.Materials@Uni-Bayreuth.de

Chapter 8

E. Comini
SENSOR
Department of Information Engineering
Brescia University and CNR-IDASC
via valotti 9
25133 Brescia
Italy

E-mail: comini@ing.unibs.it

Chapter 9

Z. Zhao and M. A. Carpenter*
College of Nanoscale Science and Engineering
University at Albany – State University of New York
257 Fuller Road
Albany

© Woodhead Publishing Limited, 2013

NY 12203
USA

E-mail: mcarpenter@albany.edu; zzhao@albany.edu

M. A. Petrukhina
Department of Chemistry
University at Albany – State University of New York
1400 Washington Avenue
Albany
NY 12222
USA

E-mail: mpetrukhina@albany.edu

Chapter 10

Y. Battie*
LCP-A2MC (EA4632)
Université de Lorraine
1 Boulevard Dominique François Arago
57070 Metz Technopôle
France

E-mail: yann.battie@univ-lorraine.fr

O. Ducloux
ONERA
29 Avenue de la division Leclerc
92322 Chatillon
France

E-mail: Olivier.ducloux@onera.fr

Chapter 11

T. Kerdcharoen*
Department of Physics
Faculty of Science
Mahidol University
272 Rama 6 Road
Ratchathewi
Bangkok 10400
Thailand

and

NANOTEC Center of Excellence at Mahidol University
National Nanotechnology Center
Thailand

E-mail: sctkc@mahidol.ac.th

C. Wongchoosuk
Department of Physics
Faculty of Science
Kasetsart University
50 Phahon Yothin Road
Chatuchak
Bangkok 10900
Thailand

E-mail: chatchawal.w@ku.ac.th

Chapter 12

V. M. Aroutiounian
Department of Physics of Semiconductors and Microelectronics
Yerevan State University
1 Alex Manoukian
Yerevan 0025
Armenia

E-mail: aroutiounv1@yahoo.com

Chapter 13

R. Binions*
School of Engineering and Materials Science
Queen Mary, University of London
Mile End Road
London
E1 4NS
United Kingdom

E-mail: r.binions@qmul.ac.uk

© Woodhead Publishing Limited, 2013

A. J. T. Naik
Department of Chemistry
University College London
Christopher Ingold Laboratories
20 Gordon Street
London
WC1H 0AJ
United Kingdom

E-mail: a.naik@ucl.ac.uk

Chapter 14

D.-D. Lee*
School of Electronics Engineering
Kyungpook National University
Daegu 702–701
Korea

E-mail: ddlee@ee.knu.ac.kr

J.-C. Kim
Department of Chemical Engineering
Kyungpook National University
Daegu 702–701
Korea

E-mail: kjchang@knu.ac.kr

Chapter 15

P. K. Guha*
Electronics and Electrical Communication Engineering Department
Indian Institute of Technology
Kharagpur
India-721302

E-mail: pkguha@ece.iitkgp.ernet.in

S. Santra
Physics and Meteorology Department
Indian Institute of Technology
Kharagpur
India-721302

E-mail: sumita.santra@gmail.com

J. W. Gardner
Microsensors and Bioelectronics Laboratory
School of Engineering
University of Warwick
Coventry CV4 7AL
UK

E-mail: J.W.Gardner@warwick.ac.uk

Chapter 16

G. G. Mandayo*
CEIT and Tecnun
University of Navarra
P. Manuel Lardizabal 15
20018 San Sebastian
Spain

E-mail: ggmandayo@ceit.es; ggmandayo@tecnun.es

J. Herrán
CIDETEC-IK4
Pº Miramón 196
2009 San Sebastian
Spain

E-mail: jherran@cidetec.es

© Woodhead Publishing Limited, 2013

Woodhead Publishing Series in Electronic and Optical Materials

1 **Circuit analysis**
J. E. Whitehouse
2 **Signal processing in electronic communications: For engineers and mathematicians**
M. J. Chapman, D. P. Goodall and N. C. Steele
3 **Pattern recognition and image processing**
D. Luo
4 **Digital filters and signal processing in electronic engineering: Theory, applications, architecture, code**
S. M. Bozic and R. J. Chance
5 **Cable engineering for local area networks**
B. J. Elliott
6 **Designing a structured cabling system to ISO 11801: Cross-referenced to European CENELEC and American Standards**
Second edition
B. J. Elliott
7 **Microscopy techniques for materials science**
A. Clarke and C. Eberhardt
8 **Materials for energy conversion devices**
Edited by C. C. Sorrell, J. Nowotny and S. Sugihara
9 **Digital image processing: Mathematical and computational methods**
Second edition
J. M. Blackledge
10 **Nanolithography and patterning techniques in microelectronics**
Edited by D. Bucknall
11 **Digital signal processing: Mathematical and computational methods, software development and applications**
Second edition
J. M. Blackledge
12 **Handbook of advanced dielectric, piezoelectric and ferroelectric materials: Synthesis, properties and applications**
Edited by Z.-G. Ye

© Woodhead Publishing Limited, 2013

13 **Materials for fuel cells**
Edited by M. Gasik
14 **Solid-state hydrogen storage: Materials and chemistry**
Edited by G. Walker
15 **Laser cooling of solids**
S. V. Petrushkin and V. V. Samartsev
16 **Polymer electrolytes: Fundamentals and applications**
Edited by C. A. C. Sequeira and D. A. F. Santos
17 **Advanced piezoelectric materials: Science and technology**
Edited by K. Uchino
18 **Optical switches: Materials and design**
Edited by S. J. Chua and B. Li
19 **Advanced adhesives in electronics: Materials, properties and applications**
Edited by M. O. Alam and C. Bailey
20 **Thin film growth: Physics, materials science and applications**
Edited by Z. Cao
21 **Electromigration in thin films and electronic devices: Materials and reliability**
Edited by C.-U. Kim
22 ***In situ* characterization of thin film growth**
Edited by G. Koster and G. Rijnders
23 **Silicon-germanium (SiGe) nanostructures: Production, properties and applications in electronics**
Edited by Y. Shiraki and N. Usami
24 **High-temperature superconductors**
Edited by X. G. Qiu
25 **Introduction to the physics of nanoelectronics**
S. G. Tan and M. B. A. Jalil
26 **Printed films: Materials science and applications in sensors, electronics and photonics**
Edited by M. Prudenziati and J. Hormadaly
27 **Laser growth and processing of photonic devices**
Edited by N. A. Vainos
28 **Quantum optics with semiconductor nanostructures**
Edited by F. Jahnke
29 **Ultrasonic transducers: Materials and design for sensors, actuators and medical applications**
Edited by K. Nakamura
30 **Waste electrical and electronic equipment (WEEE) handbook**
Edited by V. Goodship and A. Stevels
31 **Applications of ATILA FEM software to smart materials: Case studies in designing devices**
Edited by K. Uchino and J.-C. Debus

© Woodhead Publishing Limited, 2013

32 **MEMS for automotive and aerospace applications**
Edited by M. Kraft and N. M. White
33 **Semiconductor lasers: Fundamentals and applications**
Edited by A. Baranov and E. Tournie
34 **Handbook of terahertz technology for imaging, sensing and communications**
Edited by D. Saeedkia
35 **Handbook of solid-state lasers: Materials, systems and applications**
Edited by B. Denker and E. Shklovsky
36 **Organic light-emitting diodes: Materials, devices and applications**
Edited by A. Buckley
37 **Lasers for medical applications: Diagnostics, therapy and surgery**
Edited by H. Jelínková
38 **Semiconductor gas sensors**
Edited by R. Jaaniso and O. K. Tan
39 **Handbook of organic materials for optical and optoelectronic devices: Properties and applications**
Edited by O. Ostroverkhova
40 **Metallic films for electronic, optical and magnetic applications: Structure, processing and properties**
Edited by K. Barmak and K. Coffey
41 **Handbook of laser welding technologies**
Edited by S. Katayama
42 **Nanolithography: The art of fabricating nanoelectronics, nanophotonics and nanobiology devices and systems**
Edited by M. Feldman
43 **Laser spectroscopy for sensing: Fundamentals, techniques and applications**
Edited by M. Baudelet
44 **Chalcogenide glasses: Preparation, properties and applications**
Edited by J.-L. Adam and X. Zhang
45 **Handbook of MEMS for wireless and mobile applications**
Edited by D. Uttamchandani
46 **Subsea optics and imaging**
Edited by J. Watson and O. Zielinski
47 **Carbon nanotubes and graphene for photonic applications**
Edited by S. Yamashita, Y. Saito and J. H. Choi
48 **Optical biomimetics: Materials and applications**
Edited by M. Large
49 **Optical thin films and coatings**
Edited by A. Piegari and F. Flory
50 **Computer design of diffractive optics**
Edited by V. A. Soifer

© Woodhead Publishing Limited, 2013

51 **Smart sensors and MEMS: Intelligent devices and microsystems for industrial applications**
Edited by S. Nihtianov and A. L. Estepa
52 **Fundamentals of femtosecond optics**
S. A. Kozlov and V. V. Samartsev
53 **Nanostructured semiconductor oxides for the next generation of electronics and functional devices: Properties and applications**
S. Zhuiykov

© Woodhead Publishing Limited, 2013

1

Fundamentals of semiconductor gas sensors

N. YAMAZOE and K. SHIMANOE,
Kyushu University, Japan

DOI: 10.1533/9780857098665.1.3

Abstract: As an introduction to this book, a variety of semiconductor gas sensors is presented. They are classified into five types, according to the transducers used: resistor, diode, MIS (metal-insulator-semiconductor) capacitor, MIS FET (metal-insulator-semiconductor field effect transistor) and oxygen concentration cell. The structure, working principle and sensing mechanism are described for each type. As the only type successfully on the market at present, the resistor is allotted considerably more space than the alternative semiconductor gas sensors, with experimental knowledge and the theory of gas response described in detail. The receptor function of metal oxides recently found in resistors is also of critical importance in other types incorporating the same oxides; the contact potential generated between oxide and metal is likely a main origin of the gas response of those devices. Finally, observations on the prospects for and problems with semiconductor gas sensors are made.

Key words: gas sensor, semiconductive oxide, field effect transistor (FET), depletion layer, contact potential, grain size effect.

1.1 Introduction

Semiconductor gas sensors using metal oxides such as SnO_2 were pioneered by two research groups in Japan.[1,2] These sensors were soon put on the market as gas leak alarms and proved to be indispensable in keeping people safe from the distressing circumstances resulting from gas leaks. At the same time, their success had worldwide impact on researchers, creating awareness of the importance of gas sensors, or chemical sensors more generally. Great effort has subsequently been made in the development of new gas sensors, including those using silicon semiconductor devices and solid electrolytes devices. If the definition of a semiconductor gas sensor is a sensor into which a semiconductor material is incorporated, there is a variety of semiconductor gas sensors of varying structures, made of different materials and involving various working principles.

© Woodhead Publishing Limited, 2013

This introduction describes the fundamental aspects of the various semiconductor gas sensors that have been developed so far, or that are proposed. First, they are classified into five types, based on the constitutional principle of sensor devices (Section 1.2). The structure of devices, their working principles and sensing mechanisms are described in subsequent sections. However, the greatest space is devoted to describing experimental knowledge and the theory of gas response of the sensors based on resistors, which have been made full use of and which still have potential for further development. It has long been queried why sensors of this type are promoted with regard to their sensitivity, as the constituent oxides are smaller than in other types of device,[3] though a semiempirical analysis has been attempted.[4, 5] This issue was recently resolved by developing a new theory on the receptor function of small-sized oxides.[6, 7] As revealed in the new theory, small semiconductors are depleted of electrons in two stages by a process of ionosorption of oxygen or oxidizing gases, resulting in the appearance of regional depletion followed by volume depletion. Gas response can be sufficiently understood based on the same theory. It is shown that the theory gives an important clue to understanding the gas response of oxides attached to potentiometric gas sensors (Section 1.5). The chapter closes with personal observations regarding semiconductor gas sensors (Section 1.6).

1.2 Classification of semiconductor gas sensors

Generally speaking, a gas sensor is composed of a receptor and a transducer, as illustrated in Fig. 1.1. The former is provided with a material or a materials system which, on interacting with a target gas, either induces a change in its own properties (work function, dielectric constant, electrode potential, mass, etc.), or emits heat or light. The transducer is a device to transform such an effect into an electrical signal (sensor response). The construction of a sensor is determined by the transducer used, with the receptor appearing to be implanted within it. From this perspective, a semiconductor gas sensor can be defined as a sensor in which a semiconductor material is used as a receptor and/or transducer.

There are two groups of semiconductors: oxide and non-oxide (typically, silicon). Non-oxide semiconductors cannot work as a receptor because they are coated with a protective insulation layer, but they can provide a transducer in the form of MIS FETs and MIS capacitors. In contrast, oxide semiconductors can work as both a receptor and a transducer (mostly in the form of a resistor) owing to their chemical and physical stability in hostile environments at elevated temperatures.

Table 1.1 shows various examples of semiconductor gas sensors classified according to the types of transducer used, and sub-classified by the kinds of receptor used, together with the kinds of signal output (response), typical sensor devices and the gases targeted. The transducers are seen to be available in

© Woodhead Publishing Limited, 2013

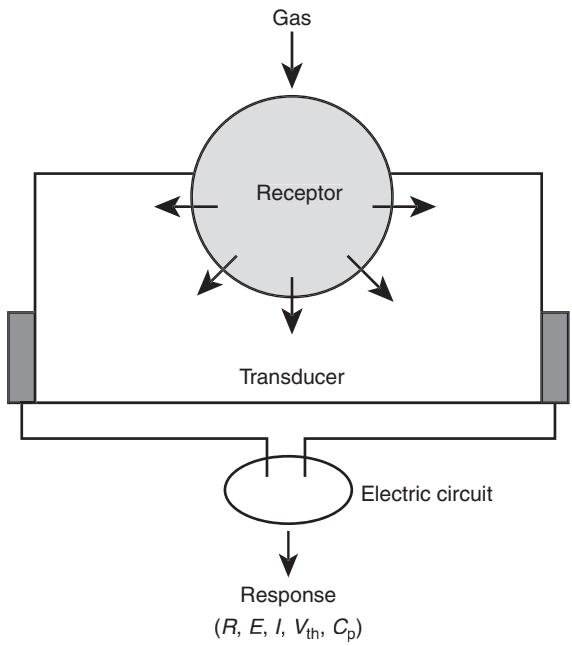

1.1 Gas sensor as constituted of a receptor and a transducer. R = resistance, E = electromotive force, I = current, V_{th} = threshold voltage (FET), C_p = capacitance.

the forms of resistors, diodes, MIS capacitors, MIS FETs or oxygen concentration cells. For each type of sensor thus classified, devices, sensing principles and the important features of semiconductor gas sensors are now described.

1.3 Resistor type sensors: empirical aspects

Of the various types of sensor, resistor sensors have received the greatest investigation and have proven their feasibility in practice. These sensors are often called 'oxide semiconductor gas sensors'. There are two subtypes: surface sensitive and bulk sensitive. This section is devoted to surface sensitive resistor sensors, except for Section 1.3.3 which briefly discusses bulk sensitive resistor sensors. It is noted that books and review articles have been published about oxide semiconductor gas sensors.[8–10]

1.3.1 Sensing materials and devices

Sensing materials

A surface sensitive resistor sensor works on a very simple principle; on exposure to a target gas in air at an elevated temperature, its resistance either

© Woodhead Publishing Limited, 2013

Table 1.1 Classification of semiconductor gas sensors according to the types of transducers and receptors used

Transducer	Response signal	Receptor	Device (example)	Target
Resistor	Resistance	Oxides	Porous SnO_2 (surface sensitive)	A variety of gases
			Sintered TiO_2 (bulk sensitive)	Air/fuel ratio (car engine)
Diode	Bias current	Oxides	Pd-TiO_2 (single crystal)	H_2
MIS capacitor	Bias potential shift	Pd	Pd-gate capacitor	H_2, NH_3
MIS FET	Threshold voltage shift	Pd	Pd-gate FET	H_2, NH_3
		Ionic conductors	Proton conductor gate FET	H_2
			$NaNO_2$-gate FET	NO_2
		Oxides	WO_3-gate FET	NO_2
		Dielectrics	Cellulose-gate FET	Humidity
Oxygen concentration cell	Cell voltage	Oxides	Pt/zirconia/oxide/Pt	A variety of gases

Note: 'Oxides' stands for semiconductive metal oxides.

decreases or increases as a function of the partial pressure of the gas. Of the many metal oxides, *n*-type oxides (such as SnO_2, In_2O_3, WO_3, ZnO and γ-Fe_2O_3) and *p*-type oxides (such as CuO and Co_3O_4) exhibit significant gas sensing properties. Mainly due to stability issues, however, SnO_2, In_2O_3, WO_3 have been adopted as the sensor materials utilized in practice. In practice, even these oxides are frequently loaded or mixed empirically with several foreign materials as a sensitizer (PdO, Pt, Fe_2O_3, etc), a skeleton material (alumina), or a binder (silica).

When an *n*-type oxide is used, resistance decreases on exposure to inflammable or reducing gases in the air (inorganic: H_2, CO, NH_3, H_2S, NO, etc; organic: CH_4, propane, alcohols, odorants, etc.), while it increases on exposure to oxidative gases (NO_2, ozone, N_2O, etc.). Apart from such redox-active gases, CO_2 and water vapor have been known to affect the resistance to a greater or lesser degree. Exploitation of the effects of CO_2 has led to the development of a semiconductor CO_2 sensor.[11]

© Woodhead Publishing Limited, 2013

Sensitizers

Gas sensing properties, especially gas responses, are known to be often improved significantly when constituent oxides are loaded with small amounts of appropriately chosen foreign materials. Examples are: SnO_2-PdO (CO, propane, etc.), SnO_2-Pt and/or PdO (methane), SnO_2-Co_3O_4 (CO), SnO_2-CuO (H_2S), SnO_2-Ag_2O (H_2), In_2O_3-PdO (CO, odorant gases), WO_3-Au (NH_3), SnO_2-La_2O_3-Pt (ethanol), SnO_2-CaO (ethanol), In_2O_3-Fe_2O_3 (ozone), SnO_2-Fe_2O_3 (NO_2), TiO_2-Cr_2O_3 (NO), etc. In this list, the materials following the oxide semiconductors are sensitizers and the target gases are shown in parentheses. As suggested from the large variation in sensitizers, the mechanisms of sensitization involved are not so simple.

It is useful to know that the dispersion of the sensitizers, except Pt, always causes the resistances of the device in base air to increase. This suggests that those interact with the oxides and increase the work function of the oxides. In view of heterogeneous catalysis, Pt, PdO, CuO, Ag_2O, Co_3O_4 and Au are well-known oxidation catalysts to reducing gases. Therefore, such catalytic activity is relevant to the sensitizing actions. It should be noted, however, that the mere promotion of oxidation reactions cannot contribute to gas response unless it has something to do with the surface properties of the oxides. In this sense, the sensitizers, except Pt, undergo redox changes such as $PdO + H_2 \rightarrow Pd + H_2O$, $Pd + (1/2)\ O_2 \rightarrow PdO$, and the changes of their redox state upon exposure to target gases can possibly induce changes in device resistance (gas response) through electronic interactions with oxides (electronic sensitization). In the case of Pt, on the other hand, it seems that the target gas (methane) is partially oxidized on Pt to HCHO or CO, which then reacts with the adsorbed oxygen of the oxide (chemical sensitization).

La_2O_3 and CaO, which have no such catalytic oxidation activity, modify the acid-base properties of the oxide surface more basic; on the acidic surface, ethanol undergoes dehydration (no consumption of O^-), $C_2H_5OH \rightarrow C_2H_4 + H_2O$; on the basic surface it undergoes oxidative dehydrogenation, $C_2H_5OH + 2\ O^- \rightarrow C_2H_4O + H_2O$. It is thus understood that, in this case, the selectivity of reaction paths is changed by the sensitizers. As shown above, Fe_2O_3 promotes response to oxidizing gases, though the mechanism of promotion is not yet clear.

There can be no doubt that sensitizers are very important for practical devices. Unfortunately, however, little basic research has been carried out on sensitizers and sensitizing actions.

Device structure

Sensor devices are fabricated into a resistor in which a porous stack of the sensing materials is attached with a heater and a resistance measuring probe (usually a pair of metal electrodes). Various structures have been devised

© Woodhead Publishing Limited, 2013

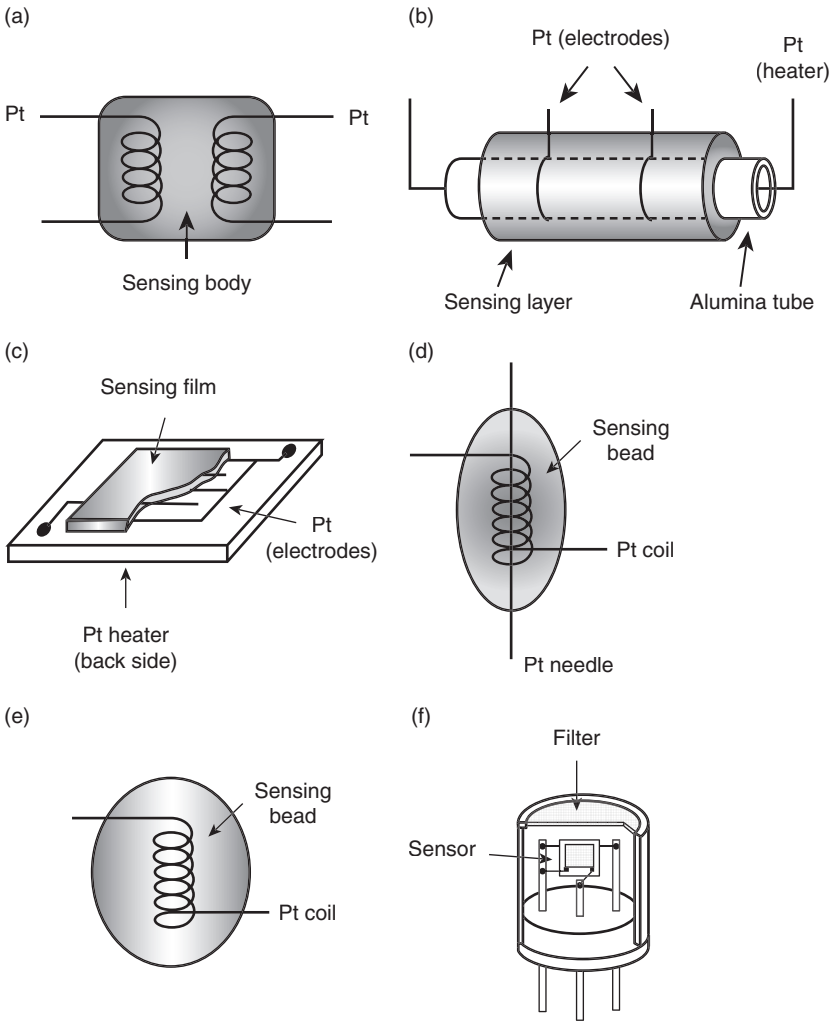

1.2 Device structures adopted for resistor type sensors in practice. (a) Sintered block, (b) thin alumina tube-coated layer, (c) screen printed thick film, (d) small bead inserted with coil and needle electrodes, (e) small bead inserted with a single coil (heater and electrode), (f) practical sensor element assembling sensor device, metal cap and filter.

in practice, as shown in Fig. 1.2. Originally fabrication was a sintered block structure (about 0.5 cm in size) with a pair of Pt coil electrodes inserted (a); one of the coils also served as a heater. This was followed by a thin alumina tube within a heavy coating (b); a pair of wire electrodes was wound on the tube and a heater was set inside it. Currently in wide use is a thick film

© Woodhead Publishing Limited, 2013

structure (c), screen-printed on an alumina substrate with a pair of electrodes and a heater printed in advance. A micro version of this structure, known as a MEMS (micro electro-mechanical system) sensor, is currently under development, as will be described later. Apart from these standard structures, bead-shaped structures have been devised for practical use. A small bead made of sensing materials (about 0.5 mm in size) is inserted with a coil and needle electrodes in (d); the coil also works as a heater. A similar bead is inserted with a single coil (heater) in (e), the so-called 'hot wire' type; a change in the resistance of the sensing materials affects the composite resistance between the two terminals of the inserted coil, which is measured precisely on a bridge circuit as gas response.

For actual use, each device is bonded to the connector pins and put inside a metal cap with a hole(s) on top, in order to remove the risk of triggering gas explosions. In addition, an adsorbent such as active carbon (often referred to as a 'filter') is placed in a layer immediately behind the hole in order to remove unpleasant gases, as shown in (f).

Fabrication

Important guidelines for device fabrication collected empirically can be summarized as follows:

1. Crystallite sizes of oxide semiconductors should be as small as possible.
2. Sensitizers should be dispersed as finely as possible.
3. Sensing layer thickness and porosity should also be optimized to improve selectivity and durability.

According to these guidelines, fabrication of devices is carried out carefully. It starts with the preparation of a fine powder of oxide semiconductor (crystallite size around 10 nm in diameter) through what is known as a 'wet' process. This is the precipitation of a precursor of the oxide from an aqueous solution of its metal salt(s), followed by the gentle washing, drying and calcination of the precursor prior to its conversion to the final powder. The powder is loaded with a small amount of a sensitizer and then converted into slurry (paste) by milling it using water or organic vehicles, together with any other necessary additives. The slurry is finally deposited over the electrodes (block or bead type), or on the substrate (thick film type), and, after drying, the deposit is sintered under specific conditions to stabilize the porous microstructure.

It is noted that all of the semiconductor gas sensors so far in use are of the thick film (or layer) type, prepared through the wet processes discussed above. Thin film type devices, especially those fabricated via physical methods such as sputtering, have frequently shown interesting sensing performances in the short term, but little use is currently made of these devices.

© Woodhead Publishing Limited, 2013

1.3.2 Gas sensing characteristics

Response and response transients

The behavior of resistance on switching between base air and gas ambient is illustrated in Fig. 1.3(a). On switching to an inflammable gas ambient, the resistance reduces from a value in air (R_a) to a stationary value (R_g), while it goes back to R_a on switching back. Empirically, gas response is defined as the ratio, R_a/R_g (normalized conductance). The rate of response or recovery is expressed empirically in terms of the time (τ) needed for a 90% full response or recovery. In the case of oxidizing gases like NO_2 which increase the resistance, gas response is defined as R_g/R_a (normalized resistance).

The dependence of R_g on the partial pressure of target gas (P_g) is known empirically to fall on linear correlations on logarithmic scales;[12] that is,

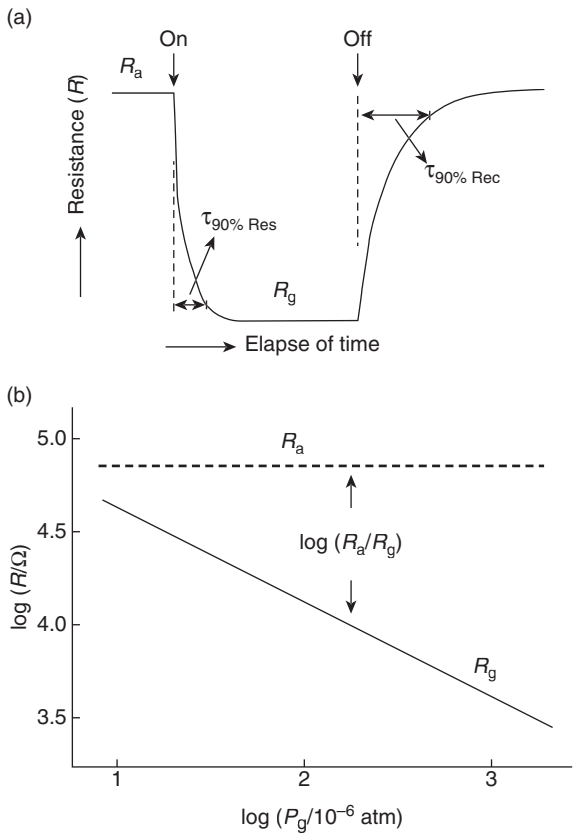

1.3 Response and recovery Transients. (a) On switching on and off an inflammable gas in air, (b) linear correlation observed between resistance (R_g) and partial pressure of the gas (P_g) on logarithmic scales (power law).

© Woodhead Publishing Limited, 2013

$R_g = cP_g^{\alpha}$ where α and c are constants (power law), as shown in Fig. 1.3(b). Accordingly, gas response also follows power law, $R_a/R_g = cP_g^{\alpha}$ (inflammable gases) or $R_g/R_a = cP_g^{\alpha}$ (oxidizing gases). The power index, α, is almost fixed depending on the kinds of target gas, taking values roughly equal to: 1/2 to many inflammable gases (H_2, CO, etc), 1 to NO_2 and 1/2 for O_3. It is noted that the resistance under exposure to varying partial pressure of oxygen (P_{O_2}) follows the power equation with $\alpha = 1/2$; namely, $R_{O_2} = c''' P_{O_2}^{1/2}$. The power indices are related to the modes of interaction between the gases and the surface of oxide semiconductors, as will be discussed later.

Sensitivity is usually defined as a slope of the correlation between gas response and P_g. In the event that power law holds well, however, this definition is meaningless since sensitivity is dependent on P_g unless α is unity. This difficulty is overcome if P_g is replaced by P_g^{α} in the above definition. The slope (sensitivity) is then nothing but the proportionality constant of the power equation. Sensitivity is determined by the physicochemical constants of semiconductor, target gas and oxygen.

Operating temperature

Response and response transients are sensitive to the operating temperature. The rates of response and recovery naturally increase with increasing temperature. On the other hand, response shows different behavior depending on whether the gas is inflammable or oxidizing. For an inflammable gas, response goes through a maximum on increasing temperature, resulting in a well-known bell-shaped correlation between the response and temperature. This dependence appears because the rate constant of the surface reaction between gas and adsorbed oxygen (k_R) increases exponentially with a rise in temperature, while the Knudsen diffusion coefficient of the gas (D_K) does so sublinearly. In the lower temperature region, $k_R < D_K$ is held so that k_R is an exclusive determinant for gas response. In higher temperatures, on the other hand, the relation is inversed, $k_R > D_K$, and the response is attenuated by the gas diffusion and reaction effect.[13, 14] In this temperature range, the gas is consumed significantly by diffusion from the surface to the inside of the porous sensing layer. The effective partial pressure of the gas in the inner region where the resistance is actually measured can be significantly lower than the nominal value outside. The ratio of the actual gas response to the ideal (free of attenuation) is known as the 'utility factor' (U). U remains unity in lower temperatures, while in higher temperatures it decreases rather sharply with increasing temperature, increasing diffusion length (sensing layer thickness) and decreasing pore size. It follows that the response maximum and the temperature at that point vary not only by the kinds of gas and oxide semiconductor, but also by the device structure (layer thickness, in particular) and the sensing materials adopted in processing.

© Woodhead Publishing Limited, 2013

Strictly speaking, there is a further possible reason for the decrease of gas response at high temperature: oxygen adsorption is decreased with increasing temperature. Therefore, if the partial pressure of the inflammable gas is too great, adsorbed oxygen is consumed (resistance reaches minimum) such that gas response will decrease with increasing temperature, reflecting the temperature dependence of the adsorbed oxygen. This discussion is valid for a small partial pressure of gas.

Oxidizing gases like NO_2, on the other hand, are adsorbed on the oxide semiconductor particles. The amount of adsorption, and therefore the gas response, increases as the temperature drops. Operating temperature is then determined as a compromise between gas response and rates of response and recovery.

Disturbances to gas response

Gas response reacts to disturbances to varying degrees. There are two kinds of disturbance: a drift of base air resistance (R_a) and a modulation of gas response (R_g) by coexistent gases. As for the former, R_a shifts downward quickly on increasing the partial pressure of coexistent water vapor (P_{H_2O}), a phenomenon known as a 'short-term effect of water vapor'. Apart from this phenomenon, P_{H_2O} seems to be related to a long-term drift of R_a; it is known that R_a undergoes seasonal changes; that is, it goes up in summer and goes down in winter. Unfortunately, these two types of drifts are yet to be clarified in detail. Practically, attempts have been made to correct the long-term drift partly by means of software.

The disturbance brought about by a modulation of gas response can be simplified if both the target gas and coexistent gas are inflammable, as in the case of sensing CO in the coexistence of H_2. The strength of the disturbance can be estimated if the sensitivity to each gas is known. To mitigate interferences by coexistent gases, nonstandard modes of sensor operation have been adopted in some cases for sensing CO and alcohol in the breath.

1.3.3 Semiconductor oxygen sensors

At sufficiently high temperatures, where the bulk diffusion of component ions oxides is activated to a significant degree, oxide semiconductors are known to change non-stoichiometry, and thus electronic conductivity changes depending on P_{O_2}. Upon exposure to a mixture of inflammable gas and air, sensors using such oxides change resistance depending on the composition of the mixture. What is responsible for the change in resistance is not the reducing gas itself but P_{O_2} in the ambient after the reducing gas has been oxidized completely. Resistor type oxygen sensors working on this principle have been proposed by using oxides such as TiO_2, Nb_2O_5 and

© Woodhead Publishing Limited, 2013

MgO-CoO. Among them, one using TiO_2 has been successfully incorporated into car engine exhaust control systems in practice. The sensor, fabricated into a well-sintered block of TiO_2 with a pair of electrodes inserted, is exposed to car engine exhausts at high temperature (e.g. 1073 K). Since the resistance decreases or increases stepwise as air/fuel (A/F) ratio crosses the border between lean burn and rich burn, it can be utilized for A/F ratio control. Its share in the market is somewhat small, however, compared with that of its competitor, zirconia oxygen sensors.

1.4 Resistor type sensors: theoretical aspects

For resistive type gas sensors, a porous assembly of fine particles (mostly grains) of oxide semiconductors should function as a receptor as well as a transducer. It has long been accepted that grains act as a receptor to gases, while the contacts between the grains act as the transducer which transforms the gas reception into a change in device resistance. However, an understanding of the receptor function and the transducer function involved had remained far from being satisfactory until basic approaches to them began very recently. This section focuses on recent advances in the basic (theoretical) approaches, though the studies are still in progress.

1.4.1 Receptor function and transducer function

Oxide semiconductors are known to exhibit unique interactions with some sorts of gases, resulting in the ionosorption of the gases. In the event that the gas in a problem situation has a large electron affinity, such as O_2 and NO_2, the host semiconductor supplies electrons to the gas to allow it to be adsorbed as anionic species such as O^-, O^{2-} or NO_2^-. In the event that the gas is low in ionization potential, like NO, on the other hand, the gas donates electrons to the semiconductor to be adsorbed as cationic species, such as NO^+. The electrons supplied or given up in these ionosorption processes are transferred from the bulk of the semiconductor to the surface, or vice versa, accompanied by a change in energy band structure (band bending) of the semiconductor. It is well-known that electron transfer from the bulk of *n*-type semiconductor results in the formation of an electron-depleted layer in the semiconductor. No doubt, an oxide semiconductor sensor, when placed in air, is subjected to the adsorption (ionosorption) of oxygen, and its resistance in air (air base) is determined usually from the equilibrium of oxygen adsorption. As very recently revealed with SnO_2 sensors, oxygen is adsorbed mainly in the form of O^{2-} in extremely dry air, whereas in the presence of low humidity (0.1% in volume and above) the adsorption in that form is suppressed almost completely by water vapor to be replaced by the adsorption in another form (O^-). In practice, it can thus be assumed

© Woodhead Publishing Limited, 2013

as a good approximation that the latter form (O^-) prevails over the former (O^{2-}) under usual sensor operating conditions. The sensor is utilized for detecting a target gas coexistent in air by means of a change in the resistance of the device. Target gases fall into two groups: gases which undergo ionosorption (such as NO_2) and inflammable gases (such as H_2, CO and C_3H_8). In cases where ionosorption takes place in addition to that of oxygen, the energy band structure changes accordingly. Usually, however, serious interference often occurs between the ionosorption of the gas and that of oxygen, reducing the resultant change in energy band structure. The key to designing a sensor sensitive to such a gas is discovering how to mitigate such interference. Inflammable gases react with the anionic adsorbates of oxygen. As a result of the reaction, electrons of the adsorbates are returned to the semiconductor, causing the energy band structure to revert to one that corresponds to smaller amounts of oxygen adsorbates. Obviously, response to a gas in this group will be enhanced as the consumption of the oxygen adsorbates is made more efficient.

Here, it is of central importance to show how the qualitative understanding mentioned above can be converted into more quantitative ones. For simplicity, let us assume that a sensor device is a porous stack of uniform grains of an *n*-type oxide semiconductor. It is accepted that each grain plays the role of a receptor, while that of the transducer is played by each contact between grains; that is the most resistive part in the device, so it determines the resistance of the whole device. However, further understanding has been less than straight forward. For some considerable time, efforts were made to understand the receptor and the transducer functions based on the surface space charge layer model and the double Schottky barrier model, as shown by (a) and (b) in Fig. 1.4, respectively. These models, (a) and (b), were guessed at by many researchers as analogies from a metal semiconductor contact diode (see, for instance, reference 9). It was assumed that the thickness of the depletion layer (w) should increase as oxygen adsorption as anionic species (typically O^-) increases, while it should decrease as the adsorbed oxygen is consumed with an inflammable gas (H_2). Correspondingly, the double Schottky barrier formed across the contact between grains should change its height, inducing changes in contact resistance and, hence, resistance in the device. Unfortunately, these models were unable to give quantitative information regarding gas response. Shortcomings of the models were made clear recently by our basic approaches, as described below.

The receptor model (a) assumes implicitly that the semiconductor grains are sufficiently large. In reality, however, they are very tiny (typically about 10 nm in diameter), so the space charge layer can easily extend over the entire area of grains; that is, w grows to grain radius (a), at P_{O_2} significantly below that in air, P_{O_2}(a). Obviously, a new process of electron depletion has to take place afterward until the grains reach electrostatic equilibrium with

© Woodhead Publishing Limited, 2013

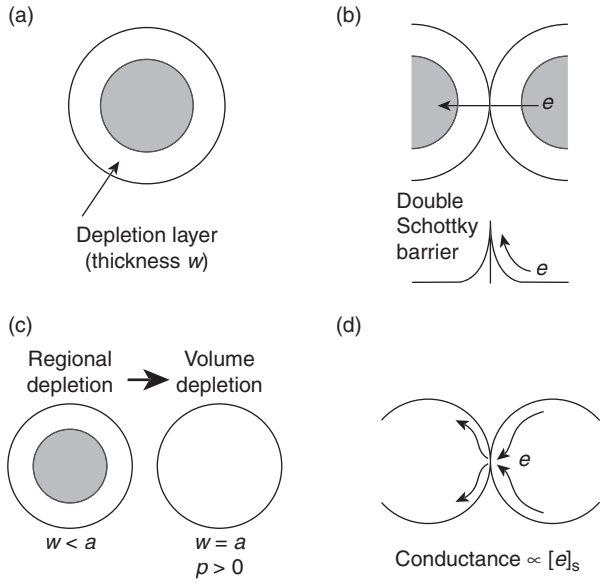

1.4 Diagrams of electron depletion for oxide grains and the resistance of contact between grains. (a) Space charge layer model, (b) double Schottky barrier model, (c) regional and volume depletion model, (d) surface conductive grains contact model.

oxygen adsorption at P_{O_2}(a). A method proposed here is one in which electron depletion is achieved by shifting the Fermi level downward by p kT, as shown in Fig. 1.5.[6,7] Here, p is the Fermi level shift as expressed in the unit of kT where kT is thermal energy. The electrons supplied to the adsorbates in this stage are squeezed out of the grains by increasing p. To distinguish the electron depletion of this type (accompanied by a change in p) from the conventional type one (accompanied by a change in w), these are denoted as volume depletion and regional depletion, respectively. The value of p or w is determined uniquely for given conditions of gas adsorption and semiconductor grains. Importantly, p or w depends on a when the conditions are otherwise fixed. As shown in Fig. 1.4(c), small oxides are usually in a state of regional depletion at low P_{O_2}, while those that are usually in a state of volume depletion in base air (the whole area being depleted) and their electronic states are controlled by p. It is noted, however, that more rigorous discussion should be extended in terms of reduced radius (n) rather than of radius (a), as discussed later.

The double Schottky barrier model (Fig. 1.4(b)) also turned out to be completely misleading. It focused attention on the electron transport path running through the centers of contacting grains. In reality, however, there

© Woodhead Publishing Limited, 2013

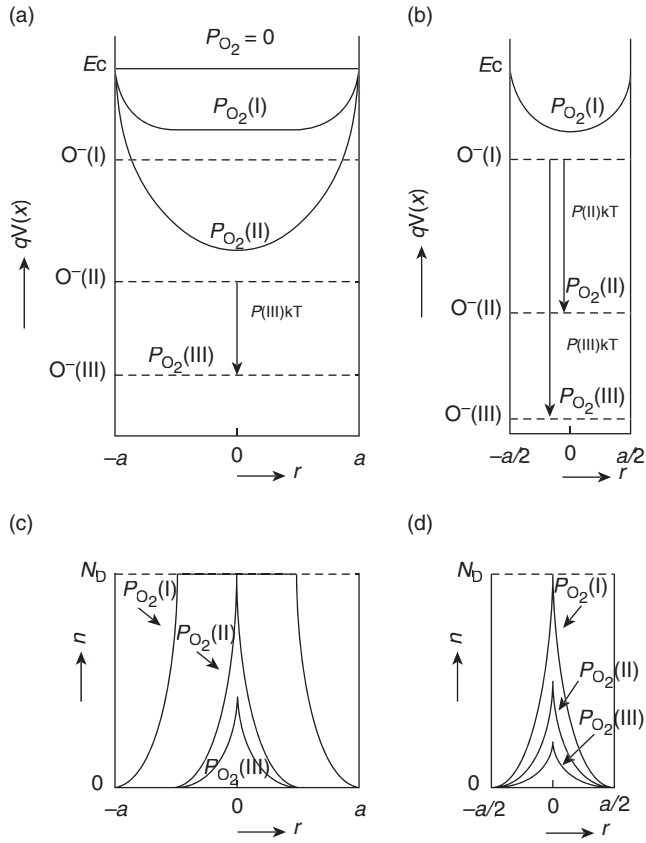

1.5 Energy band diagrams: (a) and (b) distributions of conduction electrons; (c) and (d) for two kinds of grains different in radius (*a* or *a*/2) at steps of increasing P_{O_2}.

are a tremendous number of other transport paths running on the surface of grains, which are free of potential barriers, as shown in Fig. 1.4(d). The electron transport through the contact can thus be achieved by migration or tunneling of the surface electrons, indifferent to the bulk electrons inside. The contact resistance and the device resistance (R) are then inversely proportional to the surface density of electrons, $[e]_S$, as long as the grains are uniform. Device resistance (R) as normalized by that at flat band state (R_0), called 'reduced resistance', is expressed by using the donor density of semiconductor (N_D) as follows:

$$\frac{R}{R_0} = N_D / [e^-]_S \qquad [1.1]$$

© Woodhead Publishing Limited, 2013

1.4.2 Response to oxygen (base air resistance)

Let us consider a case where oxygen is adsorbed as O^- on an oxide grain of radius a. The adsorption equilibrium is written as follows:

$$O_2 + 2e^- = 2\,O^- \quad K_{O_2}\,P_{O_2}[e^-]_S^2 = [O^-]^2 \qquad [1.2]$$

Here, K_{O_2} is the adsorption constant and $[O^-]$ the surface concentration of O^-. Note that $[e]_S$ is a variable of the grain. At the same time, we have to consider the electrostatic equilibrium of the grain. Assuming that there is no surface state other than O^-, $[e^-]_S$ and $[O^-]$ can be expressed as a function of p, respectively, for volume depletion as follows:[15]

$$[O^-] = -\frac{Q_{SC}}{q} = N_D L_D \left\{\left(\frac{n}{3}\right) - A(n)\exp(-p)\right\} \qquad [1.3]$$

$$[e^-]_S = N_D \exp\left\{-\left(\frac{1}{6}\right)n^2 - p\right\} \qquad [1.4]$$

Here, Q_{SC} is the total surface charge density of the grain, which is assumed to be ascribed solely to $[O^-]$ in this case. q is the elementary charge of proton. L_D is the Debye length defined as $L_D = (\varepsilon kT/q^2 N_D)^{1/2}$, where ε is permittivity, and n is reduced radius defined as $n = a/L_D$. $A(n)$ stands for the number of free electrons remaining in the conduction band at $p = 0$ as normalized by $N_D L_D$ and the surface area of the grain. Assuming Boltmann's distribution law for the tailing of electrons, it is given by the following integral:

$$A(n) = \left(\frac{1}{n^2}\right)\int_0^n R^2 \exp\left\{-\left(\frac{1}{6}\right)R^2\right\} \mathrm{d}R$$

There are three simultaneous equations, equations [1.2]–[1.4], correlating among three variables, $[e^-]_S$, $[O^-]$ and p. It is thus possible to determine each variable as a function of $K_{O_2}P_{O_2}$. The solution for $[e]_S$ is transformed into normalized resistance through equation [1.1].

$$\frac{N_D}{[e^-]_S} = \frac{R}{R_0} = c(n) + \left(\frac{S}{a}\right)\left(K_{O_2}P_{O_2}\right)^{1/2} \qquad [1.5]$$

S is the shape factor for the semiconductor crystals used; i.e. $S = 3$ for spheres, 2 for columns and 1 for plates. Constant $c(n)$ is given by $c(n) = (3/n)\exp(n^2/6)\,A(n)$; it increases from unity as n increases; first, gradually when n is small, and then exponentially afterward.

© Woodhead Publishing Limited, 2013

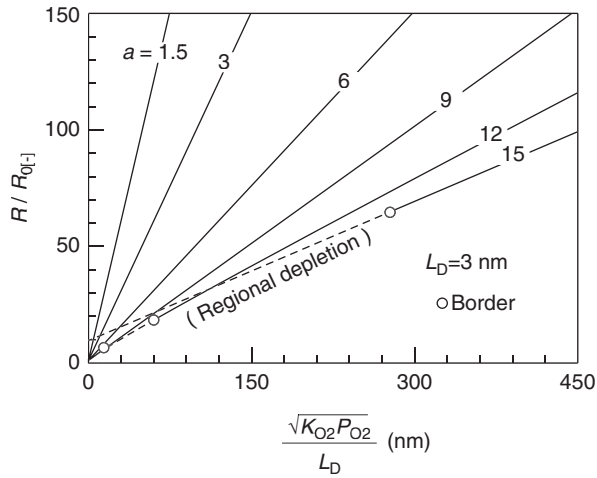

1.6 Reduced resistance (R/R_0) as correlated with $(K_{O_2}P_{O_2})^{1/2}/L_D$ for devices using oxide grains different in reduced size (n).

The correlations given by equation [1.5] are illustrated in Fig. 1.6, where reduced resistance (R/R_0) is related to $(K_{O_2}P_{O_2})^{1/2}$ for variously sized grains (L_D is assumed to be 3 nm). The linear correlations coincide with the power index (1/2) to P_{O_2}, as previously mentioned. Its slope is given by ($3/a$), indicating that sensitivity to oxygen increases as a decreases. As also indicated in Fig. 1.6, the correlation is bent in the initial region of P_{O_2} for larger grains where regional depletion takes place. Remarkably, it can be shown that R/R_0 is almost independent of a in the regional area. Such correlations have, in fact, been confirmed experimentally. It is also noted that, under a particular condition, oxygen adsorption to form another species (O^{2-}) also takes place, which is demonstrated by the linear dependence of R/R_0 on $P_{O_2}{}^{1/4}$ in the stage of volume depletion.

1.4.3 Response to inflammable gases

Simple inflammable gases like H_2 and CO react with adsorbed oxygen (O^-) in one step, while the supply for the O^- consumed is the ambient. In a steady state, the following reactions proceed at an equal rate:

$$O_2 + 2e^- \rightarrow 2O^- \quad (R1) \qquad H_2 + O^- \rightarrow H_2O + e^- \quad (R2)$$

When the rate of the reverse reaction of (R1) is negligible, the surface density of O^- at the steady state is expressed as follows:

© Woodhead Publishing Limited, 2013

$$[O^-] = \left\{ \frac{\left(k_1 P_{O_2}(a)\right)}{\left(k_2 P_{H_2}\right)} \right\} [e^-]_S^2 \qquad [1.6]$$

Here, $P_{O_2}(a)$ and P_{H_2} are partial pressures of oxygen in air and hydrogen, respectively, while k_1 and k_2 are the rate constants of (R1) and (R2), respectively. Equation [1.6] is a constraint connecting $[e^-]_S$ and $[O^-]$ in this case. Then, the equations for $[e^-]_S$, $[O^-]$ and p can be solved as previously performed. By using equation [1.1], reduced resistance under exposure to H_2, R_g/R_0 is derived for volume depletion as follows:

$$\frac{R_g}{R_0} = c(n)/2 + \left\{ c\left((n)/2\right)^2 + \left(\frac{3N_D}{a} \right) \frac{\left(k_1 P_{O_2}(a)\right)}{\left(k_2 P_{H_2}\right)} \right\}^{1/2} \qquad [1.7]$$

This equation is consistent with the power law (−1/2) to H_2. Reduced resistance in air, R_a/R_0, is obtained by substituting $P_{O_2}(a)$ for P_{O_2} in equation [1.5]. The conventional response to H_2, $R_a/R_g = (R_a/R_0)/(R_g/R_0)$, can then be derived, which is expressed as follows when $R_a/R_g >> 1$:

$$\frac{R_a}{R_g} = \left\{ \frac{S\left(k_2/k_{-1}\right)}{\left(aN_D\right)} \right\}^{1/2} P_{H_2}{}^{1/2} \,(\text{volume depletion}) \qquad [1.8]$$

S is the shape factor and equals 3 for spheres; k_{-1} is the rate constant of the reverse reaction of (R_1), $k_{-1} = k_1/K_{O_2}$. The response is thus shown to be linear to $P_{H_2}{}^{1/2}$, which accords with the experimental data as shown in Fig. 1.7, where $(R_a/R_g)^2$ is correlated with P_{H_2} instead. The proportionality constant (sensitivity) is promoted with increasing rate constant ratio (k_2/k_{-1}) and by decreasing grain radius (a) and donor density (N_D). The effects of grain size can thus be rationalized theoretically. However, it should be noted that there are many other inflammable gases which react with O^- in more complex ways. Treatments of the responses to those gases have yet to be undertaken.

1.4.4 Response to oxidizing gases

Let NO_2 be an example of an oxidizing gas. It is adsorbed on the grains to form NO_2^- as follows:

$$NO_2 + e^- = NO_{2-} \qquad K_{NO_2} P_{NO_2} [e^-]_S = [NO_{2-}] \qquad [1.9]$$

© Woodhead Publishing Limited, 2013

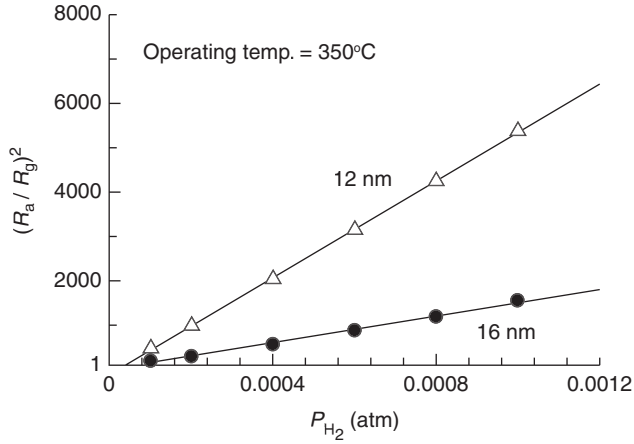

1.7 Correlations between gas response $(R_a/R_g)^2$ and partial pressure of hydrogen (P_{H_2}) as observed with SnO_2 grains of 12 and 16 nm in diameter at 573 K.

K_{NO_2} and P_{NO_2} are the equilibrium adsorption constant and partial pressure of NO_2, respectively. In base air, oxygen is adsorbed, too, according to equation [1.2], so that there are two kinds of adsorbates accommodating electrons transferred from the grain. Through the same procedure used in the previous sections, it can be derived that reduced resistance to NO_2 in the stage of volume depletion is expressed as:

$$\frac{R_g}{R_0} = c(n) + \left(\frac{S}{a}\right)(K_{O_2} P_{O_2}(a))^{1/2} + \left(\frac{S}{a}\right) K_{NO_2} P_{NO_2} \qquad [1.10]$$

There is thus linear correlation between resistance and P_{NO_2}, with its slope being inversely proportional to the grain size (a).

Gas response (R_g/R_a) is derived from equations [1.10] and [1.5], if the grains are already in the stage of volume depletion in air and $R_g/R_a >> 1$, to be as follows:

$$\frac{R_g}{R_a} = \{K_{NO_2} / (K_{O_2} P_{O_2}(a))^{1/2}\} P_{NO_2} \qquad [1.11]$$

The response is independent of a in this case, because the dependence of R_g/R_0 and R_a/R_0 on a is cancelled out. If regional depletion prevails in air, however, a totally different situation arises. Now, R_a/R_0 is almost independent of a, as stated previously, so that equation [1.11] is replaced, approximately, by equation [1.12]. The response is then inversely proportional to a.

© Woodhead Publishing Limited, 2013

$$\frac{R_g}{R_a} = \left(\frac{R_0}{R_a}\right)\left(\frac{S}{a}\right) K_{NO_2} P_{NO_2} \qquad [1.12]$$

Devices based on WO_3 have been found to be sensitive to NO_2, as shown in Fig. 1.8, where granular and lamellar crystals of WO_3 are used in Figs 1.8(a) and 1.8(b), respectively. The lamellar crystals with smaller *a* are seen

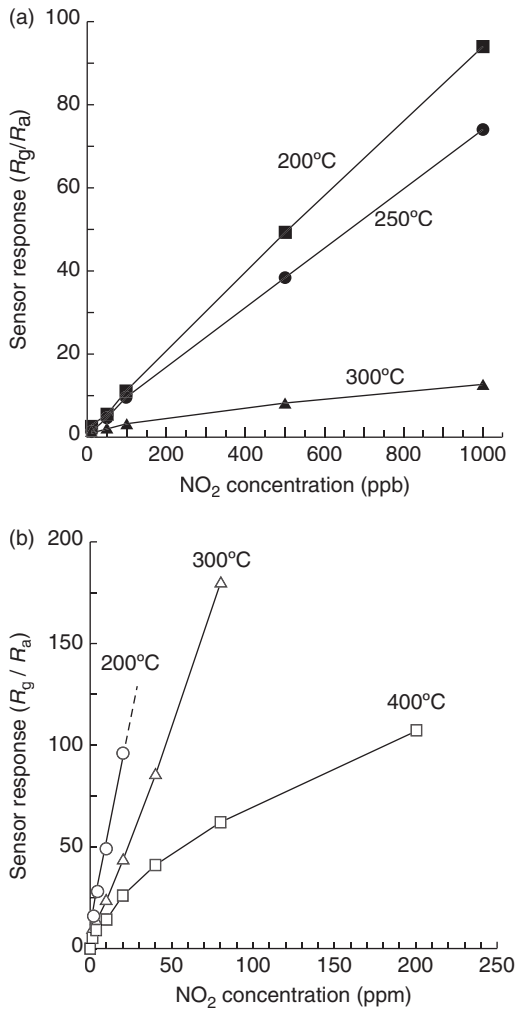

1.8 Correlations between gas response (R_g/R_a) and partial pressure of nitrogen dioxide as observed with WO_3-based devices at various temperatures. (a) Granular WO_3 as pyrolyzed from ammonium tungstate, (b) lamellar WO_3 with crystallites of about 13 nm in size prepared through a colloidal process.

© Woodhead Publishing Limited, 2013

to be particularly sensitive to NO_2, in agreement with equation [1.12], being capable of detecting NO_2 at 10 ppb. The response is linear to P_{NO_2} at lower operating temperatures. It is suggested that this material allows NO_2 to be adsorbed efficiently, while keeping O_2 adsorption at a minimal level ($K_{NO_2} >> K_{O_2}$), thus imposing the situation rationalized by equation [1.12].

1.4.5 Extensions

The theory of gas response can be applied or extended to the analyses of other related phenomena of gas sensors, though such work is still in its early stages. For example, the rates of response and recovery have been formulated theoretically.[16] It has also been derived that a type of sensitization takes place when semiconductor grains are dispersed with an additive that deprives them of conduction electrons and thus affects the reduction of the effective radius of the grains.[17]

The theory also provides a useful tool to understand the nature and roles of the metal-oxide semiconductor contacts involved in semiconductor gas sensors.[18] Under conditions where oxide grains are covered with a sufficiently large density of adsorbates (surface states), their energy band structure is known to remain unaltered, even when they are brought in contact with a metal (pinning). Instead, contact potential (δ_{CP}, in volts) is generated across the contact to compensate the work function difference in between, in addition to the conduction band edge difference (δ_{EC}) appearing in between, as shown in Fig. 1.9. The expression for volume depletion of δ_{CP} is as follows:

$$q\,\delta_{CP} = q(\phi_m - \phi_s),\ q\,\phi_s = q\,\phi_{s,0} + (\delta_{RD}(n) + p\,)\,kT \qquad [1.13]$$

Here, $q\phi_m$ and $q\phi_s$ are the work function values of the metal and semiconductor (ϕ in volts), respectively, and $\phi_{s,0}$ is the value of ϕ_s at flat band state. The expression $\delta_{RD}(n)\,kT$ gives the total lowering of the Fermi level during regional depletion, which is given by $\delta_{RD}(n) = n^2/(2S)$ where S is the shape factor. For a resistor type sensor, δ_{CP} acts as a directional barrier to drifting electrons. It reduces the drift mobility of the electrons traveling against it and eventually increases the resistance of the contact involved. It follows that the contacts between electrode metal and oxide grains are more resistive and more gas-sensitive than the other usual contacts between oxide grains. This has been confirmed to be the case with a narrow gap-electrodes attached device in which the aperture between electrodes was as small as 1 μm or below.[19]

Metal-semiconductor contact also appears to play a key role in the potentiometric gas sensors attached with oxide semiconductors. In these devices,

© Woodhead Publishing Limited, 2013

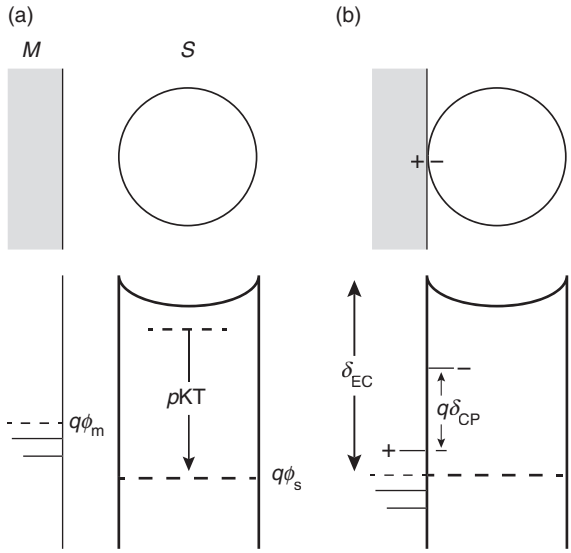

1.9 Energy band diagrams of oxide grain and metal electrode before and after contact under exposure to base air.
Note: The band diagrams remain unaltered (pinning) while contact potential is generated in between upon contact.

gas response seems to reflect the change of contact potential imposed by switching from base air to the target gas ambient, $\delta_{CP}(g) - \delta_{CP}(a)$, as described later. Through equation [1.13] and other relations, it is correlated with the gas response of resistor type sensors in ideal cases as follows:

$$\delta_{CP}(g) - \delta_{CP}(a) = \phi_S(g) - \phi_s(a) = \left(\frac{RT}{F}\right) \mathrm{In}\left(\frac{R_g}{R_a}\right) \qquad [1.14]$$

Here, R and F are gas constant and Faraday constant, respectively, and $RT/F = kT/q$.

1.5 Non-resistive sensors

Various non-resistive gas sensors using semiconductors have been proposed. As described below, these sensors, constructed based on various principles, provide useful information to learn how receptor function and transducer function are generated and combined together into gas sensors, though most of the sensors are yet to be exploited further for use in practice.

© Woodhead Publishing Limited, 2013

1.5.1 Field effect transistor type gas sensors

Principle

The typical structure and characteristic of Pd-gate FET gas sensors are illustrated in Figs 1.10(a) and (b). As is well-known, a FET, usually attached with a normal metal-gate, is a device for controlling drain current by gate voltage applied. Under well-controlled conditions, drain current starts to flow when gate voltage (V) exceeds a threshold voltage (V_{th}) and, on a further increase in V, it increases proportionally to $(V - V_{th})^2$, as shown in Fig. 1.10(b). It is endowed with gas sensing ability when the metal gate is attached with an adequate foreign material. If the new gate system modulates the electrical field underneath depending on the gas ambient, the drain current of the

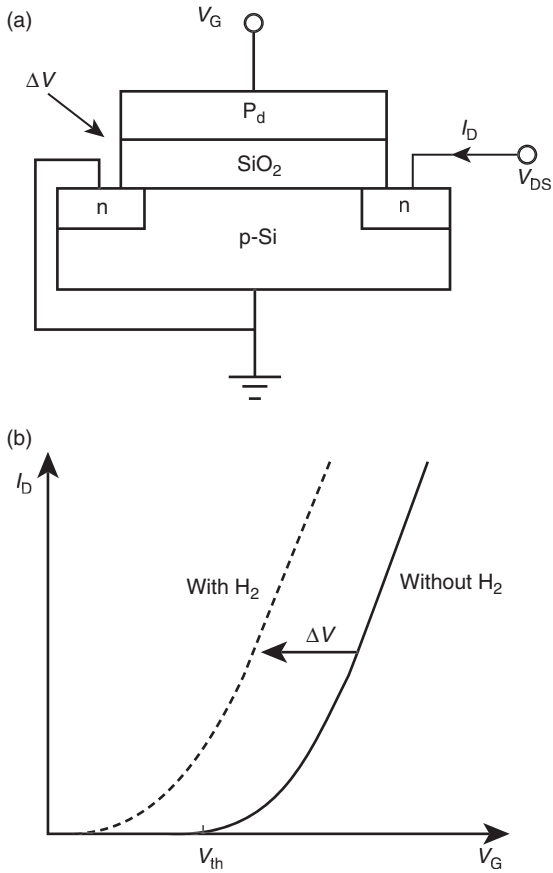

1.10 (a) Structure of Pd-gate FET. (b) Drain current (I_D) characteristics observed: V_G, gate voltage, V_{DS} (source–drain voltage).

© Woodhead Publishing Limited, 2013

device at a fixed gate voltage will change accordingly. Alternatively, actual devices focus attention to V_{th} and its shift is taken as gas response.

The FET gas sensor first proposed was Pd-gate FET; Pd particles were dispersed in the gate region.[20] It responded to H_2 and NH_3 in air at 423 K. Reportedly, the H atoms dissociated from these molecules are dissolved into Pd metal and polarize in the vicinity of the border to the underlying insulator layer (SiO_2) to modulate the electrical field underneath. However, with no supporting evidence having been found, this speculation should be reconsidered. Later, various materials were introduced successfully into the gate. Those are typified in three groups: i.e. solid electrolytes, oxide semiconductors and dielectrics. As observed, combinations of these materials with the gate metal form gas-sensitive functional systems: half cell, metal-semiconductor contact, or capacitor, respectively.

Solid electrolyte-gate field effect transistor

Three-phase contact between metal, solid electrolyte and gas is known to act as an active site for electrochemical reactions (half cell reaction). If the solid electrolyte is a proton conductor, for instance, the following reaction takes place in the presence of H_2, and the half cell equilibrium is expressed by the following Nernst equation:

$$H_2 = 2H^+ + 2e^-,\ \Phi_M - \Phi_{SE} = -\left(\frac{RT}{2F}\right) In\, P_{H_2} + \text{Constant} \qquad [1.15]$$

The electrical potentials of metal and solid electrolyte are Φ_M and Φ_{SE}, respectively. The constant is determined by the kinds of materials involved. The same half cell is formed when the proton conductor is placed between the gate metal and the insulator layer of the FET. Thus, Φ_{SE} is raised by an amount as indicated by equation [1.15] higher than Φ_M, which is now controlled externally as gate voltage. This means that, at a fixed gate voltage, Φ_{SE} increases and, hence, the electrical field underneath also increases with increasing P_{H_2}. In the alternative mode of operation, V_{th} shifts down as P_{H_2} increases, following Nernst's equation. Such behavior has been confirmed experimentally with an antimonic acid layer attached device, which responded well to H_2 diluted in N_2 at room temperature.[21] The response to H_2 in air deviated considerably from this behavior due to the occurrence of mixed potential.

Similarly, devices sensitive to NO_2 or CO_2 can be fabricated by attaching $NaNO_2$ (Na+ ionic conductor) or Li_2CO_3-based composite salt (Li+ ionic conductor) to the gate, respectively.[22,23] The response mechanisms involved can be understood in the same way. In the NO_2 device, for example, the half cell reaction is expressed as follows:

© Woodhead Publishing Limited, 2013

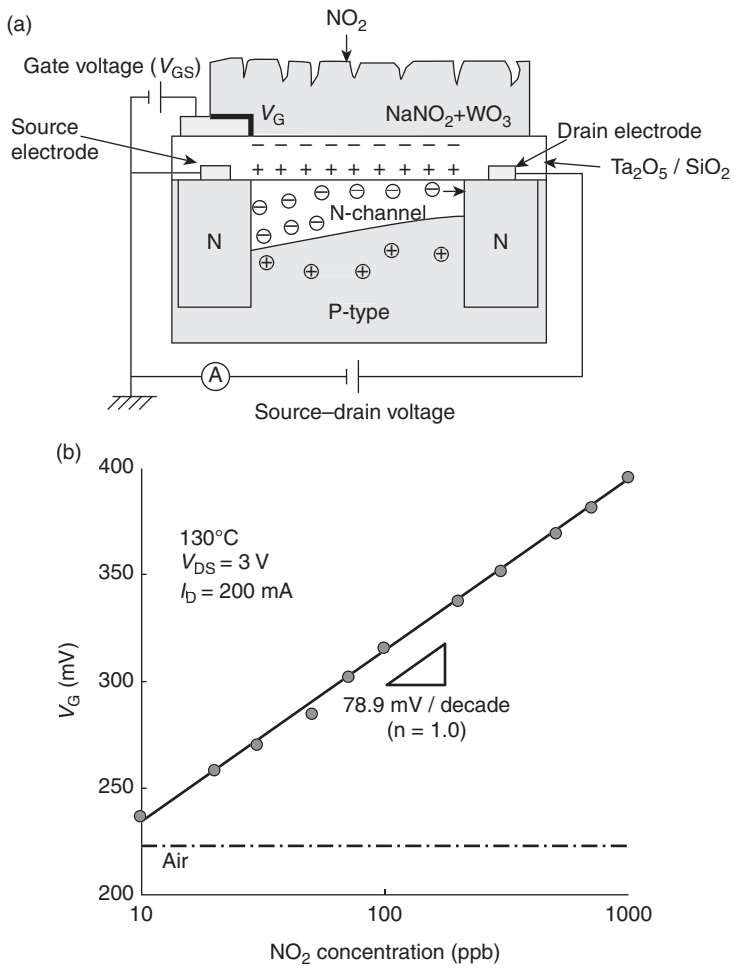

1.11 $NaNO_2$-gate FET sensor. (a) Construction of $NaNO_2$-gate FET sensor, (b) NO_2 sensing characteristics observed.

$$NO_2 + e^- + Na^+ = NaNO_2,\ \Phi_M - \Phi_{SE} = \left(\frac{RT}{F}\right)\ln P_{NO_2} + \text{Constant} \qquad [1.16]$$

$\Phi_{SE} - \Phi_M$ should shift down and so V_{th} should shift up, with increasing P_{NO_2}. This behavior has been confirmed experimentally, as shown in Fig. 1.11. The device was fairly sensitive, responding to a few tens ppb NO_2 in air, showing a Nernst slope fairly close to that of the one-electron reaction expected.

In conventional electrochemistry, a half cell is always combined with another (reference half cell), and its electrochemical equilibrium is investigated through the cell voltage (EMF). In contrast, the half cell of the present

© Woodhead Publishing Limited, 2013

device is combined with an FET underneath and its electrochemical equilibrium is investigated through V_{th}.

Oxide semiconductor-gate field effect transistor

Oxide semiconductors have been introduced into the gate of a FET. A typical example would be the WO_3-gate FET, which was sensitive to NO_2 in air, as shown in Fig. 1.12.[24] Obviously, the high sensitivity originates from the excellent receptor function of WO_3 to NO_2. In current devices, metal-semiconductor contact is made between the gate metal and fine WO_3 crystals, and the resulting contact potential seems to play a decisive role. Due to the contact potential, $\Phi_S - \Phi_M$ goes up or down with a change in P_{NO_2}, according to equation [1.13]. Here, Φ_S is the electrical potential of WO_3. In the same way as the previous devices were treated, the gas response in threshold voltage mode is derived by using equation [1.14], given as follows:

$$V_{th}(g) - V_{th}(a) = \left(\frac{RT}{F}\right)\left\{\ln P_{NO_2} + \left[\ln\left(\frac{R_0}{R_a}\right)\left(\frac{S}{a}\right)K_{NO_2}\right]\right\} \qquad [1.17]$$

When P_{NO_2} is sufficiently large, equation [1.17] is seen to be very similar to equation [1.16], with the response linearly correlated with P_{NO_2} on a semilogarithmic scale with the same Nernst slope. However, the constants appearing in both the equations have totally different meanings from each other. The constant in equation [1.17] mainly reflects the sensitivity of the

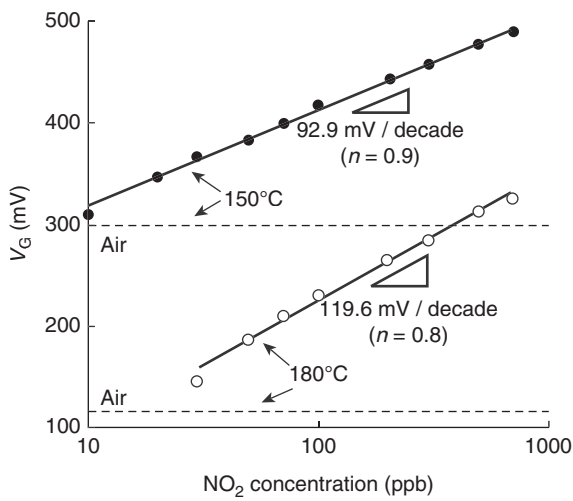

1.12 NO_2 sensing characteristics as observed with WO_3-gate FET sensor.

© Woodhead Publishing Limited, 2013

receptor function of the grains to NO_2. It determines the position of the semilogarithmically linear correlation along the vertical axis and, so, the lower detection limit of P_{NO_2}.

Dielectric material-gate field effect transistor

When a layer of dielectric material is introduced beneath the gate metal, a capacitor is formed on top of the FET, its capacitance varying depending on the dielectric constant and layer thickness of the material. The presence of the capacitor naturally imposes modulation of the electrical field underneath, which is otherwise controlled by the gate voltage only. If the dielectric layer is porous and capable of absorbing a polar-molecule gas effectively to change its dielectric constant, the resulting device is made sensitive to the gas through the change in capacitance; V_{th} moves further away from the air level as the gas partial pressure increases. Based on this principle, the devices sensitive to polar gases (such as water vapor and ethanol gas) have been fabricated fairly successfully by using dielectric materials such as cellulose and its derivatives.[25]

1.5.2 Oxygen concentration cell type sensors

An oxygen concentration cell is constructed by using stabilized zirconia (an O^{2-} ionic conductor) and it is known to work well as an oxygen sensor. If an oxide semiconductor such as SnO_2 is deposited between the sensing electrode (Pt) and zirconia (Fig. 1.13(a)), the device is also made sensitive to various reducing and oxidizing gases other than oxygen.[26] The response (EMF) to such a non-oxygen gas, starting from 0 in base air, increases or decreases linearly with the increasing logarithm of the partial pressure of the gas (Fig. 1.13(b)), while EMF to a fixed gas ambient varies somewhat drastically with the kind and size of the oxides used. For a considerable time, such a response to non-oxygen gases has been considered to be ascribable to the mixed potential generated at the zirconia/oxide semiconductor interface and, for this reason, such devices have been called 'mixed potential' type sensors. The mixed potential is postulated to be generated to H_2 in air, for instance, through the following pair of redox reactions:

$$O_2 + 4e^- \rightarrow 2O^{2-}, \qquad O^{2-} + H_2 \rightarrow H_2O + 2e^-$$

However, it is hard to understand why the response is promoted by a decreasing size of oxides (grain size effect) based on this theory.

Basic approaches to this group of sensors are highly desired in order to reveal the fundamental mechanism of gas sensing involved.

© Woodhead Publishing Limited, 2013

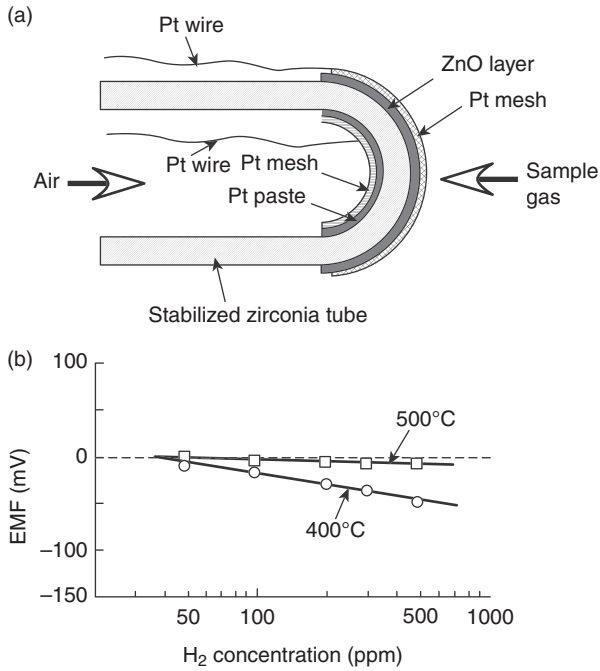

1.13 Oxygen concentration cell type gas sensors attached with oxide semiconductors. (a) Device structure, (b) responses to reducing or oxidizing gases.

1.5.3 Other gas sensors

This section describes types of semiconductor gas sensor that have not been mentioned so far.

Metal-insulator-semiconductor capacitor type sensors

The structure of a metal-insulator-semiconductor (MIS) capacitor and its capacitance vs. applied voltage characteristics are shown in Figs 1.14(a) and (b),[27] respectively. A MIS capacitor is obtained if a MIS FET is deprived of the source–drain current channel (see Fig. 1.10). To provide the MIS capacitor with gas sensing ability, foreign materials (solid electrolytes, oxide semiconductors, or dielectrics) are placed under the metal layer, in the same way as in a MIS FET. In these devices, the capacitance depends on the voltage applied to the metal layer (relative to the semiconductor), whereas at a fixed voltage it changes on switching from air base to gas ambient. In order to keep the capacitance the same, the applied voltage is obliged to shift up or down on changes in the ambient, and this shift is taken as the response of the device to the gas.

© Woodhead Publishing Limited, 2013

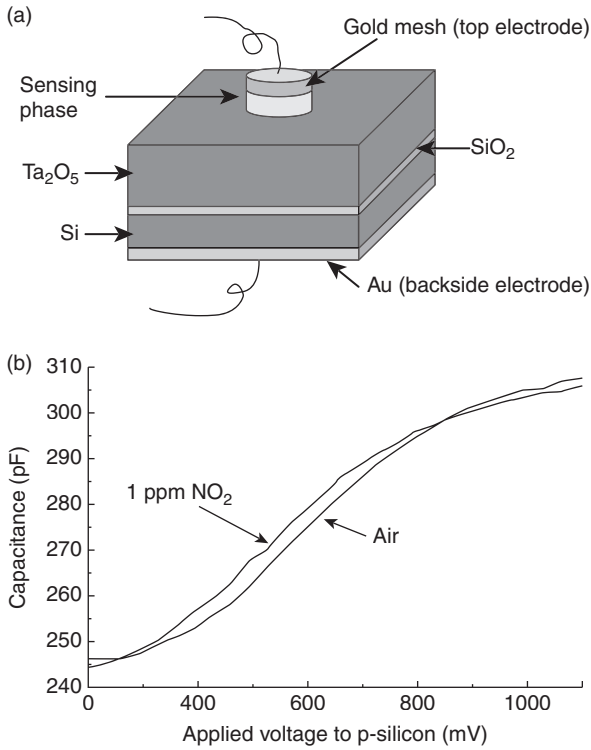

1.14 MIS capacitor. (a) Structure of MIS capacitor, (b) capacitance vs applied voltage characteristic obtained.

Diode type sensors

Non-ohmic contact between metal and semiconductor shows a rectifying property, which is utilized in what is known as a 'metal-semiconductor contact diode' (Schottky diode). Many researchers have attempted to apply the same principle to gas sensors. Various combinations between metals (Pt, Pd, Ag, etc.) and oxide semiconductors (TiO_2, ZnO, etc.) have been chosen to fabricate diode devices. In many cases, the resulting devices showed a reducing gas-dependent rectifying property; in H_2 containing ambient, forward current density was promoted conspicuously with increasing P_{H_2}, while reverse current density was also promoted as well, which was unexpected. Such gas dependent-behavior is of sufficient interest from a standpoint of developing gas sensors. At the same time, however, it suggests the need to reconsider the gas sensing mechanism involved. A matter of concern is whether the contacts formed there are, in fact, of the non-ohmic type, as expected. It has been recognized in other semiconductor sensors that the same contact is achieved through generating contact potential instead of undergoing electron transfer,

© Woodhead Publishing Limited, 2013

as stated previously. The contact potential can be responsible not only for the rectifying property, but also for the promotion of current density, forward as well as reverse, with increasing P_{H2}. Therefore, further careful investigations are needed into this type of gas sensor.

1.6 Future trends

Semiconductor gas sensors will become more and more important in the future. Seeds and needs for them, basic approaches needed and challenges desired are described below as a personal view of the present authors.

1.6.1 Needs and seeds

There is a great variety of gases around us of different properties, origin and concentration. Some are hazardous and should be kept under control, while others may be vital for life or symptomatic of health conditions. Gas sensors are needed for various purposes: safety, amenity, energy saving, health, foods, environmental protection, and so on. As is well-known, the application of gas sensors in practice began with inflammable gas alarms to protect people from fatal gas hazards such as gas explosions, incomplete combustion accidents and exposure to poisonous gases. Fire alarms using a semiconductor gas sensor in combination with a smoke or thermal detector and breath alcohol checkers for preventing drunken driving are also examples of gas sensors used for safety purposes. For the purposes of amenity and energy saving, air quality sensors have been installed in air cleaners, while a pair of sensors sensitive to CO and NO_2 has been incorporated into a car auto-damper system. Odor sensors and breath odor checkers also belong to this category.

Gas sensors are important in other categories, too, though their development is more difficult because the target gases concerned are usually of very low concentrations. For example, volatile organic compounds (VOCs) are one of the urgent targets; if generated in houses, those may cause sick house syndrome, while some of them are even carcinogenic. Various hazardous gases frequently used in factories, laboratories and hospitals should be controlled with the use of gas sensors to protect the health of people working there. Sensing of bio-activity related gases is also important in health and foods. Detection of disease-related gases is drawing increasing attention for medical purposes. Sensory monitoring of air pollutants has been a deep concern to many researchers but, unfortunately, for a variety of reasons this is yet to receive attention. Semiconductor gas sensors, which are endowed with high sensitivity compared with other gas sensors, are, in principle, the best-suited for such applications, though a great deal of effort should be put into substantiating new frontiers for gas sensors.

© Woodhead Publishing Limited, 2013

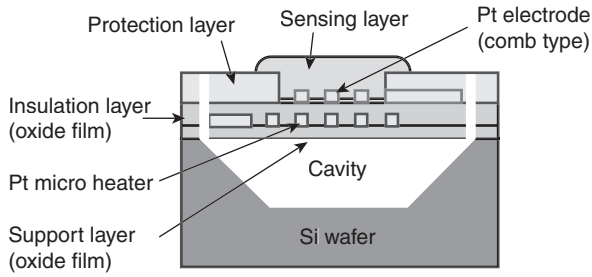

1.15 MEMS gas sensor.

As a new seed in gas sensors, micro sensors fabricated by using MEMS technology, known as 'MEMS sensors', have recently been exploited extensively, aiming at realizing battery-driven gas sensors. As shown in Fig. 1.15, the gas sensing layer (about 100 μm x 100 μm wide and a few tens nm thick) is deposited on a diaphragm, which is suspended over a cavity created within a silicon chip. Electrodes and a heater are printed on the diaphragm beforehand. As a typical feature of such a micro-device, the sensing layer temperature can be changed quickly (within 30 ms), so that the device can be compatible with temperature-programmed operation. This feature would seem to bring about new intelligent functions to gas sensors. Temperature-programmed gas response diagrams, for instance, may be useful for the identification of target gases.

1.6.2 Basic approaches desired

Semiconductor gas sensors have so far been developed on the basis of experience and intuition. Tremendous efforts have been devoted to discovering new sensing materials, new ways of materials processing, new types of device, new targets for gas sensing and so on, putting emphasis on gas sensing performances. This approach, however, is not always so effective for further advances of gas sensors. With the receptor function of small oxide semiconductors having been clarified, there is now a keen need for approaches shedding light on the more basic side of gas sensors. The knowledge thus accumulated will be useful in establishing guidelines for designing semiconductor gas sensors. Matters for further investigation include:

- establishing methods to characterize and control semiconductive properties, especially the donor density, of oxides;
- seeking quantitative correlations between sensitivity data and catalytic oxidation data for a series of inflammable gases;
- seeking quantitative correlations between semiconductor properties and gas sensing properties for oxides;

© Woodhead Publishing Limited, 2013

- basic analyses of the existing state and the roles of sensitizers;
- basic analyses of the effects of mixing one oxide semiconductor with another.

Preparation of discrete nano-crystals of oxide semiconductors has become increasingly popular recently. Sensors using nano-crystals of exotic morphology have been fabricated and often shown to exhibit interesting gas sensing properties. Unfortunately, however, origins of such interesting properties have received scant investigation from a basic standpoint, making it difficult to draw on information useful in the design of gas sensors. In fact, nano-sized crystallites have already been utilized in practical gas sensors. It would be informative to undertake a critical evaluation of the differences brought about by such a change in morphology.

1.6.3 Challenges

There are subjects of research which are worth challenging in order to progress the innovation of semiconductor gas sensors. Some examples are listed below:

1. Elucidation of control of water vapor effects: Disturbances by water vapor have been a major origin of errors in gas response. Elimination of them upgrades the quality of gas sensing.
2. Verification of ultrasensitive gas sensors: New frontiers of gas sensor applications often demand that they cope with reducing gases at sub-ppm levels. It is necessary, first, to prove that such high-sensitive sensors can be devised.
3. Contact potential-conscious sensor design: Gas response of a resistor type sensor seems to be promoted significantly by contact potential if a properly designed composite gas sensing layer is used.
4. Exploration to make FET type and oxygen concentration cell type gas sensors more flexible in operating temperature: FET-based on silicon cannot function at temperatures higher than ca.180°C, whereas the cell using zirconia cannot function at temperatures lower than ca. 550°C; neither is able to work in the most important temperature range for gas sensing. Exploration for new semiconductors and new solid electrolytes is desired to eliminate these limitations.

1.7 References

1. Seiyama, T., Kato, A., Fujiishi, K. and Nagatani, M. (1962) *Analytical Chemistry*, **34**, 1502.
2. Taguchi, N. (1962) *Published patent application in Japan*, S37-47677, Oct.

© Woodhead Publishing Limited, 2013

3. Xu, C., Tamaki, J., Miura, N. and Yamazoe N. (1991) *Sensors and Actuators B: Chemical*, **3**, 147.
4. Rothschild, A. and Komen, Y. (2004) *Journal of Electroceramics*, **13**, 697.
5. Rothschild, A. and Komen, Y. (2004) *Journal of Applied Physics*, **95**, 6374.
6. Yamazoe, N. and Shimanoe, K. (2008) *Journal of The Electrochemical Society*, **155**, J85.
7. Yamazoe, N. and Shimanoe, K. (2008) *Journal of The Electrochemical Society*, **155**, J93.
8. Watson, J. (1984) *Sensors and Actuators*, **5**, 29.
9. Madou, M. and Morrison, S. R. (1989) *Chemical Sensing with Solid State Devices*, Academic Press, Boston.
10. Korotcenkov, G. (2011) *Chemical Sensors: Fundamentals of Sensing Materials*, Momentum Press, New Jersey.
11. Yoshioka, T., Mizuno, N. and Iwamoto, M. (1991) *Chemistry Letters*, **20**, 1249.
12. Clifford, P. K. and Tuma, D. T. (1982/1983) *Sensors and Actuators*, **3**, 233.
13. Sakai, G., Matsunaga, N., Shimanoe, K. and Yamazoe, N. (2001) *Sensors and Actuators B: Chemical*, **80**, 125.
14. Yamazoe, N. and Shimanoe, K. (2011) *Sensors and Actuators B: Chemical*, **154**, 277.
15. Yamazoe, N. and Shimanoe, K. (2011) *Sensors and Actuators B: Chemical*, **158**, 28.
16. Yamazoe, N. and Shimanoe, K. (2010) *Sensors and Actuators B: Chemical*, **150**, 132.
17. Yamazoe, N. and Shimanoe, K. (2009) *Thin Solid Films*, **517**, 6148.
18. Yamazoe, N., Shimanoe, K. and Sawada, C. (2007) *Thin Solid Films,* **515**, 8302.
19. Tamaki, J., Niimi, J., Ogura, S. and Konishi, S. (2006) *Sensors and Actuators B: Chemical*, **117**, 353.
20. Lundström, I., Shivaraman, M. S., Svensson, C. and Lundkvist, L. (1975) *Applied Physics Letters*, **26**, 55.
21. Miura, N., Harada, T., Yoshida, N., Shimizu, Y. and Yamazoe, N. (1995) *Sensors and Actuators B: Chemical*, **24–5**, 499.
22. Nakata, S., Shimanoe, K., Miura, N. and Yamazoe, N. (2001) *Sensors and Actuators B: Chemical*, **77**, 512.
23. Shimanoe, K., Goto, K., Obata, K., Nakata, S., Sakai, G. and Yamazoe, N. (2004) *Sensors and Actuators B: Chemical*, **102**, 14.
24. Nakata, S., Shimanoe, K., Miura, N. and Yamazoe, N. (2003) *Electrochemistry*, **71**, 503.
25. Karube, I., Tamiya, E., Sode, K., Yokoyama, K., Kitagawa, Y., Suzuki, H. and Asano, Y. (1988) *Analytica Chimica Acta*, **213**, 69.
26. Lu, G., Miura, N. and Yamazoe, N. (1996) *Journal of The Electrochemical Society*, **143**, L154.
27. Zamani, C., Shimanoe, K. and Yamazoe, N. (2005) *Sensors and Actuators B: Chemical*, **109**, 216.

© Woodhead Publishing Limited, 2013

2

Conduction mechanism in semiconducting metal oxide sensing films: impact on transduction

N. BÂRSAN, M. HUEBNER and U. WEIMAR,
University of Tübingen, Germany

DOI: 10.1533/9780857098665.1.35

Abstract: This chapter gives an overview of the conduction mechanisms in semiconducting metal oxide (SMOX) sensing films and their impact on the transduction of surface chemistry into a measurable sensor signal (relative change of resistance). Following general discussion on the functioning of sensors based on SMOX porous, sensing films, modelling of the conduction in *p*- and *n*-type materials is performed. The theoretical results explain why the sensor signals are lower for *p*-type oxides when compared with *n*-type oxides. The modelling concepts are verified by applying them to experimental results obtained with sensors based on both *n*- and *p*-type SMOXs with good results.

Key words: semiconducting metal oxide (SMOX), sensing and transduction of SMOXs, *p*- and *n*-type MOXs, conduction mechanism, modelling, measurements taken in working conditions.

2.1 Introduction

Chemoresistive gas sensors based on semiconducting metal oxides (SMOXs), are very successful, being sold in millions, in applications as diverse as the detection of explosive gas leakages in residential premises, or the control of air intake in car interiors (Bârsan *et al.*, 2007). There is a continuous effort to extend their applications in markets as different as indoor air quality, or consumer goods (Applied Sensor, Reutlingen, Germany (http://www.appliedsensor.com/applications). After the initial publication of gas sensitive effects on germanium by Brattain and Bardeen (1953), metal oxides were identified as possible sensitive materials by Heiland (1954), Bielanski *et al.* (1957) and Seiyama *et al.* (1962), and were brought to the market by Taguchi (1971), who founded the largest manufacturer of SMOX sensors: Figaro Engineering (Figaro, Osaka, Japan (http://www.figarosens.com)).

The success of this type of device is based on their good price–performance ratio; they are:

© Woodhead Publishing Limited, 2013

- inexpensive (the price range is a few euros per sensor);
- easy to use (there is a direct relationship between the concentration of the target gas and the sensor resistance);
- very sensitive (generally being able to measure down to a few ppm, or even a few hundred ppb);
- very stable (with reported life times extending into decades);
- easy to integrate in arrays for more ambitious analytical tasks;
- reasonably low power consumption when realized on micro-machined membranes using a pulsed temperature mode (realized by battery operation).

The gas detection with SMOX-based gas sensors is, in principle, simple: in air, at temperatures between 150°C and 400°C, oxygen is adsorbed on the surface of the metal oxides by trapping electrons from the bulk with the overall effect of increasing the resistance of the sensor (for *n*-type materials), or decreasing it (for *p*-type materials). The additional occurrences of gases in the atmosphere that react with the pre-adsorbed oxygen, or directly with the oxide, determine the relative changes of the sensor resistance (sensor signals). From this very naïve picture, one can already get the idea that one has to examine two aspects: the surface reaction taking place between the material and the gases (called the 'receptor function') and the transduction of it into the corresponding changes in the electrical resistance of the sensor. This contribution examines the influence of the conduction mechanism on the transduction of surface reactions into sensor signals. Section 2.2 looks at the understanding of the functioning of SMOX-based sensors, then Section 2.3 examines the main differences brought about by the type of conduction of the material. Section 2.4 presents examples of applying simultaneous work function and conductance measurements to the theoretical study of the conduction mechanisms, and the chapter closes with Section 2.5 which offers a set of conclusions and an outlook for future studies.

2.2 General discussion about sensing with semiconducting metal oxide gas sensors

All SMOX-based gas sensors are realized by depositing a sensing layer over an insulating substrate provided with electrodes and a heater. The electrodes are used for the readout of sensor resistance; the heater raises the temperature of the SMOXs sufficiently high to allow for their fast and reproducible operation, generally between 150°C and 400°C. An example is presented in Fig. 2.1.

In this example, the sensing layer, in the form of a thick porous film, is deposited by applying screen-printing technology onto a planar alumina substrate equipped with interdigitated Pt electrodes on its front, for the

© Woodhead Publishing Limited, 2013

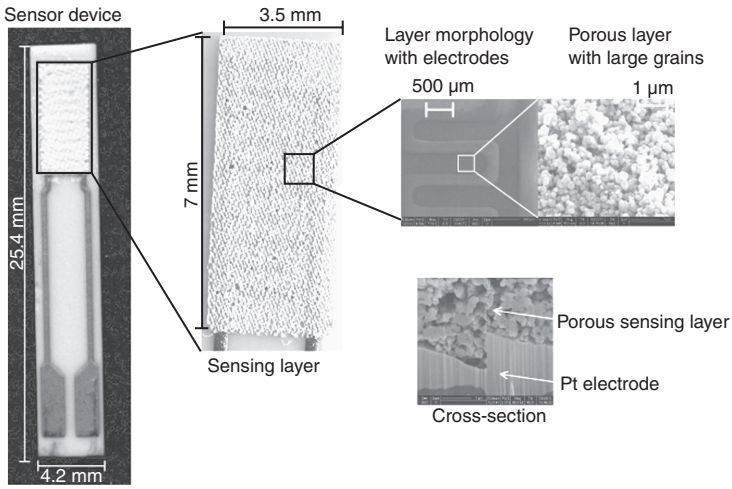

2.1 Design of the sensor substrate used at the University of Tübingen.

readout of the electrical resistance, and a Pt heater on its reverse, which allows the sensor to operate at well-controlled temperatures. All commercial sensors are based on thick porous layers, for reasons that will be given below; in addition to screen printing, other coating technologies (e.g. drop coating) can be applied. Although the working principles of such devices seem quite simple, the sensing process – which includes surface reactions, corresponding charge transfer processes and their translation into variations of the electrical resistance of the sensor – is very complex. Figure 2.2 presents a diagram of the various elements involved in the simple case of CO detection with an *n*-type SMOX (e.g. a SnO_2-based gas sensor).

Figure 2.2 demonstrates how, due to the chemisorption of atmospheric oxygen, a depletion layer is formed on the surface of the grains comprising the sensing layer. The presence of reducing gases, such as CO, reduces the negative charge trapped on the surface by the formation of CO_2. The measurable result is a decrease in the sensor's resistance (R). The surface reaction and corresponding conduction are indicated by the arrows.

The grains of the sensing layer are loosely sintered together; in the example, it is considered that any influence of the surface does not extend into the whole grain, so one can consider that there are two distinctly separate areas: a space charge layer on the surface and, unaffected by exposure to gas, the bulk. In dry air, atmospheric oxygen interacts with the surface of SnO_2, acceptor levels are created, and electrons from the conduction band are trapped at these levels – forming molecular and/or atomic oxygen ions. Consequently, the depletion layer appears on the surface of the grains; in the energy band representation this is formalized as a bending of the upward

© Woodhead Publishing Limited, 2013

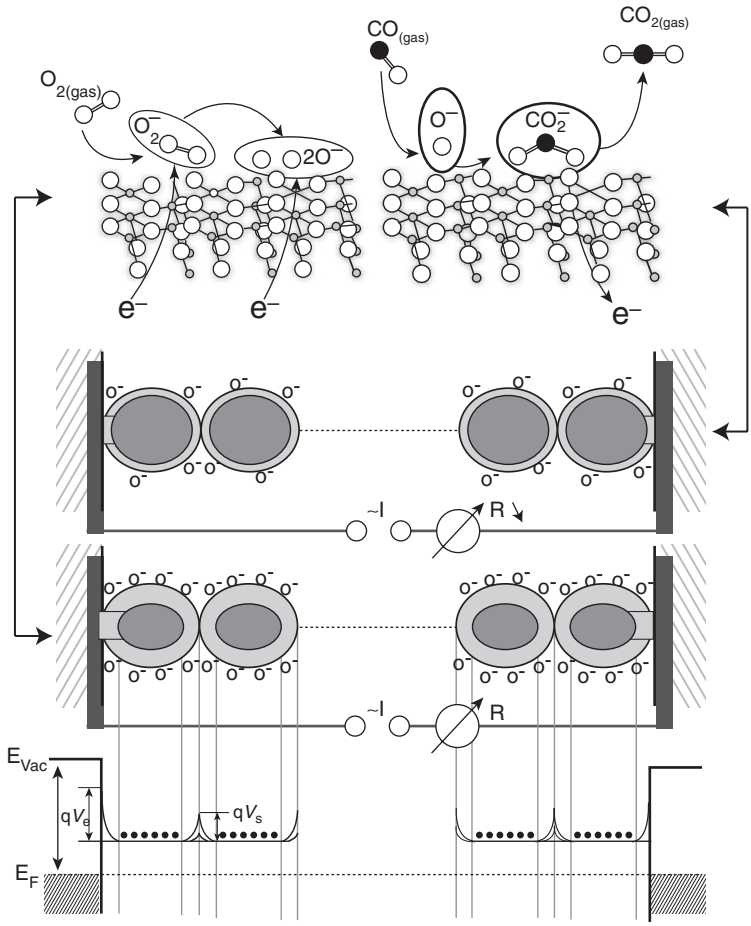

2.2 Diagram representing how surface reactions are transduced into a measurable signal (qV_s is the height of the back to back Schottky barriers formed between the grains, qV_e is the height of the barrier formed at the interface between the electrode and the oxide).

band, meaning that the electrons need more energy to reach the surface (against the electric field of the negatively charged surface). Hence, the conduction in the sensing layer is controlled by the back-to-back Schottky barriers formed between the grains. It is generally accepted that the CO is reacting with pre-adsorbed oxygen, forming CO_2 that disperses in the atmosphere (Cox and Henrich, 1994). These surface reactions – the ionosorption of oxygen and its consumption by the presence of CO – are the chemical basis of sensing; they describe the receptor function of the sensitive material. The charge transfer, associated with the surface chemical reactions, determines the measured effect; namely, the resistance change: the reaction

© Woodhead Publishing Limited, 2013

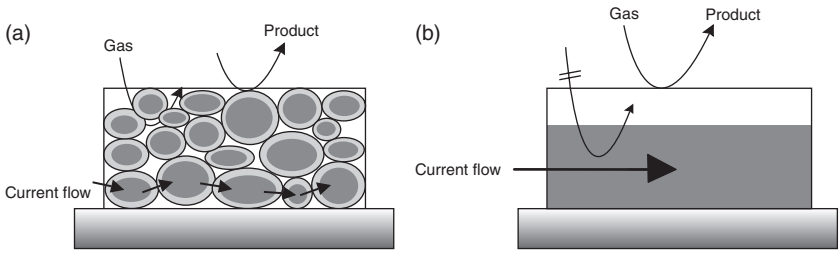

2.3 Diagram showing the difference between (a) a porous and (b) a compact layer.

of CO with the ionosorbed oxygen decreases the surface negative charge, the consequence being a reduction of the energy barrier height between the grains. That enables a progressively greater number of electrons to flow from one electrode to the other, which translates into a reduction of resistance in the sensor. Assuming that the intrinsic characteristics of the material remain constant, the relationship between the change of the surface charge and the change of the resistance depends on the morphology of the thick film layer. A useful criterion for classification takes into consideration the accessibility of the sensing layer's bulk to gases and Fig. 2.3 illustrates a simple distinction between compact and porous layers.

In the case of a compact layer, gas interaction only takes place on the geometric surface; the flow of current is only influenced by the thickness of the depletion layer on the surface of the layer. For porous layers, the gas can penetrate into the entire layer and, in that way, each individual grain is affected by the surrounding gaseous composition. The current is consequently determined by the barriers between all the grains.

For compact layers, the bulk is not accessible to gases and the interaction only takes place on the geometric surface (the as-formed electron depleted layer is colored light gray, in contrast to the electron-rich bulk region colored dark gray. Here, the assumption that the constant material properties do not depend on the process by which the layer is formed ensures that, for both type of layer, there are surface and bulk zones). The electrical current therefore flows parallel to the surface and the conduction process takes place in the lower resistive bulk area, with the consequence that it is only indirectly influenced by the modulation of the low resistive cross-section area. This explains why the relative resistance changes for such kinds of layer are low.

In the case of porous layers, the gaseous species can penetrate into the bulk, which makes the active surface much deeper. Here, the electrical current is forced to cross the surface by passing from one grain to the next and, accordingly, is directly influenced by the energy barriers between the grains

© Woodhead Publishing Limited, 2013

(grain boundary model). These are the main reasons why the best results for *n*-type metal oxide-based gas sensors are obtained by using porous thick film layers, where the conduction mechanism is controlled by the back-to-back Schottky barriers. Furthermore, the dimensions of the grains in porous layers (d) have to be taken into consideration. There are two cases – depending on the relation between the dimension of the grains, d, and the Debye length, Ld – which show a different dependency between the conductance and the target gas concentration:

- Case 1: grains large enough to have an unaffected bulk area ($d >> L_D$);
- Case 2: grains smaller than, or comparable to, the Debye length ($d \leq L_D$).

A detailed discussion about the modelling of the two cases is given in Bârsan (1994) and Bârsan and Weimar (2001).

It must be noted that, because of the access of the gases to the whole volume, the interaction can take place in different parts of the sensor device; meaning that, in principle, it is possible to have contributions from the entire sensor and not only from the sensitive material. Figure 2.4 presents a scanning electron microscopy (SEM) diagram showing the cross-section of an SnO_2 porous thick film sensor and the different contact possibilities. In addition to the grain–grain contacts (a), Fig. 2.4 shows additional interfaces that can play a role in sensing and transduction: the grain–electrode–Al_2O_3 substrate contact (c) and/or the grain–Al_2O_3 substrate contact (b). The most obvious contribution might be related to (c), due to the fact that the current needs to go through the electrodes and that, due to the noble metal nature of these electrodes, there is a possibility of catalytic effects. The insulating nature of the inert substrate means that (b) is a significantly less probable influencing factor. Further, it was shown that the electrical contribution of the electrode–SMOX interface is a series resistance that does not change under target gas exposure (Bârsan and Weimar, 2001), the influence of which it is possible to minimize by making sure that the number of grain–grain contacts between the electrodes is much greater than 2. This simply implies that the use of gaps between the electrodes is much greater than the grain size. The proven chemical effect of the electrodes (Dutraive *et al.*, 1995; Weimar *et al.*, 1997) has to be considered as an influencing factor for the average grain–grain sensing unit in the layer.

Discussion in the following sections will focus on the part of the conduction process/mechanism in *p*- and *n*-type SMOXs. A theoretical discussion (modelling of the conduction) about the different dependencies between the surface chemistry and the corresponding resistance of the layer will be performed. By the use of measurement techniques undertaken during working conditions, the validity of the models will be proven experimentally. In doing so, one needs to use a parameter that is directly linked to both surface reactivity and conduction.

© Woodhead Publishing Limited, 2013

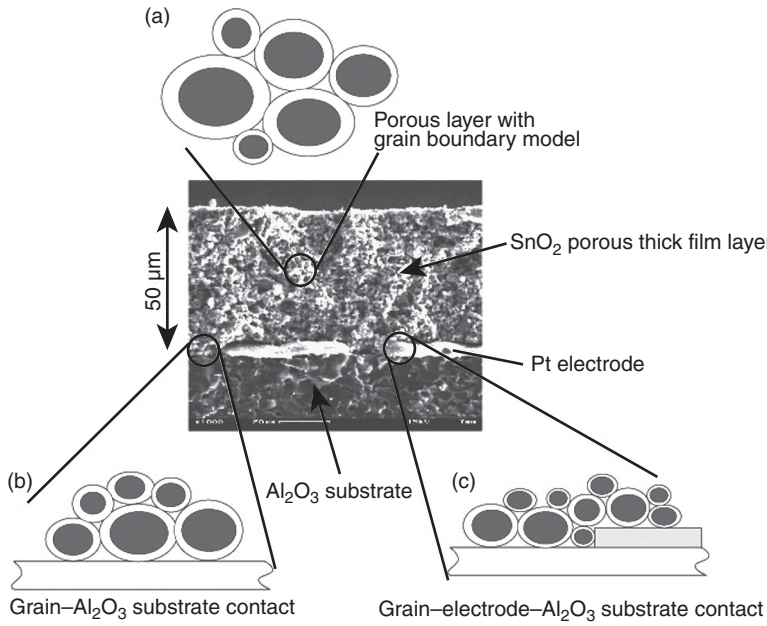

2.4 Different gas interactions in porous layers. The gas penetrates into the layer and interaction can therefore take place at the grain–grain boundaries (a), the grain–Al_2O_3 substrate contact (b) and at the grain–electrode–Al_2O_3 substrate contact (c).

The ideal candidate is the change in the surface band bending ($q\Delta V$) of the SMOX because its magnitude under gas exposure is a measure of surface reactivity and also controls the electrical transport from one electrode to the other. Consequently, one needs a technique which is able to directly measure its changes on gas exposure; the well-established Kelvin probe method (Oprea *et al.*, 2009) for the measurement of work function changes ($\Delta\Phi$) was selected for this purpose. Work function changes can be caused by changes in the band bending ($q\Delta V$), the electron affinity ($\Delta\chi$) or the bulk position of the Fermi level ($\Delta(E_{C,B} - E_F)$ = electrochemical potential), as shown in Fig. 2.5 which describes the influence of CO reaction in air on the work function of SnO_2.

$$\Delta\Phi = q\Delta V + \Delta\chi + \Delta(E_{C,B} - E_F) \qquad [2.1]$$

The latter contribution can be excluded in the temperature range in which SMOX sensors are usually operated because the thermal energy is not sufficiently high for bulk reactions with the atmospheric gases (e.g. oxygen bulk diffusion) to take place.

Electron affinity depends on the concentration of surface dipoles, generally linked to surface species related to the reaction with water vapour (Bârsan

© Woodhead Publishing Limited, 2013

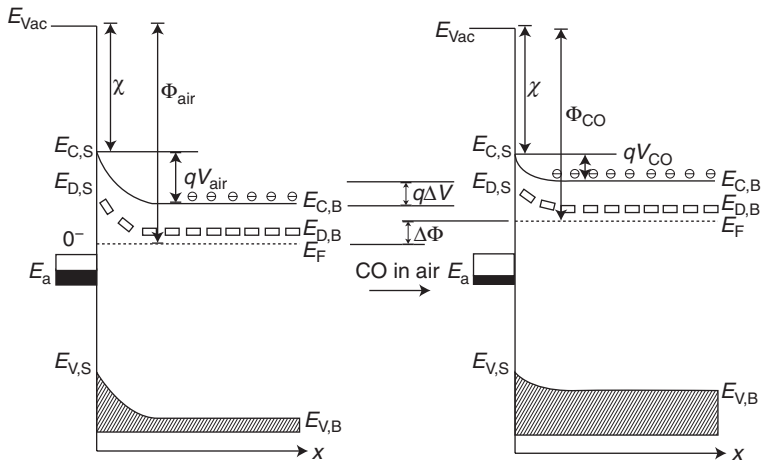

2.5 Energy band representation of SnO_2 showing the different contributions to the work function of CO sensing in dry air conditions. Following symbols are used for the different parameters: E_{Vac} = vacuum level; $E_{C,S(B)}$ = conduction band at the surface (in the bulk); $E_{D,S(B)}$ = donor levels at the surface (bulk); E_a = surface acceptor levels; E_F = Fermi level; $E_{V,S(B)}$ = valence band at the surface (bulk); χ = electron affinity; $\Phi_{air}(CO)$ = work function in air (upon CO exposure); $qV_{air}(CO)$ = band bending in air (upon CO exposure); $q\Delta V$ = change of band bending; $\Delta\Phi$ = change of work function; and x = distance from the surface.

and Weimar, 2003). By ensuring that the electron affinity is constant ($\Delta\chi = 0$), one obtains direct access to the changes in the band bending ($q\Delta V$) by using the Kelvin probe technique, which can be achieved by keeping the system in very dry conditions. The corresponding changes in the resistance can be easily measured with the sensor device being used. Consequently, one can measure the dependence of the resistance on the surface band bending in different conditions and, therefore, the conduction mechanism can be identified.

2.3 Sensing and transduction for *p*- and *n*-type semiconducting metal oxides

In the field of SMOX-based gas sensors, by far the most studied material is the *n*-type SnO_2. Moreover, most of the commercial sensors marketed today are based on it, generally in combination with noble metal additives (Ihokura and Watson, 1994; Williams, 1999). The other material used in commercial sensors in applications involving the detection of oxidizing gases is WO_3, which is also an *n*-type semiconductor. This is intriguing, because since

© Woodhead Publishing Limited, 2013

the early 1980s considerable efforts were directed towards finding alternative materials with a better or different sensing performance, amongst them *p*-type oxides, such as Cr_2O_3 and CuO (see Kim *et al.*, 2008; Li *et al.*, 2008; Miremadi *et al.*, 1994; Shimizu *et al.*, 2001; Zhang *et al.*, 2006 for reports on their sensing performance to different gases: H_2, O_2, EtOH, CO, NO_2, etc.). Much lower sensor signals were consistently observed – defined for *n*-type SMOX sensors as shown in Equation [2.2] and for *p*-type SMOX sensors in Equation [2.3] – when compared with SnO_2-based sensors in spite of well-known high surface reactivity (*R* denotes the electrical resistance of the sensor, *G* denotes the electrical conductance).

$$S_n = \frac{R_{\text{air}}}{R_{\text{gas}}} = \frac{G_{\text{gas}}}{G_{\text{air}}} \quad [2.2]$$

$$S_p = \frac{R_{\text{gas}}}{R_{\text{air}}} = \frac{G_{\text{air}}}{G_{\text{gas}}} \quad [2.3]$$

An example for this observation is given in Fig. 2.6, where the EtOH sensing behaviour of *p*-type Cr_2O_3 (open symbols) is compared with that of undoped SnO_2 (filled symbols) exposed to CO. For both materials, huge changes in the work function ($\Delta\Phi$, continuous lines with squares) upon target gas exposure (EtOH and CO) were measured, indicating a high surface reactivity (change

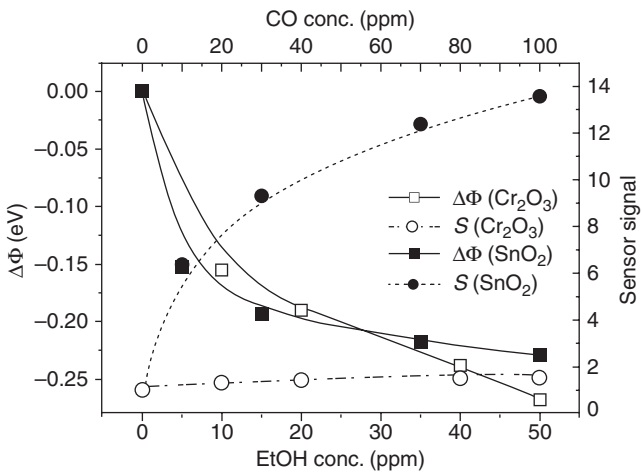

2.6 Comparison between *p*-type Cr_2O_3 and *n*-type SnO_2. For similar changes in the work function upon exposure to EtOH and CO, respectively, the *n*-type material shows much higher changes in the resistance (sensor signal *S*).

© Woodhead Publishing Limited, 2013

of band bending). In the case of *n*-type SnO_2, these changes are translated into rather 'large' sensor signals (dotted line with filled circles). For *p*-type Cr_2O_3, similar changes resulted in much lower levels of signal (dotted line with open circles). The reason for this was recently unveiled when it was demonstrated that large changes in the surface band bending ($q\Delta V$) do not result in large changes in resistance (sensor signals) because of the conduction mechanism (Bârsan *et al.*, 2010; Pokhrel *et al.*, 2008).

To understand and explain this huge difference in the relationship between the surface chemistry and the changes in conductance, one has to look in more detail at the conduction processes in these materials. The focus will be, first, on the modelling of the conduction for *p*-type metal oxides to determine the relationship between resistance and band bending in normal operational conditions. Subsequently, *n*-type materials will be examined for conditions in which the conduction mechanism changes.

2.3.1 Modelling of conduction for *p*- and *n*-type semiconducting metal oxides in normal conditions (operation in air)

Even if the initial modelling were based on results obtained on Cr_2O_3 (Bârsan *et al.*, 2010), the large grain size of that material would have the effect of making the weight of surface phenomena even less significant because of the possible conduction contribution of the bulk. Accordingly, in order to simplify the case under investigation, CuO was used as a prototype *p*-type metal oxide for the gas sensing performance in response to CO; its grain size making it feasible to consider that the surface plays the dominant role in conduction (Huebner *et al.*, 2011a). The validity of the findings, though, is not limited to CuO. The *p*-type semiconducting behaviour of CuO is related to the presence of acceptor levels – attributed to copper vacancies – in the band gap, which determine the appearance of holes in the valence band. The adsorption of oxygen on the surface of CuO is considered to be at the origin of CO sensing and can be described by Equation [2.4]:

$$\frac{1}{2}O_2^{air} + S_A \leftrightarrow O^-_{(ad)} + h^+ \qquad [2.4]$$

whereas O_2^{air} represents atmospheric oxygen, S_A an adsorption site for oxygen, $O^-_{(ad)}$ the resulting chemisorbed oxygen species and h^+ the created hole in the valence band. The interaction of atmospheric O_2 with the surface of the SMOX determines the formation of acceptor levels, and the electron transfer from the valence band to the surface leads to the formation of ionosorbed oxygen species resulting in upward band bending. The negative charged surface is compensated by an increased hole concentration in the

© Woodhead Publishing Limited, 2013

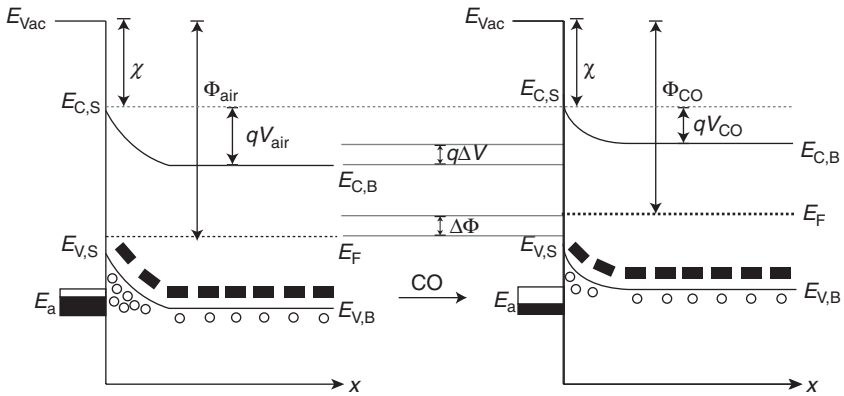

2.7 Energy bands representation for a *p*-type SMOX material. The reaction of CO as target gas with the *p*-type material causes a decrease in the band bending ($q\Delta V$) and therefore changes in the work function ($\Delta\Phi$). The symbols used for the different parameters are as given for Fig. 2.5 (the left side describes the situation in air, the right side the situation under CO exposure).

valence band that determines the formation of an accumulation layer. This is a very important difference when one compares the case of *p*-type materials with *n*-type materials: in *p*-type, the conductivity of the surface increases because of the adsorption of atmospheric oxygen. This situation, represented by energy bands, is shown on the left-hand side of Fig. 2.7. The effect of CO exposure, very similar to the general reaction mechanism for SnO_2 explained in Section 2.2, is the consumption of ionosorbed oxygen species that determines the reduction of negative charge trapped at the surface:

$$CO^{gas} + O^{-}_{(ad)} + h^{+} \rightarrow CO_2^{gas} + S_A \qquad [2.5]$$

whereas CO^{gas} represents the carbon monoxide in the gas phase, $O^{-}_{(ad)}$ preadsorbed oxygen species, h^{+} a hole in the valence band, CO_2^{gas} the formed product and S_A a free adsorption site for oxygen. As a consequence, the hole concentration near the surface decreases; in energy terms, this situation is described by a decrease in the surface band bending. Hence, the conductivity at the surface decreases and the overall sensor resistance increases.

Figure 2.8 illustrates the differences in the conduction mechanisms between 'similar' porous layers of *p*-type and *n*-type materials. The 'similarity' – meaning comparable grain size, morphology and parameters of the depletion/accumulation layers – is considered in order to focus on the conduction mechanism only. The left-hand side of Fig. 2.8 describes an *n*-type SMOX for a porous layer consisting of loosely sintered grains with a radius larger than the Debye length (not fully depleted). In this case, one can

© Woodhead Publishing Limited, 2013

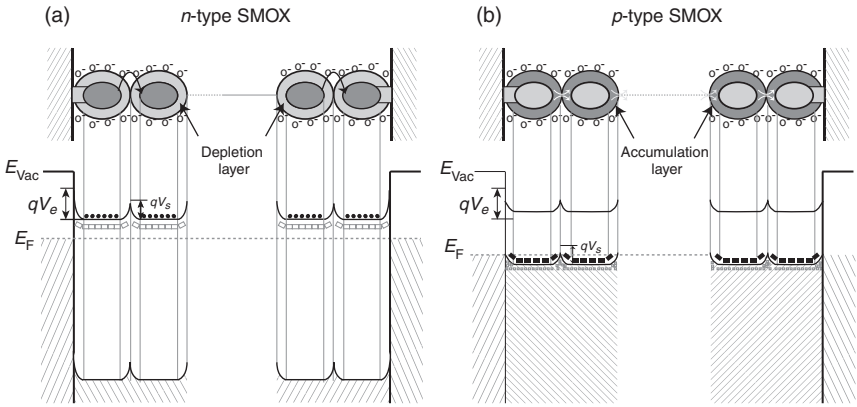

2.8 Illustration of the conduction processes and the corresponding energy bands for an *n*-type SMOX material (a) described by a depletion layer, and for a *p*-type SMOX material (b) with an accumulation layer.

differentiate between a gas sensitive surface depletion layer (upward band bending, light gray) with a large electrical resistance and an unaffected bulk region (dark gray) with a lower electrical resistance. The electric current through the layer from one electrode to the other is therefore determined by the concentration of electrons (n_S) having sufficient energy to overcome the potential barrier (qV_S) between the grains (back-to-back Schottky barriers). The dependence between this concentration and the surface band bending can be described by a Boltzmann distribution by assuming that the Schottky approximation is valid:

$$n_S = n_b \exp\left(-\frac{qV_S}{kT}\right) \qquad [2.6]$$

whereas n_b represents the electron density in the bulk and kT the thermal energy (≈ 0.05 eV). For the conductance, one can consequently write:

$$G_n \propto \exp\left(-\frac{qV_S}{kT}\right) \qquad [2.7]$$

As shown in Fig. 2.7, the upward band bending in the case of *p*-type MOXs determines the formation of an accumulation layer for holes. Accordingly, the conductivity in the surface space charge layer increases in comparison with the bulk, and conduction takes place differently compared with that described by the depletion layer. The current will now flow through the accumulation parallel to the surface and also through the bulk; this situation can be described by two resistors in parallel. The latter contribution from the

© Woodhead Publishing Limited, 2013

bulk depends on the nature of the material and the morphology of the layer. It is obvious that larger grains have a higher bulk influence, which makes the surface effect – and, therefore, the sensing – less important. In this case (e.g. for Cr_2O_3 with rather large grains), a complex relationship between the conductance/resistance and the band bending was obtained (Bârsan *et al.*, 2010). A much simpler relationship is devised by ensuring that the grains are quite small (e.g. as in the case of CuO (≈ 25 nm) (Huebner *et al.*, 2011a), so that the contribution to the conductance of the bulk can be ignored. Hence, one can assume that the conduction process is now dominated by the average hole concentration in the accumulation layer ($G_p \propto \tilde{p}_S$).

Considering that also in this situation the Boltzmann statistics are valid, the average hole concentration $\tilde{p}_S$ can be easily calculated by using a one-dimensional approach.

$$\tilde{p}_S = \frac{1}{x_0}.\int_0^{x_0} p_b \exp\left(\frac{qV(x)}{kT}\right)dx \qquad [2.8]$$

whereas p_b represents the hole density in the bulk and x_0 the width of the space charge layer. To evaluate the integral in Equation [2.8], one has to solve the Poisson equation for the accumulation layer if the conductance is determined by the holes. After the first integration of Poisson's equation, one obtains (Morrison, 1977):

$$\frac{dV(x)}{dx} = \sqrt{\frac{2kTp_b}{\varepsilon\varepsilon_0}}.\exp\left(\frac{qV(x)}{2kT}\right) \qquad [2.9]$$

where V represents the potential at a certain point x and $\varepsilon\varepsilon_0$ the relative permittivity of the material. By using the definition of the Debye length $\left(L_D = \sqrt{kT\varepsilon\varepsilon_0/q^2p_b}\right)$ and the boundary conditions that $V = V_S$ for $x = 0$, the following relationship between the distance from the surface, x, and the potential $V(x)$ is obtained for the second integration:

$$x = \sqrt{2}.L_D.\left[\exp\left(-\frac{qV_S}{2kT}\right) - \exp\left(-\frac{qV(x)}{2kT}\right)\right] \qquad [2.10]$$

Now, the integral in Equation [2.8] can be calculated by changing the variables and by using Equation [2.10]. For the average concentration of holes in the surface space charge layer, one obtains:

$$\tilde{p}_S = p_b \exp\left(\frac{qV_S}{2kT}\right) \qquad [2.11]$$

© Woodhead Publishing Limited, 2013

Hence, one can write for the dependence of the conductance and the surface band bending:

$$G_p \propto \exp\left(\frac{qV_S}{2kT}\right) \quad [2.12]$$

Comparing the latter expression with the corresponding one for *n*-type porous thick film layers (Equation [2.7]), one can clearly observe that the same surface chemistry (same change in the surface band bending) is translated differently into a change of the conductance/resistance depending on what kind of material is used. Considering the sensor signal as the relative change of the sensor resistance due to exposure to the target gas, $S_{n,p}$, one obtains that the signal of a *p*-type is simply the square root of the signal for the *n*-type MOX:

$$S_p = \sqrt{S_n} \quad [2.13]$$

This fact clearly shows why the use of *p*-type materials as chemoresistive gas sensors is not optimal. Although these materials may be highly reactive to the target gases, the output electrical signal is quite low, as already shown in Fig. 2.6 for Cr_2O_3.

To calculate the band bending changes from the changes in the resistance, one has to use the following dependency:

$$q\Delta V = -2kT.\ln\left(\frac{R_{\text{gas}}}{R_{\text{air}}}\right) \quad [2.14]$$

More details about the calculations can be found in Huebner *et al.* (2011a).

The classical, state-of-the-art preparation technology for SMOX-based gas sensors – thick, porous sensing layers – is not the best choice for *p*-type materials. In their case, the direct readout of the changes in the surface band bending would be more efficient; in the case of a resistive readout, thin, compact films with electrodes deposited on the top would be more appropriate.

2.3.2 Modelling of the conduction for *n*-type semiconducting metal oxide: extension to low oxygen concentrations

As already mentioned, for the case of *n*-type SnO_2 porous layers the conduction mechanism in an oxygen containing background is determined by the appearance of a depletion layer at the surface of the grains. The negative surface charge related to ionosorbed oxygen species is compensated by a positive space charge layer near the surface, resulting in an upward

© Woodhead Publishing Limited, 2013

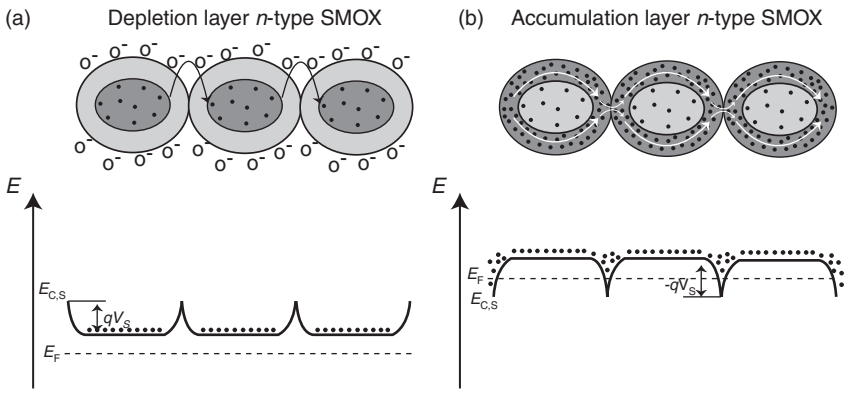

2.9 Presentation of the conduction processes for *n*-type SnO_2 in (a) a depletion layer model and (b) an accumulation layer model.

band bending. In cases where the dimension of the grains is larger than the Debye length, one can distinguish between a rather resistive space charge layer on the surface and a bulk area with a lower resistance. The conduction is therefore controlled by the barrier height on the surface of the grains. Only the electrons which have sufficient energy to overcome the back-to-back Schottky barriers between the grains can move from one electrode to another. The diagram of the conduction process in the depletion layer in Fig. 2.9 helps achieve a better understanding. The dependence of the conductance and the surface band bending can be easily expressed by Equation [2.7], assuming that the Schottky approximation is valid and that the bulk donors are fully ionized.

By decreasing the amount of oxygen in the background (or by increasing the concentration of the reducing gases), one consequently also decreases the initial upward band bending on the surface of the grains; in certain conditions, it is possible to reach a flat band situation. That means that there are no energy differences between the surface and the bulk, as well as the fact that the concentration of the free charge carriers is constant. A similar situation is possible also in air when the Debye length exceeds the grain size: fully depleted grains. There, the position of the Fermi level relative to the minimum of the conduction band does not correspond to the Fermi level of the bulk conditions (Bârsan and Weimar, 2001).

If the oxygen concentration in the atmosphere were lowered, the flat band situation could most probably be reached in the absence of oxygen, if one considers that the full height of the upward band bending is only determined by the ionosorption of oxygen; that means that there are no intrinsic electron traps on the surface. If the band bending is further decreased (e.g. by exposure to reducing gases that will form surface donors (Huebner *et al.*, 2011b)), one would record a downward band bending at the surface,

© Woodhead Publishing Limited, 2013

meaning the formation of an accumulation layer and, therefore, the conduction mechanism will change. This situation is presented in the right-hand side of Fig. 2.9. The easiest way for the electrical current to travel from one electrode to another is now through the accumulation layer on the surface (lowest resistivity). Hence, one can also assume, as in the case of *p*-type MOXs, that the conductance is simply proportional to the average electron concentration in the accumulation layer ($G_n \propto \tilde{n}_S$). The challenge is now to find a relationship which describes the dependence between the changes in the band bending and the changes in the resistance for the accumulation layer.

The procedure is very similar to that shown previously for the *p*-type material and is described in detail in Bârsan *et al.* (2011). By assuming that also in the accumulation layer conditions the Boltzmann statistics are valid and that one can use a one-dimensional approach, one can write for the average electron concentration:

$$\tilde{n}_S = \frac{1}{x_0}.\int_0^{x_0} n_b \exp\left(-\frac{qV(x)}{kT}\right)dx \qquad [2.15]$$

The only difference compared with the accumulation layer for the *p*-type SMOX is that the electrons are the charge carriers and that the accumulation is therefore described by a downward band bending. Again, here one has to solve the Poisson equation (Morrison, 1977); with its solution, the average electron concentration $\tilde{n}_S$ can be calculated. One obtains:

$$\tilde{n}_S = n_b.\exp\left(-\frac{qV_S}{2kT}\right) \qquad [2.16]$$

The dependence of the conductance on the surface band bending in the case of the accumulation layer can therefore be described by:

$$G_n \propto \exp\left(-\frac{qV_S}{2kT}\right) \qquad [2.17]$$

By comparing Equations [2.17] and [2.7], it becomes obvious that the impact of the surface band bending on the conductance is very different depending on the condition (depletion vs accumulation layer). If the conduction is described by the accumulation layer, the relative change of the resistance is simply the square root of the relative change in relation to the depletion layer model, assuming that in both cases one measures the same surface band bending changes:

$$S_{\text{acc}} = \sqrt{S_{\text{dep}}} \qquad [2.18]$$

© Woodhead Publishing Limited, 2013

The latter expression implies that the 'largest' signals are obtained in the case of the depletion layer model. The effect of the surface chemistry on the resistance changes becomes weaker where the conduction moves into the accumulation layer.

The analytical solution (Equation [2.16]) obtained for the average electron concentration in the accumulation layer is only valid in conditions where one can use the Boltzmann statistics. If the conduction band edge at the surface crosses the Fermi level, this assumption is no longer valid. One then has to use the Fermi–Dirac statistics instead of the Boltzmann statistics in order to determine the dependence of the electron concentration on the surface band bending. The average electron concentration in the accumulation in this case can be calculated numerically (Bârsan *et al.*, 2011). By comparing the trend of the analytical and the numerical solutions, both describing how the average electron concentration in the accumulation layer depends on the surface band bending, the following statements can be made:

- both trends are similar (same slope) up to around 0.3 eV after the crossing of the surface conduction band edge with the Fermi level position;
- with further increasing of the surface band bending, the trends are strongly divergence, which reflects the lack of appropriateness of the Boltzmann approximation.

The slope of the 'correct' numerical solution is getting lower (a smaller coefficient than $(2kT)^{-1}$ in the exponent in the Equation [2.17]), indicating that the influence of the band bending on the resistance is becoming weaker.

The latter calculations in Equations [2.15] to [2.17] show that the conduction mechanism for an *n*-type SnO_2 sensor might change from one controlled by a depletion layer to one dominated by transport through the accumulation layer, depending on the operational conditions. This fact has to be borne in mind, especially if the concentration range to be explored is very large.

2.4 Investigation of the conduction mechanism in semiconducting metal oxide sensing layers: studies in working conditions

The ideas and models presented in Section 2.3 are applied to SnO_2 and CuO as model systems for *n*- and *p*-type SMOXs.

2.4.1 Sample preparation and experimental conditions

The *n*-type semiconducting SnO_2 powder was synthesized by a conventional wet-chemistry solgel procedure ($SnCl_{4(aq)}$ and $NH_{3(aq)}$) followed by

© Woodhead Publishing Limited, 2013

a calcination treatment at 1000°C for 8 hours (Diéguez *et al.*, 1999). For the highly crystalline *p*-type CuO nano-particles, a soft chemistry route was employed using a mixture of copper-acetate, oleic acid and trioctylamine (Huebner *et al.*, 2011a). The investigated porous thick film layers were obtained by using the automatic screen-printing procedure. Therefore, the powders were mixed with an appropriate amount of an organic vehicle to obtain a homogenous paste which was subsequently printed onto the alumina substrates. For the electrical readout, the substrates are provided with interdigitated Pt electrodes, and a Pt heater on the backside allowed the operation at well-controlled temperatures (see Fig. 2.1). To remove the residual organic solvent, the sensors were finally heated in a moving belt oven (SnO_2: 400°C–600°C; CuO: 300°C–450°C).

To investigate the conduction mechanism in the sensing layers, simultaneous DC-resistance and work function change measurements were taken in working conditions using the Kelvin probe technique (McAllister KP 6500 Kelvin Probe). The latter is a non-contact, non-destructive method which measures the changes in the contact potential differences (CPD) between the sensor and a vibrating reference electrode. Variations in the CPD induced by the changes in the surrounding atmosphere (e.g. CO exposure) represent the changes in the material's work function (Oprea *et al.*, 2009).

$$\Delta\mathrm{CPD} = -\Delta\Phi/q \qquad [2.19]$$

By choosing conditions in such a way that possible contributions from the electron affinity ($\Delta\chi$) to the work function changes can be ignored (very dry conditions excluding influences of surface dipoles from humidity), the changes in the surface band bending can be directly measured as changes in the contact potential difference (ΔCPD). In these circumstances, one can directly correlate the changes in the surface band bending with the corresponding sensor resistance change. It is important to note that both measured parameters are average values corresponding to an average sensing unit of the layer, which includes all influences from grain size dispersion, influence of substrate and electrode, etc.

2.4.2 Conduction mechanism of *p*-type CuO – experimental results

Simultaneous DC-resistance (Keithley 2000 multimeter) and work function change measurements on exposure to CO (10, 30, 50, 70 and 100 ppm) of a CuO based porous thick film gas sensor were performed at 150°C in dry air conditions. The time dependencies of the resistance and the CPD are presented in Fig. 2.10. One observes that the resistance increases on CO exposure, whereas the work function decreases. This indicates that there are

© Woodhead Publishing Limited, 2013

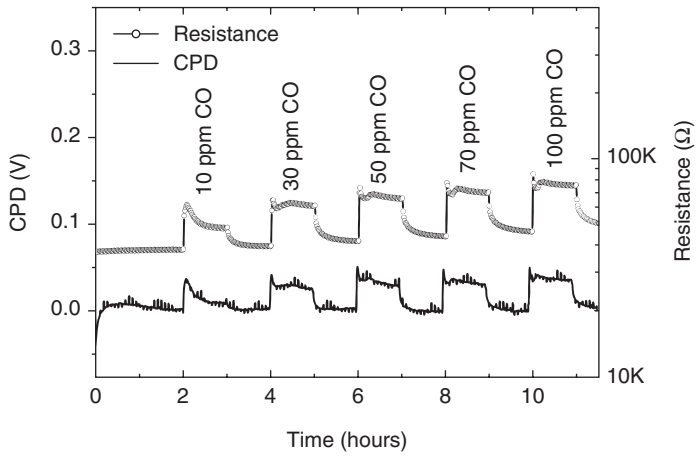

2.10 Simultaneous contact potential differences (CPD) and electrical resistance changes of a CuO sensor (operated at 150°C) due to exposure to different concentrations of CO (10, 30, 50, 70 and 100 ppm) in dry air conditions.

fewer holes in the accumulation layer and a decrease of the upward band bending occurs (see also Fig. 2.7). One expects that, in dry conditions, CO reacts with pre-adsorbed oxygen, resulting in the cancellation of a hole and the formation of CO_2 as described by Equation [2.5].

In these circumstances, the measured changes in the work function on exposure to CO should only be caused by changes in the band bending. To prove this assumption, the different contributions which may cause changes in the work function on increasing CO concentrations are shown in Fig. 2.11. The changes of the work function ($\Delta\Phi$, dark gray with stars) are directly measured, the changes in the band bending ($q\Delta V$, black line with dots) are extracted from the resistance changes by using the relationship for the dependence of the resistance and the surface band bending (Equation [2.14]). The changes of the electron affinity ($\Delta\chi$, open squares) are calculated according to the following equation:

$$\Delta\chi = \Delta\Phi - q\Delta V \qquad [2.20]$$

One clearly observes that no changes occur in the electron affinity during the reaction of CO with CuO in dry air conditions; all changes in the work function are caused by changes in the band bending.

The fitting curve describing the dependence between the sensor signal ($S_p = R_{gas}/R_{air}$) and the corresponding changes in the work function/band bending is given in Fig. 2.12. The value for the slope, as obtained, fairly accurately reflects the dependence gained from the theory (experimental value of 2.000 ± 0.034 and theoretical value of 2).

© Woodhead Publishing Limited, 2013

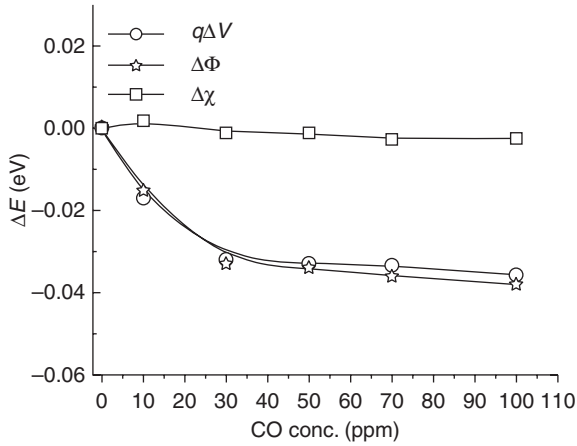

2.11 Changes of band bending ($q\Delta V$), work function ($\Delta\Phi$) and possible changes of the electron affinity ($\Delta\chi$) with increasing CO concentrations (10, 30, 50, 70 and 100 ppm) of the CuO sensor in dry air condition operated at 150°C. ΔE represents the changes of all contributions in the unit of eV.

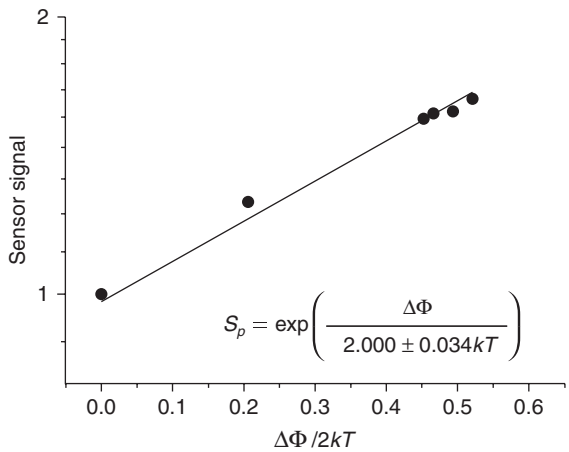

2.12 Fitting curve describing the dependence between the sensor signal (S_p) and the corresponding changes in the work function. The value obtained for the slope reflects the dependence gained from the theory quite effectively.

The experimental results show a good match to the theory. In addition, it was becoming clear that the use of *p*-type materials as chemoresistive gas sensing materials is not optimal. The same surface chemistry (same band bending) results in a much lower sensor signal for the *p*-type material compared with *n*-type materials, where the conduction is described by a

© Woodhead Publishing Limited, 2013

depletion layer model (upward band bending). Further, the reaction of CO with pre-adsorbed oxygen species is supported because no changes in the electron affinity are observed.

To extend the findings to more realistic orientated conditions, similar experiments in a background of 50% relative humidity (25°C) were performed. Figure 2.13 presents the different contributions: the measured changes in the work function (stars), the calculated band bending changes (black with circles) from the measured resistance changes and the extracted electron affinity (squares) changes on CO exposure in the humid background. There, the situation is completely different compared with the experiments in dry air: significantly larger changes in the work function are observed whereas, at the same time, the decrease in the band bending is much smaller. This implies that, on CO exposure in the presence of humidity, a strong decrease occurs in electron affinity. For a better understanding of the difference observed between Figs 2.11 and 2.13, the influence of the humidity itself and its effect on the different contributions is depicted in Fig. 2.14. The exposure to water vapour not only determines a large decrease in the band bending (increasing resistance, circles), but also an increase in the electron affinity (squares), which indicates a change in the concentration of surface dipoles. The reaction of water with the surface of CuO can be expressed as follows (see also (Huebner *et al.*, 2011b)):

$$O^{-}_{(ad)} + H_2O^{gas} + 2Cu_{Cu} + h^{+} \leftrightarrow 2(Cu^{+}_{Cu} - OH^{-}) + S_A \qquad [2.21]$$

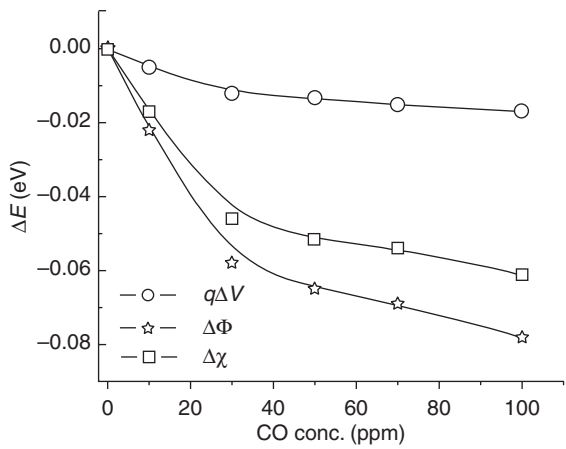

2.13 Changes of band bending ($q\Delta V$), work function ($\Delta\Phi$) and possible changes of the electron affinity ($\Delta\chi$) with increasing CO concentrations (10, 30, 50, 70 and 100 ppm) of the CuO sensor in 50% relative humidity (25°C) operated at 150°C.

© Woodhead Publishing Limited, 2013

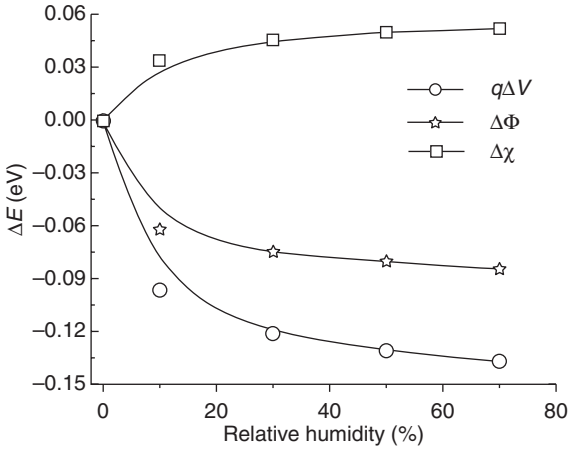

2.14 Changes of band bending ($q\Delta V$), work function ($\Delta\Phi$) and possible changes of the electron affinity ($\Delta\chi$) of the CuO sensor on exposure to humidity levels (10, 30, 50 and 70% relative humidity at 25°C) at an operational temperature of 150°C.

A water molecule from the atmosphere (H_2O^{gas}) reacts with pre-adsorbed oxygen ions ($O^-_{(ad)}$) and two Cu sites ($2Cu_{Cu}$) on the surface under the formation of two terminal hydroxyl groups ($2(Cu^+_{Cu} - OH^-)$). The appearance of the two terminal hydroxyl groups is responsible for the increase in the electron affinity (formation of local surface dipoles) and the cancellation of a hole (h^+) determines the decrease in the band bending. S_A is the freed adsorption site for chemisorbed oxygen.

Consequently, there is competition between CO and H_2O for oxygen ions as reaction partners in the presence of humidity. This explains the observed behaviour in Fig. 2.13. The effect of CO exposure in humid conditions is reduced (smaller sensor signals); and the buildup of the dipoles is hindered due to fewer adsorption sites for water vapour, which determines the monitored decrease in the electron affinity.

This example demonstrates how one can identify the sensing mechanism of CO and CuO in the presence of humidity by using working conditions DC-resistance and work function change measurements in combination with appropriate modelling of the conduction.

2.4.3 Conduction mechanism of *n*-type SnO_2 – experimental results

The experiments were performed on an SnO_2-based gas sensor operated at 300°C. Investigations were made into the influences of CO and H_2 in

© Woodhead Publishing Limited, 2013

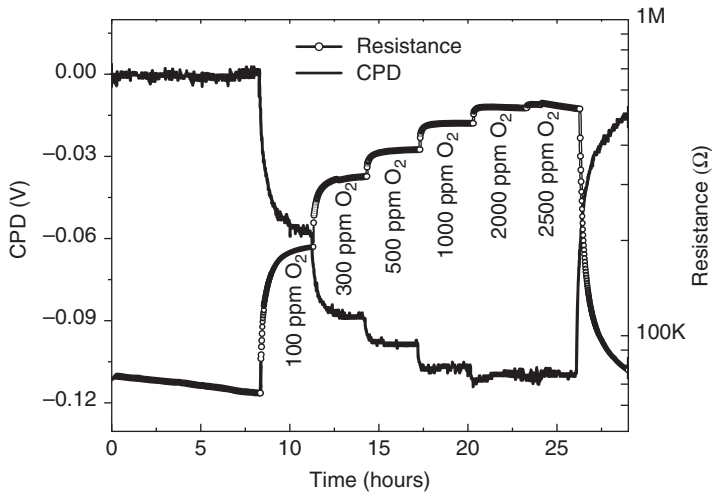

2.15 Simultaneous contact potential differences (CPD) and electrical resistance changes of an SnO_2 sensor (operated at 300°C) with stepwise increasing amounts of oxygen (100, 300, 500, 1000, 2000 and 2500 ppm).

different oxygen backgrounds, and that of oxygen itself on the resistance and the band bending.

In Fig. 2.15, the measured changes of the resistance and the CPD during stepwise increasing oxygen concentrations from zero (N_2 atmosphere) up to 2500 ppm are shown. One observes a steep increase in both resistance and work function at the lower concentrations due to the adsorption of oxygen, resulting in ionosorbed oxygen species on the surface; a form of saturation occurs as oxygen reaches 2000 ppm.

Figure 2.16 illustrates the behaviour of the resistance and the CPD on exposure to four CO pulses (10, 30, 70 and 100 ppm) in the absence (Fig. 2.16(a)) and in the presence (Fig. 2.16(b)) of 22 000 ppm of oxygen. A huge drop is observed in both the resistance and the work function due to exposure to CO; except for the first pulse (10 ppm), the equilibrium state in the work function is reached in the allotted three hours of CO exposure. The recovery process, however, is very slow for both parameters; the baseline could not be reached again in the three hours allowed for recovery. The presence of oxygen in the background determines a higher baseline resistance (formation of ionosorbed oxygen) and a decrease in the relative changes of both the resistance and the work function in comparison with the absence of oxygen. The response and recovery times in the presence of oxygen are considerably more rapid.

Figure 2.17 illustrates the time dependence of the resistance and the CPD of a similar experiment using five pulses of H_2 (10, 20, 30, 50 and 100 ppm)

© Woodhead Publishing Limited, 2013

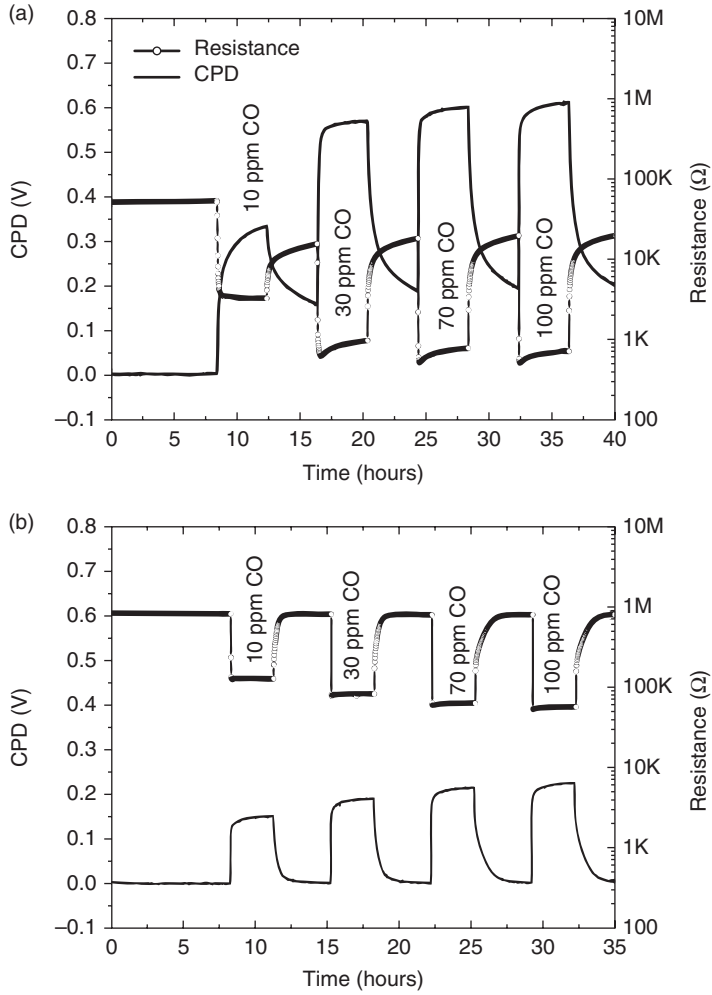

2.16 Simultaneous contact potential differences (CPD) and electrical resistance changes of an SnO_2 sensor (operated at 300°C) during exposure to four pulses of CO (10, 30, 70 and 100 ppm) in the absence of oxygen (a) and in a background of 22 000 ppm of oxygen (b).

instead of CO in the absence of oxygen (Fig. 2.17(a)) and in a background of 22000 ppm of oxygen (Fig. 2.17(b)). In the case of hydrogen, the drop in the resistance and in the work function in the absence of oxygen is much more dramatic (the material becomes almost conductive). The response and recovery times are more rapid compared with CO. In the presence of oxygen, as expected, increases in the baseline resistance and the decrease of the signals were observed.

© Woodhead Publishing Limited, 2013

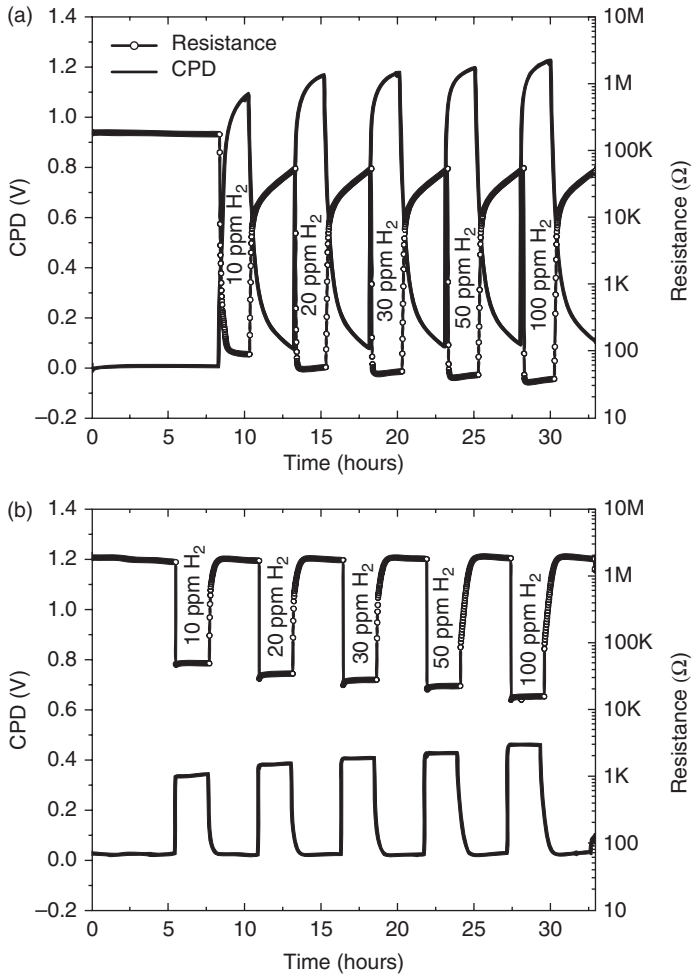

2.17 Simultaneous contact potential differences (CPD) and changes in electrical resistance of an SnO_2 sensor (operated at 300°C) during exposure to five pulses of H_2 (10, 20, 30, 50 and 100 ppm) in the absence of oxygen (a) and in a background of 22 000 ppm of oxygen (b).

Figure 2.18 presents an overview of all the results obtained by simultaneous DC-resistance and work function change measurements, including similar experiments in a background of 200 ppm of oxygen. There, the resistance and the corresponding band bending changes – extracted from the changes in the work function – are plotted semi-logarithmically. As a reference, the situation in nitrogen was chosen ($q\Delta V = 0$). The existence of three different areas with a seamless transfer in between each other is obvious. Each of

© Woodhead Publishing Limited, 2013

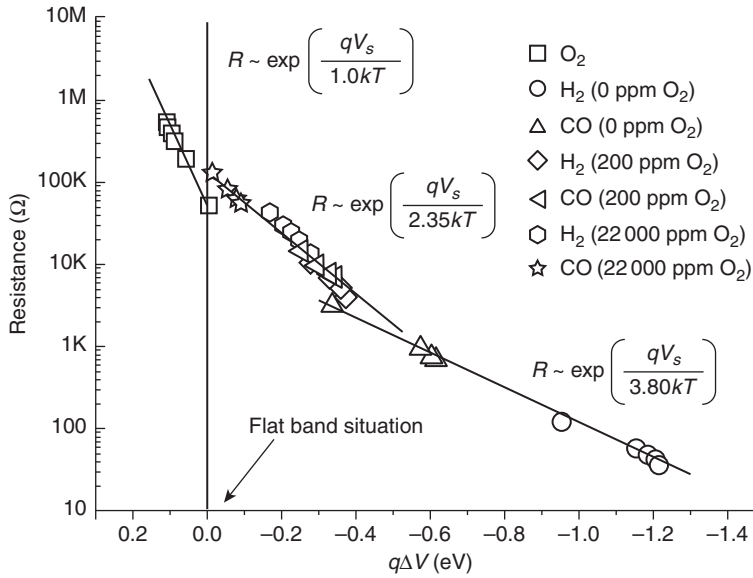

2.18 Dependence of the resistance and the corresponding band bending changes ($q\Delta V$). The flat band situation is the situation in a dry N_2 background. The three different areas/models are indicated by lines.

them can be aacurately-fitted by a proper exponential dependency of the resistance and the corresponding band bending. The calculated slopes are $((1.0 \pm 0.1)kT)^{-1}$, $((2.35 \pm 0.12)kT)^{-1}$ and $((3.80 \pm 0.05)kT)^{-1}$, respectively.

The trend observed in the experimental data is in line with the theoretical modelling presented in Section 2.3.2. The conduction moves from a mechanism controlled by the presence of the depletion layer (theoretical value: 1; experimental value: 1.0 ± 0.1) to one controlled by transport through the accumulation layer where the Boltzmann statistics are still valid (theoretical value: 2; experimental value: 2.35 ± 0.12) to the extreme case in which the Fermi level extends deep into the conduction band on the surface. It could be demonstrated in the theory (Bârsan *et al.*, 2011) that, in this area, the value should increase above 2, reflecting that the influence of the surface band bending on the resistance decreases. This decrease is also supported by the experimental/phenomenological parameter showing a value of 3.80 ± 0.05.

The latter results correlate the measured resistances with the measured changes in the work function obtained from several individual measurements in different combinations of O_2, CO and H_2. The fact that the experimental points are sitting on the same curve combining the individual conduction mechanisms indicates that the reactions involving these gases

© Woodhead Publishing Limited, 2013

have very similar effects. The upward band bending is determining a conduction mechanism dominated by the surface depletion layer; the downward band bending changes the conduction mechanism to one dominated by accumulated electrons in the surface layer. In the latter case, the deeper the conduction band edge on the surface falls below the Fermi level (higher concentrations of CO and H_2 in the absence of oxygen), the weaker the effect of the band bending on the sensor signal becomes.

The switch from one conduction model to the other takes place directly in a dry nitrogen atmosphere; this indicates that, under these conditions, a flat band situation is present (absence of active intrinsic surface traps).

The significance of the results presented is not only limited to the conditions used here. In higher oxygen backgrounds (synthetic air), one could also find resistance changes on exposure to reducing gases (high concentrations) of a few orders of magnitude, which could result in a switch between the different conduction mechanisms. This could explain why it is sometimes so difficult to describe the dependence of the full sensor response on the target gas concentration over a large concentration range with a single curve.

2.5 Conclusion and future trends

The contribution presented here highlights the importance of the conduction mechanism in the SMOX sensing layers for the performance of the corresponding gas sensors. It basically demonstrates that high surface reactivity and the considerable charge transfer processes associated with it are not sufficient for 'large' sensor signals. These depend to a large extent on the way in which the surface changes are translated into measurable changes of the electrical resistance of the sensor, which depend on the conduction mechanism.

The proposed conduction models, which are based on simple assumptions and confirmed by the experimental results, explain the weaker performance of the devices based on *p*-type materials when compared with those based on *n*-type materials. They also open up new opportunities for investigation in combination with working conditions characterization techniques.

Future work will concentrate on applying the models for more complicated and realistic operational conditions in the direction indicated by the CuO investigation presented in Section 2.4.2. The understanding of the effect of the presence of humidity in the ambient is of crucial importance, as is the understanding of the effect of surface dopants and bulk doping.

2.6 References

Bârsan, N. (1994) 'Conduction models in gas-sensing SnO_2 layers: grain-size effects and ambient atmosphere influence', *Sensors and Actuators B: Chemical*, **17**(3), 241–6, DOI: 10.1016/0925–4005(93)00873-W

© Woodhead Publishing Limited, 2013

Bârsan, N., Huebner, M. and Weimar, U. (2011) 'Conduction mechanisms in SnO_2 based polycrystalline thick film gas sensors exposed to CO and H_2 in different oxygen backgrounds', *Sensors and Actuators B: Chemical*, **157**(2), 510–17, DOI: 10.1016/j.snb.2011.05.011

Bârsan, N., Koziej, D. and Weimar, U. (2007) 'Metal oxide-based gas sensor research: how to?' *Sensors and Actuators B: Chemical*, **121**(1), 18–35, DOI: 10.1016/j.snb.2006.09.047

Bârsan, N., Simion, C., Heine, T., Pokhrel, S. and Weimar, U. (2010) 'Modeling of sensing and transduction for p-type semiconducting metal oxide based gas sensors', *Journal of Electroceramics*, **25**(1), 11–19, DOI: 10.1007/s10832–009–9583-x

Bârsan, N. and Weimar, U. (2001) 'Conduction model of metal oxide gas sensors', *Journal of Electroceramics*, **7**(3), 143–67, DOI: 10.1023/A:1014405811371

Bârsan, N. and Weimar, U. (2003) 'Understanding the fundamental principles of metal oxide based gas sensors; the example of CO sensing with SnO_2 sensors in the presence of humidity', *Journal of Physics-condensed Matter*, **15**(20), R813–R839, PII S0953–8984(03)33587–8

Bielanski, A., Deren, J. and Haber, J. (1957) 'Electric conductivity and catalytic activity of semiconducting oxide catalysts', *Nature*, **179**(4561), 668–9, DOI: 10.1038/179668a0

Brattain, W. and Bardeen, J. (1953) 'Surface properties of germanium', *Bell Telephone System Technical Publications Monograph*, **2086**, 1–41.

Cox, P. A. and Henrich, V. E. (1994) *The Surface Science of Metal Oxides*, Cambridge University Press, ISBN 0–521–44389-X

Diéguez, A., Romano-Rodríguez, A., Morante, J. R., Kappler, J., Bârsan, N. and Goepel, W. (1999) 'Nanoparticle engineering for gas sensor optimisation: improved sol-gel fabricated nanocrystalline SnO_2 thick film gas sensor for NO_2 detection by calcination, catalytic metal introduction and grinding treatments', *Sensors and Actuators B: Chemical*, **60**(2–3), 125–37, DOI: 10.1016/S0925–4005(99)00258–0

Dutraive, M. S., Lalauze, R. and Pijolat, C. (1995) 'Sintering catalytic effects and defect chemistry in polycrystalline tin dioxide', *Sensors and Actuators B: Chemical*, **26**(1–3), 38–44, DOI: 10.1016/0925–4005(94)01552-S

Heiland G (1954) 'Zum Einfluss von Wasserstoff auf die elektrische Leitfähigkeit von ZnO-Kristallen', *Zeitschrift der Physik*, **138**, 459–64, DOI: 10.1007/BF01327362

Huebner, M., Simion, C. E., Tomescu-Stanoiu, A., Pokhrel, S., Bârsan, N. and Weimar, U. (2011a) 'Influence of humidity on CO sensing with p-type CuO thick film gas sensors', *Sensors and Actuators B: Chemical*, **153**, 347–53, DOI: 10.1016/j.snb.2010.10.046

Huebner, M., Pavelko, R. G., Bârsan, N. and Weimar, U. (2011b) 'Influence of oxygen backgrounds on hydrogen sensing with SnO_2 nanomaterials', *Sensors and Actuators B: Chemical*, **154**(2), 264–9, DOI: 10.1016/j.snb.2010.01.049

Ihokura, K. and Watson, J. (1994) *Stannic Oxide Gas Sensors; Principles and Applications*, Boca Raton, CRC Press.

Kim, Y. S., Hwang, I. S., Kim, S. J., Lee, C. Y. and Lee, J. H. (2008) 'CuO nanowire gas sensors for air quality control in automotive cabin', *Sensors and Actuators B: Chemical*, **135**(1), 298–303.

© Woodhead Publishing Limited, 2013

Li, Y., Liang, J., Tao, Z. and Chen, J. (2008) 'CuO particles and plates: Synthesis and gas-sensor application', *Materials Research Bulletin*, **43**(8–9), 2380–5, DOI: 10.1016/j.materresbull.2007.07.045

Morrison, S. R. (1977) *The Chemical Physics of Surfaces*, New York, Plenum, ISBN 0–306–30960–2

Miremadi, B. K., Singh, R. C., Chen, Z., Morrison, S. R. and Colbow, K. (1994) 'Chromium oxide gas sensors for the detection of hydrogen, oxygen and nitrogen oxide', *Sensors and Actuators B: Chemical*, **21**(1), 1–4, DOI: 10.1016/0925–4005(93)01208-L

Oprea, A., Bârsan, N. and Weimar, U. (2009) 'Work function changes in gas sensitive materials: Fundamentals and applications', *Sensors and Actuators B: Chemical*, **142**(2), 470–93, DOI: 10.1016/j.snb.2009.06.043

Pokhrel, S., Simion, C. E., Quemener, V., Bârsan, N. and Weimar, U. (2008) 'Investigations of conduction mechanism in Cr_2O_3 gas sensing thick films by ac impedance spectroscopy and work function changes measurements', *Sensors and Actuators B: Chemical*, **133**(1), 78–83, DOI: 10.1016/j.snb.2008.01.054

Seiyama, T., Kato, A., Fujiishi, K. and Nagatani, M. (1962) 'A new detector for gaseous components using semiconductive thin films', *Analytical Chemistry*, **34**, 1502f, DOI: 10.1021/ac60191a001

Shimizu, Y., Nakashima, N., Hyodo, T. and Egashira, M. (2001) 'NOx sensing properties of varistor-type gas sensors consisting of micro p-n junctions', *Journal of Electroceramics*, **6**, 209–17, DOI: 10.1023/A:1011448513611

Taguchi, N. (1971) *US Patent No. 3631436*.

Weimar, U., Morante, J. R., Schweizer-Berberich, M., Bârsan, N. and Goepel, W. (1997), 'Electrode effects on gas sensing properties of nanocrystalline SnO_2 gas sensors', *In Conference Proceedings EUROSENSORS XI, Warschau (Poland), ISBN 83-908335-0-6*, 1377–80.

Williams, D. E. (1999) 'Semiconducting oxides as gas-sensitive resistors', *Sensors and Actuators B: Chemical*, **57**(1–3), 1–16, DOI: 10.1016/S0925–4005(99)00133–1

Zhang, J., Liu, J., Peng, Q., Wang, X. and Li, Y. (2006) 'Nearly monodisperse Cu2O and CuO nanospheres: Preparation and applications for sensitive gas sensors', *Chemistry of Materials*, **18**(4), 867–71, DOI: 10.1021/cm052256f

© Woodhead Publishing Limited, 2013

3

Electrode materials and electrode-oxide interfaces in semiconductor gas sensors

S. P. LEE, Kyungnam University, Korea

DOI: 10.1533/9780857098665.1.64

Abstract: The electrodes used in a gas sensor allow contact to be made to the sensing material itself so that its electrical properties can be measured. They require mechanical and chemical stability with the substrate and an optimal geometry for detecting the response of sensors to gases. This chapter provides some background to the electrode materials for semiconductor gas sensors, including the chemistry of electrode-oxide semiconductor interfaces, the transport mechanism across the junction and gas/solid interactions in the interfaces.

Key words: electrode materials, electrode-oxide interfaces in gas sensors, physics of barrier formation, carrier transport theory, gas–solid interaction.

3.1 Introduction

The surface and interface science for semiconductor gas sensors have been extensively studied since Seiyama *et al*.[1] reported that the charge carriers in the surface of an oxide semiconductor in contact with a gas varied according to the gas concentration. The electrode materials and geometry have advanced considerably in the last few decades. The physics of the energy barrier in an electrode-semiconductor interface could be significant compared with the energy barrier in the contact of a doped semiconductor. Charge transfer during the chemical reaction of gas in the electrode–semiconductor interfaces leads to a uniform Fermi level instead of energy band bending. This chemical reaction in the interfaces would affect the conductance of the sensor, as well as chemical reaction in the semiconductor surface. To design reliable semiconductor gas sensors requires the understanding of electrode-semiconductor interfaces, and control of the geometric and electronic structures of electrodes.

The aim of this chapter is to describe and review the interface chemistry and transition theory of the electrode-oxide semiconductor layer in gas sensor operation. Section 3.2 deals with criteria for selecting the metal and semiconductor materials used in the fabrication of gas sensors. The chemistry and

© Woodhead Publishing Limited, 2013

physics of barrier formation in the metal-oxide semiconductor interfacial layer are outlined in Section 3.3. The recent investigations into the charge carrier transport model, including the tunnel effect in the electrode-oxide semiconductor interface, are discussed in Section 3.4. Section 3.5 surveys research and development works that have been undertaken on gas/solid interactions in electrode-semiconductor interfaces.

3.2 Electrode materials for semiconductor gas sensors

Electrodes of semiconductor gas sensors have a function of conductor to an external circuit as a contact material. Contact resistance that is formed in the electrode-oxide semiconductors may in some cases have significant contribution on the response of the sensors. Electrode materials are also utilized as catalyst activators in the sensor operation. In special cases, for electrode materials to operate at high temperature in automotive and aerospace industries, they have to endure at temperature up to 600°C. Therefore, the electrode materials of semiconductor gas sensors are responsible for their sensitivity and selectivity to specific gases.

3.2.1 Metals and conduction

Understanding of the behavior of electrons in solids is one of the keys to understanding electrode materials. The electron theory of solids is capable of explaining the electrical, optical, magnetic, thermal and chemical properties of materials. In other words, electron theory provides important fundamentals for a technology which is often considered to be the basis for modern civilization. Electrical conduction involves the motion of charges in a material under the influence of an applied electric field. A material can be generally classified as a conductor if it contains a large number of free electrons or mobile charge carriers. In metals, due to the nature of metallic bonding, the valence electrons from the atoms form a sea of electrons that are free to move within the metal and are therefore called 'conduction electrons'. This is especially true for pure metals, where atom size and packing are uniform and nothing is present to dissipate the free motion of electrons. Alloying disrupts the uniformity of the structure and reduces the electrical conductivity. An increase in temperature also disrupts the structure due to lattice vibration, and results in a decrease in electrical conductivity.

Good electrical conductors, such as metals, are also known to be good thermal conductors. The conduction of thermal energy from higher to lower temperature regions in a metal involves the conduction electrons carrying the energy. Consequently, there is an innate relationship between the

© Woodhead Publishing Limited, 2013

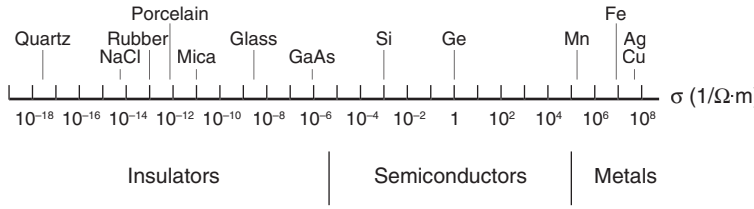

3.1 Room temperature conductivity of various materials.

electrical and thermal conductivities, which is supported by theory and experiments.[2]

The conductivity, σ, of different materials spans about 25 orders of magnitude, as shown in Fig. 3.1. This is the largest-known variation in a physical property. It is generally accepted that, in metals and alloys, the electrons – particularly the outer or 'valence electrons, – play an important role in electrical conduction. Before doing so, let us revisit some fundamental equations of physics pertaining to electrical conduction. These laws have been extracted from experimental observations.[3]

Ohm's law:

$$V = R \cdot I \qquad [3.1]$$

relates the potential difference V (in volts) with the electrical resistance R (in ohms) and the electrical current I (in amperes).

A differential form of Ohm's law is:

$$J = \sigma \cdot \varepsilon \qquad [3.2]$$

which links current density, $J = I/A$ – i.e., the current per unit area (A/m^2), with conductivity σ and electric field strength

$$\varepsilon = \frac{V}{L} \qquad [3.3]$$

The resistance of a conductor can be calculated from its physical dimensions by

$$R = \frac{L\rho}{A} \qquad [3.4]$$

where L is the length of the conductor, A is its cross-sectional area and ρ is the specific resistance, or resistivity. The conductivity is in inverse proportion to the resistivity:

$$\rho = \frac{1}{\sigma} \qquad [3.5]$$

© Woodhead Publishing Limited, 2013

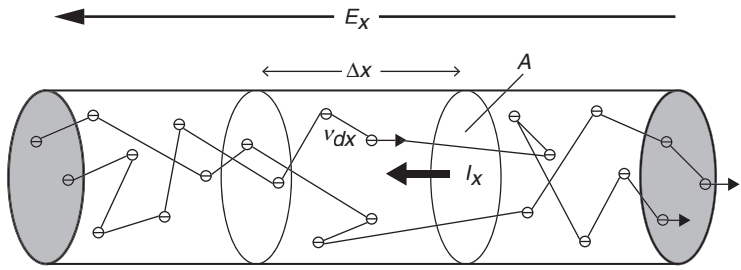

3.2 Drift of electrons in a conductor in the presence of an applied electrical field.

Figure 3.2 shows the net flow of electrons in a conductor cross-sectional area A in the presence of an applied field E_x. Notice that the direction of electron motion is opposite to that of the electric field E_x and of conventional current, because the electrons experience a coulombic force qE_x, in the x direction, due to their negative charge. We know that the conduction electrons are actually moving around randomly in the metal, but we will assume that, as a result of the application of the electric field E_x, they all acquire a net velocity in the x direction. Otherwise, there would be no net flow of charge through area A.

The average velocity of the electrons in the x direction at time t is denoted as $v_{dx}(t)$. This is called the 'drift velocity', which is the instantaneous velocity v_x in the x direction averaged over many electrons, (~10^{28} m^{-3}); that is

$$v_{dx} = \frac{1}{N}[v_{x1} + v_{x2} + v_{x3} + \cdots + v_{xN}] \qquad [3.6]$$

where v_{xi} is the x direction velocity of i^{th} electron and N is the number of conduction electrons in the metal. Suppose that n is the number of electrons per unit volume in the conductor ($n = N/V$). In time Δt, electrons move a distance $\Delta x = v_{dx}\Delta t$, so the total charge Δq crossing the area A is $enA\Delta x$. This is valid because all the electrons within distance Δx pass through A; thus, $n(A\Delta)$ is the total number of electrons crossing A in time Δt.

The current density in the x direction is:

$$J_x = \frac{\Delta q}{A\Delta t} = \frac{enAv_{dx}\Delta t}{A\Delta t} = env_{dx} \qquad [3.7]$$

This general equation relates J_x to the average velocity v_{dx} of the electrons. It must be appreciated that the average velocity may not be consistent, because the applied field, for example, may be changing: $E_x = E_x(t)$.

$$J_x(t) = env_{dx}(t) \qquad [3.8]$$

© Woodhead Publishing Limited, 2013

To relate the current density to the electric field E_x, we must examine the effect of the electric field on the motion of the electrons in the conductor. To do so, we will consider copper crystal.

The copper atom has a single valence electron in its 4*s* subshell, and this electron is loosely bound. The solid metal consists of positive ion cores, Cu+, at regular sites, in the face-centered cubic crystal structure.[2] The valence electrons detach themselves from their parents and wander around freely in the solid, forming a kind of electron cloud or gas. These mobile electrons are free to respond to an applied field, creating a current density J_x. The valence electrons in the electron gas are therefore conduction electrons.

3.2.2 Influence of electrode material

Toohey[4] summarized the study on the interaction between electrodes and sensor materials, and the influence of electrode materials in sensing behavior. The most common electrode material in practical and experimental sensors appears to be platinum, although gold and silver are occasionally used. Chemically, both are relatively inert. As pure metals they can be sputtered, or evaporation-coated, onto a substrate, and both are available in ink formulations for screen-printing. Ball- or wedge-bonding with platinum, gold, or aluminum wire allows the sensor device to be packaged in a conventional semiconductor header. A study of SnO_2 and SnO_2–Mn_2O_3 hydrogen sensors with gold, palladium and platinum electrodes showed that changing from platinum to gold could produce axis-fold increase in sensitivity and a shift in peak sensitivity temperature from ~375 to ~450°C (Fig. 3.3).[5] Also, while the pure tin dioxide sensors had linear *I–V* characteristics under all conditions, the mixed oxide devices showed nonlinearity for high hydrogen

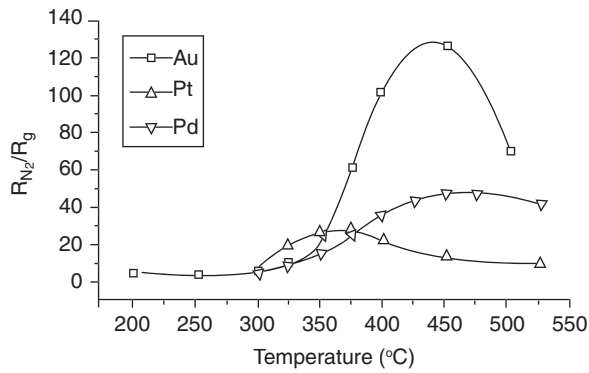

3.3 Sensitivity influence of three electrodes on a SnO_2–Mn_2O_3 (10:1) sensor for hydrogen gas.

© Woodhead Publishing Limited, 2013

concentrations with palladium or gold electrodes, but not when platinum was used. This suggests that the electrode–sensor contact was an appreciable component of the total sensor impedance.

Two different interdigitated electrode geometry configurations and two different electrode materials, Au and Pt, were analyzed with regard to their sensitivity characteristics to CO by Capone *et al*.[6] Au electrodes were not particularly stable compared with the more resistant Pt electrodes. Increasing the temperature, Au atoms diffused from the contact into a Ti layer and/or into SnO_2 bulk. Under the same geometry, sensors with Pt electrodes had shown a higher resistance compared with sensors with Au electrodes. Saukko *et al*.[7] studied the influence of electrode materials on the properties of a tin oxide-based gas sensor. The energy barrier between the electrode and the sensing semiconductor could be significant compared with the energy barriers between the semiconductor grains. Then, chemical reactions between the gas atmosphere and the metal-semiconductor interface would strongly affect the overall conductance of the sensor. They found a considerable difference in the conductance responses of the same SnO_2 thick-films to H_2 and CO when samples with Pt and Au electrodes were compared. The sample with Pt electrodes was more sensitive to H_2, whereas Au electrodes seemed to give a better response to CO.

The resistance of a tin oxide gas sensor consists of bulk resistance, surface resistance and contact resistance. The reduction of contact resistance is useful for improving the properties of oxide semiconductor gas sensors. An ohmic contact between the electrode and sensing material can reduce the contact resistance. Zhou *et al*.[8] compared conventional tin dioxide-gold electrode structures with devices in which an n^+ layer was introduced between the sensor and electrode. The use of the metal-n^+-n contact not only improved the sensitivity of the sensor to alcohol, but also the sensor selectivity to other gases did not change with the addition of an n+ layer.

Schottky-type sensors typically comprise a metal in contact with a semiconductor material, or a metal in contact with a thin insulating layer on a semiconductor material. When a metal is brought in contact with a semiconductor, the Fermi level of the semiconductor adjusts to and aligns with the Fermi level of the dominant metal by an amount equal to the difference between the two work functions of the two materials. This adjustment of the Fermi levels also occurs if there is a very thin insulating layer between the metal and the semiconductor.[9, 10] For hydrogen detection, Pd or Pt are the metals most often used in Schottky-type sensors. Hydrogen molecules adsorb onto the surface of the catalytic metal and dissociate into hydrogen atoms. Some of the atoms then diffuse through the metal film to the metal–insulator interface, where they are polarized and form a dipolar layer, which changes the metal work function and, hence, the Schottky barrier height. This change in the Schottky barrier height causes a shift in the

© Woodhead Publishing Limited, 2013

current–voltage (*I–V*) characteristics and thus the response can be measured as the change in voltage when the diode is operated at constant bias current. Various combinations of metal/semiconductor have been used for hydrogen detection. The first hydrogen-sensitive Schottky diodes were reported by Shivaraman *et al*.[11] and Steele and MacIver[12]. Both diodes used palladium as the metal and the semiconductor substrates used were n-Si and CdS, respectively. In 1979, Ito[13] had predicted that Schottky diodes consisting of similar metals and ionic semiconductors (such as SnO_2, In_2O_3, $KTaO_3$, ZnO, etc.) would also be sensitive to hydrogen. Comparative studies between Schottky diodes using Pd and Pt as the catalytic metals indicated the superior performance of Pt in terms of speed of response and sensitivity to hydrogen.[14, 15] In addition to Pd and Pt, other hydrogen-sensitive metals and alloys had been proposed including Ru,[16] Ni,[17] Au,[18] Ag,[19] IrPt and PdAg.[20] Song *et al*.[20] tested the response to hydrogen gas of AlGaN/GaN Schottky diodes with Pt, IrPt and PdAg from 200°C to 800°C. From 200°C to 300°C, PdAg diodes exhibited significantly higher sensitivity compared with Pt and IrPt diodes. Above 400°C, however, IrPt and Pt diodes showed higher sensitivity, while the sensitivity of PdAg diodes degraded due to the poor thermal stability (Fig. 3.4).[19]

One of the main disadvantages regarding the metal oxide-based gas sensors is a gradual loss of stability and reliability: the problems of ageing and drift of the sensors. Capone *et al*.[21] studied the influence of the ageing of the Ti/Au interdigitated electrical contacts on the responses of pure and Ni-, Os-, Pt- and Pd-doped SnO_2 thin films. They found that the use of Ti/Pt electrical contacts, which were more stable than Ti/Au or Ti/Pd/Au structures, could reduce one of the possible causes of ageing that produced the drift of

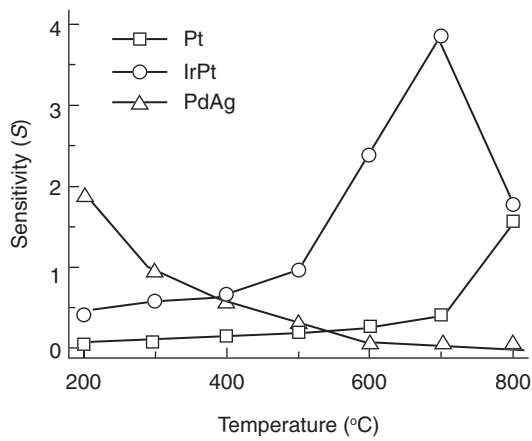

3.4 The comparison of hydrogen sensitivity in AlGaN/GaN Schottky diodes with different catalytic metals.

© Woodhead Publishing Limited, 2013

the sensor responses. SEM (scanning electron microscope) and XPS (X-ray photoelectron spectroscopy) analysis had shown the degradation of the Au layer on the fingers in an Ti/Au system due to the diffusion of gold at the high working temperature of the sensors.

3.2.3 Electrode geometry

Traditionally, solid-state gas sensors have a two-electrode configuration, where the gas sensing material is located between two metal electrodes, and a third metal electrode, which is usually platinum, is used for the heating of the sensor device. There are numerous methods by which such sensors can be realized. Figure 3.5 shows traditional gas sensor-electrode geometries. To make measurements on a semiconductor gas sensing material it is possible to use a compressed sintered or unsintered pellet with metal contacts on each face.

However, in a practical device the sensing material present is usually a thin (e.g. sputtered or vacuum-evaporated) or thick (e.g. screen-printed) film on a substrate, and almost invariably the electrodes have interdigitated geometry. The advantages of this configuration are: that it permits a large electrode-film contact area within a small overall footprint, and that both electrodes are fabricated together on the substrate before the sensing film is deposited. This provides great flexibility in the fabrication process, as it need not be compatible with the sensing material.[4]

The widths chosen for the digits and intervening spaces can affect the performance of the device. If the electrode spacing is small, the current flowing between them will sample only the region of film immediately above

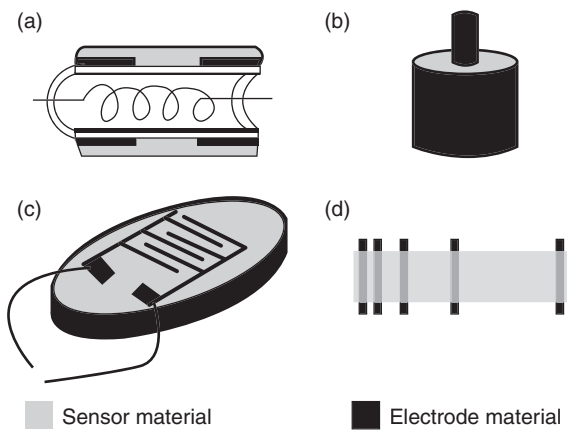

3.5 Various electrode structures used with gas sensors: (a) tube, (b) cylinder, (c) inter digit, and (d) transmission line.[4]

© Woodhead Publishing Limited, 2013

them; if the spacing is large, the current will tend to spread out 'vertically' throughout the film, and so sample a larger proportion of it.[22] Also, the sensor–electrode interface may itself make a significant contribution to the gas-sensitive resistance of the device. Varying the electrode width–electrode gap ratio will vary the relative contributions of the 'interface' and 'pure film' resistances.

In particular, Jain *et al.*[23] have studied the influence of electrode geometry and position in an attempt to improve sensor sensitivity and selectivity. They compare the results of placing electrodes high up in the sensor face and further down in the active layer–substrate interface; they also studied the effect of interlacing the electrodes. Vilanova *et al.*[24] studied the influence of electrode position, electrode gap and active layer thickness for high, medium and poor catalytic activity sensor/gas pairs. The purely geometric effect arises because the film conductance does not change instantly or uniformly when the gas ambient changes: the gas must diffuse through the film, reacting with the particle surfaces as it does so. This leads to variations in local film conductance. A numerical simulation indicated, for example, that where a sensor is highly sensitive to the test gas, sensitivity increased with electrode spacing when the electrodes were underneath the film (Fig. 3.6), but decreased with spacing when the electrodes were deposited on top of the film.[24] If electrode spacing was decreased to less than the film thickness,

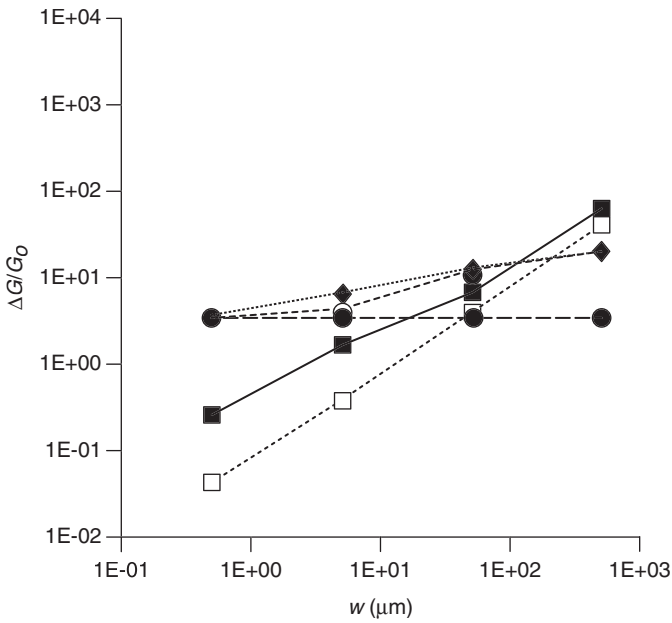

3.6 Sensitivity vs electrode gap (*w*) for electrodes placed at the bottom.[24]

© Woodhead Publishing Limited, 2013

it was possible to detect a less-reactive gas in the presence of a gas that was more reactive.

Gardner[25] derived expressions which defined the response of a pair of planar conductometric gas sensors according to the electrode thickness and an electrode gap. The steady-state conductance in air, G_o, of a homogeneous film of conductivity, σ_o, and thickness, L, lying on semi-infinite electrodes can be found by integrating the current density over a closed surface, whence:

$$G_o = \frac{\sigma_o b}{\pi} \ln \left[\frac{1 + \left(1 + \frac{w^2}{L^2}\right)^{1/2}}{\frac{w}{2L}} \right] \qquad [3.9]$$

where w is the separation of the electrodes and b is the length of the electrodes. It is assumed that the edge effects can be ignored ($b \gg w$). When a gas of concentration C_0 is introduced, it can diffuse into the porous film and react at sites dispersed uniformly throughout the film. These reaction sites modify the local conductivity of the film according to a function that depends on the local gas concentration C_x. The steady-state response R (fractional change in conductance) of the sensor by integrating the concentration-dependent current density can be given by:

$$R = \frac{G(C_x) - G_o}{G_o \pi} = \frac{\sigma(C_x) - \sigma_o}{\sigma_o} = \frac{\int_{x/L=0}^{x/L=1} F(C_x) \left[\left(\frac{x}{L}\right)^2 + \left(\frac{w}{2L}\right)^2 \right]^{1/2} d\left(\frac{x}{L}\right)}{\ln \left\{ \left[1 + \left(1 + \frac{w^2}{4L^2}\right)^{1/2} \right] \Big/ \left(\frac{w}{2L}\right) \right\}} \qquad [3.10]$$

In the case of the narrow-gap sensor, the base-line conductance G_{on} and the response of the narrow-gap sensor R_n become:

$$G_{on} = \frac{\sigma_o b}{\pi} \ln \left(\frac{4L}{w_n} \right)$$

where $w_n/L \ll 1$

$$R_n = \frac{\int_{x/L=0}^{x/L=1} F(C_x) \left[\left(\frac{x}{L}\right)^2 + \left(\frac{w_n}{2L}\right)^2 \right]^{\frac{1}{2}} d\left(\frac{x}{L}\right)}{\ln \left(\frac{4L}{w_n} \right)} \qquad [3.11]$$

© Woodhead Publishing Limited, 2013

In the case of the wide-gap sensor, the base-line conductance G_{ow} can be simplified by using the first term in Maclaurin's expansion of the log to give:

$$G_{ow} \approx \frac{2}{\pi}\frac{\sigma_o bL}{\pi w_w} \qquad [3.12]$$

The sensing electrodes behave like a parallel-plate structure. As the electric field inside the film is nearly constant and independent of the distance x, the response of the wide-gap sensor R_w can be reduced to:

$$R_w \approx \int_{x/L=0}^{x/L=1} F(C_x)d\left(\frac{x}{L}\right) \qquad [3.13]$$

Under a uniform gas profile (*type I*), the steady-state response function is given by the power law:

$$F_1(C_o) = k_2 C_o^n \qquad 0 < n < 1 \qquad [3.14]$$

where C_o is the external gas concentration, k_2 is the gas-sensitivity parameter for a semiconducting oxide material, and exponent n normally lies between 0.3 and 0.9. The steady-state response of this type of sensor pair is straightforward as in the concentration profile (Fig. 3.7a). When a semiconducting oxide material is doped with catalyst of high activity (*moving-boundary gas profile, type II*), it is probable that the gas entering the film is rapidly consumed and so does not penetrate all the way into the film (Fig. 3.7b).[25] The response function can be written as:

$$F_{II}(C_x) = \begin{cases} k_2 C_o^n & x_b \le x \le L \\ 0 & 0 \le x < x_b \end{cases} \qquad [3.15]$$

The response of the wide-gap sensor becomes simply the fraction of the film penetrated by the gas multiplied by the isotherm, hence:

$$R_w \approx k_2 C_o^n \int_{x_b/L}^{1} d\left(\frac{x}{L}\right) = k_2 C_o^n \left(1 - \frac{x_b}{L}\right) \qquad [3.16]$$

The response of the narrow-gap sensor can also be found from Equations [3.11] and [3.15]:

$$R_n \approx k_2 C_o^n \frac{\ln\left\{2\Big/\left[\frac{x_b}{L} + \left(\frac{x_b^2}{L^2} + \frac{{w_n}^2}{4L^2}\right)\frac{1}{2}\right]\right\}}{\ln\left(\frac{4L}{w_n}\right)} \qquad [3.17]$$

© Woodhead Publishing Limited, 2013

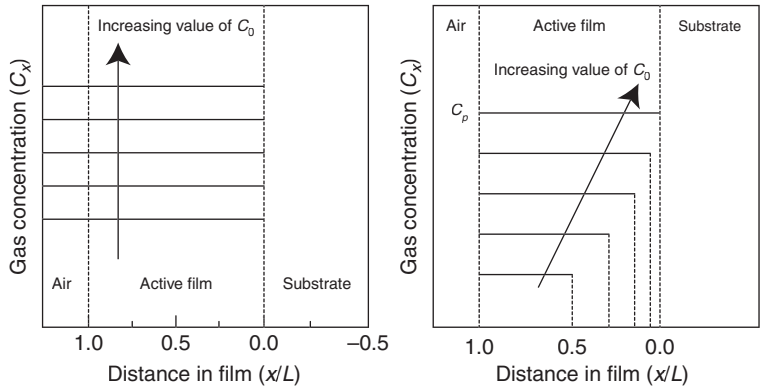

3.7 Gas profile in the active film: (a) uniform and (b) moving boundary.

Hoefer *et al*.[26, 27] used an array of electrodes of differing width and separation to examine contact resistance effects in tin dioxide sensors. The transmission-line method they used involves measuring the total resistance of a semiconductor sample as a function of electrode separation. It was shown that the modified sheet resistance displayed greater sensitivity to CO and NO_2 than either the sheet resistance itself, or the contact resistance. In this case, wide electrodes with narrow spacing would produce the most sensitive detection. An array of electrodes varying in width and spacing, but all using the same sensing material, could be used to resolve a mixture of CO, CH_4, NO_2 and water vapor into separate measurements of each component by first determining the relative sensitivity of the total resistance of each electrode pair to the individual gases.[28]

On the other hand, electrodes with different geometry were applied to the semiconductor gas sensors. Korotcenkov[29] reviewed practical aspects in the design of one-electrode semiconductor gas sensors. Figure 3.8 shows standard two-electrode and one-electrode sensors schematically in planar view. The schematic electrical circuits of these sensors are also shown in Fig. 3.8, where R_{Pt} is a coil resistance of Pt spiral, R_{MeO} is the inter-turn resistance of metal-oxide ceramics and R_S is a total resistance of the sensor. The physical configuration of ceramics type and thin film type one-electrode semiconductor gas sensors are shown in Figs 3.9 and 3.10.[29]

In the one-electrode sensors, the metal resistor simultaneously acts as the heater and the measuring electrode. The operation principle of the one-electrode sensor is based on the shunting of the Pt electrode by the semiconductor oxide, coating the metal spiral or strip. Typically, one-electrode sensors are incorporated in a Wheatstone Bridge circuit, or in the simplest electrical format; the change of voltage drop at the sensor is determined. For

© Woodhead Publishing Limited, 2013

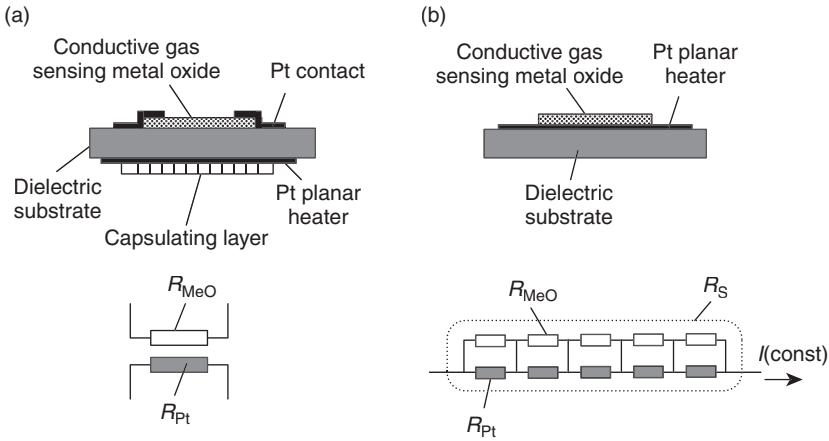

3.8 Planar constructions of (a) standard (two-electrode), and (b) one-electrode semiconductor gas sensors.

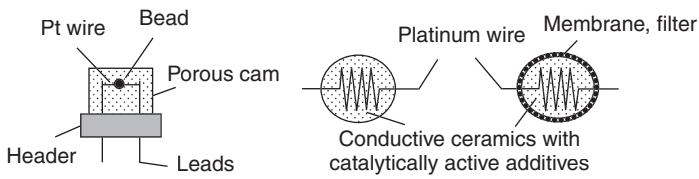

3.9 Schematic view of ceramics type, one-electrode, semiconductor gas sensor.

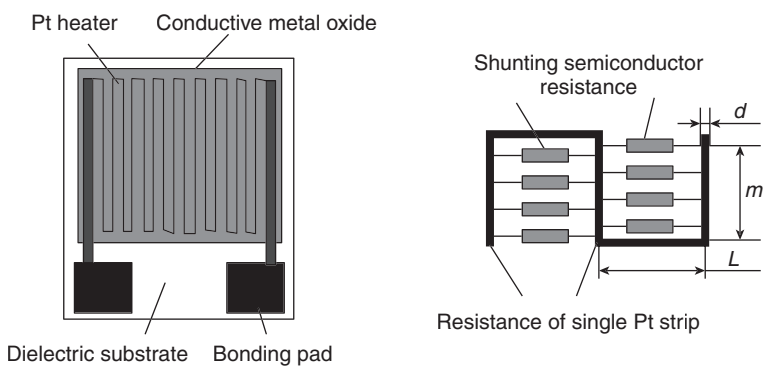

3.10 Schematic view of thin film type, one-electrode, semiconductor gas sensor and its circuit.

© Woodhead Publishing Limited, 2013

the design of one-electrode semiconductor sensors, SnO_2[30–33] and In_2O_3[31,34,35] have mainly been used. Taking into account the design features of one-electrode sensors, the impedance matching between metal oxide and Pt strip resistance (R(MeO) and R(Pt)) may be achieved through:

(1) the control of the diameter of the Pt wire in ceramic type sensors, and Pt strip thickness and width in planar-type sensors (Fig. 3.10);
(2) the control of the distance between Pt turns in ceramic sensors and Pt strips in planar sensors;
(3) the control of metal-oxide thickness;
(4) the control of metal-oxide bulk resistance.

It is important to note that for oxidizing and reducing gas sensors, the requirements on the film resistance values will vary in order to achieve an optimal gas response.

Faglia *et al*.[36] used four probe array analysis in the gas detection system to distinguish between the grain contribution and the contact contribution. This suggested that the contact contribution was very important for CO detection, while the material contributes to CH_4 detection in tin oxide gas sensors. For four-electrode semiconductor sensor design, $CrTiO_3$ (CTO)[37] and WO_3/TiO_2[38] have mainly been used.

It is clear that the material and geometry of the electrodes can influence gas sensor behavior. Many researchers are investigating the fabrication of gas sensors using nanoparticulate materials as the sensitive layer. While it is possible to use 'normal' sized electrodes with widths and separations of several microns for these devices, it is of interest to examine the changes in response which are obtained when nanoelectrodes are used; i.e. contacts of comparable dimensions to a single particle – around 5 nm. Potential advantages of nanoelectrodes include:[4]

(i) the possibility of addressing single nanodots;
(ii) the ability to vary the relative contributions of electrode–dot and dot–dot contacts to the total sensor resistance;
(iii) where a nanodot film consists of conducting and nonconducting particles, decreasing the electrode size could increase sensitivity by around an order of magnitude or more by 'softening' the percolation threshold;[39]
(iv) small electrode systems use less sensor chip real estate; however, producing structures of these sizes is problematic.

3.2.4 Properties of paste materials for electrodes

To complete the general discussion of conductors, this section will summarize the properties of some of the most widely-used conductor inks. It is not

© Woodhead Publishing Limited, 2013

intended to list the properties of specific paste formulations as this type of information is readily obtainable from manufacturers' literature and inks are constantly being superseded by improved compositions.[40]

Silver

Silver inks were probably the first thick film inks to be developed and were used mainly in the construction of capacitors. There are several points in favor of silver as a conductive ink. Not only is it the least expensive metal which is compatible with the normal thick film process, but it also may be made to have good bond strength and high conductivity, and is easily wetted by tin-lead solder. Although its leach resistance to this solder is poor, this is easily overcome by slight modification of the solder. Silver compositions are also compatible with several resistor and dielectric systems. The major disadvantage of silver is its strong tendency to migrate over the surface of insulants and resistors when subjected to electrical fields under conditions of high humidity; this may lead to the lowering of resistance or complete short circuits in other thick film components.

Gold

Gold inks may be constituted to have high conductivity, similar to that of silver, and produce films which are stable under all normal service conditions. They are compatible with most dielectric and some resistor systems, although they are not generally suitable for terminating the palladium/silver type of resistors. The main disadvantages of gold are its high cost and its unsuitability for solder joining. Tin-lead solders are unsuitable for use with gold conductors and cannot easily be modified, as in the case of silver, although special solders such as gold–tin alloys may be used.

Gold is normally used in circuits where high conductivity and reliability are required and in applications where silicon devices are to be eutectically bonded, or where ultrasonic bonds have to be made, to gold or aluminum wires. A further use of gold is in the closure of hermetic packages, where lids may be sealed to gold metallization using a solder alloy consisting of gold (80%)/tin (20%). The advantage of gold in this situation is that, in a neutral atmosphere, the solder seal may be made without the use of flux.

Platinum

Platinum inks are the most expensive thick film conductive ink, but are occasionally used where extreme resistance to molten solder and to bold strength degradation by solder is required.

© Woodhead Publishing Limited, 2013

Palladium–silver

Palladium–silver alloys are perhaps the most widely-used conductor compositions. They are less expensive than gold alloys, are compatible with most dielectric and resistor systems, and are suitable for ultrasonic wire bonding. The sheet resistivity is typically in the region of 0.01 to 0.04 Ω/sq and, although this figure is considerably higher than the resistivity of pure metal conductors, it is lower than the figures for gold alloy conductors.

The addition of palladium to silver greatly reduces the rate of dissolution of the metal in molten solder. Increasing the palladium content thus provides greater leach resistance, but at the expense of solderability and conductivity. It also increases the cost. It is common practice, therefore, for ink manufacturers to produce a range of palladium–silver alloys of different palladium content so that the best compromise may be chosen for any particular application.

Palladium–silver pastes can be fired with excellent initial bond strength to the substrate, but this rapidly degrades if the circuits are stored at elevated temperatures (above 70°C) when the conductors are tinned. A further disadvantage is the possibility of silver migration under conditions of high humidity. The rate of migration is, however, considerably reduced by the presence of the palladium.

Platinum–silver

Increasing world demand for palladium and wild fluctuations in its price have recently persuaded some ink manufacturers to add platinum–silver alloys to their range of conductors as alternatives to palladium–silver. Sheet resistance range from 0.01 to 0.04 Ω/sq with increasing platinum content, and in this and most other respects the two ranges are found to be generally equivalent. Platinum–silvers are not, however, recommended for hybrid applications involving ultrasonic aluminum wire bonding.

Platinum–gold

Platinum–gold systems possess many of the advantages of both gold and platinum. They have excellent solderability combined with outstanding resistance to solder leaching, and are also suitable for both wire and die bonding. They are compatible with most other thick film materials and, whilst the initial bond strength tends to be lower than that of palladium–silver alloys, they have much greater resistance to solder bond strength degradation. The chief disadvantages lie in their high cost and rather high electrical resistivity (0.08–0.1 Ω/sq).

© Woodhead Publishing Limited, 2013

Palladium–gold

This alloy system has generally similar properties to platinum–gold and is less costly. The solder leach resistance and solder ageing are, however, inferior to the more expensive material. Resistivity is of the order of 0.04–0.10 Ω/sq.

3.3 Electrode-oxide semiconductor interfaces

The physical understanding of the electrode-oxide semiconductor interfaces are described in this section. Interfaces of this type occur in oxide semiconductor gas sensors and metal-insulator-semiconductors (MIS) devices. When a metal is contacted with oxide, the potential barrier arises from the separation of changes of the metal-oxide interface as well as the metal-semiconductor contacts.

The first significant step towards understanding the mechanism of the electrode-oxide semiconductor is given in an ideal case contact. Another advance in our understanding of the electrode-oxide semiconductor junction is concerned with contacts with surface states, and interfacial layer and an image force.

3.3.1 Ideal contact of metal and oxide semiconductor

The potential barrier which forms when a metal is contacted with an oxide semiconductor arises from the separation of charges at the metal-oxide semiconductor interface, such that a high-resistance region devoid of mobile carriers is created in the oxide semiconductor. This is similar with the Schottky–Mott model that explains the barrier height of metal-semiconductor contact.[41] According to this model, the barrier results from the difference in the work functions of the two substances. The energy-band diagrams in Fig. 3.11 illustrate the process of barrier formation. Figure 3.11(a) shows the electron energy-band diagram of a metal of work function $\Phi_m (= e\phi_m)$ and an *n*-type semiconductor of work function $\Phi_s (= e\phi_s)$ which is smaller than Φ_m. The work function of a metal is defined as the amount of energy required to raise an electron from the Fermi level to the vacuum level. The vacuum level is the energy level of an electron just outside the metal with zero kinetic energy and is the reference level in Fig. 3.11(a). The work function Φ_m has a volume contribution due to the periodic potential of the crystal lattice and a surface contribution due to the possible existence of a dipole layer at the surface. The work function Φ_s of the semiconductor is defined similarly and is a variable quantity because the Fermi level in the semiconductor varies with the doping. An important surface parameter which does not depend on doping is the electron affinity χ, defined as the energy difference of an electron

© Woodhead Publishing Limited, 2013

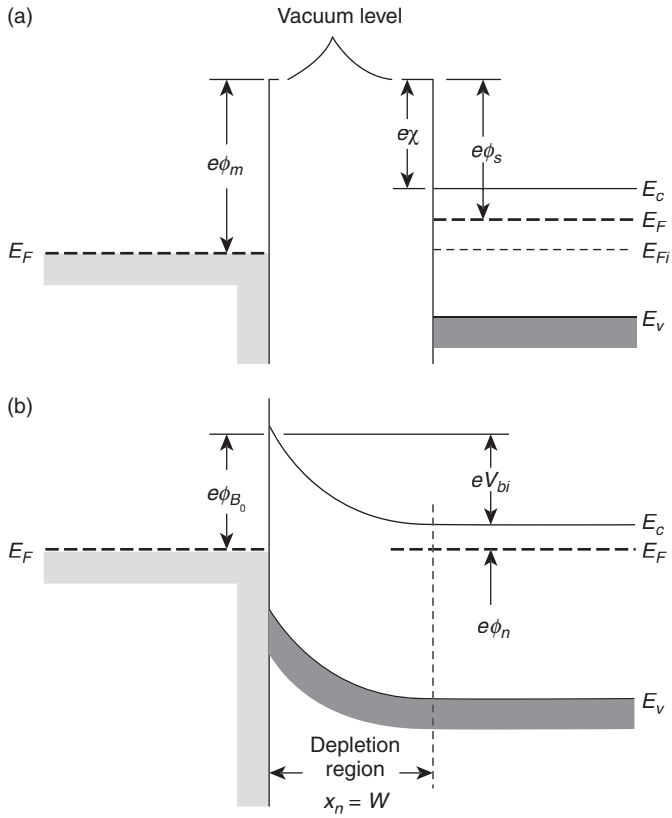

3.11 Energy-band diagram of metal contact to *n*-type semiconductor with $\Phi_m > \Phi_s$; (a) neutral materials separated from each other, and (b) thermal equilibrium situation after the contact has been made. x_n is the penetration of the depletion region into the *n* material, *W* is the width of the depletion region and E_{Fi} is the intrinsic Fermi level.

between the vacuum level and the lower edge of the conduction band. The work functions Φ_m and Φ_s and the electron affinity χ are usually expressed in electron volts (eV). Note that the semiconductor shown in Fig. 3.11(a) does not contain any charges at the surface, so the band structure of the surface is the same as that of the bulk and there is no band bending.

Figure 3.11(b) shows the energy-band diagram after the contact is made and equilibrium has been reached. When the two substances are brought into intimate contact, electrons from the conduction band of the semiconductor, which have higher energy than the metal electrons, flow into the metal till the Fermi level on the two sides is brought into coincidence. As the electrons move out of the semiconductor into the metal, the free electron concentration in the semiconductor region near the boundary decreases.

© Woodhead Publishing Limited, 2013

Since the separation between the conduction band edge E_c and Fermi level E_F increases with decreasing electron concentration and, in thermal equilibrium, E_F remains constant throughout, the conduction band edge E_c bends up, as shown in Fig. 3.11(b). The conduction band electrons which cross over into the metal leave a positive charge of ionized donors behind, so the semiconductor region near the metal becomes depleted of mobile electrons. Thus, a positive charge is established on the semiconductor side of the interface and the electrons, which cross over into the metal form a thin sheet of negative charge contained within the Thomas–Fermi screening distance from the interface (≈ 0.5Å). Consequently, an electrical field is established from the semiconductor to the metal, as shown in Fig. 3.11(b). Note that the width of the space charge layer in the semiconductor is appreciable because the donor concentration in the semiconductor is several orders of magnitude smaller than the electron concentration in the metal.[41]

Let us now investigate how much the energy bands in the semiconductor will bend upward. It should be evident that, since the band gap of the semiconductor is not changed by making contact with the metal, the valence band edge E_v will move up parallel to the conduction band edge E_c. Also, the vacuum level in the semiconductor will follow the same variations as E_c. This is because the electron affinity of the semiconductor is assumed to remain unchanged even after the metal contact is made. Thus, for a metal-semiconductor system in thermal equilibrium, the important point which determines the barrier height is that the vacuum level must remain continuous across the transition region. Hence, the vacuum level from the semiconductor side must approach the vacuum level on the metal side gradually to preserve the continuity. The amount of band bending, then, is equal to the difference between the two vacuum levels, which is equal to the difference between the two work functions. This difference is given by $eV_{bi} = (\Phi_m - \Phi_s)$, where V_{bi} is expressed in volts and is known as 'contact potential difference', or the built-in potential of the junction: eV_{bi} obviously is the potential barrier which an electron moving from the semiconductor into the metal has to surmount. However, the barrier looking from the metal towards the semiconductor is different and is given by:[41, 42]

$$\Phi_{B0} = (\Phi_m - \chi) \qquad [3.18]$$

Since

$$\Phi_s = \chi + \Phi_n$$

we have

$$eV_{bi} = \Phi_{B0} - \Phi_n \qquad [3.19]$$

© Woodhead Publishing Limited, 2013

where $\Phi_n = (E_c - E_F)$ represents the penetration of the Fermi level in the band gap of the semiconductor and e is the electronic charge. Equation [3.18] was stated by Schottky[43] and, independently, by Mott[44].

The exact shape of the potential barrier can be calculated from the charge distribution within the space charge layer. In most cases, the height ϕ_{B0} of the potential barrier is orders of magnitude larger than the thermal voltage, kT/e, and the space charge region in the semiconductor becomes a high-resistivity depletion region devoid of mobile carriers. The shape of the barrier is then determined from the donor distribution in the semiconductor. Schottky assumed the semiconductor to be uniformly doped up to the metal interface, which gives rise to a uniform charge density in the depletion region. The electrical field strength for this constant space charge rises linearly with the distance from the edge of the space charge layer and the resulting parabolic barrier is known as a 'Schottky barrier'.[43] Mott[44] assumed a thin layer of semiconductor, devoid of any charge, sandwiched between a uniformly doped semiconductor and the metal. The electrical field strength in the thin region is constant and the potential increases linearly across this region. This type of barrier is known as the 'Mott barrier'. The Mott barrier is encountered in situation where a thin layer of low-doped, nearly intrinsic semiconductor is interposed between a metal and a heavily-doped semiconductor.

The above description applies only to an n-type semiconductor whose work function is less than the metal work function Φ_m. The electron energy-band diagrams for an n-type semiconductor with $\Phi_m < \Phi_s$ are shown in Fig. 3.12. Figure 3.12(a) shows the energy bands for separated materials. After the contact is made, electrons flow from the metal into the conduction band of the semiconductor, leaving behind a positive charge on the metal and causing an accumulation of electrons on the semiconductor side of the boundary. When equilibrium is reached, the Fermi level in the semiconductor is raised by an amount $(\Phi_s - \Phi_m)$, as shown in Fig. 3.12(b). The accumulation layer charge in the semiconductor is confined to a thickness of the order of Debye length and is, essentially, a surface charge. Since the concentration of electrons in the metal is very large, the positive charge on the metal side is also a surface charge contained within a distance of about 0.5 Å from the metal-semiconductor interface. It is clear that no depletion region is formed in the semiconductor and there is no potential barrier for the electron flow either from the semiconductor towards the metal, or in the opposite direction. The electron concentration is increased in the region near the interface and the region of highest resistivity in the system is the bulk semiconductor region.

The foregoing discussion has shown that, in case of an n-type semiconductor, a metal-semiconductor contact is rectifying if $\Phi_m > \Phi_s$ and is non-rectifying if $\Phi_m < \Phi_s$. The opposite is true for a metal p-type semiconductor contact. The work functions of various metals and semiconductors are given in Table 3.1.[41, 44–48]

© Woodhead Publishing Limited, 2013

Table 3.1 Work functions of some metals and semiconductors

Material	Work function, $\Phi(eV)$	Material	Work function, $\Phi(eV)$
Ag	4.26	Pt	5.65
Al	4.28	Ti	4.33
Au	5.10	W	4.55
Cr	4.50	SnO_2[44, 45]	4.04~4.53
Ni	5.15	TiO_2[46]	Nanocrystalline: 5.23
Pd	5.12		Single crystal: 4.83
		ZnO[47]	7.30

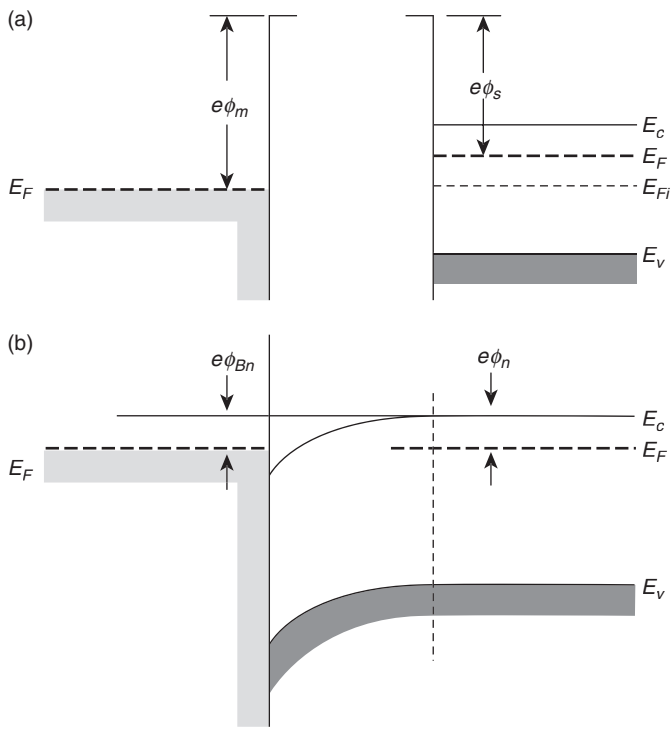

3.12 Energy-band diagram of metal contact to *n*-type semiconductor with $\Phi_m < \Phi_s$: (a) neutral materials separated from each other and (b) contact under thermal equilibrium.[41]

3.3.2 Contacts with surface states and an interfacial layer

The periodicity of the crystal lattice terminates at the surface of a semiconductor. In a crystal, the surface atoms only have neighbors on the semiconductor side; on the vacuum side, there are no neighbors with whom the surface atoms can make bonds. Thus, each of the surface atoms has one

© Woodhead Publishing Limited, 2013

broken bond in which only one electron is present. The broken bonds are known as 'dangling bonds'. Dangling bonds give rise to localized energy states at the surface of the semiconductor with energy levels lying in the forbidden gap. These surface states are usually continuously distributed in the band gap and are characterized by a neutral level Φ_0. The position of this neutral level is such that, when there is no band bending in the semiconductor, the states are occupied by electrons up to Φ_0, making the surface electrically neutral. The states below Φ_0 are donor-like because they are neutral when occupied and are positive when empty. Obviously, the states above Φ_0 behave as acceptors. On the clean surface of the semiconductor, the density of surface states equals the density of surface atoms. Adsorbed layers of foreign atoms may considerably reduce this density by completing the broken bonds. The surface states modify the charge in the depletion region and, thus, affect the barrier height. Figure 3.13(a) shows the electron energy-band diagram of an *n*-type semiconductor under flat band condition. When a metal is now brought in contact with the semiconductor and equilibrium is reached, the Fermi level in the semiconductor must change by an amount equal to the contact potential by exchanging charge with the metal. If the density of surface states at the semiconductor surface is considerable, then the charge exchange takes place largely between the metal and the surface states, and the space charge in the semiconductor remains almost unaffected. As a result, the barrier height in Fig. 3.13(b) becomes independent of the metal work function. In this case, the barrier height is said to be pinned by surface states.[49] Considering a continuum of interface states, a phenomenological formula for the Schottky barrier height can be formulated.[50,51]

$$\Phi_{B0} = S(s)\chi + \Phi_0(s) \qquad [3.20]$$

where $\Phi_0(s)$ represents the contribution of the surface states and the interface index $S(s) = d\,\Phi_{B0}/d\chi$ gives the dependence of the barrier height on the metal electro-negativity.

The interface between metals and nonmetals has been classified into four broad types according to the resulting interfacial atomic configuration:[52]

(1) The nonmetal is an insulator (or a semiconductor) and the metal is physisorbed on its surface.
(2) The nonmetal is a highly polarizable semiconductor and the metal makes a weak chemical bond, but does not react with it to form a bulk compound.
(3) The highly polarizable semiconductor reacts with the metal and forms one or more chemical compounds.
(4) A thin film of oxide is left during the surface preparation of a highly polarizable semiconductor, which prevents an intimate contact between the metal and the conductor. The film is referred to as an 'interfacial layer'.

© Woodhead Publishing Limited, 2013

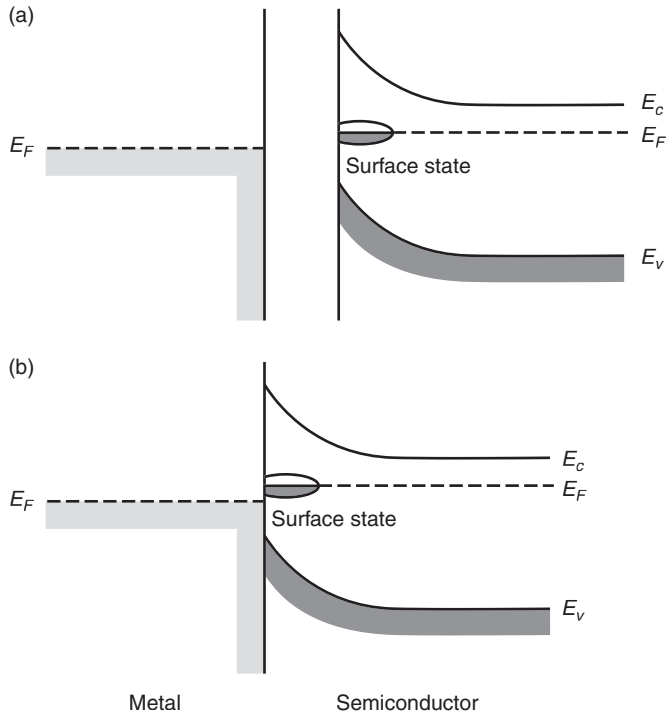

3.13 Energy-band diagram of the band bending interface in the presence of surface states for a metal/*n*-type semiconductor: (a) under flat band condition and (b) after contact formation.

The type (1) interface is an ideal Schottky barrier contact in which the barrier height varies directly with the metal work function in accordance with Equation [3.18]. The type (2) interface approximates to a Bardeen barrier,[49] provided that the surface states are assumed to be spaced inside the semiconductor so as to allow a potential drop across this region. In the clean contacts of this type, one would expect the barrier height to show a weak dependence on Φ_m. The type (3) interface represents a case of strong chemical bonding between the metal and the semiconductor and, hence, we would expect the barrier height to depend on some quantity related to chemical or metallurgical reactions at the interface. The type (4) contact is the one most frequently encountered in actual metal-semiconductor devices.

In most metal-semiconductor contacts, the semiconductor surface before metal deposition is prepared by chemical cleaning and a thin insulating oxide layer is invariably left on the surface of the semiconductor. The thickness of this interfacial layer depends on the method of surface preparation and, for a good Schottky contact, must be less than about 20Å. The energy-band diagram of a contact with an interfacial oxide layer is

© Woodhead Publishing Limited, 2013

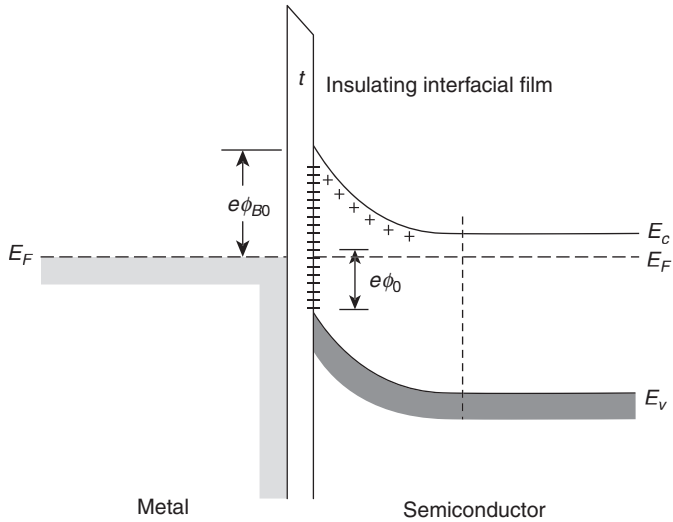

3.14 Electron energy-band diagram of a metal-semiconductor contact with surface states and interfacial layer.

shown in Fig. 3.14. In this figure, potential drops linearly across the interfacial oxide layer because this layer is assumed to be an ideal insulator devoid of any charge. It has also been assumed that the lower edge of the conduction band of the insulator lies below the vacuum level. When the interfacial layer is sufficiently thin (<30Å), the potential drop across it is negligibly small compared with that in the semiconductor depletion region. Such a thin layer is transparent to the electrons as the electrons can tunnel through it in either direction. For these reasons, the barrier height Φ_{B0} and the contact potential difference V_{bi} remain almost unaffected by the presence of a thin interfacial layer.

In this state, the charge in the depletion region vanishes and the charge on the metal side is balanced by the charge in the interface states on the semiconductor side. This flat band barrier height is given by:[53]

$$\Phi^*_{B0} = C_1(\Phi_m - \chi) + (1 - C_1)(E_g - \Phi_0) = C_1\Phi_m + C_2 \qquad [3.21]$$

where

$$C_1 = \frac{\in_i}{\in_i + e^2 t D_s}$$

Here, $\in_i = \in_r \in_0$ is the permittivity of the insulating layer, t is its thickness, e is the electronic charge and D_s is the density of interface states per unit area per eV. The position of the neutral level Φ_0 is measured from the top of

© Woodhead Publishing Limited, 2013

the valence band. From Equation [3.21] it is seen that as D_s tends to zero, C_1 becomes unity and Φ^*_{B0} tends to the Schottky limit of Equation [3.18].

The expression for the flat band barrier height is modified when there is a charge present in the interfacial oxide layer. Considering the case of the *n*-type semiconductor, if there is a fixed charge Q_{ox} per unit area within the oxide layer then Equation [3.21] is replaced by:[54]

$$\Phi^*_{B0} = C_1(\Phi_m - \chi) + (1 - C_1)(E_g - \Phi_0) - \frac{C_1 t Q_{ox}}{\in i} \qquad [3.22]$$

3.3.3 Image force effects on the barrier height

The other effect which makes the barrier height depend on the electrical field in the depletion region is the lowering of the image force barrier. This is not dependent on the presence of the interfacial oxide layer and occurs even when such a layer is absent. Lowering of the image force barrier can be understood by referring to Fig. 3.15. When an electron is at a distance x from the metal, there exists an electrical field perpendicular to the metal surface. This field may be calculated by assuming a hypothetical positive image charge e located at a distance $(-x)$ inside the metal. The force of attraction F between the electron and its image charge is $e^2/4\pi\in_d(2x)^2$, and the electron has a negative potential energy $F \bullet x = -e^2/16\pi\in_d x$ relative to that of an electron at infinity, as shown by the dashed curve in Fig. 3.15. This potential energy must be added to the barrier energy $-eE_x$ to obtain the total energy of the electron. It can be seen from Fig. 3.15 that the maximum in energy occurs at a distance x_m from the metal surface, and it can also be shown that the magnitude $\Delta\Phi_{B0}$ $(= e\Delta\phi_{B0})$ of the barrier lowering is given by:[55]

$$\Delta\Phi_{B0} = \left[\frac{s^B N_d}{8\pi^2 \in_d^2 \in_s}(V_{bi} - V)\right]^{1/2} \qquad [3.23]$$

Here, N_d is the donor concentration in the semiconductor and V is the applied voltage. The image force permittivity $\in_d$ may be different from the static permittivity $\in_s$ of the semiconductor. This is because the electron approaches the barrier with the thermal velocity ($\approx 10^7$ cm/sec) and, if its transit time through the barrier region is small compared with the dielectric relaxation time, then the semiconductor does not become fully polarized. However, it is found in practical situations that the electron transit time through the barrier region is sufficiently large to justify $\in_d = \in_s$.

The image force lowering of the barrier results from the field produced by an electron and will be absent when there is no electron present in the

© Woodhead Publishing Limited, 2013

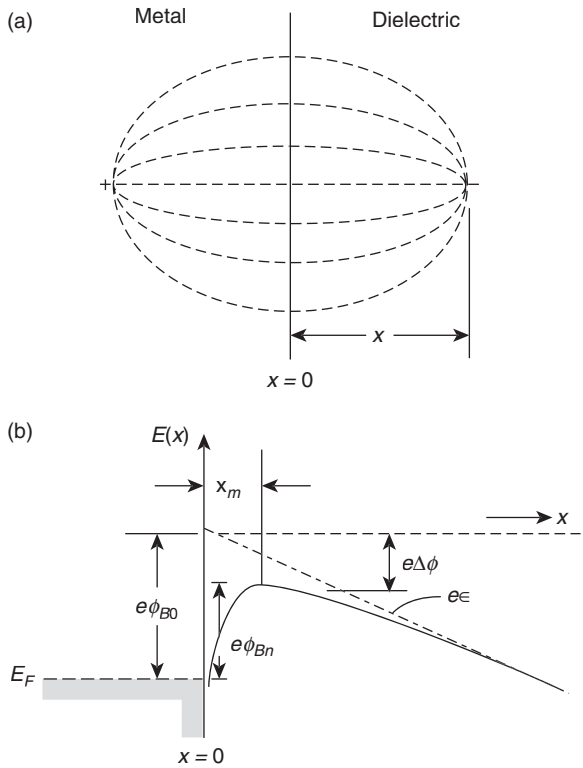

3.15 (a) Image charge and electric field lines at a metal-dielectric interface and (b) electron energy diagram showing the image force lowering of the barrier.[55]

semiconductor conduction band near the top of the barrier. Hence, when the barrier height is measured by a method which does not require movement of the electron over the barrier, the obtained value of Φ_{B0} is not lowered by the image force.

3.4 Charge carrier transport in the electrode-oxide semiconductor interfaces

One of the important issues of semiconductor gas sensors is the understanding of charge transfer reactions at surfaces and interfaces, and of charge transport in oxide semiconductors. Gas adsorption at surfaces of oxide semiconductors may lead to charge transfer reactions and to the change of electrical conductivity in the chemical sensors. This section deals with electrical characteristics, transport mechanism and the layer structure in the metal-semiconductor interface.

© Woodhead Publishing Limited, 2013

3.4.1 Electric field and capacitance in the metal-semiconductor interface

The electrical field and potential distribution in the depletion region of a Schottky barrier junction depend on the barrier height, the applied voltage, and the impurity concentration. These dependences are frequently needed and can be obtained by the solution of a one-dimensional Poisson equation. Figure 3.16(a) shows the energy-band diagram of a reverse-biased Schottky barrier junction made on an *n*-type semiconductor. We assume the semiconductor to be nondegenerate and uniformly doped, and divide it into a space charge region and a neutral region devoid of any space charge. At any point in the semiconductor, the Poisson equation can be written as:[41, 42]

$$\frac{d^2\phi}{dx^2} = -\frac{e}{\in_s}[N_d + p(x) - n(x)] \qquad [3.24]$$

where $\in_s$ is the semiconductor permittivity, N_d is the donor concentration, and $n(x)$ and $p(x)$ are the electron and the hole concentrations at any point x in the semiconductor, respectively. It is assumed that all the donors are ionized. Taking the potential ϕ to be zero in the neutral bulk region of the semiconductor at the edge of the space charge layer, one can write:

$$n(x) = n_0 exp\left[\frac{e\phi(x)}{kT}\right], \qquad p(x) = p_0 exp\left[-\frac{e\phi(x)}{kT}\right] \qquad [3.25]$$

where n_0 and p_0 represent the equilibrium electron and hole concentrations in the neutral semiconductor. Substituting the values of $n(x)$ and $p(x)$ in Equation [3.24], one obtains:

$$\frac{d^2\phi}{dx^2} = -\frac{e}{\in_s}\left\{N_d - n_0 exp\left[\frac{e\phi(x)}{kT}\right] + p_0 exp\left[-\frac{e\phi(x)}{kT}\right]\right\} \qquad [3.26]$$

A closed form solution of this equation is not possible. An additional simplifying assumption made in the analysis is the so-called 'depletion approximation'. In this approximation, the free carrier concentrations are assumed to fall abruptly from their equilibrium values n_0 and p_0 in the bulk neutral region to a negligibly small value in the barrier space charge region. In reality, this transition occurs smoothly over a distance in which the bands bend by about $3\,kT$, but the calculations made using the depletion approximation are sufficiently accurate for most purposes. Thus, using the depletion approximation, Equation [3.26] can be written as:

© Woodhead Publishing Limited, 2013

$$\frac{d^2\phi}{dx^2} = -\frac{e}{\in_s} N_d \qquad 0 < x < W$$

$$= 0 \qquad\qquad x > W \qquad [3.27]$$

where W represents the width of the depletion region. Integrating Equation [3.27] with respect to x and using the condition that $d\phi/dx = 0$ at $x = W$, we obtain the electrical field $\varepsilon(x)$ in the depletion region:

$$\varepsilon(x) = -\frac{d\phi}{dx} = \varepsilon_m \left(1 - \frac{x}{w}\right) \qquad [3.28]$$

where

$$\varepsilon_m = -\frac{eN_d}{\in_s} W$$

is the maximum electric field which occurs at $x = 0$. A second integration with the boundary condition $\phi = 0$ at $x = W$ leads to the following relation:

$$\phi(x) = \frac{eN_d}{2 \in_s} W^2 \left(1 - \frac{x}{W}\right)^2 \qquad [3.29]$$

Thus, the potential varies parabolically with the distance in the depletion region and has its maximum value $\phi(0) = V_d$ given by:

$$V_d = (V_{bi} - V) = \frac{eN_d}{2 \in_s} W^2 \qquad [3.30]$$

where V is the externally applied voltage. For a forward bias, $V = V_F$ and, for a reverse bias, $V = -V_R$. The negative sign in the equation shows that the potential at $x = 0$ is negative with respect to that at $x = W$.

The depletion region width W is obtained from the below relation:

$$W = \left\{ \frac{2 \in_s}{eN_d} |V_{bi} - V| \right\}^{1/2} \qquad [3.31]$$

The width of the depletion region at zero bias is obtained by putting $V = 0$. From Equation [3.31], it can be seen that W decreases below its value W_0 in the event of a forward bias, and increases above W_0 in the event of a reverse bias. Figures 3.16(b) and 3.16(c) show the electrical field and the potential distributions for the Schottky barrier junction.

© Woodhead Publishing Limited, 2013

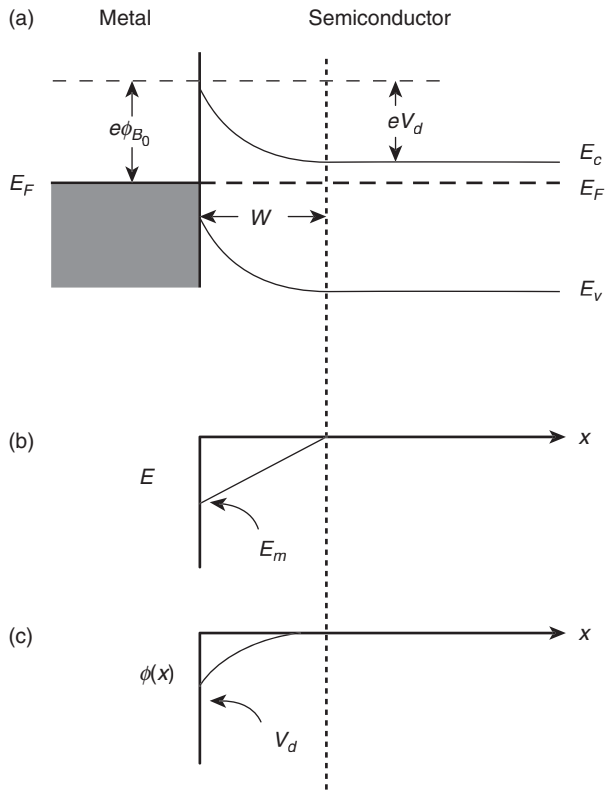

3.16 Electrical field and potential distribution in the metal-semiconductor interface: (a) energy-band diagram, (b) electrical field, and (c) potential distribution.

In the depletion approximation, we have neglected the electron and hole concentrations in comparison with the donor concentration N_d. In a strong n-type semiconductor, the hole concentration is negligible but, at the edge of the depletion region $x = W$, the electron concentration $n(W) = n_0 = N_d$ and decreases exponentially with the decreasing potential $\phi(x)$. It should be clear that the concentration $n(x)$ becomes negligibly small compared with N_d when $e\phi(x)$ in Equation [3.25] is $-4\ kT$ or less. Thus, the depletion approximation is valid only when the potential drop V_d across the depletion region is large compared with about $4\ kT/e$.

A change in the voltage across the Schottky barrier junction causes a change in the width of the depletion region, and this change is accomplished by the movement of charge carriers into the space charge layer or out of this region. This change in the depletion region charge gives rise to a capacitance. Referring to Fig. 3.16(a) and ignoring the charge in the surface

© Woodhead Publishing Limited, 2013

states, there are three sources of charge in the region of the barrier. First, there is the charge Q_d in the depletion region, which results from the movement of electrons out of the semiconductor into the metal. Second, there is a charge Q_m on the metal surface which is caused by the electrons that have crossed from the semiconductor into the metal. Finally, if the band bending is sufficiently large, a charge Q_h will occur due to holes which exist in the semiconductor region immediately adjacent to the metal contact.[40] Electrical neutrality in the junction region requires that $Q_d + Q_m + Q_h = 0$, where each of these charges represents the charge per unit area of the junction. Suppose now that the bias across the junction is increased by a small amount ΔV_d. The space charge layer capacitance C' per unit area is defined by the relation:

$$C' = \frac{dQ_d}{dV_d} = -\frac{d}{dV_d}(Q_m + Q_h) \qquad [3.32]$$

Let us ignore the effect of minority carriers and take $Q_h = 0$ so that $Q_d = -Q_m$. Applying Gauss's Law at the metal-semiconductor boundary, we obtain:

$$\in_s \varepsilon_m = Q_d \qquad [3.33]$$

The maximum electrical field strength is assumed to occur at $x = 0$. The field E_m has been calculated in Equation [3.28], assuming the depletion approximation. A more accurate expression for ε_m is obtained by integrating Equation [3.26], assuming that band bending is small so that $p(x)$ is negligible everywhere and:

$$\frac{d^2\phi}{dx^2} = -\frac{e}{\in_s}\left\{N_d - n_0 \exp\left[\frac{e\phi(x)}{kT}\right]\right\} \qquad [3.34]$$

Multiplying both sides of this relation by $2d\phi/dx$ and integrating from $x = 0$ to $x = W$, with $\phi(0) = -V_d$ and $\phi(W) = 0$ and assuming $N_d = n_0$, we obtain:

$$\left(\frac{d\phi}{dx}\right)^2_{x=0} = \varepsilon_m^2 = \frac{2e}{\in_s} N_d \left(V_d - \frac{kT}{e}\right) \qquad [3.35]$$

where $V_d = (V_i - V)$ is the voltage drop across the depletion region and the built-in voltage V_i is taken to be positive. The depletion region charge Q_d per unit area is then given by:

$$Q_d = \in_s \varepsilon_m = \left[2e \in_s N_d \left(V_d - \frac{kT}{e}\right)\right]^{1/2} \qquad [3.36]$$

© Woodhead Publishing Limited, 2013

and the depletion region capacitance C can be written as:

$$C = A\frac{dQ_d}{dV_d} = A\left\{\frac{e \in_s N_d}{2[V_{bi} - (kT/e) - V]}\right\}^{1/2} \quad [3.37]$$

where A represents the area of the Schottky barrier contact. Since charge Q_d varies with the voltage in a nonlinear manner, the capacitance is a nonlinear function of voltage and can be defined only as a differential capacitance presented to a small change ΔV_d in the voltage of the depletion region.

If an interfacial oxide layer is present between the metal and the semiconductor, a portion of the applied voltage appears across this layer and modifies the dependence of the depletion region charge Q_d on the applied voltage. The capacitances of the interfacial layer and the depletion region are effectively in series, and the overall capacitance in general may be a complicated function of the interfacial layer parameters and the applied voltage. However, when the interfacial layer is thin (about 30Å or less) electrons can tunnel through the layer from the metal to the semiconductor and the resulting Schottky barrier is nearly ideal. The current–voltage characteristics of the nearly ideal diode are described in terms of an ideality factor n given by:

$$\frac{1}{n} = \left(\frac{\partial \Phi_B}{e\partial V}\right) \quad [3.38]$$

where $\partial\Phi_B/\partial V$ represents the change in the barrier height with applied voltage because of the presence of the interfacial layer. If the states at the oxide-semiconductor interface are uniformly distributed in energy, then n is nearly independent of the applied voltage.

In order to obtain the C–V characteristics for the nearly ideal case, we substitute $eV_i = (\Phi_B - \Phi_n)$ in Equation [3.36] and write:

$$Q_d = [2 \in \varepsilon_s N_d(\Phi_B - \Phi_n - kT - eV)]^{1/2} \quad [3.39]$$

and

$$C = A\left|\frac{dQ_d}{dV}\right| = eA\left\{\frac{\in_s N_d}{2[\Phi_{B0} - \Phi_n - kT - eV]}\right\}^{1/2}\left(1 - \frac{\partial \Phi_B}{e\partial V}\right) \quad [3.40]$$

which, after substituting for $\partial\Phi_{B0}/\partial V$ in terms of the ideality factor n, becomes:

$$C = A\left|\frac{dQ_d}{dV}\right| = eA\left\{\frac{\in_s N_d}{2[\Phi_{B0} - \Phi_n - kT - eV]}\right\}^{1/2} \quad [3.41]$$

© Woodhead Publishing Limited, 2013

The barrier height ϕ_{B0} for a constant n can be written as:

$$\Phi_B = \Phi_{B0} + \frac{\partial \Phi_B}{\partial V} V = \Phi_{B0} + \left(1 - \frac{1}{n}\right) eV \qquad [3.42]$$

where Φ_{B0} represents the zero bias barrier height. Combining Equations [3.41] and [3.42], one obtains:

$$\frac{1}{C^2} = \frac{2nA^{-2}}{e^2 \in_s N_d} [n(\Phi_{B0} - \Phi_n - kT) - eV] \qquad [3.43]$$

From Equation [3.43], one observes that the effect of the interfacial layer is to scale up both the slope and the intercept. Thus, the $1/C^2$ versus voltage V plot underestimates the dopant concentration and results in a larger intercept V_0 over its values in the ideal case without the interfacial layer. For a nearly ideal Schottky barrier, n is 1.1 or less so that the value of N_d is not changed to an appreciable degree but V_0 is significantly increased.

3.4.2 Transport mechanism across the junction barrier

The current flows in a Schottky barrier because of charge transport from the semiconductor to the metal, or vice versa. There are four different mechanisms by which the carrier transport can occur:

(1) thermionic emission over the barrier;
(2) tunneling through the barrier;
(3) carrier recombination (or generation) in the depletion region; and
(4) carrier recombination in the neutral region of the semiconductor which is equivalent to the minority carrier injunctions.[42]

Figure 3.17 depicts these processes for a forward biased Schottky barrier made on an *n*-type semiconductor. The inverse processes occur under reverse bias.

Referring to Fig. 3.17, an electron emitted over the barrier from the semiconductor into the metal must move through the high field depletion region. In traversing this region, the motion of the electron is governed by the drift and the diffusion processes. The emission of electrons into the metal is controlled by the density of available states in the metal. Thus, the two processes – the emission over the barrier, and the drift and diffusion in the depletion region – are effectively in series and whichever offers the higher resistance determines the current. In their original treatment, Wanger,[56] and Schottky and Spenke[57] assumed that the current was limited by the drift and

© Woodhead Publishing Limited, 2013

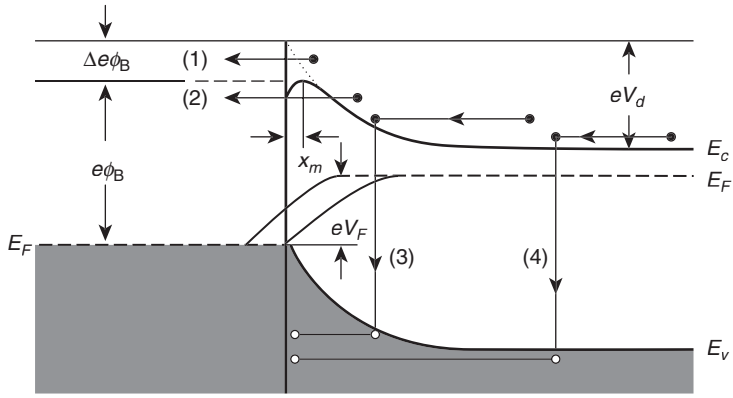

3.17 Energy-band diagram of a forward biased Schottky barrier junction on an *n*-type semiconductor showing different transport processes.[55]

diffusion processes. The diffusion theory leads to the following expression for the diode current:[58]

$$I = eAN_c\mu\varepsilon_m exp\left(-\frac{\phi_B}{kT}\right)\left[exp\left(\frac{eV}{kT}\right)-1\right] \qquad [3.44]$$

where A is the diode cross-sectional area, N_c is the effective density of states in the conduction band of the semiconductor, μ is the electron mobility, and all other symbols have their usual meanings. Since the maximum field E_m in Equation [3.44] is voltage dependent, the pre-exponential factor in this equation does not saturate as it should in an ideal Schottky diode. Subsequent work by Bethe showed that the diode current is limited by thermionic emission over the barrier and is not in agreement with Equation [3.44]. The difference between the two mechanisms is shown by the position of the quasi-Fermi level in the depletion region. According to the diffusion theory, the electrons are in equilibrium with the lattice even when the junction is forward biased, so that their quasi-Fermi level coincides with the metal Fermi level at the interface, as shown by dotted curve in Fig. 3.17. In the thermionic emission theory, on the other hand, the electrons entering the metal have energy higher than the metal electrons and their quasi-Fermi level is almost horizontal through the depletion region, as shown by the dashed curve.

The effect of drift and diffusion in the depletion region is assumed to be negligible in the thermionic emission theory and the barrier height is assumed to be large compared with kT. From Fig. 3.17, it is obvious that only those electrons whose kinetic energy exceeds the height of the potential barrier will be able to reach the top of the barrier. Assuming that the

© Woodhead Publishing Limited, 2013

electrons have a Maxwellian distribution of velocities, the number of electrons n^* per unit area which have sufficient energy to move over the barrier from the semiconductor into the metal is given by:

$$n^* = n_0 exp\left[\frac{-e(V_{bi} - V)}{kT}\right] \quad [3.45]$$

where n_0 represents the electron concentration in the neutral semiconductor outside the depletion region and V is the voltage applied to the semiconductor.

For a nondegenerate semiconductor:

$$n_0 = N_c exp\left(\frac{-\phi_n}{kT}\right) \quad [3.46]$$

And, since $\Phi_B = eV_i + \Phi_n$ from Equation [3.45], we obtain:

$$n^* = N_c exp\left[-\frac{(\phi_B - eV)}{kT}\right] \quad [3.47]$$

If these electrons are assumed to have an isotropic distribution of velocities then, from the kinetic theory, the flux of electrons incident on the barrier is $(n^*\overline{v})/4$. Supposing that all the incident electrons cross over into the metal and
none is reflected back, the current I_{SM} due to passing of electrons from the semiconductor to the metal is given by:

$$I_{SM} = \frac{eA\overline{v}}{4} N_c exp\left[-\left(\frac{\phi_B - eV}{kT}\right)\right] \quad [3.48]$$

where $\overline{v}$ is the average thermal velocity of electrons in the semiconductor. Although the electrons flow from the semiconductor into the metal, the current I_{SM} flows from the metal to the semiconductor and is taken to be positive in Fig. 3.17.

For an unbiased junction under thermal equilibrium, no net current can flow. Consequently, the current given by Equation [3.48] must be balanced by an opposite current I_{MS} due to the crossing of electrons from the metal into the semiconductor, making $I = I_{SM} + I_{MS} = 0$ and:

$$I_{MS} = -\frac{eA\overline{v}}{4} N_c exp\left(-\frac{\phi_B}{kT}\right) \quad [3.49]$$

In the presence of an applied bias V, the barrier for electron flow from the metal to the semiconductor remains practically unchanged at ϕ_B and so

© Woodhead Publishing Limited, 2013

is the current $I_{MS} = -I_0$. The current I_{SM}, however, is given by Equation [3.48] and, combining this equation with Equation [3.49], we obtain:

$$I = I_0\left[exp\left(\frac{eV}{kT}\right) - 1\right] \qquad [3.50]$$

For a Maxwellian distribution, the average velocity $\overline{v} = \left(8kT/\pi m^*\right)^{1/2}$ and substituting $N_c = 2\left(2\pi m^* kT/h^2\right)^{3/2}$, the current I_0 can be written as:

$$I_0 = ART^2 exp\left(-\frac{\phi_B}{kT}\right) \qquad [3.51]$$

where

$$R = \frac{4\pi m^* ek^2}{h^3}$$

is the Richardson constant for thermionic emission from the metal into the semiconductor with electron effective mass m^*, h is the Plank's constant and A is the diode area.

3.4.3 Tunneling through the barrier

The thermionic emission diffusion theory of Crowell and Sze[59] assumes that the electron distribution function remains Maxwellian in the barrier depletion region, and that the classical drift and diffusion equations can be used throughout this region. Near the top of the barrier, the electrical field is very high and the distribution function changes considerably within a mean free path. Under these conditions, it is no longer possible to split the current into drift and diffusion components. Moreover, we should not expect the distribution function near the top of the barrier to be Maxwellian and isotropic. As the electrons entering the metal are assumed not to return, the distribution function near the boundary must be anisotropic. However, the transport equations derived from the first-order solution of the Boltzmann equation are found to be inadequate near the top of the barrier and a new set of transport equations has been proposed. These considerations show that the problem of hot electrons in a rapidly varying field has not been solved to date and we do not yet have an exact theory of the Schottky barrier current–voltage characteristics.

Besides the diffusion and thermionic emission mechanisms, electrons can also be transported across the barrier by quantum mechanical tunneling.

© Woodhead Publishing Limited, 2013

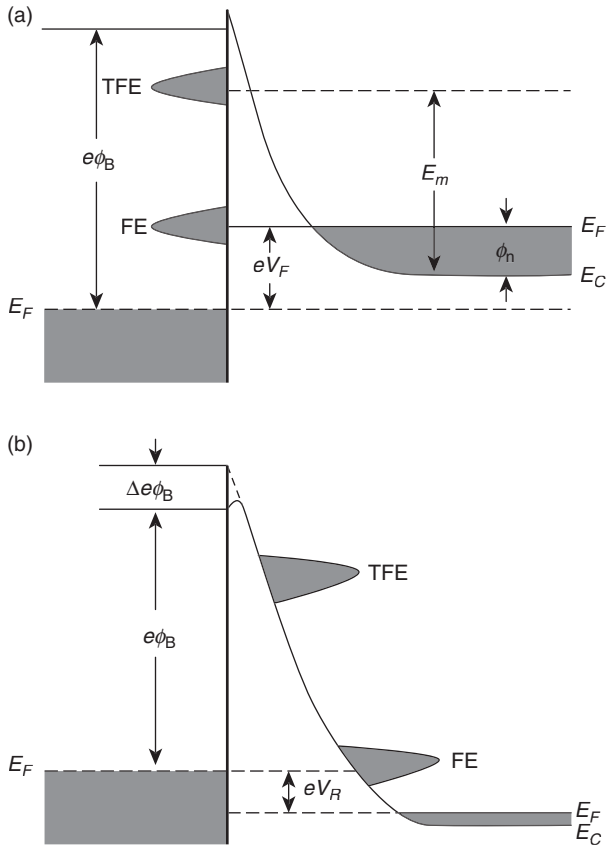

3.18 Field emission and thermionic field emission tunneling through a Schottky barrier on an *n*-type semiconductor: (a) forward bias and (b) reverse bias.

The two ways in which tunneling can occur in a Schottky barrier junction are shown in Fig. 3.18 for both forward bias and reverse bias. The semiconductor in Fig. 3.18 is assumed to be doped to degeneracy such that the Fermi level lies above the bottom of the conduction band. Because of heavy doping, the depletion region is very thin and, at low temperatures, electrons with energy close to the Fermi level can tunnel from the semiconductor into the metal. This process is known as 'field emission' (FE). At higher temperatures, a significant number of electrons are able to rise high above the Fermi level, where they see a thinner and lower barrier. These electrons thus can tunnel into the metal before reaching the top of the barrier. This tunneling of thermally excited electrons is known as 'thermionic field emission' (TFE). Since the number of electrons decreases rapidly with energy above the Fermi level, and the barrier thickness and height also decreases,

© Woodhead Publishing Limited, 2013

there exists an energy E_m at which the contribution of TFE becomes maximum. If the temperature is gradually raised still further, a limit is reached at which practically all the electrons are able to reach the top of the barrier and thermionic emission predominates.

Tunneling through a Schottky barrier has been analyzed theoretically by Padovani and Stratton,[60] and by Crowell and Rideout.[61] The main results of their study are described below. Field emission in the forward direction occurs only in degenerate semiconductors and, except for very low forward biases, the *I–V* characteristic in the presence of tunneling can be described by the relation:

$$I = I_s exp\left(\frac{eV}{E_0}\right) \qquad [3.52]$$

where

$$E_0 = E_{00} coth\left(\frac{E_{00}}{kT}\right)$$

and

$$E_{00} = \frac{eh}{4\pi}\left(\frac{N_d}{m^* \in_s}\right)^{\frac{1}{2}}$$

where m^* is the electron effective mass and h is Planck's constant. The pre-exponential factor I_s in Equation [3.52] is only weakly dependent on voltage and is a complicated function of barrier height, parameters of the semiconductor and the temperature. The ratio kT/E_{00} is a measure of the relative importance of TFE and tunneling. At low temperatures, E_{00} may become large compared with kT and we have $E_0 \approx E_{00}$, then the slope of $\ln I$ versus the V plot is constant and independent of T. This is the case for FE. At high temperatures where $E_{00} << kT$, we get $E_0 = kT$ and the slope of the $\ln I$ versus the V plot is e/kT, which corresponds to TE. For intermediate values of temperature, the slope can be written as e/nkT with:

$$n = \frac{E_{00}}{kT}\coth\left(\frac{E_{00}}{kT}\right) \qquad [3.53]$$

3.4.4 Structure of the interfacial layer

From the previous discussion, we have seen that real focus for the discussion of the microscopics of the Schottky barrier is understanding the mechanisms which determine the interfacial layer. The interplay of a variety of effects

© Woodhead Publishing Limited, 2013

Table 3.2 Enumeration of the layer-by-layer stages of Schottky barrier formation

0. Clean surface
a. Ordered
b. Disordered
1. Dilute limit
a. Chemisorption
b. Reaction
2. Metal nucleation
a. Eutectic formation
b. Compound formation
c. Interdiffusion and interaction
3. Asymptotic overlayer

then determines the interfacial composition, interfacial width and the number of interfacial states. The complexity of the general problem arises from the diversity of concurrent effects that can be at work in specific material situations. Schottky barriers are fabricated with the layer-by-layer approach, or the deposition of the metal on the semiconductor.

Before treating the details of the barrier evolution stages, it is worth describing the details of the overall process to motivate the division into the stages enumerated in Table 3.2 into which the evolution can be decomposed.[62]

The details of the formation of the interfacial layer are the focus of this section without concurrently emphasizing the processes which generate the interface stated. This separation better allows the individual aspects to be identified, but should not imply a decoupling of the two phenomena. The interface layer can have a multiplicity of zones with a division between metallic and semiconducting regions, as depicted in Fig. 3.19.

On the semiconducting side, the interfacial layer has two zones. The first zone lies within the evanescent tail of the metal. The second zone is the remaining region where, due to interdiffusion, a composition or doping different from the original bulk semiconductor exists. A similar description can be characterized on the metal side and the new alloyed metal zone may be of sufficient width to become the metal forming the barrier. This new interfacial metal can have different characteristics from the originally deposited metal.

State 0: The clean semiconductor surface

The layer-by-layer evolution starts from the clean semiconductor surface. The clean semiconductor surfaces can be divided into two types of regime: ordered and disordered. In the case of cleaved surfaces, disordering usually results from structured damage induced by the cleaving process employed. The non-cleavage faces are typically cleaned by a sputtering technique

© Woodhead Publishing Limited, 2013

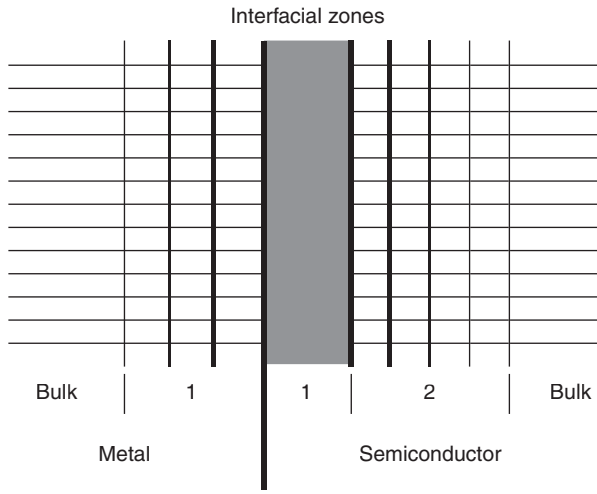

3.19 Schematic depiction of metal-semiconductor interfacial zones.[62]

which usually leaves the surface disordered and, in the case of compound semiconductors, non-stoichiometric. Thermal annealing will usually restore the ordering. The most perfect non-cleavage surfaces are those grown *in situ* with MBE techniques.

Most vacuum-semiconductor interfaces reconstruct or relax so that they show lateral periodicities or coordinates different from a strict truncation of the bulk lattice. A variety of driving forces for these reconstructions have been identified, but in general they can be summed up as deriving from the surface lowering its energy by remaining semiconducting. The reconstruction has a strong influence on the spectrum of intrinsic surface states and their energy position. The character of surface states observed with electron spectroscopy is very sensitive to the presence of adsorbates or overlayers.

Stage 1: The dilute limit

The initial stage of interface development constitutes the dilute limit. The dilute limit is characterized by a density of metal atoms small enough that a continuous metal film does not form. The structural aspects of the dilute limit are complex and depend strongly on the semiconductor during deposition. Changes in the surface structure at this stage of deposition are known as 'impurity stabilized'. Deposition rate effects are not well-explored but have been demonstrated with respect to nucleation of single crystal metals. An important aspect of the dilute limit is that the heat of condensation of the metal atom may be sufficient to dislodge semiconductor surface

© Woodhead Publishing Limited, 2013

atoms. If there is a tendency to surface reaction, then this also strongly influences this stage.

Stage 2: Monolayer formation

The monolayer formation stage plays the most important part in determining the characteristics of the interface. As the density of atoms increases, metal nuclei begin to form. The nucleation of the metal film is a very complex subject. Characteristic of the monolayer formation stage is the production of interdiffusion due to the heat released as the metal nucleates. This heat augments electromigration due to the heat released as the presence of the dipole. In some cases, the release of this heat can drive other reactions over their activation barrier. The approach to monolayer formation may have several substages at which ordered metal overlayers may result. The structural aspects of the monolayer stage are strongly dependent on the deposition temperature and subsequent annealing history.

Stage 3: Addition monolayers and interdiffusion

The final characteristics of the interface can continue to be driven as additional monolayers are added. Strain fields due to lattice mismatch and grain boundary phenomena can play an important role. Usually, the interface reaches a stable configuration within 3 to 10 monolayers for most metals on semiconductors. Interfaces are often metastable, however, and the interdiffusion is accelerated at increased temperature or under biased conditions. The application of core level photoemission to this problem confirmed what had already been deduced with Auger spectroscopy, but on a finer dimensional scale. An overriding fact of metal-semiconductor interfaces is the intrinsic aspects of interfacial interdiffusion and interaction. These two aspects of the chemistry often tend to overwhelm issues that might be deduced from the clean separate surfaces. The interdiffusion can result in interface layers with radically different characteristics from the supposed components.

3.5 Gas/solid interactions in the electrode-oxide semiconductor interfaces

Semiconductor sensors can be used to identify the presence of gases or to detect amount of gas. The interaction of gas with the sensing element in the electrode-oxide semiconductor interface can cause changes in electrical properties. Most known sensing mechanisms for the detector of reducing gases are applied to hydrogen and carbon monoxide. Selective-hydrogen sensors are based on the specific interactions (catalytic reactivity and solubility) of hydrogen with some noble elements such as palladium and platinum.[63–67] On the other hand, the control of electrode gap, the formation of

© Woodhead Publishing Limited, 2013

porous electrode and the electrode with micro holes are applied to enhance the sensor performance in other reduced gas sensors.

3.5.1 Dipole formation in the interfacial layer

It is known that a number of metals – e.g. Pd or Pt – adsorb and dissolve hydrogen, and that the adsorbed atoms change the work function of the metal surfaces. By using a thin metal film as the catalytic metal electrode of the Schottky devices, hydrogen and other gases that react with the catalytic metal can be detected. Hydrogen molecules are adsorbed and dissociated on the outer metal surface. Then, the atomic hydrogen permeates through the bulk lattice toward the metal-semiconductor, causing a perturbation at this interface that gives rise to a change in the sensor output signal.[63–69] Two hypothetical steps were proposed to explain the detection mechanism:[66]

(1) the hydrogen atom is polarized at the metal-semiconductor interface, which gives rise to a dipole layer, or
(2) an excess of charge states at the metal-semiconductor interface is created in the presence of hydrogen and reduces the Schottky barrier height.

Figure 3.20 shows the band diagrams both without and with hydrogen adsorption. The hydrogen-polarized layer, arising from the intrinsic electrical field of the diode, redistributes the charges in the depletion region and abates the degree of band bending. Hence, the corresponding current is correlated with the number of hydrogen atoms adsorbed at the metal-semiconductor interface. When atomic hydrogen has been formed on the outer metal surface, which is exposed to the ambient, an equilibrium is reached between the hydrogen concentration at this metal surface and that at the metal-semiconductor interface. Based on this model, the change in the *I–V* characteristics and the decrease in the Schottky barrier height are strongly related to the hydrogen concentration.

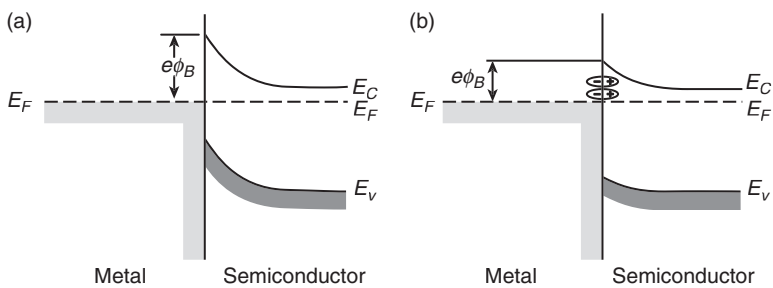

3.20 Energy-band diagram of a Schottky junction; (a) without hydrogen adsorption and (b) with hydrogen adsorption.

© Woodhead Publishing Limited, 2013

3.5.2 Effects of hydrogen adsorption in the Schottky barrier junction

According to the dipole model, originally developed by Lundstrom,[70, 71] the hydrogen sensitivity of catalytic gate devices is based on the dissociation of molecules on the catalytic metal surface and the diffusion through the metal film to form a polarized layer at the metal–insulator interface. The polarized layer gives rise to a shift of capacitance–voltage curve of an MOS capacitor or the current–voltage curve of a Schottky diode. Catalytic gate devices also respond to hydrogen-containing molecules such as hydrocarbons, provided that the molecules are also dissociated on the catalytic metal surface. Oxygen atoms are also dissociated on the catalytic metal surface. Water formation with oxygen atoms from oxygen-containing molecules consumes hydrogen and, therefore, decreases the sensor response. In other words, catalytic metal gates have a direct response to hydrogen and hydrocarbons, as well as an indirect response to oxygen molecules, whose effect is to decrease the direct response.

The hydrogen response of field-effect devices in normal air depends on several significant steps. First, the hydrogen molecule has to dissociate on the catalytic metal surface. This dissociation occurs in competition with adsorption of other molecules in the ambient – in particular, oxygen molecules. Since the oxygen concentration is normally around 20%, a certain minimum hydrogen concentration is needed to give a significant hydrogen concentration on the catalytic metal surface. For nonporous Pd, this concentration is typically around 1 ppm if a couple of mV response is needed, while it is higher for nonporous Pt. When atomic hydrogen has formed on the metal surface, an equilibrium between the hydrogen concentration at the metal surface and the hydrogen concentration at the metal–insulator interface is reached by diffusion of hydrogen atoms through the metal film. A very important part of this process is the surface reactions occurring at the metal–air interface. Hydrogen is supplied by the dissociation of hydrogen molecules from the gas phase, but there is also a back reaction due to the surface reactions between adsorbed hydrogen atoms and adsorbed oxygen atoms, resulting in water molecules that desorb rapidly from the surface at normal operation temperatures. In addition to this back reaction, adsorbed hydrogen atoms can also associate and desorb again as hydrogen molecules. These reactions are summarized in Fig. 3.21.[72]

When hydrogen atoms are adsorbed to the surface adsorption sites (s) of the metal, reaction is expressed as:[65]

$$H_{2,\text{gas}} + 2s \leftrightarrow 2H_s \qquad [3.54]$$

Because oxygen is present in the ambient air, it can also be adsorbed on the metal surface and react with the adsorbed hydrogen to form OH–s, which

© Woodhead Publishing Limited, 2013

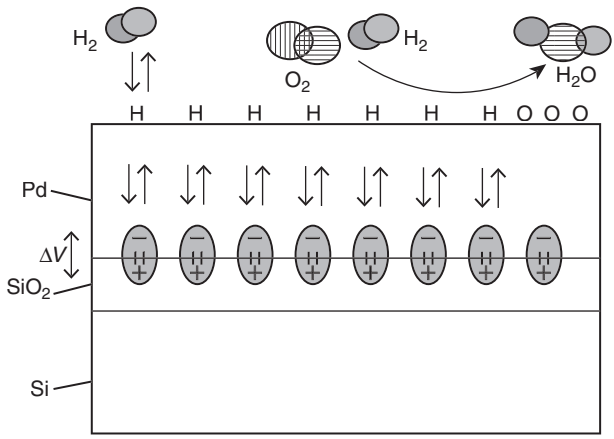

3.21 Surface reactions, diffusion and trapping on the catalytic metal surface of a Pd-MIS device.

can then react with H–*s* to form water (H_2O). The corresponding reactions are expressed as:

$$O_{2,gas} + 2s \leftrightarrow 2O_s \quad [3.55]$$

$$O_S + H_S \leftrightarrow OH_S + s \quad [3.56]$$

$$H_S + OH_S \leftrightarrow H_2O + 2s \quad [3.57]$$

$$2H_S + O_S \leftrightarrow H_2O + 3s \quad [3.58]$$

Except some of the dissociated hydrogen atoms react with the oxygen molecules, surface oxygen and hydroxyl group, the other adsorbed hydrogen atoms diffuse through the metal film into the metal-oxide interface and then further penetrate into the oxide film.

$$s_i = H_S \leftrightarrow s + H_{s_i} \quad [3.59]$$

$$s_O + H_s \leftrightarrow s + H_{s_O} \quad [3.60]$$

where s_i and s_O are the hydrogen adsorption sites in the interface and the oxide layer, respectively. The adsorption sites at the interface are located at the oxygen atoms on the oxide surface,[73] and the absorption sites in the oxide layer are located at the silicon or oxygen atoms (SiO_2 devices).[74] Because the oxygen atoms existing at the oxide surface provide more trap

© Woodhead Publishing Limited, 2013

sites for forming the hydrogen dipoles, a large number of hydrogen atoms could then be adsorbed at the metal-oxide, thereby acting as a dipole layer. Consequently, the resultant barrier height ϕ_{B,H_2} is reduced and becomes smaller than $\phi_{B,air}$ due to the formation of dipoles. The hydrogen atoms absorbed within the oxide layer react with the oxide atoms and subsequently release the electrons, which raises the Fermi level of the oxide. Then the oxide barrier $V_{O,air}$ between metal and oxide is gradually reduced to V_{OB,H_2} during the reaction process.

3.5.3 Adsorption of other gases in the Schottky barrier junction

A semiconductor gas sensor generally consists of a thin or thick film of particulate semiconductor material, whose macroscopic conductance is measured using a pair of electrodes with dimensions much larger than the particle size. Gas phase species can become adsorbed on the particles. If physisorption occurs, there is little direct effect on the macroscopic conductivity, although occupation of surface sites by the physisorbed species may block adsorption of other species. If chemisorptions occur, with charge transfer between the adsorbate and the semiconductor, the charged surface layer produces bending of the conduction and valence band edges. When particles are essentially separate, with no grain intergrowth, the band bending leads to a potential barrier between neighboring particles and a change in the macroscopic conductance relative to that of a pristine film with no adsorbate. Where some particle intergrowth has occurred, the depletion region induced by chemisorption narrows the conductive regions (necks) between grains, again leading to a decrease in macroscopic conductance relative to the film with no adsorption.[3] In either case, it will be seen that changes in the number of species adsorbed, or in their relative charges, will lead to changes in the macroscopic conductance, as depicted in Fig. 3.22.[75] It is the basis of the gas sensing mechanism in conductometric ('chemresistor') sensors based on tin dioxide and other semiconductors.

For the detection of CO gas, the operation of a sensor requires oxygen as a constituent of the background gas. The reaction of CO with the adsorbed oxygen and/or oxygen in the oxide semiconductor causes the reactant product, CO_2, to be desorbed from the device.[76,77] The desorption and reaction of CO gas at steady state proceed via the following reaction at the metal-oxide semiconductor interface:

$$2e^- + O_2 \leftrightarrow 2O^-_{ads} \qquad [3.61]$$

$$CO + O^-_{ads} \leftrightarrow CO_{2,des} + e^- \qquad [3.62]$$

© Woodhead Publishing Limited, 2013

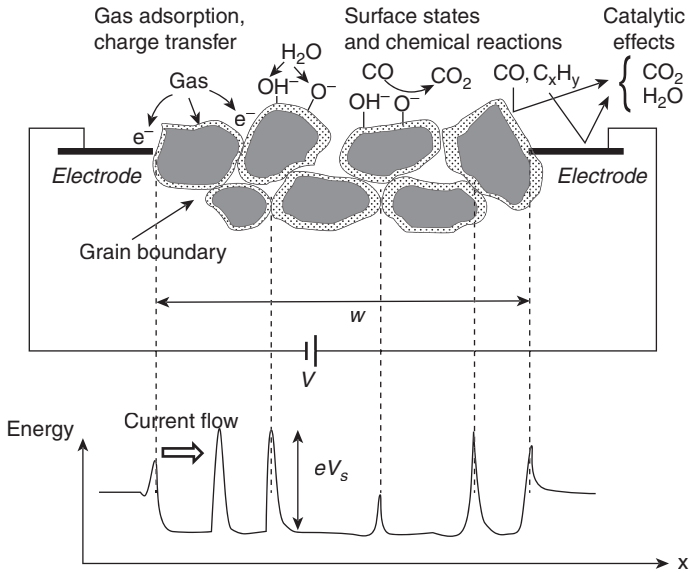

3.22 Schematic of a conductometric gas sensor with electrodes placed high up in the sensor face.

Oxygen can dissociate on the metal and oxygen atoms so formed may spill over onto the oxide semiconductor surface, a well-known phenomenon in catalysis.[78,79] The adsorption (reduction) of the chemisorbed O^- ion at the metal-oxide semiconductor interface increase(decrease) the resistance of the oxide semiconductor. In metal-insulator-semiconductor (MIS) gas (CO, NO_x, etc.) sensors which have the metal-oxide semiconductor gate layer, the behavior and gas adsorption mechanism are somewhat different from those of conventional noble gate hydrogen sensors. The chemisorption process leads to the creation of dipole moments and changes of work function, thus directly shifting the threshold voltage due to the change of carriers in the inversion layer. The consequent change in voltage across the dipole layer can be solved using Poisson's equation, the result of which is given by:[80]

$$\Delta V_{th} = -N_\theta \frac{\mu}{\varepsilon} \qquad [3.63]$$

where N_θ is the density of the adsorption site, μ is the dipole moment of the dipole layer and ε is the permittivity. The change in voltage across the dipole bilayer leads to a shift of V_{th} in the negative gate bias direction. In the *I–V* characteristics of the metal-insulator-semiconductor field effect transistor (MISFET), I_{Dsat} can be expressed as:

© Woodhead Publishing Limited, 2013

$$I_{Dsat} = \frac{C(V_G - \Delta V_{th})^2}{2} \quad [3.64]$$

where C is a constant determined by the device design.

3.6 Conclusion

Charge carrier transport in the electrode-semiconductor interface has been a subject of much interest over the last few decades. In the electrode-semiconductor interface, charge transport theory seems to be a seemingly simple system that can be explained by potential barrier formation; nevertheless, it may possibly be explained in several different mechanisms depending on the types and shapes of sensors. The best conclusion for this is that it is not one single mechanism which will account for all the different material situations encountered. Even though the electrode of gas sensors is known to affect the sensing mechanism of semiconductor gas sensors, it is still unclear how much the electrode influences the sensors. The anticipation that the electrode will improve the properties of gas sensors leads scholars researching on gas sensors to choose an optimum electrode material and modify electrode geometry according to its sensor construction. In the near future, totally new mechanisms that cannot be explained by current models may be proposed and applied for nano-sized gas sensors currently being researched.

3.7 References

1. Seiyama, T., Kato, A., Fulishi, K. and Nagatani, M., 'A new detector for gaseous components using semiconductive thin films', *Anal. Chem*., 1962, **34**, 1502–03.
2. Kasap, S., *Principles of electrical engineering materials and devices*, New York, McGraw-Hill, 1997.
3. Hummel, R., *Electronic properties of materials*, New York, Springer-Verlag, 1985.
4. Toohey, M. J., 'Electrodes for nanodot-based gas sensors', *Sensor Actuat. B*, 2005, **105**, 232–50.
5. Gourari, H., Lumbreras, M., Van Landschoot, R. and Schoonman, J., 'Electrode nature effects on stannic oxide type layers prepared by electrostatic spray deposition', *Sensor Actuat. B*, 1999, **58**, 365–9.
6. Capone, S., Siciliano, P., Quaranta, F., Rella, R., Epifani, M. and Vasanelli, L., 'Moisture influence of geometry effect of Au and Pt electrodes on CO sensing response of SnO_2 microsensors based on sol-gel thin film', *Sensor Actuat. B*, 2001, **77**, 503–11.
7. Saukko, S. and Lantto, V., 'Influence of electrode material on properties of SnO_2-based gas sensor', *Thin Solid Films*, 2003, **436**, 137–40.

© Woodhead Publishing Limited, 2013

8. Zhou, X., Xu, Y., Cao, Q. and Niu, S., 'Metal–semiconductor ohmic contact of SnO_2-based ceramic gas sensors', *Sensors Actuat. B*, 1997, **41**, 163–7.
9. Sze, S., *Semiconductor Devices*, Hoboken, Wiley, 2002.
10. Hubert, T., Boon-Brett, L., Black, G. and Banach, U., 'Hydrogen sensors – A review', *Sensor Actuat. B*, 2011, **157**, 329–52.
11. Shivaraman, M., Lundstrom, I., Svensson, C., and Hammarsten, H., 'Hydrogen sensitivity of palladium thin-oxide silicon Schottky barriers', *Electron. Lett*., 1976, **12**, 483–4.
12. Steele, M. and MacIver, B., 'Palladium/cadmium-sulfide Schottky diodes for hydrogen detection', *Appl. Phys. Lett*., 1976, **28**, 687–8.
13. Ito, K., 'Hydrogen sensitive Schottky barrier diodes', *Surf. Sci*., 1979, **86**, 345–52.
14. Cheng, C., Tsai, Y., Lin, K., Chen, H., Hsu, W., Chuang, H., Chen, C. and Liu, W., 'Hydrogen sensing characteristics of Pd- and Pt-Al0.3Ga0.7As metal semiconductor (MS) Schottky diodes', *Semicond. Sci. Tech*., 2004, **19**, 778–82.
15. Kim, J., Gila, B., Chung, G., Abernathy, C., Pearton, S. and Ren, F., 'Hydrogen sensitive GaN Schottky diodes', *Solid State Electron*., 2003, **47**, 1069–73.
16. Basu, S., Roy, S. and Jacob, C., 'Ruthenium as Schottky metal for SiC-based high temperature hydrogen sensors', *Mater. Technol. Hydrogen Economy*, 2004, **801**, 193–8.
17. Salehi, A. and Nazerian, V., 'Characterization of magnetic Ni/n-Si Schottky contact for hydrogen gas sensing applications', *Sensor Actuat. B*, 2007, **122**, 572–7.
18. Pandis, C., Brilis, N., Bourithis, E., Tsamakis, D., Ali, H., Krishnamoorthy, S., Iliadis, A. and Kompitsas, M., 'Low-temperature hydrogen sensors based on Au nanoclusters and Schottky contacts on ZnO films deposited by pulsed laser deposition on Si and SiO_2 substrates', *IEEE Sens. J.*, 2007, **7**, 448–54.
19. Hossein-Babaei, F. and Purahmad, M., 'Wide dynamic range hydrogen sensing using silver-rutile Schottky diode', in: *Proceedings of The Third International Conference on Sensing Technology*, 2008, 72–5.
20. Song, J., Lu, W., Flynn, J. and Brandes, G., 'AlGaN/GaN Schottky diode hydrogen sensor performance at high temperatures with different catalytic metals', *Solid State Electron*., 2005, **49**, 1330–4.
21. Capone, S., Epifani, M., Francioso, L., Kaciulis, S., Mezzi, A., Siciliano, P. and Taurino, A., 'Influence of electrodes ageing on the properties of the gas sensors based on SnO_2', *Sensor Actuat. B*, 2006, **115**, 396–402.
22. Williams, D. and Pratt, K., 'Theory of self-diagnostic sensor array devices using gas-sensitive resistors', *J. Chem. Soc. Faraday Trans*., 1995, **91**, 1961–6.
23. Jain, U., Harker, A., Stoneham, A. and Williams, D., 'Effect of electrode geometry on sensor response', *Sensor Actuat. B*, 1990, **2**, 111–14.
24. Vilanova, X., Llobet, E., Brezmes, J., Calderer, J. and Correig, X., 'Numerical simulation of the electrode geometry and position effects on semiconductor gas sensor response', *Sensors Actuat. B*, 1998, **48**, 425–31.
25. Gardner, J., 'Intelligent gas sensing using an integrated sensor pair', *Sensors Actuat. B*, 1995, **26**(27), 261–6.
26. Hoefer, U., Steiner, K. and Wagner, E., 'Contact and sheet resistances of SnO_2 thin films from transmission-line model measurements, *Sensor Actuat. B*, 1995, **26**, 59–63.
27. Hoefer, U., Böttner, H., Felske, A., Kühner, G., Steiner, K. and Sulz, G, 'Thin-film SnO_2 sensor arrays controlled by variation of contact potential – a suitable

© Woodhead Publishing Limited, 2013

tool for chemometric gas mixture analysis in the TLV range', *Sensor Actuat. B*, 1997, **44**, 429–33.
28. Reeves, G. and Harrison, H., 'Obtaining the specific contact resistance from transmission line model measurements', *IEEE Electron Device Lett.*, 1982, **3**, 111–13.
29. Korotcenkov, G., 'Practical aspects in design of one-electrode semiconductor gas sensors: Status report', *Sensor Actuat. B*, 2007, **121**, 664–78.
30. Song, K., Joo, B., Choi, N., Lee, Y., Lee, S., Huh, J. and Lee, D., 'A micro hot-wire sensors for gas sensing applications', *Sensor Actuat. B*, 2004, **102**, 1–6.
31. Korotcenkov, G., Boris, I., Brinzari, V., Lychkovsky, Yu., Karkotsky, G., Golovanov, V., Cornet, A., Rossinyol, E., Rodriguez, J. and Cirera, A., 'Gas sensing characteristics of one-electrode gas sensors on the base of doped In_2O_3 ceramics', *Sensor Actuat. B*, 2004, **103**, 13–22.
32. Jones, E., 'The pellistor catalytic gas sensor', in: Moseley, P. and Tofield, B. (eds.), *Solid-state Gas Sensors*, Institute of Physics, Bristol, 1987, 17–31.
33. Fukui, K., 'Detection and measurements of odour by sintered tin oxide', *Sensor Actuat. B*, 1991, **5**, 27–32.
34. Malchenko, S., Lychkovski, Y. and Baykov, M., 'One electrode semiconductor sensors for detection of toxic and explosive gases in air', *Sensor Actuat. B*, 1992, **7**, 505–6.
35. Malchenko, S., Lychkovski, Y. and Baykov, M., 'In_2O_3-based gas sensors', *Sensor Actuat. B*, 1993, **13**(14), 159–61.
36. Ivanovskaya, M. and Bogdanov, P., 'Effect of NiII ions on the properties of In_2O_3-based ceramic sensors', *Sensor Actuat. B*, 1998, **53**, 44–53.
37. Faglia, G., Comini, E., Sberveglieri, G., Rella, R., Siciliano, P. and Vasanelli, L., 'Square and collinear four probe array and Hall measurements on metal oxide thin film gas sensors', *Sensor Actuat. B*, 1998, **53**, 69–75.
38. Williams, D., 'Semiconducting oxides as gas-sensitive resistors', *Sensor Actuat. B*, 1999, **57**, 1–16.
39. Gerlich, M., Kornely, S., Fleischer, M., Meixner, H. and Kassing, R., 'Selectivity enhancement of a WO_3/TiO_2 gas sensor by the use of a four-point electrode structure', *Sensor Actuat. B*, 2003, **93**, 503–8.
40. Bläser, D., Rühl, Th., Diehl, C., Ulrich, M. and Kohl, D., 'Nanostructured semiconductor gas sensors to overcome sensitivity limitations due to percolation effects', *Phys. A*, 1999, **266**, 218–23.
41. Holmes, P. and Loasby, R., *Handbook of thick film technology*, Glasgow, Electrochemical Pub., 1976, 105–13.
42. Neamen, D., *Semiconductor physics and devices*, New York, McGraw-Hill, 2003, 326–49.
43. Tyagi, M., 'Physics of Schottky barrier junction', in Sharma, B., *Metal-semiconductor Schottky barrier junction and their application*, New York, Plenum, 1984, 1–17.
44. Schottky, W., 'Halbleitertheorie der Sperrschicht', *Naturwissen(s)chaften*, 1938, **26**, 843.
45. Mott, N., 'Note on the contact between a metal and an insulator or semiconductor', *Proc. Camb. Phil. Soc.*, 1938, **34**, 568–72.
46. Islam, M. and Hakim, M., 'Electron affinity and work function of polycrystalline SnO_2 thin film', *J. Mat. Sci. Lett.*, 1986, **5**, 63–5.

© Woodhead Publishing Limited, 2013

47. Feucht, D., 'Heterojunctions in photovoltaic devices', *J. Vac. Sci. Technol*., 1977, **14**, 57–64.
48. Gutmann, S., Wolak, M., Conrad, M., Beerbom, M. and Schlaf, R., 'Effect of UV and X-ray Radiation on the Work Function of TiO_2 Surfaces', *J. Appl. Phys.*, 2010, **107**, 103705.
49. Frese, Karl, W., 'Simple method for estimating energy levels of solids', *J. Vac. Sci. Technol*., 1979, **16**, 1042–4.
50. Bardeen, J., 'Surface states and rectification at a metal-semiconductor contact', *Phys. Rev.*, 1947, **71**, 717–27.
51. Milnes, A. and Feucht, D. J., *Heterojunctions and metal-semiconductor junctions* (chs 6 and 7), New York, Academy Press, 1972.
52. Mead, C., 'Metal-semiconductor surface barriers', *Solid State Electron*, 1966, **9**, 1023–32.
53. Andrew, J. and Phillips, J., 'Chemical bonding and structure of metal-semiconductor interfaces, *Phys. Rev. Lett.*, 1969, **22**, 1433–6.
54. Cowley, A. and Sze, S., 'Surface states and barrier height of metal-semiconductor systems', *J. Appl. Phys*, 1965, **36**, 3212–20.
55. Wada, O., Majerfeld, A. and Robson, P., 'InP Schottky contacts with increased barrier height', *Solid State Electron*, 1982, **25**, 381–7.
56. Rhoderick, E., *Metal-semiconductor Contacts*, Oxford, Clarendon, 1978.
57. Wagner, C., 'Theory of current rectifier', *Phys. Z.*,1931, **32**, 641–5.
58. Schottky, W. and Spenke, E., 'Quantitative treatment of the space charge and boundary-layer theory of the crystal rectifier', *Wiss. Veroff. Siemens-Werken*, 1939, **18**, 225–91.
59. Sze, S., *Physics of semiconductor devices*, New York, John Wiley & Sons, 1981.
60. Crowell, C. and Sze, S., 'Current transport in metal-semiconductor barrier, *Solid State Electron*, 1966, **9**, 1035–48.
61. Padovani, F. and Stratton, R., 'Field and thermionic-field emission in Schottky barriers', *Solid State Electron*, 1966, **9**, 695–707.
62. Crowell, C. and Rideout, V., 'Normalized thermionic-field emission in metal-semiconductor barriers', *Solid State Electron*, 1969, **12**, 89–105.
63. Bachrach, R., 'Interface chemistry and structure of Schottky barrier formation', in Sharma, B., *Metal-semiconductor Schottky barrier junctions and their application*, New York, Plenum, 1984, 61–112.
64. Lundstrom, I. and Svensson, C., *In solid state chemical sensors;* Janata, J. and Huber, J. (eds.), New York, Academic Press, 1985.
65. Potje-Kamloth, L., Semiconductor junction gas sensors', *Chem. Rev*., 2008, **108**, 367–99.
66. Lee, C. and Yan, J., 'Sensing mechanisms of Pt/β-Ga_2O_3/GaN hydrogen sensor diodes', *Sensor Actuat. B*, 2010, **147**, 723–9.
67. Hubert, T., Boon-Brett, L., Black, G. and Banach, U., 'Hydrogen sensors – A review', *Sensor Actuat. B*, 2011, **157**, 329–52.
68. Ruths, P., Ashok, S., Fonash, S. and Ruths, J., 'A study of Pd-Si MIS Schottky-barrier diode hydrogen detector', *IEEE Trans. Electron. Devices*, 1981, ED-**28**, 1003–9.
69. Johansson, M., Lundstrom, I. and Ekedahl, L., 'Bridging the pressure gap for palladium metal-insulator-semiconductor hydrogen sensors in oxygen containing environments', *J. Appl. Phys*., 1998, **84**, 44–51.

© Woodhead Publishing Limited, 2013

70. Card, H. and Rhoderick, E., 'Studies of tunnel MOS diodes I. Interface effects in silicon Schottky diodes', *J. Phys. D: Appl. Phys*., 1971, **4**, 1589–601.
71. Lundström, I., Shivaraman, M., Svensson, C. and Lundkvist, I., 'A hydrogen-sensitive MOS field effect transistor', *J. Appl. Phys. Lett*., 1975, **26**, 55–7.
72. Lundström, I., 'Hydrogen sensitive MOS structures: Part 1: Principles and applications', *Sensor Actuat.*, 1981, **1**, 403–26.
73. Lundström, I., Sundgren, H., Winquist, F., Eriksson, M., Krantz-Rulcker, C. and Lloyd-Spetz, A., 'Twenty-five years of field effect gas sensor research in Linkoping, *Sensor Actuat. B*, 2011, **157**, 329–52.
74. Eriksson, M., Salomonsson, A. and Lundström, I., 'The influence of the insulator surface properties on the hydrogen response of field-effect gas sensors', *J. Appl. Phys*., 2005, **98**, 034903.
75. Capone, S., Siciliano, P., Quaranta, F., Rella, R., Epifani, M. and Vasanelli, L., 'Moisture influence of geometry effect of Au and Pt electrodes on CO sensing response of SnO_2 microsensors based on sol-gel thin film', *Sensor Actuat. B*, 2001, **77**, 503–11.
76. Morrison, S., 'Mechanism of semiconductor gas sensor operation', *Sensor Actuat. B*, 1987, **11**, 283–7
77. Eggins, B., *Chemical sensors and biosensors*, New York, Wiley, 2002, 49.
78. Yanagida, H., 'Gas sensing characteristics of porous zinc oxide ceramic with and without platinum catalyst', *Proc. Int. Meet. on chemical sensors*, 1983, 95–100.
79. Pajonk, G., Teichner, S. and Germain, J., *Studies in surface science and catalysis*, New York, Elsevier, 1983, 17.
80. Fukuda, H., Kasama, K. and Nomura, S., 'Highly sensitive MISFET sensors with porous Pt–SnO_2 gate electrode for CO gas sensing applications', *Sensor Actuat. B*, 2000, **64**, 163–8.

© Woodhead Publishing Limited, 2013

4

Recent trends in silicon carbide (SiC) and graphene-based gas sensors

M. ANDERSSON, A. LLOYD SPETZ
and R. PEARCE, Linköping University, Sweden*

DOI: 10.1533/9780857098665.2.117

Abstract: The introduction of silicon carbide (SiC) as the semiconductor in gas sensitive field effect devices has tremendously improved this sensor platform extending the temperature range and number of detectable gases. Here we review the recent trends in research, starting with transducer mechanisms, and the latest findings regarding the detection mechanism, and present new material combinations as sensing layers and describe smart operation of the field effect sensors enabling one sensor to act as a sensor array. The introduction of epitaxially-grown graphene on SiC as a gas sensing layer shows the potential of ppb detection of NO_2.

Key words: field effect gas sensors, SiC gas sensors, smart sensing, temperature cycling, epitaxial graphene on SiC gas sensors.

4.1 Introduction

Chemical sensors based on field effect transistors (FETs) were introduced in the 1970s when, first, the ion sensitive FET (ISFET) for pH-measurements (Bergveld, 1970) and, later, the hydrogen-sensitive metal oxide semiconductor FET (MOSFET) (Lundström *et al*., 1975) were invented. Since the mid-1980s, FETs have been developed that are also sensitive to other gaseous substances – such as ammonia, hydrocarbons and carbon monoxide (Lundström *et al*., 2007; Lloyd Spetz *et al*., 2009). The first devices were based on silicon and, in respect of the MOSFET device, a catalytically active gate metal such as palladium, platinum, or iridium provided its gas sensitivity. Besides transistors, also metal oxide semiconductor (MOS) capacitors and Schottky diodes with catalytic gate contacts have been developed for gas-sensing purposes, the basic sensing mechanism being common to all the different field effect sensor devices. Upon exposure of the sensors to a certain substance or gas mixture, the interaction between the gas and gate contact

* R. Pearce, National Physical Laboratory, UK, from March 2012.

© Woodhead Publishing Limited, 2013

changes the electrical field across the MOS structure, in turn modulating the current through or, in case of a capacitor, the capacitance over the device.

With the introduction of the first metal insulator semiconductor (MIS)[1] gas sensor devices based on SiC in the early 1990s (Hunter *et al*., 1992; Spetz *et al*., 1992), new possibilities opened up for the application of field effect sensors. The wide band gap of SiC permits operational temperatures beyond the limit of approximately 200°C for Si-based sensors without suffering intrinsic conduction effects. Extending the range of sensor operation temperatures allowed exploration of gas metal interactions and catalytic reactions occurring above 200°C, facilitating detection of more compounds. SiC is also relatively chemically inert, preventing device degradation caused by reactions with other materials or substances, also being effective at elevated temperatures. SiC-based field effect sensors have therefore been utilized in a number of high temperature and corrosive applications such as combustion control, for example in car exhausts and small- and medium-scale power plants (Wingbrant *et al*., 2003; Unéus *et al*., 2005; Andersson *et al*., 2007), and the monitoring of ammonia slip from diesel exhaust and flue gas after treatment systems (Wingbrant *et al*., 2005; Andersson *et al*., 2006). Commercial sensor systems based on SiC are available through a spin-off company launched in 2007 (SenSiC AB, Kista, Stockholm, Sweden, www.sensic.se). Monitoring the regeneration of NO_x storage catalysts has also been suggested as an application suitable for field effect sensors based on SiC (Schalwig *et al*., 2004). Field effect devices based on other wide band gap semiconductors – such as diamond (Gurbuz *et al*., 1998), gallium nitride and aluminium gallium nitride (Schalwig *et al*., 2002a; Eickhoff *et al*., 2003) – have also been demonstrated for gas-sensing purposes.

The last five years have seen the development of new devices, new materials combinations and new operation modes of SiC-based field effect sensors, and with the advent of epitaxially-grown graphene on SiC (Yakimova *et al*., 2010), the field is expanding even further. Based on theoretical modelling and materials research, selectivity and sensitivity towards various gases are currently also being improved by the development of new combinations of gas-sensitive layers. Recent trends, reviewed in this chapter, include simplification of device designs to reduce fabrication costs and increase stability, as well as novel designs to facilitate sensors for new applications. Dynamic sensor operation through temperature and bias cycling is another recent line of development to enhance stability, as well as selectivity towards certain substances. The very promising possibilities for even ultra-sensitive detection of gaseous compounds, down to single molecule detection, with SiC/graphene sensor structures are discussed at the end of the chapter.

[1] The acronym MOS is reserved for the case of MIS structures based on silicon and silicon dioxide as the semiconductor and insulator, respectively.

© Woodhead Publishing Limited, 2013

4.2 Background: transduction and sensing mechanisms

In this section, first the basic physical principle and electrical operation of the transducer platform, the FET device, is given. Then the sensing mechanism, when the devices are used as gas sensors, is given in general and for hydrogen as well as non-hydrogen containing gases. For this section we also refer to the reference Andersson *et al*. (2013).

4.2.1 Transducer platform

The MIS capacitor represents the heart of most field effect sensor devices, and the physics of MIS capacitors is of importance and is treated in semiconductor physics and other sensor books (Sze, 1981; Lundström, 1995; Dimitrijev, 2000). Here, we will only give the basic physical principles regarding the metal insulator semiconductor field effect transistor (MISFET), since this is the ultimate transducer for commercial sensor devices.

Regarding the transistor-based devices, the basic principles of operation can be exemplified considering the n-channel enhancement-type (p-doped semiconductor substrate) MISFET displayed in Fig. 4.1. The MIS capacitor structure is an integral part of the transistor device, separating the n-doped source and drain regions, and with its metal contact forming the gate (G in Fig. 4.1). The source and p-type substrate (or 'body', as it is often called) terminals are normally grounded, whereas a bias is applied to the drain and gate contacts (see Fig. 4.1), V_{DS} and V_{GS}, respectively.

When no bias is applied to the gate terminal ($V_{GS} = 0$), as in Fig. 4.1(a), no conductive path from source to drain exists, preventing current flow between these two terminals. However, for a gate bias larger than the so-called threshold voltage V_T ($V_{GS} > V_T$), an n-type (inversion) layer, commonly referred to as the 'channel', develops at the surface of the semiconductor allowing electrons to flow between the source and drain terminals in response to a drain bias, as in Fig. 4.1(b).

For small drain voltages, the channel has the characteristics of a resistor, the conductance of which is determined by its dimensions, the mobility of the electrons, and the inversion layer density of electrons. This electron density is a function of the gate bias, why the channel conductance can be modulated by the gate voltage V_{GS}; the larger the gate bias the larger the electron concentration of the channel and thus its conductivity (compare V_{GS1} and V_{GS2} in Fig. 4.1). When increasing the drain to source voltage beyond the difference between V_{GS} and V_T, the drain current I_D is no longer affected by the drain bias, see Figs 4.1(c) and 4.1(d). Thus, the drain current basically saturates for $V_{DS} \geq V_{GS} - V_T$. The saturation voltage ($V_{DS,sat} = V_{GS}$

© Woodhead Publishing Limited, 2013

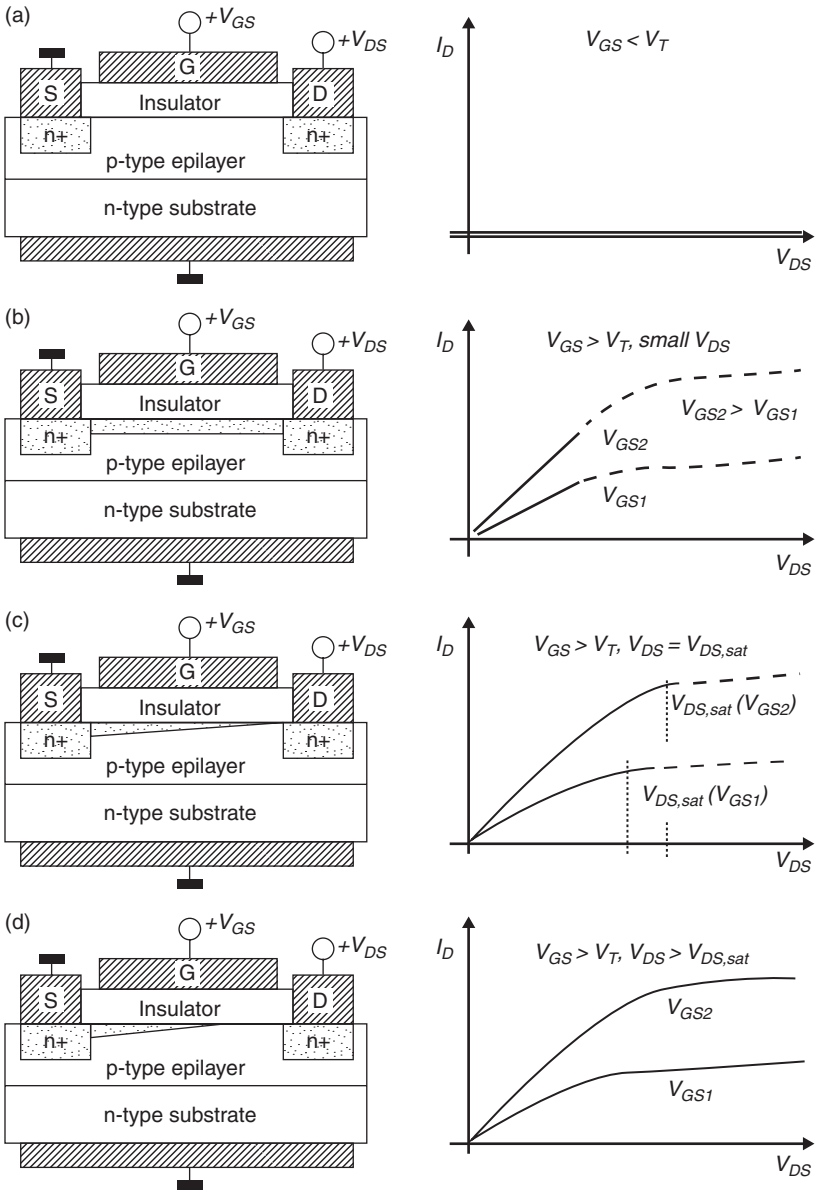

4.1 This figure displays the n-channel enhancement-type MISFET and the state of its inversion layer (channel), as well as the corresponding I/V characteristics under various gate and drain bias conditions.

© Woodhead Publishing Limited, 2013

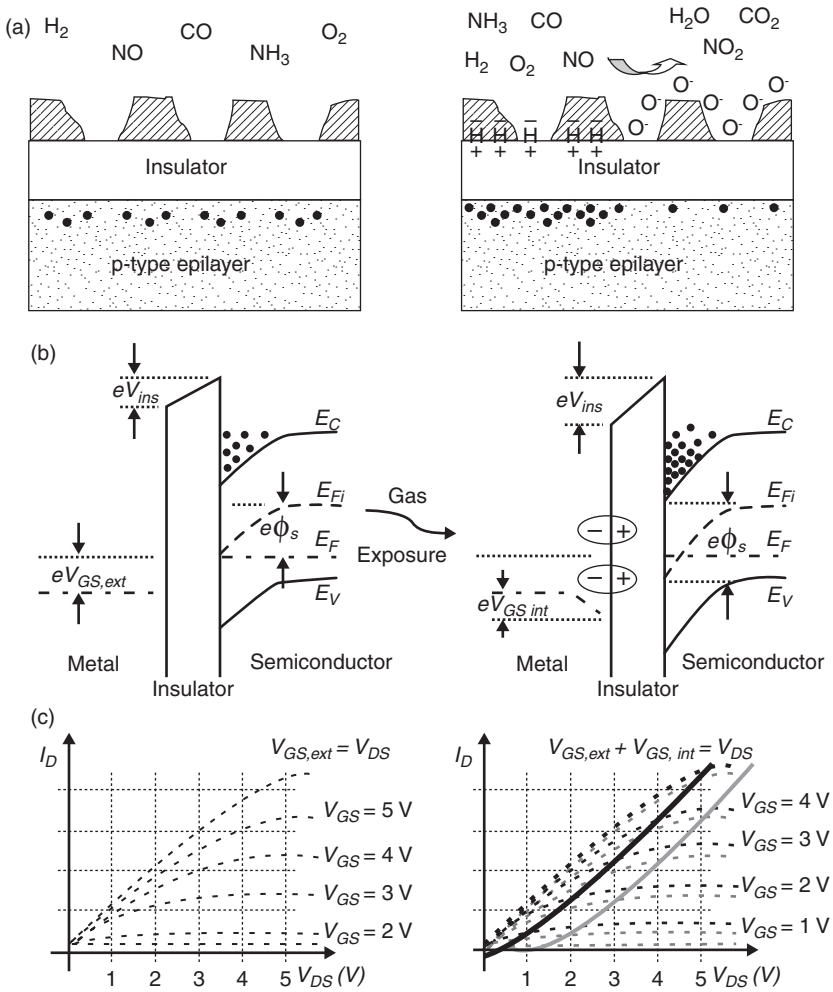

4.2 In (a) examples of reactions on the catalytic metal gates are displayed, as well as the effect of hydrogen and oxygen anion adsorption on the number of charge carriers in the channel. In (b) and (c) the corresponding changes of the energy band diagram and the I/V characteristics following hydrogen exposure (black) are given.

– V_T), and thus the saturation current $I_{D,sat}$, is solely determined by the gate bias. As long as the applied drain to source voltage is larger than the saturation voltage, the applied gate voltage will determine the drain current, as can also be seen from Fig. 4.2.

© Woodhead Publishing Limited, 2013

Transistor-based sensor devices are normally operated in saturation mode. The drain current versus gate voltage relationship for the saturation region quantitatively is described by:

$$I_{D,sat} = \frac{W\mu_n\varepsilon_{ins}}{2Ld_{ins}}[V_{GS} - V_T]^2 \quad [4.1]$$

$$V_T = \frac{2d_{ins}[eN_a\varepsilon_S\Phi_F]^{1/2}}{\varepsilon_{ins}} - \frac{Q_{SS}d_{ins}}{\varepsilon_{ins}} + \Phi_{ms} + 2\Phi_F \quad [4.2]$$

where W and L are the channel width and length, respectively; μ_n is the channel electron mobility; ε_{ins} and d_{ins} are the insulator permittivity and thickness, respectively; e is the elementary charge; N_a the bulk doping concentration; ε_s the semiconductor permittivity; Q_{SS} the insulator charge density; Φ_{ms} the metal-to-semiconductor work function difference; and Φ_F the Fermi potential, which is the potential difference between the Fermi level and the intrinsic Fermi level.

For a more in-depth treatment of field effect device theory and operation see, for instance, Lundström (1995) and Neamen (2003).

4.2.2 Transduction mechanisms

Parameters such as device dimensions, electron mobility, permittivity and doping concentration are inherent to the choice of materials, the design and the processing of field effect sensor devices. Once fabricated, the values of these are fixed but, as seen from Equations [4.1] and [4.2], charges located in or at the surface of the insulator, Q_{SS}, the metal-to-semiconductor work function difference Φ_{ms}, and any internal gate voltage drop,[2] adding to the externally applied gate bias, can also have an influence on the drain current. Any change in the values of one or more of these parameters will change the I/V characteristics of the FET devices.

Thus, if the interactions between the gas and gate materials upon exposure to a certain substance leads to the introduction of an internal gate voltage drop, a change in gate insulator charge, and/or a change in gate metal work function, the substance could be detected through a change in drain current. This requires the injection of charge to or charge separation at the gate contact/insulator interface, or species capable of changing the metal work function to adsorb on the inner surface of the gate contact material.

[2] V_{GS} could be viewed as composed of two parts, the externally applied bias $V_{GS,ext}$ and any internal voltage drop $V_{GS,int}$ inside the device, according to $V_{GS} = V_{GS,ext} + V_{GS,int}$.

© Woodhead Publishing Limited, 2013

Examples of changes in I_D vs V_{GS} characteristics for the situation of a gas-induced internal voltage drop are given in Fig. 4.2(c).

When atoms or molecules adsorb on a surface, there is most often some kind of charge transfer between the adsorbates and the surface, and thus separation of charge, as well as a change in work function of the material. One kind of field effect-based gas sensor, the suspended gate FET (SGFET), utilizes this latter phenomenon. The design of SGFETs includes a very small air gap between the gate contact material and the insulator, just large enough to facilitate rapid diffusion of gas molecules to the gate contact surface facing the insulator. Any change in drain current, i.e. sensor signal, upon gas exposure is directly related to the change in work function of the gate material, resulting from adsorption of one or more gaseous substances to its surface. For most transistor-based field effect sensors, the drain current is kept constant, however, and the resulting drain voltage used as a sensor signal. Most commonly, the transistor drain and gate (enhancement-type devices), or source and gate (depletion-type devices) terminals are also connected when operated as a gas sensor, making it a simple two-terminal device.

4.2.3 Sensing mechanisms

General

Work function changes and the creation of internal voltage drops are merely the general mechanisms behind the conversion of chemical interactions between the gas and the sensor device into an electrical output. Voltage drops can be introduced and work function changes can be achieved in a number of different ways. In order to be useful for specific applications, the sensors must, however, be able to distinguish between different gas mixtures and/or quantify one or more substances with good resolution. The sensitivity and selectivity towards the substance(s) of interest are important figures of merit for a specific sensor, as are detection limit, speed of response and stability.

As noted above, any charge separation at the interface or work function changes do not provide much information as to the gas composition. The sensor's sensitivity and selectivity to the analyte of interest is therefore largely determined by the specific interactions between the various ambient gaseous substances and the gate materials exposed to the surrounding gas. These interactions include adsorption and reactions of atoms and molecules on the surfaces of the gate materials, as well as desorption from the same surfaces.

In general, adsorption and desorption are dependent on, for example, the ambient temperature, the partial pressure of the substance, the desorption

© Woodhead Publishing Limited, 2013

energy and the sticking coefficient $S_0(T)$. The sticking coefficient gives the probability for adsorption of a molecule incident on an empty adsorption site, and is dependent on temperature and the activation energy for adsorption. The sticking coefficient is therefore different for different molecules, surface compositions and orientations. Furthermore, the adsorption of molecules on the sensor surface may be direct, or via precursor states, it may be dissociative or non-dissociative and there may be interaction between adsorbed species on the surface. All these details of the adsorption will affect the equilibrium state of the molecules on the sensor surface. Also, other constituents of the surrounding gas matrix may adsorb to the surface and affect the coverage of the target substance in different ways (e.g. by reducing or blocking adsorption of this substance, or removing it from the surface through chemical reactions).

At steady state, equilibrium usually develops between the adsorption, chemical surface reactions and desorption of the different substances in the surrounding gas matrix. An overview of the surface processes and examples of their influence on the device characteristics is given in Fig. 4.2. Considering the operational temperature of the sensor to be constant, and the sticking coefficients, interaction and desorption energies to be inherent to the molecules and the surface, the steady-state condition on the surface is dependent on the partial pressures of the gas matrix constituents and, therefore, reflects the composition of the surrounding gas. Several different gas matrices may, however, give rise to the same equilibrium surface conditions for a certain surface and operational temperature. Conversely, a different surface, or a change in operational temperature, may give rise to a different equilibrium surface condition for the same gas matrix, highlighting the importance and possibilities regarding the choice of gate material and sensor operational temperature, as also exemplified below.

Detection of hydrogen-containing gases

Hydrogen, H_2, adsorbs dissociatively on catalytic gate metals such as Pd, Pt and Ir. In the presence of hydrogen alone, the steady-state surface coverage of hydrogen atoms follows the simple Langmuir relation (Fogelberg *et al.*, 1995; Ekedahl *et al.*, 1998) and is only dependent on ambient hydrogen pressure. Normally, also other substances are present in the surrounding atmosphere and may affect the equilibrium coverage of hydrogen in different ways. Notably, oxygen also adsorbs dissociatively on commonly-used gate metals at sensor operating temperatures – the recombination and desorption rates, however, being very low at these temperatures. Below 300°C, oxygen can basically be removed at any appreciable rate only through reaction with other atoms or molecules, such as chemisorbed hydrogen in the formation of water. In normal air, the pressure-dependent hydrogen coverage for

© Woodhead Publishing Limited, 2013

every gate material is determined by the adsorption and desorption characteristics of hydrogen and its reaction with adsorbed oxygen. Variations in hydrogen and oxygen partial pressures thus lead to a change in coverage.

The generated hydrogen atoms are, to some extent, also withdrawn from the surface by rapid diffusion through the metal contact to the metal/insulator interface. Due to the very rapid diffusion, the surface coverage and interface hydrogen concentration are in equilibrium. As concluded from IR spectroscopy (Wallin *et al.*, 2005), the hydrogen atoms adsorb to oxygen atoms in the surface of oxidic insulators, forming OH groups on the oxide accompanied by substantial charge transfer. Since OH groups have a large dipole moment, the interface layer of dipoles introduces a sharp potential step at the interface, earlier referred to as an internal voltage drop V_{int}. This voltage drop adds to the externally applied bias, resulting in a shift of the I/V characteristics of the sensor, as illustrated in Fig. 4.2(c), and is given by:

$$\Delta V_{int} = n_H \cdot \frac{p}{\varepsilon} \qquad [4.3]$$

where p is the dipole moment of an OH group, ε the permittivity of free space and n_H is the number of hydrogen atoms per unit area at the interface, which is related to the metal surface coverage of hydrogen (Eriksson *et al.*, 1997; Usagawa and Kikuchi, 2011). The size of the I/V shift is thus a measure of the ambient partial pressure of hydrogen, in relation to other gases such as oxygen. A corresponding energy band diagram illustrating the effect of this dipole layer can be found in Fig. 4.2(b).

From a sensor response point of view, it has been shown that dipole formation is the dominant effect regarding hydrogen detection. Work function changes due to adsorption on the metal side of the interface only have a minor influence on the sensor signal, introducing a small shift in the I/V or C/V characteristics in the opposite direction to that generated by dipole formation (Eriksson and Ekedahl, 1998). Further evidence for the importance of an oxidic insulator surface has been obtained from sensors based on both SiC and GaN Schottky diodes (Schalwig *et al.*, 2002b; Weidemann *et al.*, 2003), for which the hydrogen response considerably improved upon the introduction of a thin oxide between the metal and the semiconductor. When comparing the hydrogen response from devices with different insulator materials (e.g. Al_2O_3, Ta_2O_5, SiO_2), the response correlates well with the insulator surface density of oxygen atoms (Eriksson *et al.*, 2005), further emphasizing the role of the oxygen as adsorption sites for the hydrogen (see Fig. 4.3). The choice of insulator thus influences the hydrogen sensitivity of field effect devices, as well as their dynamic range.

In the case of other molecules containing hydrogen, the same basic principles as for hydrogen apply if free hydrogen atoms can be generated upon

© Woodhead Publishing Limited, 2013

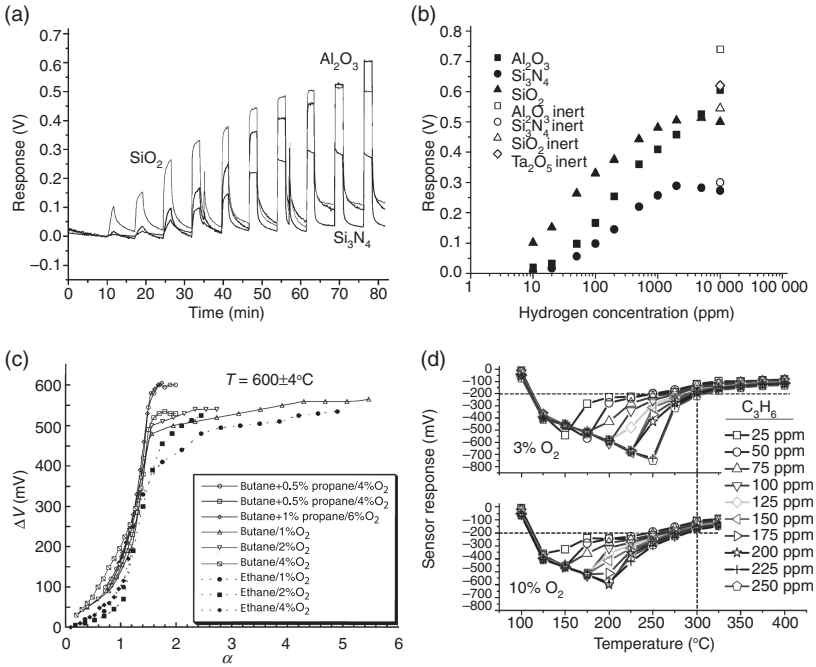

4.3 This figure displays, in (a) and (b), the response to hydrogen in the range 10 ppm to 1% in air or N_2 (indicated as 'inert' in (b)) at 140°C for Pd/Pt gate field effect sensors with various insulator materials. In (c) and (d) the response ΔV to saturated hydrocarbons at 600°C as a function of equivalence ratio α is given, as well as the response to unsaturated hydrocarbons at temperatures of 100–400°C and concentrations well below the equivalence ratio. The equivalence ratio is defined as the ratio of the actual fuel-to-oxidizer ratio to the stoichiometric fuel-to-oxidizer ratio. Panels (a) and (b) are reprinted with permission from the *Journal of Applied Physics* 98:3 (2005), 034903. © 2012 American Institute of Physics (Eriksson *et al.*, 2005). Panel (c) is reprinted with permission from *Sensors and Actuators* B43 (1997), 52–5. © 1997 Elsevier (Baranzahi *et al.*, 1997). Panel (d) is reprinted with permission from the Proceedings of the IEEE International Conference on Sensors, Atlanta, Georgia, USA, October 2007, 493–4. © 2007 IEEE (Andersson *et al.*, 2007)

adsorption. At temperatures of approximately 600°C and above, field effect sensors with catalytic metal gates exhibit a binary response to hydrocarbons, irrespective of hydrocarbon identity (see Fig. 4.3) (Baranzahi *et al.*, 1997). As long as the oxygen concentration is such that complete oxidation of the hydrocarbons can take place on the gate metal, the high reaction rates keep the surface fairly clean from hydrocarbons and, to a large extent, oxygen covered. Any hydrocarbons sticking to the surface are oxidized directly upon adsorption without generation of any free hydrogen atoms.

© Woodhead Publishing Limited, 2013

When increasing the hydrocarbon concentration beyond the stoichiometric hydrocarbon to oxygen ratio, the hydrocarbons reduce the gate metal surface and effectively deplete it of oxygen. Dissociation, rather than oxidation, is the dominating process, producing free hydrogen atoms which can reach the interface and induce an internal voltage drop.

At lower temperatures, certain hydrocarbons – e.g. unsaturated hydrocarbons such as C_2H_4 and C_3H_6 – may still reduce the catalytic metal surface and produce free hydrogen even in the presence of excess amounts of oxygen (Burch and Watling, 1997, 1998). The underlying reason is the higher sticking probability of these hydrocarbons compared with oxygen and the lower rates of oxidation at lower temperatures. Pt gate sensors operated at 200–300°C therefore also exhibit a binary switch in sensor response, the switch point being dependent on oxygen concentration and temperature (due to the temperature dependence of the sticking coefficients), see Fig. 4.3. For decomposition of saturated hydrocarbons on the catalytic sensor surface in an atmosphere of excess oxygen, all decomposed hydrogen atoms end up as water molecules, which desorb from the sensor surface. Therefore no free hydrogen atoms are generated and no sensor response obtained from these substances for excess oxygen conditions (Burch and Watling, 1998; Andersson *et al.*, 2004).

Another hydrogen containing substance which has attracted a great deal of interest in the field of high-temperature gas sensors is ammonia (NH_3). Ammonia has not been observed to dissociate upon adsorption to Pt at temperatures below approximately 225°C (Chilton, 1960). Furthermore, there is some evidence of the dissociation occurring being oxygen-mediated on Pd-MOS sensor devices (Fogelberg *et al.*, 1987), leading to direct oxidation of adsorbed ammonia. The view that no free hydrogen atoms are generated on the Pt surface accords with the observations from sensors with dense, homogeneous Pt gates, for which no ammonia response is obtained. In case of a discontinuous gate metal (see Fig. 4.2), exposing parts of the oxide to the ambient, the field effect devices exhibit similar sensing characteristics as for hydrogen (Spetz *et al.*, 1987; Löfdahl, 2001a).

The generally-accepted view emphasizes the importance of the three phase boundaries between oxide, metal and the gas phase as the site for ammonia dissociation to create OH groups on the surface of the oxide (Löfdahl, 2001b). At the metal/oxide border, hydrogen from the ammonia molecule may be directly transferred to oxygen atoms in the surface of the oxide, possibly as a proton, the charged complex being stabilized by its proximity to the metal. Fourier Transform Infrared (FTIR) spectroscopic measurements on a model system consisting of a Pt impregnated SiO_2 powder revealed the formation of OH groups at temperatures above 225°C upon exposure to ammonia (Wallin *et al.*, 2007). The amount of OH groups formed correlated well with the Pt loading (coverage), which has been interpreted as the OH groups

© Woodhead Publishing Limited, 2013

being located close to the metal/oxide border. Local response measurements performed on capacitive field effect sensor devices by laterally-resolved photo current measurements have provided similar results, relating the generation of OH groups to the metal/oxide border. Furthermore, these investigations also indicated the possibility for diffusion of hydrogen/protons into the metal/oxide interface underneath the metal (Löfdahl, 2001b), inducing the same kind of internal voltage drop as in the case of hydrogen exposure.

As previously mentioned, oxygen also adsorbs dissociatively on Pt and negatively-charged oxygen atoms may spill over to exposed areas of the oxide surface in devices with a discontinuous gate contact. At steady state, an equilibrium between oxygen coverage on the Pt surface and concentration of oxygen anions on the oxide surface would then develop. It has been suggested that the response of porous Pt gate sensors to reducing substances such as hydrogen, hydrocarbons and ammonia may partly originate from the reverse spill-over of oxygen anions and their removal on the Pt surface through reactions with adsorbed hydrogen, hydrocarbon and ammonia molecules (Schalwig *et al*., 2002c; Yamaguchi *et al*., 2007). It should be noted that the removal of negative charge from the oxide surface has the same effect on the I/V or C/V characteristics of field effect sensors as the voltage drop introduced by OH group formation.

Detection of non-hydrogen-containing gases

Carbon monoxide (CO) is an example of a reducing, non-hydrogen-containing substance for which the interaction with Pt gate field effect sensors may cause a substantial change in the I/V or C/Vcharacteristics of a device. Without being able to generate any free hydrogen upon adsorption, the CO sensitivity has been stipulated to be at least partly caused by the removal of oxygen anions (Schalwig *et al*., 2002c), as discussed above, and/or the reduction (Nakagomi *et al*., 1997; Becker *et al*., 2011) of a surface platinum oxide (Dean *et al*., 1988). The CO response also correlates well with the CO oxidation characteristics on silica-supported Pt (Andersson *et al*., 2010; Becker *et al*., 2011) At the same point where the oxidation rate suddenly drops when increasing the CO/O_2 ratio or decreasing the temperature, the sensor signal exhibits a binary switch from a small to a large response (see also Fig. 4.4) (Andersson *et al*., 2011; Darmastuti *et al*., 2011). In analogy with the previously discussed case regarding hydrocarbons, the higher sticking probability of CO compared with oxygen at lower temperatures leads to the Pt surface being practically covered with CO (unless the CO/O_2 ratio is too small), almost excluding oxygen adsorption, at CO concentrations well below the oxygen concentration. With no or very little oxygen on the surface, the CO oxidation rate is very low. At higher temperature or higher oxygen concentration, the poisoning of the sensor by adsorbed CO on the sensor surface recovers as the CO is removed and the Pt surface rapidly reverts to being

© Woodhead Publishing Limited, 2013

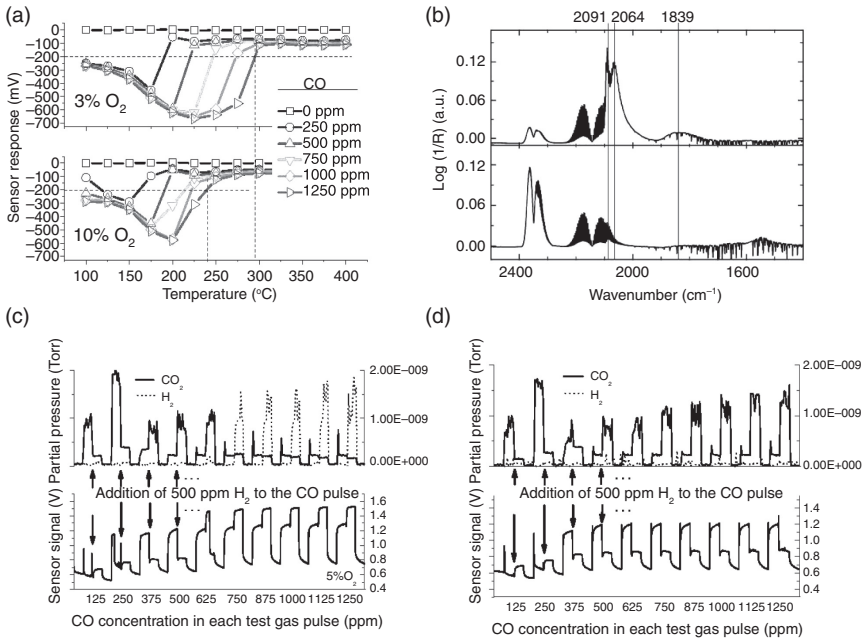

4.4 In (a), the CO/O_2 and temperature-dependent binary switch of the response of Pt gate field effect sensors towards CO is exemplified. Panel (b) displays the disruption of the adsorbed CO layer on the Pt surface upon hydrogen exposure; the spectral peaks at 1839, 2091 and 2064 cm^{-1} (upper panel: 250 ppm CO in 5% O_2) correspond to CO adsorbed on Pt, whereas the peaks at wave numbers slightly below 2400 cm^{-1} (lower panel: 500 ppm H_2 added to 250 ppm CO in 5% O_2) represents gaseous CO_2. In (c) and (d), the sensor response towards CO in the range of 125–1250 ppm in the absence/presence of hydrogen (500 ppm) is given for two different oxygen concentrations (lower panels), as well as the downstream H_2 and CO_2 partial pressures (upper panels). Panel (a) is reprinted with permission from the Proceedings of the IEEE International Conference on Sensors, Atlanta, Georgia, USA, October 2007, 493–4. © 2007 IEEE (Andersson *et al.*, 2007). Panel (b) is reprinted with permission from the *IEEE Sensors Journal*, 11(7), 1527–34. © 2011 IEEE (Becker *et al.*, 2011). Panels (c) and (d) are reprinted with permission from the Proceedings of the IEEE International Conference on Sensors, Limerick, Ireland, October 2011, 493–4. © 2011 IEEE (Darmastuti *et al.*, 2011).

dominated by adsorbed oxygen. A large response of Pt gate field effect devices to CO therefore correlates with a surface completely covered by CO, whereas a small CO response is encountered whenever the Pt surface is oxygen dominated. Not only porous Pt gate contacts exhibit these characteristics, however. Dense films without any exposed oxide areas also show the same binary switch in sensor signal (Andersson and Lloyd Spetz, 2010). Furthermore, upon introduction of hydrogen at a constant concentration,

© Woodhead Publishing Limited, 2013

the large CO response of Pt gate sensors can either increase or decrease, depending on the CO/O_2 ratio and temperature, see Figs. 4.4(c) and (d). It has also been concluded that the presence of hydrogen can break the self-poisoning of the CO oxidation (Becker 2011) (Fig. 4.4(b)). This indicates that hydrogen may be able to penetrate/adsorb on a Pt surface covered by CO and, if the CO concentration in relation to the oxygen concentration is small, disrupt the CO coverage.

If, on the other hand, the CO/O_2 ratio is too high in comparison with the hydrogen concentration, or the Pt surface temperature too low, the surface remains covered by CO and, effectively, depleted of oxygen. Without any oxygen on the surface, there is no risk of adsorbing hydrogen on the Pt surface being oxidized. A much higher proportion of hydrogen atoms can therefore reach the interface. As a consequence, a CO-covered surface will exhibit a very much larger sensitivity to small concentrations of hydrogen, suggesting the CO response partly being mediated through an increased sensitivity to the background concentration of hydrogen present in all gas mixtures. Further support for the influence of hydrogen on the CO response is given from UHV studies on Si-based field effect devices (Eriksson and Ekedahl, 1997; Medlin *et al.*, 2003).

As exemplified above, the application-specific performance of a sensor is thus influenced by adsorption, reactions between adsorbed species and desorption characteristics of the individual substances present in the gas mixture. These characteristics depend on the materials interacting with the substances, the structure of the materials and the operation temperature; therefore, the selectivity and sensitivity to the gases of interest can be influenced by the choice of gate materials, their structure and the temperature. For the development of sensors for new applications, it is therefore important to gain knowledge about gas solid interactions and sensor mechanisms to be able to tailor devices with good selectivity and sensitivity to the target substance(s).

4.3 Recent material developments for improved selectivity of SiC gas sensors

The ability of hydrogen atoms to diffuse through the commonly-used gate materials renders most of the field effect sensors developed so far to exhibit hydrogen sensitivity. Also, nitride-based insulators have a tendency to oxidize over time, providing the necessary sites for hydrogen adsorption (Eriksson *et al.*, 2005). In developing sensors for specific applications, the issue of cross-sensitivity to hydrogen and substances containing hydrogen therefore has to be taken into account. For most applications, this cross-sensitivity has been a limit for the development of field effect-based devices for sensing of substances that do not contain hydrogen, such as oxygen, nitrogen oxides and sulphur oxides. In order to widen the area of application for

© Woodhead Publishing Limited, 2013

field effect sensors by increasing selectivity towards other substances than hydrogen or hydrogen containing gases, one line of development has been the introduction of new materials combinations.

4.3.1 New material combinations

From theoretical considerations and experimental results, indications exist which suggest that hydrogen termination – and thus, OH group formation – is energetically unfavourable on most magnesium oxide (MgO) surfaces (Chizallet *et al*., 2006; Darmastuti *et al*., 2011). It has also been postulated that hydrogen adsorption at the insulator/metal interface of the MgO/Pt system would occur on the metal, rather than the insulator side of the interface. Experimental results point in the same direction, field effect sensors based on MgO/Pt structures exhibiting no or very little response/sensitivity to hydrogen. The very small hydrogen-induced response is also in the opposite direction to the normal hydrogen response of SiO_2/Pt structures, as briefly discussed earlier, indicating hydrogen adsorption to the metal side of the interface (Eriksson and Ekedahl, 1998). Furthermore, the CO sensitivity of devices comprising dense Pt gate films on top of MgO is extremely low or non-existent, providing further indications for the CO response of SiO_2/Pt-based sensors at least partly being mediated by an increase in sensitivity towards background hydrogen.

Tailor-made sensing layers for oxygen

With the introduction of MgO as the top part of the insulating layer in field effect sensors, the cross-sensitivity to hydrogen or substances containing hydrogen can thus be markedly reduced. This has also been shown for field effect devices with other gate contacts than Pt. By using conducting oxides as gate material – such as iridium oxide (IrO_2) or ruthenium oxide (RuO_2), for which the work function changes as a function of oxidation state (Sang *et al*., 2003) – it has been shown that the sensitivity towards oxygen, and thereby the gas-sensing abilities of field effect sensors, can also be retained when MgO is used as the insulator (Andersson and Lloyd Spetz, 2009) (see Fig. 4.5). This realizes oxygen sensors with no need for reference gas, unlike the lambda (in the US, universal heated exhaust gas oxygen, UHEGO) sensor (Logothetis *et al*., 1992).

Partial oxidation or reduction upon exposure to different oxygen concentrations at elevated temperatures changes the work function of the gate material at the gate material/insulator boundary and thereby, as discussed in Section 4.2, also the C/V or I/V characteristics of the device. Similar sensors employing ruthenium oxide nanoparticles deposited on SiO_2 as gate

© Woodhead Publishing Limited, 2013

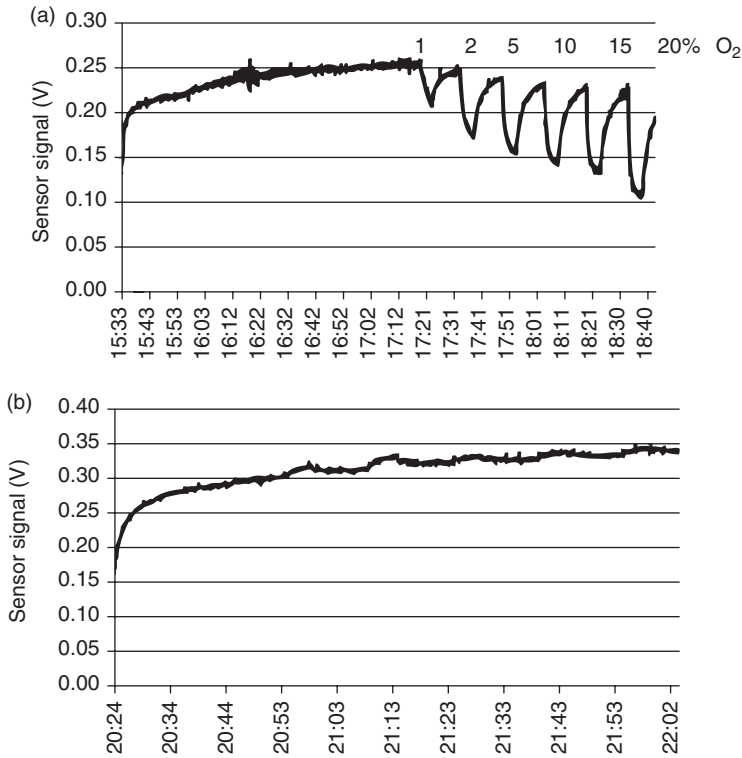

4.5 (a) The response of a $Pt/IrO_2/MgO$ sensor towards 1, 2, 5, 10, 15 and 20% O_2 in a background of 0.1% O_2 in N_2 at 500°C. (b) The response to 200, 500 and 1000 ppm CO and 100, 250 and 500 ppm propene for the same sensor. Reprinted with permission from the Proceedings of the IEEE International Conference on Sensors, Christchurch, New Zealand, October 2009, 2031–5. © 2009 IEEE (Andersson *et al.*, 2009).

material, on the other hand, exhibit more or less the same response characteristics to hydrogen and substances containing hydrogen as Pt/SiO_2 and Ru/SiO_2 structures (Salomonsson *et al.*, 2006).

Tailoring layers for CO_2 and NO_x

Not only have the cross-sensitivity issues been addressed in the development of new sensing materials and materials combinations also possible solutions have been investigated for the detection of substances (e.g. CO_2 and NO_2) which have not been possible to detect with the field effect sensors developed so far. Ion-conducting materials sandwiched between a porous metal gate contact and the insulator have been studied since 2000 (Nakagomi and Lloyd Spetz, 2006). Upon exposure of such structures to the target gas (e.g.

© Woodhead Publishing Limited, 2013

O_2), the target gas adsorbs on the metal gate surface, picking up charge from the metal and thereby forming the corresponding ion (e.g. by formation of oxygen anions O^-). At the three phase boundaries between the metal, ion conductor and the gas phase, these ions spill over to, and can be incorporated in, the material at vacant positions. Most often, but not always, the material is partly composed of the same atom/ion as the target gas for detection (in the case of oxygen, the ion conductor is normally an oxide, such as zirconium oxide ZrO_2, commonly doped by some other element, e.g. yttrium, to create more of oxygen vacancies) (Visser *et al.*, 2001).

At elevated temperatures, the ions start to become mobile, moving through the material from high to low concentration by diffusion through vacancies. As a result, charges are introduced into the electronically non-conducting material and to the interface between the ion-conducting and insulating layers, thereby, as described in Section 4.2, changing the C/V or I/V characteristics of the device. This diffusion is counteracted by the drift due to the electrical field created between the interface and the gate electrode, the latter being held at a constant potential. At equilibrium, the net ion current is zero and the potential drop across the ion-conducting layer in simple terms is theoretically given by the Nernst relation (Equation [4.4]).

$$\Delta V = V_{offset}(T) + \left(\frac{RT}{nF}\right) \cdot \ln\left(\frac{[A]_{surface}}{[A]_{interface}}\right) \qquad [4.4]$$

where V_{offset} is a potential difference inherent to the material or materials combination, R the molar gas constant, T temperature, n the number of electrons transferred per reaction, F the Faraday constant and $[A]_{surface}$ and $[A]_{interface}$ the concentration of species A at the surface and interface, respectively: see, for instance, Reinhardt *et al.* (2002) and Garzon *et al.* (2004).

In conjunction with SiC-based field effect sensors, this concept was mainly used earlier for the detection of oxygen. Examples of ion-conducting materials introduced between the porous gate contact and the insulator include ZrO_2 (Miyahara *et al.*, 1987; Tobias *et al.*, 2000), CeO_2 (Jacobsén *et al.*, 2001) and $BaSnO_3$ (Cerdá *et al.*, 2002; Cerdá *et al.*, 2003). ZrO_2 has been shown to work fairly well for oxygen assessments at high temperatures (600°C and above), whereas devices based on the ion conductor LaF_3 exhibit a good oxygen sensitivity at lower temperatures, down to room temperature (Krause *et al.*, 1994; Vasiliev *et al.*, 1998). Furthermore, the combination of MgO (as insulator) and LaF_3 in field effect devices has also given indications on the possibility for oxygen sensing with markedly reduced cross-sensitivity to hydrogen or substances containing hydrogen. Possibilities for oxygen sensing at lower operating temperatures, as compared to the above-mentioned MgO/conducting oxide combinations, have thus been implicated (Andersson *et al.*, 2009).

© Woodhead Publishing Limited, 2013

Recently, the concept has also been utilized for the development of field effect devices sensitive to carbon dioxide (CO_2) and nitrogen dioxide (NO_2). By the introduction of a solid electrolyte for which, instead of oxygen anions, carbonates ($CO_3^{(2-)}$) or nitrites/nitrates (NO_2^-/NO_3^-) are incorporated in the ion conducting layer, new possibilities have emerged. In combination with a catalytic gate electrode, from which the carbonates/nitrates are generated upon adsorption of CO_2/NO_2 (through the reaction with adsorbed oxygen anions), field effect sensor devices based on the same principles as oxygen sensors can be realized (Zamani *et al.*, 2005; Kida *et al.*, 2008). In analogy with the oxygen sensors, the transfer of charge, in the form of CO_3^{2-} or NO_3^-, from the gate electrode into the electronically non-conducting solid electrolyte gives rise to a change in the C/V or I/V characteristics of the device. Earlier investigations have also shown promising results regarding NO_2 sensing with Si-based MIS capacitor structures employing $NaNO_2$ as the ion-conducting material (Zamani *et al.*, 2005).

For the detection of CO_2 with a carbonate-based electrolyte, device operating temperatures of 400°C and above are, however, required. At temperatures above 200°C, Si devices suffer from intrinsic conduction effects and can therefore not be applied for carbonate-based CO_2 sensors. Owing to its wide band gap, no such limitations are encountered for SiC-based devices, allowing the development of a SiC field effect CO_2 sensor based on the binary lithium carbonate (Li_2CO_3)/barium carbonate ($BaCO_3$) solid electrolyte (see Fig. 4.6). The binary ion conductor exhibits, in addition to good CO_2 sensitivity, an excellent stability under humid conditions. As can be seen from Fig. 4.6, the electrolyte was deposited on top of MgO and a highly porous Pt gate electrode with promising results regarding CO_2 monitoring (Inoue *et al.*, 2010). In this case, MgO also acts as a passivation layer, preventing lithium ions (Li+) from diffusing into the insulating layer during processing and operation of the device.

4.4 Dynamic sensor operation

To improve selectivity towards certain gaseous substances for which detection and quantification otherwise might prove difficult due to interference from other gases, the remedy has often been the introduction of more sensors, each with its own cross-sensitivity pattern. Normally, the combination of sensors and sensitivity patterns is very complicated, involving a large number of different kinds of sensors or similar sensors operated at different temperatures. The large number of sensor signals and their individual cross-sensitivities makes it necessary to reduce dimensionality by using multivariate data analysis and to use pattern recognition methods to retrieve the desired information.

© Woodhead Publishing Limited, 2013

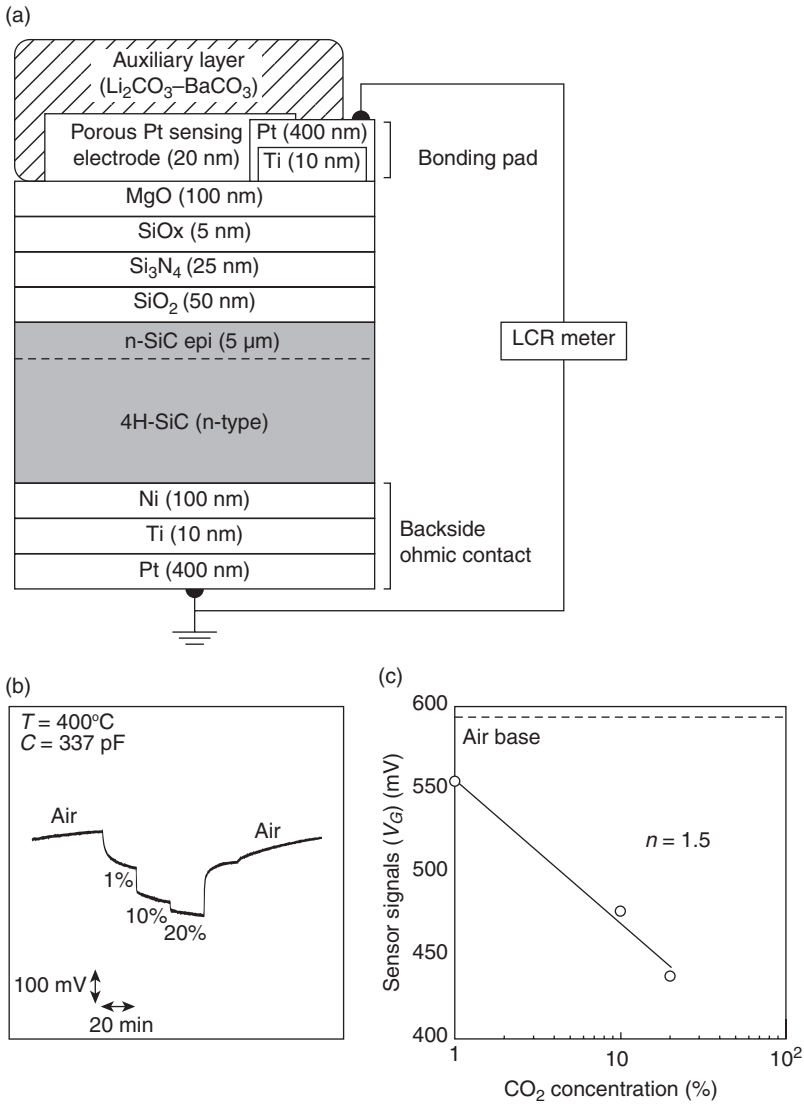

4.6 (a) Schematic drawing of the MISiC field effect-based CO_2 sensor with a binary carbonate (Li_2CO_3-$BaCO_3$) auxiliary layer (LCR meter: inductance, capacitance and resistance meter). (b) and (c) Response characteristics during CO_2 exposure at 400°C for the device in (a). Reprinted with permission from *Electrochemical and Solid State Letters* 14:1 (2010), J4–7. © 2010 The Electrochemical Society (Inoue *et al.*, 2010).

© Woodhead Publishing Limited, 2013

The most common method to reduce dimensionality is Principal Components Analysis (PCA) (Chatfield, 1980; Wold *et al.*, 2001). Multivariate methods such as PCA have, for example, been used in conjunction with SiC-based field effect devices to monitor the combustion process in bio mass fuelled power plants (Unéus *et al.*, 2005) for the estimation of ammonia concentration in typical flue gases (Andersson *et al.*, 2004) and for fast lambda control of a gasoline engine (Larsson *et al.*, 2002).

Another example of a multivariate analysis method is Linear Discriminants Analysis (LDA) (Duda *et al.*, 2000; Gutierrez-Osuna, 2002). In analogy with the method of PCA, new variables (discriminant functions – DFs) are introduced which are linear combinations of the original. Whereas PCA is an unsupervised method, in LDA the assignment of sensor observations into pre-defined groups – e.g. corresponding to concentrations of a certain target gas – is taken into account already when constructing the new variables. The linear combinations of sensor signals are calculated such that the distances between the centres of pre-defined groups are maximized in the new projected data set, while minimizing the scatter among observations within the different groups. This makes LDA a supervised method.

As was discussed earlier, the interactions between a certain gate material and the substances of the surrounding gas matrix are temperature-dependent. Different substances show different temperature dependence, which is why operation of a sensor at a number of different temperatures can provide more information about the gas matrix composition, or the concentration of a specific gas in a background of other gases. Instead of an array of sensors, each operated at a different temperature, the operation of one sensor in a cyclic temperature mode can provide just as much, or even more, information. Not only is the application of more temperatures simplified, but there is also the benefit of automatically obtaining information from non-equilibrium conditions, when changing from one temperature to another, aiding in the discrimination between gases and concentrations. The mean value of the sensor signal at different temperatures, as well as the derivatives of the signal corresponding to temperature changes, can then be extracted and treated by multivariate methods (just as for the case of signals from many individual sensors).

This approach has been developed using commercial resistive-type metal oxide semiconductor sensors – for example, for early fire detection in coal mines (Lee and Reedy, 1999; Reimann *et al.*, 2009). This concept is now also under development for field effect sensor devices based on SiC for the detection and quantification of, for example, NO_2. It has initially been demonstrated that discrimination between different gases (such as H_2, NH_3 and CO) and different concentrations seems possible for both Pt and Ir gate field effect sensors (Bur *et al.*, 2010; Bur *et al.*, 2011a).

© Woodhead Publishing Limited, 2013

As an example, consider the temperature cycle developed for NO_x assessment illustrated in Fig. 4.7 (Bur *et al.*, 2011b; Bur *et al.*, 2012). In a first step, ramping the sensor operation temperature from 100°C to 400°C, the temperatures for which the sensor exhibits maximum sensitivity towards NO_x as well as the greatest response in comparison with interfering gases such as NH_3, CO and hydrocarbons were identified and included in the temperature cycle. On the same basis, the cycle was divided into 10 intervals from which various features were extracted. Examples of features are the mean, maximum and minimum values, as well as the initial derivative and integral of each interval. Furthermore, a stepwise LDA was performed, the purpose of which was to determine the significance of the different features regarding their contribution to the overall quantification of NO_x. The sensor signal and each feature was thereby also filtered, to suppress the noise but preserve the original sensor signal features, and normalized not to skew the significance among features due to larger absolute values or noise. The final LDA model was based on the features of mean value, slope, standard deviation and Euclidian norm of each interval. The preliminary results indicated good possibilities for the estimation of NO_x levels in a background of typical exhaust and flue gases (see Fig. 4.7) (Bur *et al.*, 2011b).

Bias cycling is another alternative for a dynamic mode of operation. The interaction between the various gaseous substances and the gate material is not only dependent on their identity and temperature, but also the gate potential. In analogy with the temperature cycling mode, a bias cycle could possibly be developed to increase selectivity towards one or more substances. Preliminary results from I/V measurements performed under various gate biases and CO concentrations suggest that the approach might be feasible for the determination of CO concentration.

The development of two different sensor operating modes may also open up possibilities regarding self-diagnostic sensor systems. Comparison of the data from two independent methods – e.g. temperature and bias cycling – may increase the chances for fault-detection and self-diagnosis of the sensor. In the event of sensor malfunction, it is not likely that the outcome of two separate evaluation schemes would be similar, the discrepancy between them therefore indicating problems. The concept has been demonstrated for a resistive-type metal oxide semiconductor sensor utilizing simultaneous temperature cycling and electrical impedance spectroscopy measurements (Reimann *et al.*, 2008).

4.5 Novel SiC and graphene-based sensor devices

One recent development in the field of SiC which has attracted much attention from across the scientific community has been the epitaxial growth of

© Woodhead Publishing Limited, 2013

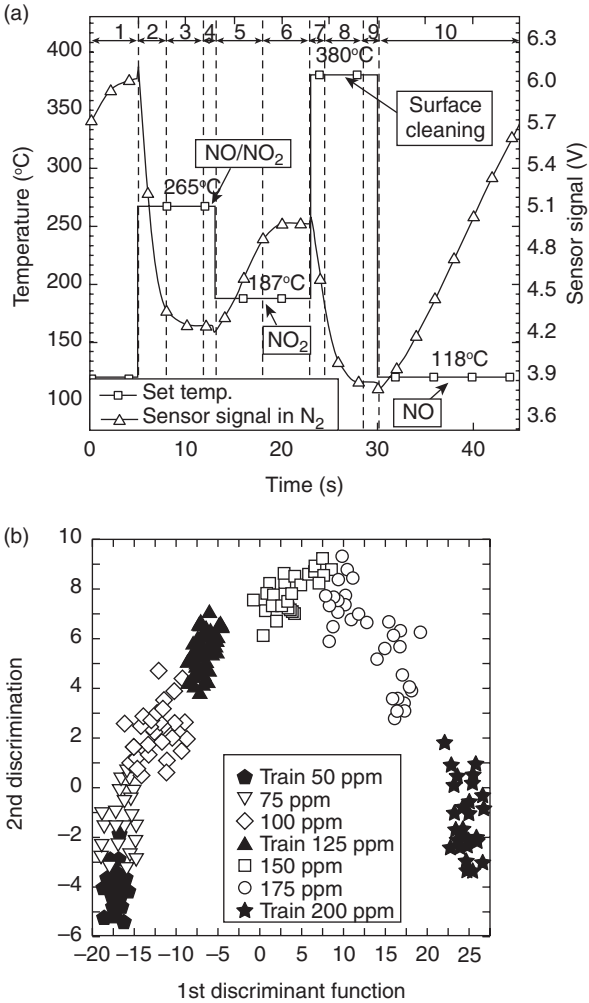

4.7 In (a) the temperature cycle developed for NO_x quantification with a Pt gate SiC-based field effect sensor is displayed. In (b) the discrimination is given between different NO_x concentrations when loading the selected features (mean value, slope, standard deviation and Euclidian norm) of each of the 10 intervals indicated in (a) into the LDA. The concentrations of 50, 125 and 200 ppm, and denoted train, have been used for developing (training) the model, whereas the other concentrations were used to evaluate the model. Reprinted with permission from the Proceedings of the IEEE International Conference on Sensors, Limerick, Ireland, October 2011, 137–40. © 2011 IEEE (Bur *et al.*, 2011b).

© Woodhead Publishing Limited, 2013

graphene layers on SiC. The growth of graphene on SiC is arguably the most promising method for large-scale, controlled growth of graphene. This new material has the potential to become an excellent sensor for applications at low temperatures. The discussion of epitaxially-grown graphene on SiC will form the last section in this chapter, and will focus mainly on the production and properties of graphene epitaxially-grown on SiC. There is also a survey of the field, including production of epitaxial graphene-based sensors and the mechanisms by which they give a response.

4.5.1 Properties of graphene

Graphene is a single graphite layer, consisting of a hexagonally arranged, sp^2 bonded, stable two-dimensional allotrope of carbon with a plethora of unique properties (Geim and Novoselov, 2004). Of particular interest are the unusual electronic properties of graphene. The band structure of graphene – first calculated by Wallace in 1947 (Wallace, 1947) – forms Dirac cones where the valence and conduction bands, formed by the π and π^* states, respectively, touch at Dirac points (Wilson, 2006) (see Fig. 4.8). As the bands touch, graphene has no band gap and, as there is zero density of states at the Fermi level, graphene is often referred to as a 'semimetal' or a 'zero-gap' semiconductor. Changes in number of even a few charge carriers away from the Fermi level can cause notable changes in conductivity (Novoselov *et al.*, 2004) (see Fig. 4.9). Changes in conductivity can be introduced by applying an external electric field, by adsorption of gases or by proximity to charges – e.g. on a substrate. Graphene is ambipolar and can either donate or accept electrons-in both cases an increase in conductivity is observed for previously undoped graphene (Schedin *et al.*, 2007).

Graphene was predicted to be thermodynamically unstable due to its two-dimensional nature (Peierls, 1935; Landau, 1937) and, instead, roll up to form one-dimensional carbon nanotubes or fullerene-like balls. This theoretically

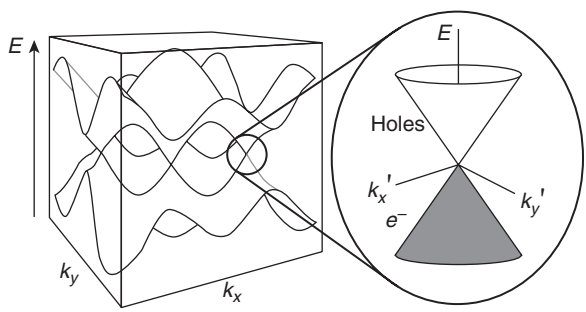

4.8 The band structure of graphene as first calculated by Wallace in 1947.

© Woodhead Publishing Limited, 2013

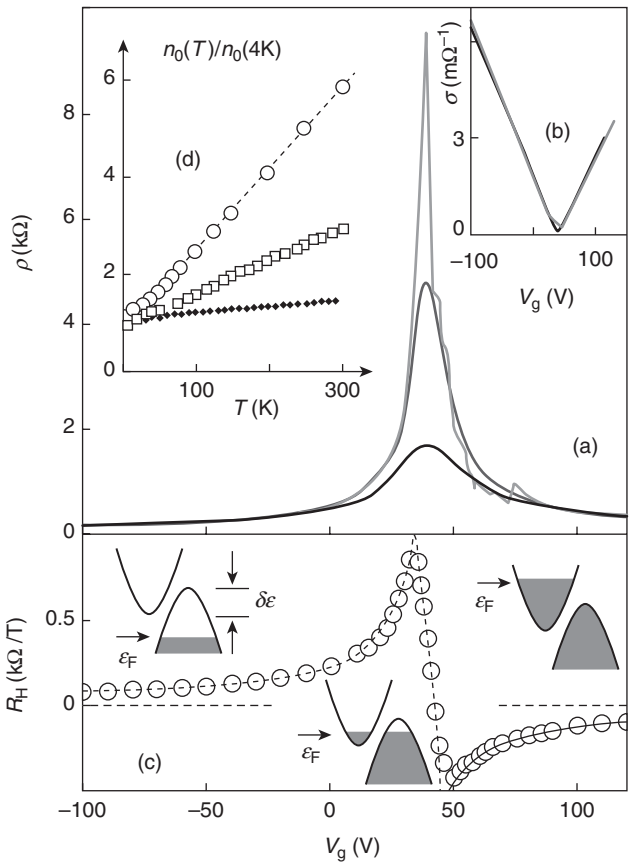

4.9 In this figure, (a) presents the field effect in few-layer graphene (FLG), showing typical dependences of graphene's resistivity ρ on gate voltage for different temperatures (T = 5, 70 and 300 K for top to bottom curves, respectively); (b) presents an example of changes in the film's conductivity $\sigma = 1/\rho(V_g)$ obtained by inverting the 70 K curve, (c) shows the Hall coefficient R_H vs V_g for the same film – ε_F denotes the Fermi level and $\delta\varepsilon$ the energy overlap between the valence and conductance bands, (d) presents the temperature dependence of carrier concentration n_0 in the mixed state for the film in (a) (open circles), a thicker FLG film (squares) and multi-layer graphene ($d \approx 5$ nm; solid circles) – the dashed curves in (b) to (d) are the dependences calculated from a model of a two-dimensional semimetal illustrated by figure (b). Reprinted with permission from *Science* 306 (2004), 666–9. © 2004 AAAS (Novoselov *et al.*, 2004).

predicted instability is observed in free-standing graphene sheet as folds and wrinkles (Meyer *et al.*, 2007), with further stability incurred from the strong van der Waals forces binding the graphene to its substrate (Riedl *et al.*, 2009).

© Woodhead Publishing Limited, 2013

4.5.2 Graphene as a gas-sensitive material

The interest in graphene as a sensor material stems from its unique electrical properties. The band structure of graphene makes it particularly sensitive to chemical doping; the withdrawal or donation of even a few electrons shifts the Fermi level significantly away from the Dirac point, thus a small change in the number of charge carriers has a significant effect on the resistance of the graphene sheet.

Apart from its singular band structure, graphene has many other properties that render it particularly suitable for applications as a gas sensor. Single-layer graphene has every atom at the surface, has high metallic conductivity, even when very few charge carriers are present (Novoselov *et al*., 2004); and few crystal defects, which leads to low Johnson noise (Novoselov *et al*., 2005; Schedin *et al*., 2007) and thermal switching noise (also referred to as 'flicker' or 'low frequency (1/f) noise') (Liu *et al*., 2009). The low noise level in graphene devices means that very small changes in resistivity – i.e. small sensor responses – can be detected, leading to highly sensitive sensors. Graphene is also chemically very stable due to its strong bonds and lack of defects. The electronic conductivity of graphene allows for direct measurement of resistance, and the robustness of graphene allows for layers only one atom thick to be processed into sensors.

The mechanism of detection in graphene sensors is still a hotly-debated topic with Schedin *et al*.(2007) describing the change in number of charge carriers with adsorption of gases. A similar mechanism was proposed with the first carbon nanotube FET sensor (Kong *et al*., 2000), whereby electron-withdrawing molecules reduce the number of electrons and increase the number of holes – so increasing the charge carriers in the p-type carbon material, and electron-donating molecules increase the number of electrons and reduce the number of holes – decreasing the charge carriers in p-type carbon materials. A concurrent sensing mechanism was proposed by Hwang *et al*. for graphene on SiO_2 (Hwang *et al*., 2007); using the results of Schedin *et al*., they calculated the Hall mobility of graphene when exposed to gases and showed that the increase in mobility upon gaseous exposure increased. Instead of gas adsorption causing a decrease in mobility due to increased impurity scattering, it is theorized that, as Hall mobility increases upon gaseous adsorption, scattering in the graphene must decrease, due to neutralization of charged scattering impurities thought to be at the surface between the graphene and the SiO_2 substrate. Evidence for an induced decrease in mobility upon adsorption of certain species on bi-layer and few-layer graphene have, however, also been presented (Klarskov *et al*., 2011; Sato *et al*., 2011).

4.5.3 Production of graphene

With the explosion of interest in graphene after the Nobel prize winning publication in 2004 (Novoselov *et al*., 2004), there followed a similar

© Woodhead Publishing Limited, 2013

explosion in publications on growth and production methods of graphene. Whilst many of these production methods were previously known, the electronic properties of the graphene produced had not been tested before and the importance of the material produced had not been fully realized. Large coverage of graphene with a uniform number of layers and a low defect concentration is required for production of devices, with the cost of production also vital if mass production is to be achieved.

The mechanical exfoliation of graphite into its constituent graphene layers was famously first achieved using sticky tape for the repeated separation of the graphene layers from each other, followed by dissolution of the graphene platelets and their subsequent disposition on a SiO_2 substrate (Novoselov *et al*., 2004). The graphene flakes are optically transparent but can be found with an optical microscope due to the optical interference with the SiO_2 substrate. The advantages of this and similar methods is the high quality of the graphene flakes produced; the disadvantages are the small size of the flakes produced, the lack of control over the number of graphene layers and the time-consuming hunting of the graphene layers. This method was an extremely expensive way of producing graphene, but prices of mechanically exfoliated graphene are falling rapidly.

The production of graphene via the reduction of graphite oxide was first described by Hanns-Peter Boehm, an X-ray crystallographer, who isolated and identified a few, or even single, graphene sheets with transmission electron microscopy and X-ray diffraction in 1962 (Fig. 4.10) (Boehm *et al*., 1962). Boehm authored the International Union of Pure and Applied Chemistry (IUPAC) report defining the term 'graphene' in 1994. The production of

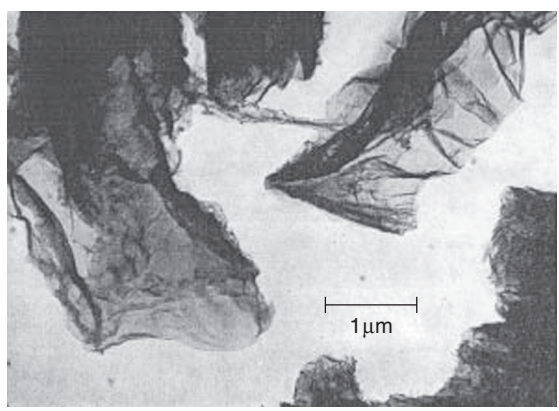

4.10 Transmission electron micrograph showing isolated graphene oxide. Reprinted with permission from *Zeitschrift für Naturforschung* 17b (1962), 150–3. © 1962 Verlag der Zeitschrift für Naturforschung. (Boehm *et al*., 1962).

© Woodhead Publishing Limited, 2013

graphene by this method requires, first, exfoliation of the graphite in solution to produce suspended flakes of graphene oxide, then reduction of the resulting graphene oxide to produce graphene layers. This method has attracted attention due to the low cost of producing graphene; however, the quality of the graphene is lower than that produced by other methods due to the inefficient reduction of functional groups.

Epitaxial growth of graphene layers on metals by chemical vapour deposition (CVD) has been demonstrated using a range of metals including ruthenium (Sutter *et al*., 2008), iridium (Van *et al*., 2011), nickel (Reina *et al*., 2008) and copper (Li *et al*., 2009). Epitaxial growth on metals has delivered large graphene areas with some control over film thickness (Zhao *et al*., 2011). The main drawback to this method is that the graphene films are produced on electrically conductive substrates, and must be removed and redeposited on a non-conductive substrate for device manufacture. Transfer of CVD-grown graphene films has been demonstrated up to the wafer scale (Lee *et al*., 2010).

The unzipping of carbon nanotubes (CNTs) to form graphene nanoribbons is an interesting way of confining the electrons in a graphene sheet to one dimension. This allows for further control over the electronic properties of graphene, such as the opening of a band gap. As the diameter of CNTs changes, so does their chirality and electronic properties, with specific diameter and chiral angles giving either semiconducting or metallic nanoribbons. Nanotube unzipping may be effected by, for example, a solution of potassium permanganate and sulphuric acid (Hiura *et al*., 1995), or by plasma etching (Huang and Dai, 2002). However, the production of single-walled nanotubes is not straightforward and, at present, it is not possible to produce CNTs in bulk with sufficient control over diameter to produce only semiconducting or only metallic CNTs.

4.5.4 Production of graphene on SiC

The epitaxial growth of graphene by the high-temperature sublimation of Si from SiC is arguably the most promising method for large-scale growth of largely defect-free graphene layers, with the benefit of production directly onto a resistive material.

Graphene grows on both of the polar faces of SiC, referred to here as the ‘Si-face’ and the ‘C-face’. On both polar faces of SiC, the first graphene layer is covalently bonded to the SiC surface: this layer is referred to as the ‘buffer’ or ‘zeroth’ layer, and it is on top of this layer that graphene layers are found. Due to its two-dimensionality, graphene is highly influenced by the substrate, with interface states between the graphene layer and the SiC donating electrons to the graphene, causing n-type behaviour (Varchon *et al*., 2007) and possibly introducing a band gap (Zhou *et al*., 2007b).

© Woodhead Publishing Limited, 2013

Recent advances in epitaxial graphene growth on SiC enable high-quality, single-layer graphene with controlled electronic properties, such as carrier concentration, over an entire wafer (Yakimova *et al.*, 2010) (see Fig. 4.11). These improvements in growth techniques have allowed control over substrate induced doping, reducing it to very low levels and preserving the linearity of the bands near the Dirac point, as has been shown by measurements of the quantum Hall effect on epitaxial single-layer graphene on SiC material (Tzalenchuk *et al.*, 2010).

It has recently been shown that growth of graphene on templated SiC by high-temperature Si sublimation can result in the formation of graphene nanoribbons (Sprinkle *et al.*, 2010). If graphene can be reduced in width to form nanoribbons, the electron confinement leads to changing electronic properties. Depending on the width and the structure of the edge of the graphene nanoribbon, metallic or semiconducting properties can prevail, with the band gap of semiconducting nanoribbons inversely scaling with width (Nakada *et al.*, 1996).

The effect of the interface on the electronic properties of graphene on SiC can be overcome by hydrogen intercalation, which effectively decouples the graphene from the SiC. It has been shown that molecular hydrogen can migrate under the buffer layer and saturate the surface Si bonds by forming

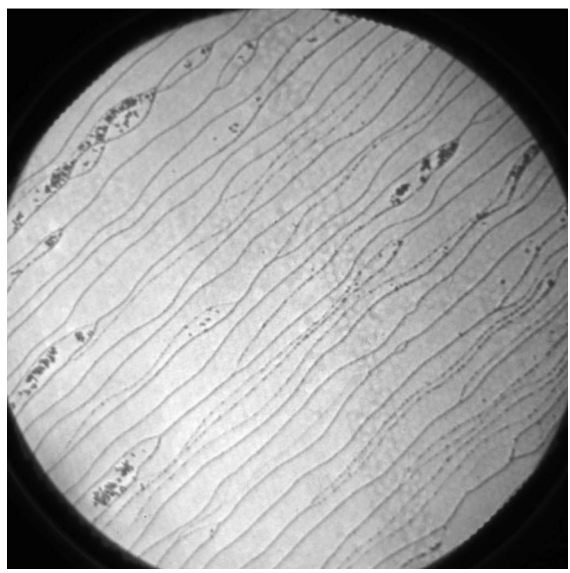

4.11 Low-energy electron microscopy (LEEM) image: single monolayer of graphene on SiC(0001), diameter 20 μm. Reprinted with permission from *Physical Review* B 78 (2008), 245403. © 2008 American Physical Society (Virojanadara *et al.*, 2008).

© Woodhead Publishing Limited, 2013

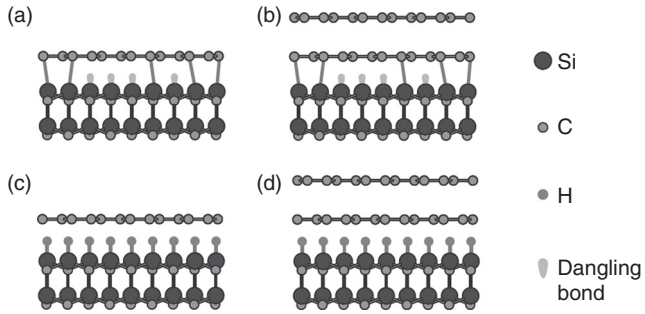

4.12 Side-view models for (a) the (6 $\sqrt{3}\times 6$ $\sqrt{3}$) R30° reconstruction of SiC(0001) ('zero-layer'), and (b) epitaxial monolayer graphene. After hydrogen intercalation, (c) the zerolayer, and (d) monolayer graphene, are decoupled from the substrate. Reprinted with permission from *Physical Review Letters*, **103**, 246804. © 2009 American Physical Society (Riedl *et al.*, 2009).

covalent bonds with the surface Si atoms, passivating the underlying SiC substrates (see Fig. 4.12) (Riedl *et al.*, 2009). The electronic properties of the buffer layer are transformed into those of a graphene monolayer, and an epitaxial graphene monolayer becomes bi-layer graphene decoupled from the SiC substrate (Watcharinyanon *et al.*, 2011).

Similar surface decoupling effects resulting in charge neutrality have been observed via graphene surface modification with strongly electron-withdrawing tetrafluro-tetracyanoquino-dimethane (F4 TCNQ) (Chen *et al.*, 2007; Coletti *et al.*, 2010) and n-doping due to the SiC substrate has been reduced via doping with Sb or Bi. (Gierz *et al.*, 2008).

4.5.5 Epitaxial graphene on SiC as gas sensors

Whilst there are relatively few reports of epitaxially-grown graphene on SiC being utilized for sensors to date, there are many indications that this material will make a successful sensor material. Authors cite the ease of fabrication of sensors due to entire substrate surface coverage and the robustness of the material as it does not require relocation from the growth substrate (Nomani *et al.*, 2010; Pearce *et al.*, 2011b). There are several differences between the sensing properties of epitaxially-grown graphene on SiC and graphene produced from highly ordered pyrolytic graphite (HOPG). One such difference is the opposite direction of response to electron-donating or electron-withdrawing molecules (Nomani *et al.*, 2010; Pearce *et al.*, 2011b). Graphene produced on SiC is an n-type conductor due to electron donation from interface states (Varchon *et al.*, 2007), whereas graphene not on SiC is a p-type conductor due to electron withdrawal by adsorbed oxygen/water

© Woodhead Publishing Limited, 2013

vapour (Collins *et al.*, 2000). Whilst this adsorption process also occurs on graphene on SiC, it is usually a smaller effect than that of electron donation from the substrate interface states, with the Fermi level remaining above the Dirac point. Interestingly, due to the effective decoupled nature of graphene grown on the carbon face of SiC, the response from devices fabricated on this face was that of a p-type conductor (see Fig. 4.13). However, devices fabricated on the Si-face show a larger response to gases than devices fabricated on the C-face (Nomani *et al.*, 2010). This increase in response on the Si-face may be due to improved graphene formation, or an increase in proximity of the Fermi level to the Dirac point.

Greater control has recently become possible over the amount of electron donation from the interface states through an increased understanding of the growth of this new material (Yakimova *et al.*, 2010), with lower

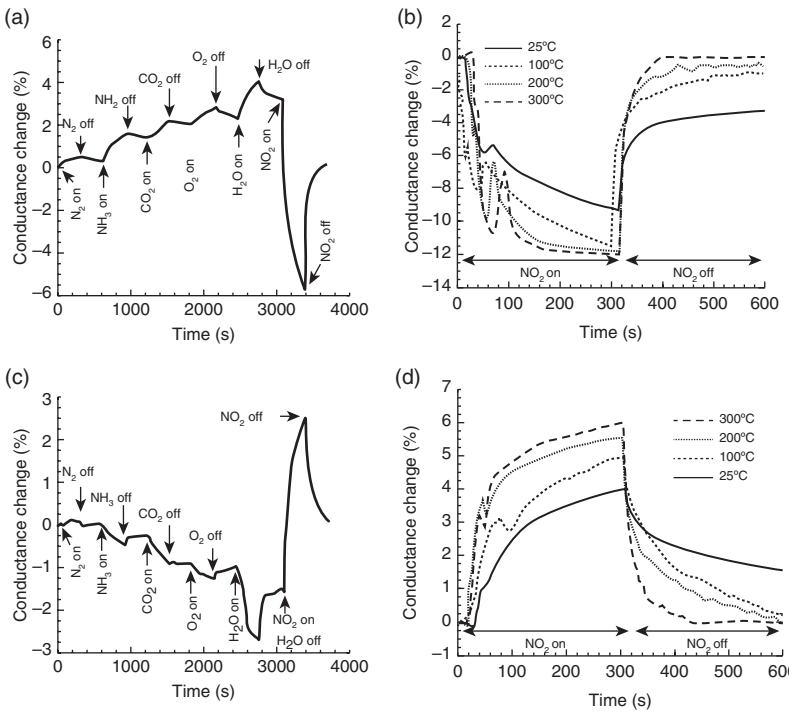

4.13 (a and c) Highly-selective NO_2 detection using epitaxial graphene films on (a) the Si-face, and (c) the C-face, in the presence of major interfering gases such as N_2, NH_3 (550 ppm), CO_2 (20%), O_2 (pure) and H_2O (saturated) at 300°C. (b and d) The temporal conductance change in graphene layers on (b) the Si-face, and (d) the C-face at different temperatures with a flow of 18 ppm NO_2. Reprinted with permission from *Sensors and Actuators* B, **150** (1), 301–7. © 2010 Elsevier (Nomani *et al.*, 2010).

© Woodhead Publishing Limited, 2013

amounts of n-type doping and increased device repeatability expected. For devices produced from low n-doped graphene on SiC, a transition between n- and p-type conduction, and therefore a change in gas response direction, is observed with increasing adsorption of electron-withdrawing gas NO_2 (see Fig. 4.14) (Pearce *et al.*, 2011b).

Epitaxial graphene has the potential to be the material of choice for sensors where detection of very low concentrations of gases and vapours is required. Response to ppb concentrations of gases such as NO_2 has been demonstrated on single-layer graphene devices (Pearce, *et al.*, 2012). This extreme sensitivity is attributed to graphene's narrow and linear density of states about the Dirac point. Due to the low doping of epitaxial graphene, the Fermi level sits close to the Dirac point where sensitivity to chemical doping is greatest. Indeed, the work function of a nominally n-doped one-layer graphene epitaxial device was shown to shift by ~500 meV with adsorption of 30 ppb of NO_2 (Pearce, *et al.*, 2012).

The substrate-induced doping in epitaxial graphene varies slightly from sample to sample with growth conditions and substrate morphology (Eriksson *et al.*, 2012). This variation in carrier concentration affects the gas concentration at which an n- and p-type transition is observed in few-layer epitaxial graphene devices (Pearce, *et al.*, 2012).

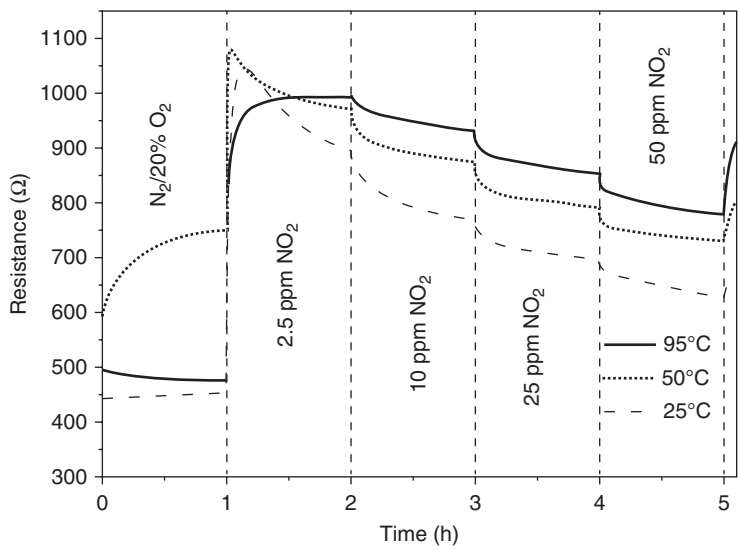

4.14 Response of single-layer graphene sensor towards stepwise increases in NO_2 in a carrier gas of N_2 with 20% O_2. Plot shows change in response direction with increasing NO_2 concentration. The dashed line shows results taken at 50°C and the dotted line shows results taken at 25°C. Reprinted with permission from *Sensors and Actuators* B, **155** (2), 451–5. © 2011 Elsevier (Pearce *et al.*, 2011b).

© Woodhead Publishing Limited, 2013

It has also been shown (Pearce *et al*., 2011b) that multi-layer (~10 layers) graphene on SiC demonstrates a significantly smaller response than single-layer graphene on SiC. This was attributed to current flow through several graphene layers and increased distance of the Fermi level from the Dirac point. The change of the Fermi level in multi-layer graphene was attributed to shielding of the uppermost graphene layer in the multi-layer stack from the SiC substrate, and adsorption of oxygen and water vapour which strongly p-dopes the surface layer.

4.5.6 Epitaxial graphene on SiC field effect transistors as gas sensors

Whilst there are many reports (Gu *et al*., 2007; Zhou *et al*., 2007a; Moon *et al*., 2009) of a large field effect observed for epitaxially-grown graphene on SiC FET structures, to date, most FETs have top gates with a dielectric layer deposited on top. These structures are not suitable for gas sensing as gases cannot diffuse through the dielectric layer. There is, however, a report of a solution-gated sensor (see Fig. 4.15) (Ang *et al*., 2008). This solution-gated sensor showed shifts in the I/V characteristics upon changing the pH due to capacitive charging of the surface by hydroxyl (OH^-) and hydroxonium ions (H_3O^+).

Epitaxial graphene devices are also hindered by the poor adhesion of contact pads, rendering conventional wire-bonding impossible. The lack of ability to wire-bond puts limitations on the sensor design, with sensor devices relying on the use of probes (Nomani *et al*., 2010), or die attachment of electrical leads (Pearce *et al*., 2011b). Patterning of the graphene using conventional photolithography and removal of residual carbon contamination on the SiC surface by plasma etching before contact deposition has also proved a successful method for producing well-adhered contact pads. The effect of residual photoresist and damage to the graphene during photolithography may cause a change in sensor response (Dan *et al*., 2009). A novel sensor design which requires no patterning of the graphene layer has been reported (Pearce *et al*., 2011a). This design (see Fig. 4.16) utilizes a suspended gate structure where the un-patterned epitaxially-grown graphene layer is sandwiched against contact pads.

4.6 Conclusion

The SiC FET devices as high-temperature gas sensors are commercially available in sensor systems for combustion control in small- and medium-scale power plants. Recent research and development which started in 2009 has realized tailor-made sensing layers for oxygen and carbon dioxide detection. Smart sensor operation using only one sensor may detect the NO_2

© Woodhead Publishing Limited, 2013

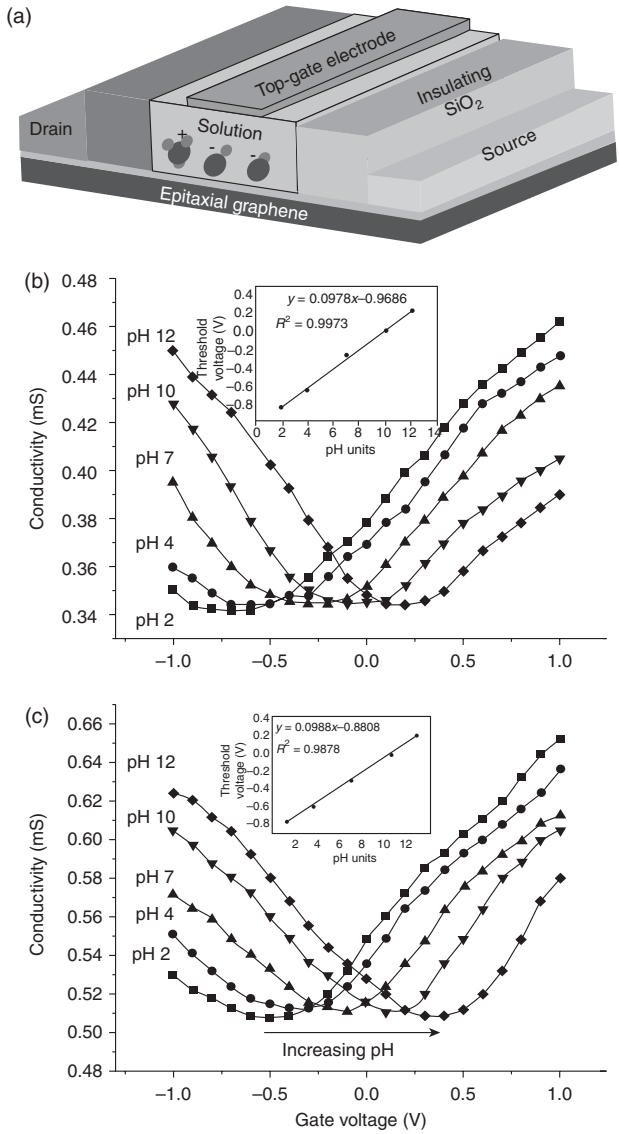

4.15 (a) Schematic of the solution-gated epitaxial graphene FET. (b and c) Conductivity versus gate potential plot of a solution gate field effect transistor (SGFET) fabricated on (b) 1–2 layers and (c) 3–4 layers, of epitaxial graphene (EG). The measurements were recorded in 10 mM KCl/10 mM phosphate buffer solution (PBS) between pH 2 and 12 at constant drain–source voltage of –1 V. The insets show the plot of shift in threshold voltage ($V_G = E_D$) versus pH, where a supra-Nernstian sensitivity of 99 meV/pH can be obtained. Reprinted with permission from the *Journal of the American Chemical Society* B, **130** (44), 14392–3. © 2008 American Chemical Society (Ang *et al.*, 2008).

© Woodhead Publishing Limited, 2013

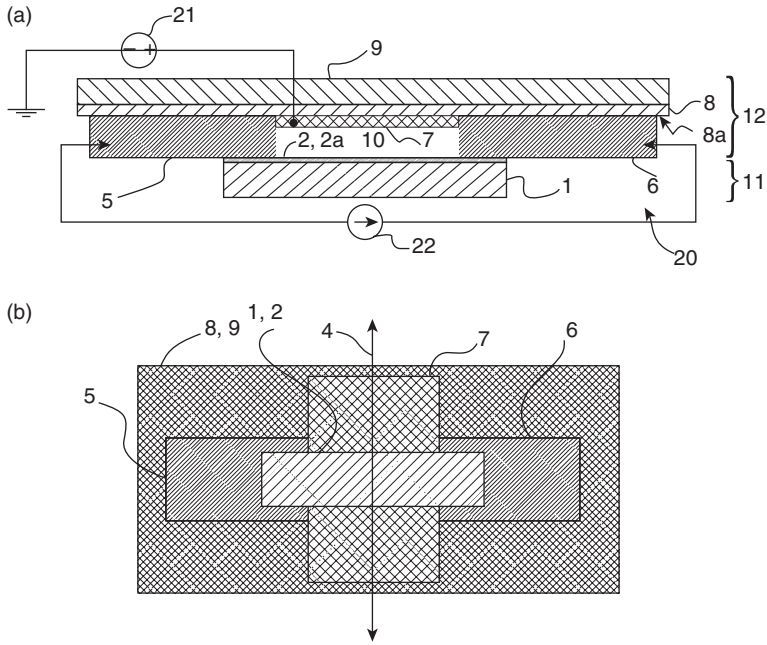

4.16 (a) Side and (b) bottom views of the transistor device. The numbering is the same in both panels. 1: graphene substrate; 2 (and 2a): graphene layer; 3: channel modification layers-not shown in these diagrams; 4: air flow between gate and channel; 5: source/drain contact/bonding pad; 6: source/drain contact/bonding pad; 7: gate; 8 (and 8a): gate insulator; 9: gate substrate; 10: air gap between gate and channel; 11: part 1 of the device, which can be contacted separately from 12; 12: part 2 of the device; 20: source and drain electrical connection; 21: electrical connection to ground or voltage source; 22: voltage / current meter (Source: taken from Pearce *et al.*, (2011a).)

concentrations in varying backgrounds of typical exhaust gases. Epitaxially-grown, defect-free, monolayer graphene on SiC is now available over large areas and has been employed in gas-sensing devices. Detection of ppb concentration of NO_2 has been demonstrated by SiC/graphene sensors devices.

4.7 References

Andersson, M., Everbrand, L. and Lloyd Spetz, A. (2007), 'A novel sensor system based on gas sensitive MISiCFET devices for combustion control in small-scale wood fired boilers', in Proceedings of the IEEE International Conference on Sensors, Atlanta, Georgia, USA, October 2007, 493–4.

Andersson, M., Ljung, P., Mattsson, M., Löfdahl, M. and Lloyd Spetz, A. (2004), Investigations on the possibilities of a MISiCFET sensor system for OBD

© Woodhead Publishing Limited, 2013

and combustion control utilizing different catalytic gate materials, *Topics in Catalysis*, **30/31**, 365–8.

Andersson, M. and Lloyd Spetz, A. (2009), 'Tailoring of field effect gas sensors for sensing of non-hydrogen containing substances from mechanistic studies on model systems', in Proceedings of the IEEE International Conference on Sensors, Christchurch, New Zealand, October 2009, 2031–5.

Andersson, M. and Lloyd Spetz, A. (2010), Tailoring of SiC based field effect gas sensors for improved selectivity to non-hydrogen containing species, *Proc. IMCS13*, Perth, Australien 12–14 July, p. 369.

Andersson, M., Pearce, R. and Lloyd Spetz, A. (2013), New generation SiC based field effect transistor gas sensors, *Sensors and Actuators B Chemical*, **179**, 95–106. Doi:10.1016/j.snb.2012.12.059

Andersson, M., Wingbrant, H., Petersson, H., Unéus, L., Svenningstorp, H., Löfdahl, M., Holmberg, M. and Lloyd Spetz, A. (2006), *Gas sensor arrays for combustion control, in Encyclopedia of Sensors Vol. **4***, Stevenson Ranch, USA, American Scientific Publishers, 139–54.

Ang, P. K., Chen, W., Wee, A. T. S. and Loh, K. P. (2008), Solution-gated epitaxial graphene as pH sensor, *Journal of the American Chemical Society*, **130**(44), 14392–3.

Baranzahi, A., Lloyd Spetz, A., Glavmo, M., Carlsson, C., Nytomt, J., Salomonsson, P., Jobson, E., Häggendal, B., Mårtensson, P. and Lundström, I. (1997), Response of metal-oxide-silicon carbide sensors to simulated and real exhaust gases, *Sensors and Actuators*, **B43**, 52–9.

Becker, E., Andersson, M., Eriksson, M., Lloyd Spetz, A. and Skoglundh, M. (2011), Study of the sensing mechanism towards carbon monoxide of platinum-based field effect sensors, *IEEE Sensors Journal*, **11**(7), 1527–34.

Bergveld, P. (1970), Development of an ion sensitive solid state device for neurophysiological measurements, *IEEE Transactions on Biomedical Engineering*, BME-**17**, 70–1.

Boehm, V. H. P., Clauss, A., Fischer, G. O. and Hofmann, U. (1962), Thinnest Carbon Films, *Z Naturforsch*, **17b**, 150–3.

Bur, C., Reimann, P., Schütze, A., Andersson, M. and Lloyd Spetz, A. (2010), Increasing the selectivity of Pt-gate SiC field effect gas sensors by dynamic temperature modulation, in Proceedings of the IEEE International Conference on Sensors, Waikoloa, USA 1–4 November, 1267–72. Doi:10.1109/ICSENS.2010.5690598

Bur, C., Reimann, P., Schütze, A., Andersson, M. and Lloyd Spetz, A. (2011a), Temperature cycled operation of SiC field effect gas sensors: Increasing the selectivity for improved sensor systems, in Proceedings of the ISOEN 2011, New York, USA, 02–05 May, Vol. **1362**, 91–2. Doi:10.1063/1.3626317

Bur, C., Schütze, A., Andersson, M. and Lloyd Spetz, A. (2011b), Hierarchical strategy for quantification of NO_x in a varying background of typical exhaust gases, in Proceedings of the IEEE International Conference on Sensors, Limerick, Ireland, 28–31 October, 137–40. Doi: 10.1109/ICSENS.2011.6127046

Bur, C., Reimann, P., Schütze, A., Andersson, M. and Lloyd Spetz, A. (2012), New method for selectivity enhancement of SiC field effect gas sensors for quantification of NOx, *Microsystem Technologies/ Smart Sensors, Actuators and MEMS*, Springer-Verlag, Berlin, 18, 7, 1015–25. Doi: 10.1007/s00542–012–1434-z

© Woodhead Publishing Limited, 2013

Burch, R. and Watling, T. C. (1997), Kinetics and mechanism of the reduction of NO by C_3H_8 over Pt/Al_2O_3 under lean-burn conditions, *Journal of Catalysis*, **169**, 45–54.

Burch, R. and Watling, T. C. (1998), The effect of sulphur on the reduction of NO by C_3H_6 and C_3H_8 over Pt/Al_2O_3 under lean-burn conditions, *Applied Catalysis B*, **17**, 131–9.

Cerdá, J., Arbiol, J., Dezanneau, G., Díaz, R. and Morante, J. R. (2002), Perovskite-type $BaSnO_3$ powders for high temperature gas sensor applications, *Sensors and Actuators B*, **84**, 21–2.

Cerdá, J., Morante, J. R. and Lloyd Spetz, A. (2003), New tunnel Schottky SiC devices using mixed conduction ceramics, *Materials Science Forum*, **433–6**, 949–52.

Chatfield, C. and Collins, A. J. (1980), *Introduction to Multivariate Analysis*, London, Chapman & Hall.

Chen, W., Chen, S., Qi, D. C., Gao, X. Y. and Wee, A. T. S. (2007), Surface transfer p-type doping of epitaxial graphene, *Journal of the American Chemical Society*, **129**, 10418–22.

Chilton, T. H. (1960), *The Manufacture of Nitric Acid by the Oxidation of Ammonia,* in Chemical Engineering Progress Monograph series **3**(56), New York, American Institute of Chemical Engineers.

Chizallet, C., Costentin, G., Che, M., Delbecq, F. and Sautet, P. (2006), Revisiting acido-basicity on the MgO surface by periodic density functional theory calculations: Role of surface topology and ion coordination on water dissociation, *Journal of Physical Chemistry B*, **110**, 15878–86.

Coletti, C., Riedl, C., Lee, D. S., Krauss, B., Patthey, L., von Klitzing, K., Smet, J. H. and Starke, U. (2010), Charge neutrality and band-gap tuning of epitaxial graphene on SiC by molecular doping, *Physical Review B*, **81**, 235401.

Collins, P. G., Bradley, K., Ishigami, M. and Zettl, A. (2000), Extreme oxygen sensitivity of electronic properties of carbon nanotubes, *Science*, **287**, 1801–4.

Dan, Y., Lu, Y., Kybert, N. J., Luo, Z. and Johnson, A. T. C. (2009), Intrinsic response of graphene vapor sensors, *Nano Letters*, **9**, 1472–5..

Darmastuti, Z., Pearce, R., Lloyd Spetz, A. and Andersson, M. (2011), 'The influence of gate bias and structure on the CO sensing performance of SiC based field effect sensors', in Proceedings of the IEEE International Conference on Sensors, Limerick, Ireland, October 2011, 133–6.

Dean, V. W., Frenklach, M. and Phillips, J. (1988), Catalytic etching of platinum foils and thin films in hydrogen-oxygen mixtures, *Journal of Physical Chemistry*, **92**, 5731–8.

Dimitrijev, S. (2000), *Understanding Semiconductor Devices*, New York, Oxford University Press.

Duda, R. O., Hart, P. E. and Stork, D. G. (2000), *Pattern Classification*, New York, Wiley.

Eickhoff, M., Schalwig, J., Weidemann, O., Görgens, L., Neuberger, R., Hermann, M., Steinhoff, G., Baur, B., Müller, G., Ambacher, O. and Stutzmann, M. (2003), Electronics and sensors based on pyroelectric Al-GaN/GaN heterostructures, *Physica Status Solidi C: Conferences 0* (6 SPEC. ISS.), 1908–18.

Ekedahl, L.-G., Eriksson, M. and Lundström, I. (1998), Hydrogen sensing mechanisms of metal-insulator interfaces, *Accounts of Chemical Research*, **31**(5), 249.

Eriksson, J., Pearce, R., Iakimov, T., Vironajadara, C., Gogova, D., Andersson, M., Syväjärvi, M., Lloyd Spetz, A. and Yakimova, R. (2012), The influence of

© Woodhead Publishing Limited, 2013

substrate morphology on thickness uniformity and unintentional doping of epitaxial graphene on SiC, *Appl. Phys. Lett.*, **100**, 241607. Doi:10.1063/1.4729556

Eriksson, M. and Ekedahl, L.-G. (1997), The influence of CO on the response of hydrogen sensitive Pd-MOS devices, *Sensors and Actuators B*, **42**, 217–23.

Eriksson, M. and Ekedahl, L.-G. (1998), Hydrogen adsorption states at the Pd/SiO_2 interface and simulation of the response of a Pd metal-oxide-semiconductor hydrogen sensor, *Journal of Applied Physics*, **83**(8), 3947–51.

Eriksson, M., Lundström, I. and Ekedahl, L.-G. (1997), A model of the Temkin isotherm behavior for hydrogen adsorption at Pd-SiO_2 interfaces, *Journal of Applied Physics*, **82**(6), 3143–6.

Eriksson, M., Salomonsson, A., Lundström, I., Briand, D. and Åbom, A. E. (2005), The influence of the insulator surface properties on the hydrogen response of field-effect gas sensors, *Journal of Applied Physics*, **98**(3), 34903–8.

Fogelberg, J., Eriksson, M., Dannetun, H. and Petersson, L.-G. (1995), Kinetic modeling of hydrogen ad/absorption in thin films on hydrogen sensitive field effect devices: Observation of large hydrogen dipoles at the Pd-SiO_2 interface, *Journal of Applied Physics*, **78**(2), 988–96.

Fogelberg, J., Lundström, I. and Petersson, L.-G. (1987), Ammonia dissociation on oxygen covered palladium studied with a hydrogen sensitive Pd-MOS device, *Physica Scripta*, **35**, 702–5.

Garzon, F. H., Mukundan, R., Lujan, R. and Brosha, E. L. (2004), Solid state ionic devices for combustion gas sensing, *Solid State Ionics*, **175**, 487–90.

Geim, A. K. and Novoselov, K. S. (2007), The rise of graphene, *Nat Mater*, **6**, 183–91.

Gierz, I., Riedl, C., Starke, U., Ast, C. R. and Kern, K. (2008), Atomic hole doping of graphene, *Nano Letters*, **8**, 4603–7..

Gu, G., Nie, S., Feenstra, R., Devaty, R., Choyke, W., Chan, W. K. and Kane, M. G. (2007), Field effect in epitaxial graphene on a silicon carbide substrate, *Applied Physics Letters*, **90**, 253507.

Gurbuz, Y., Kang, W. P., Davidson, J. L. and Kerns, D. V. (1998), High-temperature tolerant diamond diode for carbon monoxide gas detection, *Journal of Applied Physics*, **84**, 6935–6.

Gutierrez-Osuna, R. (2002), Pattern analysis for machine olfaction, *IEEE Sensors Journal*, **2**(3), 189–202.

Hiura, H., Ebbesen, T. W. and Tanigaki, K. (1995), Opening and purification of carbon nanotubes in high yields, *Advanced Materials*, **7**, 275–6.

Huang, S. and Dai, L., (2002), Plasma etching for purification and controlled opening of aligned carbon nanotubes, *Journal of Physical Chemistry B*, **106**, 3543–5.

Hunter, G. W., Neudeck, P., Jefferson, G. D., Madzar, G. C., Liu, C. C. and Wu, Q. H. (1992),'The development of hydrogen sensor technology at NASA Lewis Research Center', in Proceedings of the 4th Annual Space System Health Management Technology Conference, Cincinatti, USA.

Hwang, E. H., Adam, S. and Das Sarma, S. (2007), Transport in chemically doped graphene in the presence of adsorbed molecules, *Physical Review B*, **76**, 195421.

Inoue, H., Andersson, M., Yuasa, M., Kida, T., Lloyd Spetz, A. and Shimanoe, K. (2010), CO_2 sensor combining a metal-insulator silicon carbide (MISiC) capacitor and a binary carbonate, *Electrochemical and Solid-State Letters*, **14**(1), J4–7. Doi: 10.1149/1.3512998

Jacobsén, S., Helmersson, U., Ekedahl, L.-G., Lundström, I., Mårtensson, P. and Lloyd Spetz, A. (2001), Pt/CeO_2 SiC Schottky diodes with high response to

© Woodhead Publishing Limited, 2013

hydrogen and hydrocarbons, Proceedings of Transducers '01 and Eurosensors XV, Munich, Germany, 832–5.

Kida, T., Kishi, S., Yuasa, M., Shimanoe, K. and Yamazoe, N. (2008), Planar NASICON-based CO_2 sensor using BiCuVOx/Perovskite-type oxide as a solid-reference electrode, *Journal of the Electrochemical Society*, **155**, J117–21.

Klarskov, M. B., Dam, H. F., Petersen, D. H., Hansen, T. M., Löwenborg, A., Booth, T. J., Schmidt, M. S., Lin, R., Nielsen, P. F. and Böggild, P. (2011), Fast and direct measurements of the electrical properties of graphene using micro four point probes, *Nanotechnology*, **22**, 445702.

Kong, J., Franklin, N. R., Zhou, C., Chapline, M. G., Peng, S., Cho, K. and Dai, H. (2000), Nanotube molecular wires as chemical sensors, *Science*, **287**, 622–5.

Krause, S., Moritz, W. and Grohmann, I. (1994), Improved long term stability for an LaF_3 based oxygen sensor, *Sensors and Actuators B*, **18**(19), 148–54.

Landau, L. D. (1937), Broken symmetry and phase transitions, *Physikalische Zeitschrift der Sowjetunion*, **11**, 26.

Larsson, O., Göras, A., Nytomt, J., Carlsson, C., Lloyd Spetz, A., Artursson, T., Holmberg, M., Lundström, I., Ekedahl, L.-G. and Tobias, P. (2002), Estimation of air fuel ratio of individual cylinders in SI engines by means of MISiC sensor signals in a linear regression model, In SAE Technical Paper Series, paper 2002–01–0847, Detroit, Michigan, USA.

Lee, A. P. and Reedy, B. J. (1999), Temperature modulation in semiconductor gas sensing, *Sensors and Actuators B*, **60**, 35–42.

Lee, Y., Bae, S., Jang, H., Jang, S., Zhu, S.-E., Sim, S. H., Song, Y. I., Hong, B. H. and Ahn, J.-H. (2010), Wafer-scale synthesis and transfer of graphene films, *Nano Letters*, **10**, 490–3.

Li, X., Cai, W., An, J., Kim, S., Nah, J., Yang, D., Piner, R., Velamakanni, A., Jung, I. and Tutuc, E. (2009), Large-area synthesis of high-quality and uniform graphene films on copper foils, *Science*, **324**, 1312.

Liu, G., Stillman, W., Rumyantsev, S., Shao, Q., Shur, M. and Balandin, A. A. (2009), Low-frequency electronic noise in the double-gate single-layer graphene transistors, *Applied Physics Letters*, **95**, 033103–3.

Lloyd Spetz, A., Skoglundh, M. and Ojamäe, L. (2009), FET Gas-Sensing Mechanism, Experimental and Theoretical Studies, in Solid State Gas Sensing, New York, Elisabetta Comini, Guido Faglia, Giorgio Sberveglieri (eds.), ch. 4, 153–79, Springer, Norwell MA, USA, 2009. ISBN: 978-0-387-09664-3

Logothetis, E. M., Visser, J. H., Soltis, R. E. and Rimai, L. (1992), Chemical and physical sensors based on oxygen pumping with solid-state electrochemical cells, *Sensors and Actuators B*, **9**, 183–9.

Lundström, I., Shivaraman, M. S. and Svensson, C. M. (1975), A hydrogen-sensitive MOS field effect transistor, *Journal of Applied Physics*, **46**, 3876–81.

Lundström, I. (1991), Field effect chemical gas sensors, in Sensors A Comprehensive Survey, Eds. Göpel W, Hesse J and Zemel J N, **2**(1), pp. 467–528, VCH Verlagsgesellschaft mbH, Wienheim.

Lundström, I., Sundgren, H., Winquist, F., Eriksson, M., Krantz-Rülcker, C. and Lloyd-Spetz, A. (2007), Twenty-five years of field effect gas sensor research in Linköping, *Sensors and Actuators B*, **121**, 247–62.

Löfdahl, M., Utaiwasin, C., Carlsson, A., Lundström, I. and Eriksson, M. (2001a), Gas response dependence on metal gate morphology of field-effect devices, *Sensors and Actuators B*, **80**, 183–92.

© Woodhead Publishing Limited, 2013

Löfdahl, M. (2001), Spatially resolved gas sensing, Linköping studies in science and technology, Dissertation no. 696, Linköping, Sweden, 115–27.

Medlin, J. W., McDaniel, A. H., Allendorf, M. D. and Bastasz, R. (2003), Effects of competitive carbon monoxide adsorption on the hydrogen response of metal-insulator-semiconductor sensors: the role of metal film morphology, *Journal of Applied Physics*, **93**(4), 2267–74.

Meyer, J. C., Geim, A. K., Katsnelson, M. I., Novoselov, K. S., Booth, T. J. and Roth, S. (2007), The structure of suspended graphene sheets, *Nature*, **446**, 60–3.

Miyahara, Y., Tsukada, K. and Miyagy, H. (1987), Field-effect transistor using a solid electrolyte as a new oxygen sensor, *Journal of Applied Physics*, **63**(7), 2431–4.

Moon, J., Curtis, D., Hu, M., Wong, D., McGuire, C., Campbell, P., Jernigan, G., Tedesco, J., VanMil, B. and Myers-Ward, R. (2009), Epitaxial-graphene RF field-effect transistors on Si-face 6H-SiC substrates, *Electron Device Letters, IEEE*, **30**, 650–2.

Nakada, K., Fujita, M., Dresselhaus, G. and Dresselhaus, M. S. (1996), Edge state in graphene ribbons: Nanometer size effect and edge shape dependence, *Physical Review B*, **54**, 17954.

Nakagomi, S. and Lloyd Spetz, A. (2006), Gas sensor device based on catalytic metal-metal oxide-SiC structure, in *Encyclopedia of Sensors Vol. **4***, Stevenson Ranch, USA, American Scientific Publishers, 155–70.

Nakagomi, S., Tobias, P., Baranzahi, A., Lundström, I., Mårtensson, P. and Lloyd Spetz, A. (1997), Influence of carbon monoxide, water and oxygen on high temperature catalytic metal-oxide silicon carbide structures, *Sensors and Actuators B*, **45**, 183–91.

Neamen, D. A. (2003), *Semiconductor physics and devices; basic principles*, New York, McGraw-Hill.

Nomani, M. W. K., Shishir, R., Qazi, M., Diwan, D., Shields, V. B., Spencer, M. G., Tompa, G. S., Sbrockey, N. M. and Koley, G. (2010), Highly sensitive and selective detection of NO_2 using epitaxial graphene on 6H-SiC, *Sensors and Actuators B: Chemical*, **150**(1), 301–7.

Novoselov, K. S., Geim, A. K., Morozov, S. V., Jiang, D., Katsnelson, M. I., Grigorieva, I. V., Dubonos, S. V. and Firsov, A. A. (2005), Two-dimensional gas of massless Dirac fermions in graphene, *Nature*, **438**, 197–200.

Novoselov, K. S., Geim, A. K., Morozov, S. V., Jiang, D., Zhang, Y., Dubonos, S. V., Grigorieva, I. V. and Firsov, A. A. (2004) Electric field effect in atomically thin carbon films, *Science*, **306**, 666–9.

Pandey, D., Prakash, G., Yu, Q., Cao, H., Jauregui, L., Pei, S. and Chen, Y. P. (2009), Surface microscopy characterizations of large size graphene films grown by surface segregation on Ni and transferred to Si/SiO_2 substrate, *ECS Transactions*, **19**(5), 75–80.

Pearce, R., Andersson, M., Hultman, L., Yakimova, R. and Lloyd Spetz, A. (2011a), *Field effect transistor for chemical sensing using graphene, chemical sensor using the transistor and method for producing the transistor*, PCT/SE2011/050565.

Pearce, R., Iakimov, T., Andersson, M., Hultman, L., Spetz, A. L. and Yakimova, R. (2011b), Epitaxially grown graphene based gas sensors for ultra sensitive NO_2 detection. *Sensors and Actuators B: Chemical*, **155**, 451–5.

Pearce, R., Yakimova, R., Eriksson, J., Hultman, L., Andersson, M. and Lloyd Spetz, A. (2012), Development of FETs and resistive devices based on epitaxially grown

© Woodhead Publishing Limited, 2013

single layer graphene on SiC for highly sensitive gas detection, *Materials Science Forum*, **717**(720), 680–90. Doi:10.4028/www.scientific.net/MSF.717–720.687

Peierls, R. E. (1935), Quelques propriétés typiques des corps solides, *Annales de L'Institut Henri Poincare*, **5**, 177.

Reimann, P., Dausend, A. and Schütze, A. (2008), A self-monitoring and self-diagnosis strategy for semiconductor gas sensor systems, in Proceedings of IEEE International Conference on Sensors, Lecce, Italy, 192–5.

Reimann, P., Horras, S. and Schütze, A. (2009), Field-test system for underground fire detection based on semiconductor gas sensors, in Proceedings of the IEEE International Conference on Sensors, 2009, Christchurch, New Zealand, 659–64.

Reina, A., Jia, X., Ho, J., Nezich, D., Son, H., Bulovic, V., Dresselhaus, M. S. and Kong, J. (2008), Large area, few-layer graphene films on arbitrary substrates by chemical vapor deposition, *Nano Letters*, **9**, 30–5.

Reinhardt, G., Mayer, R. and Rösch, M. (2002), Sensing small molecules with amperometric sensors, *Solid State Ionics*, **150**, 79–92.

Riedl, C., Coletti, C., Iwasaki, T., Zakharov, A. A. and Starke, U. (2009), Quasi-free-standing epitaxial graphene on SiC obtained by hydrogen intercalation, *Physical Review Letters*, **103**, 246804.

Salomonsson, A., Petoral Jr., R.M., Uvdal, K., Aulin, C., Käll, P.-O., Ojamäe, L., Strand, M. Sanati, M. and Lloyd Spetz, A. (2006), Nanocrystalline ruthenium oxide and ruthenium in sensing applications – an experimental and theoretical study, *Journal of Nanoparticle Research*, **8**, 899–910. Doi: 10.1007/s11051-005-9058–1.

Sang, Y. H., Ho, W. J. and Jong-Lam, L. (2003), IrO_2 Schottky contact on n-type 4H-SiC, *Applied Physics Letters*, **82**(26), 4726–8.

Sato, Y., Takai, K. and Enoki, T. (2011), Electrically controlled adsorption of oxygen in bilayer graphene devices, *Nano letters*, **11**, 3468–75.

Schalwig, J., Müller, G., Eickhoff, M., Ambacher, O. and Stutzmann, M. (2002), Group III-nitride based gas sensors for combustion monitoring, *Materials Science and Engineering B*, **93**, 207–14.

Schalwig, J., Müller, G., Karrer, U., Eickhoff, M., Ambacher, O., Stutzmann, M., Görgens, L. and Dollinger, G. (2002), Hydrogen response mechanism of Pt-GaN Schottky diodes, *Applied Physics Letters*, **80**(7), 1222–4.

Schalwig, J., Kreisl, P., Ahlers, S. and Müller, G. (2002), Response mechanism of SiC-based MOS field-effect gas sensors, *IEEE Sensors Journal*, **2**(5), 394–402.

Schalwig, J., Ahlers, S., Kreisl, P., Bosch-v. Braunmühl, C. and Müller, G. (2004), A solid-state gas sensor array for monitoring NOx storage catalytic converters, *Sensors and Actuators B*, **101**, 63–71.

Schedin, F., Geim, A. K., Morozov, S. V., Hill, E. W., Blake, P., Katsnelson, M. I. and Novoselov, K. S. (2007), Detection of individual gas molecules adsorbed on graphene, *Nat Mater*, **6**, 652–5.

Spetz, A., Arbab, A. and Lundström, I. (1992), Gas sensors for high temperature operation based on metal oxide silicon carbide (MOSiC) devices, in Proceedings of Eurosensors VI, San Sebastian, Spain, 19–23.

Spetz, A., Armgarth, M. and Lundström, I. (1987), Optimization of ammonia-sensitive structures with platinum gates, *Sensors and Actuators*, **11**, 349–65.

© Woodhead Publishing Limited, 2013

Sprinkle, M., Ruan, M., Hu, Y., Hankinson, J., Rubio, R. M., Zhang, B., Wu, X., Berger, C. and de Heer, W. A. (2010), Scalable templated growth of graphene nanoribbons on SiC, *Nat Nano*, **5**, 727–31.

Sutter, P. W., Flege, J.-I. and Sutter, E. A. (2008), Epitaxial graphene on ruthenium, *Nat Mater*, **7**, 406–11.

Sze, S. M. (1981) *Physics of semiconductor devices*, New York, John Wiley & Sons.

Tobias, P., Macak, K., Helmersson, U., Lundström, I. and Lloyd Spetz, A. (2000), Zirconia based oxygen sensor without the need of a reference electrode, in Proceedings of the 8th International Meeting on Chemical Sensors, Basel, Switzerland, 149.

Tzalenchuk, A., Lara-Avila, S., Kalaboukhov, A., Paolillo, S., Syväjärvi, M., Yakimova, R., Kazakova, O., Janssen, T. J. B. M., Fal'ko, V. and Kubatkin, S. (2010), Towards a quantum resistance standard based on epitaxial graphene, *Nat Nano*, **5**, 186–9.

Unéus, L., Artursson, T., Mattsson, M., Ljung, P., Wigren, R., Mårtensson, P., Holmberg, M., Lundström, I., Lloyd Spetz, A. (2005), Evaluation of on-line flue gas measurements by MISiCFET and metal oxide sensors in boilers, *IEEE Sensors Journal*, **5**(1), 75–81.

Usagawa, T. and Kikuchi, Y. (2011), Device characteristics for Pt-Ti-O gate Si-MISFETs hydrogen gas sensors, *Sensors and Actuators B*, **160**(1), 105–14.

Van, C., Kimouche, A., Plantey, A., Fruchart, O., Guillemaud, P., Bendiab, N. and Coraux, J. (2011), Epitaxial graphene prepared by chemical vapor deposition on single crystal thin iridium films on sapphire, *Applied Physics Letters*, **98**, 181903.

Varchon, F., Feng, R., Hass, J., Li, X., Nguyen, B. N., Naud, C., Mallet, P., Veuillen, J. Y., Berger, C., Conrad, E. H. and Magaud, L. (2007), Electronic structure of epitaxial graphene layers on SiC: Effect of the substrate, *Physical Review Letters*, **99**, 126805.

Vasiliev, A., Moritz, W., Fillipov, V., Bartholomäus, L., Terentjev, A. and Gabusjan, T. (1998), High temperature semiconductor sensor for the detection of fluorine, *Sensors and Actuators B*, **49**, 133–8.

Virojanadara, C., Syväjärvi, M., Yakimova, R., Johansson, L. I., Zakharov, A. A. and Balasubramanian, T. (2008), Homogeneous large-area graphene layer growth on 6H -SiC(0001), *Physical Review B*, **78**, 245403.

Visser, J. H. and Soltis, R. E. (2001), Automotive exhaust gas sensing systems, *IEEE Transactions on Instrumentation and Measurement*, **50**(6), 1543–50.

Wallace, P. R. (1947), The band theory of graphite, *Physical Review*, **71**, 622.

Wallin, M., Grönbeck, H., Lloyd Spetz, A., Eriksson, M. and Skoglundh, M. (2005), Vibrational analysis of H2 and D2 adsorption on Pt/SiO_2, *Journal of Physical Chemistry B*, **109**, 9581–8.

Wallin, M., Byberg, M., Grönbeck, H., Skoglundh, M., Eriksson, M. and Lloyd Spetz, A. (2007), Vibrational analysis of H2 and NH_3 adsorption on Pt/SiO2 and Ir/SiO2 model sensors, in Proceedings of IEEE International Conference on Sensors, Atlanta, USA, 1315–17.

Watcharinyanon, S., Virojanadara, C., Osiecki, J. R., Zakharov, A. A., Yakimova, R., Uhrberg, R. I. G. and Johansson, L. I. (2011), Hydrogen intercalation of graphene grown on 6H-SiC(0001), *Surface Science*, **605**, 1662–8.

© Woodhead Publishing Limited, 2013

Weidemann, O., Hermann, M., Steinhoff, G., Wingbrant, H., Lloyd Spetz, A., Stutzmann, M. and Eickhoff, M. (2003), Influence of surface oxides on hydrogen-sensitive Pd-GaN Schottky diodes, *Applied Physics Letters*, **83**(4), 773–5.

Wilson, M. (2006), Electrons in atomically thin carbon sheets behave like massless particles, *Physics Today*, **59**, 21–3.

Wingbrant, H., Svenningstorp, H., Salomonsson, P., Tengström, P., Lundström, I. and Lloyd Spetz, A. (2003), Using a MISiCFET device as a cold start sensor, *Sensors and Actuators B*, **93**, 295–303.

Wingbrant, H., Svenningstorp, H., Salomonsson, P., Kubinski, D., Visser, J. H., Löfdahl, M. and Lloyd Spetz, A. (2005), Using a MISiC-FET sensor for detecting NH_3 in SCR systems, *IEEE Sensors Journal*, **5**(5), 1099–105.

Wold, S., Sjöström, M. and Eriksson, L. (2001) PLS-regression: a basic tool of chemometrics, *Chemometrics and Intelligent Laboratory Systems*, **58**, 109–30.

Yakimova, R., Virojanadara, C., Gogova, D., Syväjärvi, M., Siche, D., Larsson, K. and Johansson, L. I. (2010), Analysis of the formation conditions for large area epitaxial graphene on SiC substrates, *Materials Science Forum*, **645–648**, 565–8.

Yamaguchi, T., Kiwa, T., Tsukada, K. and Yokosawa, K. (2007), Oxygen interference mechanism of platinum-FET hydrogen gas sensor, *Sensors and Actuators A*, **136**(1), 244–8.

Zamani, C., Shimanoe, K. and Yamazoe, N. (2005), A new capacitive-type NO_2 gas sensor combining an MIS with a solid electrolyte, *Sensors and Actuators B*, **109**, 216–20.

Zhao, L., Rim, K. T., Zhou, H., He, R., Heinz, T. F., Pinczuk, A., Flynn, G. W. and Pasupathy, A. N. (2011), Influence of copper crystal surface on the CVD growth of large area monolayer graphene, *Solid State Communications*, **151**, 509–13.

Zhou, S., Gweon, G. H., Fedorov, A., De Heer, W., Lee, D. H., Guinea, F., Neto, A. and Lanzara, A. (2007a), Substrate-induced band gap opening in epitaxial graphene, *Arxiv preprint arXiv:0709.1706*.

Zhou, S. Y., Gweon, G. H., Fedorov, A. V., First, P. N., de Heer, W. A., Lee, D. H., Guinea, F., Castro Neto, A. H. and Lanzara, A. (2007b), Substrate-induced bandgap opening in epitaxial graphene, *Nat Mater*, **6**, 770–5.

© Woodhead Publishing Limited, 2013

5

Recent advances in wide bandgap semiconductor-based gas sensors

F. REN and S. J. PEARTON, University of Florida, USA

DOI: 10.1533/9780857098665.2.159

Abstract: We review recent progress in wide bandgap thin-film and nanorod sensors made from GaN or ZnO and related materials for applications in the detection of gases such as oxygen, carbon dioxide and hydrogen. Practical aspects are covered, such as the use of differential sensor pairs to eliminate the effects of temperature variations and of the effect of humidity on the detection sensitivity.

Key words: gallium nitride, zinc oxide, heterostructure, nanorods, semiconductors.

5.1 Introduction

Semiconductor-based sensors can be fabricated using mature techniques from the Si chip industry and/or novel nanotechnology approaches. Silicon-based sensors are still the dominant component of the semiconductor segment due to their low cost, and their reproducible and controllable electronic response. However, these sensors are not suited for operation in harsh environments – for instance, high temperature, high pressure or corrosive ambients. Si will be etched by some of the acidic or basic aqueous solutions encountered in biological sensing. By sharp contrast, GaN is not etched by any acid or base at temperatures below a few hundred degrees. Therefore, wide bandgap group III nitride compound semiconductors are alternative options to supplement silicon in these applications because of their chemical resistance, high temperature/high power capability, high electron saturation velocity and simple integration with existing GaN-based ultraviolet (UV) light-emitting diodes, UV detectors and wireless communication chips.

The GaN materials system is attracting much interest for commercial applications of green, blue, and UV light emitting diodes (LEDs) and laser diodes, as well as high speed and high frequency power devices. Due to the wide bandgap nature of the material, it is thermally very stable, and electronic devices can be operated at temperatures up to 500°C.

© Woodhead Publishing Limited, 2013

The GaN-based materials are also chemically stable, and no known wet chemical etchant can etch these materials; this makes them highly suitable for operation in chemically harsh environments. Due to their high electron mobility, GaN material based high electron mobility transistors (HEMTs) can operate at a very high frequency with a higher breakdown voltage, better thermal conductivity and wider transmission bandwidths than Si or GaAs devices (Zhang *et al.*, 2003a; Makimoto *et al.*, 2004; Saito *et al.*, 2006).

An overlooked potential application of the GaN HEMT structure is sensors (Pearton *et al.*, 2010; Chu *et al.*, 2011; Lo *et al.*, 2011, 2012; Ren, 2011, 2012). The high electron sheet carrier concentration of nitride HEMTs is induced by piezoelectric polarization of the strained AlGaN layer in the hetero-junction structure of the AlGaN/GaN HEMT and the spontaneous polarization is considerable in wurtzite III-nitrides. This provides an increased sensitivity relative to simple Schottky diodes fabricated on GaN layers or field effect transistors (FETs) fabricated on the AlGaN/GaN HEMT structure. The gate area of the HEMT can be used to modulate the drain current in the FET mode or for use as the electrode for the Schottky diode. A variety of gas, chemical and health-related sensors based on HEMT technology have been demonstrated with proper surface functionalization on the gate area of the HEMTs, including the detection of hydrogen, mercury ion, prostate specific antigen (PSA), DNA and glucose (Lothian *et al.*, 1992; Luther *et al.*, 1999; Johnson *et al.*, 2000; Neuberger *et al.*, 2001; Schalwig *et al.*, 2002b; Eickhoff *et al.*, 2003; Kim *et al.*, 2003a; Mehandru *et al.*, 2004; Pearton *et al.*, 2004; Shen *et al.*, 2004; Kang *et al.*, 2004a, 2004b; Kouche *et al.*, 2005; Kryliouk *et al.*, 2005; Tien *et al.*, 2005a, 2005b; Wang *et al.*, 2005a, 2005b, 2005c; Kang *et al.*, 2005b, 2005c, 2005e; Kang *et al.*, 2006; Wang *et al.*, 2006; Gangwani *et al.*, 2007; Jun *et al.*, 2007; Pearton *et al.*, 2007; Kang *et al.*, 2007a, 2007b, 2007c; Wang *et al.*, 2007a, 2007b, 2007c; Anderson *et al.*, 2008; Chen *et al.*, 2008; Johnson *et al.*, 2009; Kang *et al.*, 2008; Lim *et al.*, 2008; Yu *et al.*, 2008; Wright *et al.*, 2009).

In this chapter, we discuss recent progress in the functionalization of these semiconductor sensors for applications in detection of different gases, and the integration of these sensors into wireless packages for remote sensing capability. In addition, gas sensors based on other wide energy bandgap semiconductors – including SiC, GaN nanowires, InN nanobelts and ZnO nanorods – are covered in this chapter.

5.2 Gas sensing

There are a variety of gases whose presence needs to be detected in industrial and medical processes. This section covers each of these gases in turn.

© Woodhead Publishing Limited, 2013

5.2.1 Oxygen sensing

The current technology for O_2 measurement, referred to as 'oximetry', is small and convenient to use. However, the O_2 measurement technology does not provide a complete measure of respiratory sufficiency. A patient suffering from hypoventilation (poor gas exchange in the lungs) given 100% oxygen can have excellent blood oxygen levels while still suffering from respiratory acidosis due to excessive CO_2. Also, the O_2 measurement is not a complete measure of circulatory sufficiency. If there is insufficient blood flow or insufficient hemoglobin in the blood (anemia), tissues can suffer hypoxia despite high oxygen saturation in the blood that does arrive. The current oxide-based O_2 sensors can operate at very high temperatures, such as the commercialized solid electrolyte ZrO_2 (700ºC), or the semiconductor metal oxides such as TiO_2, Nb_2O_5, $SrTiO_3$ and CeO_2 (> 400ºC). However, it remains important to develop a low operational temperature and a high sensitivity O_2 sensor in order to build a small, portable and low cost O_2 sensor system for biomedical applications.

Oxide-based materials are widely used and studied for oxygen sensing because of their low cost and good reliability. The commercialized solid electrolyte ZrO_2 (Logothetis, 1991) has been widely used in automobiles for oxygen sensing in combustion processes. The electrolyte metal oxide oxygen sensor usually uses a reference gas and operates at a high temperature (700°C) (Xu *et al.*, 2000). Semiconductor metal oxides such as TiO_2, Ga_2O_3, Nb_2O_5, $SrTiO_3$ and CeO_2 do not need a reference gas, but they still need to be operated at a considerably high temperature (> 400°C) in order to reach high sensitivity, which means a high power consumption for heating up the sensors (Gerblinger *et al.*, 1995; Trinchi *et al.*, 2003; Castaneda, 2007; Mohammadi and Fray, 2007; Sotter *et al.*, 2007; Yakimova *et al.*, 2007). For biomedical applications (such as monitoring oxygen in the breath for a lung transplant patient), a portable and low power consumption O_2 sensor system is needed. Therefore, it is crucial to develop a low operating temperature and high sensitivity O_2 sensor for those applications.

The conductivity mechanism of most metal oxide-based semiconductors results from electron hopping from intrinsic defects in the oxide film and these defects are related to the oxygen vacancies generated during oxide growth. Typically, the higher the concentration of oxygen vacancies in the oxide film, the more conductive is the film. InZnO (IZO) films have been used in fabricating thin-film transistors, and the conductivity of the IZO is also found to depend on the oxygen partial pressure during oxide growth (Lim *et al.*, 2007; Wang *et al.*, 2007, 2008). The IZO is a good candidate for O_2 sensing applications.

A schematic of the oxygen sensor is shown in Fig. 5.1(a). Figure 5.1(b) shows the device had a strong response when it was tested at 120°C in pure

© Woodhead Publishing Limited, 2013

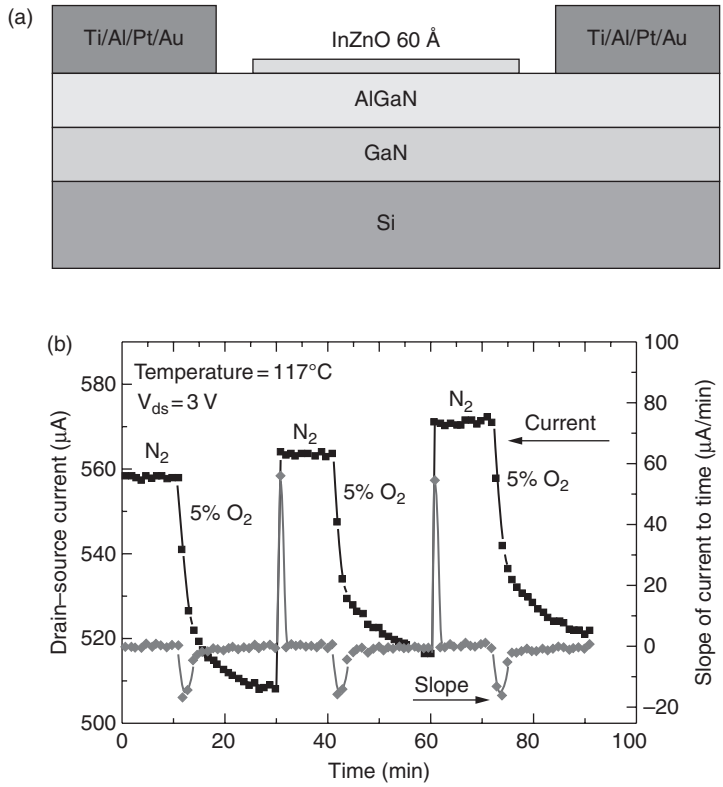

5.1 (a) Schematic of an AlGaN/GaN HEMT-based O_2 sensor; (b) drain current of an IZO functionalized HEMT sensor measured at fixed source–drain during exposure to different 5% O_2 concentration ambients. Notes: The drain bias voltage was 3.0 V and measurements were conducted at 117°C.

nitrogen and 5% oxygen in nitrogen, alternately, at $V_{ds} = 3$V. When the device was exposed to the 5% oxygen, the drain–source current decreased, whereas when the device was exposed to nitrogen, the current increased. The IZO film provides a high oxygen vacancy concentration, which makes the film readily sense oxygen and create a potential on the gate area of the AlGaN/GaN HEMT. A sharp drain–source current change demonstrates the combination of the advantage of the high electron mobility of the HEMT and the high oxygen vacancy concentration of the IZO film. Because of these advantages, this oxygen sensor can operate with high sensitivity at a relatively low temperature compared with many oxide-based oxygen sensors which operate from 400°C to 700°C.

In summary, it is clear that, through a combination of IZO films and the AlGaN/GaN HEMT structure, a low operation temperature and low power consumption oxygen sensor can be achieved. The sensor can be used either

© Woodhead Publishing Limited, 2013

in the steady-state or in the annealed mode, which provides flexibility in various applications. This device shows promise for portable, fast response and high sensitivity oxygen detectors.

5.2.2 Carbon dioxide sensing

The detection of carbon dioxide (CO_2) gas has attracted attention in the context of global warming, biological and health-related applications, such as indoor air quality control, process control in fermentation and in the measurement of CO_2 concentrations in the exhaled breath of patients with lung and stomach diseases (Machado *et al.*, 2005; Namjou *et al.*, 2006; Thorpe *et al.*, 2006; Thorpe *et al.*, 2008). In medical applications, it can be critical in hospital to monitor the CO_2 and O_2 concentrations in the circulatory systems of patients with lung diseases. The current technology for CO_2 measurement typically uses IR instruments, which can be very expensive and bulky.

The most common approach for CO_2 detection is based on non-dispersive infrared (NDIR) sensors, which are the simplest of the spectroscopic sensors (Manuccia and Eden, 1985; Wormhoudt, 1985; Kimmig *et al.*, 2000; Chu and Lo, 2008). The best detection limits for the NDIR sensors are currently in the range of 20–10 000 ppm. The key components of the NDIR approach are an infrared (IR) source, a light tube, an interference filter and an infrared (IR) detector. In operation, gas enters the light tube. Radiation from the IR light source passes through the gas in the light tube to impinge on the IR detector. The interference filter is positioned in the optical path in front of the IR detector such that the IR detector receives the radiation of a wavelength that is strongly absorbed by the gas whose concentration is to be determined while filtering out the unwanted wavelengths. The IR detector produces an electrical signal that represents the intensity of the radiation impinging on it. It is generally considered that NDIR technology is limited by power consumption and size.

In recent years, monomers or polymers containing amino-groups – such as tetrakis(hydroxyethyl)ethylenediamine, tetraethylene-pentamine and polyethyleneimine (PEI) – have been used for CO_2 sensors to overcome the power consumption and size issues found in the NDIR approach (Kong and Dai, 2001; Satyapal *et al.*, 2001; Shim *et al.*, 2001; Dell'Amico *et al.*, 2003). Most of the monomers or polymers are utilized as coatings for surface acoustic wave transducers. The polymers are capable of adsorbing CO_2 and facilitating a carbamate reaction. PEI has also been used as a coating on carbon nanotubes for CO_2 sensing by measuring the conductivity of nanotubes on exposure to the CO_2 gas. For example, CO_2 adsorbed by a PEI coated nanotube portion of a nanotube field effect transistor (NTFET) sensor lowers the total pH of the polymer layer and alters the charge transfer to the semiconducting nanotube channel, resulting in a change in the NTFET

© Woodhead Publishing Limited, 2013

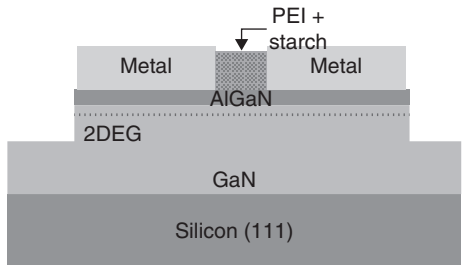

5.2 Schematic of an AlGaN/GaN HEMT-based CO_2 sensor.

electronic characteristics (Ong and Grimes, 2001; Varghese *et al.*, 2001; Star *et al.*, 2004; Kuzmych *et al.*, 2007).

A cross-section of the device is shown in Fig. 5.2. The interaction between CO_2 and the amino group-containing compounds with the influence of water molecules is based on an acid-base reaction. The purpose of adding starch to the PEI in our experiment was to enhance the absorption of the water molecules into the PEI/starch thin film. Several possible reaction mechanisms have been suggested. The key reaction was that primary amine groups, $-NH_2$, on the PEI main chain reacted with CO_2 and water forming $-NH_3^+$ ions and the CO_2 molecule became $OCOOH^-$ ions. Thus, the charges, or the polarity, on the PEI main chain were changed. The electrons in the two-dimensional electron gas (2DEG) channel of the AlGaN/GaN HEMT are induced by piezoelectric and spontaneous polarization effects. This 2DEG is located at the interface between the GaN layer and AlGaN layer. There are positive counter-charges at the AlGaN surface layer induced by the 2DEG. Any slight changes in the ambient of the AlGaN/GaN HEMT affect the surface charges of the AlGaN/GaN HEMT. The PEI/starch was coated on the gate area of the HEMT. The charges of the PEI changed through the reactions between $-NH_2$ and CO_2, as well as water molecules. These are then transduced into a change in the concentration of the 2DEG in the AlGaN/GaN HEMTs.

Figure 5.3 shows the drain current of PEI/starch functionalized HEMT sensors measured exposed to different CO_2 concentration ambients. The measurements were conducted at 108°C and a fixed source–drain bias voltage of 0.5 V. The current increased with the introduction of CO_2 gas. This was due to the increase in net positive charges on the gate area, thus inducing electrons in the 2DEG channel. The response to CO_2 gas has a wide dynamic range from 0.9% to 40%, as shown in Fig. 5.4. Higher CO_2 concentrations were not tested because there is little interest in these for medical-related applications. The response times were in the order of 100 s. The signal decay time was slower than the rise time, and was due to the longer time required to purge CO_2 from the test chamber.

The effect of ambient temperature on CO_2 detection sensitivity was investigated. The drain current changes were linearly proportional to the CO_2

© Woodhead Publishing Limited, 2013

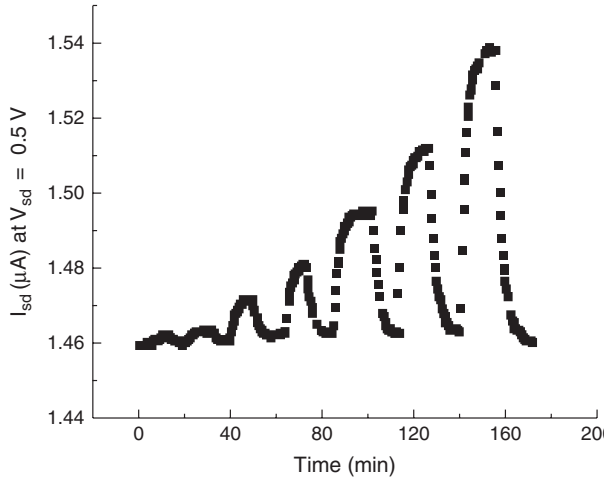

5.3 Drain current of a PEI/starch functionalized HEMT sensor measured at fixed source–drain during exposure to different CO_2 concentration ambients. Notes: the drain bias voltage was 0.5 V and measurements were conducted at 108°C.

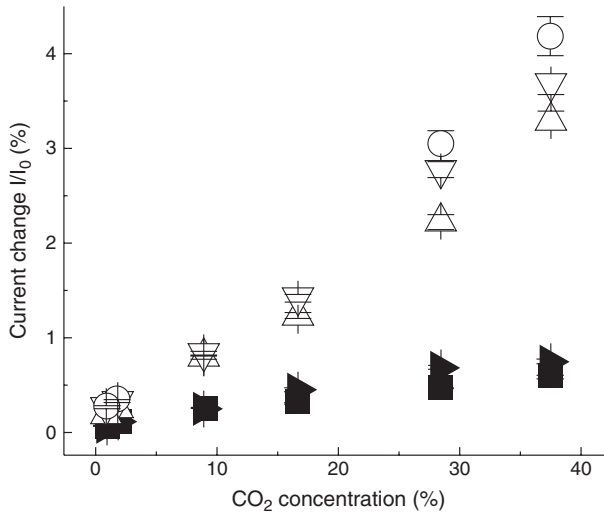

5.4 The drain current changes of an HEMT sensor as a function of CO_2 concentration.

concentration for all the tested temperatures. However, the HEMT sensors showed higher sensitivity for the higher testing temperatures. There was a noticeable change of the sensitivity from the sensors tested at 61°C to those tested at 108°C. This difference is likely due to higher ambient temperature increasing the reaction rate between the amine groups and CO_2, as well as

© Woodhead Publishing Limited, 2013

the diffusion of CO_2 molecules into the PEI thin film. The sensors exhibited reversible and reproducible characteristics.

In conclusion, PEI/starch functionalized HEMT sensors for CO_2 detection with a wide dynamic range from 0.9% to 50%. The sensors were operated at low bias voltage (0.5 V) for low power consumption applications. The sensors showed higher sensitivity at the testing temperature, which was higher than ~100°C. The sensors showed good repeatability. This electronic detection of CO_2 gas is a significant step towards a compact sensor chip which can be integrated with a commercial available handheld wireless transmitter to realize a portable, fast and high sensitive CO_2 sensor.

5.2.3 Ethylene sensing

Of particular interest in developing wide bandgap sensors are methods for detecting ethylene (C_2H_4), which presents problems because of its strong double bonds and, hence, the difficulty in dissociating it at modest temperatures (Vasiliev *et al.*, 1998; Savage *et al.*, 2000; Mitzner *et al.*, 2003). Ideal sensors have the ability to discriminate between different gases, and arrays that contain different metal oxides (e.g. SnO_2, ZnO, CuO, WO_3) on the same chip can be used to obtain this result. Another prime focus should be the thermal stability of the detectors, since they are expected to operate for long periods at elevated temperature (Mitra *et al.*, 1998; Rao, 2000; Gila *et al.*, 2001; Ling *et al.*, 2001; Chang *et al.*, 2002; Kim *et al.*, 2002; Hu *et al.*, 2003; Wollenstein *et al.*, 2003). Metal-oxide-semiconductor (MOS) diode-based sensors have significantly better thermal stability than a metal-gate structure and better sensitivity than Schottky diodes on GaN. In this work, we show that both AlGaN/GaN MOS diodes and Pt/ZnO bulk Schottky diodes are capable of detection of low concentrations (10%) of ethylene at temperatures of 50–300°C (ZnO) or 25–400°C (GaN).

Figure 5.5(a) shows a schematic of the completed AlGaN/GaN MOS-HEMT. The difference in forward diode current at 400°C of the Pt/Sc_2O_3/AlGaN/GaN MOS-HEMT diode both in pure N_2 relative to a 10% C_2H_4/90%N_2 atmosphere is illustrated in Fig. 5.5(b). At a given forward bias, the current increases on introduction of the C_2H_4. In analogy with the detection of hydrogen in comparable SiC and Si Schottky diodes, a possible mechanism for the current increases involves atomic hydrogen which is either decomposed from C_2H_4 in the gas phase, or chemisorbed on the Pt Schottky contacts then catalytically decomposed to release atomic hydrogen. The hydrogen can then diffuse rapidly through the Pt metallization and the underlying oxide to the interface, where it forms a dipole layer and lowers the effective barrier height. We emphasize that other mechanisms could be present; however, the activation energy for the current recovery is ~1 eV,

© Woodhead Publishing Limited, 2013

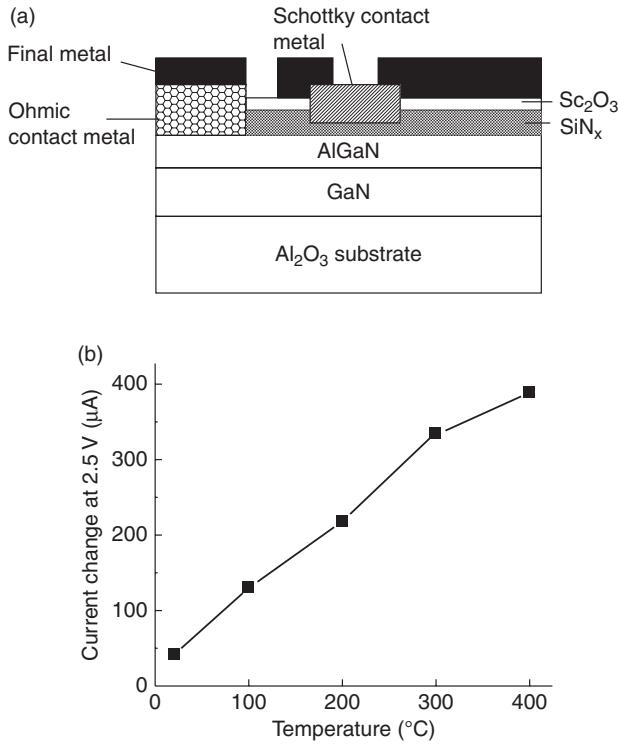

5.5 (a) Diagram of an AlGaN/GaN MOS diode; (b) change in current at fixed bias when ethylene is introduced into the test chamber with the sensor held at different temperatures.

similar to the value for atomic hydrogen diffusion in GaN (Nickel and Fleischer, 2003), which suggests that this is at least a plausible mechanism. As the detection temperature is increased, the response of the MOS-HEMT diodes increases due to more efficient cracking of the hydrogen on the metal contact. Note that the changes in both current and voltage are quite large and readily detected. In analogy with results for MOS gas sensors in other materials systems, the effect of the introduction of the atomic hydrogen into the oxide is to create a dipole layer at the oxide/semiconductor interface that will screen some of the piezo-induced charge in the HEMT channel. The time constant for response of the diodes was determined by the mass transport characteristics of the gas into the volume of the test chamber and was not limited by the response of the MOS diode itself.

5.3 Hydrogen sensing

Hydrogen gas (H_2) is a colorless, odorless, combustible gas. It has many industrial applications, mostly in the processing of fossil fuels, metal refining, and

© Woodhead Publishing Limited, 2013

the production of hydrochloric acid, methanol and ammonia. It has been used as the combustion material on the Space Shuttle solid rocket booster, and was used as a lifting gas until the now-infamous Hindenburg disaster occurred in 1937. Hydrogen poses several safety concerns. The upper and lower flammability limits of hydrogen in air are 4% and 75% by volume. Furthermore, pure hydrogen flame emits ultraviolet light, thus it is nearly invisible to the naked eye. Finally, when stored in liquid form, it is a cryogen. Therefore, in industrial processes where hydrogen is used, a robust sensor is essential.

An emerging application for hydrogen is in fuel cell electric vehicles. Such vehicles operate on the principle of electricity generation from the reaction of hydrogen and oxygen to form H_2O. This electricity directly drives a motor on each wheel. The only emission is water vapor. This emerging technology has been proposed for next-generation zero carbon emission vehicle technology. However, a concern with this technology is the wide-scale use of hydrogen gas. All fueling stations will have to store and dispense gas and, in the event of a crash, vehicles would leak a hydrogen plume if the tank ruptures. Therefore, a sensor will have to be very robust, detect low hydrogen concentrations, have a large detection range and have the ability to be deployed in city-scale networks.

Hydrogen sensor technology has been traditionally based on the cracking of the molecule in the presence of a catalytic metal, such as Pt or Pd. By integrating these metals on the gate electrode of the HEMT, the change of the sensing material's conductivity can be amplified through a Schottky diode or field effect transistor (FET) operation. It is generally accepted that H_2 is dissociated when adsorbed on Pt and Pd at room temperature. The reaction is as follows:

$$H_{2(ads)} \rightarrow 2\,H^+ + 2e^-$$

Dissociated hydrogen causes a change in the channel and conductance, creating a measurable signal. This makes sensors based on an integrated semiconductor device extremely sensitive to a broad, dynamic range of hydrogen concentrations.

Wide bandgap semiconductor sensors based on gallium nitride (GaN) and silicon carbide (SiC) can be operated at lower current levels than conventional Si-based devices and offer the capability of detection at elevated temperatures due to their low intrinsic carrier concentrations. The ability of electronic devices fabricated in these materials to function in high temperature, high power and high flux/energy radiation conditions enable performance enhancements in a wide variety of spacecraft, satellite, homeland defense, mining, automobile, nuclear power and radar applications. This chapter will discuss advances in hydrogen sensor technology using wide bandgap semiconductor devices and the implementation of sensors in wireless networks.

© Woodhead Publishing Limited, 2013

5.3.1 AlGaN/GaN HEMT Schottky diode-based hydrogen sensor

GaN materials systems are attracting significant interest for commercial and military applications, ranging from radar and unmanned vehicles to cable television amplifiers and wireless base stations. Due to the wide bandgap nature of the material, it is thermally very stable, and electronic devices can be operated at temperatures up to 500°C. The material is also chemically stable, with the only known wet etchant being molten NaOH or KOH, making it highly suitable for operation in chemically harsh environments or in radiation fluxes. Due to the high electron mobility, nitride-based HEMTs can operate from very high frequency (VHF) through X-band frequencies with higher breakdown voltage, and offer better thermal conductivity, and wider transmission bandwidths than Si or GaAs devices. GaN-based HEMTs can also operate at significantly higher power densities and higher impedance than GaAs devices currently in use (Pearton *et al.*, 1999; Eastman *et al.*, 2001; Keller *et al.*, 2001; Mishra *et al.*, 2002; Adivarahan *et al.*, 2003, Lu *et al.*, 2003; Mehandru *et al.*, 2003; Saito *et al.*, 2003; Tarakji *et al.*, 2003; Zhang *et al.*, 2003b; Zhang *et al.*, 2003c; Iwakami *et al.*, 2004; Hikita *et al.*, 2005; Nakazawa *et al.*, 2005; Palacios *et al.*, 2005; Valizadeh and Pavlidis, 2005).

5.3.2 Basic Schottky diode hydrogen sensor

AlGaN/GaN HEMTs show promising performance for use in broad-band power amplifiers in base station applications due to the high sheet carrier concentration, electron mobility in the two-dimensional electron gas (2DEG) channel and high saturation velocity. An overlooked potential application of the AlGaN/GaN high electron mobility transistor structure is in sensors. The high electron sheet carrier concentration of nitride HEMTs is induced by piezoelectric polarization of the strained AlGaN layer and the spontaneous polarization is considerable in wurtzite III-nitrides. This provides an increased sensitivity relative to simple Schottky diodes fabricated on GaN layers (Baranzahi *et al.*, 1995; Luther *et al.*, 1999; Schalwig *et al.*, 2001; Schalwig *et al.*, 2002a; Kim *et al.*, 2003; Weidemann *et al.*, 2003; Kim *et al.*, 2003b; Kang *et al.*, 2004a; Kang *et al.*, 2004b; Kang *et al.*, 2005; Kouche *et al.*, 2005; Matsuo *et al.*, 2005; Voss *et al.*, 2005; Wang *et al.*, 2005; Yun *et al.*, 2005; Song *et al.*, 2005a; Song *et al.*, 2005b; Ali *et al.*, 2006; Huang *et al.*, 2006). The gate area can be functionalized so that current changes can be detected for a variety of gases, liquids and biomolecules.

Hydrogen sensors are particularly interesting for the emerging fuel cell vehicle market. There are also applications for detection of combustion gases for fuel leak detection in spacecraft, automobiles and aircraft, fire detectors, exhaust diagnosis and emissions from industrial processes (Baranzahi

© Woodhead Publishing Limited, 2013

et al., 1995; Chen *et al.*, 1998; Svenningstorp *et al.*, 1999; Schalwig *et al.*, 2002a; Eickhoff *et al.*, 2003; Kim *et al.*, 2004; Pearton *et al.*, 2004; Kang *et al.*, 2004a, Kouche *et al.*, 2005; B. S. Kang *et al.*, 2005a; Hung *et al.*, 2012). A variety of gas, chemical and health-related sensors based on HEMT technology have been demonstrated with proper surface functionalization on the gate area of the HEMTs, including the detection of hydrogen, mercury ion, prostate specific antigen (PSA), DNA and glucose (Kang *et al.*, 2007a, 2007b, 2007c; Wang *et al.*, 2007c).

In GaN HEMT, the sensing mechanism is ascribed to the dissociation of the molecular hydrogen on a catalytic metal gate contact, followed by diffusion of the atomic hydrogen and, thus, the changing of the effective barrier height on Schottky diode structures. This effect has been used in Si, SiC, ZnO and GaN-based Schottky diode combustion gas sensors (Eberhardt *et al.*, 1981; Hartnagel *et al.*, 1995; Mitra *et al.*, 1998; Chang *et al.*, 2002; Voss *et al.*, 2005; Wang *et al.*, 2005; Anderson *et al.*, 2007; Anderson *et al.*, 2008; REB, 2010; Kim *et al.*, 2012). Furthermore, under forward bias conditions, the positively charged atomic hydrogen will be screened by the applied bias; under reverse bias conditions, the positive charge will be attracted to the surface. Therefore, reverse bias conditions are expected to yield improved sensitivity.

Device structure and fabrication

Simple two-terminal Schottky diodes are effective hydrogen sensors. The use of an AlGaN/GaN HEMT substrate improves the sensitivity, as the 2DEG will serve to amplify the effect of hydrogen absorption, discussed below. The HEMT structure is grown via metalorganic chemical vapor deposition (MOCVD) or molecular beam epitaxy (MBE) and consists of an AlN buffer layer on a sapphire (Al_2O_3) substrate, followed by a GaN buffer layer (0.5–2 μm), followed by an $Al_{0.3}GaN$ barrier layer (25–35 nm). The basic device fabrication begins with a mesa etch for isolation in a Cl_2/Ar inductively coupled plasma (ICP) etch system. The next step is deposition of ohmic metal via e-beam evaporation and lift-off. The metal scheme is typically Ti/Al/Pt/Au, although Ti/Al/TiB2/Ti/Au has been shown to improve reliability. The metal stack is annealed in a rapid thermal anneal (RTA) system at 850°C for 30 s in flowing N_2 to form the contact. The next step is the deposition of the sensing metal, which is also the Schottky contact. In a FET configuration, this would be the gate metal step, and would consist of a thin Ni or Pt layer to form the contact, followed by a thick Au layer for stability and probing. In this configuration, however, a thin Ni or Pt layer is desirable, as it will serve as the catalytic surface. Finally, an overlay metal is deposited, typically Ti/Au by e-beam evaporation and lift-off, to enable probing. This

© Woodhead Publishing Limited, 2013

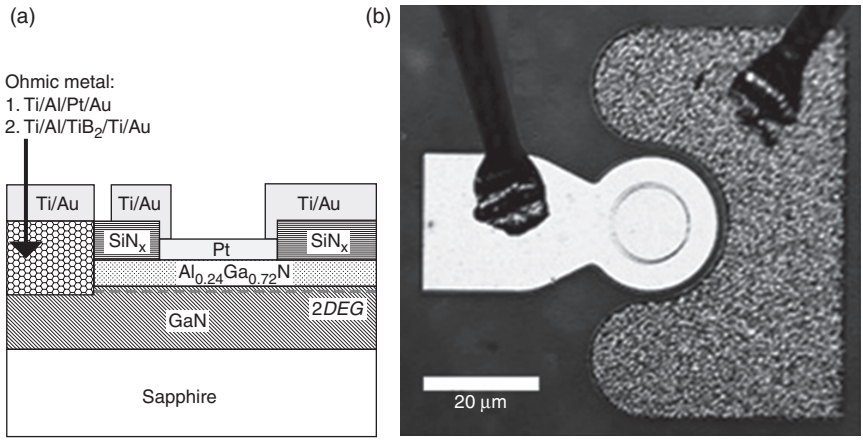

5.6 (a) Cross-sectional schematic of a completed Schottky diode on an AlGaN/GaN HEMT layer structure; (b) plan-view photograph.

is deposited as a ring around the catalytic metal with a large metal trace for wire bonding and probing. Figure 5.6 presents a device cross-section diagram and optical image of a packaged device.

Testing procedure

The system built for gas sensor testing consists of an environmental chamber with an electrical feed-through to a semiconductor parameter analyzer for monitoring the device current-voltage (I-V) characteristics (Fig. 5.7). Mass flow controllers are used to introduce test gases and nitrogen to the chamber and vary the concentration, and the chamber passes through a furnace for testing at elevated temperature. The hydrogen concentration can be controlled down to 1 ppm, or up to % levels, and the temperature range is from 25 to 500°C.

Experimental results

A basic demonstration of the hydrogen sensitivity of an AlGaN/GaN Schottky diode is presented in Fig. 5.8, which shows the linear (Fig. 5.8(a)) and log scale (Fig. 5.8(b)) forward I-V characteristics at 25°C of the HEMT diode, both in air and in a 1% H_2 in air atmosphere. For these diodes, there is a clear increase in current on the introduction of H_2, as a result of a lowering of the effective barrier height through the mechanism previously discussed. The H_2 catalytically decomposes on the Pt metallization and diffuses rapidly to the interface, where it forms a dipole layer. A more

© Woodhead Publishing Limited, 2013

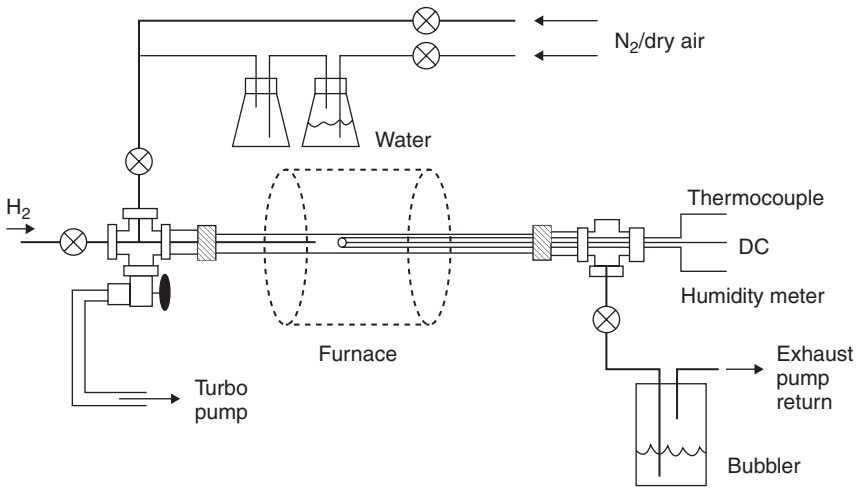

5.7 Diagram of the hydrogen sensing system.

detailed calculation of the reduction in barrier height is discussed below. The differential change in forward current on the introduction of hydrogen into the ambient is ~1 mA.

To test the time response of the sensors, a 10% H_2/90% N_2 ambient was switched into the chamber through a mass flow controller for periods of 10, 20 or 30 s and then switched back to pure N_2. Figure 5.9 shows the time dependence of forward current at a fixed bias of 2V under these conditions. The response of the sensor is rapid (< 1 s), with saturation taking close to 30 s. On switching off the hydrogen-containing ambient, the forward current decays exponentially back to its initial value. This time constant is determined by the transport properties of the test chamber and is not limited by the response of the diode itself.

For further study, devices were tested under both forward and reverse bias conditions at room temperature (25°C) in a nitrogen atmosphere at hydrogen concentrations ranging from 0 to 500 ppm, controlled by diluting the gas mix with nitrogen using mass flow controllers. Again, there was an increase in current under both forward and reverse bias conditions on exposure to hydrogen, as shown in Fig. 5.10. This result is consistent with previously discussed mechanisms (Neuberger *et al.*, 2001; Hunter *et al.*, 2002). The hydrogen atoms form a dipole layer, lowering the Schottky barrier height, and increasing net positive charges on the AlGaN surface, as well as negative charges in the 2DEG channel. The calculated barrier height decrease for 500 ppm and 100 ppm hydrogen is 5 meV and 1 meV, respectively. The ideality factors were calculated to be 1.25 and 1.23 in 500 and 100 ppm hydrogen, respectively, compared with 1.26 in 100% nitrogen.

© Woodhead Publishing Limited, 2013

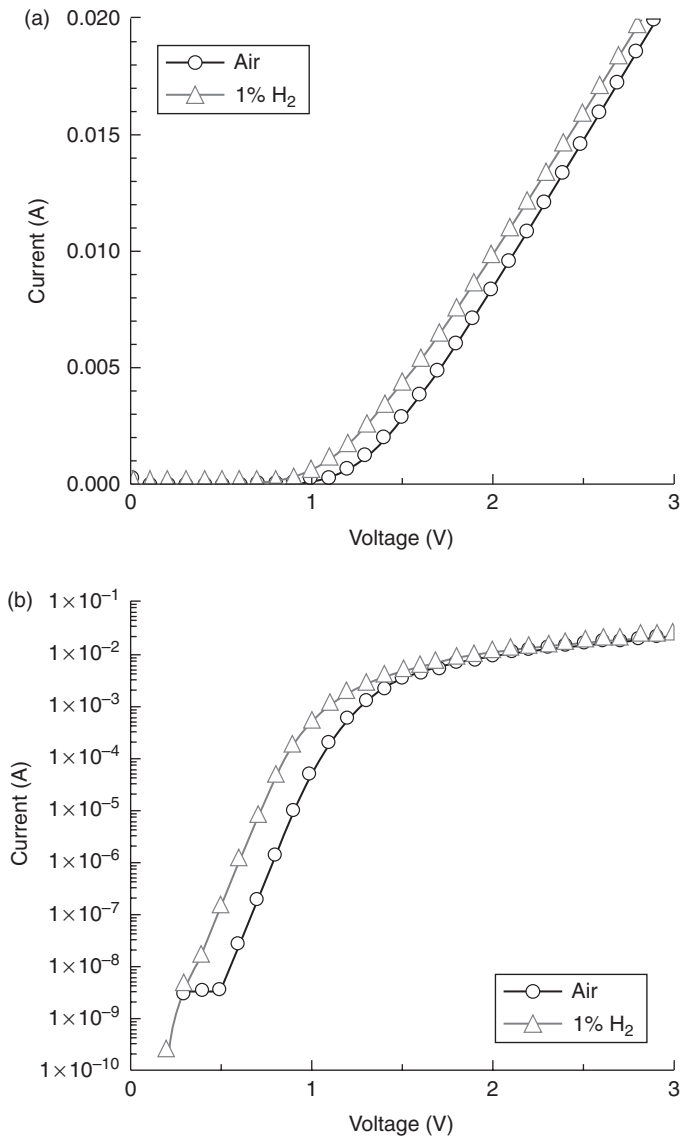

5.8 I-V characteristics in linear (a) or log (b) form of a Pt-gated diode measured in air or 1% hydrogen ambient at 25°C.

However, a plot of hydrogen sensitivity (defined as the drain current change over the initial drain current) versus bias voltage shows different characteristics for forward and reverse bias polarity conditions at 500 ppm of H_2, as shown in Fig. 5.11. For the forward bias condition, there is a maximum sensitivity obtained around 1 V and further increase of bias voltage reduces the sensitivity.

© Woodhead Publishing Limited, 2013

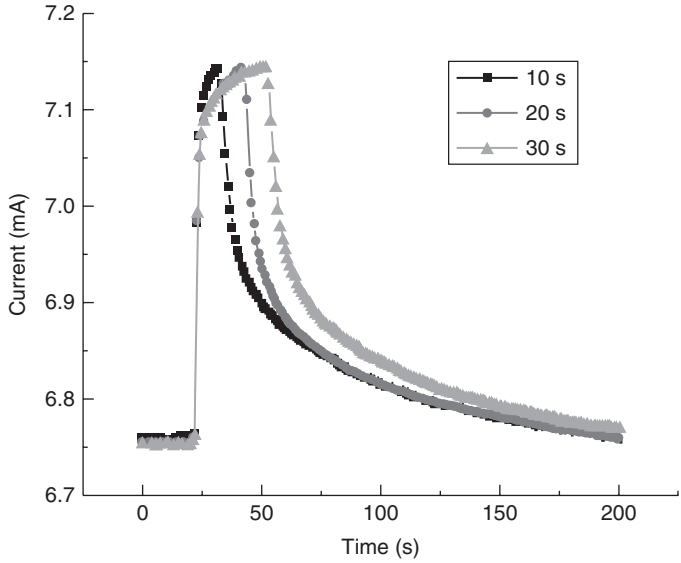

5.9 Time response at 25°C of a MOS-HEMT-based diode forward current at a fixed bias of 2 V when switching the ambient from N_2 to 10% H_2/90% N_2 for periods of 10, 20 or 30 s and then back to pure N_2.

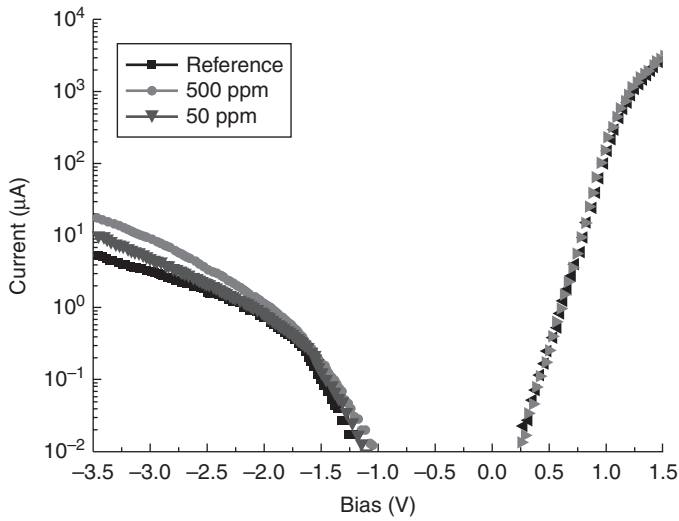

5.10 Forward and reverse bias plot of a diode current in varying atmospheres.

© Woodhead Publishing Limited, 2013

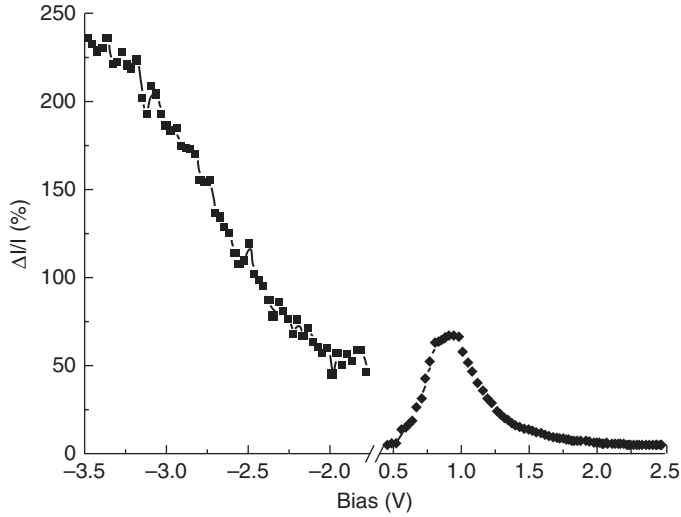

5.11 Percentage change in current as a function of bias at 500 ppm H_2.

The sensitivity for the reverse bias condition is quite different and increases proportionally to the bias voltage. We have proposed the following mechanism for the change in sensitivity under forward and reverse bias conditions:

(1) The initial increase in the sensitivity is due to the reduction in the Schottky barrier height.
(2) Further increase in forward bias allows electrons to flow across the Schottky barrier. These excess electrons bind with H+, form atomic hydrogen and gradually destroy the dipole layer at the interface, thereby losing the hydrogen detection sensitivity.
(3) For the reverse bias condition, electrons given away by the hydrogen atom may be swept across the depletion region. At higher reverse bias voltage, a higher driving force is applied to the electrons to move across the depletion region. Thus, the dipole layer is amplified at the Pt/AlGaN interface for higher reverse bias voltage. Due to this dipole layer amplification, detection sensitivity is enhanced at higher reverse bias voltage.

Detection sensitivity as a function of hydrogen concentration is quantified in Fig. 5.12. It is clear that the diodes are much more sensitive under reverse bias conditions, as predicted from the proposed mechanism. A detection limit of 100 ppm is achieved under forward bias, but the reverse bias detection limit is an order of magnitude lower, 10 ppm. The change in current at 10 ppm is 14% and over 200% at 500 ppm under reverse bias conditions, where forward bias operation results in changes of 25–75% over

© Woodhead Publishing Limited, 2013

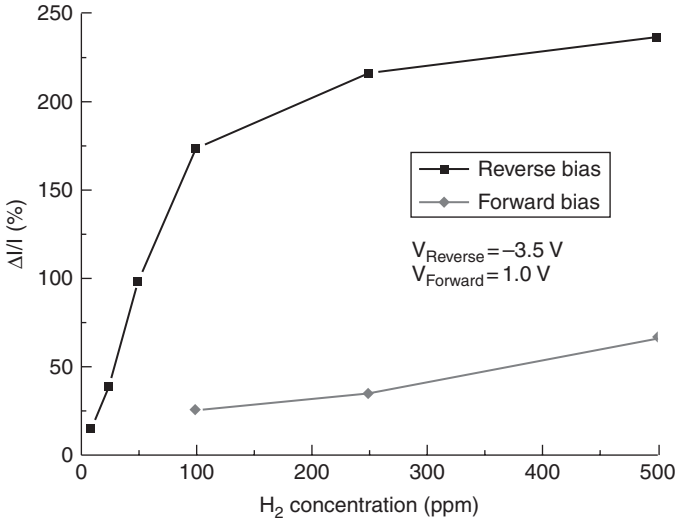

5.12 Percentage change in current as a function of hydrogen concentration under both forward and reverse bias.

the 100–500 ppm range. This is consistent with published reports indicating improved sensitivity under reverse bias (Schalwig *et al.*, 2001). The reliability of the hydrogen sensor may be quite different under the two bias voltage polarities, since different degradation mechanisms in GaN devices are accelerated by either the presence of high voltage depletion regions (reverse bias), or current injection (forward bias) (Steinhoff *et al.*, 2003).

5.3.3 TiB_2 ohmic contacts

Boride-based ohmic contacts on HEMTs show lower contact resistance than Ti/Al/Pt/Au after extended aging at 350°C (Khanna *et al.*, 2006). TiB_2-based ohmic contacts show improved stability for long-term operation (Wang *et al.*, 2007a). The structure of the ohmic contacts is Ti (200Å)/Al (1000Å)/TiB_2 (400Å)/Ti (200Å)/Au (800Å). All of the metals were deposited by Ar plasma-assisted radio frequency (RF) sputtering at pressures of 15–40 mTorr and RF (13.56 MHz) powers of 200–250 W. The contacts were annealed at 850°C for 45 s under a flowing N_2 ambient in a Heatpulse 610T system. Figure 5.13 shows the time dependence of forward current at 1.5 V gate bias for devices with both types of ohmic contacts. These tests were carried out in the field, where temperature and humidity were not controlled. There are several features of note. First, the current is much higher in the diodes with TiB_2-based contacts because of their lower contact resistance (1.6×10^{-6} Ω.

© Woodhead Publishing Limited, 2013

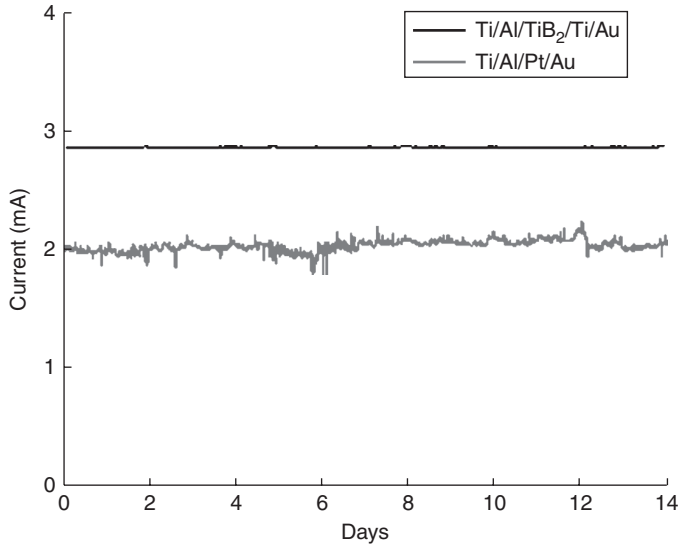

5.13 Variation in forward current at fixed bias for diodes with boride-based ohmic contacts (upper trace) or conventional ohmic contacts (lower trace) as a function of time under field conditions where the temperature increases during the day and decreases at night.

cm^2 vs 7.5×10^{-6} $\Omega.cm^2$ for the conventional Ti/Al/Pt/Au). Second, there is much better stability of the devices with TiB_2-based contacts. There is much less temperature dependence to the contact resistance of the boride contacts and this translates to less variation in gate current as the temperature cycles from day to night.

5.3.4 Effect of humidity on hydrogen sensors

Most of the hydrogen sensing studies to date have been conducted with hydrogen balanced with dry nitrogen, and a few experiments were performed in dry air conditions. However, in real applications for detecting hydrogen leaks humidity may play a significant role on the hydrogen sensing, and humidity in major cities in the US is often quite high, > 50% (CityRating.com, 2002). Therefore, it is important to study the effect of humidity on AlGaN/GaN HEMT-based hydrogen sensors.

Figure 5.14 shows the time dependence of the diode current for an HEMT sensor biased at a −1.5 V and exposed 1% H_2 balanced with air with different relative humidity. The 1% H_2 mixture was switched into the chamber through a mass flow controller for 180 s and then switched back to humid

© Woodhead Publishing Limited, 2013

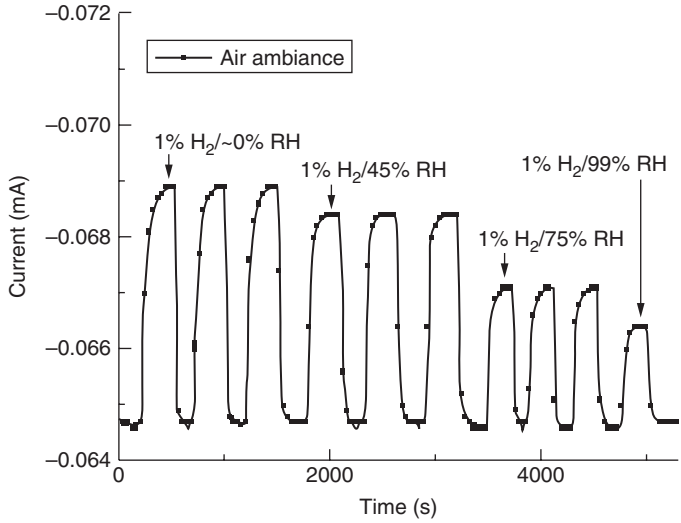

5.14 Time dependence of the absolute value of the AlGaN/GaN HEMT diode current biased at –1.5 V as the gas ambient switched back and forth between 1% hydrogen balance and air with different humidity.

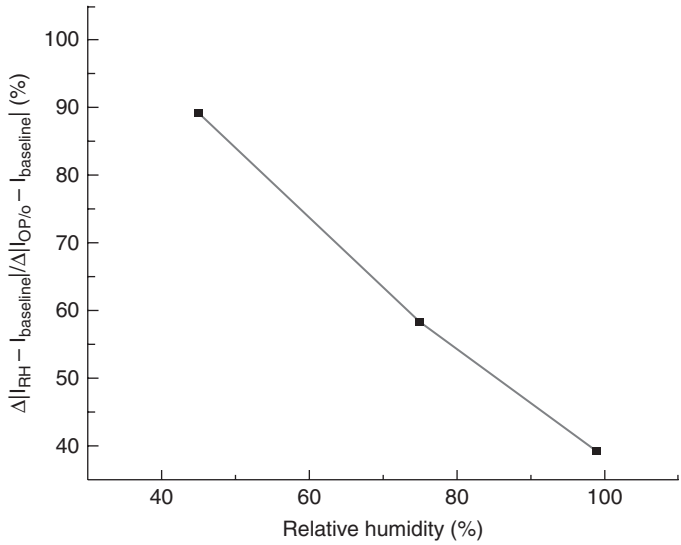

5.15 Hydrogen sensitivity as a function of the humidity. Bias voltage = –1.5 V.

© Woodhead Publishing Limited, 2013

air. Both sensing response and recovery times of the sensor were less than 1 minute, and the sensor also demonstrated good recyclability.

However, the sensitivity for 1% H_2 linearly decreased as the relative humidity increased, as illustrated in Fig. 5.15. Both relative humidity and oxygen partial pressure have been reported to degrade the electrocatalytic activity of platinum (Conway *et al.*, 1990; Harrington, 1997; Markovic and Ross, 2002; Paik *et al.*, 2004; Xu *et al.*, 2007). The absorbed water vapor and oxygen blocked available surface adsorption sites of platinum for H_2, and lowered the concentration of hydrogen at the metal/semiconductor interface.

The sensor exhibited a fast response for recovery time, when the gas ambient switched from hydrogen-containing humid air to non-hydrogen containing humid air. However, a slow recovery time was observed when the gas ambient switched from hydrogen-containing humid air to non-hydrogen containing dry air, as illustrated in Fig. 5.16. This slow recovery behavior was similar to the results obtained in our previous study conducted using dry nitrogen as the background ambient, which showed a long and slow recovery time (Wang *et al.*, 2006; Wang *et al.*, 2007a). The slow recovery time in that work was, we now believe, mistakenly attributed to longer times required to purge the residue hydrogen from the gas chamber. In this work, we note that the presence of water molecules in the ambient shortened the

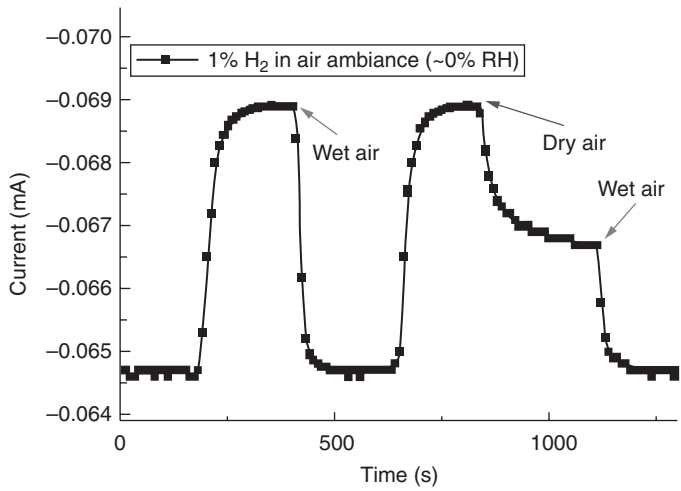

5.16 Time dependence of recovery time characteristics of the AlGaN/GaN HEMT diode current biased at –1.5 V as the gas ambient switched back and forth between 1% hydrogen balance and air with 100% humidity as well as dry air.

© Woodhead Publishing Limited, 2013

recovery time. It has been reported that Pd or Pt adsorbs H_2O and catalytically dissociates the adsorbed H_2O to form OH molecules with the assistance of surface chemisorbed atomic oxygen (Zhao *et al.*, 2008; Huang *et al.*, 2009). The atomic H would readily react with OH to form H_2O; thus, the presence of humidity consumed the atomic hydrogen and reduced the sensor recovery time.

5.3.5 Differential sensor

A differential pair of AlGaN/GaN HEMT diodes could be used for hydrogen sensing at near room temperature. This configuration provides a built-in control diode to reduce false alarms due to temperature swings, humidity changes, or voltage transients. Figure 5.17 shows an optical microscope image of the completed devices. The active device has 10 nm Pt exposed to the atmosphere, while the reference diode has Ti/Au covering the Pt layer.

Figure 5.18 shows the absolute and differential forward current-voltage (I-V) characteristics at 25°C of the HEMT active (Fig. 5.18(a)) and reference (Fig. 5.18(b)) diodes, both in air and in a 1% H_2 in air atmosphere. For the active diode, the current increases on the introduction of H_2, through a lowering of the effective barrier height. The H_2 catalytically decomposes on the Pt metallization and diffuses rapidly to the interface, where it forms a dipole layer. The differential change in forward current on the introduction of hydrogen into the ambient is ~1–4 mA over the voltage range examined and peaks at low bias. This is roughly double the detection sensitivity of comparable GaN Schottky gas sensors tested under the same conditions,

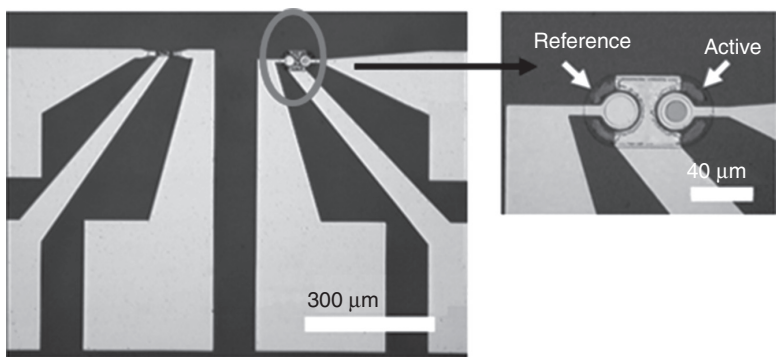

5.17 Microscopic images of differential sensing diodes. Notes: the opening of the active diode was deposited with 10 nm Pt, and the reference diode was deposited with Ti/Au.

© Woodhead Publishing Limited, 2013

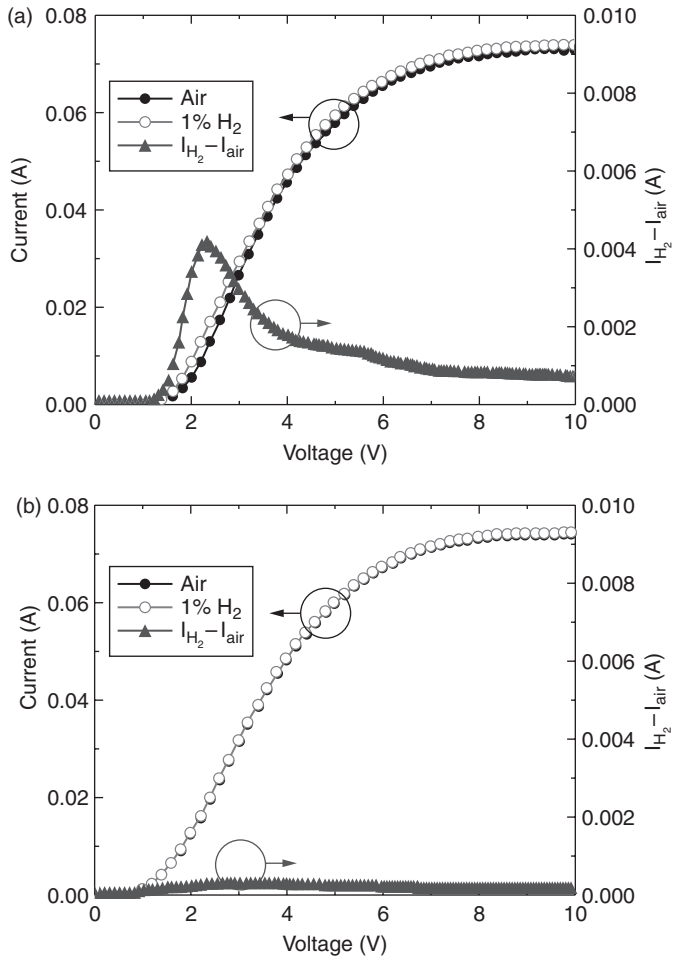

5.18 Absolute and differential current of HEMT active (a) and reference (b) diodes measured at 25°C.

confirming that the HEMT-based diode has advantages for applications requiring the ability to detect hydrogen even at room temperature.

As the detection temperature is increased to 50°C, the differential current response of the HEMT diode pair was almost constant over a wide range of voltages due to more efficient cracking of the hydrogen on the metal contact, as shown in Fig. 5.19. The maximum differential current is similar to that at 25°C, but the voltage control to achieve maximum detection sensitivity for hydrogen is not as significant at 50°C.

© Woodhead Publishing Limited, 2013

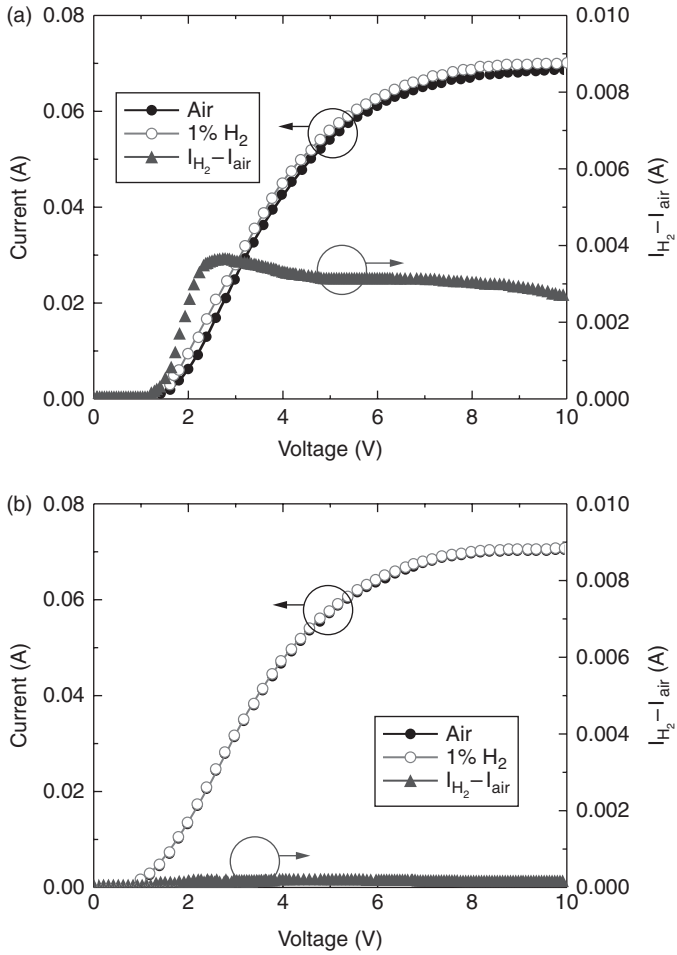

5.19 Absolute and differential current of HEMT active (a) and reference (b) diodes measured at 50°C.

5.4 GaN Schottky diode sensor

Schottky diodes are the simplest sensor type to fabricate and can be operated in two different modes. In this section we cover their use for gas sensing.

5.4.1 N-face and Ga-face comparison

Wurtzite GaN is a polar material. Therefore, along the c-axis, there are N-face (N-polar) or Ga-face (Ga-polar) orientations on the GaN surface.

© Woodhead Publishing Limited, 2013

Since there are different reactivities for the N-face and Ga-faces (Starke *et al.*, 2000; Mayumi *et al.*, 2001; Northrup and Neugebauer, 2004), it is interesting to note how these different surfaces react with different chemicals. The polarity determined by the GaN surface has been used to improve the performance of AlGaN/GaN HEMTs (Ambacher *et al.*, 1999). The Ga-polar surface is intentionally grown to make the spontaneous polarization compatible with the piezoelectric polarization to enhance the two-dimensional electron gas in AlGaN/GaN HEMTs (Ambacher *et al.*, 1999). However, the density functional theory suggests that hydrogen has a much higher affinity for the N-face surface of GaN than the Ga-face (Northrup and Neugebauer, 2004). High resolution electron energy loss spectroscopy (HREELS) showed a strong preference of N-sites for the adsorption of hydrogen gas or atomic H (Starke *et al.*, 2000). It was also shown that, below 820, N-polar GaN has a much faster reaction rate than that of the Ga-polar GaN surface (Mayumi *et al.*, 2001). Thus, one might expect the polarity of the surface to play an important role in hydrogen sensing characteristics. Recent results showed that Schottky diodes fabricated on N-face GaN provided much higher sensitivity than Ga-face GaN and Ga-face AlGaN/GaN HEMTs (Wang *et al.*, 2009a; Wang *et al.*, 2009b).

In N-polar GaN Schottky diodes, because of the higher surface reactivity with hydrogen inducing higher polarity, the Schottky barrier heights are reduced much more than those of Ga-polar Schottky diodes. Therefore, the N-polar GaN Schottky diodes have much higher sensitivity than Ga-polar GaN.

Device structure and fabrication

The GaN layer structures were grown on C-plane Al_2O_3 substrates with a low temperature GaN buffer by metalorganic chemical vapor deposition (MOCVD), as described previously (Sun *et al.*, 2008; Sun *et al.*, 2009). A key aspect for the N-polar growth is control of heteroepitaxial evolution with the use of two dissimilar conditions: one to enhance the vertical island formation, and the other to promote the lateral coalescence process. The degree of surface roughening through island nucleation can be controlled as seen by the low reflectance region, followed by designed rapid lateral growth (coalescence) to smooth out the surface. All epilayers at the end of coalescence are optically smooth and free of pits (Sun *et al.*, 2008; Sun *et al.*, 2009). Both Ga- and N-polar layers were grown to a thickness of ~1.3 μm on sapphire substrates. The layers exhibited n-type carrier densities of 1.5×10^{18} cm^{-3} (mobility of 245 cm^2/Vs) for the undoped N-face samples and 1×10^{18} cm^{-3} (mobility of 410 cm^2/Vs) for the Si-doped Ga-face samples. For comparison, we also used standard Ga-polar AlGaN/GaN heterostructure samples with a sheet carrier density of 9×10^{12} cm^{-2} for comparison as

© Woodhead Publishing Limited, 2013

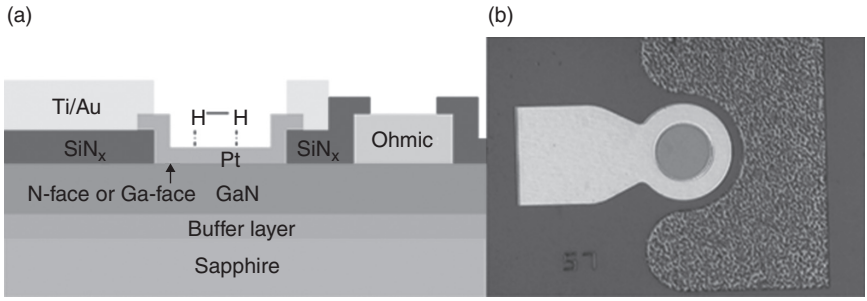

5.20 (a) Cross-sectional diagram of a Schottky diode made of Ga-polar or N-polar; (b) plan-view photograph of device.

sensors, since we have found these to exhibit higher hydrogen sensitivities than GaN diodes (Pearton *et al.*, 2004; Kang *et al.*, 2004b).

For all samples, ohmic contacts were formed by lift-off of e-beam deposited Ti (200 Å)/Al (1000 Å)/Ni (400 Å)/Au (1200 Å) subsequently annealed at 850°C for 45 s under a flowing N_2 ambient. The surface was encapsulated with 2000 Å of plasma enhanced chemical vapor deposited SiN_x at 300°C. Windows in the SiN_x were opened by dry etching and 100 Å of Pt deposited by e-beam evaporation for Schottky contacts. The final metal was e-beam deposited Ti/Au (200 Å/1200 Å) interconnection contacts. Figure 5.20 presents a diagram of the structure of the device and a bird's-eye view.

Experimental results

Schottky diode I-V characteristics seen in N-polar GaN, Ga-polar GaN and Ga-polar HEMTs before and after exposure to 4% H_2 in N_2 are illustrated in Fig. 5.21(a). The absolute and percentage change in current as a function of voltage as a result of hydrogen exposure are shown in Fig. 5.21(b). Note the remarkably greater effect of hydrogen exposure on the N-face diode. This diode actually reverts from rectifying to near-ohmic behavior after exposure to the 4% H_2 in N_2. The maximum percentage current changes were correspondingly much larger than for the Ga-face GaN or HEMT diodes: namely, 10^6 compared to 10 for the Ga-polar and 170 for the HEMT diode.

Figure 5.22 shows the time dependence of current change in the three types of sensors as a function of cycling the ambient from N_2 to 4% H_2 in N_2 and then back to N_2. The devices were operated at slightly different biases that were found to maximize their response. The N-polar diodes show much larger relative responses, but do not recover their original current within the time frame of the measurement, in contrast to the Ga-face and HEMT diodes. It is possible that some hydrogen was strongly bonded with nitrogen,

© Woodhead Publishing Limited, 2013

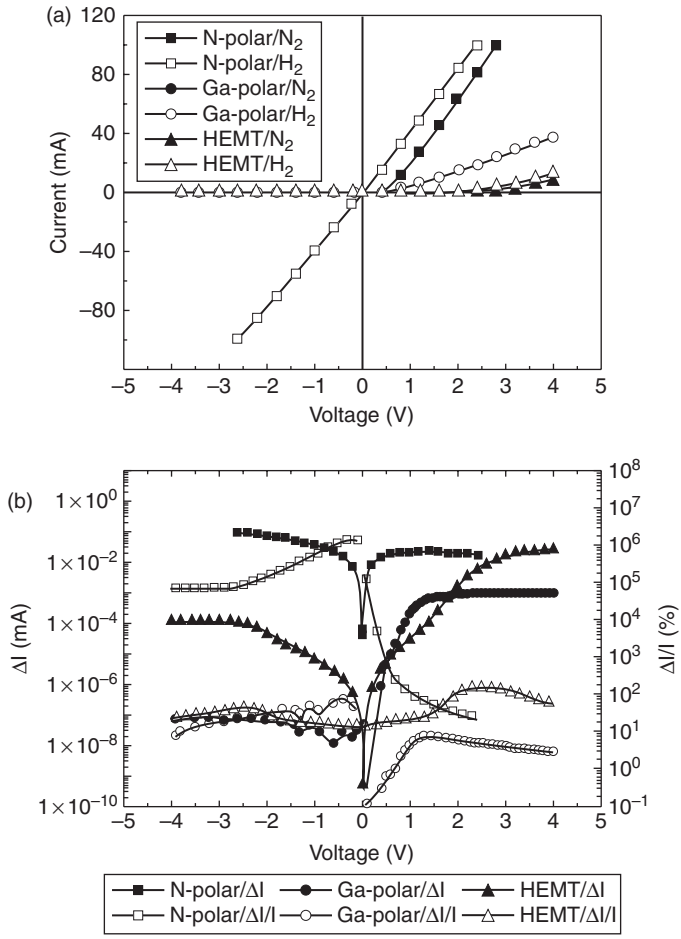

5.21 (a) I-V characteristics from the three types of diodes (Schottky diodes made of N-polar GaN, Ga-polar GaN and Ga-polar HEMT) before and after exposure to 4% H_2 in N_2; (b) the absolute and percentage change in current as a function of voltage as a result of hydrogen exposure.

with the thermal energy at room temperature not being sufficiently high to break the bonding.

As illustrated in Fig. 5.23(a), a shift from rectifying to near-ohmic behavior in the top frame upon initial exposure to the hydrogen-containing ambient was observed. This sudden current change in the reversed bias region demonstrated the effectiveness of using an N-polar GaN Schottky diode as the hydrogen sensor. However, the recovery time of the N-polar GaN Schottky diode was significantly longer compared with that of the GaN-

© Woodhead Publishing Limited, 2013

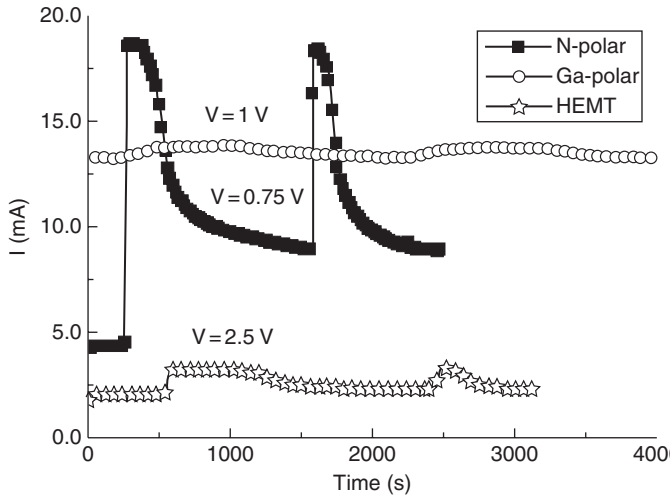

5.22 Time dependence of current change in the three types of sensors as a function of cycling the ambient from N_2 to 4% H_2 in N_2 at room temperature.

polar Schottky diode, as previously discussed. Figure 5.23(b) shows the recovery of the I-V characteristics in N-polar Schottky diode at 5-minute intervals after switching back to an N_2 ambient at room temperature. Even cycling the diodes to 150°C in N_2 after hydrogen sensing was not sufficient to restore the initial current, in sharp contrast to the other types of diodes where full recovery of the current was achieved at room temperature after approximately 15 minutes. This is consistent with the predicted stability of the H-covered N-polar GaN surface (Mayumi *et al.*, 2001; Northrup and Neugebauer, 2004).

5.4.2 W/Pt contacted GaN Schottky diodes

W/Pt contacted GaN Schottky diodes also show forward current changes of > 1 mA at low bias (3V) in the temperature range 350–600ºC when the measurement ambient is changed from pure N_2 to 10% H_2/90% N_2. We have found that use of a MOS diode structure with an Sc_2O_3 gate dielectric and the same W/Pt metallization show these same reversible changes in forward current on exposure to H_2-containing ambient over a much broader temperature range (90ºC to > 625ºC). The increase in current in both cases is the result of a decrease in the effective barrier height of the MOS and Schottky gates of 30–50 mV 10% H_2/90% N_2 ambient relative to pure N_2, and is due to catalytic dissociation of the H_2 on the Pt contact, followed by diffusion to

© Woodhead Publishing Limited, 2013

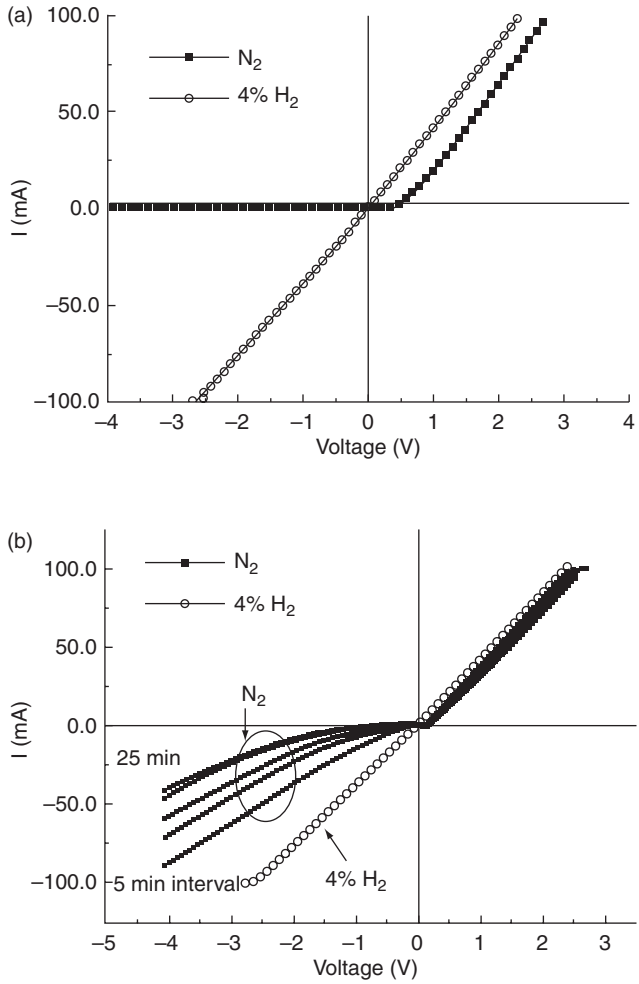

5.23 (a) I-V characteristics of the N-polar diodes before and after exposure to the H_2-containing ambient; (b) recovery of I-V characteristics in an N-face diode as a function of time in N_2 ambient after initial sensing of hydrogen.

the W/GaN or Sc_2O_3/GaN interface. The presence of the oxide lowers the temperature at which the hydrogen can be detected and, in conjunction with the use of high-temperature stable W metallization, enhances the potential applications of these wide bandgap sensors. Figure 5.24 presents the change in current in AlGaN/GaN and W/Pt GaN diodes at 500°C when the ambient is switched from N_2 to 10% H_2 in N_2, and shows that the relative change in current is greater with the MOS structure.

© Woodhead Publishing Limited, 2013

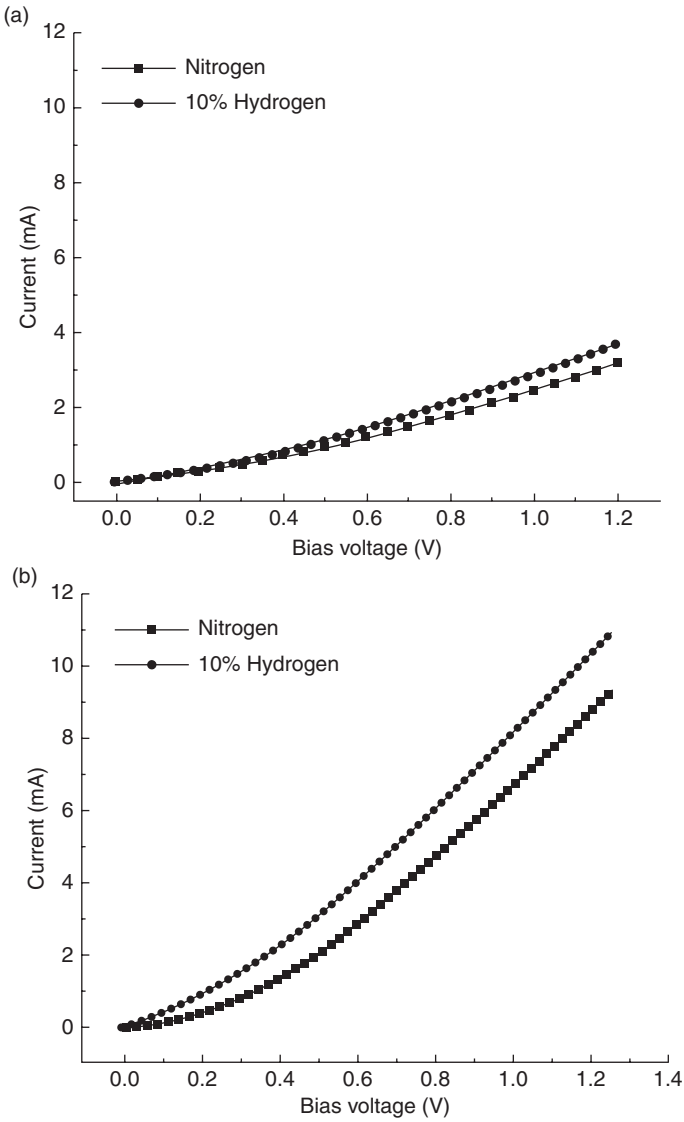

5.24 Change in current in (a) AlGaN/GaN and (b) W/Pt GaN diodes at 500°C when the ambient is switched from N_2 to 10% H_2 in N_2.

5.5 Nanostructured wide bandgap materials

Nanostructured wide bandgap materials functionalized with Pd or Pt are even more sensitive than their thin film counterparts because of the large surface-to-volume ratio (Lim *et al.*, 2008; Johnson *et al.*, 2009). 1-D semiconductor nanomaterials (such as carbon nanotubes (CNTs), Si nanowires,

© Woodhead Publishing Limited, 2013

GaN nanowires and ZnO nanowires) are good candidates to replace 2-D semiconductors due to the advantages listed below.

1. The 1-D structure has a large surface-to-volume ratio, which means that a significant fraction of the atoms can participate in surface reactions.
2. The Debye length (λ_D) for 1-D nanomaterials is comparable to their radius over a wide temperature and doping range, which promotes greater sensitivity than is found in a 2-D thin film.
3. A 1-D nanostructure is usually stoichiometrically better controlled than a 2-D thin film, and has a greater level of crystallinity than the 2-D thin-film. With 1-D structures, common defect problems in 2-D semiconductors could be easily solved.
4. Further decreasing the diameter, the onset of quantum effects is expected to be seen.
5. Low cost and low power consumption, together with their high compatibility with microelectronic processing make the 1-D nanostructure potential and practical materials for sensors. Impressive results have been demonstrated with GaN, InN and ZnO nanowires or nanobelts that are sensitive to hydrogen down to approximately 20 ppm at room temperature.

5.5.1 Hydrogen sensors based on ZnO nanorods

One of the main demands for such sensors is the ability to selectively detect hydrogen at room temperature in the presence of air. In addition, for most of these applications, the sensors should have very low power requirements and minimal weight. Nanostructures are natural candidates for this type of sensing. One important aspect is to increase their sensitivity for detecting gases such as hydrogen at low concentrations or temperatures, since typically an on-chip heater is used to increase the dissociation efficiency of molecular hydrogen to the atomic form and this adds complexity and power requirements. Previous work has shown that Pd-coated or doped CNTs become more sensitive to the detection of hydrogen through catalytic dissociation of H_2 to atomic hydrogen (Lu *et al.*, 2004; Sayago *et al.*, 2005; Kang *et al.*, 2005d). ZnO is also an attractive material for sensing applications, and nanowires and nanorods in this system have been reported for pH, gas, humidity and chemical sensing (Huang *et al.*, 2001; Keem *et al.*, 2004; Wan *et al.*, 2004a; Wan *et al.*, 2004b). These nanostructures could also have novel applications in biomedical science because ZnO is bio-safe (Wang, 2004). ZnO nanorods are relatively straightforward to synthesize by a number of different methods (Wu *et al.*, 2000; Pan *et al.*, 2001; Zheng *et al.*, 2001; He *et al.*, 2003; Lao *et al.*, 2003; Liu *et al.*, 2003; Ng *et al.*, 2003; Poole *et al.*, 2003;

© Woodhead Publishing Limited, 2013

Zhang *et al.*, 2003; Park *et al.*, 2003a; Park *et al.*, 2003b; Park *et al.*, 2003c; Heo *et al.*, 2004; Wang, 2004).

In ZnO devices, gas sensing mechanisms suggested include the exchange of charges between adsorbed gas species and the ZnO surface, leading to changes in depletion depth (Kim *et al.*, 2003b) and changes in surface or grain boundary conduction by gas adsorption/desorption (Vasiliev *et al.*, 1998; Kim *et al.*, 2003a). It should be noted that hydrogen introduces a shallow donor state in ZnO and this change in near-surface conductivity may also play a role. In the presence of a catalytic metal, the resulting charged atomic hydrogen will further change the conductivity, thus improving sensitivity.

Device structure and fabrication

The first step is the growth of ZnO nanorods. The structures are grown by MBE using Zn metal and O_2 plasma discharge as the source chemicals. To establish nucleation sites for the nanorods, a thin Au layer (2 nm) is deposited and annealed on a sapphire substrate. This process will form islands, rather than a continuous thin film. After two hours' MBE growth time at 600ºC, single-crystal nanorods with a typical length around 2~10 μm and a diameter in the range of 30–150 μm have been grown. Figure 5.25 shows a scanning electron micrograph of the as-grown rods.

The device structure is a simple two-terminal resistor, so Al/Ti/Au electrodes are deposited using e-beam evaporation with a shadow mask with

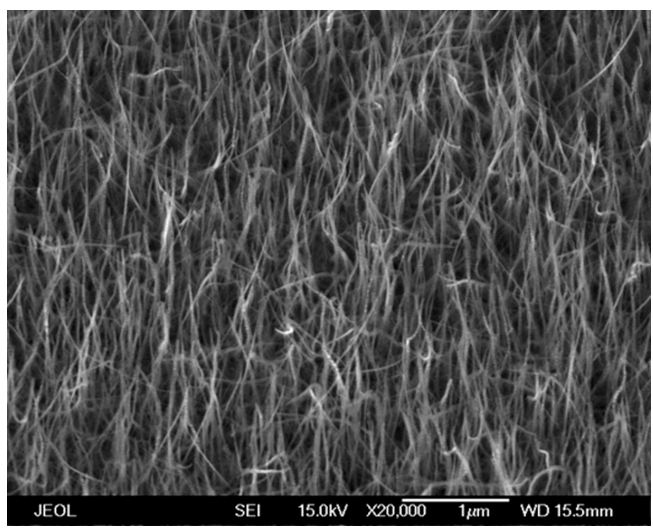

5.25 SEM image of ZnO nanorods.

© Woodhead Publishing Limited, 2013

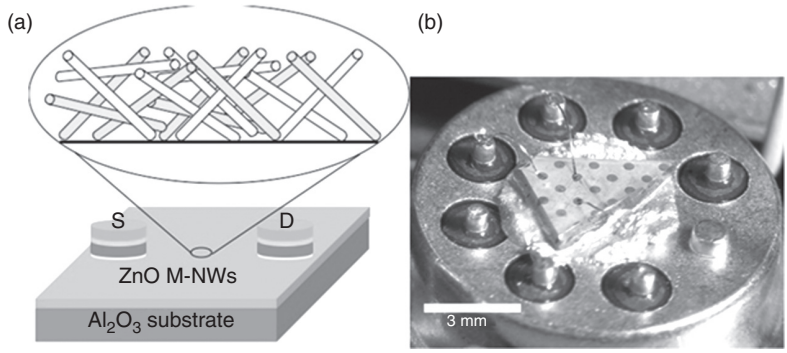

5.26 (a) Diagram of contact geometry for multiple nanorod gas sensor; (b) packaged, wire-bonded device for testing. S, source; D, drain; M-NWs, multiple nanowires.

a spacing of ~30 μm. The nanowires alone are sensitive to hydrogen, but studies have shown that a blanket deposition of catalytic metal clusters will improve sensitivity. The metal is deposited using e-beam evaporation, and the film is only 10 nm thick, so that nucleation clusters form but no continuous thin film. Current-voltage measurements confirmed that there was no conduction through the metal clusters, and there was no thin ZnO film formed using the nanorod growth conditions. Figure 5.26 presents a cross-sectional diagram of the contact geometry for a multiple nanorod gas sensor, and a packaged, wire-bonded device.

Experimental results

A preliminary investigation established the effect of catalytic metal coatings on ZnO nanorods. The time-dependent response of uncoated and Pd-coated nanorods to varying hydrogen concentrations from 10–500 ppm, with recovery in N_2, is shown in Fig. 5.27. There is clearly a strong increase (approximately a factor of 5) in the response of the Pd-coated nanorods to hydrogen relative to the uncoated devices. The addition of the Pd appears to be effective in catalytic dissociation of the H_2 to atomic hydrogen. In addition, there was no response to the presence of O_2 in the ambient at room temperature, and the relative response of Pt-coated nanorods is a function of H_2 concentration in N_2. The Pd-coated CNTs detected hydrogen down to < 10 ppm, with relative responses of > 2.6 % at 10 ppm and > 4.2% at 500 ppm H_2 in N_2 after an exposure of 10 minutes. By comparison, the uncoated devices showed relative resistance changes of ~0.25% for 500 ppm H_2 in N_2 after an exposure of 10 minutes and the results were not consistent for lower concentrations.

To study the transient sensor response, the resistance change of the Pt-coated multiple ZnO nanorods was monitored as the gas ambient was

© Woodhead Publishing Limited, 2013

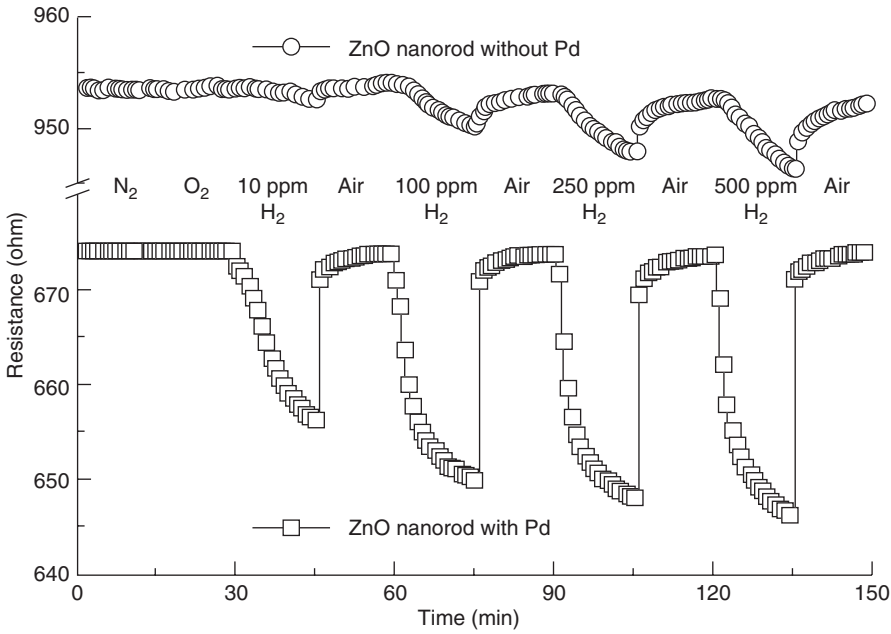

5.27 Time dependence of resistance of either Pd-coated or uncoated multiple ZnO nanorods as the gas ambient is switched from N_2 to various concentrations of H_2 in air (10–500 ppm).

switched from vacuum to N_2, oxygen or various concentrations of H_2 in air (10–500 ppm) and then back to air, as shown in Fig. 5.28. This data confirms the absence of sensitivity to O_2. The resistance change during the exposure to hydrogen was slower in the beginning and the rate resistance change reached a maximum at 1.5 minutes of the exposure time. This could be due to some Pd becoming covered with native oxide and this native oxide removed by exposure to hydrogen. Since the available surface of Pd for catalytic chemical absorption of hydrogen increased after the removal of oxides, the rate of resistance change increased. However, the Pd surface gradually saturated with the hydrogen and resistance change rate decreased. When the gas ambient switched from hydrogen to air, the oxygen reacted with hydrogen right away, and the resistance of the nanorods changed back to the original value instantly.

Figure 5.29 shows the Arrhenius plot of the rate of nanorod resistance change. The rate of resistance change for the nanorods exposed to 500 ppm H_2 in N_2 was measured at different temperatures. An activation energy of 12 kJ/mole was extracted from the slope of the Arrehnius plot. This value is greater than that of the typical diffusion process. Therefore, the dominant mechanism for this sensing process should be the chemisorption of hydrogen to the Pd surface.

© Woodhead Publishing Limited, 2013

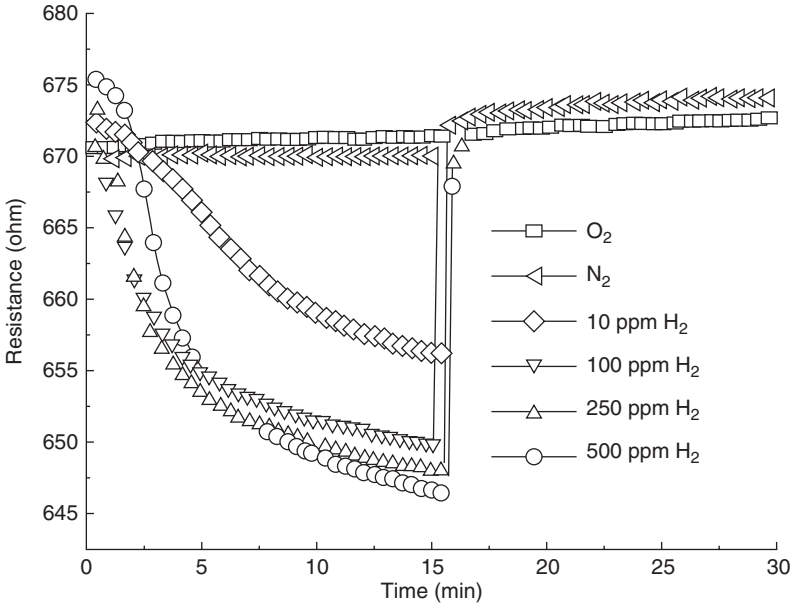

5.28 Relative response of Pd-coated nanorods as a function of H_2 concentration in N_2.

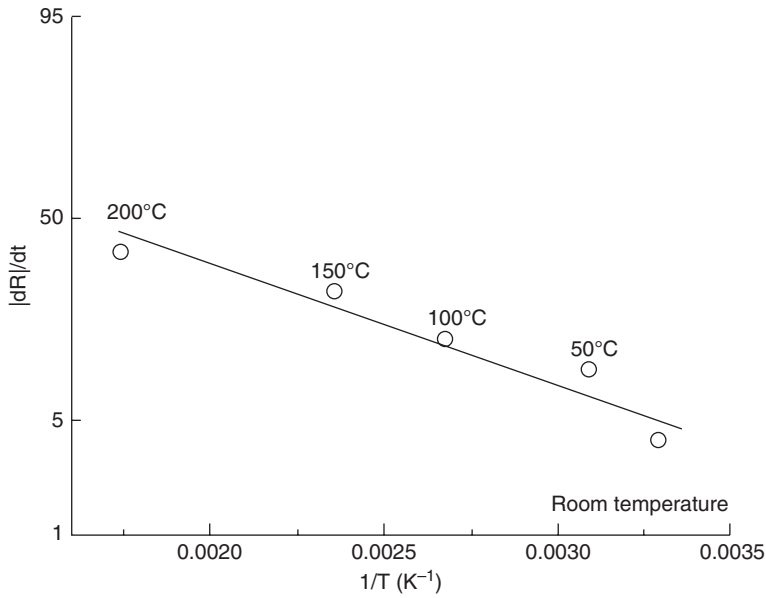

5.29 Time dependence of resistance change of Pd-coated multiple ZnO nanorods as the gas ambient is switched from N_2 to oxygen or various concentrations of H_2 in air (10–500 ppm) and then back to N_2. Slope = –1420; activation energy (E) = 11.8 kJ/mol.

© Woodhead Publishing Limited, 2013

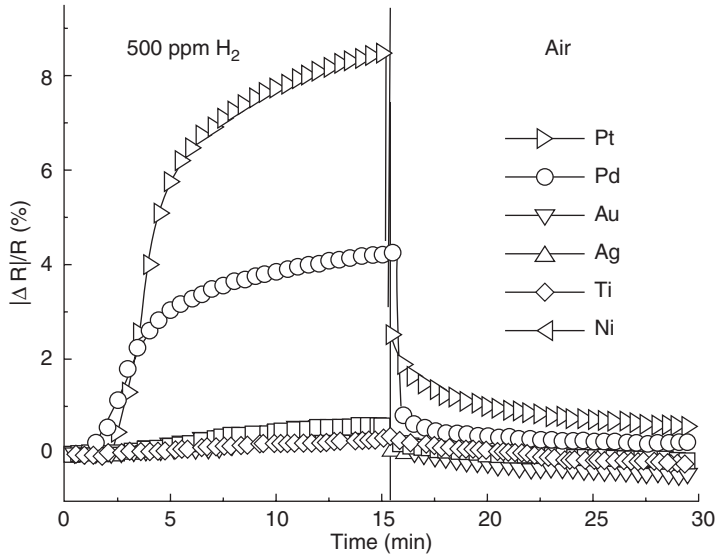

5.30 Time dependence of relative resistance response of metal-coated multiple ZnO nanorods as the gas ambient is switched from 500 ppm of H_2 in air to N_2 over time. Note: There was no response to O_2.

Having established improved sensitivity by coating the nanorods with catalytic metal, we then investigated the effects of different metals to further improve sensitivity and response. Using the same coating procedure described above, we investigated the effect of metal coatings of Ti, Ni, Ag, Au, Pt and Pd. Figure 5.30 shows the time dependence of the relative resistance change of either metal-coated or uncoated multiple ZnO nanorods as the gas ambient is switched from air to 500 ppm of H_2 in N_2. These were measured at a bias voltage of 0.5 V. There is a strong enhancement in response to Pd, and a lesser enhancement response to Pt coatings; however, the other metals produce little or no change. This is consistent with the known catalytic properties of these metals for hydrogen dissociation. Pd has a higher permeability than Pt but the solubility of H_2 is larger in the former (Spetz *et al.*, 2000). Moreover, studies of the bonding of H to Ni, Pd and Pt surfaces have shown that the adsorption energy is lowest on Pt (Connolly *et al.*, 2002).

The power requirements for the sensors were very low, which is a key requirement for a competitive, marketable sensor. Figure 5.31 shows the I-V characteristics measured at 25°C in both a pure N_2 ambient and after 15 minutes in a 500 ppm H_2 in N_2 ambient. Under these conditions, the resistance response is 8% and is achieved for a power requirement of only 0.4 mW. This compares well with competing technologies for hydrogen detection, such as Pd-loaded carbon nanotubes (Lu *et al.*, 2004; Sayago *et al.*, 2005).

© Woodhead Publishing Limited, 2013

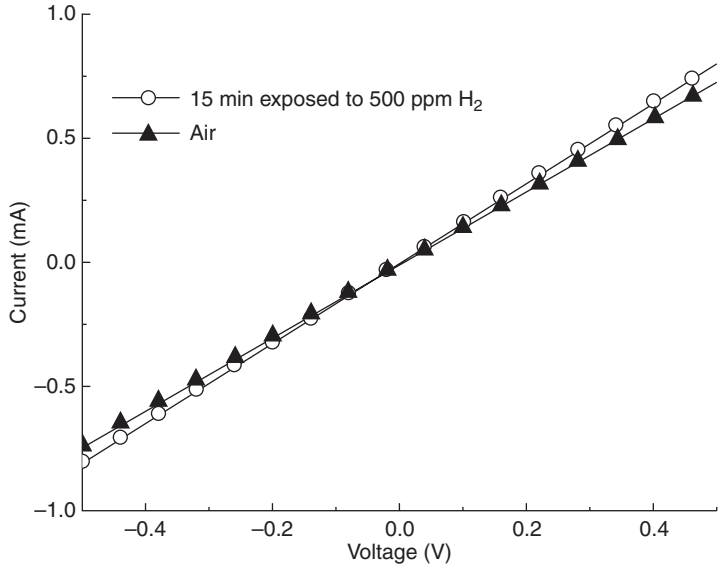

5.31 I-V characteristic of Pt-coated ZnO nanowires in air and after 15 minutes in 500 ppm H_2 in air.

5.5.2 GaN nanowires

Figure 5.32(a) shows scanning electron microscopy (SEM) micrographs of as-grown nanowires. A layer of 10 nm-thick Pd was deposited by sputtering onto the nanowires to verify the effect of the catalyst on gas sensitivity. Figure 5.32(b) shows the measured resistance at a bias of 0.5 V as a function of time from Pd-coated and uncoated multiple GaN nanowires exposed to a series of H_2 concentrations (200–1500 ppm) in N_2 for 10 minutes at room temperature. Pd-coating of the nanowires improved the sensitivity to ppm level H_2 by a factor of up to 11. The addition of Pd appears to be effective in the catalytic dissociation of molecular hydrogen. Diffusion of atomic hydrogen to the metal/GaN interface alters the surface depletion of the wires and, hence, the resistance at fixed bias voltage (Voss *et al.*, 2005). The resistance change depended on the gas concentration but the variations were small at H_2 concentration above 1000 ppm. The resistance after exposing the nanowires to air was restored to approximately 90% of the initial level within 2 minutes (Lim *et al.*, 2008; Johnson *et al.*, 2009).

5.5.3 InN nanobelts

Similar results can be obtained with InN nanostructures. The hydrogen sensing characteristics of multiple InN nanobelts grown by metalorganic

© Woodhead Publishing Limited, 2013

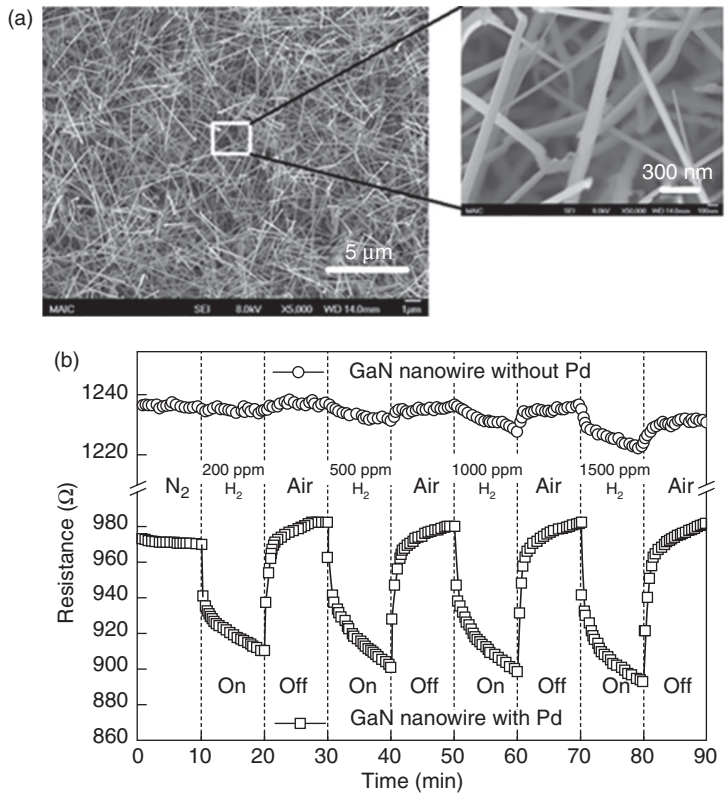

5.32 (a) SEM images of as-grown GaN nanowires; (b) measured resistance at an applied bias of 0.5 V as a function of time from Pd-coated and uncoated multiple GaN nanowires exposed to a series of H_2 concentrations (200–1500 ppm) in N_2 for 10 min at room temperature.

chemical vapor deposition have been reported previously (Lim *et al.*, 2008; Wright *et al.*, 2009). Pt-coated InN sensors could selectively detect hydrogen at the tens of ppm level at 25°C, while uncoated InN showed no detectable change in current when exposed to hydrogen under the same conditions. On exposure to various concentrations of hydrogen (20–300 ppm) in N_2 ambient, the relative resistance change increased from 1.2% at 20 ppm H_2 to 4% at 300 ppm H_2, as shown in Fig. 5.33. Approximately 90% of the initial InN resistance was recovered within 2 minutes by exposing the nanobelts to air. Temperature-dependent measurements showed greater resistance change and faster response at high temperature compared with those at room temperature due to an increase in the catalytic dissociation rate of H_2, as well as diffusion rate of atomic hydrogen into the Pt/InN

© Woodhead Publishing Limited, 2013

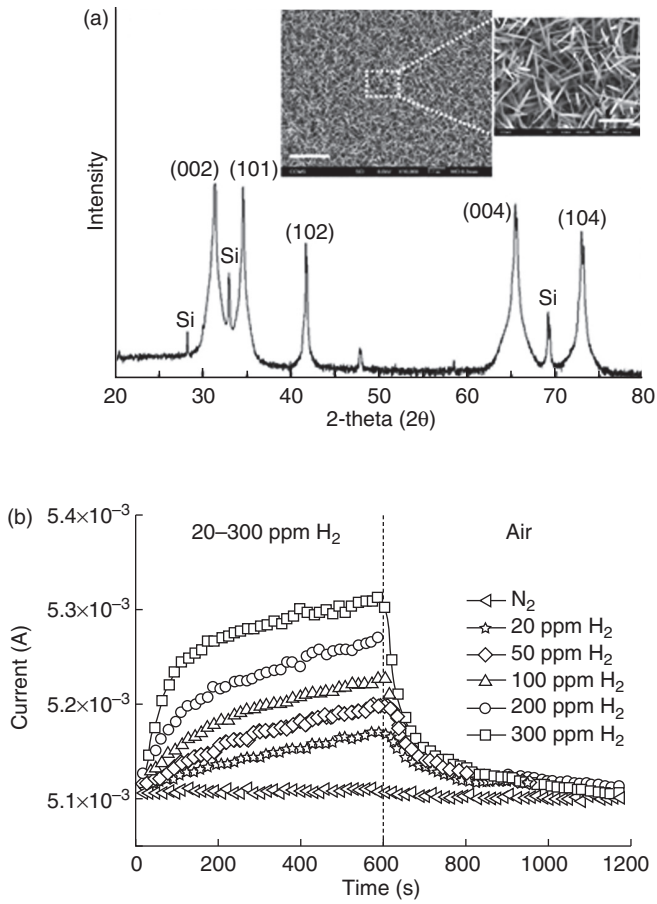

5.33 (a) X-ray diffraction spectrum of MOCVD-grown InN nanobelts; (b) change in current at fixed bias for switching from 20–300 ppm H_2 in air to pure air for Pt-coated InN nanobelts. Note: the inset in (a) shows SEM images of the nanobelts.

interface. The Pt-coated InN nanobelt sensors were operated at low power levels (~ 0.5 mW).

5.5.4 Single ZnO nanowire

Figure 5.34 shows a diagram of a single ZnO nanowire sensor and an SEM micrograph. Figure 5.35 illustrates the time dependence of resistance of Pt-coated ZnO nanowires as the gas ambient is switched from N_2 to various concentrations of H_2 in N_2 (10–500 ppm) over time. There are several aspects that are noteworthy. First, there is a strong increase (approximately

© Woodhead Publishing Limited, 2013

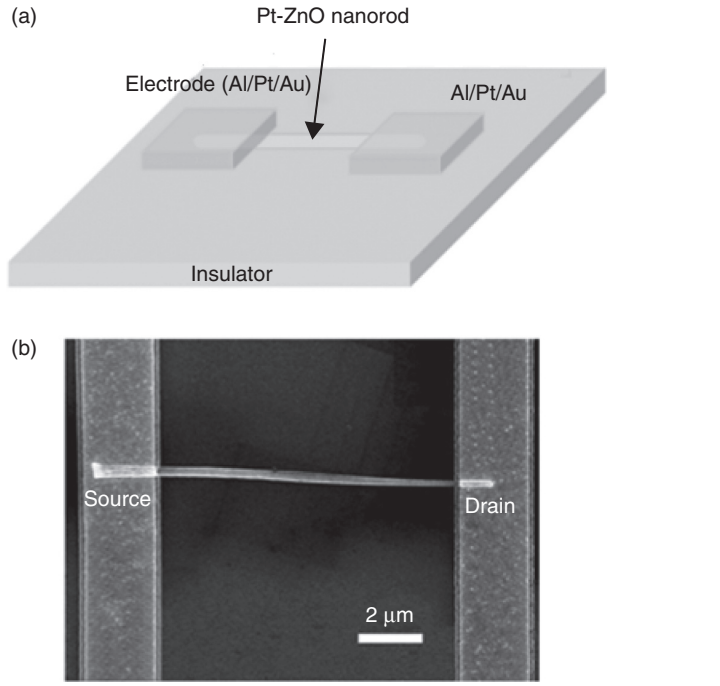

5.34 (a) Schematic of ZnO nanowire sensor; (b) SEM of completed device.

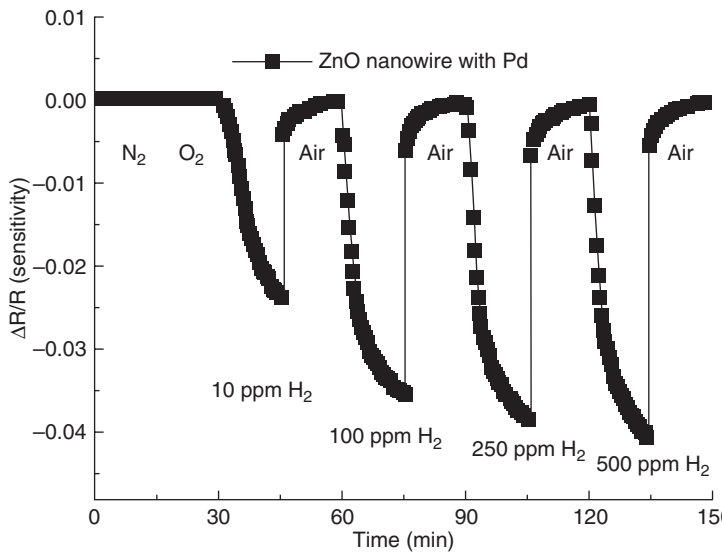

5.35 Change in resistance (R) as a function of time when switching to ambient containing H_2.

© Woodhead Publishing Limited, 2013

a factor of 10) in the response of the Pt-coated nanowires to hydrogen relative to the uncoated devices. The addition of the Pt appears to be effective in the catalytic dissociation of the H_2 to atomic hydrogen. Second, there was no response of either type of nanowire to the presence of O_2 in the ambient at room temperature. Third, the effective conductivity of the Pt-coated nanowires is higher due to the presence of the metal. Fourth, the recovery of the initial resistance is rapid (90%, < 20 s) on removal of the hydrogen from the ambient by either O_2 or air, while the nanowire resistance continues to change at least 15 minutes after the introduction of the hydrogen. The reversible chemisorption of reactive gases at the surface of metal oxides such as ZnO can produce a large and reversible variation in the conductance of the material. The gas sensing mechanism suggested includes the desorption of adsorbed surface hydrogen and grain boundaries in poly-ZnO; and the exchange of charges between adsorbed gas species and the ZnO surface, leads to changes in depletion depth and changes in surface or grain boundary conduction by gas adsorption/desorption (Hartnagel *et al.*, 1995; Mitra *et al.*, 1998; Chang *et al.*, 2002; Mitzner *et al.*, 2003; Lim *et al.*, 2008). The detection mechanism is still not firmly established in these devices and needs further study. It should be remembered that hydrogen introduces a shallow donor state in ZnO and this change in near-surface conductivity may also play a role.

5.6 Silicon carbide Schottky diode hydrogen sensor

Silicon carbide (SiC) Schottky diodes with Ni, Pd or Pt contacts are also sensitive to the presence of hydrogen in the ambient. These diodes can be operated up to 150°C for extended periods without deterioration of the Pt contact, although this is a significant concern for higher temperatures due to the possibility of $PtSi_2$ formation. For very high operating temperatures, it is desirable to use either a metal-oxide-semiconductor (MOS) approach, or else employ more thermally stable metallization, such as W or WSi_x. Figure 5.36 shows the forward I-V characteristics in N_2 or 10% H_2 in N_2 ambients at both 25°C and 150°C. The change in forward current upon changing the gas became greater at higher temperatures due to the increased dissociation efficiency of the gas molecules. This dissociation can occur through a catalytic reaction with the Pt gate, or through additional surface reactions on the semiconductor.

Figure 5.37 shows the time response of a SiC diode at 150°C on switching the gas introduced into the enclosure from N_2 to 10% H_2 in N_2. Note that the change in voltage required to maintain a forward current of 30 mA is very rapid (< 1 s), with saturation occurring ~4 s after the switching of the gases. The diffusion of hydrogen through the Pt layer is not the limiting

© Woodhead Publishing Limited, 2013

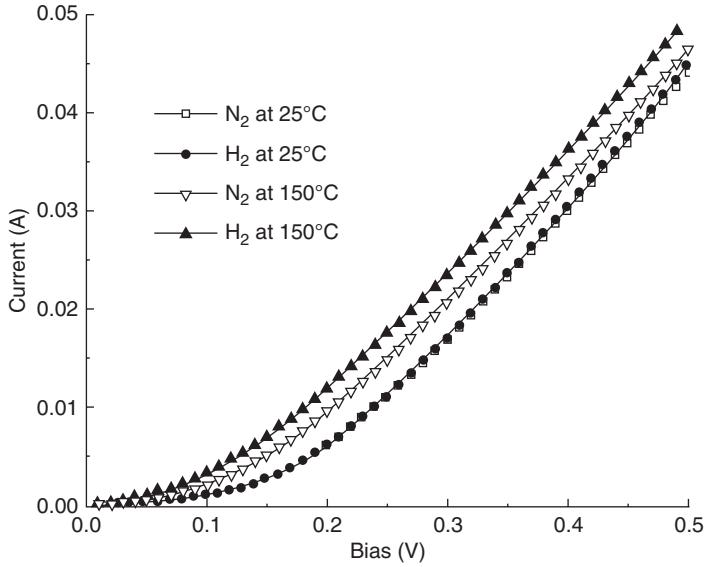

5.36 Low bias forward I-V characteristics from SiC sensor in 10% H_2 in N_2 or pure N_2 ambients at different temperatures (size of contact is 0.5 cm × 0.5 cm).

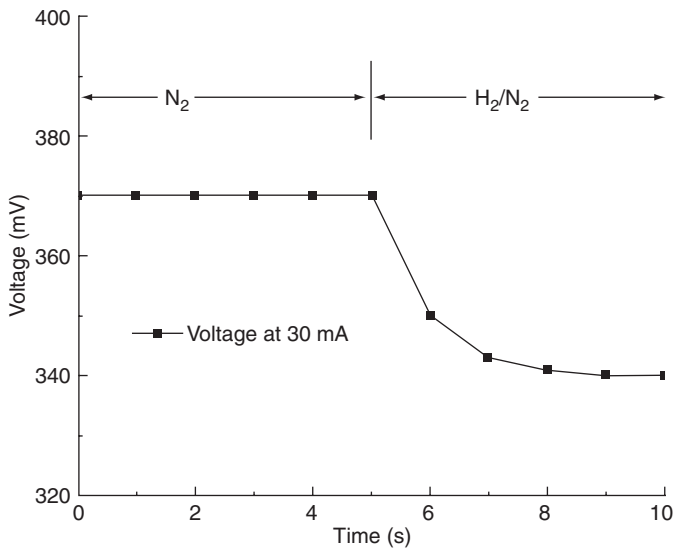

5.37 Time response of SiC sensor upon changing from pure N_2 to 10% H_2 in N_2 ambient at 150°C. Note: the y-axis shows the forward bias required to maintain a current of 30 mA.

© Woodhead Publishing Limited, 2013

factor in the time response of the diodes but, rather, the mass transport of gas into the enclosure, as we have observed by altering the introduction rate. Similarly, the initial recovery of the characteristics after the introduction of the initial N_2 ambient is most likely dominated by the removal of hydrogen atoms from the Pt/SiC interface or SiC interface. These results demonstrate the ability of SiC diodes to perform as rapid, sensitive gas sensors over a broad range of temperatures.

In conclusion, Pt/4H-SiC diode rectifiers of the type used for high-power electronic applications are also shown to be effective in gas sensor H_2 detection. The time response of the diodes is limited by the gas mass flow transport characteristics, with the intrinsic response due to changes in the interfacial OH-dipole layer being very rapid.

5.7 Wireless sensor network development

We have demonstrated a wireless hydrogen sensing system using commercially available wireless components and GaN Schottky diodes as the sensing devices. The sensors used in the circuit have shown current stability for more than one year in an outdoor environment. The advantage of a wireless network sensing system is that it enables monitoring of independent sensor nodes and transmits wireless signals, so the sensor nodes can be placed anywhere within the range of a base station. This is especially useful in manufacturing plants and hydrogen-fuelled automobile dealerships, where a number of sensors, possibly each detecting different chemicals, would be required. We have also developed an energy-efficient transmission protocol to reduce the power consumption of the remote sensor nodes. This extends battery life to a highly significant degree, thus making the system truly wireless. Experimental results showed that a 150-meter transmission distance can be achieved with 10 mW total power consumption. The entire sensor package can be built for less than $50, making it extremely competitive in today's market (Eickhoff *et al.*, 2001; Neuberger *et al.*, 2001; Schalwig *et al.*, 2001).

5.7.1 Sensor module

The sensor module was fully integrated on an FR4 PC board and packaged with a battery, as shown in Fig. 5.38(a). The dimension of the sensor module package was: $4.5 \times 2.9 \times 2$ inch^3. The maximum line of sight range between the sensor module and the base station was 150 meters. The base station of the wireless sensor network server was also integrated in a single module ($3.0 \times 2.7 \times 1.1$ inch^3) and ready to be connected to laptop by a USB cable, as shown in Figs 5.38(b) and (c). The base station draws its power from the

© Woodhead Publishing Limited, 2013

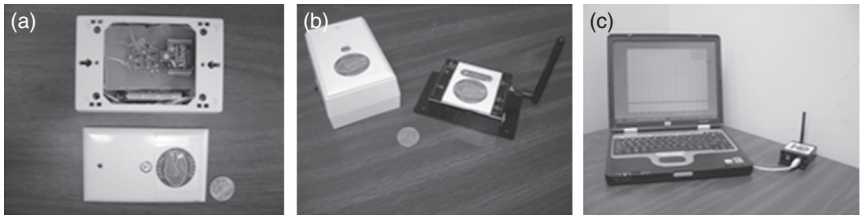

5.38 Sensor system. (a) Sensor with sensor device; (b) sensor and base station; (c) computer interface with base station.

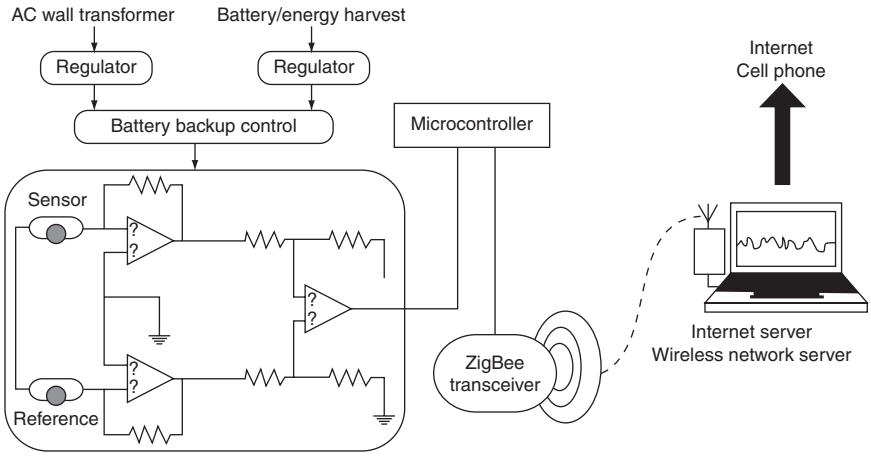

5.39 Block diagram of sensor module and wireless network server.

laptop's USB interface and does not require any battery or wall transformer (Eickhoff *et al.*, 2001; Neuberger *et al.*, 2001; Schalwig *et al.*, 2001).

Description of wireless transceiver

The sensor devices are based on the technology described in the previous sections, and demonstrate comparable characteristics. An instrumentation amplifier is used for the detection circuit to sense the change of current in the device. The current variation, embodied as a change in the output voltage of the detection circuit, is fed into the microcontroller. The microcontroller calculated the corresponding current change and controlled the ZigBee transceiver to transmit the data to the wireless network server. The block diagram of the sensor module and the wireless network server are shown in Fig. 5.39 (Eickhoff *et al.*, 2001; Neuberger *et al.*, 2001; Schalwig *et al.*, 2001).

© Woodhead Publishing Limited, 2013

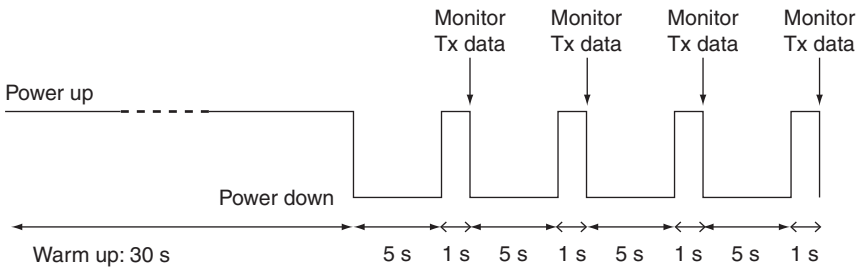

5.40 System timing of a wireless sensor node.

The Zigbee-compliant wireless network supports the unique needs of low-cost, low-power sensor networks, and operates within the ISM 2.4 GHz frequency band. The transceiver module is completely turned down for most of the time, and is turned on to transmit data in extremely short intervals. The timing of the system is shown in Fig. 5.40. When the sensor module is turned on, it is programmed to power up for the first 30 s. Following the initialization process, the detection circuit is periodically powered down for 5 s and powered up again for another 1 s, achieving a 16.67% duty cycle. The ZigBee transceiver is enabled for 5.5 ms to transmit the data only at the end of every cycle. This gives an RF duty cycle of only 0.09% (Eickhoff *et al.*, 2001; Neuberger *et al.*, 2001; Schalwig *et al.*, 2001).

Description of web server

A web server was developed using MATLAB to share the collected sensor data via the Internet. The interface of the server program, shown in Fig. 5.41, illustrates three emulated sensors with different baseline currents. If the current of any sensor increases to a level that indicates a potential hydrogen leakage, the alarm would be triggered. A client program was also developed to receive the sensor data remotely. As shown in Fig. 5.41, the remote client was able to obtain a real-time log of the system for the previous 10 minutes via the client program. In addition, a full data log was obtained by accessing the server as an ftp client, as the server program incorporates a full data logging functionality. When an alarm was triggered, the client was able to deactivate the alarm remotely by clicking a button on the interface. The server program for the wireless sensor network could also report a hydrogen leakage emergency through the phone line. When the current of any sensor exceeded a certain level, indicating a potential hydrogen leakage, the server would automatically call the phone-dial program, reporting the emergency to the appropriate personnel (Eickhoff *et al.*, 2001; Neuberger *et al.*, 2001; Schalwig *et al.*, 2001).

© Woodhead Publishing Limited, 2013

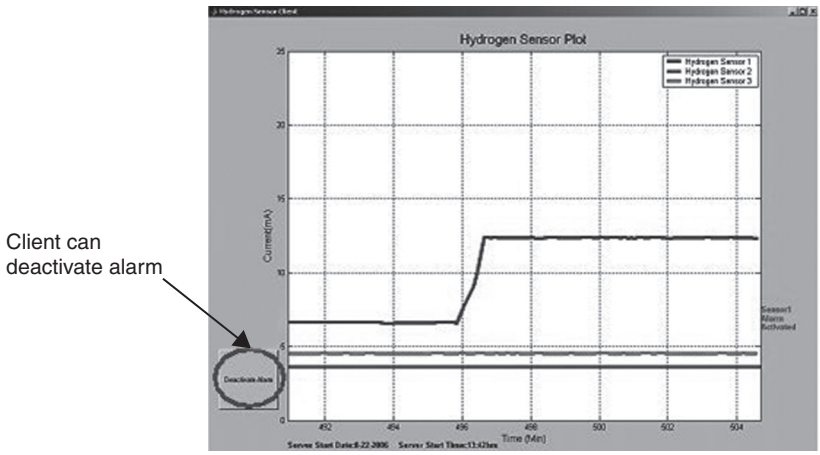

5.41 Interface of online hydrogen level monitoring.

5.7.2 Field test

Field tests have been conducted both at University of Florida and at Greenway Ford in Orlando, FL. The setup at Greenway Ford was aimed to test the stability of the sensor hardware and the server software under actual operational conditions. (Eickhoff *et al.*, 2001; Neuberger *et al.*, 2001; Schalwig *et al.*, 2001).

Initial field test results

Outdoor tests have been conducted to test the sensor's response to different concentrations of hydrogen at different distances. The tested hydrogen concentrations include: 1%, 4% and 100%, and the distance from the outlet of hydrogen to the sensor ranges from 1 foot to 6 feet. Hydrogen was detected in all these cases, triggering the program to send an alarm to a cell phone. Initial results of field testing indicated that the reliability of the sensors could be of concern, as the single diode sensors showed a periodic rise and fall in current level, which can be attributed to a temperature effect. There was also a long-term current degradation, attributed to ohmic contact degradation.

Improved field test results

False alarms and stability are two problems that arise when considering marketable applications. These can be caused by voltage swings in the device, or simply by temperature changes altering the current level. A differential pair

© Woodhead Publishing Limited, 2013

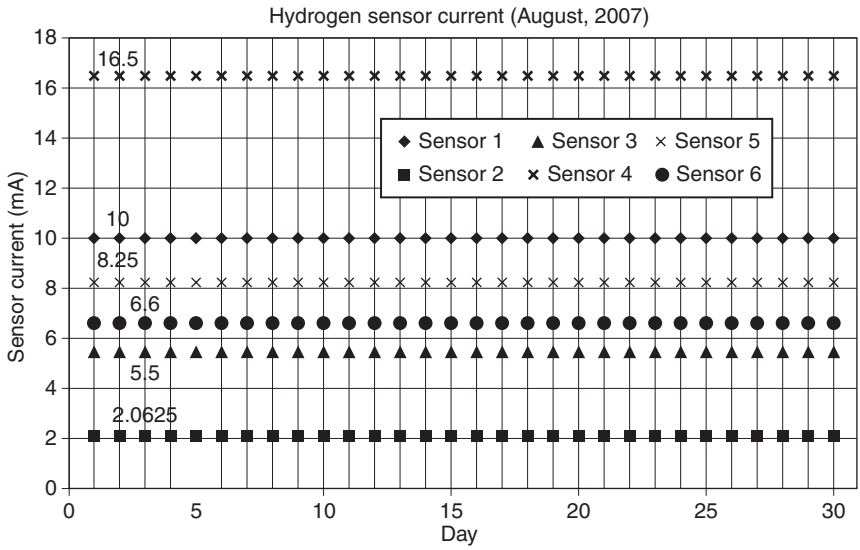

5.42 Field test results over a one-month period for differential diode sensors with boride-based ohmic contacts.

configuration of AlGaN/GaN HEMT diodes with a built-in control diode has been shown to reduce false alarms (Wang *et al.*, 2006). To avoid thermal effects, the sensor was redesigned with a differential detection system involving a reference diode (which was encapsulated) and an active diode (which was open to the ambient). Detection is achieved by monitoring the difference in current between the two devices.

An additional key required for long-term monitoring is availability of stable ohmic contacts. Boride-based contacts on HEMTs have lower contact resistance than Ti/Al/Pt/Au after extended aging at 350°C (Khanna *et al.*, 2006). Also, TiB_2-based ohmic contacts show improved stability for long-term operation (Wang *et al.*, 2007a). The combination of differential diode sensors and boride-based ohmic contacts has significantly improved stability and reliability. Recent field data are shown in Fig. 5.42, and the data can be monitored in real-time at the following website: http://ren.che.ufl.edu/app/realtimeSensing.htm

5.8 Conclusion

AlGaN/GaN HEMTs, GaN as well as SiC diodes, GaN nanowires and ZnO nanorods appear well-suited to sensing applications for combustible gases. The changes in forward current for Ga-faced AlGaN/GaN HEMTs are approximately double those of simple Ga-faced GaN Schottky diode

© Woodhead Publishing Limited, 2013

gas sensors tested under similar conditions, and suggest that integrated chips involving gas sensors and HEMT-based circuitry for off-chip communication are feasible in the AlGaN/GaN system. New development in N-faced GaN Schottky diodes shows much higher sensitivity than Ga-faced diodes due to high polarity formed on the surface termination. Devices show improved sensing capabilities under reverse bias polarity. Due to the amplification of the dipole layer at the interface under reverse bias conditions, instead of screening under forward bias conditions, the sensitivity of hydrogen detection is higher under reverse bias conditions. By using reverse bias conditions combined with the improved stability from boride contacts, the overall stability of the GaN system is very attractive for long-term applications requiring high sensitivity. Pt-coated ZnO nanowires also demonstrate a superior response compared with other metals. The recovery characteristics are rapid following the removal of hydrogen from the ambient. The primary advantages of ZnO nanorods are that they can be placed on cheap transparent substrates such as glass (making them attractive for low-cost sensing applications) and can operate at very low power levels.

A low-power wireless sensor network has been demonstrated. This type of network can accommodate different sensors at each node, and has been engineered to have a long battery life, making the system truly wireless. These sensors could conceivably be placed at strategic locations on a large scale, and have been field-tested. In the anticipated mass deployment of hydrogen fuel cell vehicles, city-level monitoring and networking will be necessary for safety. This work shows that the technology exists for a low-cost, large-scale sensor deployment.

5.9 Acknowledgments

Grateful thanks to all those who have contributed to this chapter: B. Chu, H. Wang, D.P. Norton and J. Lin, University of Florida, USA; T.J. Anderson, Naval Research Laboratory, USA; C. Li, Texas Tech University, USA; Y.-L. Wang, National Tsing Hua University, Taiwan; J. Kim, Korea University, Korea; L.-C. Tien, National Dong Hwa University, Taiwan; J.W. Johnson, Kopin Corp., USA; and A. Dabiran, SVT Associates, USA.

The work at the University of Florida is partially supported by the Office of Naval Research (ONR) under Contract number 00075094, monitored by Dr Chagaan Baatar; the NSF under contract number ECCS 0901711, monitored by Dr Yogesh B. Gianchandani; NASA Kennedy Space Center Grant NAG 10–316, monitored by Mr Daniel E. Fitch; and by Superfund Basic Research Program Grant RO1ES015449.

© Woodhead Publishing Limited, 2013

5.10 References

Adivarahan, V., Gaevski, M., Sun, W. H., Fatima, H., Koudymov, A., Saygi, S., Simin, G., Yang, J., Khan, M. A., Tarakji, A., Shur, M. S. and Gaska, R. (2003) 'Submicron gate Si_3N_4/AlGaN/GaN-metal-insulator-semiconductor heterostructure field-effect transistors', *IEEE Electron Device Letters*, **24**(9), 541–543.

Ali, M., Cimalla, V., Lebedev, V., Romanus, H., Tilak, V., Merfeld, D., Sandvik, P. and Ambacher, O. (2006) 'Pt/GaN Schottky diodes for hydrogen gas sensors', *Sensors and Actuators B-Chemical*, **113**(2), 797–804.

Ambacher, O., Smart, J., Shealy, J. R., Weimann, N. G., Chu, K., Murphy, M., Schaff, W. J., Eastman, L. F., Dimitrov, R., Wittmer, L., Stutzmann, M., Rieger, W. and Hilsenbeck, J. (1999) 'Two-dimensional electron gases induced by spontaneous and piezoelectric polarization charges in N- and Ga-face AlGaN/GaN heterostructures', *Journal of Applied Physics*, **85**(6), 3222–3233.

Anderson, T., Wang, H., Kang, B., Ren, F., Pearton, S., Osinsky, A., Dabiran, A. and Chow, P. (2008) 'Effect of bias voltage polarity on hydrogen sensing with AlGaN/GaN Schottky diodes', *Applied Surface Science*, **255**(5), 2524–2526.

Anderson, T., Wang, H. T., Kang, B. S., Li, C., Low, Z. N., Lin, J., Pearton, S. J., Painter, J., Balaban, C., Osinsky, A., Dabiran, A., Chow, P. and Ren, F. (2008) *Advances in Wireless Hydrogen Sensor Networks*, translated by Sacramento, CA.

Anderson, T., Wang, H. T., Kang, B. S., Li, C., Low, Z. N., Lin, J., Pearton, S. J., Ren, F., Dabiran, A., Osinsky, A. and Painter, J. (2007) 'A New Advance in Hydrogen Sensors', [online], available: http://www.hydrogenandfuelcellsafety.info/2007/jul/sensors.asp [accessed

Baranzahi, A., Spetz, A. L. and Lundstrom, I. (1995) 'Reversible hydrogen annealing of metal-oxide-silicon carbide devices at high-temperatures', *Applied Physics Letters*, **67**(21), 3203–3205.

Castaneda, L. (2007) 'Effects of palladium coatings on oxygen sensors of titanium dioxide thin films', *Materials Science and Engineering B-Solid State Materials for Advanced Technology*, **139**(2–3), 149–154.

Chang, C.J., Hung, S.T., Ren, F., Pearton, S.J., Lo, C.F., Chen C.C and Kravchenko, I.I. (2012) 'Oxygen sensing properties of SnO_2-Gated AlGaN/GaN high electron mobility transistors at low temperatures', *Journal of Vacuum Science and Technology B*, **30**(2012), 041214-1-041214-5

Chang, J. F., Kuo, H. H., Leu, I. C. and Hon, M. H. (2002) 'The effects of thickness and operation temperature on ZnO : Al thin film CO gas sensor', *Sensors and Actuators B-Chemical*, **84**(2–3), 258–264.

Chen, K., Wang, H., Kang, B., Chang, C., Wang, Y., Lele, T., Ren, F., Pearton, S., Dabiran, A., Osinsky, A. and Chow, P. (2008) 'Low Hg(II) ion concentration electrical detection with AlGaN/GaN high electron mobility transistors', *Sensors And Actuators B-Chemical*, **134**(2), 386–389.

Chen, L. Y., Hunter, G. W., Neudeck, P. G. and Knight, D. (1998) 'X-ray photoelectron spectroscopy study of the heating effects on Pd/6H-SiC Schottky structure', *Journal of Vacuum Science & Technology a-Vacuum Surfaces and Films*, **16**(5), 2890–2895.

Chu, C. S. and Lo, Y. L. (2008) 'Fiber-optic carbon dioxide sensor based on fluorinated xerogels doped with HPTS', *Sensors and Actuators B-Chemical*, **129**(1), 120–125.

© Woodhead Publishing Limited, 2013

Chu, B.H., Chang, C.Y., Kroll, K., Denslow, N., Wang, Y.L., Pearton, S.J. Lin, J., Dabiran, A.M.,Wowchak, A.M., Cui, B., Chow, P.P., Johnson, J.W., Rajagopal, P., Roberts, J.C., Piner, E.L., Linthicum K.J. and Ren, F. (2011) 'Detection of vitellogenin, an endocrine disruptor biomarker, Using AlGaN/GaN HEMTs', *Physica Status Solidi C*, **7/8**(3), 2486–2489.

CityRating.com (2002) 'Relative Humidity', [online], available: http://www.cityrating.com/relativehumidity.asp [accessed

Connolly, E. J., O'Halloran, G. M., Pham, H. T. M., Sarro, P. M. and French, P. J. (2002) 'Comparison of porous silicon, porous polysilicon and porous silicon carbide as materials for humidity sensing applications', *Sensors and Actuators a-Physical*, **99**(1–2), 25–30.

Conway, B., Barnett, B., Angerstein Kozlowska, H. and Tilak, B. (1990) 'A surface electrochemical basis for the direct logarithmic growth law for initial stages of extension of anodic oxide films formed at noble metals', *The Journal of chemical physics*, **93**, 8361.

Dell'Amico, D. B., Calderazzo, F., Labella, L., Marchetti, F. and Pampaloni, G. (2003) 'Converting carbon dioxide into carbamato derivatives', *Chemical Reviews*, **103**(10), 3857–3897.

Eastman, L. F., Tilak, V., Smart, J., Green, B. M., Chumbes, E. M., Dimitrov, R., Kim, H., Ambacher, O. S., Weimann, N., Prunty, T., Murphy, M., Schaff, W. J. and Shealy, J. R. (2001) 'Undoped AlGaN/GaN HEMTs for microwave power amplification', *IEEE Transactions on Electron Devices*, **48**(3), 479–485.

Eberhardt, W., Greuter, F. and Plummer, E. W. (1981) 'Bonding of H to Ni, Pd, and Pt surfaces', *Physical Review Letters*, **46**(16), 1085–1088.

Eickhoff, M., Neuberger, R., Steinhoff, G., Ambacher, O., Muller, G. and Stutzmann, M. (2001) 'Wetting behaviour of GaN surfaces with Ga- or N-face polarity', *Physica Status Solidi B-Basic Research*, **228**(2), 519–522.

Eickhoff, M., Schalwig, J., Steinhoff, G., Weidemann, O., Görgens, L., Neuberger, R., Hermann, M., Baur, B., Müller, G. and Ambacher, O. (2003) 'Electronics and sensors based on pyroelectric AlGaN/GaN heterostructures–part B: Sensor applications', *physica Status Solidi (c)*, **6**, 1908–1918.

Gangwani, P., Pandey, S., HaIdar, S., Gupta, M. and Gupta, R. S. (2007) 'Polarization dependent analysis of AlGaN/GaN HEMT for high power applications', *Solid-State Electronics*, **51**(1), 130–135.

Gerblinger, J., Lohwasser, W., Lampe, U. and Meixner, H. (1995) 'High-temperature oxygen sensor-based on sputtered cerium oxide', *Sensors and Actuators B-Chemical*, **26**(1–3), 93–96.

Gila, B. P., Johnson, J. W., Mehandru, R., Luo, B., Onstine, A. H., Allums, K. K., Krishnamoorthy, V., Bates, S., Abernathy, C. R., Ren, F. and Pearton, S. J. (2001) 'Gadolinium oxide and scandium oxide: Gate dielectrics for GaN MOSFETs', *Physica Status Solidi a-Applied Research*, **188**(1), 239–242.

Harrington, D. A. (1997) 'Simulation of anodic Pt oxide growth', *Journal of Electroanalytical Chemistry*, **420**(1–2), 101–109.

Hartnagel, H., Dawar, A., Jain, A., Jagadish, C. and Pearton, S. (1995) *Semiconducting transparent thin films*, Institute of Physics Pub.

He, M. Q., Fahmi, M. M. E., Mohammad, S. N., Jacobs, R. N., Salamanca-Riba, L., Felt, F., Jah, M., Sharma, A. and Lakins, D. (2003) 'InAs nanowires and whiskers grown by reaction of indium with GaAs', *Applied Physics Letters*, **82**(21), 3749–3751.

© Woodhead Publishing Limited, 2013

Heo, Y. W., Norton, D. P., Tien, L. C., Kwon, Y., Kang, B. S., Ren, F., Pearton, S. J. and LaRoche, J. R. (2004) 'ZnO nanowire growth and devices', *Materials Science & Engineering R-Reports*, **47**(1–2), 1–47.

Hikita, M., Yanagihara, M., Nakazawa, K., Ueno, H., Hirose, Y., Ueda, T., Uemoto, Y., Tanaka, T., Ueda, D. and Egawa, T. (2005) 'AlGaN/GaN power HFET on silicon substrate with source-via grounding (SVG) structure', *IEEE Transactions on Electron Devices*, **52**(9), 1963–1968.

Hu, Y., Zhou, X., Han, Q., Cao, Q. and Huang, Y. (2003) 'Sensing properties of CuO-ZnO heterojunction gas sensors', *Materials Science and Engineering B*, **99**(1–3), 41–43.

Huang, F. C., Chen, Y. Y. and Wu, T. T. (2009) 'A room temperature surface acoustic wave hydrogen sensor with Pt coated ZnO nanorods', *Nanotechnology*, **20**(6).

Huang, J. R., Hsu, W. C., Chen, Y. J., Wang, T. B., Lin, K. W., Chen, H. I. and Liu, W. C. (2006) 'Comparison of hydrogen sensing characteristics for Pd/GaN and Pd/A1(0.3)Ga(0.7)As Schottky diodes', *Sensors and Actuators B-Chemical*, **117**(1), 151–158.

Huang, M. H., Mao, S., Feick, H., Yan, H. Q., Wu, Y. Y., Kind, H., Weber, E., Russo, R. and Yang, P. D. (2001) 'Room-temperature ultraviolet nanowire nanolasers', *Science*, **292**(5523), 1897–1899.

Hung, S.-T., Chang, C.-J., Hsu, C.-H., Chu, B. H., Lo, C. F., Hsu, C.-C., Pearton, S. J., Holzworth, M. R., Whiting, P. G., Rudawski, N. G., Jones, K. S., Dabiran, A. and Chow, P. (2012) 'SnO_2 functionalized AlGaN/GaN high electron mobility transistor for hydrogen sensing applications, *International Journal of Hydrogen Energy* **37**(11), 13783–13788

Hunter, G., Thomas, V., Neudeck, P., Liu, C., Makel, D., Ward, B., Chen, L., Robert, S. and Field, L. (2002) 'Development of SiC gas sensor systems', *Proceedings Of the Electrochemical Society*, **3**(2002), 93–111.

Iwakami, S., Yanagihara, M., Machida, O., Chino, E., Kaneko, N., Goto, H. and Ohtsuka, K. (2004) 'AlGaN/GaN heterostructure field-effect transistors (HFETs) on Si substrates for large-current operation', *Japanese Journal of Applied Physics Part 2-Letters & Express Letters*, **43**(7A), L831-L833.

Johnson, J., Choi, Y. H., Ural, A., Lim, W., Wright, J. S., Gila, B. P., Ren, F. and Pearton, S. J. (2009) 'Growth and Characterization of GaN Nanowires for Hydrogen Sensors', *Journal of Electronic Materials*, **38**(4), 490–494.

Johnson, J. W., Luo, B., Ren, F., Gila, B. P., Krishnamoorthy, W., Abernathy, C. R., Pearton, S. J., Chyi, J. I., Nee, T. E., Lee, C. M. and Chuo, C. C. (2000) 'Gd_2O_3/GaN metal-oxide-semiconductor field-effect transistor', *Applied Physics Letters*, **77**(20), 3230–3232.

Jun, J., Chou, B., Lin, J., Phipps, A., Shengwen, X., Ngo, K., Johnson, D., Kasyap, A., Nishida, T., Wang, H., Kang, B., Ren, F., Tien, L., Sadik, P., Norton, D., Voss, L. and Pearton, S. (2007) 'A hydrogen leakage detection system using self-powered wireless hydrogen sensor nodes', *Solid-State Electronics*, **51**(7), 1018–1022.

Kang, B., Heo, Y., Tien, L., Norton, D., Ren, F., Gila, B. and Pearton, S. (2005a) 'Hydrogen and ozone gas sensing using multiple ZnO nanorods', *Applied Physics A-Materials Science & Processing*, **80**(5), 1029–1032.

Kang, B., Kim, S., Ren, F., Gila, B., Abernathy, C. and Pearton, S. (2005b) 'Comparison of MOS and Schottky W/Pt-GaN diodes for hydrogen detection', *Sensors And Actuators B-Chemical*, **104**(2), 232–236.

© Woodhead Publishing Limited, 2013

Kang, B., Kim, S., Ren, F., Johnson, J., Therrien, R., Rajagopal, P., Roberts, J., Piner, E., Linthicum, K., Chu, S., Baik, K., Gila, B., Abernathy, C. and Pearton, S. (2004a) 'Pressure-induced changes in the conductivity of AlGaN/GaN high-electron mobility-transistor membranes', *Applied Physics Letters*, **85**(14), 2962–2964.

Kang, B., Louche, G., Duran, R., Gnanou, Y., Pearton, S. and Ren, F. (2004b) 'Gateless AlGaN/GaN HEMT response to block co-polymers', *Solid-State Electronics*, **48**(5), 851–854.

Kang, B., Mehandru, R., Kim, S., Ren, F., Fitch, R., Gillespie, J., Moser, N., Jessen, G., Jenkins, T. and Dettmer, R. (2005c) 'Hydrogen sensors based on Sc_2O_3/AlGaN/GaN high electron mobility transistors', *Physica Status Solidi (c)*, **2**(7), 2672–2675.

Kang, B., Pearton, S., Chen, J., Ren, F., Johnson, J., Therrien, R., Rajagopal, P., Roberts, J., Piner, E. and Linthicum, K. (2006) 'Electrical detection of deoxyribonucleic acid hybridization with AlGaN/GaN high electron mobility transistors', *Applied Physics Letters*, **89**(12).

Kang, B., Ren, F., Heo, Y., Tien, L., Norton, D. and Pearton, S. (2005d) 'pH measurements with single ZnO nanorods integrated with a microchannel', *Applied Physics Letters*, **86**(11).

Kang, B., Ren, F., Wang, L., Lofton, C., Tan, W., Pearton, S., Dabiran, A., Osinsky, A. and Chow, P. (2005e) 'Electrical detection of immobilized proteins with ungated AlGaN/GaN high-electron-mobility transistors', *Applied Physics Letters*, **87**(2).

Kang, B., Wang, H., Lele, T., Tseng, Y., Ren, F., Pearton, S., Johnson, J., Rajagopal, P., Roberts, J., Piner, E. and Linthicum, K. (2007a) 'Prostate specific antigen detection using AlGaN/GaN high electron mobility transistors', *Applied Physics Letters*, **91**(11).

Kang, B., Wang, H., Ren, F., Gila, B., Abernathy, C., Pearton, S., Dennis, D., Johnson, J., Rajagopal, P., Roberts, J., Piner, E. and Linthicum, K. (2008) 'Exhaled-breath detection using AlGaN/GaN high electron mobility transistors integrated with a Peltier element', *Electrochemical And Solid State Letters*, **11**(3), J19-J21.

Kang, B., Wang, H., Ren, F., Gila, B., Abernathy, C., Pearton, S., Johnson, J., Rajagopal, P., Roberts, J., Piner, E. and Linthicum, K. (2007b) 'pH sensor using AlGaN/GaN high electron mobility transistors with Sc_2O_3 in the gate region', *Applied Physics Letters*, **91**(1).

Kang, B., Wang, H., Ren, F., Pearton, S., Morey, T., Dennis, D., Johnson, J., Rajagopal, P., Roberts, J., Piner, E. and Linthicum, K. (2007c) 'Enzymatic glucose detection using ZnO nanorods on the gate region of AlGaN/GaN high electron mobility transistors', *Applied Physics Letters*, **91**(25).

Kang, B. S., Kim, S., Ren, F., Gila, B. P., Abernathy, C. R. and Pearton, S. J. (2005) 'Comparison of MOS and Schottky W/Pt-GaN diodes for hydrogen detection', *Sensors and Actuators B-Chemical*, **104**(2), 232–236.

Kang, B. S., Mehandru, R., Kim, S., Ren, F., Fitch, R. C., Gillespie, J. K., Moser, N., Jessen, G., Jenkins, T., Dettmer, R., Via, D., Crespo, A., Gila, B. P., Abernathy, C. R. and Pearton, S. J. (2004a) 'Hydrogen-induced reversible changes in drain current in Sc_2O_3/AlGaN/GaN high electron mobility transistors', *Applied Physics Letters*, **84**(23), 4635–4637.

Kang, B. S., Ren, F., Gila, B. P., Abernathy, C. R. and Pearton, S. J. (2004b) 'AlGaN/GaN-based metal-oxide-semiconductor diode-based hydrogen gas sensor', *Applied Physics Letters*, **84**(7), 1123–1125.

© Woodhead Publishing Limited, 2013

Kang, B. S., Wang, H. T., Lele, T. P., Tseng, Y., Ren, F., Pearton, S. J., Johnson, J. W., Rajagopal, P., Roberts, J. C., Piner, E. L. and Linthicum, K. J. (2007a) 'Prostate specific antigen detection using AlGaN/GaN high electron mobility transistors', *Applied Physics Letters*, **91**.

Kang, B. S., Wang, H. T., Ren, F., Gila, B. P., Abernathy, C. R., Pearton, S. J., Johnson, J. W., Rajagopal, P., Roberts, J. C., Piner, E. L. and Linthicum, K. J. (2007b) 'pH sensor using AlGaN/GaN high electron mobility transistors with Sc_2O_3 in the gate region', *Applied Physics Letters*, **91**(1).

Kang, B. S., Wang, H. T., Ren, F., Pearton, S. J., Morey, T. E., Dennis, D. M., Johnson, J. W., Rajagopal, P., Roberts, J. C., Piner, E. L. and Linthicum, K. J. (2007c) 'Enzymatic glucose detection using ZnO nanorods on the gate region of AlGaN/GaN high electron mobility transistors', *Applied Physics Letters*, **91**(25).

Keem, K., Kim, H., Kim, G. T., Lee, J. S., Min, B., Cho, K., Sung, M. Y. and Kim, S. (2004) 'Photocurrent in ZnO nanowires grown from Au electrodes', *Applied Physics Letters*, **84**(22), 4376–4378.

Keller, S., Wu, Y. F., Parish, G., Ziang, N. Q., Xu, J. J., Keller, B. P., DenBaars, S. P. and Mishra, U. K. (2001) 'Gallium nitride based high power heterojunction field effect transistors: Process development and present status at UCSB', *IEEE Transactions on Electron Devices*, **48**(3), 552–559.

Khanna, R., Pearton, S. J., Ren, F. and Kravchenko, II (2006) 'Comparison of electrical and reliability performances of TiB_2-, CrB_2-, and W_2B_5-based Ohmic contacts on n-GaN', *Journal of Vacuum Science & Technology B*, **24**(2), 744–749.

Kim, H., Lim, W., Lee, J.H., Pearton, S.J., Ren F . and Jang, S. (2012) 'Highly sensitive AlGaN/GaN diode-based hydrogen sensors using platinum nanonetworks', *Sensors and Actuators B*, **164**(10) 64–69.

Kim, J., Gila, B., Chung, G., Abernathy, C., Pearton, S. and Ren, F. (2003) 'Hydrogen-sensitive GaN schottky diodes', *Solid-State Electronics*, **47**(6), 1069–1073.

Kim, J., Gila, B. P., Abernathy, C. R., Chung, G. Y., Ren, F. and Pearton, S. J. (2003a) 'Comparison of Pt/GaN and Pt/4H-SiC gas sensors', *Solid-State Electronics*, **47**(9), 1487–1490.

Kim, J., Mehandru, R., Luo, B., Ren, F., Gila, B. P., Onstine, A. H., Abernathy, C. R., Pearton, S. J. and Irokawa, Y. (2002) 'Characteristics of MgO/GaN gate-controlled metal – oxide – semiconductor diodes', *Applied Physics Letters*, **80**(24), 4555–4557.

Kim, J., Ren, F., Gila, B. P., Abernathy, C. R. and Pearton, S. J. (2003b) 'Reversible barrier height changes in hydrogen-sensitive Pd/GaN and Pt/GaN diodes', *Applied Physics Letters*, **82**(5), 739–741.

Kim, S., Kang, B. S., Ren, F., Ip, K., Heo, Y. W., Norton, D. P. and Pearton, S. J. (2004) 'Sensitivity of Pt/ZnO Schottky diode characteristics to hydrogen', *Applied Physics Letters*, **84**, 1698–1700.

Kimmig, L., Krause, P., Ludwig, M. and Schmidt, K. (2000) 'Non-dispersive infrared gas analyzer', US Patent, US 6166383A.

Kong, J. and Dai, H. J. (2001) 'Full and modulated chemical gating of individual carbon nanotubes by organic amine compounds', *Journal of Physical Chemistry B*, **105**(15), 2890–2893.

Kouche, A. E. L., Lin, J., Law, M. E., Kim, S., Kim, B. S., Ren, F. and Pearton, S. T. (2005) 'Remote sensing system for hydrogen using GaN Schottky diodes', *Sensors and Actuators B-Chemical*, **105**(2), 329–333.

© Woodhead Publishing Limited, 2013

Kryliouk, O., Park, H., Wang, H., Kang, B., Anderson, T., Ren, F. and Pearton, S. (2005) 'Pt-coated InN nanorods for selective detection of hydrogen at room temperature', *Journal Of Vacuum Science & Technology B*, **23**(5), 1891–1894.

Kuzmych, O., Allen, B. L. and Star, A. (2007) 'Carbon nanotube sensors for exhaled breath components', *Nanotechnology*, **18**.

Lao, J. Y., Huang, J. Y., Wang, D. Z. and Ren, Z. F. (2003) 'ZnO nanobridges and nanonails', *Nano Letters*, **3**(2), 235–238.

Lim, W., Wang, Y. L., Ren, F., Norton, D. P., Kravchenko, II, Zavada, J. M. and Pearton, S. J. (2007) 'Room-temperature-deposited indium-zinc oxide thin films with controlled conductivity', *Electrochemical and Solid State Letters*, **10**(9), H267-H269.

Lim, W., Wright, J. S., Gila, B. P., Johnson, J. L., Ural, A., Anderson, T., Ren, F. and Pearton, S. J. (2008) 'Room temperature hydrogen detection using Pd-coated GaN nanowires', *Applied Physics Letters*, **93**(7).

Lim, W. T., Wright, J. S., Gila, B. P., Pearton, S. J., Ren, F., Lai, W. T., Chen, L. C., Hu, M. S. and Chen, K. H. (2008) 'Selective-hydrogen sensing at room temperature with Pt-coated InN nanobelts', *Applied Physics Letters*, **93**(20).

Ling, Z., Leach, C. and Freer, R. (2001) 'Heterojunction gas sensors for environmental NO_2 and CO_2 monitoring', *Journal of the European Ceramic Society*, **21**(10–11), 1977–1980.

Liu, C. H., Yiu, W. C., Au, F. C. K., Ding, J. X., Lee, C. S. and Lee, S. T. (2003) 'Electrical properties of zinc oxide nanowires and intramolecular p-n junctions', *Applied Physics Letters*, **83**(15), 3168–3170.

Lo, C.F., Chu, B.H., Pearton, S.J., Dabiran, A.M., Chow, P.P., Dore, S., Hung, S.C.,Chen, C.W. and Ren F . (2011), 'Effect of Temperature on CO Detection Sensitivity of ZnO nanorod-gated AlGaN/GaN HEMTs', *Applied Physics Letters* **99**(15), 142107-1-142107-3.

Lo, C.F., Liu, L., Chu, B.H., Ren, F., Pearton, S.J., Doré, S., Hsu, C.-H., Kim, J., Dabiran, A.M. and Chow, P.P. (2012), 'Carbon monoxide detection sensitivity of ZnO nanorod-gated AlGaN/GaN high electron mobility transistors in different temperature environments', *Journal of Vacuum Science and Technology B* **30** (6), 010606-1-010606-6.

Logothetis, E. (1991) 'Automotive oxygen sensors', *Chemical Sensor Technology*, **3**, 89–104.

Lothian, J. R., Kuo, J. M., Ren, F. and Pearton, S. J. (1992) 'Plasma and wet chemical etching of IN0.5GA0.5P', *Journal of Electronic Materials*, **21**(4), 441–445.

Lu, W., Kumar, V., Piner, E. L. and Adesida, I. (2003) 'DC, RF, and, microwave noise performance of AlGaN-GaN field effect transistors dependence of aluminum concentration', *IEEE Transactions on Electron Devices*, **50**(4), 1069–1074.

Lu, Y. J., Li, J., Han, J., Ng, H. T., Binder, C., Partridge, C. and Meyyappan, M. (2004) 'Room temperature methane detection using palladium loaded single-walled carbon nanotube sensors', *Chemical Physics Letters*, **391**(4–6), 344–348.

Luther, B. P., Wolter, S. D. and Mohney, S. E. (1999) 'High temperature Pt Schottky diode gas sensors on n-type GaN', *Sensors and Actuators B-Chemical*, **56**(1–2), 164–168.

Machado, R. F., Laskowski, D., Deffenderfer, O., Burch, T., Zheng, S., Mazzone, P. J., Mekhail, T., Jennings, C., Stoller, J. K., Pyle, J., Duncan, J., Dweik, R. A. and Erzurum, S. C. (2005) 'Detection of lung cancer by sensor array analyses of

© Woodhead Publishing Limited, 2013

exhaled breath', *American Journal of Respiratory and Critical Care Medicine*, **171**(11), 1286–1291.

Makimoto, T., Yamauchi, Y. and Kumakura, K. (2004) 'High-power characteristics of GaN/InGaN double heterojunction bipolar transistors', *Applied Physics Letters*, **84**(11), 1964–1966.

Manuccia, T. and Eden, J. (1985) 'Infrared optical measurement of blood gas concentrations and fiber optic catheter',

Markovic, N. M. and Ross, P. N. (2002) 'Surface science studies of model fuel cell electrocatalysts', *Surface Science Reports*, **45**(4–6), 121–229.

Matsuo, K., Negoro, N., Kotani, J., Hashizume, T. and Hasegawa, H. (2005) 'Pt Schottky diode gas sensors formed on GaN and AlGaN/GaN heterostructure', *Applied Surface Science*, **244**(1–4), 273–276.

Mayumi, M., Satoh, F., Kumagai, Y., Takemoto, K. and Koukitu, A. (2001) 'Influence of polarity on surface reaction between GaN{0001} and hydrogen', *Physica Status Solidi B-Basic Research*, **228**(2), 537–541.

Mehandru, R., Kim, S., Kim, J., Ren, F., Lothian, J. R., Pearton, S. J., Park, S. S. and Park, Y. J. (2003) 'Thermal simulations of high power, bulk GaN rectifiers', *Solid-State Electronics*, **47**(6), 1037–1043.

Mehandru, R., Luo, B., Kang, B., Kim, J., Ren, F., Pearton, S., Pan, C., Chen, G. and Chyi, J. (2004) 'AlGaN/GaN HEMT based liquid sensors', *Solid-State Electronics*, **48**(2), 351–353.

Mishra, U. K., Parikh, P. and Wu, Y. F. (2002) 'AlGaN/GaN HEMTs – An overview of device operation and applications', *Proceedings of the IEEE*, **90**(6), 1022–1031.

Mitra, P., Chatterjee, A. P. and Maiti, H. S. (1998) 'ZnO thin film sensor', *Materials Letters*, **35**(1–2), 33–38.

Mitzner, K. D., Sternhagen, J. and Galipeau, D. W. (2003) 'Development of a micromachined hazardous gas sensor array', *Sensors and Actuators B-Chemical*, **93**(1–3), 92–99.

Mohammadi, M. R. and Fray, D. J. (2007) 'Semiconductor TiO_2-Ga_2O_3 thin film gas sensors derived from particulate sol-gel route', *Acta Materialia*, **55**(13), 4455–4466.

Nakazawa, S., Ueda, T., Inoue, K., Tanaka, T., Ishikawa, H. and Egawa, T. (2005) 'Reclessed-gate AlGaN/GaN HFETs with lattice-matched InAlGaN quaternary alloy capping layers', *IEEE Transactions on Electron Devices*, **52**(10), 2124–2128.

Namjou, K., Roller, C. B. and McCann, P. J. (2006) 'The breathmeter – A new laser device to analyze your health', *IEEE Circuits & Devices*, **22**(5), 22–28.

Neuberger, R., Muller, G., Ambacher, O. and Stutzmann, M. (2001) 'High-electron-mobility AlGaN/GaN transistors (HEMTs) for fluid monitoring applications', *Physica Status Solidi a-Applied Research*, **185**(1), 85–89.

Neuberger, R., Müller, G., Ambacher, O. and Stutzmann, M. (2001) 'Ion-induced modulation of channel currents in AlGaN/GaN high-electron-mobility transistors', *Physica Status Solidi (a)*, **183**(2), R10-R12.

Ng, H. T., Li, J., Smith, M. K., Nguyen, P., Cassell, A., Han, J. and Meyyappan, M. (2003) 'Growth of epitaxial nanowires at the junctions of nanowalls', *Science*, **300**(5623), 1249–1249.

Nickel, N. H. and Fleischer, K. (2003) 'Hydrogen local vibrational modes in zinc oxide', *Physical Review Letters*, **90**(19).

© Woodhead Publishing Limited, 2013

Northrup, J. E. and Neugebauer, J. (2004) 'Strong affinity of hydrogen for the GaN(000–1) surface: Implications for molecular beam epitaxy and metalorganic chemical vapor deposition', *Applied Physics Letters*, **85**(16), 3429–3431.

Ong, K. and Grimes, C. (2001) 'A carbon Nanotube-based Sensor for CO_2 Monitoring', *Sensors*, **1**(6), 193–205.

Paik, C. H., Jarvi, T. D. and O'Grady, W. E. (2004) 'Extent of PEMFC cathode surface oxidation by oxygen and water measured by CV', *Electrochemical and Solid State Letters*, **7**(4), A82-A84.

Palacios, T., Rajan, S., Chakraborty, A., Heikman, S., Keller, S., DenBaars, S. P. and Mishra, U. K. (2005) 'Influence of the dynamic access resistance in the g(m) and f(T) linearity of AlGaN/GaN HEMTs', *IEEE Transactions on Electron Devices*, **52**(10), 2117–2123.

Pan, Z. W., Dai, Z. R. and Wang, Z. L. (2001) 'Nanobelts of semiconducting oxides', *Science*, **291**(5510), 1947–1949.

Park, W. I., Jun, Y. H., Jung, S. W. and Yi, G. C. (2003a) 'Excitonic emissions observed in ZnO single crystal nanorods', *Applied Physics Letters*, **82**(6), 964–966.

Park, W. I., Yi, G. C., Kim, J. W. and Park, S. M. (2003b) 'Schottky nanocontacts on ZnO nanorod arrays', *Applied Physics Letters*, **82**(24), 4358–4360.

Park, W. I., Yi, G. C., Kim, M. and Pennycook, S. J. (2003c) 'Quantum confinement observed in ZnO/ZnMgO nanorod heterostructures', *Advanced Materials*, **15**(6), 526–529.

Pearton, S. J., Kang, B. S., Kim, S. K., Ren, F., Gila, B. P., Abernathy, C. R., Lin, J. S. and Chu, S. N. G. (2004) 'GaN-based diodes and transistors for chemical, gas, biological and pressure sensing', *Journal of Physics-Condensed Matter*, **16**(29), R961-R994.

Pearton, S. J., Lele, T., Tseng, Y. and Ren, F. (2007) 'Penetrating living cells using semiconductor nanowires', *Trends in Biotechnology*, **25**(11), 481–482.

Pearton, S. J., Zolper, J. C., Shul, R. J. and Ren, F. (1999) 'GaN: Processing, defects, and devices', *Journal of Applied Physics*, **86**(1), 1–78.

Pearton, S.J., Ren, F., Wang, Yu-Lin., Chu, B.H., Chen, K.H., Chang, C.Y., Lim, Wantae., Lin, Jenshan. and Norton, D.P. (2010), 'Recent advances in wide bandgap semiconductor biological and gas sensors', *Progress in Materials Science*, **55**(1), 1–60.

Poole, P. J., Lefebvre, J. and Fraser, J. (2003) 'Spatially controlled, nanoparticle-free growth of InP nanowires', *Applied Physics Letters*, **83**(10), 2055–2057.

Rao, B. B. (2000) 'Zinc oxide ceramic semi-conductor gas sensor for ethanol vapour', *Materials Chemistry and Physics*, **64**(1), 62–65.

Ren, F.,Chu, B.H., Chen, K.H., Chang, C.Y., Chen V. and Pearton, S.J. (2012) 'GaN based sensors', in *GaN and ZnO-Based Materials and Devices*, ed. S.J. Pearton (Springer, NY 2012).

Ren, F. and Pearton, S.J. (2011) *Semiconductor Devices-Based Sensors for Gas, Chemical and Biomedical Applications* (CRC Press, Boca Raton, 2011).

REB (2010) 'Hydrogen separation and membrane reactors', [online], available: http://www.rebresearch.com/H2perm2.htm, http://www.rebresearch.com/H2sol2.htm.

Saito, W., Domon., T., Omura, I., Kuraguchi, M., Takada, Y., Tsuda, K. and Yamaguchi, M. (2006) 'Demonstration of 13.56-MHz class-E amplifier using a high-voltage GaN power-HEMT', *IEEE Electron Device Letters*, **27**(5), 326–328.

© Woodhead Publishing Limited, 2013

Saito, W., Takada, Y., Kuraguchi, M., Tsuda, K., Omura, I., Ogura, T. and Ohashi, H. (2003) 'High breakdown voltage AlGaN-GaN Power-HEMT design and high current density switching behavior', *IEEE Transactions on Electron Devices*, **50**(12), 2528–2531.

Satyapal, S., Filburn, T., Trela, J. and Strange, J. (2001) 'Performance and properties of a solid amine sorbent for carbon dioxide removal in space life support applications', *Energy & Fuels*, **15**(2), 250–255.

Savage, S., Konstantinov, A., Saroukhan, A. and Harris, C. (2000) *High Temperature 4H-SiC FET for Gas Sensing Applications*, translated by Research Triangle Park, NC (USA): Transtec Publications; 1999, 1431–1434.

Sayago, I., Terrado, E., Lafuente, E., Horrillo, M. C., Maser, W. K., Benito, A. M., Navarro, R., Urriolabeitia, E. P., Martinez, M. T. and Gutierrez, J. (2005) 'Hydrogen sensors based on carbon nanotubes thin films', *Synthetic Metals*, **148**(1), 15–19.

Schalwig, J., Muller, G., Ambacher, O. and Stutzmann, M. (2001) 'Group-III-nitride based gas sensing devices', *Physica Status Solidi a-Applied Research*, **185**(1), 39–45.

Schalwig, J., Muller, G., Eickhoff, M., Ambacher, O. and Stutzmann, M. (2002a) 'Gas sensitive GaN/AlGaN-heterostructures', *Sensors and Actuators B-Chemical*, **87**(3), 425–430.

Schalwig, J., Muller, G., Karrer, U., Eickhoff, M., Ambacher, O., Stutzmann, M., Gorgens, L. and Dollinger, G. (2002b) 'Hydrogen response mechanism of Pt-GaN Schottky diodes', *Applied Physics Letters*, **80**(7), 1222–1224.

Shen, L., Coffie, R., Buttari, D., Heikman, S., Chakraborty, A., Chini, A., Keller, S., DenBaars, S. P. and Mishra, U. K. (2004) 'High-power polarization-engineered GaN/AlGaN/GaN HEMTs without surface passivation', *IEEE Electron Device Letters*, **25**(1), 7–9.

Shim, M., Javey, A., Kam, N. W. S. and Dai, H. J. (2001) 'Polymer functionalization for air-stable n-type carbon nanotube field-effect transistors', *Journal of the American Chemical Society*, **123**(46), 11512–11513.

Song, J. H., Lu, W., Flynn, J. S. and Brandes, G. R. (2005a) 'AlGaN/GaN Schottky diode hydrogen sensor performance at high temperatures with different catalytic metals', *Solid-State Electronics*, **49**(8), 1330–1334.

Song, J. H., Lu, W., Flynn, J. S. and Brandes, G. R. (2005b) 'Pt-AlGaN/GaN Schottky diodes operated at 800 degrees C for hydrogen sensing', *Applied Physics Letters*, **87**(13).

Sotter, E., Vilanova, X., Llobet, E., Vasiliev, A. and Correig, X. (2007) 'Thick film titania sensors for detecting traces of oxygen', *Sensors and Actuators B-Chemical*, **127**, 567–579.

Spetz, A. L., Tobias, P., Uneus, L., Svenningstorp, H., Ekedahl, L. G. and Lundstrom, L. (2000) 'High temperature catalytic metal field effect transistors for industrial applications', *Sensors and Actuators B-Chemical*, **70**(1–3), 67–76.

Star, A., Han, T. R., Joshi, V., Gabriel, J. C. P . and Gruner, G. (2004) 'Nanoelectronic carbon dioxide sensors', *Advanced Materials*, **16**(22), 2049-+.

Starke, U., Sloboshanin, S., Tautz, F. S., Seubert, A. and Schaefer, J. A. (2000) 'Polarity, morphology and reactivity of epitaxial GaN films on Al_2O_3(0001)', *Physica Status Solidi a-Applied Research*, **177**(1), 5–14.

© Woodhead Publishing Limited, 2013

Steinhoff, G., Hermann, M., Schaff, W. J., Eastman, L. F., Stutzmann, M. and Eickhoff, M. (2003) 'pH response of GaN surfaces and its application for pH-sensitive field-effect transistors', *Applied Physics Letters*, **83**(1), 177–179.

Sun, Q., Cho, Y. S., Kong, B. H., Cho, H. K., Ko, T. S., Yerino, C. D., Lee, I. H. and Han, J. (2009) 'N-face GaN growth on c-plane sapphire by metalorganic chemical vapor deposition', *Journal of Crystal Growth*, **311**(10), 2948–2952.

Sun, Q., Cho, Y. S., Lee, I. H., Han, J., Kong, B. H. and Cho, H. K. (2008) 'Nitrogen-polar GaN growth evolution on c-plane sapphire', *Applied Physics Letters*, **93**(13).

Svenningstorp, H., Tobias, P., Lundstrom, I., Salomonsson, P., Martensson, P., Ekedahl, L. G. and Spetz, A. L. (1999) 'Influence of catalytic reactivity on the response of metal-oxide-silicon carbide sensor to exhaust gases', *Sensors and Actuators B-Chemical*, **57**(1–3), 159–165.

Tarakji, A., Fatima, H., Hu, X., Zhang, J. P., Simin, G., Khan, M. A., Shur, M. S. and Gaska, R. (2003) 'Large-signal linearity in III-N MOSDHFETs', *IEEE Electron Device Letters*, **24**(6), 369–371.

Thorpe, M. J., Balslev-Clausen, D., Kirchner, M. S. and Ye, J. (2008) 'Cavity-enhanced optical frequency comb spectroscopy: application to human breath analysis', *Optics Express*, **16**(4), 2387–2397.

Thorpe, M. J., Moll, K. D., Jones, R. J., Safdi, B. and Ye, J. (2006) 'Broadband cavity ringdown spectroscopy for sensitive and rapid molecular detection', *Science*, **311**(5767), 1595–1599.

Tien, L., Sadik, P., Norton, D., Voss, L., Pearton, S., Wang, H., Kang, B., Ren, F., Jun, J. and Lin, J. (2005a) 'Hydrogen sensing at room temperature with Pt-coated ZnO thin films and nanorods', *Applied Physics Letters*, **87**(22).

Tien, L., Wang, H., Kang, B., Ren, F., Sadik, P., Norton, D., Pearton, S. and Lin, J. (2005b) 'Room-temperature hydrogen-selective sensing using single Pt-coated ZnO nanowires at microwatt power levels', *Electrochemical And Solid State Letters*, **8**(9), G230-G232.

Trinchi, A., Li, Y. X., Wlodarski, W., Kaciulis, S., Pandolfi, L., Russo, S. P., Duplessis, J. and Viticoli, S. (2003) 'Investigation of sol-gel prepared Ga-Zn oxide thin films for oxygen gas sensing', *Sensors and Actuators A-Physical*, **108**(1–3), 263–270.

Valizadeh, P. and Pavlidis, D. (2005) 'Investigation of the impact of Al mole-fraction on the consequences of RF stress on AlxGa1-xN/GaN MODFETs', *IEEE Transactions on Electron Devices*, **52**(9), 1933–1939.

Varghese, O., Kichambre, P., Gong, D., Ong, K., Dickey, E. and Grimes, C. (2001) 'Gas sensing characteristics of multi-wall carbon nanotubes', *Sensors and Actuators B: Chemical*, **81**(1), 32–41.

Vasiliev, A., Moritz, W., Fillipov, V., Bartholomaus, L., Terentjev, A. and Gabusjan, T. (1998) 'High temperature semiconductor sensor for the detection of fluorine', *Sensors and Actuators B-Chemical*, **49**(1–2), 133–138.

Voss, L., Gila, B. P., Pearton, S. J., Wang, H. T. and Ren, F. (2005) 'Characterization of bulk GaN rectifiers for hydrogen gas sensing', *Journal of Vacuum Science & Technology B*, **23**(6), 2373–2377.

Wan, Q., Li, Q. H., Chen, Y. J., Wang, T. H., He, X. L., Gao, X. G. and Li, J. P. (2004a) 'Positive temperature coefficient resistance and humidity sensing properties of Cd-doped ZnO nanowires', *Applied Physics Letters*, **84**(16), 3085–3087.

© Woodhead Publishing Limited, 2013

Wan, Q., Li, Q. H., Chen, Y. J., Wang, T. H., He, X. L., Li, J. P. and Lin, C. L. (2004b) 'Fabrication and ethanol sensing characteristics of ZnO nanowire gas sensors', *Applied Physics Letters*, **84**(18), 3654–3656.

Wang, H., Anderson, T., Kang, B., Ren, F., Li, C., Low, Z., Lin, J., Gila, B., Pearton, S., Osinsky, A. and Dabiran, A. (2007a) 'Stable hydrogen sensors from AlGaN/GaN heterostructure diodes with TiB_2-based Ohmic contacts', *Applied Physics Letters*, **90**(25), 252109.

Wang, H., Anderson, T., Ren, F., Li, C., Low, Z., Lin, J., Gila, B., Pearton, S., Osinsky, A. and Dabiran, A. (2006) 'Robust detection of hydrogen using differential AlGaN/GaN high electron mobility transistor sensing diodes', *Applied Physics Letters*, **89**(24).

Wang, H., Kang, B., Chancellor, T., Lele, T., Tseng, Y., Ren, F., Pearton, S., Dabiran, A., Osinsky, A. and Chow, P. (2007b) 'Selective detection of Hg (II) ions from Cu(II) and Pb(II) using AlGaN/GaN high electron mobility transistors', *Electrochemical And Solid State Letters*, **10**(11), J150-J153.

Wang, H., Kang, B., Ren, F., Fitch, R., Gillespie, J., Moser, N., Jessen, G., Jenkins, T., Dettmer, R., Via, D., Crespo, A., Gila, B., Abernathy, C. and Pearton, S. (2005a) 'Comparison of gate and drain current detection of hydrogen at room temperature with AlGaN/GaN high electron mobility transistors', *Applied Physics Letters*, **87**(17), 172105.

Wang, H., Kang, B., Ren, F., Tien, L., Sadik, P., Norton, D., Pearton, S. and Lin, J. (2005b) 'Detection of hydrogen at room temperature with catalyst-coated multiple ZnO nanorods', *Applied Physics A-Materials Science & Processing*, **81**(6), 1117–1119.

Wang, H., Kang, B., Ren, F., Tien, L., Sadik, P., Norton, D., Pearton, S. and Lin, J. (2005c) 'Hydrogen-selective sensing at room temperature with ZnO nanorods', *Applied Physics Letters*, **86**(24), 243503.

Wang, H. T., Anderson, T. J., Kang, B. S., Ren, F., Li, C. Z., Low, Z. N., Lin, J. S., Gila, B. P., Pearton, S. J., Osinsky, A. and Dabiran, A. (2007a) 'Stable hydrogen sensors from AlGaN/GaN heterostructure diodes with TiB2-based Ohmic contacts', *Applied Physics Letters*, **90**(25).

Wang, H. T., Kang, B. S., Chancellor, T. F., Lele, T. P., Tseng, Y., Ren, F., Pearton, S. J., Johnson, W. J., Rajagopal, P., Roberts, J. C., Piner, E. L. and Linthicum, K. J. (2007b) 'Fast electrical detection of Hg(II) ions with AlGaN/GaN high electron mobility transistors', *Applied Physics Letters*, **91**(4).

Wang, H. T., Kang, B. S., Ren, F., Fitch, R. C., Gillespie, J. K., Moser, N., Jessen, G., Jenkins, T., Dettmer, R., Via, D., Crespo, A., Gila, B. P., Abernathy, C. R. and Pearton, S. J. (2005) 'Comparison of gate and drain current detection of hydrogen at room temperature with AlGaN/GaN high electron mobility transistors', *Applied Physics Letters*, **87**(17).

Wang, H. T., Kang, B. S., Ren, F., Pearton, S. J., Johnson, J. W., Rajagopal, P., Roberts, J. C., Piner, E. L. and Linthicum, K. J. (2007c) 'Electrical detection of kidney injury molecule-1 with AlGaN/GaN high electron mobility transistors', *Applied Physics Letters*, **91**(22).

Wang, Y. L., Chu, B. H., Chang, C. Y., Chen, K. H., Zhang, Y., Sun, Q., Han, J., Pearton, S. J. and Ren, F. (2009a) 'Hydrogen sensing of N-polar and Ga-polar GaN Schottky diodes', *Sensors and Actuators B-Chemical*, **142**(1), 175–178.

© Woodhead Publishing Limited, 2013

Wang, Y. L., Covert, L. N., Anderson, T. J., Lim, W. T., Lin, J., Pearton, S. J., Norton, D. P., Zavada, J. M. and Ren, F. (2008) 'RF characteristics of room-temperature-deposited, small gate dimension indium zinc oxide TFTs', *Electrochemical and Solid State Letters*, **11**(3), H60-H62.

Wang, Y. L., Ren, F., Lim, W., Norton, D. P., Pearton, S. J., Kravchenko, II and Zavada, J. M. (2007) 'Room temperature deposited indium zinc oxide thin film transistors', *Applied Physics Letters*, **90**(23).

Wang, Y. L., Ren, F., Zhang, U., Sun, Q., Yerino, C. D., Ko, T. S., Cho, Y. S., Lee, I. H., Han, J. and Pearton, S. J. (2009b) 'Improved hydrogen detection sensitivity in N-polar GaN Schottky diodes', *Applied Physics Letters*, **94**(21).

Wang, Z. (2004) 'Nanostructures of zinc oxide', *Materials Today*, **7**(6), 26–33.

Weidemann, O., Hermann, M., Steinhoff, G., Wingbrant, H., Spetz, A. L., Stutzmann, M. and Eickhoff, M. (2003) 'Influence of surface oxides on hydrogen-sensitive Pd : GaN Schottky diodes', *Applied Physics Letters*, **83**(4), 773–775.

Wollenstein, J., Plaza, J. A., Cane, C., Min, Y., Bottner, H. and Tuller, H. L. (2003) 'A novel single chip thin film metal oxide array', *Sensors and Actuators B-Chemical*, **93**(1–3), 350–355.

Wormhoudt, J. (1985) *Infrared methods for gaseous measurements: theory and practice*, CRC.

Wright, J. S., Lim, W., Gila, B. P., Pearton, S. J., Ren, F., Lai, W. T., Chen, L. C., Hu, M. S. and Chen, K. H. (2009) 'Pd-catalyzed hydrogen sensing with InN nanobelts', *Journal of Vacuum Science & Technology B*, **27**(3), L8-L10.

Wu, X. C., Song, W. H., Huang, W. D., Pu, M. H., Zhao, B., Sun, Y. P. and Du, J. J. (2000) 'Crystalline gallium oxide nanowires: intensive blue light emitters', *Chemical Physics Letters*, **328**(1–2), 5–9.

Xu, H., Kunz, R. and Fenton, J. M. (2007) 'Investigation of platinum oxidation in PEM fuel cells at various relative humidities', *Electrochemical and Solid State Letters*, **10**(1), B1-B5.

Xu, Y. L., Zhou, X. H. and Sorensen, O. T. (2000) 'Oxygen sensors based on semiconducting metal oxides: an overview', *Sensors and Actuators B-Chemical*, **65**(1–3), 2–4.

Yakimova, R., Steinhoff, G., Petoral, R. M., Vahlberg, C., Khranovskyy, V., Yazdi, G. R., Uvdal, K. and Spetz, A. L. (2007) 'Novel material concepts of transducers for chemical and biosensors', *Biosensors & Bioelectronics*, **22**(12), 2780–2785.

Yu, X., Li, C., Low, Z. N., Lin, J., Anderson, T. J., Wang, H. T., Ren, F., Wang, Y. L., Chang, C. Y., Pearton, S. J., Hsu, C. H., Osinsky, A., Dabiran, A., Chow, P., Balaban, C. and Painter, J. (2008) 'Wireless hydrogen sensor network using AlGaN/GaN high electron mobility transistor differential diode sensors', *Sensors and Actuators B-Chemical*, **135**(1), 188–194.

Yun, F., Chevtchenko, S., Moon, Y. T., Morkoc, H., Fawcett, T. J. and Wolan, J. T. (2005) 'GaN resistive hydrogen gas sensors', *Applied Physics Letters*, **87**(7).

Zhang, A. P., Rowland, L. B., Kaminsky, E. B., Kretchmer, J. W., Beaupre, R. A., Garrett, J. L., Tucker, J. B., Edward, B. J., Foppes, J. and Allen, A. F. (2003a) 'Microwave power SiC MESFETs and GaNHEMTs', *Solid-State Electronics*, **47**(5), 821–826.

Zhang, A. P., Rowland, L. B., Kaminsky, E. B., Tilak, V., Grande, J. C., Teetsov, J., Vertiatchikh, A. and Eastman, L. F. (2003b) 'Correlation of device performance and defects in AlGaN/GaN high-electron mobility transistors', *Journal of Electronic Materials*, **32**(5), 388–394.

© Woodhead Publishing Limited, 2013

Zhang, A. P., Rowland, L. B., Kaminsky, E. B., Tucker, J. B., Kretchmer, J. W., Allen, A. F. and Cook, J. (2003c) '9.2W/mm (13.8W) AlGaN/GaN HEMTs at 10 GHz and 55 V drain bias', *Electronics Letters*, **39**(2), 245–247.

Zhang, B. P., Binh, N. T., Segawa, Y., Wakatsuki, K. and Usami, N. (2003) 'Optical properties of ZnO rods formed by metalorganic chemical vapor deposition', *Applied Physics Letters*, **83**(8), 1635–1637.

Zhao, Z. Y., Knight, M., Kumar, S., Eisenbraun, E. I. and Camenter, M. A. (2008) 'Humidity effects on Pd/Au-based all-optical hydrogen sensors', *Sensors and Actuators B-Chemical*, **129**(2), 726–733.

Zheng, M. J., Zhang, L. D., Li, G. H., Zhang, X. Y. and Wang, X. F. (2001) 'Ordered indium-oxide nanowire arrays and their photoluminescence properties', *Applied Physics Letters*, **79**(6), 839–841.

© Woodhead Publishing Limited, 2013

6

Micromachined semiconductor gas sensors

D. BRIAND, Ecole Polytechnique Fédérale de Lausanne, Switzerland and J. COURBAT, Innovative Sensor Technology IST AG, Switzerland

DOI: 10.1533/9780857098665.2.220

Abstract: This chapter reviews micromachined semiconductor gas sensors. First, the chapter briefly discusses the history of this technology. It then addresses the micro-hotplates concept that has led to the development of different types of micromachined gas sensor devices. The different realizations of micromachined semiconductor gas sensors are presented: thin- and thick-film metal-oxide, field effect, and those using complementary metal-oxide semiconductors (CMOSs) and silicon-on-insulator (SOI) technologies. Finally, recent developments based on gas sensitive nanostructures, polymers, printing and foil-based technologies are highlighted.

Key words: silicon micromachining, micro-hotplates, semiconductor, metal-oxide, field-effect, gas sensors, CMOS and SOI, nanowires, printing, polymeric, plastic.

6.1 Introduction

Metal-oxide gas sensors based on screen-printing thick layers on alumina substrates to form a platinum heater and electrodes, and to pattern the thick metal-oxide gas sensitive film, have been commercialized for a few decades. At the beginning of the 1980s, micromachining of silicon took considerable strides and led to the emergence of new micro-electro-mechanical systems (MEMS) devices. The use of microfabrication techniques to realize microsensors and MEMS devices has brought different advantages than miniaturization, such as batch processing, formation of arrays, reduced power consumption and new modes of operation. Some work has been undertaken by micromachining anodic alumina (Mardilovich *et al.*, 2000; Vasiliev *et al.*, 2008) but the extensive developments were carried out based on silicon micromachining (Simon *et al.*, 2001).

This chapter therefore focuses on silicon micromachined semiconductor gas sensors. After a brief history of silicon hotplates and metal-oxide

© Woodhead Publishing Limited, 2013

gas sensors, more information will be provided on the micro-hotplate concept, realizations and reliability. The core of the chapter comprises a section on micromachined thin- and thick-film metal-oxide gas sensors addressing temperature modulation. Finally, some highlights and trends are noted concerning complementary metal-oxide semiconductor (CMOS) and silicon-on-insulator (SOI) implementation of metal-oxide gas sensors, micromachined field-effect gas sensors, integration of nanowires and polymeric substrates.

6.2 A brief history of semiconductors as gas sensitive devices

In 1952 Brattain and Bardeen reported on the change of the semiconducting properties of germanium with a variation of the partial pressure of oxygen in the surrounding atmosphere (Brattain, 1952). Seiyama published 10 years later results demonstrating the gas sensing effect on metal-oxides (Seiyama *et al.*, 1962). Taguchi brought metal-oxide semiconductor gas sensors to market using an alumina ceramic tube mounted with the metal-oxide and electrodes and a heater coil passing through it. He founded in 1969 the company Figaro Engineering Inc., which is still today the largest manufacturer of semiconductor gas sensors world-wide. Nowadays, the commercially available devices are mostly manufactured using screen-printing on small and thin ceramic substrates exhibiting a power consumption of 0.2 to 1 W. In 1988, Demarne *et al.*, demonstrated and patented the first thin-film metal-oxide gas sensors based on a micromachined silicon substrate. The micro-hotplate was made of a thermally insulating silicon oxide membrane. It embedded a gold heater. Gold electrodes were patterned on top and covered with a thin tin dioxide film. The device operated with a significantly reduced power consumption of about 100 mW to reach 300°C, a value still much lower than commercially available devices on alumina substrates.

Motorola licensed the technology and put effort into developing mass produced metal-oxide gas sensors using silicon micromachining (Fig. 6.1). Polysilicon heaters were introduced in an oxide-nitride membrane, using gold electrodes as before. They ceased work on the chemical sensor in 1998, but the technology was taken over by MicroChemical Systems SA in Switzerland and has evolved to be aligned with the developments reported by other research and industrial groups. Micromachined thick-film semiconductor gas sensors were introduced by drop-coating the metal-oxide on a thin dielectric membrane with platinum used both for heaters and electrodes, offering improved performances and robustness (Briand *et al.*, 2000a). This technology has been exploited since then by AppliedSensor GmbH (Section 6.4.2). Temperature modulation was introduced as a mode of operation due to the low thermal mass of the micro-hotplates. This mode of operation is now mainly applied to applicative scenarios to minimize power consumption; to reduce the influence

© Woodhead Publishing Limited, 2013

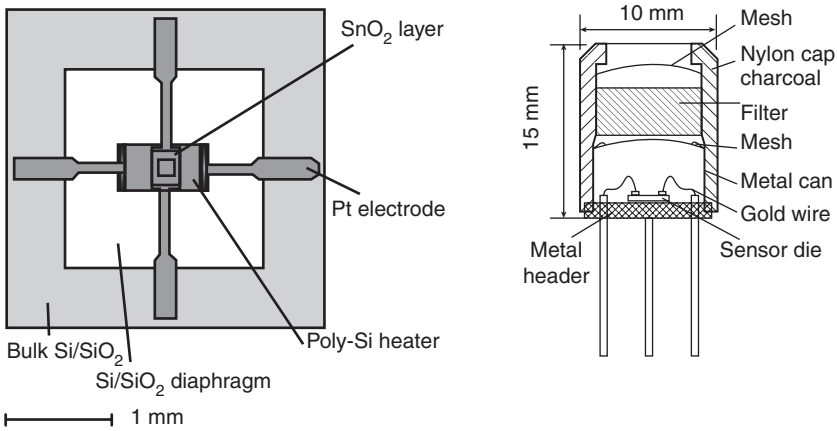

6.1 Diagram of the MGS 1100 sensor from Motorola. Micromachined sensor element is illustrated on the left, and the sensor housing on the right. The sensitive films were obtained by rheotaxial growth and thermal oxidation of tin layers (RGTO) deposited on the silicon oxide-nitride membrane. From Simon *et al.* (2001).

of humidity, for example, to enhance the discrimination capabilities of these sensors; and to improve their stability over time (Section 6.4.3).

Since 2000, the field has been evolving towards the use of SOI wafers, the implementation of these sensors in CMOS technology and on polymeric substrates, and the identification of suitable modes of operation for different applications. The field is now strongly focusing on nanomaterials (Ho *et al.*, 2011), especially nanostructured metal-oxides, but one can question whether this would be the solution to the main problems remaining with thin- and thick-film devices. Despite the extensive work carried out in this regard, very little has transferred to and been exploited by industry so far. Micro-hotplates being a mature and robust technology, the main issue remains of the synthesis of performing materials and their effective integration into a robust manufacturing process.

Research and developments since the end of the 1980s has reported a huge set of metal-oxide materials and hotplate combinations. Due to limitations of space, it has been necessary to be selective regarding the work to be presented in this chapter, which is far from exhaustive. More details on the different configurations of alumina- and silicon-type metal-oxide gas sensors can be found in Simon *et al.* (2001).

6.3 Micro-hotplate concept and technologies

Silicon micromachining has been used to generate thermally insulated heating elements suspended on a dielectric membrane. By patterning metallic

© Woodhead Publishing Limited, 2013

electrodes (Au, Pt) on top of the membrane, these structures have been applied as low-power transducers in metal-oxide gas sensors. This section provides information on the design, fabrication, characteristics and reliability of micro-hotplates used in semiconductor gas sensors.

6.3.1 Concept and thermal design

The operation of a metal-oxide gas sensor relies on the change in resistance of an n- or p-type semiconducting layer – mainly SnO_2 – when exposed to reducing or oxidizing gases.

A diagram of a typical cross-sectional view of a silicon micromachined metal-oxide (MOX) sensor is presented in Fig. 6.2. Their development has evolved towards silicon substrates to produce devices suitable for commercialization due to their low-cost, low-power consumption and high reliability. To lower the resistivity of the gas sensitive film, as well as to improve the kinetics of the chemical reactions, the metal-oxide layer is heated with a micro-heater. The heated area is usually embedded in a thin dielectric membrane to improve the thermal insulation and to reduce the power consumption of the device, which is typically in the order of a few tens of milliwatts at 300°C, and its thermal time constant (few to tens of milliseconds). Thermal programming allows kinetically controlled selectivity.

Figure 6.3 illustrates the heat losses that occur in a micro-hotplate when operating. The thermal energy, Q, generated by the Joule effect in the micro-heater, is given by:

$$\Delta Q = R \cdot I^2 \cdot \Delta t \qquad [6.1]$$

where I is the current flowing through the heater with a resistance R during Δt time. This heat is dissipated in the device and in the surrounding environment by three means:

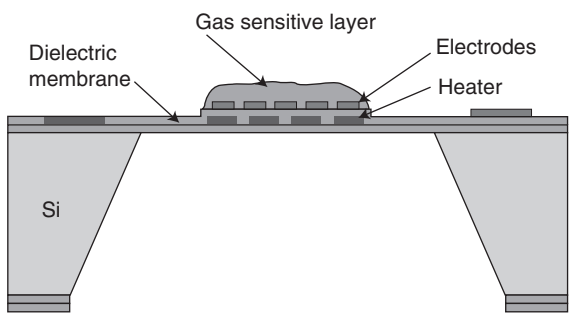

6.2 Cross-sectional diagram of a micromachined metal-oxide gas sensor.

© Woodhead Publishing Limited, 2013

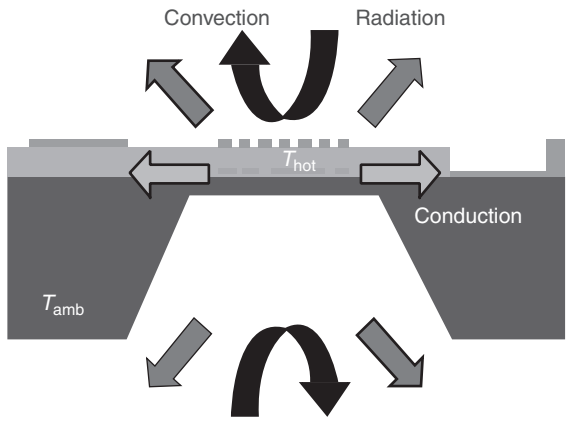

6.3 Heat losses in a micro-heating device: conduction, convection and radiation.

- conduction in the device;
- convection in the surrounding media (typically air);
- radiation.

Thus, the heat generated by the micro-heater is equal to the sum of the heat lost by conduction in the device, Q_{cond}, by convection in the air, Q_{conv}, and by radiation, Q_{rad}:

$$R \cdot I^2 \cdot \Delta t = \Delta Q_{cond} + \Delta Q_{conv} + \Delta Q_{rad} \quad [6.2]$$

The thermal design of micro-hotplates is mainly based on finite element simulation with the objective of optimizing the power consumption and obtaining a uniform temperature distribution over the active area. A precise model to evaluate the uniformity of power consumption and temperature over the heated area requires many empirical parameters to be known or measured accurately (Ali *et al.*, 2008; Courbat *et al.*, 2010a). Different heater layouts have been published, mainly meander or spiral shapes (Briand *et al.*, 2000a; Elmi *et al.*, 2008a), spiral shapes exhibiting better spatial temperature uniformity (Faglia *et al.*, 1999; Graf *et al.*, 2004a).

6.3.2 Micro-hotplate realization and performance

Micro-hotplates are made using a combination of thin-film and silicon micromachining processes. There are two main kinds of micromachined silicon substrates: closed-membrane and bridge-membrane. They consist of a suspended thin dielectric membrane, made of silicon nitride and/or silicon oxide, that is released using silicon micromachining on either the obverse or

© Woodhead Publishing Limited, 2013

reverse faces. The typical thickness of the membranes is from 0.5 to 2 μm. Closed membranes have lateral dimensions of about 0.5 to 1 mm, with approximately half the length being used as the active area. The typical lateral dimensions of bridge membranes lie between 100 and 200 μm. A silicon plug/island or a highly thermal conductive material, such as silicon carbide, can be implemented to improve uniformity of temperature. Also, silicon microelectronics components can be integrated on the thermally insulated area of the device. Diagrams of these structures are presented in Fig. 6.4. A bridge-membrane exhibits lower power consumption due to better thermal

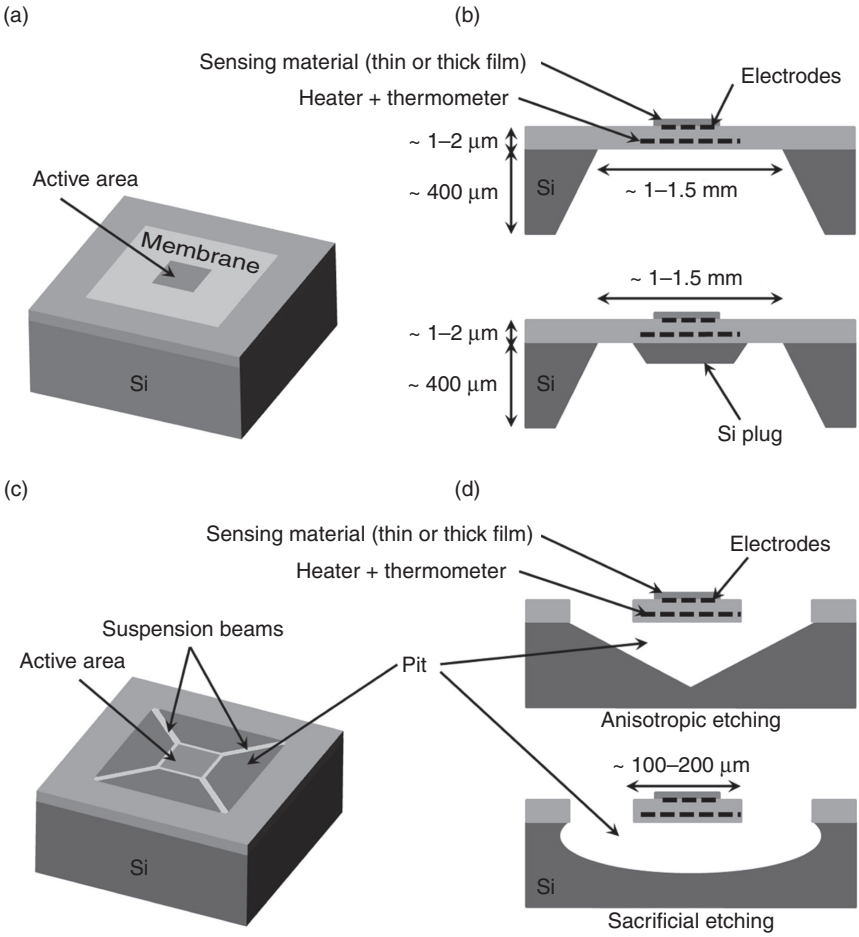

6.4 Diagram of a suspended-membrane-type gas sensor: (a and b) reverse of silicon micromaching; (c and d) obverse surface micromachining – (a and c) top view, (b and d) side view. Adapted from Simon *et al.* (2001).

© Woodhead Publishing Limited, 2013

insulation from the silicon substrate, while a closed-membrane is more convenient for patterning the sensing element.

Micro-hotplates with a bridge-membrane design based on CMOS-compatible processes were proposed by Cavicchi *et al.* (1995). The architecture of the hotplate is presented in Fig. 6.5. During the 2000s, the Swiss Federal Institute of Technology Zurich (ETHZ), Switzerland, came up with different generations of CMOS micromachined metal-oxide gas sensors with integrated driving and read-out circuitries (Graf *et al.*, 2006a). The heat necessary for the chemical reactions between the gaseous environment and the sensing layer was provided by the Joule effect through a field-effect transistor (FET) or polysilicon resistor. For improved reliability, platinum and tungsten are preferred as heater material at the time of writing. More details on the heater performances are provided in Section 6.3.3, on reliability. The heater and thermometer, which are needed to control the sensor operation temperature, can be either a dual purpose unit or two separate components. Polysilicon and platinum have often been used; microelectronic components, such as a forward bias silicon p-n junction as a temperature sensor, can be considered when silicon is available on the membrane.

With a resolution in the micrometer range for the photolithographic patterning of the electrodes, the gas sensitive area can be significantly reduced

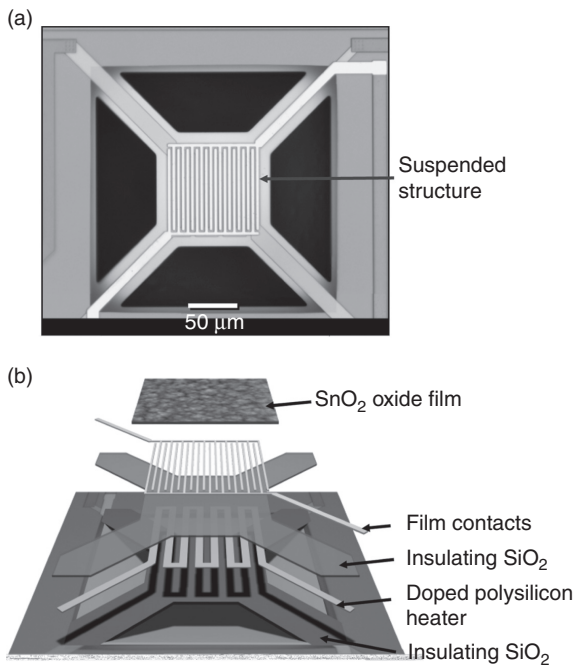

6.5 Obverse of CMOS silicon micromachined hotplate: (a) optical picture; (b) diagram. Courtesy of Dr Steve Semancik, NIST, USA.

© Woodhead Publishing Limited, 2013

in comparison with screen-printing on ceramic substrates. Regarding the electrode material, platinum is favored since it shows very good chemical stability and can provide higher gas responses (Barsan *et al.*, 1999). The two main approaches for the deposition of the gas sensitive sensing layer are either thin- or thick-film techniques. A thin film is usually realized by evaporation or sputtering; a thick film is deposited by screen-printing, spray pyrolysis, or drop-coating (Simon *et al.*, 2001). Once deposited, these materials usually require annealing at high temperatures (350°C to 800°C) in an oxygen-containing atmosphere to modify the morphology (e.g. grain size) and microstructure (e.g. porosity, surface-to-volume ratio). The parameters of this annealing step have to be carefully selected in order to be compatible with the micro-hotplate itself. Some temperature limitations occur with micro-hotplates based on a CMOS-compatible process.

Several micromachined hotplates for metal-oxide gas sensors have been reported in the literature. However, robust and established technologies all make use of the closed-membrane design in combination with platinum as the electrode material. Recent papers show that platinum is now mainly used as a heater material with tungsten applied in CMOS-compatible devices. The characteristics of some representative examples are summarized in Table 6.1. The optimization of the micromachined platform is very close to the optimum achievable, with a minimum active area – and, therefore, power consumption – reached. According to the resolution of the photolithographic process, it is becoming difficult to further reduce the size of the hotplates and yet retain an exploitable sensing layer and heater resistance values. The next steps are towards using nano-patterning techniques, self-heated metal-oxide nanostructures and printing on flexible polymeric substrates, as presented in Section 6.7 on trends and perspectives.

6.3.3 Micro-hotplate reliability

Operating at a relatively high temperature, the electro-thermo-mechanical reliability of micromachined hotplates is an important aspect for metal-oxide gas sensors.

Numerical thermo-mechanical studies have been performed to improve the robustness of the membrane, addressing buckling and stress concentration (Puigcorbé *et al.*, 2003). Thermo-mechanical reliability depends on the design and materials used. In general, the membranes made of dielectric materials deposited at a higher temperature (e.g. low-pressure chemical vapor deposition – LPCVD) are more robust. The membrane is usually formed of a stress-compensated stack of thin films of silicon nitride, silicon oxynitride and/or silicon oxide. A heater embedded in between LPCVD low-stress silicon nitride thin films has proven to be robust (Demarne *et al.*,

© Woodhead Publishing Limited, 2013

Table 6.1 Comparison of various micro-hotplate designs that have been reported in the literature

Year	Author	Active area (1000 μm²)	Hotplate area (1000 μm²)	Power at 300°C (mW)	Power/ heater area (mW/1000 μm²)	CMOS Yes/No	Membrane (M)/bridge (B)	Material membrane or bridge	Heater
1990	Dibbern	202.5	1822.5	55	0.27	No	M	Oxynitride	NiFe
1993	Suehle	10	40	40	4.00	Yes	B	CMOS films	Poly Si
1995	Zanini	722.5	1440	90	0.12	No	M	Oxynitride	Pt
1995	Gardner	472.5	3596.4	40	0.08	No	M	Nitride	Pt
1996	Aigner	300	1000	35	0.12	No	M	Nitride	Pt
1996	Lee	10	1000	18	1.80	No	M	Oxynitride	Poly Si Pt
1997	Gotz	250	1210	55	0.22	No	M	Oxynitride	Poly Si
1998	Guidi	562.5	2250	67	0.12	No	M	Nitride	Pt
1998	Astie	230	3240	125	0.54	No	M	Si/SiO	Poly Si
1999	Horrillo	250	1210	38	0.15	No	M	Nitride	Poly Si
2001	Udrea	90	250	100	1.11	Yes	M	CMOS films	FET
2001	Benn	40	NA	8.6	0.215	No	B	SiC	SiC-N
2002	Afridi	10	44	27.5	2.75	Yes	B	CMOS films	Poly-Si
2002	Briand	202.5	1000	50	0.25	No	M	Nitride	Pt/FET
2002	Mo	6.4	25.6	6	0.94	No	B	Oxynitride	Pt
2002	Chan	14.4	57.6	60	4.17	No	B	Oxynitride	Poly-Si
2003	Lee	31.4	1000	30	0.95	No	M	Nitride	Pt
2003	Tsamis	10	NA	15	1.50	No	B	Porous Si	Poly-Si Pt
2004	Fujres	10	NA	7.5	0.75	No	B	Nitride	Pt
2004	Baroncini	250	1000	20	0.08	No	M	Nitride	Pt

© Woodhead Publishing Limited, 2013

2004	Laconte	57.6	409.6	13	0.22	No	M	Oxynitride	Poly-Si
2005	Graf	70.7	250	50	0.71	Yes	M	CMOS films	Poly-Si
2005	Lee	3990	NA	73	0.02	No	B	Nitride	Pt
2006	Elmi	20.1	NA	6	0.30	No	B	Oxynitride	Pt
2006	Belmonte	160	NA	30	0.19	No	B	Oxynitride	Pt
2007	Guo	36.1	90	23	0.64	No	B	Oxynitride	Pt
2008	Barborini	1000	NA	24	0.02	No	B	Oxynitride	Pt
2008	Briand	250	2250	60	0.24	No	M	Polyimide	Pt
2008	Ali	17.67	250	14	0.79	Yes	M	CMOS films	W
2008	Ali	0.452	70.7	6	13.27	Yes	M	CMOS films	W

Notes: Where exact values are not given, they have been deduced from the information given in the particular paper. NA: not available.
Source: Adapted from Ali *et al.* (2008), in which all references can be found.

© Woodhead Publishing Limited, 2013

1988; Briand *et al.*, 2000a). This dielectric material is, however, not commonly available in MEMS foundries.

Accelerated aging tests have also been developed to determine and analyze the failure mechanisms by thermally cycling the device, by ramping up the power until breakdown, or by operating it at temperatures higher than their normal use (Bosc *et al.*, 1998; Briand *et al.*, 2003). Cracks in the dielectric membrane, electromigration and electro-stress-migration have been identified as the main causes of failure (Briand *et al.*, 2005). At high temperatures, the migration of the platinum atoms in the heater meander was linked to the mechanical stress in the dielectric membrane. State-of-the-art technologies can allow temperature cycling up to several millions of cycles before failure, enabling temperature modulation of the sensor (Section 6.4.3).

The heater material is a crucial point for the stability of this type of device during operation. Driven by CMOS compatibility, Poly-Si was first used but it suffers from an inappropriate drift of its electrical resistivity at high temperature (Ehmann *et al.*, 2001). Platinum is the material that has been implemented for the heater for improved reliability. It is used in most micromachined metal-oxide sensors on the market at the time of writing, not only for the heater, but also for the electrodes. Courbat *et al.* (2008) showed that adding a small amount of another refractory metal (such as iridium) to the platinum can improve its resistance to electromigration. However, Mo exhibited superior performances to platinum, allowing higher operational temperatures (Mele *et al.*, 2012).

TiN – a CMOS-compatible material – has been applied as a heating element showing relatively better performances than platinum (Creemer *et al.*, 2008). FETs have also been implemented as heaters in CMOS technology but this requires a silicon area in or underneath the membrane (Graf *et al.*, 2005). A very low-power micromachined hotplate platform was designed using silicon-on-insulator (SOI) technology and a robust tungsten heater (Ali *et al.*, 2008). This device is now commercially available in the products portfolio from Cambridge CMOS Sensors Ltd in the UK. One constraint is the obligation to work with the thin films available in the CMOS process. Depending on the process, the CMOS dielectric stack of films is not always optimum and post-processes can be necessary. For instance, this can involve the deposition of the metallic electrodes (Pt, Au), or a passivation and stress compensating dielectric thin film.

6.4 Micromachined metal-oxide gas sensors

In the main, two types of metal-oxide gas sensitive films have been integrated into micromachined hotplate transducers: thin and thick films. The different developments will be presented in this section. The integration of a third type of structure – nanowires, into which considerable efforts are

© Woodhead Publishing Limited, 2013

being made at the time of writing – will be presented in Section 6.7.1, Trends and perspectives. Other chapters in this book address in detail the synthesis, sensing mechanisms and properties related to these different sensing films.

In this section, for better readability and to allow comparison between results, all responses are given as R_{gas}/R_{air} if $R_{gas} > R_{air}$, or as R_{air}/R_{gas} if $R_{air} > R_{gas}$, where R_{air} is the baseline resistance of the sensors in air and R_{gas} is its resistance when exposed to the analyte under examination.

6.4.1 Thin gas sensitive films

First, micromachined gas sensors were obtained using thin-film deposition technologies. That technique, used for semiconductor manufacturing, is available in most clean-rooms with evaporation or sputtering machines. The motivation at that time was to produce MEMS-based metal-oxide gas sensors using thin-film technology only, being a disruptive technology compared with the thick-film technologies used on alumina.

The first silicon micromachined thin-film metal-oxide gas sensor was developed at CSEM SA, Switzerland by Demarne and Grisel (1988); this was commercialized at the beginning of the 1990s by Microsens SA in Switzerland. It consisted in a SiO_2 membrane embedding a gold-based meander-shaped heater. A thin film of SnO_x was sputtered and patterned by lift-off. Two configurations were proposed, without and with a silicon plug to make the temperature reached in the active area of the device more uniform. To attain 300°C, the supplied powers were, respectively, 104 mW and 183 mW. Motorola also showed a significant interest in the development of commercial micromachined thin-film gas sensors for CO detection (Lyle *et al.*, 1997). They ceased their activities in that field at the end of the 1990s. Development was pursued by MiCS (MicroChemical Systems SA) in Switzerland, now part of the SGX Sensortech group.

Other techniques have been used for the fabrication of thin-film metal-oxide gas sensors. At NIST in the USA, Cavicchi *et al.* (1995) and Semancik *et al.* (2001) produced gas sensors by chemical vapor deposition (CVD). By applying a current and thus heating the hotplate, sensing films could be deposited locally (i.e. only on heated active areas) using an adequate organometallic precursor. SnO_2 and ZnO films were obtained with tetramethyltin and diethylzinc in an oxygen atmosphere. They were deposited onto different seed layers, which played a significant role in terms of gas selectivity.

Besides CVD and sputtering from a target of the desired material, thin films were obtained by sputtering or evaporation through the rheotaxial growth and thermal oxidation (RGTO) process. This method consists in depositing thin layers of a metal, followed by its thermal oxidation in an oxygen-rich atmosphere. Tin oxide layers of 350 nm in thickness were obtained with this technique from sputtered Sn by Faglia *et al.* (1999) for the design

© Woodhead Publishing Limited, 2013

of CO sensors. The highest sensitivity to CO was obtained at an operating temperature of 400°C. Responses of between 2 and 3 were obtained when the device was exposed to 25 ppm of CO, the alarm level in many countries. With the same technique, Elmi *et al.* (2008b) grew SnO_2 films on very low power hotplates. A temperature of 300°C was reached with a supply power of 6 mW. The sensor had a response of 7.5 when exposed to 100 ppb of NO_2 at 200°C and 5 under 10 ppm of CO at 450°C.

In 2003, the European Aeronautic Defence and Space company (EADS) in Germany developed gas sensors based on silicon technology to replace thick-film devices, which were usually based on alumina substrates and had a high level of power consumption (Müller *et al.*, 2003). A main drawback Muller *et al.*, identified in Si-based devices was their fragile membrane. Therefore, they built their devices – an array of three hotplates – from SOI to keep the top Si layer as a robust suspended membrane. A fabrication yield of 100% was achieved with a top Si layer thicker than 5 μm. Typical power consumptions were in the range of 50 mW to 80 mW to reach an operating temperature of 300°C. The active area of the device could be operated at different temperatures and functionalized through thin- and/or thick-film technology. Friedberger *et al.* (2003) evaporated Sn and obtained SnO_2 by RGTO. The sensing film had good sensitivity towards hydrocarbon and hydrogen, but a very low response to CO.

Wöllenstein *et al.* (2003) developed an array combining several gas sensing layers by successive photolithography steps, and sputtering or e-beam evaporation. A device with four different metal-oxide layers could be produced. The films had to be deposited in a specific order, depending on the temperature required for stabilization. The layer with the highest annealing temperature was deposited first. Titanium doped chromium oxide (CTO) was produced by successively evaporating Cr and Ti layers, which were subsequently annealed at 850°C. ZnO films were obtained by direct current (DC) magnetron sputtering from a Zn target combined with an Ar/O_2 plasma. Pt-doped SnO_2 films were obtained by radio frequency (RF) magnetron reactive sputtering from a SnO_2 target followed by the deposition of a few tens of a nanometer of Pt. The sintering of ZnO and SnO_2 films occurred at a temperature of 700°C and could be performed simultaneously. As for ZnO, WO_3 was sputtered from a W target in an Ar/O_2 plasma with a low deposition rate to ensure proper oxidation of the material. The last material that could be deposited was V_2O_5. It was performed by e-beam evaporation of vanadium under controlled oxygen pressure. To reach a fully-oxidized film, the evaporation was followed by an additional oxidation treatment at 500°C in synthetic air. The silicon wafer was then bonded to a micromachined glass component acting as a structural element. To reduce power consumption as much as possible, the reverse of the Si wafer was wet-etched in a KOH solution. Etching stopped at the dielectric thin films and at the highly-doped Si layer. Gas sensing measurements are presented

© Woodhead Publishing Limited, 2013

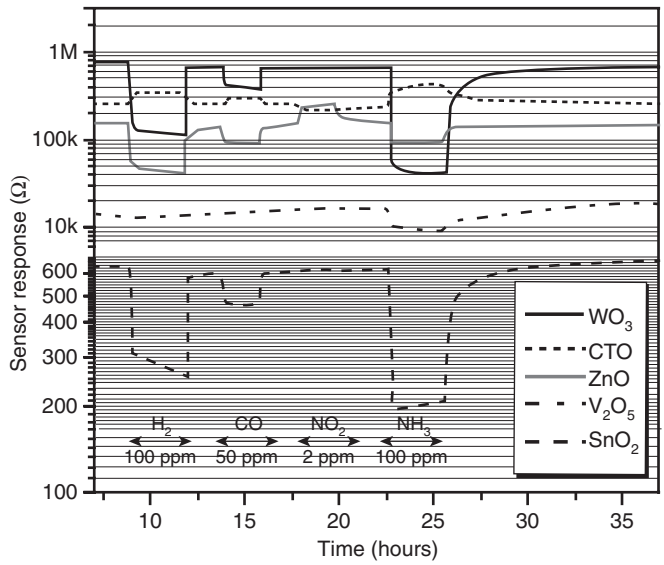

6.6 Gas measurement obtained from the sensor array. The sensing materials exhibited different behavior toward the analytes. From Wöllenstein *et al.* (2003).

in Fig. 6.6. The sensors were operated at about 200 mW to reach a temperature of 400°C. They were exposed to H_2, CO, NO_2 and NH_3 as testing gases. Discrimination can be made between them since some material resistive variation was observed only for specific gases. ZnO was the only layer exhibiting a response to NO_2, and V_2O_5 to NH_3.

6.4.2 Thick gas sensitive films

In the mid-1990s, thick-film-based metal-oxide sensors began to attract attention. There were issues regarding the stability and reproducibility of metal-oxide thin films. New deposition methods brought from outside the semiconductor industry were used – mainly pipetting, drop-coating and screen-printing. The first combination of a thick-film sensing layer combined with a micro-hotplate was carried out by Barsan (see Gardner *et al.*, 1995), by pipetting pure SnO_2, 0.2% Pt-doped SnO_2, or 0.2% doped-SnO_2 on gold electrodes patterned on micromachined hotplates. A polycrystalline structure was obtained by sintering the SnO_2 layers at 600°C in air. A power supply of 60 mW was needed to operate the sensor at 400°C. The pure SnO_2-based sensors showed the best sensitivity to organic solvents. It exhibited a resistance variation of 32% when exposed to 25 ppm of n-octane. The sensor's response and recovery times were, respectively, 40 seconds and 60 seconds. Drop-coating of Pd-doped SnO_2 pastes was first introduced by

© Woodhead Publishing Limited, 2013

Heilig *et al.* (1997). The sensing material was deposited on micromachined hotplates for the discrimination of CO, NO_2 and their binary mixtures. Briand *et al.* (2000a) used this technique for the deposition of 2% Pd-doped SnO_2 paste (Kappler *et al.*, 1998) on interdigitated Pt-electrodes. The diameter of the drop was 400 μm with a thickness of a few tens of microns. It was deposited on a membrane of 1×1 mm^2 and 1 μm thick. The sensing material could be annealed on a chip using the sensor's heater. For operating the device, a temperature of 300°C was reached with a power supply of 70 mW. The device showed a response of 2.2 and 1.4, respectively, to 10 ppm of CO and 2000 ppm of CH_4. Despite their high thickness, drop-coating has led to highly stable, reproducible sensors with very good sensitivity. These results led to the large-scale commercialization of drop-coated metal-oxide gas sensors by AppliedSensor GmbH, Germany, for the automotive market (Blaschke *et al.*, 2006). The micro-hotplate technology developed by Briand *et al.* (2000a) has been combined with much thinner optimized SnO_2 and WO_3 films, having a thickness of less than 5 μm (Fig. 6.7). Typical gas responses are displayed in Fig. 6.8. The metal-oxide drop was then further reduced by using capillaries for its deposition and could reach a diameter of about 20 μm (Courbat *et al.*, 2012). Smaller hotplates can be thus used, leading to a potential further decrease in power consumption.

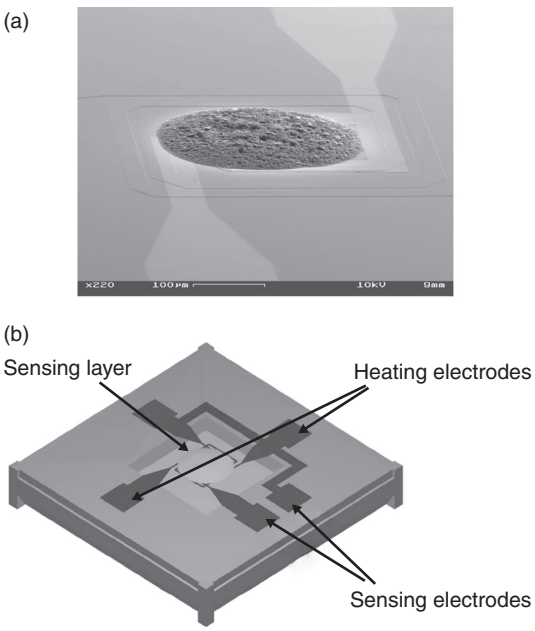

6.7 (a) SEM image of a drop-coated metal-oxide gas sensor from AppliedSensor GmbH. (b) Three-dimensional schematic drawing of the sensor structure. From Blaschke *et al.* (2006).

© Woodhead Publishing Limited, 2013

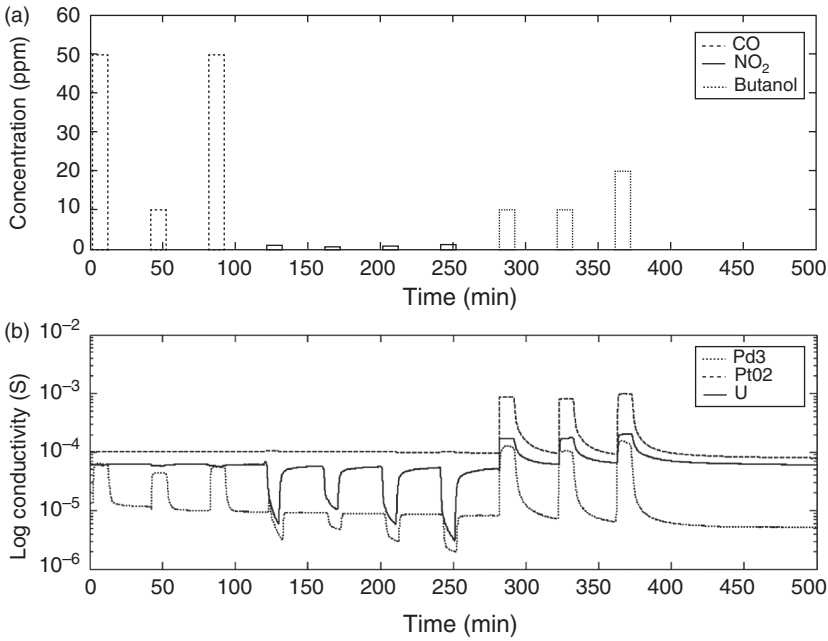

6.8 Gas response (b) of 3% Pd-doped SnO_2 (Pd3), 0.2% Pt-doped SnO_2 (Pt02) and undoped SnO_2 (U) to changes in concentrations of CO, NO_2 and butanol (a). From Blaschke *et al.* (2006).

Drop-coating was then used by many other groups. Among others, Puigcorbé *et al.* (2002) and, later, Cerdà Belmonte *et al.* (2006) from Morante's group in Spain used it for the deposition of SnO_2 and $BaSnO_3$. Espinosa *et al.* (2010) in Italy deposited drops made of 1% Pt-doped WO_3, 1% Pt-doped SnO_2, 1% Pd-doped SnO_2 and 1% Au-doped SnO_2 on a suspended micro-hotplate with a diameter of 80 μm. It required about 8 mW to reach an operating temperature of 400°C. As test gas, the sensing films were tested with ethylene, acetaldehyde, ethanol and ammonia. For a few years, Figaro Engineering Inc. investigated the potential commercialization of micromachined metal-oxide gas sensors (Ishibashi and Kaneyasu, 2009). The device was based on a suspended membrane etched from the front. The power consumption was typically in the range of 19 mW to 20 mW to attain the operating temperature. They dispensed different metal-oxide materials that were then annealed with the integrated heater on the chip. The layer thicknesses were between below 1 μm to about 50 μm, depending on the gas to be detected.

A second technique widely used for the deposition of thick-film metal-oxides on alumina substrates is screen-printing. Looking at the success met by the thick drop-coated films, screen-printing was reconsidered. Vincenzi *et al.* (2001) screen-printed Pd-doped SnO_2 paste onto

© Woodhead Publishing Limited, 2013

micromachined micro-hotplates. The paste also contained a glass frit (a low melting temperature glass) to increase its viscosity and improve adhesion to the substrate. Particular care had to be taken to avoid breaking the SiO_2/Si_3N_4 membrane during film deposition. This was achieved by using a special stencil, which reduced pressure on the membrane. The sensing film was $250 \times 350\ \mu m^2$ and had a thickness of about 40 μm. The film was then fired at 650°C for 1 hour, using the sensor's heater. For gas detection, the devices operated at 400°C with a power of 30 mW and were evaluated with CO, CH_4 and NO_2. Fairly low responses – 1.2 for 50 ppm of CO, 1.03 for 1000 ppm of CH_4 and 1.7 for 0.1 ppm of NO_2 – were obtained. It was ascribed to the glass frit, which insulated the SnO_2. To avoid breaking the membranes during screen-printing, Llobet *et al.* (2003) deposited a 5 μm thick, undoped SnO_2 sensing film before releasing the membrane. It led to a significantly improved yield of 95% after encapsulation of the sensors. They showed responses of about 3 to 25 ppm ethanol and to 625 ppm of ammonia and 8 to 62.5 ppm of acetone. From the same group, Ivanov *et al.* (2005) screen-printed SnO_2 and WO_3 pastes on micromachined transducers. When exposed to CO, low responses were obtained by SnO_2 and no response was observed with WO_3. In the case of an exposure to 1 ppm of NO_2, responses of 3.63 with SnO_2 at 250°C and 8.91 with WO_3 at 200°C were measured. Moreover, Ivanov *et al.*, sputtered the same materials so as to investigate and compare the sensing properties of thin- and thick-film metal-oxide layers. The results revealed that thick-film gas sensing layers have a higher degree of sensitivity than thin-film layers. This is due to the nature of the deposited film, which is more compact in the case of thin films, thus reducing the surface-to-volume ratio (Barsan *et al.*, 1999).

SnO_2 screen-printing paste contains a binder to control the rheological properties and to ensure a good adhesion of the film to the substrate. Glasses bring problems of SnO_2 percolation and thus reduce the conductivity. Remedy to this issue, Viricelle *et al.* (2006) evaluated different inks with an optional organic binder, instead of a mineral binder, and with Sn alkoxide, which lead to the formation of SnO_2 during thermal annealing. Sensor films with a low conductance were obtained when no binder was used because of numerous cracks in the layer. The presence of both the organic binder and the alkoxide gave good results in terms of paste adhesion and conductivity, but the pattern resolution achieved was limited. However, nowadays, screen-printing resolution down to 20 μm has been demonstrated in the field of printed electronics and better results could be expected for metal-oxide pastes.

Beside drop-coating and screen-printing, a further technology – flame spray pyrolysis (FSP) – showed promising results. The deposition technique consists in spraying liquid precursors, which form a flame. The precursors react in the gas phase with the subsequent particle formation. This method

© Woodhead Publishing Limited, 2013

allows a good control on morphology – amorphous or crystalline – as well as doping. Films with thicknesses of a few micrometers which do not require any annealing can be obtained. Sahm *et al.* (2004) used this method for the deposition of SnO_2 on alumina substrates. Gas measurements were performed. The SnO_2 sensing film showed a good response to low concentrations of NO_2 (below 200 ppb) and propanal, and a low response to CO, which is typical for undoped SnO_2 films. Kühne *et al.* (2008) used the same method for the deposition of Pt-doped SnO_2 onto micromachined hotplates. The sensing film was patterned through a shadow mask. The transducer coated with the sensing film is presented in Fig. 6.9(a). The devices operated at 250°C with a power supply of about 25 mW. It showed a good response towards ethanol concentrations between 25 and 100 ppm, as illustrated in Fig. 6.9(b).

6.4.3 Temperature modulation

Metal-oxide gas sensors can be operated in two modes: constant temperature (i.e. isothermal), or temperature-modulated. In constant temperature mode, the selectivity can be enhanced by using an array of sensors covered with different materials or dopants (Wöllenstein *et al.*, 2003; Panchapakesan *et al.*, 2006), or by operating at different temperatures (Cavicchi *et al.*, 1995; Heilig *et al.*, 1997). However, the use of several sensors considerably increases the complexity and the power consumption of the system. Additionally, a drawback with constant temperature operation is that a mixture of oxidizing and reducing gases can offset each other and no signal variation will be observed (Barsan *et al.*, 1999). With the micromachining of the devices, their thermal response times were drastically reduced to the millisecond range. This allowed their operation in a pulsed or cycled temperature mode to avoid the interference of humidity, and allowed the discrimination of several gases with one single sensor. This measurement technique was first introduced by Sears *et al.* (1989). They applied a sine signal to the sensor heater and measured the response of the SnO_2 gas sensing layer when exposed to different analytes. They observed that methane and propane gave a higher response with a heater at its maximum temperature, while CO is better measured in a cooling state. Each gas can be identified by a specific temporal response pattern, which depends on its chemical reaction with the gas sensitive material (Lee and Reedy, 1999).

Major investigations related to temperature-modulated micromachined metal-oxide gas sensors were performed in Semancik's group. Ratton *et al.* (1997) applied a saw-tooth signal shape to the heater to reach temperatures up to 550°C. The behavior of methanol, ethanol, acetone and formaldehyde was studied. The sensor signal was processed through the Gram-Schmidt approach, Fast Fourier Transform (FFT), Haar Wavelet Transform and the Granger approach to reduce the number of coefficients describing the signal and to retain as much relevant information as possible. Best results were

© Woodhead Publishing Limited, 2013

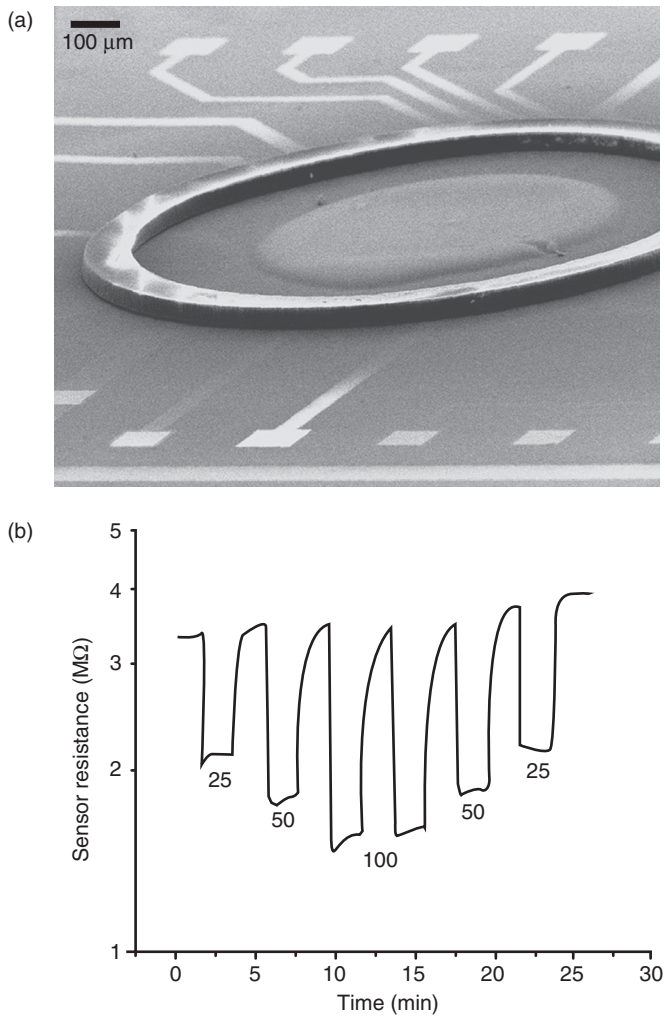

6.9 (a) SEM image of a Pt-doped SnO_2 film deposited by flame spray pyrolysis; (b) gas response to ethanol. Adapted from Kühne *et al.* (2008). Values given are EtOH concentrations (ppm); 90% r.h. (20°C); T_m = 250°C.

achieved with the Haar Transform, which efficiently compressed the information while removing noise and drift effects. Kunt *et al.* (1998) used the same device to discriminate methanol and ethanol using temperature modulation. Both gases responded differently to the temperature change, as can be seen in Fig. 6.10. In this study, they optimized the temperature profile to improve response selectivity between these two gases.

The sensitivity can be further improved by taking advantage of the unsteady state of the number of oxygen species at the surface of the metal-oxide when

© Woodhead Publishing Limited, 2013

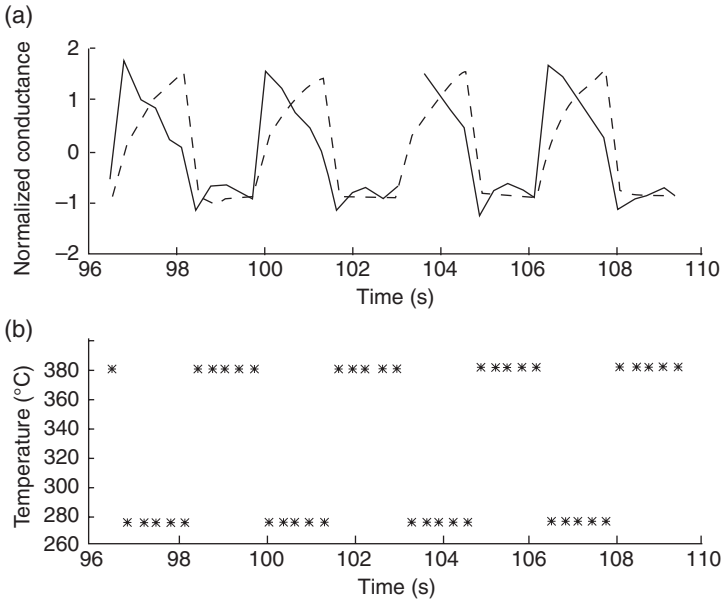

6.10 (a) Conductance response of a SnO_2 gas sensing layer to ethanol (dashed line) and methanol (solid line) for temperature pulses of 275°C and 380°C (b). From Kunt *et al.* (1998).

its temperature is changing. Llobet *et al.* (2002) showed that the transient response of thermally-cycled metal-oxide sensors decreases the sensor's response to humidity and to the drift in the resistance of the gas sensitive layer. Several options of temperature variations have been presented in the literature to improve selectivity. Different waveforms at different frequencies have been applied to the heater of the gas sensor to achieve thermal cycling of its temperature. The sensor response can be then analyzed by signal processing. FFT was used by Nakata *et al.* (2006). They applied a sine wave and its second harmonic to the sensor heater to improve the selectivity of a SnO_2 semiconductor gas sensor. Depending on the phase shift of the second signal compared with the first, discrimination between alcohols, hydrocarbons and aromatic compounds could be performed. Figure 6.11 shows the sensor response to ethanol, ethane and toluene as representative examples of these gas families. Llobet *et al.* (2002) used discrete wavelet transform and an artificial neural network to measure and discriminate CO, NO_2 and their mixture. The wavelet technique gave better results than FFT in terms of data compression, and tolerance to noise and drift in the sensor response.

A system based on simpler electronics relies on pulsing the temperature (i.e. the heater is only switched on and off). Depending on the duty cycle, it

© Woodhead Publishing Limited, 2013

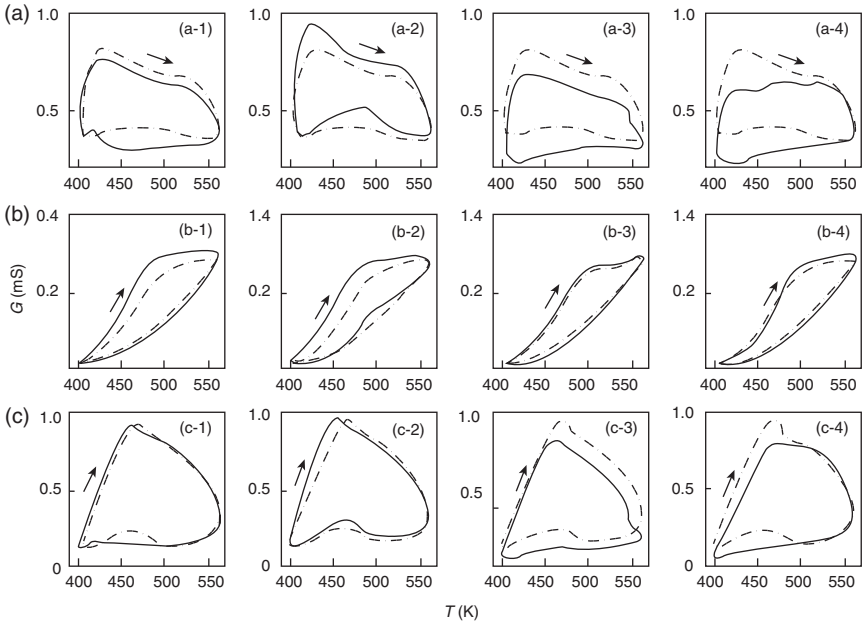

6.11 Sensor temperature vs sensor conductance of the sensor when a sine wave was applied to the heater without the second harmonic (dashed line) and with the second harmonic (solid line) with a phase shift of (1) 0 rad, (2) $\pi/2$ rad, (3) π rad, (4) $3\pi/2$ rad. The sample gases tested were 1000 ppm of (a) ethanol, (b) ethane, (c) toluene. From Nakata *et al.* (2006).

allows a significant reduction in power consumption (Courbat *et al.*, 2012). Among other techniques, this was used by Faglia *et al.* (1999) for the detection of CO with an Au-doped SnO_2 film. They used a square signal with a period between 0.5 seconds to 180 seconds. The heater was powered for 100 ms, which was sufficient to reach a steady state. Beside a reduction in power consumption, Faglia *et al.*, observed an increase in sensor response, compared with DC measurements, for periods up to 20 seconds. Therefore, such a method can allow a reduction in power consumption while improving sensing performances.

6.4.4 Packaging

Silicon micromachined semiconductor gas sensors are mainly packaged using standard metallic transistor outline (TO) headers as support, and wire bonding is used for their electrical connection. Typically, a metallic cap with a grid is fixed to the TO header with a hydrophobic gas permeable membrane on top of it. A filtering agent can be also included in the package.

© Woodhead Publishing Limited, 2013

The use of silicon microfabrication techniques brings not only the ability to process the sensors at wafer-level but also, as demonstrated in Raible *et al.*, in 2006, the encapsulation and testing of the sensors at wafer-level. This concept allows liquid-tight sealing of gas sensor devices, which protects them during production (e.g., wafer dicing) and later in the application, while still allowing the target gases to reach the sensing layer. The basis of wafer-level packaging is the combination of a structured Pyrex wafer with a micromachined substrate wafer. Thereafter, thick-film SnO_2 layers are deposited and stabilized before a diffusion membrane is attached, which seals the wafer stack as shown in Fig. 6.12. The wafer stack is finally diced into individual sensor elements which can be mounted on printed circuit board using different interconnection methods, such as chip on board, flip-chip, tape automated bonding and so on (Fig. 6.13).

Briand *et al.* (2007) reported on a higher level integration of wafer-level packaged micromachined metal-oxide gas sensors. The concept was based

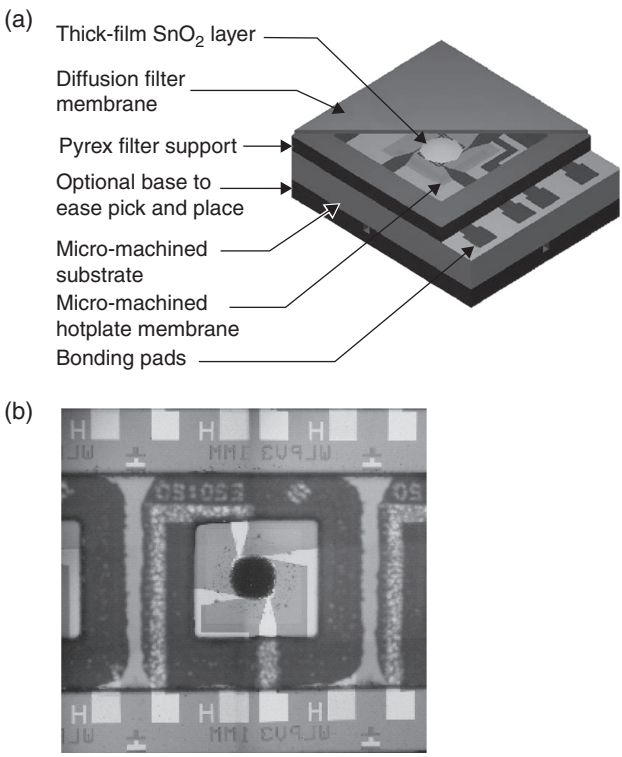

6.12 (a) Diagram of the wafer-level packaged metal-oxide sensor; (b) optical picture of an individual sensor area with the Pyrex rim and the metal-oxide drop before the fixation of the gas permeable membrane. From Raible *et al.* (2006).

© Woodhead Publishing Limited, 2013

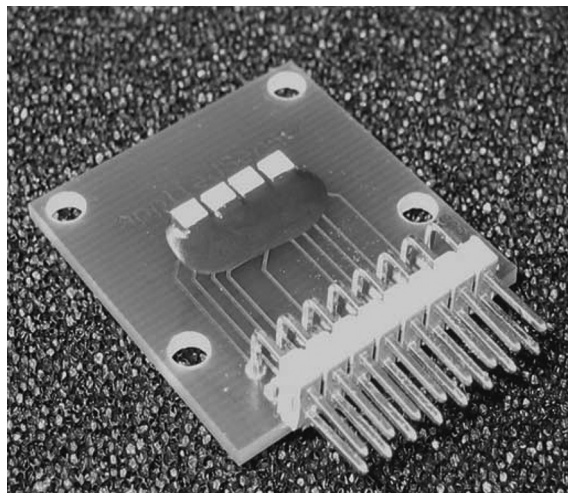

6.13 Chip on board wafer-level packaged metal-oxide gas sensors on printed circuit board. From Raible *et al.* (2006).

on the insertion of the metal-oxide drop into the micromachined cavity in the silicon substrate with the platinum electrodes at its bottom. Using this approach, the Pyrex rim was no longer necessary and the gas permeable membrane could be fixed directly onto the silicon substrate to close the cavities containing the drop-coated metal-oxide film (Fig. 6.14). For a 200 μm-wide deep reactive-ion etched (DRIE) membrane, a power consumption of 15 mW was reached at 300°C. DRIE technology also allows the reduction of the chip size to a minimum, compared with KOH etching. Following the trends in the field of sensor packaging and mounting, surface mount devices (SMDs) are appearing on the market using a plastic, molded package as a cost-effective approach.

6.5 Complementary metal-oxide semiconductor (CMOS)-compatible metal-oxide gas sensors

CMOS-compatible and SOI-based micro-hotplates used as transducers for metal-oxide gas sensors were reported, respectively, by Suehle *et al.* (1993) and Laconte *et al.* (2004). They addressed the realization of the hotplates themselves in a CMOS-compatible process with an integrated poly-Si heater. But the real benefit of this technology comes with the integration of the complete driving and read-out electronics on the sensor chip. Beside the potential reduction of power consumption and the cost of the sensor system, the number of bonding wires can be decreased, as can the packaging. The integration of the electronic circuitry can also improve signal response fidelity due to on-chip signal processing, and

© Woodhead Publishing Limited, 2013

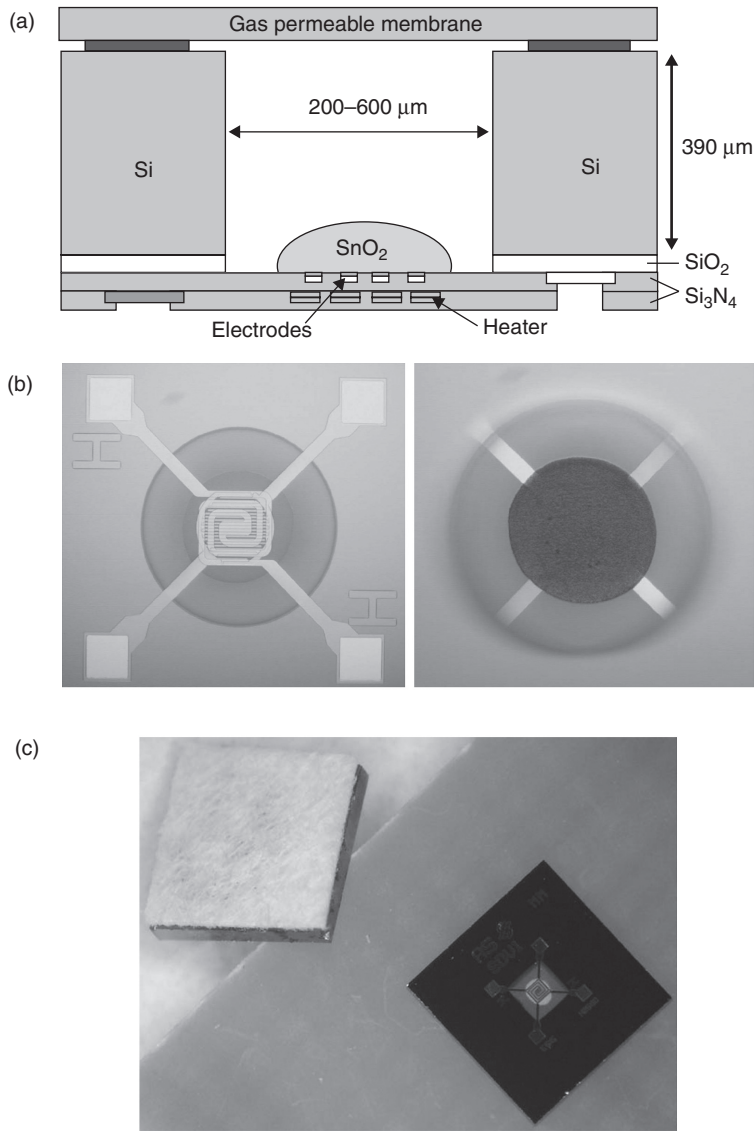

6.14 (a) Diagram of the wafer-level packaged semiconductor gas sensors with the metal-oxide film deposited in the silicon micromachined cavity; (b) and (c) optical images of the DRIE etched 200 μm-wide drop-coated metal-oxide device (b) before and (c) after encapsulation at the wafer-level. From Briand *et al.* (2007).

amplification and conditioning of small sensor signals. Benefits can be brought to the operation of the sensor by allowing the implementation of driving, signal conditioning and compensation strategies. However, if the yield of the formation of the sensing layer on the sensor chip is not

© Woodhead Publishing Limited, 2013

sufficiently high, the failure cost will be significantly higher, together with the loss of the electronics.

Four main concerns need to be addressed when integrating metal-oxide sensors in a CMOS-compatible process:

- The dielectric membrane of the micro-hotplates will be composed of CMOS dielectric films. It can be formed through a silicon micromachining post-process either on the back or the front.
- The standard electrically conductive materials are doped polysilicon and aluminum, which are not suitable to be used as heaters (Section 6.3.3) or electrodes (oxidation of Al) for the sensor. Implementing platinum, the commonly used material, as heater and electrode material involves post-processing steps.
- The post-deposition of the metal-oxide sensing layer needs to be CMOS-compatible, and its post-deposition annealing is limited in terms of temperature and time.
- Once the CMOS metal-oxide sensor chip is available, the miniaturization of the device brings different issues to the CMOS electronics design. We refer the reader to the comprehensive review published by Gardner *et al*. (2010), for more information about electronics circuitry design.

Afridi *et al.* (2002) have reported on an array of four bridge-type front micromachined hotplates with post-processed gold electrodes and including interface electronics. The metal-oxide films, tin oxide and titanium dioxide, were deposited using an LPCVD process when operating the micro-hotplates at different temperatures. A decoder was used to select a given micro-heater and sensing resistive layer, with a bipolar transistor or a metal-oxide-semiconductor field-effect transistor (MOSFET) switch, respectively. The signal-to-noise ratio was improved using an on-chip operational amplifier.

ETH Zurich, in Switzerland, has extensively developed CMOS-compatible metal-oxide gas sensors with on-chip integrated circuitry (Graf *et al.*, 2004; Barrettino *et al.*, 2006). Post-processing was used to include platinum electrodes on the hotplate coated with a drop-coated Pd-doped tin oxide film. Annealing of the metal-oxide film was performed at a maximum temperature of 400°C, which prevented any degradation of the device. Figure 6.15 presents an advanced analog/digital monolithic sensor system (Graf *et al.*, 2006a). Its fabrication was performed using an industrial CMOS process followed by post-processing steps for the patterning of the platinum electrodes, the release of the membrane by silicon micromachining, and the deposition of the sensing layer. Dielectric thin films available in the CMOS process were used for the thermally-insulated membrane, electrical insulation and passivation. The active area featured a circular-shape resistive heater, a temperature sensor and electrodes to contact

© Woodhead Publishing Limited, 2013

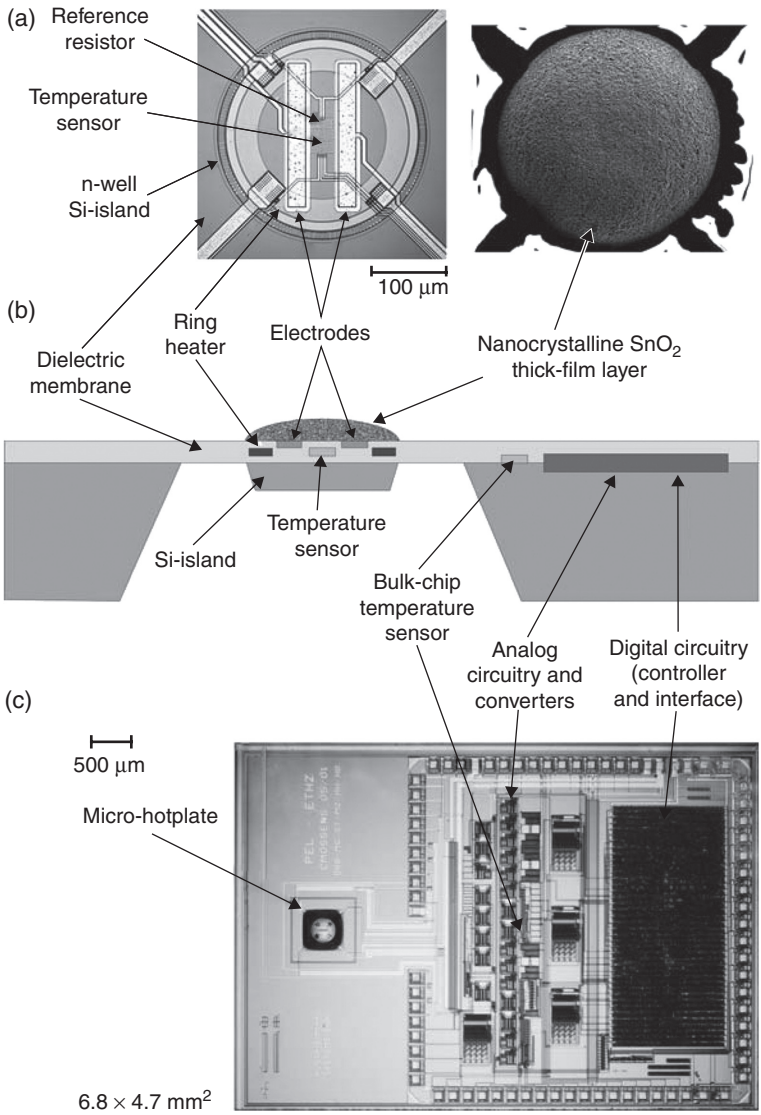

6.15 Monolithic metal-oxide-based gas sensor system in CMOS technology: (a) close-up of the micro-hotplate (left) and SEM-micrograph of a micro-hotplate with a drop-coated nanocrystalline thick-film layer (right); (b) cross-sectional diagram of the heated area of the sensor chip; (c) micrograph of the CMOS-based overall sensor system chip featuring micro-hotplates and circuitry. Graf *et al.* (2006a).

© Woodhead Publishing Limited, 2013

the sensing layer. In Fig. 6.15(c), the micro-hotplate, the analog circuitry (including analog-to-digital and digital-to-analog converters), and the digital circuitry are distinguishable. The digital part included a programmable digital temperature controller and a digital interface. This enabled control of the sensor temperature, as well as a read-out of the temperature of the hotplate and the gas sensor signal. A logarithmic converter connected to the resistance layout of the sensitive layer not only allowed a first-order signal linearization, but also helped to address the large variation range of the metal-oxide resistance from 1 kΩ to 100 MΩ. A stand-alone version of the monolithic sensor system (including three transistor-heated micro-hotplates (Graf *et al.*, 2005) with fully digital temperature controllers and a digital interface)) was developed to take complete advantage of this technology.

Robust high-temperature tungsten-based SOI micro-hotplates were reported by Ali *et al.* (2008) and have been successfully commercialized by Cambridge CMOS Sensors Ltd in the UK. The hotplates are fabricated using a standard SOI CMOS process in a commercial foundry, followed by a DRIE post-processing step to release the dielectric silicon dioxide closed-type membrane. The process was performed on 150 mm SOI wafers with a 0.25 μm-thick silicon device layer sitting on a 1 μm-thick box oxide layer used as etch stop during the DRIE of silicon. The silicon device layer is very thin and can be removed from the whole membrane area for better thermal insulation. One of the tungsten metal layers was used as heater, and exhibited very stable behavior at a high temperature of 500°C. An ultra-low power consumption of 12 mW and a fast transient time of 2 ms to reach 600°C were reported. Figure 6.16 presents a diagram of this device. The complete integration of the CMOS electronic circuitry with the sensor element is still to be demonstrated.

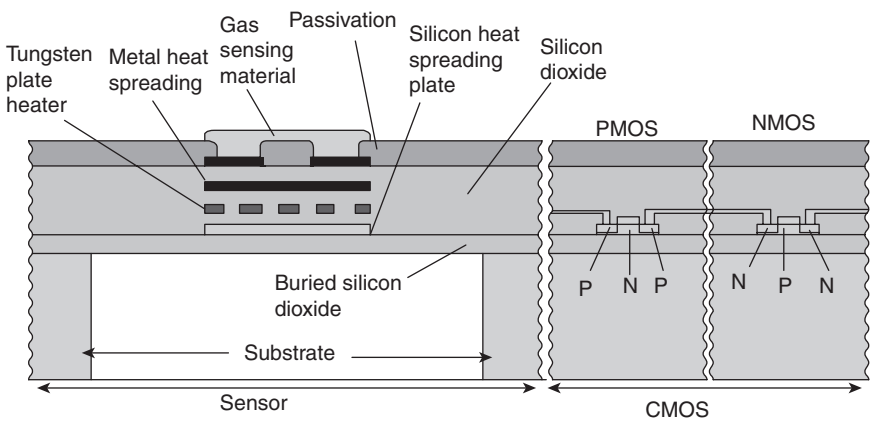

6.16 Design of tungsten SOI chip: gas sensor and integrated CMOS circuitry. From Ali *et al.* (2008).

© Woodhead Publishing Limited, 2013

6.6 Micromachined field-effect gas sensors

The field-effect gas sensing principle was first demonstrated by Prof. Lundström in 1975 by replacing the standard aluminum gate of a MOSFET with a catalytic metal, such as palladium, for the detection of hydrogen (Lundström *et al.*, 1975). By heating up the device, hydrogen molecules dissociate in hydrogen atoms, which diffuse through the catalytic metal, reaching the metal-dielectric interface of the FET devices. Electric dipoles are created, which induce a change in the I-V curve characteristics of the FET device. By tuning the catalytic gate material of the device, a series of gases (mainly containing hydrogen atoms) can be sensed using the FET as a transducer (Lundström *et al.*, 2007). Extensive literature can be found on the topic and AppliedSensor GmbH is now commercializing the technology mainly for application in the fuel cell market. Modulating the temperature is also of interest for this sensing principle, and some work has been undertaken in that direction. However, low power and low thermal mass devices are desirable for this purpose (Kreisl *et al.*, 2005). These devices have also been developed on silicon carbide for applications in harsh environment (Lloyd Spetz *et al.*, 1997).

At the end of the 1990s, in the framework of the European project Chemical Imaging for Automotive Applications (CIA), reducing the power consumption of GasFETs was identified as being of interest to the automotive market. Developments have been undertaken by Briand *et al.* (2001) to achieve the thermal insulation of a GasFETs array based on the micro-hotplate concept. At that time, the technology was further developed for its integration into an electronic nose by Nordic Sensors Technologies, Sweden (now AppliedSensor).

Basically, using silicon micromachining, an array of four GasFETs devices, with different catalytic layers (Pd, Ir, Pt), were located on a silicon island thermally insulated from the silicon chip frame by a thin-film dielectric membrane made of silicon nitride (Briand *et al.*, 2000b; Fig. 6.17). A two-step wet silicon anisotropic etching in KOH was developed to achieve a 10 μm-thick silicon plug underneath the dielectric membrane, in which the electrical components were located. A doped silicon resistor used as heater and a diode used as a temperature sensor were integrated into the design, as shown in Fig. 6.17.

Processing, however, remained heavy, with many photolithographic steps. Power consumption was significantly reduced to 90 mW for an operational temperature of 170°C. But the most interesting feature was the fast modulation of the temperature. A thermal time constant of less than 100 ms could be reached with sensing devices configured in this way. Modifications of the kinetics of the gas reactions with the sensing film occurred when modulating the temperature. They depended on the sensor

© Woodhead Publishing Limited, 2013

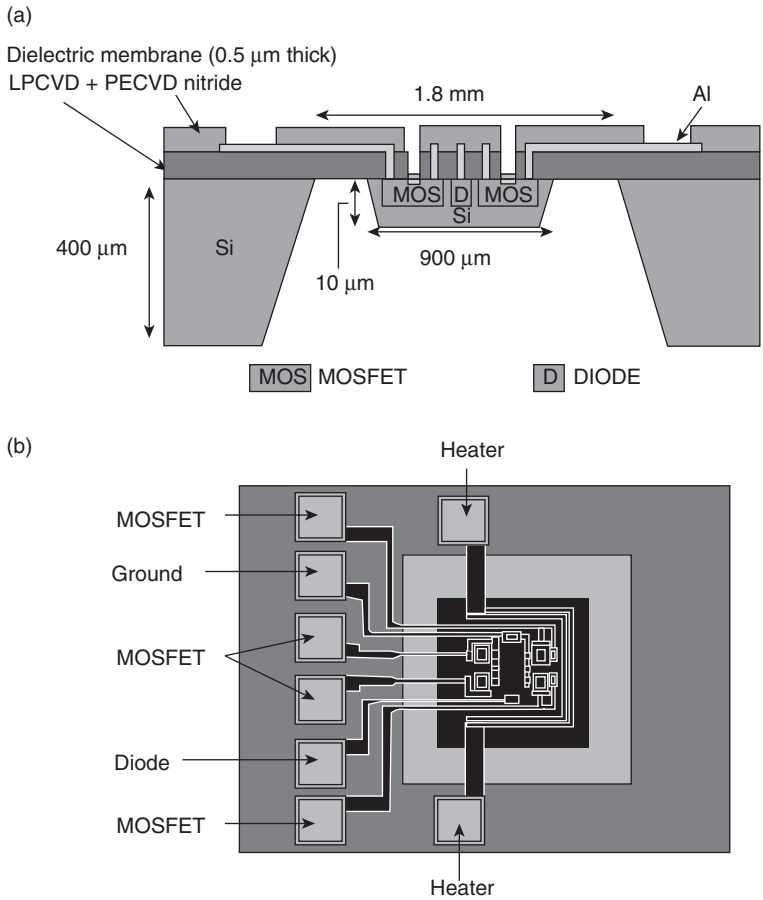

6.17 (a) Diagram of cross-sectional view of the low-power MOSFET array gas sensor. The electronic components are located in a silicon island insulated from the silicon chip frame by a dielectric membrane made of two nitride layers; (b) Optical image of the low-power micromachined MOSFET gas sensor showing the electronic devices in the silicon island suspended by a dielectric membrane. From Briand *et al.* (2000b).

'history', on the nature of the gaseous atmosphere and on the type of materials used as the catalytic film. Reduction of the recovery time of the device was achieved by performing a temperature pulse following the gas exposure, and the discrimination of gases in a mixture using temperature cycling (100°C to 200°C) was especially valuable, with an effective resolution at a temperature modulation of 'low' frequency (0.1 Hz) and large amplitude (Briand *et al.*, 2003). The data were Fourier transformed before

© Woodhead Publishing Limited, 2013

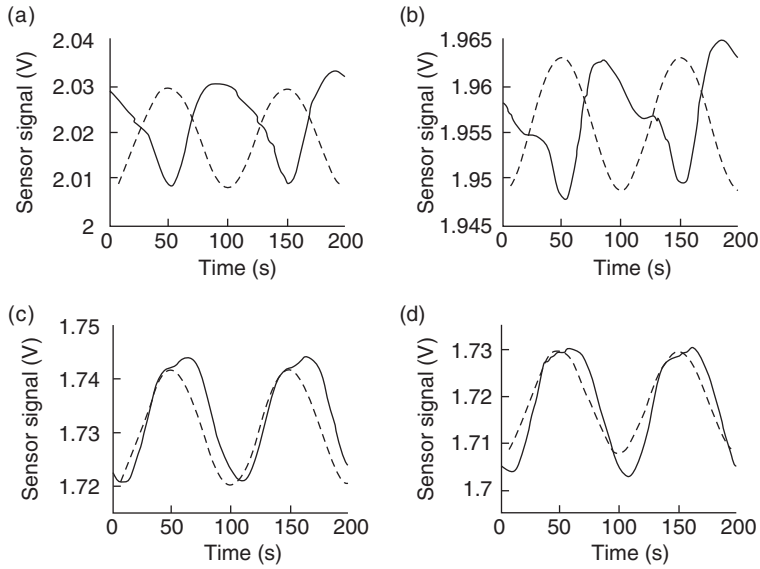

6.18 Ir-MOSFET voltage (continuous line) at a temperature variation between 150°C and 200°C at 0.01 Hz (dashed line) in the presence of (a) pure synthetic air; (b) 100 ppm H_2; (c) 10 ppm NH_3; (d) 10 ppm NH_3 and 100 ppm H_2. From Briand *et al.* (2003).

the evaluation was made using principal components analysis (PCA) plots. Discrimination was shown for gaseous mixtures of hydrogen and ammonia (10 to 100 ppm) in air (Fig. 6.18).

6.7 Trends and perspectives

The current trends with metal-oxide gas sensors are to improve their sensitivity, selectivity, stability and response time; and to reduce their power consumption, define the adapted mode of operations, and tune the materials to target new applications – for all of which, better performances, low cost and low power are required. The use of nanostructures is considered to improve the sensing characteristics of metal-oxide gas sensors and to induce new phenomena (see other chapters), even though some fundamental problems remain at all scales. The use of plastic substrates has been proposed to reduce power consumption and manufacturing efforts by using large-scale fabrication methods, such as printing techniques. The next sub-sections introduce the latest developments in integrating metal-oxide nanostructures onto hotplates and metal-oxide sensors onto polymeric foil.

© Woodhead Publishing Limited, 2013

6.7.1 Nanostructured gas sensing layers on micro-hotplates

Nanowires are seen as a solution with which to improve the sensitivity, selectivity, stability and response time of metal-oxide gas sensors. Meier *et al.* (2007) grew SnO_2 nanowires of 100 nm in diameter by the vapor-solid growth method. For testing, they were deposited onto micromachined hotplates with a focused ion beam scanning electron microscope (FIB-SEM), as shown in Fig. 6.19. Due to their diameter being similar to the Debye length, a completely depleted conduction channel can be obtained. Maximum response to CO and NH_3 occurred at about 260°C.

Materials other than SnO_2 also exhibited good gas sensing performances. Ryu *et al.* (2008) fabricated In_2O_3 nanowires by a laser ablation method. The nanowires were then sonicated in isopropanol to obtain a suspension, which was deposited onto micro-hotplates. When operating at 275°C, responses of

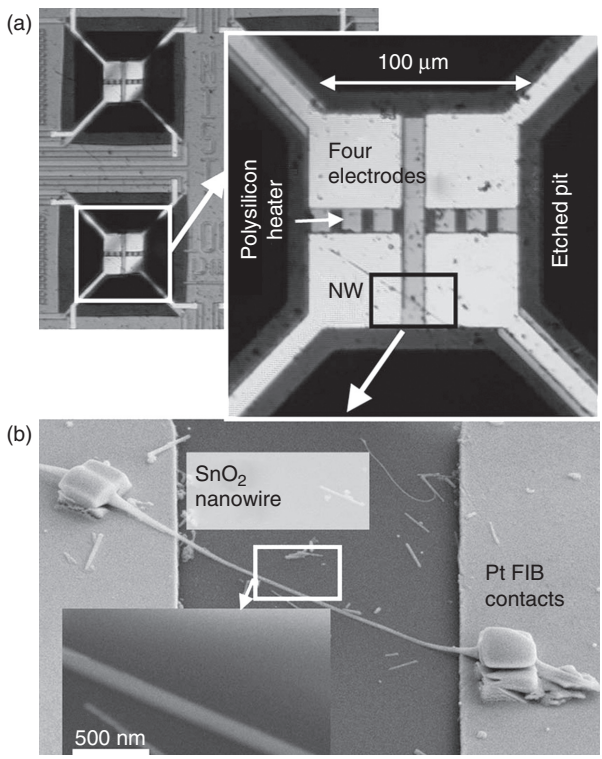

6.19 (a) Optical image of micro-hotplates with nanowires, NW. (b) SEM images of SnO_2 nanowire on a micro-hotplate. From Meier *et al.* (2007).

© Woodhead Publishing Limited, 2013

1.6 to 50 ppm of ethanol, of 2 to 100 ppm of CO and of 0.5 to 50 ppm of H_2 were measured. In addition, the micromachined gas sensor exhibited a short gas response time of about 22 seconds.

A main issue towards reducing the power consumption of metal-oxide gas sensors is their operating temperature, which is reduced in some cases by using nanostructures. Previous examples used micro-hotplates to reach the optimum thermal operating conditions. In an alternative move, Prades *et al.* (2010) addressed this problem by directly using the probing current applied to the nanowires as the heat source. This significantly simplified the device by avoiding the need for the integration of a heater into the hotplate. Moreover, it reduced the heated area and, consequently, power consumption. Currents in the range of 0.1 to 300 nA were flowing through an SnO_2 nanowire to heat it up to 300°C. The measured power consumption was 30 μW, two to three orders of magnitude lower than 'standard' micromachined metal-oxide gas sensors, making them compatible with energy harvesting systems. Very fast sensors were obtained with response times in the millisecond range. They had a good response to CO and NO_2. Si nanowires were used as gas sensors by McAlpine *et al.* (2007). The devices could operate at room temperature, drastically reducing their power consumption. They could be thus transferred on polyethylene terephthalate (PET) plastic foil as substrate (Fig. 6.20). A response of about 2 was obtained under an exposure of 2 ppm of NO_2. The detection of NO_2 concentrations as low as 20 ppb was possible. The device response time was up to few minutes,

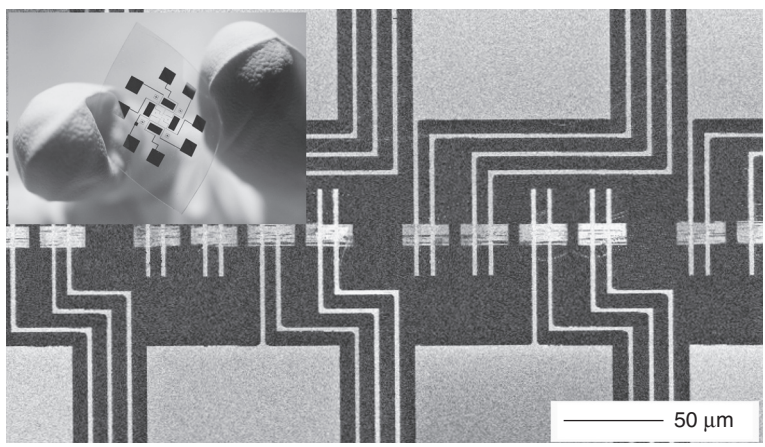

6.20 SEM image of an array of SNAP nanowire sensors. Each device (horizontal strip) is contacted by two Ti electrodes (oriented vertically) that extend to larger pads (top and bottom image edges). Inset: Digital photograph of the flexible sensor chip. From McAlpine *et al.* (2007).

© Woodhead Publishing Limited, 2013

depending on the gas concentration. Purge cycles with vacuum and fresh air were necessary for the sensor to recover after an exposure to NO_2. The nanowires could be functionalized with alkane-, aldehyde- and amino-silane to improve selectivity and allow differentiation of a binary mixture of acetone and hexane.

The fabrication of nanowires has been mastered and they have shown to be suitable for gas sensing. However, several issues remain for their large-scale use in commercial devices and for the achievement of reproducible results. It mainly concerns the precise location of the nanowires on a specific area and their electrical contact. From an operation point of view, to benefit from their low operational temperature for gas detection, sensitivity to humidity and slower desorption kinetics will need to be addressed in some cases.

6.7.2 Semiconductor gas sensors on polymeric foil

The use of plastic substrates, since 2008, has been seen as a solution to further decreasing sensor cost and manufacturing complexity, compared with devices manufactured on silicon or ceramic substrates. Plastic additionally shows other benefits, such as compatibility with large-scale fabrication (roll-to-roll), printing compatibility, light weight and conformality. Such devices aim at new applications where low cost is a prerequisite: smart-sensing labels, wearable devices, consumer goods, and so on. However, metallic oxides films are usually annealed at high temperature, and the main challenge of processing them and operating them on plastic substrates is the limited thermal budget. Nanowires, the flame spray pyrolysis deposition technique, and low sintering temperature nanoparticle inks are potential candidates for integration at a relatively low temperature onto polymeric transducing platforms of performing metal-oxide materials.

Briand *et al.* (2008) were the first to demonstrate the use of polyimide (PI) as a substrate for the fabrication of plastic-based metal-oxide gas sensors. Two types of devices were fabricated by standard microfabrication equipments. The first solution consisted in using silicon as the substrate, which was spin-coated with a PI layer. Once the bulk silicon was dry etched, a PI membrane embedding a Pt-based heater and with electrodes on top was released. The second solution was based on the use of a commercially available PI foil as the substrate. A Pt-heater was patterned and covered with a photosensitive spin-coatable PI layer used as a dielectric film to electrically insulate the electrodes on top. In both configurations, the interdigitated electrodes were drop-coated with a Pd-doped SnO_2 layer as the gas sensing film with a maximum annealing temperature at 450°C. These devices showed good gas sensing performances but suffered from excessive

© Woodhead Publishing Limited, 2013

power consumption when operating at 325°C: 82 mW for devices on silicon and 130 mW for the device on PI foil. To reduce power consumption, Courbat *et al.* (2010a) investigated the miniaturization of drop-coated metal-oxide gas sensors on PI foil. Their transducers were optimized in terms of power consumption and temperature uniformity through electrothermal simulations. Devices from 100 μm down to 15 μm were produced. With the idea of reducing power consumption further, the PI foil could be dry-etched in an O_2/CF_4 plasma to obtain closed and suspended membranes about 3 μm thick. The deposition of the metal-oxide layer (Pd-doped SnO_2) was carried out with micropipettes (Courbat *et al.*, 2012). The smallest droplet had a diameter of 20 μm (Fig. 6.21(a)). A power consumption as low as 6 mW was required to reach 300°C with a 15 μm-wide heater with a closed

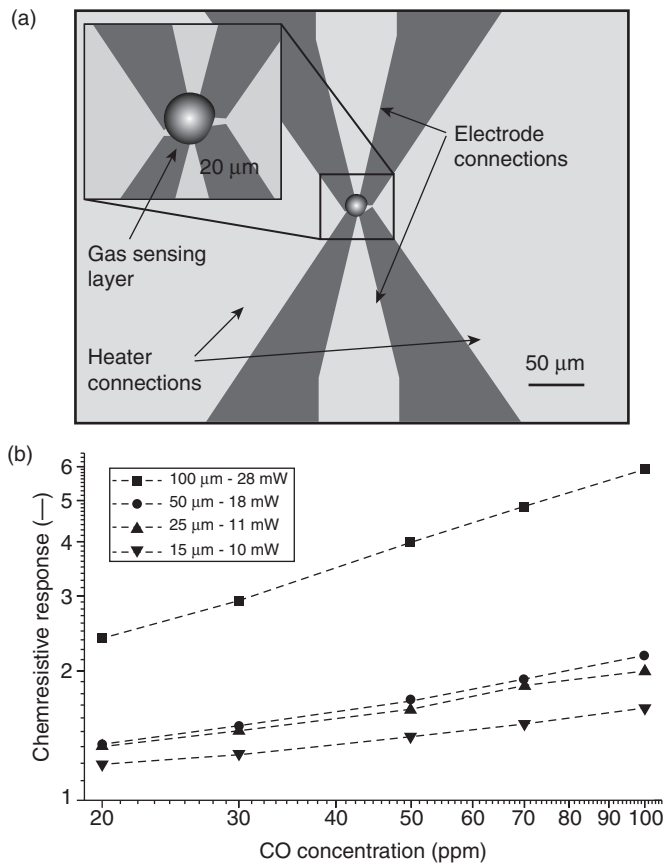

6.21 (a) Optical image (top view) of metal-oxide gas sensor on PI; (b) gas response to CO for several sensor sizes when operating at 250°C. Adapted from Courbat *et al.* (2012).

© Woodhead Publishing Limited, 2013

membrane in a continuous operating mode. With a simplified fabrication process avoiding the bulk micromachining of the PI foil, only 10 mW was necessary with a heater of the same size. These sensors could operate for more than one year at 200°C (Courbat *et al.*, 2011). The sensors worked in both continuous and pulsed modes, which decreases the power consumption to the sub-mW level. The devices showed to be effective for the detection of CO (Fig. 6.21(b)), CH_4 and NO_2. Further, a method for the encapsulation of chemical sensors at foil level was demonstrated (Courbat *et al.*, 2010b). It consisted in a pre-patterned rim made of a dry photoresist film laminated onto the PI substrate containing the gas sensors. They were covered with a water-repellent gas permeable membrane.

Recently, since 2010, with the emergence of printing techniques, new deposition methods compatible with large area manufacturing have been applied to gas sensing materials. Shen (2012) inkjet-printed pure and doped-SnO_2 on silicon and alumina substrates. The use of inkjet printing facilitated doping by the consecutive printing of SnO_2 and a dopant. A pure SnO_2-based sensor exhibited a response of about 7 to 50 ppm of ethanol and 55 when exposed to 50 ppm of H_2S when operating, respectively, at 425°C and 179°C. However, their printed layers required annealing at 550°C, making them incompatible with plastic substrates. This drawback was counteracted by Peter *et al.* (2011), who developed a titanium-doped chromium oxide (CTO) ink that did not require any firing. The adhesion to the silicon substrate and the film stability were improved by sintering the printed layer at 400°C. This temperature is, however, compatible with a high performance polymer such as some PIs. Moreover, being an additive technique, inkjet printing is of significant interest with regard to the local patterning of different sensing films on one substrate. In the case of arrays, all sensing material can be deposited simultaneously, simplifying fabrication of the device. Inkjet printing of gas sensitive metal-oxide films is now being implemented in the production line of gas sensor manufacturers, notably at IST AG in Switzerland.

Kukkola *et al.* (2011) used another technique compatible with roll-to-roll processing: gravure printing. They deposited WO_3 sensing films on interdigitated electrodes patterned on Kapton® HN PI foil from DuPont. However, the fabrication of an integrated heating element was not addressed in this study. For gas response measurement, the sensor was placed in a heated gas cell at 200°C. A gas response was obtained for a concentration of 5 ppm.

PET foils were used by McAlpine *et al.* (2007) as the substrate onto which nanotubes were deposited (see Section 6.7.1). The device showed itself to be suitable for measuring NO at room temperature. ZnO nanowires were grown on PI-based micro-hotplates by Zappa *et al.* (2012). Zn was sputtered onto the substrate through a shadow mask and then oxidized for 12 hours

© Woodhead Publishing Limited, 2013

at 300°C. Such a relatively low temperature was required to avoid damaging the plastic foil. The ZnO nanotubes showed a response towards NO_2.

The operation of metal-oxide gas sensors on plastic foil was successfully demonstrated. However, to make them fully compatible with large-scale fabrication techniques, additional work is required. So far, inkjet and gravure printing have been applied for the deposition of the gas sensing layer. However, the full printing of the transducers including the sensing layer still needs to be demonstrated.

6.8 Conclusion

Micromachined semiconductor gas sensors based on silicon micro-hotplate technology is now a mature technology with a few examples of devices on the market, mainly based on thick-film metal-oxides (notably SnO_2 and WO_3). Since the end of the 1980s, the technology has evolved significantly and offers very good models for their design and robust processes for their fabrication. Various efforts have led to devices that performing very well at operational temperatures above 500°C, with homogeneous temperature distribution over the sensing area and minimum power consumption. Power consumption for continuous operation is in the order of a few mW, and sub-mW consumption can be reached using a pulsing mode of operation. These platforms can now welcome many different types of semiconducting gas sensing materials, with various formations of device array, with the very interesting possibility of modulating the operational temperature and integrating the electronics with the sensor silicon chip. The concept of micro-hotplates has been extended to field-effect gas sensors also with reduced power consumption and thermal cycling capabilities. Trends and perspectives are mainly in relation to nanotechnology-based devices, with the integration of nanostructured gas sensing films on conventional micro-hotplates and especially on polymeric-based micro-hotplates. New processing methods are also being investigated for the integration of metal-oxide sensing layers onto micro-hotplate devices, such as flame spray pyrolysis, nanowires synthesis and the printing of metal-oxide sensing layers, mainly using inkjet. Finally, the authors of this chapter have been working on – and will hopefully achieve in the near future – a fully-printed version of metal-oxide gas sensors on large-area polymeric foil.

6.9 References

Afridi, M. Y., Suehle, J. S., Zaghoul, M. E., Berning, D. W., Hefner, A. R., Cavicchi, R. E., Semancik, S., Montgomery, C. B. and Taylor, C. J. (2002), 'A monolithic CMOS Microhotplate-based gas sensor system', *IEEE Sens. J.*, **2**(6), 644–55.

Ali, S. Z., Udrea, F., Milne, W. I. and Gardner, J. W. (2008), 'Tungsten based SOI microhotplates for smart gas sensors', *J. Microelectromech. S.*, **17**(6), 1408–17.

© Woodhead Publishing Limited, 2013

Barrettino, D., Graf, M., Taschini, S., Hafizovic, S., Hagleitner, C., Hierlemann, A. (2006), 'CMOS monolithic metal-oxide gas sensor microsystems', *IEEE Sens. Journal*, **6** (2), 276–86.

Barsan, N., Schweizer-Berberich, M. and Göpel, W. (1999), 'Fundamental and practical aspects in the design of nanoscaled SnO_2 gas sensors: a status report', *Fresnius J. Anal. Chem.*, **365**(4), 287–304.

Blaschke, M., Tille, T., Robertson, P., Mair, S., Weimar, U. and Ulmer, H. (2006), 'MEMS gas-sensor array for monitoring the perceived car-cabin air quality', *IEEE Sens. J.*, **6**(5), 1268–308.

Bosc, J.-M., Guo, Y., Sarihan, V. and Lee, T. (1998), 'Accelerated life testing for micromachined chemical sensors', *IEEE Trans. Rel.*, **47**(2), 135–41.

Brattain, W. H. and Bardeen, J. (1952), 'Surface properties of germanium', *Bell Syst. Tech. J.*, **32**, 1.

Briand, D., Beaudoin, F., Courbat, J., de Rooij, N. F., Desplats, R. and Perdu, P. (2005) 'Failure analysis of micro-heating elements suspended on thin membranes', *Microelec. Rel.*, **45**, 1786–9.

Briand, D., Colin, S., Courbat, J., Raible, S., Kappler, J. and de Rooij, N. F. (2008), 'Integration of MOX gas sensors on polyimide hotplates', *Sens. Actuators B*, **130**, 430–5.

Briand, D., Guillot, L., Raible, S., Kappler, J. and de Rooij, N. F. (2007), 'Highly integrated wafer level packaged MOX gas sensors', in *Proceedings of the Transducers'07 conference*, Lyon, France, June 10–14, 2007, 2401–4.

Briand, D., Krauss, A., van der Schoot, Weimar U., Barsan, N., Göpel, W. and de Rooij, N. F. (2000a), 'Design and fabrication of high-temperature micro-hotplate for drop-coated gas sensors', *Sens. Actuators B*, **68**, 223–33.

Briand, D., Sundgren, H., van der Schoot, B., Lundström, I. and de Rooij, N. F. (2001), 'Thermally isolated MOSFET for gas sensing application', *IEEE Electr. Device L*, **22**(1), 11–13.

Briand, D., Tomassone, G.-M. and de Rooij, N. F. (2003) 'Accelerated ageing of micro-hotplates for gas sensing applications', in *Proceedings of IEEE Sensors 2003 conference*, Toronto, Canada, 1314–17.

Briand, D., van der Schoot, B., de Rooij, N. F., Sundgren, H. and Lundström, I. (2000b), 'A low-power micromachined MOSFET gas sensor', *J. Microelectromech. S.*, **9**(3), 303–8.

Briand, D., Wingbrant, H., Sundgren, H., van der Schoot, B., Ekedahl, L.-G., Lundström, I. and de Rooij, N. F. (2003), 'Modulated operating temperature for MOSFET gas sensors: Hydrogen recovery time reduction and gas discrimination', *Sens. Actuators B*, **93**, 276–85.

Cavicchi, R. E., Suehle, J. S., Kreider, K. G., Gaitan, M. and Chaparala, P. (1995), 'Fast temperature programmed sensing for micro-hotplate gas sensors', *IEEE Electron Device Lett.*, **16**(6), 286–8.

Cerdà Belmonte, J., Puigcorbé, J., Arbiol, J., Vilà, A., Morante, J. R., Sabaté, N., Gràcia, I. and Cané, C. (2006), 'High-temperature low-power performing micromachined suspended micro-hotplate for gas sensing applications', *Sens. Actuators B*, **114**, 826–35.

Courbat, J., Briand, D. and de Rooij, N. F. (2008) 'Reliability improvement of suspended platinum-based micro-heating elements', *Sens. Actuators A*, **142**, 284–91.

Courbat, J., Briand, D. and de Rooij, N. F. (2010b), 'Foil level packaging of a chemical gas sensor', *J. Micromech. Microeng.*, **20**, 055026.

© Woodhead Publishing Limited, 2013

Courbat, J., Briand, D. and de Rooij, N. F. (2011), 'Reliability of micro-hotplates on polyimide foil', in *Proceedings Transducers'11 Conference*, Beijing, China, 338–41.

Courbat, J., Briand, D., Yue, L., Raible, S. and de Rooij, N. F. (2012), 'Drop-coated metal-oxide gas sensor on polyimide foil with reduced power consumption for wireless applications', *Sens. Actuators B*, **161**, 862–8.

Courbat, J., Canonica, M., Teyssieux, D., Briand, D. and de Rooij, N. F. (2010a), 'Design and fabrication of micro-hotplates made on a polyimide foil: electrothermal simulation and characterization to achieve power consumption in the low mW range', *J. Micromech. Microeng.*, **21**, 015014.

Creemer, J. F., Briand, D., Zandbergen, H. W., van der Vlist, W., de Boer, C. R., de Rooij, N. F. and Sarro, P. M. (2008), 'Microhotplates with TiN heaters', *Sens. Actuators A*, **148**, 416–21.

Demarne, V. and Grisel, A. (1988), 'An integrated low-power thin-film CO gas sensor on silicon', *Sens. Actuators*, **13**, 301–13.

Ehmann, M., Ruther, P., von Arx, M. and Paul, O. (2001), 'Operation and short-term drift of polysilicon-heated CMOS microstructures at temperatures up to 1200 K', *J. Micromech. Microeng*, **11**(4), 397–401.

Elmi, I., Zampolli, S. and Cardinali, G. C. (2008a), 'Optimization of a wafer-level process for the fabrication of highly reproducible thin-film MOX sensors' *Sens. Actuators B*, **131**, 548–55.

Elmi, I., Zampolli, S., Cozzani, E., Mancarella, F. and Cardinali, G. C. (2008b), 'Development of ultra-low-power consumption MOX sensors with ppb-level VOC detection capabilities for emerging applications', *Sens. Actuators B*, **135**, 342–51.

Espinosa, E., Ionescu, R., Zampolli, S., Elim, I., Cardinali, G. C., Abad, E., Leghrib, R., Ramírez, J. L., Vilanova, X. and Llobet, E. (2010), 'Drop-coated sensing layers on ultra low power hotplates for an RFID flexible tag microlab', *Sens. Actuators B*, **144**, 462–6.

Faglia, G., Comini, E., Cristalli, A., Sberveglieri, G. and Dori, L. (1999), 'Very low power consumption micromachined CO sensors', *Sens. Actuators B*, **55**, 140–6.

Friedberger, A., Kreisl, P., Rose, E., Müller, G., Kühner, G., Wöllenstein, J. and Böttner, H. (2003), 'Micromechanical fabrication of robust low-power metal oxide gas sensors', *Sens. Actuators B*, **93**, 345–9.

Gardner, J. W., Guha, P. K., Udrea, F. and Covington, J. (2010), 'CMOS Interfacing for Integrated Gas Sensors: A Review', *IEEE Sens. J.*, **10**(12), 1833–48.

Gardner, J. W., Pike, A., de Rooij, N. F., Koudelka-Hep, M., Clerc, P. A., Hierlemann, A. and Göpel, W. (1995), 'Integrated array sensor for detecting organic solvents', *Sens. Actuators B*, 26–7, 135–9.

Graf, M., Barrettino, D., Zimmermann, M., Hierlemann, A., Baltes, H., Hahn, S., Barsan, N. and Weimar, U. (2004a), 'CMOS monolithic metal-oxide sensor system comprising a microhotplate and associated circuitry', *IEEE Sens. J.*, **4**(1), 9–16.

Graf, M., Gurlo, A., Bârsan, N., Weimar, U. and Hierlemann, A. (2006a), 'Microfabricated gas sensor systems with sensitive nanocrystalline metal-oxide films', *Journal of Nanopart. Res.*, **8**(6), 823–39.

Graf, M., Müller, S. K., Barrettino, D. and Hierlemann, A. (2005), 'Transistor heater for microhotplate-based metal-oxide microsensors', *IEEE Elect. Dev. Lett.*, **26**(5), 295–7.

Heilig, A., Bârsan, N., Weimar, U., Schweizer-Berberich, M., Gardner, J. W. and Göpel, W. (1997), 'Gas identification by modulating temperatures of SnO_2-based thick film sensors', *Sens. Actuators B*, **43**, 45–51.

© Woodhead Publishing Limited, 2013

Ho, G. W. (2011), 'Gas sensors with nanostructures oxide semiconductor materials', *Sci. Adv. Mat.*, **3**(2), 150–68.

Ishibashi, N. and Kaneyasu, K. (2009), 'Development and application of semiconductor gas sensor using MEMS technology', presented at *3rd GOSPEL Workshop: Gas Sensors Based on Semiconducting Metal Oxide – New Directions*, Tübingen, Germany, November 30–December 1, 2009.

Ivanov, P., Stankova, M., Llobet, E., Vilanova, X., Brezmes, J., Gràcia, I., Cané, C., Calderer, J. and Correig, X. (2005), 'Nanoparticle metal-oxide films for micro-hotplate-based gas sensor systems', *IEEE Sens. J.*, **5**(5), 798–809.

Kappler, J., Barsan, N., Weimar, U., Dieguez, A., Alay, J. L., Romano-Rodriguez, A., Morante, J. R. and Göpel, W. (1998) 'Correlation between XPS, Raman and TEM measurements and the gas sensitivity of Pt and Pd doped SnO2 based gas sensors', *Fresenius J. Anal. Chem.*, **361**(2), 110–14.

Kühne, S., Graf, M., Tricoli, A., Mayer, F., Pratsinis, S. E. and Hierlemann, A. (2008), 'Wafer-level flame-spray-pyrolysis deposition of gas-sensitive layers on microsensors', *J. Micromech. Microeng.*, **18**, 035040.

Kunt, T. A., McAvoy, T. J., Cavicchi, R. E. and Semancik, S. (1998), 'Optimization of temperature programmed sensing for gas identification using micro-hotplate sensors', *Sens. Actuators B*, **53**, 24–43.

Kreisl, P., Helwig, A., Müller, G., Obermeier, E. and Sotier, S. (2005), 'Detection of hydrocarbon species using silicon MOS field-effect transistors operated in a non-stationary temperature-pulse mode', *Sens. Actuators B*, **106**, 442–9.

Kukkola, J., Jansson, E., Popov, A., Lappalainen, J., Mäklin, J., Halonen, N., Tóth, G., Shchukarev, A., Mikkola, J.-P., Jantunen, H., Kordás, K., Hast, J., Hassinen, T., Sunnari, A., Jokinen, K., Haverinen, H., Sliz, R., Jabbour, G., Fabritius, T., Myllylä, R., Vasiliev, A. and Zaretskiy, N. (2011), 'Novel printed nanostructured gas sensors', *Procedia Engineering*, **25**, 896–9.

Laconte, J., Dupont, C., Flandre, D. and Raskin, J.-P. (2004), 'SOI CMOS compatible low power microheater optimization for the fabrication of smart gas sensors', *IEEE Sensors J.*, **4**(5), 670–80.

Lee, A. P. and Reedy, B. J. (1999), 'Temperature modulation in semiconductor gas sensing', *Sens. Actuators B*, **60**, 35–42.

Llobet, E., Brezmes, J., Ionescu, R., Vilanova, X., Al-Khalifa, S., Gardner, J. W., Barsan, N. and Correig, X. (2002), 'Wavelet transform and fuzzy ARTMAP-based pattern recognition for fast gas identification using a micro-hotplate gas sensor', *Sens. Actuators B*, **83**(1–3), 238–44.

Llobet, E., Ivanov, P., Vilanova, X., Brezmes, J., Hubalek, J., Malysz, K., Gràcia, I., Cané, C. and Correig, X. (2003), 'Screen-printed nanoparticles tin oxide films for high-yield sensor microsystems', *Sens. Actuators B*, **96**, 94–104.

Lloyd-Spetz, A., Baranzahi, A., Tobias, P. and Lundström, I. (1997), 'High temperature sensors based on metal-insulator-silicon carbide devices, *Phys. Status Solidi A.*, **162**(1), 493–511.

Lundström, I., Shivaraman, S., Svensson, C. and Lundkvist, L. (1975), 'A hydrogen-sensitive MOS field-effect transistor', *Appl. Phys. Lett.*, **26**, 55–7.

Lundström, I., Sundgren, H., Winquist, F., Eriksson, M., Krantz-Rülcker, C. and Lloyd-Spetz, A. (2007), 'Twenty-five years of field effect gas sensor research in Linköping', *Sens. Actuators B*, **121**(1), 247–62.

Lyle, R. P., Hughes, H. G. and Walters, D. (1997), 'Micromachined silicon CO gas sensors', *Electrochem. Soc. Proc.*, **97**(5), 188–98.

© Woodhead Publishing Limited, 2013

McAlpine, M. C., Ahmad, H., Wang, D. and Heath, J. R. (2007), 'Highly ordered nanowire arrays on plastic substrates for ultrasensitive flexible chemical sensors', *Nat. Mater.*, **6**, 379–84.

Mardilovich, P., Routkevitch, D. and Govyadinov, A. (2000), 'Hybrid micromachining and surface microstructuring of alumina surface', *Conf. Proc. of Microfabricated Systems and MEMS V*, 198th ECS Meeting, pp. 33–42.

Meier, D. C., Semancik, S., Button, B., Strelcov, E. and Kolmakov, A. (2007), 'Coupling nanowire chemiresistors with MEMS microhotplate gas sensing platforms', *Appl. Phys. Lett.*, **91**, 063118.

Mele, L., Santagata, F., Iervolino, E., Mihailovic, M., Rossi, T., Tran, A. H., Schellevis, H., Creemer, J. F. and Sarro, P. M. (2012), 'A molybdenum MEMS microhotplate for high-temperature operation' *Sens. Actuators A*, **188**, 173–80.

Müller, G., Friedberger, A., Kreisl, P., Ahlers, S., Schulz, O. and Becker, T. (2003), 'A MEMS toolkit for metal-oxide-based gas sensing systems', *Thin Solid Film*, **436**, 34–45.

Nakata, S., Okunishi, H. and Nakashima, Y. (2006), 'Distinction of gases with a semiconductor sensor under a cyclic temperature modulation with second-harmonic heating', *Sens. Actuators B*, **119**, 556–61.

Panchapakesan, B., Cavicchi, R., Semancik, S. and DeVoe, D. L. (2006), 'Sensitivity, selectivity and stability of tin oxide nanostructures on large area arrays of microhotplates', *Nanotechnology*, **17**(2), 415–25.

Peter C., Kneer, J. and Wöllenstein, J. (2011), 'Inkjet printing of titanium doped chromium oxide for gas sensing application,' *Sens Lett*, **9**, 1–5.

Prades, J. D., Jimenez-Diaz, R., Hernandez-Ramirez, F., Cirera, A., Romano-Rodriguez, A. and Morante, J. R. (2010), 'Harnessing self-heating in nanowires for energy efficient, fully autonomous and ultra-fast gas sensors', *Sens. Actuators B*, **144**, 1–5.

Puigcorbé, J., Vilà, A., Cerdà, J., Cirera, A., Gràcia, I., Cané, C. and Morante, J. R. (2002), 'Thermo-mechanical analysis of micro-drop coated gas sensors', *Sens. Actuators A*, 97–8, 379–85.

Puigcorbé, J., Vogel, D., Michel, B., Vilà, A., Gràcia, I., Cané, C. and Morante, J. R. (2003), 'Thermal and mechanical analysis of micromachined gas sensors', *J. Micromech. Microeng.*, **14**, 548–56.

Raible, S., Briand, D., Kappler, J. and de Rooij, N. F. (2006), 'Wafer level packaging of micromachined gas sensors', *IEEE Sens. J*, **6**(5), 1232–5.

Ratton, L., Kunt, T., McAvoy, T., Fuja, T., Cavicchi, R. and Semancik, S. (1997), 'A comparative study of signal processing techniques for clustering microsensor data (a first step towards an artificial nose)', *Sens. Actuators B*, **41**, 105–20.

Ryu, K., Zhang, D. and Zhou, C. (2008), 'High-performance metal oxide nanowire chemical sensors with integrated micromachined hotplates', *Appl. Phys. Lett.*, **92**, 093111.

Sahm, T., Mädler, L., Gurlo, A., Barsan, N., Pratsinis, S. E. and Weimar, U. (2004), 'Flame spray synthesis of tin dioxide nanoparticles for gas sensing', *Sens. Actuators B*, **98**, 148–53.

Sears, W. M., Colbow, K. and Consadori, F. (1989), 'General-characteristics of thermally cycled tin oxide gas sensors', *Semicond Sci. Technol.*, **4**(5), 351–9.

Seiyama, T., Kato, A., Fujushi, K. and Nagatani, M. (1962), 'A new detector for gaseous components using semiconductive thin films', *Anal. Chem.*, **34**, 1502–3.

© Woodhead Publishing Limited, 2013

Semancik, S., Cavicchi, R. E., Wheeler, M. C., Tiffany, J. E., Poirier, G. E., Walton, R. M., Suehle, J. S., Panchapakesan, B. and DeVoe, D. L. (2001), 'Microhotplate platforms for chemical sensor research', *Sens. Actuator B*, **77**, 579–91.

Shen, W. (2012), 'Properties of SnO2 based gas-sensing thin films prepared by ink-jet printing', *Sens. Actuators B*, 166–7, 110–16.

Simon, I., Barsan, N., Bauer, M. and Weimar, U. (2001), 'Micromachined metal oxide gas sensors: Opportunities to improve sensor performance', *Sens. Actuators B*, **73**, 1–26.

Suehle, J. S., Cavicchi, R. E., Gaitan, M. and Semancik, S. (1993), 'Tin oxide gas sensor fabricated using CMOS micro-hotplates and in-situ processing' *IEEE Electr. Device. Lett.*, **14**, 118–20.

Vasiliev, A., Pavelko, R. G., Gogish-Klushin, S. Y., Kharitonov, D. Y., Gogish-Klushina, O. S., Sokolov, A. V., Pisliakov, A. V. and Samotaev, N. N. (2008), 'Alumina MEMS platform for impulse semiconductor and IR optic gas sensors', *Sens. Actuators B*, **132**(1), 216–23.

Vincenzi, D., Butturi, M. A., Guidi, V., Carotta, M. C., Martinelli, G., Guarnieri, V., Brida, S., Margesin, B., Giacomozzi, F., Zen, M., Pignatel, G. U., Vasiliev, A. A. and Pisliakov, A. V. (2001), 'Development of a low-power thick-film gas sensor deposited by screen-printing technique onto a micromachined hotplate', *Sens. Actuators B*, **77**, 95–9.

Viricelle, J.-P., Pijolat, C., Riviere, B., Rotureau, D., Briand, D. and de Rooij, N. F. (2006), 'Compatibility of screen-printing technology with micro-hotplate for gas sensor and solid oxide fuel cell development', *Sens. Actuators B*, **118**, 263–8.

Wöllenstein, J., Plaza, J. A., Cané, C., Min, Y., Böttner, H. and Tuller, H. L. (2003), 'A novel single chip thin film metal oxide array', *Sens. Actuators B*, **93**, 350–5.

Zappa, D., Briand, D., Comini, E., Courbat, J., de Rooij, N. F. and Sberveglieri, G. (2012), 'Zinc oxide nanowires deposited on polymeric hotplates for low-power gas sensors', in *Proceedings of the Eurosensors 2012 conference*, Cracow, Poland.

© Woodhead Publishing Limited, 2013

7

Semiconducting direct thermoelectric gas sensors

F. RETTIG and R. MOOS, University of Bayreuth, Germany

DOI: 10.1533/9780857098665.2.261

Abstract: This chapter deals with semiconducting direct thermoelectric gas sensors based on oxide materials. The principle of the sensor is based on a direct measurement of the position of the Fermi level, which can be strongly dependent on the concentration of an analyte in the ambience. The direct thermoelectric gas sensor principle measures a path-independent quantity – the thermovoltage. This makes the sensors extremely resistant to damage stemming from abrasives in gas streams. This chapter shows the importance of developing an adequate transducer, and includes a careful analysis of the sensor signals obtained. From a technological point of view, an integration of an equipotential layer for better signal quality will appear to be necessary. Considerable effort is spent on the thermal design of the transducers using finite element method (FEM) modeling. The gas sensitive material itself is analyzed by an FEM model in terms of semiconductor equations combined with thermoelectric equations. The R&D efforts described culminate in a transfer to real-world sensors, which is reported in the final section. The direct thermoelectric gas sensors manufactured show a fast response, and are stable and reproducible. Direct thermoelectric gas sensors can be an alternative to the commonly-used resistive or conductometric gas sensors.

Key words: gas sensor, thermopower, thermoelectric, simulation, tin oxide.

7.1 Introduction

This introductory section will describe the various issues that are motivating research on direct thermoelectric gas sensors before presenting a brief introduction to thermoelectric power for the general reader. The principles of direct and indirect thermoelectric gas sensors are then outlined, while early research work is reviewed in the final subsection.

7.1.1 Motivation for research on direct thermoelectric gas sensors

Gas sensors play an important role in many applications, and have been extensively developed during the past few decades. This is especially the

© Woodhead Publishing Limited, 2013

case for applications in monitoring automotive exhaust gases (lambda probe) and air quality (AQ sensors). Although the lambda probe itself cannot reduce polluting emissions from automobiles, it allows the adjustment of a stoichiometric mixture of air and fuel (Riegel *et al.*, 2002). A modern concept with two lambda probes even allows detection of a defect in a three-way catalyst (Moos, 2005). AQ sensors can monitor the air quality in houses and cars (Denk *et al.*, 1999), as well as detecting concentrations of unburnt hydrocarbons (Williams, 1999), an important point in fire prevention. Other applications include alerting people when harmful gases are in the ambient atmosphere. (Yamazoe, 2005).

Since the 1960s, many research activities have been addressed to resistive (also known as 'conductometric') gas sensors. Since the development of Taguchi's sensor based on SnO_2 (Taguchi, 1970), many semiconducting materials have been investigated and analyzed. Besides SnO_2, the most prominent examples are: TiO_2 (Logothetis and Kaiser, 1983; Takami, 1988); $SrTiO_3$ (Gerblinger and Meixner, 1991; Schönauer, 1991); $SrTi_xFe_{1-x}O_{3-\delta}$ (Williams, 1985; Moos *et al.*, 2000); WO_3 (Cantalini *et al.*, 1996); Ga_2O_3 (Lampe *et al.*, 1994); Cr_2O_3 (Jayaraman *et al.*, 1999; Niemeyer *et al.*, 2002; Ruiz *et al.*, 2003); or ZnO (Chou *et al.*, 2006). Many of these materials are discussed elsewhere in this book. The appeal of resistive gas sensors is the relative simplicity of manufacturing resistive sensors combined with an uncomplicated principle for taking measurements. Some of these materials have been tested in automotive exhausts (e. g. Gerblinger and Meixner, 1991; Lampe *et al.*, 1994; Takami, 1988; Moos *et al.*, 2003). However, harsh environments are a challenge for resistive gas sensors, since poisoning or deterioration of the gas sensitive materials by aggressive components like SO_2 or NO_x may occur, or abrasion of the gas sensitive layer by particle-containing high velocity gas streams may cause irreversible harm to the gas sensors (Rettig *et al.*, 2004). This is easy to understand since each geometric change – which may occur, for instance, by abrasion – can have a marked effect on the resistance and cause flawed concentration readings. Protective layers were proposed to overcome these problems (Gerblinger *et al.*, 1993; Rettig *et al.*, 2003).

For application in exhausts, potentiometric or amperometric gas sensors based on ion conduction membranes of yttria stabilized zirconia (YSZ) are typically used (Ivers-Tiffée *et al.*, 2001; Riegel *et al.*, 2002). Such sensors provide sufficient stability against harsh environments. The potentiometric principle offers the possibility of measuring a path-independent quantity – the electrical potential difference (voltage). In theory, abrasion does not significantly affect the sensor signals. These advantages come at the cost of a more complicated design where potentiometric and amperometric gas sensors are concerned, – for instance, the classical lambda probe requires an air reference (Somov and Guth, 1998), or a pumped reference (Baunach *et al.*, 2006).

Semiconducting direct thermoelectric gas sensors (DTEGs) do not have the disadvantages of resistive or potentiometric gas sensors. The measurand

© Woodhead Publishing Limited, 2013

is a path-independent thermovoltage and no gas reference is required. The typical materials used in resistive gas sensors can also be utilized for DTEGs. In this chapter, it will be shown that intrinsic semiconducting materials have an enhanced sensitivity compared with classical *p*- or *n*-type conducting materials. These advantages are the main drivers for the research and development of DTEGs.

In the next section, a short introduction is given to the term 'thermoelectric power' or 'Seebeck coefficient', and some early research activities on DTEGs are summarized. The main part of this chapter deals with measurement techniques, modeling and simulation of DTEGs based on semiconducting oxides. Recent results obtained with some semiconducting materials, together with a consideration of ionic DTEGs, complete the main part of this chapter. The chapter concludes with a discussion on the disadvantages and drawbacks of DTEGs, and possible future research topics.

7.1.2 Thermoelectric power

The intention of this section is to give the inexperienced reader a short introduction to the physical background of thermopower, also known as 'thermoelectric power'. The reader is referred to *Thermoelectricity* (Heikes and Ure, 1961), for a more detailed analysis.

The simplest treatment of the thermopower for semiconductors is based on the fact that the velocity of electrons increases with increasing temperature. Let us assume a wire that is divided along its length into a low-temperature section and a high-temperature section. In cross-section, at the point in the middle where the two sections meet, all electrons that pass the interface are counted. After a certain time, more electrons will have traveled from the high-temperature section to the low-temperature section than vice versa. As a result, an electrical voltage evolves between both sections to compensate the driving force. In the book of Heikes and Ure (1961) a detailed calculation is given for a semiconductor assuming a Boltzmann distribution of the electrons and a temperature gradient in a certain direction. The thermovoltage is caused by the thermal diffusion of the charge carriers in the temperature gradient in the different sections of the wire. The calculation clearly demonstrates that temperature-dependent contact voltages do not play a role in the measured thermovoltage. As a result, the thermopower (Seebeck coefficient), η, of pure *n*-type, pure *p*-type and mixed *n*–*p*-type conductors can be expressed, respectively, by Equations [7.1], [7.2] and [7.3] (e.g. Choi *et al.*, 1986):

$$\eta_{\text{n-conductor}} = -\frac{k_B}{e}\left(\ln\frac{N_C}{n} + A_e\right) \qquad [7.1]$$

$$\eta_{\text{p-conductor}} = \frac{k_B}{e}\left(\ln\frac{N_V}{p} + A_h\right) \qquad [7.2]$$

© Woodhead Publishing Limited, 2013

$$\eta = \frac{\sigma_n \eta_n + \sigma_p \eta_p}{\sigma_n + \sigma_p} \quad [7.3]$$

In these equations, k_B is the Boltzmann constant, e is the electron charge, N_C and N_V are the effective densities of states in the conduction band and in the valence band, A_e and A_h are the transport constants representing the scattering mechanism, n and p are the concentration of electrons in the conduction band and holes in the valence band, and σ_n and σ_p are the conductivities of the electrons and the holes.

The second, more general, treatment is based on nonequilibrium thermodynamics. Fluxes and forces are connected by a matrix. The diagonal elements (the main effects) of this matrix are well-known – for example, the diffusion coefficient (which is the connection between a particle flux under a concentration gradient) or the thermal conductivity (which relates the temperature gradient with the heat flux). One of the non-diagonal elements is the Seebeck coefficient (= thermopower, η), which relates a temperature gradient with a particle flux. Based on this, general equations are obtained that describe the heat and particle flow in a thermal and concentration profile:

$$\begin{aligned} &\mathrm{div}(\sigma \cdot \mathrm{grad} V_{\text{thermoelectric}} + \sigma\eta \cdot \mathrm{grad} T) = 0 \\ &\mathrm{div}(\sigma\eta T \cdot \mathrm{grad} V_{\text{thermoelectric}} + \kappa \cdot \mathrm{grad} T) \approx 0 \end{aligned} \quad [7.4]$$

Here, σ is the conductivity, $V_{\text{thermoelectric}}$ is the thermovoltage, η the Seebeck coefficient, T the temperature, and κ is the thermal conductivity for a vanishing electrical field. The second equation is here set to zero, since Joule heating as a second order effect does not play a significant role. More details can be found in Rettig (2008), or Nagy and Nayfeh (2000).

7.1.3 Direct and indirect thermoelectric gas sensors

Thermoelectric gas sensors can be divided more or less arbitrarily into direct and indirect thermoelectric gas sensors. Until recently, research has been mainly addressed to indirect gas sensors, and DTEGs have rarely been studied. Figure 7.1 explains the working principle for both types of thermoelectric gas sensor.

Indirect thermoelectric gas sensors use the heat of an exothermic reaction that stems from a combustible analyte. The temperature on a catalytically coated area of a (usually planar) substrate increases with the concentration of the analyte (Shin *et al*., 2003). The temperature difference between a catalytically inactive area on the substrate is usually measured either by thermocouples or by thermopiles. Therefore, this type of sensor is called an 'indirect thermoelectric gas sensor'. Its measurement principle is similar to pellistor sensors (Willet, 2005). The thermoelectric material itself should not be catalytically active. The catalytically active coating of the thermoelectric

© Woodhead Publishing Limited, 2013

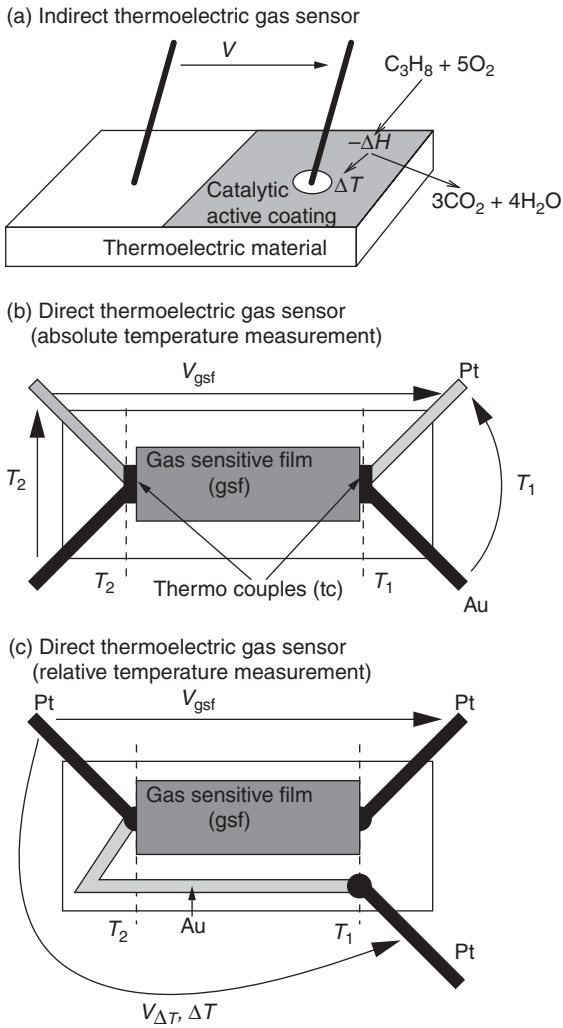

7.1 Principle of the set-up of (a) indirect, and (b) and (c) direct, thermoelectric gas sensors. The difference between (b) and (c) is the method of measuring the temperature difference ΔT. Reprinted from Rettig (2008) with permission from Shaker-Verlag.

material defines both the sensitivity and the selectivity of the sensors. As an example, the reader is referred to Shin *et al*. (2003) or Balducci *et al*. (2005), where further information on indirect thermoelectric gas sensors is given.

In contrast, in direct thermoelectric gas sensors (DTEGs) the Seebeck coefficient (thermopower, η) of the gas sensitive material itself changes when the concentration of the analyte varies in the ambient atmosphere. The density of the free electrons and/or defect electrons (holes) – or, in other words, the Fermi level – is directly affected by a changing analyte gas

© Woodhead Publishing Limited, 2013

concentration. There are several possible physical effects to explain how the Fermi level can be dependent on the gas phase. Chemisorption, for instance, may occur following the reaction:

$$O_2 + 2e^- \leftrightarrow 2O^-_{ads} \qquad [7.5]$$

This chemisorption process captures electrons from the gas sensitive material. Therefore, a space charge region evolves from the interface of the material and the gas phase. In porous structures, this interface is typically the grain surface. For an *n*-type semiconductor like SnO_2, electrons are depleted in this region, resulting in an increased resistance not only for the whole grain, but also for the whole gas sensitive film. If reducing gases are present, they may consume the chemisorbed oxygen and the electron is transferred back to the gas sensitive material, the space charge regions vanishes partly, and the resistance of the gas sensitive material decreases, often by decades.

Typically, at higher temperatures one finds effects in which the bulk of the material is involved. The electron concentration in the bulk material can be modulated by ex- or in-corporation of oxygen according to:

$$\frac{1}{2}O_2 + 2e^- + V_O^{\bullet\bullet} \leftrightarrow O_O^x \qquad [7.6]$$

Then, the oxygen partial pressure of the surrounding gas atmosphere is the driver for a change in the electron concentration. These examples clearly show that DTEGs are based on the same physical principles as conductometric gas sensors, since in both cases the analyte concentration modulates the electron density. However, the measurand is different. In conductometric devices, the material property 'conductivity' changes and, hence, the resistance of a sensor varies with the analyte concentration. In contrast, the determination of thermopower is more complicated, since not only the thermovoltage has to be measured, but also a known temperature difference has to be applied or, at least, measured.

7.1.4 Early research activities

The concept of DTEGs is not a recent one. Several authors worked on this topic in the 1980s, but no systematic studies were conducted at that time. Pisarkiewicz and Stapinski (1989) reported on the change of the Seebeck coefficient of SnO_2 when applying reducing gases. The effect was attributed to a modulation of the depletion layer at the grain surfaces affecting the Fermi level. Siroky (1993) used a thermoelectric gas sensor based on SnO_2 to detect flammable gases. Here, it was considered to measure thermopower and conductivity in parallel. Mizsei (1995) also explained the change of the thermoelectric power of palladium-activated tin oxide SnO_2 in the presence of H_2 with the affected depletion layer. Moos (1998) described a method for

© Woodhead Publishing Limited, 2013

measuring the oxygen content of a gas by using the thermoelectric effect of a bulk material. Ionescu (1998) reported on a SnO_2 gas sensor with increased selectivity using simultaneous measurement of resistance and the Seebeck coefficient. In 2000, Liess and Steffes (2000) presented a DTEG based on In_2O_3, and Smulko *et al*. (2005) used thermoelectric voltage fluctuations for gas sensing. However, it should be noted that this early work was scattered research, without a holistic consideration of the material and the correspondingly requisite transducers and evaluating systems. Additionally, these early approaches did not classify their devices as DTEGs.

7.2 Direct thermoelectric gas sensors

The following sections present the optimization of the transducers and the gas sensitive materials as well as results for different direct thermoelectric gas sensors. Section 7.2.1 covers the measurement technique for DTEGs. Section 7.2.2 describes the theoretical design of transducers and gas-sensitive materials, to enable the design of accurate, fast and long-term stable DTEGs. Section 7.2.3 presents results for different DTEGs with different materials. Section 7.2.4 describes ionic direct thermoelectric gas sensors as alternatives to semiconducting oxide materials.

7.2.1 Measurement techniques

Compared with the relatively simple resistance measurement, DTEGs require a more sophisticated set-up. The measurand thermopower (Seebeck coefficient) is defined by:

$$\eta_{gsf} = \eta_{Pt} - \frac{\Delta V_{gsf}}{\Delta T} \qquad [7.7]$$

In Equation [7.7], η_{gsf} is the Seebeck coefficient of the gas sensitive film, ΔV_{gsf} is the measured thermovoltage of the gas sensitive film, and ΔT is the temperature difference at the junctions between the gas sensitive layer and the conductor tracks. Due to the fact that the conductor tracks also add a thermovoltage, the thermopower of the gas sensitive layer has to be corrected by the thermopower of the conductor track material (here, platinum), η_{Pt}.

There are two ways to determine the temperature difference between the junctions of the conductor tracks and the gas sensitive film. Figure 7.1 depicts both possibilities: in (b), the temperature difference, ΔT, is directly determined, whereas in (c), the temperatures at both junctions, T_1 and T_2, are measured separately and the temperature difference ΔT is calculated. Due to the fact that not only the temperature difference, but also the temperature of the

© Woodhead Publishing Limited, 2013

gas sensor has to be controlled precisely, the option presented in Fig. 7.1(c) is advantageous. Combinations of both options are also possible.

The thermovoltages of metallic thermocouples are usually easy to measure, although the voltages are in the microvolt range. In contrast, the internal resistances of semiconducting oxides are by orders higher. Such high ohmic voltage sources are difficult to measure (Keem and Honig, 1975; Keithley, 2004). Therefore, a transducer for a direct thermoelectric gas sensor has to be developed, to ensure an accurate performance. The transducer which will be discussed below allows a maximum internal resistance of the gas sensitive layer of about 1 MΩ.

According to Equation [7.7], it would be possible to apply the temperature difference statically, but a temperature modulation technique enables one to measure the thermovoltages of the sensor material more precisely. In addition, some plausibility checks are possible. Furthermore, it is well-known that materials may decompose slowly in a temperature gradient due to the Soret effect (Timm and Janek, 2005).

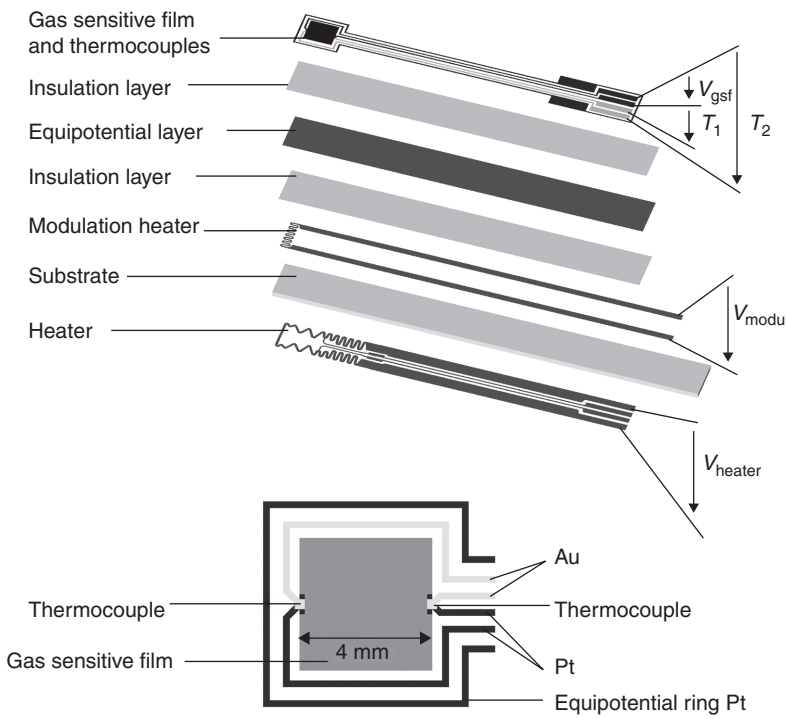

7.2 Set-up of the direct thermoelectric gas sensors presented in this chapter. The applied and measured voltages are also indicated. Reprinted from Rettig and Moos (2009) with permission from IOP-Publishing Ltd.

© Woodhead Publishing Limited, 2013

Figure 7.2 shows the design of a thermoelectric gas sensor device manufactured according to planar ceramic multi-layer technology. The heater brings the tip of the sensor to operation temperature by applying a heater voltage, V_{heater}. The modulation heater generates the temperature difference for the gas sensitive layer. For this purpose, a sinusoidal modulation voltage, V_{modu}, is applied. The equipotential layer will be explained in the next paragraph. The gas sensitive layer and two thermocouples are located on the top of the sensor. With the help of the thermocouples, the temperatures T_1 and T_2 are determined. The thermovoltage of the gas sensitive film, V_{gsf}, is measured over the platinum legs of the thermocouples. According to Equation [7.7], the thermopower of the gas sensitive layer can be calculated. More information on the challenges faced in manufacturing such sensors can be found in Rettig (2008).

Figure 7.3 shows experimental data relating to direct thermoelectric gas sensors: (a)–(d) stem from a sensor without an equipotential layer. The temperature difference in Fig. 7.3(a) is clearly sinusoidal, whereas the thermovoltage, V_{gsf}, of the gas sensitive layer differs significantly from sinusoidal behavior. The distorted signal, V_{gsf}, prevents a linear regression with ΔT. The reason for the distortion becomes apparent from Fig. 7.3(d), where a Fourier analysis of the thermovoltage of the gas sensitive layer, V_{gsf}, is shown. Besides the expected signal of 10 mHz, an additional signal at 5 mHz is found. This is the frequency of the applied modulation voltage, V_{modu}. According to Equation [7.8], the temperature modulation frequency, $f_{\Delta T}$, is twice the modulation frequency, f_{modu}:

$$\begin{aligned} P &= \frac{V_{\text{modu}}^2}{R} = \frac{V_{0,\text{modu}}^2}{R} \cdot \cos^2(\pi f_{\text{modu}} t) \\ &= \frac{V_{0,\text{modu}}^2}{2R} \cdot (1 + \cos(4\pi f_{\text{modu}} t)) = \frac{V_{0,\text{modu}}^2}{2R} \cdot (1 + \cos(2\pi f_{\Delta T} t)) \end{aligned} \quad [7.8]$$

The 5 mHz signal is an interference of the modulation voltage, V_{modu}, with the thermopower due to a small residual conductivity of the substrate material at elevated temperatures of several hundred °C. The finite resistance of the substrate material and the modulation voltage, in the range of several volts, in combination with the relatively high resistance of the gas sensitive layer and the small thermovoltages, indicates that the amplitudes of thermovoltage and the disturbing voltage are in the same order. The low resistance of the thermocouples is a short circuit for the disturbing modulation voltage and, therefore, the disturbing voltage collapses – in contrast to the situation where the gas sensitive layer has a significantly higher resistance. Therefore, the low resistance of the thermocouples compared with the high resistance of the gas sensitive layer is the reason why the temperatures measured by the thermocouples remain almost unaffected by the modulation.

It would be possible to implement a Fourier analysis to calculate the thermopower of the gas sensitive layer from the distorted voltage of the gas

© Woodhead Publishing Limited, 2013

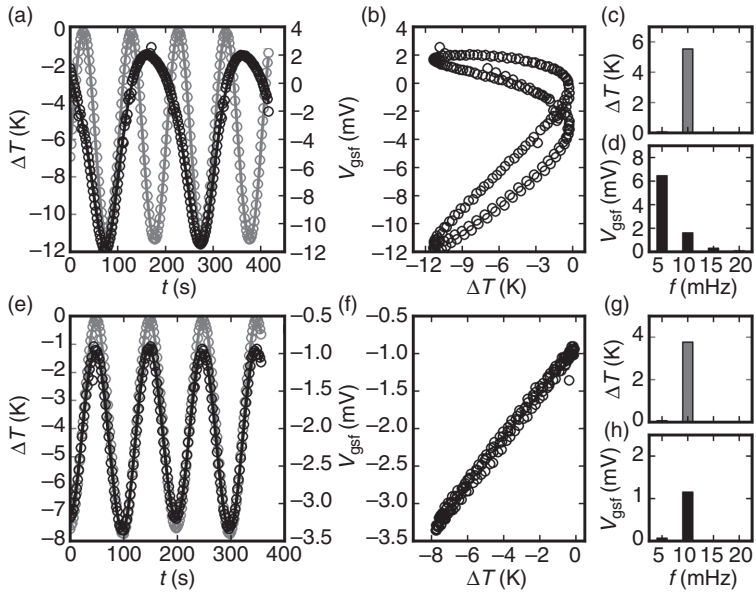

7.3 Measured and analyzed signals of a DTEG (a), (b), (c), (d) without equipotential layer, and (e), (d), (f), (g), (h) with equipotential layer. The time resolved signals of the temperature difference, ΔT, and the measured thermovoltage, V_{gsf}, are shown in (a) and (e). The $\Delta T(V_{gsf})$ diagram is given in (b) and (f). The result of the Fourier analysis of ΔT and V_{gsf} can be found in (c), (d), (g) and (h).

sensitive layer (Rettig and Moos, 2007), but an improved design of a DTEG with an additional equipotential layer offers the possibility to measure almost sinusoidal signals of the temperature difference, ΔT, and the thermovoltage of the gas sensitive layer, V_{gsf}. Figure 7.3(e)–(h) shows the results of a sensor with an equipotential layer. Both the Fourier analysis of V_{gsf} and ΔT show contributions of nearly one frequency at 10 mHz (Figs 7.3(g) and (h)) – that is, the signals are almost sinusoidal (Fig. 7.3(e)) and, therefore, the slope of a linear regression can be used to determine the thermopower of the gas sensitive film (Fig. 7.3(f)).

More details on the design of the equipotential layer can be found in Rettig and Moos (2007). The higher the internal resistance of the gas sensitive material, the more necessary the equipotential layer becomes to improve the signal quality of the DTEGs. Although the modulation technique improves accuracy, there is a fundamental drawback of the temperature modulation (Fig. 7.3(e)): at least one complete modulation period is required to obtain a first reading for the thermopower of the material. With a frequency of 10 mHz, the response time of such a sensor is about 100 seconds. Even if the material itself responds much more rapidly to changing

© Woodhead Publishing Limited, 2013

analyte concentrations, the measurement technique impedes a faster sensor response. The next section deals with a solution to the problem of reducing the response time, and presents a simulation of the electrical and thermoelectric material properties.

7.2.2 Modeling and simulation of thermoelectric gas sensors

According to Simon *et al*. (2001), the *thermal* time constant (relaxation time after a sudden temperature step) of typical gas sensors manufactured in thick-film technology on planar alumina substrates is around 10 seconds. This thermal time constant is valid for large temperature steps. It is mainly driven by the convection coefficient of the gas sensor substrate. However, for temperature modulation, large temperature differences are not necessary. A temperature difference of 20°C suffices for a DTEG. In order to reduce the response time of the sensor, the temperature modulation frequency has to be increased significantly.

The idea of a higher modulation frequency can be explained by a simple model known from Earth sciences. If one applies a sinusoidal temperature change to the ground, it is interesting to consider the depth to which ground temperature modulations are present. If one considers, for instance, a daily temperature change (hot days and cold nights), the penetration depth of the thermal wave is around 10 cm. For yearly temperature modulations (hot summers and cold winters), the thermal wave can penetrate to a depth of around 1 m. That is the reason why water pipes should be installed at least to this depth, otherwise the water would freeze. As a result, the frequency of the thermal modulation has a major influence on the penetration depth (Kittel and Krömer, 1980). Based on this concept, a one-dimensional model has been built up that describes the thermal behavior of a DTEG. A more detailed explanation of the model can be found in Rettig and Moos (2009).

The set-up of the one-dimensional model is shown in Fig. 7.4. Due to the fact that the ratio of the cross-section to the perimeter is small, it is possible to introduce surface-related convective heat loss as a volume heat loss into the one-dimensional partial differential equation:

$$\rho c_{\mathrm{p}} \frac{\partial T}{\partial t} - \kappa \frac{\partial^2 T}{\partial x^2} = \frac{1}{2d} q_0 \left(1 + \exp(2j\pi ft)\right) - \frac{h_{\mathrm{conv}} \cdot P_{\mathrm{sensor}}}{A_{\mathrm{sensor}}} (T - T_{\mathrm{a}}) \quad \text{for } x < d/2 \qquad [7.9]$$

$$\rho c_{\mathrm{p}} \frac{\partial T}{\partial t} - \kappa \frac{\partial^2 T}{\partial x^2} = -\frac{h_{\mathrm{conv}} \cdot P_{\mathrm{sensor}}}{A_{sensor}} (T - T_{\mathrm{a}}) \quad \text{for } x \geq d/2 \qquad [7.10]$$

© Woodhead Publishing Limited, 2013

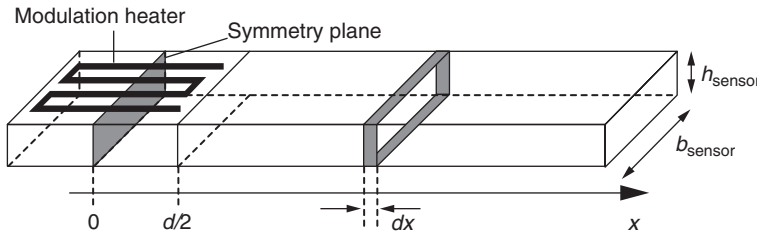

7.4 Set-up for the one-dimensional model for the thermal simulation of a direct thermoelectric gas sensor. Reprinted from Rettig and Moos (2009) with permission from IOP-Publishing Ltd.

Equations [7.9] and [7.10] were used to simulate the thermal behavior of the sensor. The density of the material is ρ, c_p is the heat capacity, T is the temperature, t the time, κ is the thermal conductivity, x is the coordinate according to Fig. 7.4, d is the lateral length of the heater, $\dot{q}$ is the heat generation of the modulation heater per volume, f is the modulation frequency, h_{conv} is the convection coefficient, P_{sensor} is the perimeter of the sensor ($P_{sensor} = 2h_{sensor} + 2b_{sensor}$), A_{sensor} is the cross-section of the sensor ($A_{sensor} = h_{sensor} \cdot b_{sensor}$) and T_a is the ambient temperature. These partial differential equations can be divided into a static differential equation and into a differential equation for a stationary harmonic solution. Details can be found in Rettig (2008) or in Rettig and Moos (2009). The solution to these equations is:

$$T_{M,S}(x) = \frac{G}{2K}\begin{cases} 1 - \exp\left(-\sqrt{K}\frac{d}{2}\right)\cosh\left(\sqrt{K}x\right) & \text{for } 0 < x \le \frac{d}{2} \\ \sinh\left(\sqrt{K}\frac{d}{2}\right)\exp\left(-\sqrt{K}x\right) & \text{for } x > \frac{d}{2} \end{cases} \qquad [7.11]$$

$$\text{with} \quad G = \frac{\dot{q}_0}{2d\kappa} \qquad \text{and} \qquad K = \frac{h_{conv}P_{sensor}}{\kappa A_{sensor}} + j\frac{2\pi f \rho c_p}{\kappa}$$

For the static part of the solution, T_S, f is zero, otherwise the actual temperature modulation frequency, f, is used to calculate the amplitude and the phase angle of the complex temperature distribution, $T_M(x)$. The considered thermal model of the sensor was verified by comparison with the measured temperature distribution of a real sensor. The factor G relates the volume source of heat $\dot{q}$ with the geometry of the modulation heater. K is, in general, the decay constant – due to the fact that it is a complex number, a decaying thermal wave is the result.

Figure 7.5(b) shows the temperature difference amplitude, $\Delta T_M(x)$, with the modulation frequency as a parameter. The experimental data were obtained by a line scan using an infrared camera. The mean applied electrical power was the same for all different modulation frequencies f. The static temperature

© Woodhead Publishing Limited, 2013

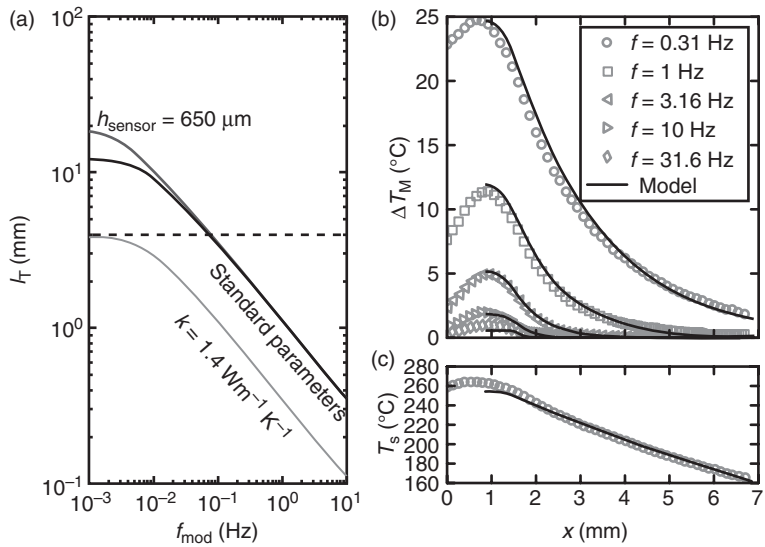

7.5 Results of the thermal modeling of a direct thermoelectric gas sensors. The decay constant (penetration depth) l_T of the thermal is shown in (a). The good agreement of both the harmonic part and the static part between model and measurement is demonstrated in panels (b) and (c). (c) Reprinted from Rettig and Moos (2009) with permission from IOP-Publishing Ltd.

distribution, $T_s(x)$, therefore agrees for all temperature modulation frequencies (Fig. 7.5(c)). This is validated by the thermal model of the sensor, as well as by the measured static temperature distribution. As expected, the amplitude of the harmonic thermal distribution decreases with increasing frequency (Fig. 7.5(b)). The length of the gas sensitive layer was designed to be 4 mm. If the modulation heater was placed at one end of the gas sensitive layer, the temperature at the other end of the gas sensitive layer would barely be affected by the harmonic part of the thermal modulation. The behavior is described best with the parameter 'penetration depth' of a thermal wave l_T. Figure 7.5(a) shows l_T as a function of the modulation frequency. A modulation frequency of $f \approx 1$ Hz results in a penetration depth of the thermal wave l_T of around 1 mm to 2 mm. Therefore, a temperature modulation frequency of 1 Hz requires a modulation heater to be placed at a distance of less than 1 mm from one end of the gas sensitive layer. Otherwise, only a small amplitude of the thermal wave will reach the gas sensitive layer.

A sensor was fabricated according to the design illustrated in Fig. 7.2. First, the platinum modulation heater was screen-printed and fired; then, the insulation layer was applied onto the modulation heater layer. After the equipotential layer and a further insulation layer, the heater and its conductor tracks were applied. Finally, the thermocouples were screen-printed on the top and

© Woodhead Publishing Limited, 2013

fired, and an insulation layer was screen-printed and fired. As a result, the distance between the modulation heater and the thermocouple was around 40–60 μm, while the other thermocouple was 4 mm away. Experimental results with different DTEGs are discussed in the next section.

The most important part of DTEGs is, of course, the gas sensitive material. Typical gas sensitive materials for classical conductometric gas sensors were not developed and optimized for the application as DTEGs. The Seebeck coefficients of these semiconducting oxide materials change with the concentration of free charge carriers, as shown in Equations [7.1]–[7.3]. The measurand resistance (conductance) is always a positive value – in contrast to the thermopower, which can have either positive or negative signs. This offers the opportunity to use different materials for DTEGs. Moos (1998) described a direct thermoelectric oxygen sensor with an intrinsic bulk material to be operated above 600°C. Another approach is considered here for simulation: gas sensitive materials for temperatures around 400°C to 600°C. In this temperature range, bulk incorporation of oxygen in these materials is a very slow process and can be ignored (Jamnik *et al.*, 2002).

Simulation results obtained for semiconductor materials are shown in the next paragraphs. Figure 7.6 depicts the geometrical model. The model has a two-dimensional rotational symmetry. The dark grey area is considered for the simulation. Each grain is described by its radius R_K. The neck radius, R_H, describes the interconnection with adjacent grains. Chemisorption takes place at the grain surface. A space charge region develops from the grain surface to the middle of the grain. The overall thermoelectric and conductive properties of the grain were calculated as follows:

First, the isothermal Poisson-Boltzmann equation was solved (Maier, 2004) from Equation [7.12]:

$$\operatorname{div}(\operatorname{grad}\Phi) = -\frac{e^2 n_i}{\varepsilon_0 \varepsilon_r k_B T}\left(\frac{p_0}{n_i}\exp(-\Phi) - \frac{n_0}{n_i}\exp(\Phi) - \frac{N_A - N_D}{n_i}\right) \qquad [7.12]$$

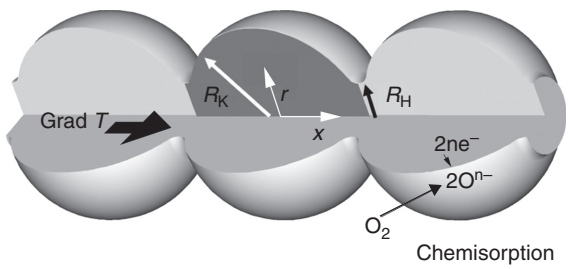

7.6 Model with rotational symmetry for the analysis of materials for DTEGs. The dark grey area was simulated with the commercial FEM-software Comsol Multiphysics. Reprinted from Rettig and Moos (2008b) with permission from Elsevier.

© Woodhead Publishing Limited, 2013

Here, Φ is the reduced potential,

$$\Phi = \frac{e\varphi}{k_B T} \quad [7.13]$$

where e is the elementary charge, φ is the electrical potential, k_B is the Boltzmann constant and T is the temperature. In Equation [7.12], n_i is the intrinsic charge carrier concentration, $\varepsilon_0 \cdot \varepsilon_r$ is the dielectric constant, p_0 and n_0 are the hole concentration in the valence band and the electron concentration in the conduction band, respectively, and N_A and N_D are the acceptor and the donor concentration in the material. Equation [7.12] is valid for materials in which electrons and holes are the mobile charge carriers. A precondition for the validity of the equation is that the conduction band and the valence band are only weakly occupied, so that the Boltzmann statistic for the charge carriers can be applied. For the simulation, Equation [7.12] was normalized regarding the space coordinates; details can be found in Rettig and Moos (2008b). The Debye length gives an idea of the extent of the space charge regions in the grain. For a *p*-type semiconductor, the Debye length $L_{D,p}$ can be calculated by:

$$L_{D,p} = \sqrt{\frac{\varepsilon_0 \varepsilon_r k_B T}{e^2 p_0}} \quad [7.14]$$

The normalized nonlinear partial differential equation (Equation [7.12]) was implemented for the rotational symmetric geometry according to Fig. 7.6 into the commercial FEM-program Comsol Multiphysics. The solution of this equation is the distribution of the reduced potential in a gas sensitive grain.

An example solution is shown in Fig. 7.7. A reduced surface potential Φ of −5 was applied to the grain surface. At a temperature of 400 °C, this reduced potential corresponds to an electrical potential φ of around 300 mV. The grain radius was R_K = 200 nm, the neck radius was R_H = 80 nm. The material itself was slightly donor-doped (N_D/n_i = 10 and N_A/n_i = 0.1) and the Debye length was 20 nm. The middle of the grain is barely influenced by the reduced surface potential, whereas almost the whole neck region is influenced by the reduced surface potential.

Using Equations [7.15] and [7.16], the charge carrier concentration distributions in the grain can be calculated (Tschöpe, 2005):

$$n = n_0 \exp(\Phi) \quad [7.15]$$

$$p = p_0 \exp(-\Phi) \quad [7.16]$$

© Woodhead Publishing Limited, 2013

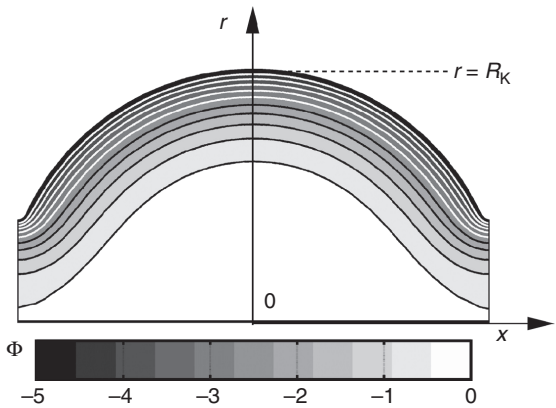

7.7 Obtained simulation data for the reduced potential Φ. A reduced surface potential was set to Φ = –5 for a grain radius of R_K = 200 nm and a neck radius of R_H = 80 nm. The material was slightly donor-doped (N_D/n_i = 10 and N_A/n_i = 0.1). The Debye length was 20 nm. Reprinted from Rettig and Moos (2008b) with permission from Elsevier.

As a result, Fig. 7.8 shows the electron concentration (top) and the hole concentration (bottom) in the different areas of the grain. At each point of the grain, $n \cdot p = n_i^2$ is valid. However, since the electron concentration can never be lower than zero, the space charge region of the electrons extends much more toward the grain center than the space charge region of the holes.

The reduced potential Φ, the electron concentration n/n_i and the hole concentration p/n_i are extracted on the *r*-axes from Fig. 7.8 and plotted in Fig. 7.9. Starting from the grain surface, an inversion area with a length of about 30 nm can be seen. In this area, the hole concentration is larger than the electron concentration, although the material is slightly donor-doped. This inversion plays a major role for the enhanced sensitivity of materials for DTEGs.

Based on Fig. 7.8, the local Seebeck coefficients and the local conductivities can be calculated by applying Equations [7.1]–[7.3] and [7.17]–[7.19].

$$\sigma_n = e\mu_n n \qquad [7.17]$$

$$\sigma_p = e\mu_p p \qquad [7.18]$$

$$\sigma = \sigma_n + \sigma_p \qquad [7.19]$$

The calculation of the local properties is possible for homogeneous semiconductors; for inhomogeneous semiconductors, the presumptions have to

© Woodhead Publishing Limited, 2013

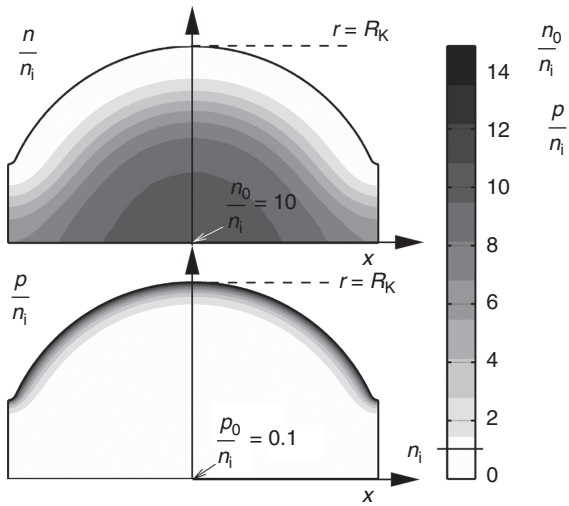

7.8 Calculated electron concentration n/n_0 and hole concentration p/p_0 for a grain radius of R_K = 200 nm and a neck radius of R_H = 80 nm based on the results of Fig. 7.7. The material is slightly donor-doped (N_D/n_i = 10 and N_A/n_i = 0.1). The Debye length is 20 nm. Reprinted from Rettig and Moos (2008b) with permission from Elsevier.

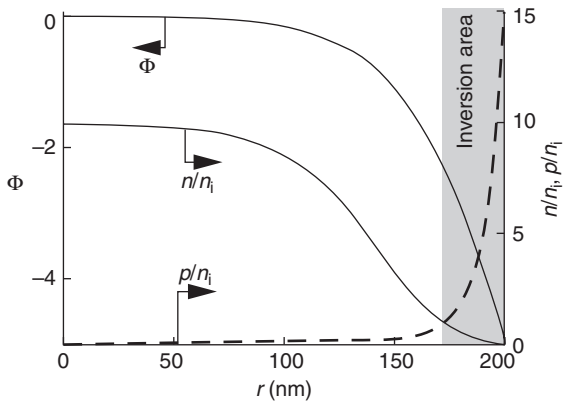

7.9 Calculated course of the electron concentration n/n_i and the hole concentration p/n_i for a grain radius of R_K = 200 nm and a neck radius of R_H = 80 nm. The curves are extracted from Fig. 7.8 on the *r*-axis. The material is slightly donor-doped (N_D/n_i = 10 and N_A/n_i = 0.1). The Debye length is 20 nm. Reprinted from Rettig (2008) with permission from Shaker-Verlag.

be checked. The space charge region extends to about 20 nm. Therefore, the local properties change significantly in this length scale. The mean free path of the charge carriers has to be significantly lower than the width of the space charge region, since otherwise the charge carriers are not able to achieve

© Woodhead Publishing Limited, 2013

the local equilibrium when travelling through the crystal. This assumption is definitively not valid for so-called 'lifetime' semiconductors (Henisch, 1984), where the restoration of the electron–hole equilibrium takes a considerable time. However, in small polaron conductors the electrons are more or less localized to single atoms and, hence, the assumption for the localized properties can be valid. For some oxide materials, a polaron-type conduction mechanism can be considered. Data for charge carrier lifetime or charge carrier mean free paths in oxides are rare. One of the few data available is published by Barsan (1994); the mean free path of the electrons in SnO_2 is lower than the Debye length by at least a factor of 25.

$$\mathrm{div}(\sigma \cdot \mathrm{grad}\phi_i) = 0 \qquad [7.20]$$

$$\mathrm{div}(\sigma \cdot \mathrm{grad}V_{ni} + \sigma\eta \cdot \mathrm{grad}T) = 0 \qquad [7.21]$$

$$\mathrm{div}(\sigma\eta T \cdot \mathrm{grad}V_{ni} + \kappa \cdot \mathrm{grad}T) = 0 \qquad [7.22]$$

Using the local properties and Equations [7.20]–[7.22] (from Nagy and Nayfeh, 2000), the effective (overall) conductivity and the effective (overall) thermopower are calculated. The starting point for the calculation was the reduced potential Φ applied on the grain surface. This surface potential is the result of the chemisorption of oxygen on the grain surface. By integration of the space charge region, the surface charge concentration can be calculated. This surface charge concentration is a (nonlinear) function of the chemisorbed oxygen and, therefore, a measure for the concentration of oxygen in the ambient atmosphere. The chemisorption itself can be described – for example, by a Wolkenstein isotherm (Wolkenstein, 1991). However, the correlation between the adsorbed amount of oxygen and the ambient oxygen concentration will not be covered here. It is sufficient to take a look at the surface charge concentration to extract some interesting results regarding new materials for DTEGs.

Figure 7.10 shows the calculated effective thermopower, η_{eff}, as a function of the normalized surface charge concentration, which is (as explained in the last paragraph) a measure for the ambient oxygen concentration. It was calculated by dividing the thermovoltage difference from the left and the right grain boundary by the temperature difference at the left and the right grain boundary. The normalization factor is the intrinsic charge carrier density, n_i. Each element of Fig. 7.10 shows the thermopower for a differently doped material with the grain size as a parameter. The slope of the curve is a measure for the sensitivity of the material. A steep slope indicates a large sensitivity. As illustrated in Fig. 7.10, acceptor-doped materials exhibit a low sensitivity, donor-doped materials show a better sensitivity,

© Woodhead Publishing Limited, 2013

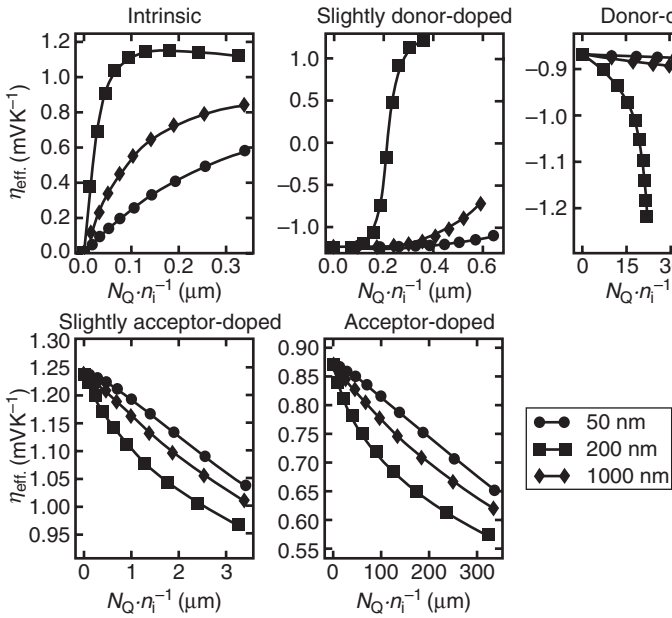

7.10 The effective thermopower, η_{eff}, as a function of the surface charge concentration $N_Q \cdot n_i^{-1}$. In each panel, the doping concentration is varied (intrinsic: $N_D/n_i = 0.1$, $N_A/n_i = 0.1$; slightly donor-doped: $N_D/n_i = 10$, $N_A/n_i = 0.1$; donor-doped: $N_D/n_i = 1000$, $N_A/n_i = 0.1$; slightly acceptor-doped: $N_D/n_i = 0.1$; $N_A/n_i = 10$; acceptor-doped: $N_D/n_i = 0.1$, $N_A/n_i = 1000$). The reduced surface potential varies from 0 to –5. Each curve is plotted for different grain radii. Reprinted from Rettig (2008) with permission from Shaker-Verlag.

while intrinsic or slightly donor-doped materials are maximally sensitive. In addition, the grain size also influences the sensitivity. The grain radius of $R_K \approx 50$ nm is near the Debye length and, therefore, the space charge region influences almost the whole grain. For large grains ($R_K \approx 1000$ nm), only the surface regions are affected. Then, the effective thermopower is insensitive to changes of the ambient oxygen concentration. The slightly donor-doped material with a grain radius of $R_K \approx 50$ nm has the maximum sensitivity. The reason is obvious from Fig. 7.9: if oxygen is adsorbed, an inversion layer is built from the surface of the grain. If a semiconductor changes from *n*-type to *p*-type semiconducting behavior, the sign change in thermopower (the sensitivity) reaches its maximal value. However, if one considers the measurand 'resistance change' of a slightly donor-doped or intrinsic material, one finds almost no sensitivity, since the conductivity always has a positive sign. As a conclusion for this section, the semiconducting materials for DTEGs should be intrinsic or slightly donor-doped for a maximal sensitivity, if they are based on the chemisorption of oxygen. For bulk materials,

© Woodhead Publishing Limited, 2013

where the entire stoichiometry of the material is changed, intrinsic materials may have also some advantages regarding sensitivity since, in this case, the sign of the thermopower also changes (Choi *et al.*, 1986; Yoo and Song, 2001). However, many of the oxide materials that are typically used for gas sensors show a significant ionic conductivity at and around the intrinsic minimum (Rothschild *et al.*, 2006). It is supposed that the ionic contribution will interact with the thermopower of electrons and holes.

7.2.3 Measurements and results

This section deals with real transducers and gas sensitive materials for DTEGs. Using the results from previous sections, accurate, rapid and long-term stable DTEGs with increased sensitivity can be designed.

A first experiment to demonstrate the advantages of DTEGs is shown in Fig. 7.11 (Moos *et al.*, 2011). Here, instead of a planar sensor, a small porous ceramic brick-shaped sample of $SrTi_{0.6}Fe_{0.4}O_{3-\delta}$ was measured, as described below. The thermopower, η, and the resistance, R, were measured simultaneously (details in Rettig *et al.*, 2005). The samples were kept at 700°C, 800°C and 900°C for 7 hours each. Within these 7 hours (duration of each run), the oxygen partial pressure was varied stepwise, and the final values of R and η were plotted. It is interesting to observe that the resistance characteristics

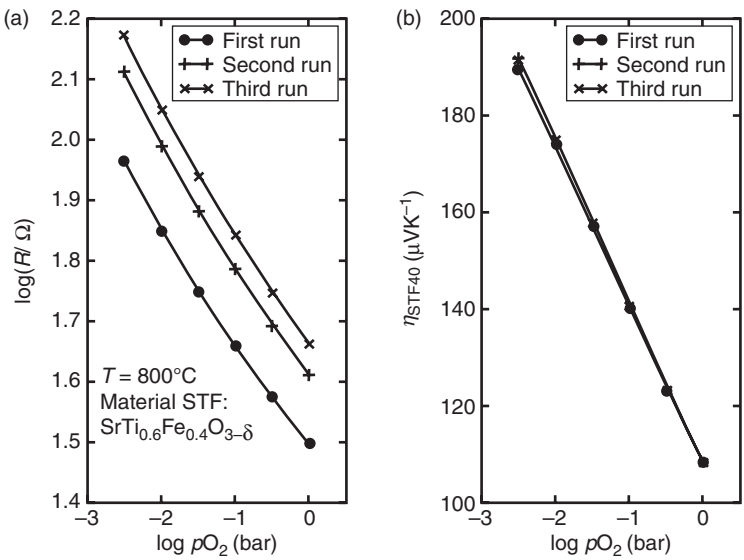

7.11 (a) Resistance, R and (b) thermopower (Seebeck coefficient), η, of a porous STF ($SrTi_{0.6}Fe_{0.4}O_{3-\delta}$) specimen when exposed to different oxygen partial pressures (from Moos *et al.*, 2011).

© Woodhead Publishing Limited, 2013

of the material shifted from run to run, presumably due to the sintering process of the sample. This large shift amounts to an error of approximately one decade in pO_2. The thermopower, η, however, remains constant. This experiment clearly highlights the advantage of the DTEGs, which is based on the geometry independence of the potential difference measurement.

As a first planar approach, a DTEG for hydrocarbons based on SnO_2 is presented. In this case, the entire sensor was still heated in a tube furnace and only the temperature modulation was applied by a planar structure. Therefore, the manufacturing procedure of this sensor was simpler compared with the sensor presented in Fig. 7.2. Figure 7.12(a) shows the design

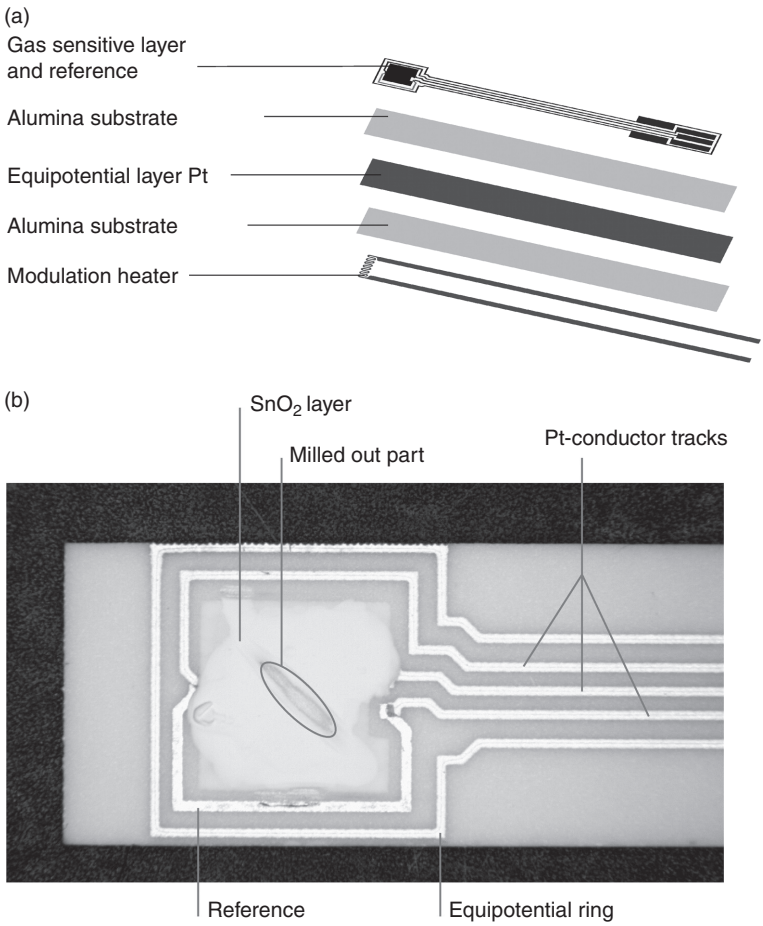

7.12 SnO_2-based DTEG (a) in thick-film technology, (b) The sensor was measured before and after milling out a part of the gas sensitive layer. Reprinted from Rettig and Moos (2007b) with permission from IEEE. © 2007 IEEE.

© Woodhead Publishing Limited, 2013

of the sensor. The upper part of the sensor containing the thermocouples and the gas sensitive layer was joined with the lower part with the modulation heater by the wet screen-printed equipotential layer. After drying and firing, the sensor was complete.

The sensor was first tested with propane and then a significant part of the gas sensitive layer was milled out. The milled-out portion of the gas sensitive layer can be seen in Fig. 7.12(b). After milling out the gas sensitive layer, the sensing response was measured again.

Figure 7.13 shows the results. The thermopower of the gas sensitive layer, η_{SnO_2}, is barely influenced after milling out a portion of the gas sensitive layer (Fig. 7.13(a)), but the resistance R_{SnO_2} is – as expected from the preceding discussion – significantly increased (Fig. 7.13(b)). If a propane concentration of 100 ppm were present in the ambience of the gas sensor, a milled-out DTEG would measure a concentration of 80 ppm propane. However, a milled-out conductometric gas sensor (Fig. 7.13(b)) would only measure a concentration of 30 ppm propane.

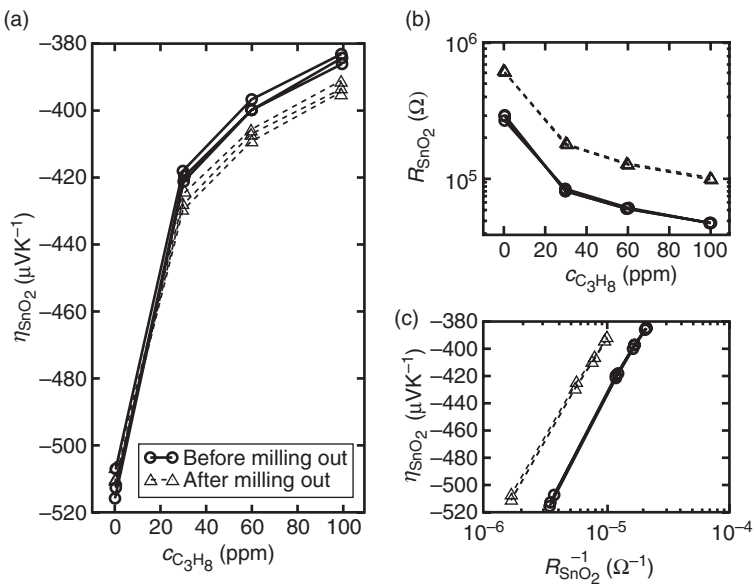

7.13 Measurement results of a DTEG as shown in Fig. 7.12, with SnO_2 as the gas sensitive material at 400°C with 1% oxygen with different propane concentrations (balance nitrogen). The curves indicate (a) the results of the thermopower η_{SnO_2}, (b) the resistance, R_{SnO_2}, and (c) the Jonker diagram, before (circles) and after (triangles) milling out a part of the gas sensitive layer. Reprinted from Rettig and Moos (2007b) with permission from IEEE. © 2007 IEEE.

© Woodhead Publishing Limited, 2013

One sees also a drift of both measurands: thermopower and resistance. At first glance, they correlate. Such an assumption can be checked with a Jonker diagram (Jonker, 1968). In such a plot, the thermopower, η_{SnO_2}, and the conductivity (or the resistance, R_{SnO_2}) are plotted against each other. If, after milling out areas of the film, the data points stay on the same curve as the points prior to milling out, the assumption would be correct. However, this is not the case, since the curves in Fig. 7.13(c) are clearly shifted to the right after the milling process. The measurand thermopower is not a function of the geometry of the gas sensitive layer. This might be advantageous for abrasive gas streams. More details of this sensor can be found in Rettig and Moos (2007b).

Figure 7.14 shows photographs of two DTEGs with SnO_2 as the gas sensitive films. The sensors were manufactured as shown in Fig. 7.2. The gas sensitive layer was applied with a brush to ensure low internal resistance of the gas sensitive layer (due to the geometry independency of the measurand thermopower, the geometry does not play a role!). The sensors also had a heater on the reverse side. It heated the entire sensor tip to the operational temperature of 400°C. The temperature modulation was applied by the modulation heater with a modulation frequency of 0.312 Hz. A continuous regression was used to extract the thermopower of the gas sensitive layer.

Figure 7.15 shows the results for both sensors. The propane concentration profile is shown in Fig. 7.15(a), the measured thermopower of the gas sensitive layer is plotted in Fig. 7.15(c). Figure 7.15(b) shows the corresponding error of the thermopower, $\Delta\eta_{SnO_2}/\eta_{SnO_2}$, determined by the error

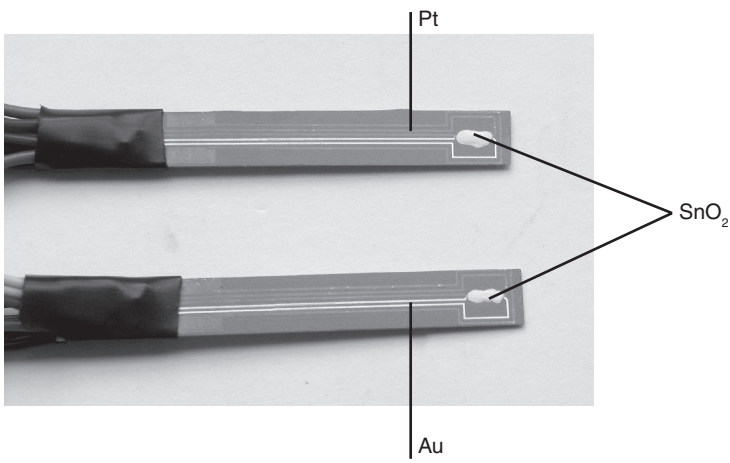

7.14 Photograph of DTEGs with SnO_2 as the gas sensitive layer. Reprinted from Rettig and Moos (2009) with permission from IOP-Publishing Ltd.

© Woodhead Publishing Limited, 2013

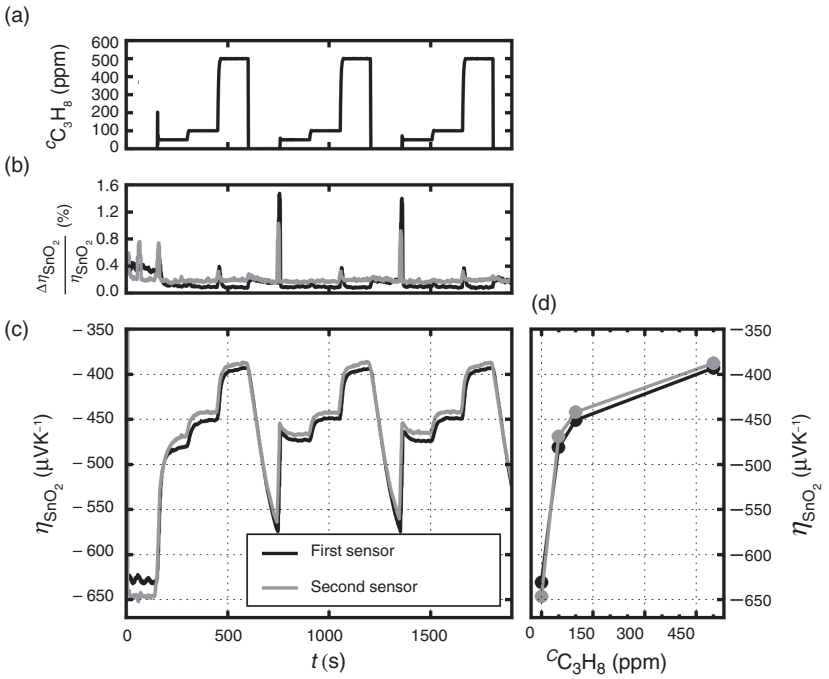

7.15 Results obtained from a DTEG with SnO_2 (see Fig. 7.14) at 400°C and 1% oxygen with different propane concentrations (balance nitrogen). The temperature modulation frequency was 0.312 Hz. The curves indicate (c) the results of the thermopower η_{SnO_2}, (b) the relative error of the thermopower $\Delta\eta_{SnO_2}/\eta_{SnO_2}$ and (d) the characteristics of the two gas sensors shown in Fig. 7.13. The transient propane profile is shown in (a). Reprinted from Rettig and Moos (2009) with permission from IOP-Publishing Ltd.

of the regression analysis. The characteristics of the sensors can be found in Fig. 7.15(d). Both sensors behave nearly identically, in the transient diagram as well as in the sensor characteristics. For a resistive gas sensor, identical behavior would be surprising, especially when the gas sensitive layer was applied using such a poorly reproducible technique. The errors $\Delta\eta_{SnO_2}/\eta_{SnO_2}$ from the continuous regression are usually below 1%. When considering the modulation frequency of 0.312 Hz, this low error is remarkable. The error can be used to check if the sensor is working correctly. If the error is above a certain level for a certain time, the sensor has to be checked. This clearly shows that accurate, rapid and reliable DTEGs can be designed. More details about this sensor can be found in Rettig and Moos (2009).

As shown above, bulk materials also show a promising oxygen gas dependent thermoelectric behavior. Therefore, two DTEGs were prepared with inks made from the same ceramic powder with which the brick-like

© Woodhead Publishing Limited, 2013

specimens of Fig. 7.11 were made. Figure 7.16(b) shows a photograph of two sensors with $SrTi_{0.6}Fe_{0.4}O_{3-\delta}$ as the oxygen gas sensitive material. The design of the sensor (Fig. 7.16(a)) was modified for this material, since the diffusion barrier material $SrAl_2O_4$ is needed to prevent an interaction of the gas sensitive material $SrTi_{0.6}Fe_{0.4}O_{3-\delta}$ (Moos *et al*., 2003) with the alumina substrate during firing. The $SrAl_2O_4$ has to be fired at 1300°C for good adhesion. The printed insulation layer introduced in Fig. 7.2 is not suitable for such high firing temperatures. For the upper part of the sensor, the $SrAl_2O_4$ was printed and fired first on the alumina substrate. Then, the Pt-conductor tracks were printed and fired. Afterwards, $SrTi_{0.6}Fe_{0.4}O_{3-\delta}$-paste was either screen-printed or applied with a brush. Finally, for the upper substrate, the Au-conductor tracks and the equipotential layer were screen-printed and fired in a separate step. The lower alumina substrate was printed with the heater, followed by the modulation heater. The heater conductor tracks and one insulation layer were screen-printed and fired in a single step. Both

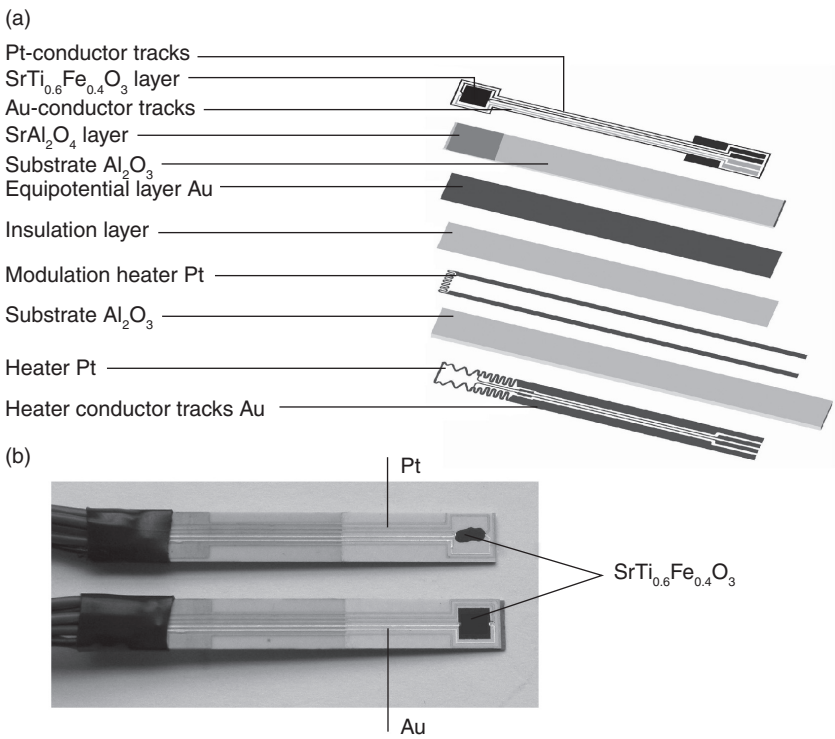

7.16 DTEGs with $SrTi_{0.6}Fe_{0.4}O_{3-\delta}$ as the gas sensitive material: (a) design, and (b) photograph. Reprinted from Rettig (2008) with permission from Shaker-Verlag.

© Woodhead Publishing Limited, 2013

substrates of the sensor were joined by applying a second wet screen-printed insulation layer on the upper substrate. After drying and firing, the sensor was ready for the measurements. Details on the complex manufacturing process of this sensor can be found in Rettig (2008). Please note the different methods by which the gas sensitive layer was applied: with a brush (Fig. 7.16(b), upper sensor, first sensor) and by screen-printing (Fig. 7.16(b), lower sensor, second sensor).

Both sensors were heated to their operational temperature of 700°C by the Pt-heater. A temperature modulation frequency of 0.156 Hz was applied to the modulation heater. The thermopower was determined by a continuous regression analysis over two periods. Due to this low modulation frequency, the sensor response time is limited to 12.8 seconds.

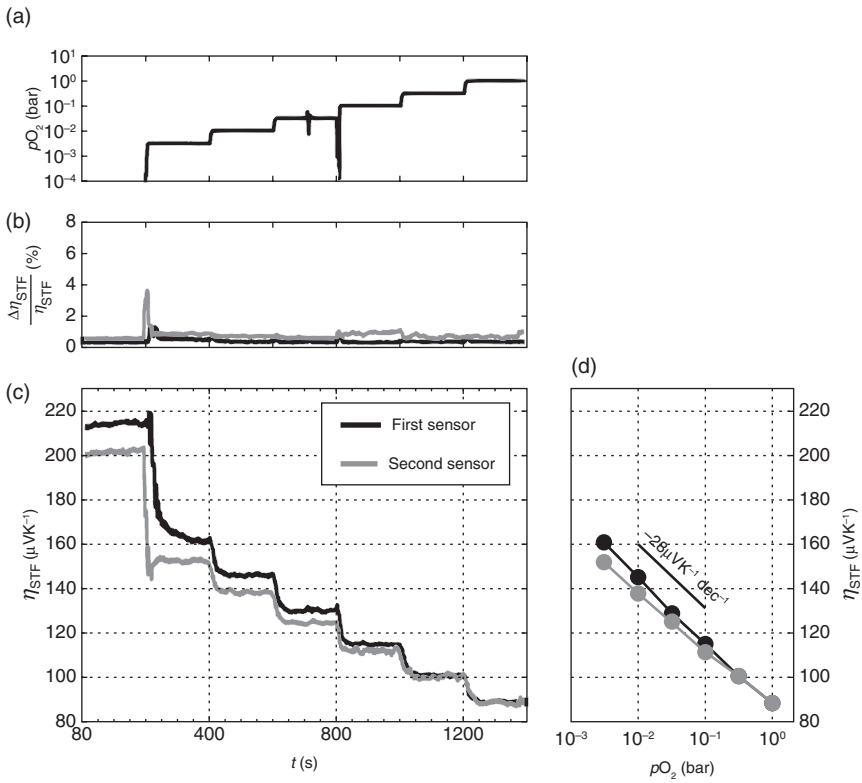

7.17 Thermopower results of a DTEG with a $SrTi_{0.6}Fe_{0.4}O_{3-\delta}$ gas sensitive film at 700°C in different oxygen concentrations (balance nitrogen). The temperature modulation frequency was 0.156 Hz. The black and the grey curves indicate (c) the results of the thermopower, η_{STF}, (b) the relative error of the thermopower, $\Delta\eta_{STF}/\eta_{STF}$, (d) the characteristics of the two gas sensors shown in Fig. 7.16. The transient oxygen profile is shown in (a). Reprinted from Rettig (2008) with permission from Shaker-Verlag.

© Woodhead Publishing Limited, 2013

The sensors were tested with different oxygen/nitrogen mixtures. Figure 7.17 shows the results of both sensors as described in Fig. 7.16. The oxygen partial pressure was varied stepwise from pure nitrogen to pure oxygen (Fig. 7.17(a)). Both sensors behaved almost identically despite the fact that the geometry of the gas sensitive layer differed significantly (Fig. 7.16(b)). Both sensors reached their equilibrium state at each oxygen concentration within 50 seconds. The relative error of the measured thermopower (Fig. 7.17(b)) was usually below 2%. However, the gas sensitive material had a relative low sensitivity toward oxygen. The slope in a half logarithmic plot is about $-28\ \mu VK^{-1}$ per decade pO_2. The material is known to have a slope of about −0.2 in a double logarithmic plot of the resistance versus the oxygen partial pressure. Therefore, the expected slope of a direct thermoelectric gas sensor would be about $40\ \mu VK^{-1}$ per decade (Moos and Härdtl, 1997). As already mentioned, the hole concentration changes in different oxygen concentrations. As a result, both the thermopower and the conductivity change. For a *p*-type material, like the one shown here, the slope in a log-log plot of resistance versus oxygen partial pressure can be transferred to a slope in a plot of the thermopower and the logarithmic oxygen partial pressure.

In Fig. 7.11, this value was almost found. The reason for this deviation from the theoretically expected slope is not clear. However, if one compares Figs 7.11 and 7.17 more closely, one finds that also the absolute value of the thermopower in Fig. 7.17 is lower than that in Fig. 7.11, e.g. η (1 bar, Fig. 7.11) $\approx 108\ \mu VK^{-1}$, whereas η (1 bar, Fig. 7.17) $\approx 85\ \mu VK^{-1}$. This behavior was also found in Röder-Roith *et al.* (2009). In this case, it was assumed that the temperature difference was not measured at the same point where the thermovoltage was determined. In other words, the temperature difference (ΔT in Equation [7.4]) was determined too large; hence, the thermovoltage, as well as the slope in the $\eta(pO_2)$ plot, appeared too small. Therefore, in Röder-Roith *et al.* (2009), a geometry correction factor was introduced and proven. Assuming the geometrical situation and a linear temperature gradient, the slope and the absolute thermopower could be increased by a factor of 1.1 (Rettig, 2008). However, the values of the bulk sample are not achieved. The different sintering temperature for the screen-printed layer (1100°C) and the bulk sample (1300°C) might be a reason. Also, the ionic thermopower of the material (Rothschild *et al.*, 2006) may contribute to the deviation from theory, because, despite the material being a *p*-type semiconductor, ionic conductivity contributes to the electrical charge transport in a non-negligible way. Overall, $SrTi_{0.6}Fe_{0.4}O_{3-\delta}$ can be used for direct thermoelectric gas sensors; however, the sensitivity is low.

The last sensor presented in this section has much higher sensitivity. According to the previous section, intrinsic gas sensitive thermoelectric materials exhibit a larger sensitivity. As intrinsic material, Fe_2O_3 was used, since

© Woodhead Publishing Limited, 2013

this material is known to have intrinsic semiconducting properties at low temperatures (Gurlo *et al*., 2004a, 2004b). This intrinsic semiconducting behavior makes the material unsuitable for conductometric gas sensors, since there is almost no change in conductivity with changing ambient pO_2. However, it is an ideal candidate for DTEGs. The design of the sensor (Fig. 7.18(a)) is quite similar to that shown in Fig. 7.2. The conductivity of an intrinsic semiconducting material is typically low, because only the intrinsic charge carriers contribute to the electrical conduction. The developed transducer for a direct thermoelectric gas sensor allows a maximum internal resistance of the gas sensitive material of about 1 MΩ. If this range is exceeded, the measured thermovoltage becomes too noisy due to disturbance from ambient voltages. For Fe_2O_3, the internal resistance of the gas sensitive layer is higher than 1 MΩ with a gas sensitive layer 4 mm long. For this reason, the distance between the two thermocouples was reduced to about 1.2 mm. As a result, the internal resistance is sufficiently low for an accurate evaluation of the thermopower. Unfortunately, however, the reproducibility of different DTEGS suffers because of the small distance between the thermocouples. The point where the temperature difference is determined is typically not the same point at which the thermovoltage of the gas sensitive layer is read out. The gas sensitive layer was applied to the transducer with a brush (Fig. 7.18(b)). Figure 7.18(c) shows a photograph of the complete gas sensor.

The sensor was heated up to 580°C and a temperature modulation frequency of 0.312 Hz was applied. The continuous linear regression to determine

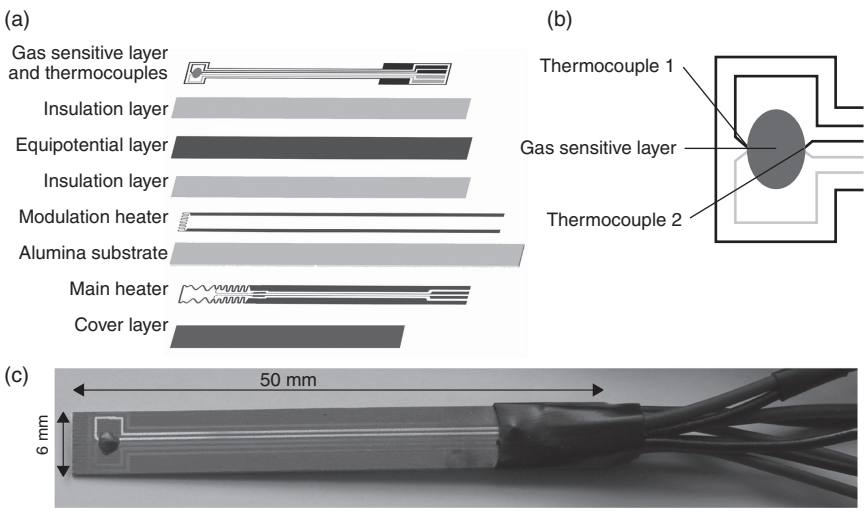

7.18 DTEGs with Fe_2O_3 as the gas sensitive material: (a) design and (b) photograph. Reprinted from Rettig and Moos (2010) with permission from Elsevier.

© Woodhead Publishing Limited, 2013

the thermopower was carried out for two periods; therefore, the response time of the sensor is limited to a regression time of 6.4 seconds. The temperature difference on the gas sensitive layer varied from −15°C to +5°C with respect to the sensor temperature of 580°C. Within this temperature difference range, the thermovoltage, ΔV_{gsf}, correlated almost linearly with the temperature difference, ΔT. The temperature at both ends of the gas sensitive layer and the thermovoltage of the gas sensitive layer was determined with a 90 ms interval. Figure 7.19 shows the results of a typical measurement run. The oxygen concentration was varied from pure nitrogen to pure oxygen in seven steps (Fig. 7.19(a)). The determined thermopower, $\eta_{Fe_2O_3}$, varied from about −400 μVK^{-1} to −50 μVK^{-1} (Fig 7.19(c)). The sensor reaches its equilibrium state within a few seconds. A more detailed timely analysis of the sensor response concluded that the measured response time ($t_{63\%}$) of 16 seconds can be assigned to the gas exchange in the test chamber. The absolute error of the thermopower $|\Delta\eta_{Fe_2O_3}|$ (Fig. 7.19(b)) is usually below 2 μVK^{-1}. The error exceeds this upper limit only after the stepwise of the oxygen concentration

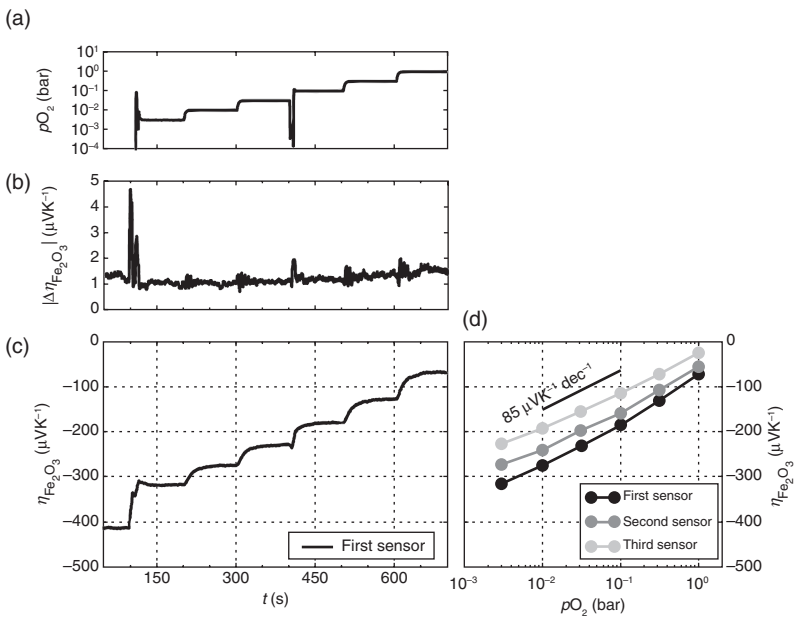

7.19 Experimental results of the DTEG with Fe_2O_3 as an oxygen sensitive layer at 580°C (sensor from Fig. 7.18). The temperature modulation frequency was 0.312 Hz. Figure 7.19(a) shows the transient oxygen profile, (b) shows the absolute error of the thermopower, $\Delta\eta_{Fe_2O_3}$, (c) depicts the transient result of the thermopower, $\eta_{Fe_2O_3}$, and (d) gives the characteristics of the three gas sensors. Reprinted from Rettig and Moos (2010) with permission from Elsevier.

© Woodhead Publishing Limited, 2013

changes. The sensor is quite rapid, even the irregularities in the gas dosing at $t = 400$ seconds are partially determined by the gas sensor. The major advantage of this gas sensor is its far higher sensitivity compared with the sensor shown in Fig. 7.17 (compare Fig. 7.19(d) with Fig. 7.17(d)). The sensitivity reaches a value of about 85 μVK^{-1} per decade and is about three times higher compared with the sensor based on $SrTi_{0.6}Fe_{0.4}O_{3-\delta}$. More details on this sensor can be found in Rettig and Moos (2010).

It was shown in this section that it is possible to manufacture accurate, rapid and sensitive DTEGs. The design of the direct thermoelectric gas sensors can be developed knowledge-based. Since intrinsic materials show the best sensitivity, the internal resistance of the gas sensitive layers has to be considered, and the insulation and equipotential layers have to be applied. An appropriate temperature modulation frequency needs to be selected to achieve good results.

7.2.4 Ionic direct thermoelectric gas (iDTEG) sensors

The direct thermoelectric gas sensors introduced in the preceding sections were based on semiconducting oxide materials. However, other materials besides electronic conductors can be employed as materials for DTEGs. Several years ago, it was shown that the thermopower η of an electrochemical cell with Pt electrodes separated by an oxygen ion conductor follows Equation [7.23] (e.g. Ahlgren and Poulsen, 1995):

$$\eta = S(T) - \frac{k_B}{4e} \times \ln(pO_2) - \frac{Q^{\bullet}_{O^{2-}}}{2eT} - \eta_{Pt} \qquad [7.23]$$

In Equation [7.23], $Q^{\bullet}_{O^{2-}}$ is the heat of transport of the oxygen ions, $S(T)$ is the entropy term and η_{Pt} is the Seebeck coefficient of platinum. In rough first order approximation, all these three terms can be considered as constant with respect to pO_2. Then, a theoretical sensitivity s of the thermoelectric cell can be derived:

$$s = \frac{d\eta}{d\log(pO_2)} = -\frac{k_B}{4e}\ln 10 \qquad [7.24]$$

According to Equation [7.24], the sensitivity should be $s \approx -50\ \mu VK^{-1}$ per decade pO_2, which is in the same order of magnitude as that of semiconductor materials.

The first implementation of such a sensor device is reported in Röder-Roith *et al.* (2009), in which 8 mol% Y_2O_3 stabilized zirconia (YSZ) was used for the gas sensitive material. The sensor set-up was similar to the sensors described above; however, an additional Pt-cermet was applied to get a high

© Woodhead Publishing Limited, 2013

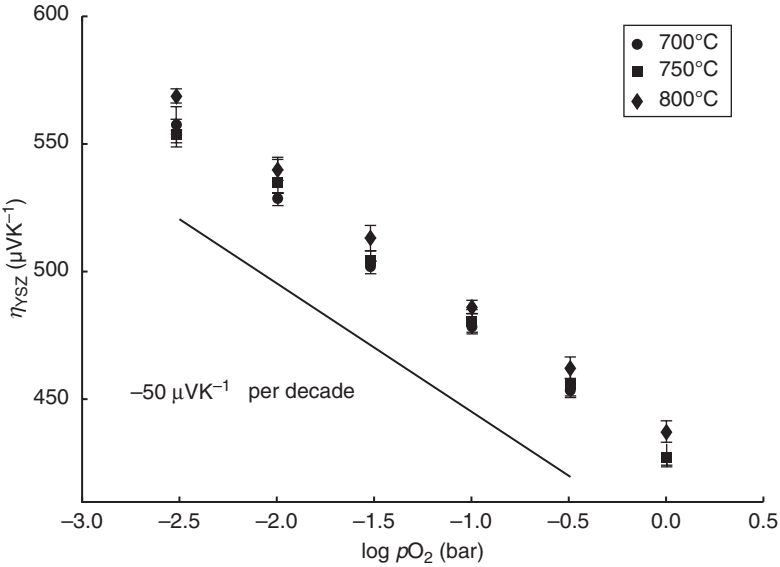

7.20 Results of an iDTEG with YSZ as an oxygen sensitive layer. Note the almost nonexistent temperature dependence of the sensor signal. Reprinted from Röder-Roith *et al.* (2009) with permission from Elsevier.

exchange rate at the YSZ-Pt interface. It becomes clear from the results in Fig. 7.20 that the sensitivity reaches the expected value. Astonishingly, but in accordance with Equation [7.24], almost no temperature dependency of η was observed. This indicates that the three pO_2-independent terms either have a negligible temperature dependency, or their temperature dependencies compensate each other. Additionally, no cross-sensitivities to NO, H_2, H_2O, CO, CO_2, or HC are observed. However, the long-term stability of this sensor has to be improved.

The perovskite-type proton conductor $BaCe_{0.95}Y_{0.05}O_{3-\delta}$ has also been considered for iDTEGs (Röder-Roith *et al.*, 2011). Although a hydrogen dependent thermopower could be measured, the different mobile species (ions, electrons, holes) allow the material to apply only in certain atmospheres with defined oxygen and hydrogen partial pressures.

7.3 Conclusion and future trends

DTEGs are an alternative to resistive gas sensors. Accurate, rapid and long-term stable gas sensors have been presented in this chapter. The main advantage of DTEGs is the measurand 'thermopower' or 'Seebeck coefficient'. In contrast to conductometric gas sensors, the measurand thermopower is not influenced by changes in the geometry of the gas sensitive

© Woodhead Publishing Limited, 2013

layer. A damage of the gas sensitive layer directly influences the resistance, but the thermopower remains virtually unaffected. An example of such an abrasion-resisting gas sensor is shown in Fig. 7.20.

Besides the sensors discussed, DTEGs have been developed with special respect to the measurement principle. First, an adequate transducer has been developed. For the DTEGs presented, a temperature modulation technique was chosen to determine the thermopower. The advantage of this technique is improved accuracy, and that the signals of the temperature differences and the thermovoltages can be analyzed either by regression analysis or by a Fourier analysis. Disturbing voltages are filtered out by these signal analyses. The disadvantage of the temperature modulation is the long response time of the sensor, which is determined here by the regression or the Fourier analysis. The problem can be overcome by rapid temperature modulation with a modulation heater placed within a distance of about 60 μm from one end of the gas sensitive layer. The thermal behavior of a direct thermoelectric gas sensor has been modeled; both the thermal model and measurement of the thermal properties of the DTEGs agree very well.

The gas sensitive layer of a DTEG determines the performance of the gas sensor. A general analysis of materials with chemisorption has been introduced. The model is based on semiconductor and thermoelectric equations. The partial differential equations (here, Poisson-Boltzmann equations) have been solved by Comsol Multiphysics. The solution has been used to calculate the isothermal and the non-isothermal properties of a gas sensitive grain. The results of the simulation concluded that small grains are generally advantageous because of higher sensitivity. Furthermore, materials with only an intrinsic charge carrier density should have the largest sensitivity compared with *n*-type or *p*-type semiconducting materials.

Four different gas sensors based on SnO_2, $SrTi_{0.6}Fe_{0.4}O_{3-\delta}$, Fe_2O_3 and YSZ demonstrated the potential of DTEGs. The classical material SnO_2 was tested with propane, while the other materials were used as oxygen sensitive materials. The temperature modulation frequency for the different materials was 0.312 Hz. The response time of the sensors was determined by the signal analyses of thermovoltage and temperature difference. It amounted to 6.4 seconds. All the sensors showed a reproducible and rapid behavior. For the DTEGs, it was shown that it is possible to mill out a significant part of the gas sensitive layer without affecting the measured thermopower significantly. With an adapted design, DTEGs may be a good alternative to resistive gas sensors.

Besides the encouraging results, DTEGs still have great potential for further improvements. The temperature modulation frequency of 0.312 Hz is not sufficient for all applications. For fast responding devices, the temperature modulation has to be in the range of 100 Hz. Manufacturing technology needs to be adjusted in order to achieve this. Micromachined ceramics or

© Woodhead Publishing Limited, 2013

silicon hot plate gas sensors may be preferred, since such a high-temperature modulation frequency needs quite small structures that may not be feasible with conventional ceramic thick-film technology.

Until now, only a few materials have been studied for DTEG application. The research focus for gas sensitive materials is usually on resistive materials. The possibility of intrinsic materials with an enhanced sensitivity (when applied in the DTEG mode) is an important property that needs to be addressed in the future. Intrinsic (low conducting) behavior can be improved, when materials with a high mobility of charge carriers are used. Then, films with a low internal resistance and a high sensitivity can be obtained. Furthermore, the aspect of utilizing ion conducting materials should be more emphasized, since a high selectivity can be expected due to the distinct ion conduction.

7.4 References

Ahlgren, E. O. and Poulsen, F. W. (1995), Thermoelectric power of stabilized zirconia. *Solid State Ionics*, **82**, 193–201.

Balducci, A., D'Amico, A., Di Natale, C., Marinelli, M., Milani, E., Morgana, M. E., Pucella, G., Rodriguez, G., Tucciarone, A. and Verona-Rinati, G. (2005). High performance CVD-diamond-based thermocouple for gas sensing. *Sensors and Actuators B: Chemical*, **111**, 102–5.

Barsan, N. (1994), Conduction models in gas-sensing SnO_2 layers: grain-size effects and ambient atmosphere influence. *Sensors and Actuators B: Chemical*, **17**(3), 241–6.

Baunach, T., Schänzlin, K. and Diehl, L. (2006), Sauberes Abgas durch Keramiksensoren. *Physik Journal*, **5**(5), 33–8.

Cantalini, C., Pelino, M., Sun, H. T., Faccio, M., Cantucci, S., Lozzi, L. and Passacantando, M. (1996), Cross sensitivity and stability of NO_2 sensors from WO_3 thin film. *Sensors and Actuators B: Chemical*, **35**(1–3), 112–18.

Choi, G. M., Tuller, H. L. and Goldschmidt, D. (1986), Electronic-transport behavior in single-crystalline $Ba_{0.03}Sr_{0.97}TiO_3$. *Physical Review B*, **34**(10), 6972–9.

Chou, S. M., Teoh, L. G., Lai, W. H., Su, Y. H. and Hon, M. H. (2006), ZnO/Al Thin Film Gas Sensor for Detection of Ethanol Vapor. *Sensors*, **6**, 1420–7

Denk, I., Ingrisch, K., Weigold, T., Baumann, K., Weiblen, K., Bauer, M., Zeppenfeld, A. and Schuhmann, B. (1999), New CO/NOx-sensor system for automotive climate control in a small size housing with high mounting flexibility, *Sensor 99 Proceedings*, 339–44.

Gerblinger, J., Lampe, U. and Meixner, H. (1993), *German patent specification*, DE4339737C1.

Gerblinger, J. and Meixner, H. (1991), Fast oxygen sensors based on sputtered strontium-titanate. *Sensors and Actuators B: Chemical*, **4**(1–2), 99–102.

Gurlo, A., Barsan, N., Oprea, A., Sahm, M., Sahm, T. and Weimar, U. (2004a), An *n*- to *p*-type conductivity transition induced by oxygen adsorption on Fe_2O_3. *Applied Physics Letters*, **85**(12), 2280–2.

Gurlo, A., Sahm, M., Oprea, A., Barsan, N. and Weimar, U. (2004b), A *p*- to *n*-transition on Fe_2O_3-based thick film sensors studied by conductance and work function change measurements. *Sensors and Actuators B: Chemical*, **102**(2), 291–8.

© Woodhead Publishing Limited, 2013

Heikes, R. R. and Ure, R. W. (1961), *Thermoelectricity*, Interscience Publishers.
Henisch, H. K. (1984), *Semiconductor contacts*, Oxford University Press.
Ionescu, R. (1998), Combined Seebeck and resistive SnO_2 gas sensors, a new selective device. *Sensors and Actuators B: Chemical*, **48**(1–3), 392–4.
Ivers-Tiffee, E., Härdtl, K. H., Menesklou, W. and Riegel, J. (2001), Principles of solid state oxygen sensors for lean combustion gas control. *Electrochimica Acta*, **47**(5), 807–14.
Jamnik, J., Kamp, B., Merkle, R. and Maier, J. (2002), Space charge influenced oxygen incorporation in oxides: in how far does it contribute to the drift of Taguchi sensors? *Solid State Ionics*, **150**(1–2), 157–66.
Jayaraman, V., Gnanasekar, K. I., Prabhu, E., Gnanasekaran, T. and Periaswami, G. (1999), Preparation and characterisation of $Cr_{2-x}Ti_xO_{3+\delta}$ and its sensor properties. *Sensors and Actuators B*, **55**(2–3), 175–9.
Jonker, G. H. (1968), Application of combined conductivity and Seebeck-effect plots for analysis of semiconductor properties. *Philips Research Reports*, **23**(2), 131–8.
Keem, J. E. and Honig, J. M. (1975), Seebeck measurements and their interpretation in high-resistivity materials case of semiconducting V_2O_3. *Physica Status Solidi A-Applied Research*, **28**(1), 335–43.
Keithley (2004), *Low level measurements handbook*. Keithley Instruments Inc.
Kittel, C. and Krömer, H. (1980), *Thermal Physics*, W. H. Freeman.
Lampe, U., Fleischer, M. and Meixner, H. (1994), Lambda measurement with Ga_2O_3. *Sensors and Actuators B: Chemical*, **17**(3), 187–96.
Liess, M. and Steffes, H. (2000), The modulation of thermoelectric power by chemisorption: a new detection principle for microchip chemical sensors. *Journal of the Electrochemical Society*, **147**(8), 3151–3.
Logothetis, E. M. and Kaiser, W. J. (1983), TiO_2 film oxygen sensors made by chemical vapour deposition from organometallics. *Sensors and Actuators*, **4**, 333–40.
Maier, J. (2004), *Physical Chemistry for Ionic Material: Ions and Electrons in Solids*, *John Wiley & Sons Ltd*.
Mizsei, J. (1995), H_2-induced surface and interface potentials on pd-activated SnO_2 sensor films. *Sensors and Actuators B: Chemical*, **28**(2), 129–33.
Moos, R. (1998), Method and apparatus for detecting the oxygen content of a gas, *US patent specification*, US6368868.
Moos, R. (2005), A Brief Overview on Automotive Exhaust Gas Sensors Based on Electroceramics. *International Journal of Applied Ceramic Technology*, **2**, 401–13.
Moos, R. and Härdtl, K. H. (1997), Defect Chemistry of Donor Doped and Undoped Strontium Titanate Ceramics between 1000°C and 1400°C, *Journal of the American Ceramic Society*, **80**, 2549.
Moos, R., Menesklou, W., Schreiner, H. J. and Härdtl, K. H. (2000) Materials for temperature independent resistive oxygen sensors for combustion exhaust gas control. *Sensors and Actuators B: Chemical*, **67**(1–2),178–83.
Moos, R., Izu, N., Rettig, F., Reiß, S., Shin, W. and Matsubara, I. (2011), Resistive Oxygen Gas Sensors for Harsh Environments, *Sensors*, **11**(4), 3439–65.
Moos, R., Rettig, F., Hürland, A. and Plog, C. (2003), Temperature-independent resistive oxygen exhaust gas sensor for lean-burn engines in thick-film technology. *Sensors and Actuators B: Chemical*, **93**(1–3), 43–50.
Nagy, P. B. and Nayfeh, A. H. (2000), On the thermoelectric magnetic field of spherical and cylindrical inclusions, *Journal of Applied Physics*, **87**, 7481–90.

© Woodhead Publishing Limited, 2013

Niemeyer, D., Williams, D. E., Smith, P., Pratt, K. F. E., Slater, B., Catlow, C. R. A. and Stoneham, A. M. (2002), Experimental and computational study of the gas-sensor behaviour and surface chemistry of the solid-solution $Cr_{2-x}Ti_xO_3$ (x <= 0.5). *Journal of Materials Chemistry*, **12**(3), 667–75.

Pisarkiewicz, T. and Stapinski, T. (1989), Influence of gas atmosphere on thermopower measurements in tin oxide thin-films. *Thin Solid Films*, **174**, 277–83.

Rettig, F., Sahner, K. and Moos, R. (2005) Thermopower of $LaFe_{1-x}Cu_xO_{3-\delta}$, *Conference proceedings of Solid State Ionics*, **15**, Baden-Baden, 569.

Rettig, F. (2008), Direkte thermoelektische Gassensoren (in German). PhD thesis, University of Bayreuth, Shaker-Verlag.

Rettig, F. and Moos, R. (2007), Direct thermoelectric gas sensors: Design aspects and first gas sensors. *Sensors and Actuators B: Chemical*, **123**(1), 413–19.

Rettig, F. and Moos, R. (2007b), Direct thermoelectric hydrocarbon gas sensors based on SnO_2, *IEEE Sensors Journal*, **7**, 1490–6.

Rettig, F. and Moos, R. (2008b), Morphology dependence of thermopower and conductance in semiconducting oxides with space charge regions. *Solid State Ionics*, **179**(39), 2299–307.

Rettig, F. and Moos, R. (2009), Temperature-modulated direct thermoelectric gas sensors: thermal modeling and results for fast hydrocarbon sensors. *Measurement Science and Technology*, **20**(6), 065205 9.

Rettig, F. and Moos, R. (2010), α-iron oxide: An intrinsically semiconducting oxide material for direct thermoelectric oxygen sensors. *Sensors and Actuators B: Chemical*, **145**(2), 685–90.

Rettig, F., Moos, R. and Plog, C. (2003), Sulfur adsorber for thick-film exhaust gas sensors. *Sensors and Actuators B: Chemical*, **93**(1–3), 36–42.

Rettig, F., Moos, R. and Plog, C. (2004), Poisoning of temperature independent resistive oxygen sensors by sulfur dioxide. *Journal of Electroceramics*, **13**(1–3), 733–8.

Riegel, J., Neumann, N. and Wiedenmann, H. M. (2002), Exhaust gas sensors for automotive emission control, *Solid State Ionics*, **152**, 783–800.

Röder-Roith, U., Rettig, R., Röder, T., Janek, J., Moos, R. and Sahner, K. (2009), Thick-film solid electrolyte oxygen sensors using the direct ionic thermoelectric effect. *Sensors and Actuators B: Chemical*, **136**(2), 530–5.

Röder-Roith, U., Rettig, F., Sahner, K., Röder, T., Janek, J. and Moos, R. (2011), Perovskite-type proton conductor for novel direct ionic thermoelectric hydrogen sensor. *Solid State Ionics*, **192**(1), 101–4.

Rothschild, A., Menesklou, W., Tuller, H. L. and Ivers-Tiffee, E. (2006), Electronic structure, defect chemistry, and transport properties of $SrTi_{1-x}Fe_xO_{3-y}$ solid solutions, *Chemistry of Materials*, **18**, 3651–9.

Ruiz, A. M., Sakai, G., Cornet, A., Shimanoe, K., Morante, J. R. and Yamazoe, N. (2003), Cr-doped TiO_2 gas sensor for exhaust NO_2 monitoring. *Sensors and Actuators B: Chemical*, **93**(1–3), 509–18.

Schönauer, U. (1991), Response-times of resistive thick-film oxygen sensors. *Sensors and Actuators B: Chemical*, **4**(3–4), 431–6.

Shin, W., Matsumiya, M., Izu, N. and Murayama, N. (2003), Hydrogen-selective thermoelectric gas sensor. *Sensors and Actuators B: Chemical*, **93**(1–3), 304–8.

Simon, T., Barsan, N., Bauer, M. and Weimar, U. (2001), Micromachined metal oxide gas sensors: opportunities to improve sensor performance. *Sensors and Actuators B: Chemical*, **73**(1), 1–26.

© Woodhead Publishing Limited, 2013

Siroky, K. (1993), Use of the Seebeck effect for sensing flammable-gas and vapors. *Sensors and Actuators B: Chemical*, **17**(1), 13–17.

Smulko, J. M., Ederth, J., Li, Y. F., Kish, L. B., Kennedy, M. K. and Kruis, F. E. (2005), Gas sensing by thermoelectric voltage fluctuations in SnO_2 nanoparticle films. *Sensors and Actuators B: Chemical*, **106**(2), 708–12.

Somov, S. I. and Guth, U. (1998), A parallel analysis of oxygen and combustibles in solid electrolyte amperometric cells, *Sensors and Actuators B: Chemical*, **47**, 131–8.

Taguchi, N. (1970), Gas detecting element and making of it, *US patent specification*, US3644795.

Takami, A. (1988), Development of titania heated exhaust-gas oxygen sensor. *American Ceramic Society Bulletin*, **67**(12), 1956–60.

Timm, H. and Janek, J. (2005), On the Soret effect in binary nonstoichiometric oxide-skinetic demixing of cuprite in a temperature gradient, *Solid State Ionics*, **176**, 1131–43.

Tschöpe, A. (2005), Interface defect chemistry and effective conductivity in polycrystalline cerium oxide, *Journal of Electroceramics*, **14**, 5–23.

Willet, M. (2005), Recent developments in catalytic gas sensors. In *1st International Workshop an Smart Gas Sensors Technology an Application*, Freiburg im Breisgau, Germany.

Williams, D. E. (1999), Semiconducting oxides as gas-sensitive resistors, *Sensors and Actuators B: Chemical*, **57**, 1–16.

Williams, D., Tofield, B. and McGeehin, P. (1985), Oxygen sensors, *European patent specification*, EP00062994.

Wolkenstein, T. (1991), *Electronic Processes on Semiconductor Surfaces during Chemisorption.* Consultants Bureau, New York.

Yamazoe, N. (2005), Toward innovations of gas sensor technology. *Sensors and Actuators B: Chemical*, **108**, 2–14.

Yoo, H. I. and Song, C. R. (2001), Thermoelectricity of $BaTiO_{3+\delta}$, *Journal of Electroceramics*, **6**, 61–74.

© Woodhead Publishing Limited, 2013

8

One- and two-dimensional metal oxide nanostructures for chemical sensing

E. COMINI, Brescia University, Italy

DOI: 10.1533/9780857098665.3.299

Abstract: Metal oxides are the most commonly used materials for chemical sensors, originally in form of thick-films. Single-crystalline one-dimensional nanostructures have considerable advantages: high surface-to-volume ratio, readily achieved reduced lateral dimensions, and their high degree of purity and crystallinity. These characteristics permit a variety of gas sensor designs, such as single wire, self-heating devices and photoactivation. Despite these advantages, large-scale integration has still not been achieved, and two-dimensional nanostructures still merit study and research.

Key words: metal oxide, chemical sensing, nanowires, films.

8.1 Introduction

Metal oxides have very different electrical properties from metals, semiconductors and insulators, and are used in many different areas such as sensors, superconductors, magnets and lighting. In relation to chemical sensing applications, the ability of metal oxides to change their electrical conductivity with the composition of the surrounding atmosphere has been known for almost sixty years.[1] In October 1968, the first generation of commercial devices were produced on a large scale by TGS (Taguchi Gas Sensor) in Japan. These sensors were made of SnO_2 thick films and were used for the detection of explosive gases.

Over the years, the demand for cheap, small, low power consuming but reliable solid-state chemical sensors has continued to grow. Consequently, significant research efforts have been made worldwide to improve on the '3Ss' (sensitivity, selectivity and stability), mainly with empirical approaches, but also some basic theoretical research and spectroscopy studies.

The metal oxide that has been paid the greatest attention for chemical sensing is SnO_2; however, other oxides – such as TiO_2, In_2O_3, WO_3, ZnO, Fe_2O_3 – have been proposed and studied. Furthermore, the use of mixed oxides, as well as the addition of noble metals, has been studied to improve not only selectivity, but also stability. One of the most important articles in

© Woodhead Publishing Limited, 2013

metal oxide chemical sensing was published in 1991 by Yamazoe.[2] It was shown that, as the crystallite size was reduced, there was a huge improvement in sensor performance. This shifted the research community focus to the performance of materials with the smallest crystallite size, while ensuring that their properties remain stable during long-term, high-temperature operation, which is necessary for metal oxide chemical sensing.

Another important discovery that changed the field of chemical sensing was the synthesis of single crystal one-dimensional oxide nanowires. These are created by the simple evaporation of the desired commercial metal oxide powders at high temperatures and their condensation at lower temperatures on the substrates. These materials have great potential thanks to their reduced lateral dimensions and single crystal habits, both for fundamental study and for potential nanodevice applications, i.e. the third generation of metal oxide gas sensors.

8.2 Deposition techniques

The technique of layer deposition and coating has a variety of industrial applications, such as protective layers, sensors, resistive films and catalyzers. We will briefly present the different deposition techniques as a function of the nanostructures obtained for:

- two-dimensional nanostructures (thin films),
- one-dimensional nanostructures (nanowires, nanorods, etc.).

8.2.1 Two-dimensional nanostructures

There are several preparation methods that have been optimized and proposed during recent years. We can, for example, distinguish between physical vapor deposition (PVD) techniques, chemical vapor deposition (CVD) techniques and techniques that do not require a vacuum.

In the case of PVD techniques, the source material to be deposited is in the solid phase. An intermediate vapor phase is then formed and finally the solid phase is deposited on the substrate. The method used for the vaporization of the source material distinguishes between the different deposition techniques. For example, heat transfer is used in thermal and electron beam evaporation, while bombardment by energetic ions is used in sputtering processes.

The thermal evaporation (TE) technique is the oldest PVD process. In this technique, the substrate is kept at a short distance from the source material, which is heated until it vaporizes. The vapor then condenses on the substrate.[3–4]

© Woodhead Publishing Limited, 2013

The equipment required to apply all these PVD methods works at pressures lower than ambient pressure: this is necessary in order to control the composition of the deposited material. To improve its purity, the mean free path of the particles must be greater than the distance between the source and the substrate. In the specific case of TE, this also allows a lower operational temperature for the vaporization. A conventional deposition system consists of a vacuum chamber, a mechanical roughing pump, a high vacuum pump, a heated crucible and a substrate holder.

In the case of TE, unintentional doping in the film can result from the high temperature of vaporization that has to be reached by the source material. Particular attention must be paid to the material composition of the crucible containing the source material and to the possible alloys that it can form with the source material at the evaporation temperature.

Electron beam evaporation (EBE) is similar to TE, except that the source material is vaporized by the heat transferred from an electron beam accelerated toward the source. On the impingement of the high-energy electrons, their kinetic energy is converted into heat and the source material can reach temperatures exceeding 300°C, causing a local melting where the beam is focused. The advantage of this technique is that the electron beam can be focused on specific areas of the source material, so that the interaction between source material and support materials can be reduced.[5–7]

Another method based on evaporation is pulsed laser deposition (PLD). The high photon flux incident on the target induces an essentially instantaneous temperature increase that causes the evaporation of the target material.[8–10] The experimental setup consists of a vacuum chamber in which there is the target material and a window through which the laser beam is focused onto the target. The ejected material that arises from a target after laser irradiation is called an 'ablation plume' (i.e., a plasma-like substance containing free electrons and ions, neutral particles, molecular fragments and chemical reaction products). The physical process of laser ablation is extremely complicated and there are several key parameters involved, such as beam energy density, the laser pulse duration, and the laser wavelength.

One of the most commonly used PVD techniques for industrial applications is sputtering. The sputtering process was discovered by W.R. Grove in 1852 while studying the discharge in a tube containing gas, but its use in industry and research began in recent decades.

In this process, the surface of the sputtering target is bombarded with gaseous ions under high voltage acceleration. Atoms or entire molecules of the target material are ejected and can reach the substrate. There is no melting of the material: the ejection of the particles from the source material (target) is a result of the momentum transferred from the incoming particle. The conventional setup for sputtering is a vacuum chamber where the working

© Woodhead Publishing Limited, 2013

gas is introduced, a high negative voltage is applied to the target, and the positively charged ionized atoms are accelerated towards it.[11–13]

To sputter conductive materials, direct current sputtering is used, while for nonconductive materials, radio frequency must be applied during the sputtering process in order to prevent the target from charging up due to the bombardment from positively charged ions. Another configuration is magnetron sputtering, where a magnetic field is added beneath the target to deflect and confine electrons, allowing for lower working pressures. In sputtering, the phase transition is obtained mechanically rather than chemically or thermally, so virtually any material can be deposited. The energy of the ejected molecules is higher with respect to TE and EBE, thus improving the crystallinity and adhesion of the thin film.

The second group of deposition techniques is CVD: a chemical reaction transforms the molecules in the gas phase, known as the 'precursors', into solid films or powders on the substrate. There are several configurations such as:

- low pressure chemical vapor deposition (LPCVD)
- atmospheric pressure chemical vapor deposition (APCVD)
- plasma enhanced chemical vapor deposition (PECVD)
- photochemical vapor deposition (PCVD)
- laser chemical vapor deposition (LCVD)
- metalorganic chemical vapor deposition (MOCVD).

In CVD, the reactant gases are diluted in carrier gases and introduced into the reaction chamber at room temperature, while the deposition surface is heated. The energy necessary to start the desired chemical reaction can be supplied as thermal energy with resistive, radiant or inductive heating, or as photon energy or glow discharge plasma. Depending on the working conditions, the reactant may experience homogeneous chemical reactions in the vapor phase before hitting the surface. Otherwise, when the reactant gases approach the surface, they slow down and heterogeneous reactions occur on the surface, forming the deposited material. Gaseous reaction by-products are then transported by the carrier gas out of the reaction chamber.

Whichever heating method is employed, CVD has to provide a volatile precursor containing the elements that compose the deposited film, transport the precursor towards the substrate surface, enhance or reduce reactions in the gas phase, and provide the surface reaction needed to form the film. The setup consists of a reaction chamber; gas/vapor delivery lines; the energy source; vacuum systems (LPCVD); an exhaust system; and gas flow, pressure and temperature monitoring systems.[14–16] Hazardous vapors are also frequently used and may be produced by chemical reactions. Thus, safety equipment may be necessary. The advantages of CVD films are good

© Woodhead Publishing Limited, 2013

adhesion, good step coverage and high versatility of materials, but a drawback is the formation of hazardous and corrosive by-products.

Beyond PVD and CVD, there are techniques from the liquid/solution phase: such as sol-gel, spray coating, spin coating, electrochemical deposition and liquid phase epitaxy. The sol-gel process is the most widely used method for the deposition of metal oxide for gas sensors.

The sol-gel process generally involves the transition from a liquid sol into a solid gel phase. Inorganic metal salts or metal organic compounds, such as metal alkoxides, may be used as precursors. The sol-gel deposition process usually has four steps:

- colloidal particles are dispersed in a liquid (sol),
- deposition of sol solution on the substrate by spraying, dipping or spinning,
- polymerization of the particles in the sol by stabilizing components removal (gel) and
- heat treatment to pyrolyze the remaining organic or inorganic components forming the final film.

The advantages of this process are the production of high-purity metal oxides, a highly controllable composition, the low temperature deposition, and a simple and economic experimental setup.[17–19] However, disadvantages such as weak adhesion and low wear-resistance limit its full industrial exploitation.

8.2.2 One-dimensional nanostructures

A nomenclature for one-dimensional materials has not yet been established. Different and creative names have been presented in the literature, such as nanotubules, whiskers, fibers, fibrils, nanocables, nanocastles, etc. Terms such as ‘nanowires’ or ‘nanorods’ were used in the literature for structures with two dimensions not exceeding a few hundreds of nanometers.

In the past decade, since 2001, the number of synthesis techniques for one-dimensional nanostructures has grown exponentially. The approaches can be divided into top-down and bottom-up techniques. The first, based on standard microfabrication technologies, allows the preparation of well-organized nanowires,[20–23] but is not yet compatible with the need for large-scale production. The second approach consists of self-assembly of molecular building blocks, synthesis via vapor-phase transport, solution-based techniques, or template growth. The advantages are the fine control in shape, morphology, structure, high purity and crystallinity, together with the low cost of the experimental equipment. The main drawback is

© Woodhead Publishing Limited, 2013

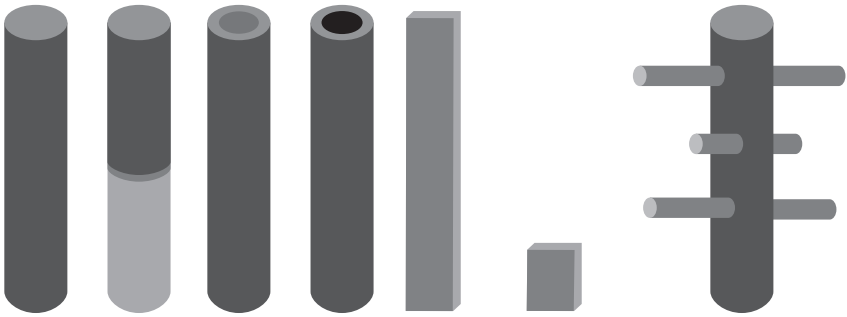

8.1 Schematic representation of some morphologies of one-dimensional nanostructures.

the integration on planar substrates needed for the exploitation of their useful properties. Several one-dimensional oxide nanostructures with different properties and morphologies have been fabricated using bottom-up synthetic routes. Most of these structures could not have been prepared easily and economically using top-down technologies. A few morphologies of these new nanostructures with potential as chemical sensing devices are summarized schematically in Fig. 8.1.

Vapor phase growth methods

In order to obtain one-dimensional structures, there has to be a preferential growth direction (i.e. a faster growth rate in a particular direction). Even though the exact mechanism responsible for one-dimensional growth in the vapor phase is still not clearly understood, vapor phase methods have been explored and are extensively used by many research groups to synthesize one-dimensional materials. The main advantage is its simplicity in terms of the procedure and the experimental set-up used.

In general, the vapor phase is obtained by evaporation, chemical reduction, or other reactions. The vapors are then transported and condensed onto the substrates surface held at lower temperatures. By controlling the supersaturation of the vapor, one-dimensional materials can be easily obtained. When the growth of the nanowire crystal directly originates from the condensation from the vapor phase without the use of a catalyzer, the term 'vapor-solid growth' is typically used. Defect-free nanowires can be produced using this technique. However, there is still no consensus on the growth mechanism. If the growth originates from the condensation onto catalyst particles, the growth is typically defined as a 'vapor liquid solid' (VLS) process. Among all vapor phase methods, the VLS process is the most successfully used and cited for generating nanowires with single-crystalline structures and in considerable amounts.

© Woodhead Publishing Limited, 2013

The mechanism for VLS was proposed by Wagner in 1964. Under deposition conditions, the catalyzer has to form a liquid solution with the desired material. It should also have a low vapor pressure and be chemically inert. In the process, the vapor diffuses into the liquid catalyzer and, as the concentration becomes too high, the growth species precipitate to form the nanowire. The liquid phase is a preferential condensation site, and this causes a higher growth rate of the VLS with respect to the VS. Furthermore, by controlling the dimension and dispersion of the catalyzer, control can be achieved over the diameter of the nanowire.

Liquid phase growth methods

There are many experimental techniques for the preparation of nanowires from the liquid phase. A considerable research effort has been expended in developing template-free methods for the deposition of one-dimensional nanostructures in a liquid environment; the most important procedures are hydrothermal methods,[24–29] electrospinning,[30–40] sonochemical[41–46] and surfactant assisted.

The Hydrothermal process has been a well-known procedure for material synthesis since the 1970s. It begins with an aqueous mixture of soluble metal salt (metal and/or metal–organic) precursors, then the solution is placed in an autoclave at a high temperature (between 100°C and 300°C) and under relatively high pressure (> 1 atm) conditions. ZnO nanorods,[47–50] CuO,[51] ceria,[52] titania[53] and MnO_2[54] have been prepared by using wet-chemical hydrothermal approaches.

Electrospinning exploits an electrical charge to force the formation of mats of fine fibers.[55] A solid fiber is produced as the electrified jet is continuously stretched due to the electrostatic repulsions between the surface charges and the evaporation of solvent. A number of oxides have been fabricated as fibrous structures: Al_2O_3, CuO, NiO, TiO_2,SiO_2, V_2O_5, ZnO, Co_3O_4, Nb_2O_5, MoO_3 and $MgTiO_3$.[56–66] The one-dimensional nanostructures produced are, in general, polycrystalline.

Template-assisted methods

There are several references reporting on template-assisted approaches for nanofabrication such as Hulteen and Martin.[67] They are regarded as one of the pioneer groups for functional nanowire array fabrication. With the use of a periodic structured template, one-dimensional nanostructures can be prepared thanks to the confinement effect of the porous template. The templates can be prepared easily with anodization. Control of the aspect ratio and the area density of one-dimensional nanostructures can be achieved by changing the diameter and length of the template, and by changing the anodization voltage.

© Woodhead Publishing Limited, 2013

The nanostructures can be deposited into the nano-pores by electrodeposition or sol-gel deposition methods. The advantages of being low cost and repeatable, together with their potential compatibility with silicon technologies, make these nanostructure synthesis procedures interesting. Despite its simplicity, template-based growth is characterized by the production of polycrystalline nanowires, which can limit their potential for both fundamental studies and applications.

8.3 Conductometric sensor

The semiconducting properties of metal oxides are due to deviation from stochiometry. In most oxides, such as tin oxide, oxygen vacancies are responsible for the n-type behavior. The normal working condition for a chemical sensor is in the presence of air at relatively high temperatures (500–800 K). At these temperatures, the metal oxide conduction is electronic and there are doubly-ionized oxygen vacancies. Oxygen in such conditions is chemisorbed on the metal oxide surface, capturing charge carriers from the conduction band and producing a space charge area. Chemical sensing is achieved in most cases by oxidation reactions between chemical species and chemisorbed oxygen, causing a decrease in the surface barrier, leading to a change in conductance. Other chemical species, such as nitrogen oxide or water vapor, may chemisorb directly on the metal oxide surfaces by trapping or releasing electrons.

8.3.1 Device integration

Device integration is very easy and well-established for thin films that can be easily patterned or deposited on the final transducers but, in the case of one-dimensional nanostructures, there still remain some open issues.

One-dimensional nanostructures should be grown directly on the transducers, but, depending on the deposition conditions, this may not always be possible due to high temperatures, pressures or the aggressive ambient required for their preparation. In these cases, they have to be transferred afterwards. The easiest way to transfer is by drop coating, but other techniques such as dielectrophoresis[68,69] or roll transfer[70] may be used. In the case of single-nanowire devices, nanomanipulation[71] can also be used.

The problem that remains in all cases is the mechanical and electrical stability of the contact achieved between the metal oxide and the metal. To obtain very stable devices, there must be a good and reliable electrical contact, with a low and stable contact resistance. This is because the metal semiconductor junction that forms at the interface between the metal oxide

© Woodhead Publishing Limited, 2013

and the metal may play a role in chemical sensing. This is even more important for single-nanowire devices because the junction is in series with the nanowire resistance; for multiple-nanowire devices, it is connected to a large number of resistances.

New lithographic techniques have been proposed for the integration of the vapor phase growth process with device fabrication.[72–74] Concerning chemical sensing, a high temperature lift-off procedure was recently developed for nanowire networks integration on sensing transducers, by using silicon oxide as a sacrificial layer.[75] This allows a clean patterning and assures the presence of uniform surfaces for the deposition of contacts.

For single-nanowire devices, highly expensive techniques (such as a focused ion beam, or a series of nano-lithographic tools) must be used, ranging from proton and electron beam nanolithography,[76] in which patterned substrates are obtained under the application of a charged particle beam, to nano-imprint lithography.[77]

8.4 Transduction principles and related novel devices

The change of the electrical properties, related to the surrounding atmosphere, can be transduced as a change of resistance, impedance or work function. The easiest measurable parameter is the sensor resistance in DC conditions. It may be measured by a voltamperometric technique at constant bias but, in commercial chemical sensors, the sensing film is usually inserted inside a voltage divider.

A typical kinetic response of conductance as a function of an introduction of a concentration step is shown in Fig. 8.2. After the reducing species is introduced at time t_1, the sensor conductance G_i increases to G_f, in the time needed to reach the new thermodynamic equilibrium of the surface reactions. If the metal oxide is not stable, or if there is an irreversible chemisorption, a steady state may not be reached.

Response time is the time necessary for the conductance to reach a threshold value (usually 90%) of the difference between G_f and G_i. Recovery time is the time necessary for the conductance to recover to a band expressed as a percentage fraction (usually 90%) of G_f–G_i. Concerning the response of chemical sensors, the linearity hypothesis is not verified, and the response when working with gas mixtures cannot be deduced by the superimposition principle, with a simple sum of the individual response.

The sensor response towards a reducing species and an n-type metal oxide may be defined as the relative change in conductance:

$$G_f/G_i$$

© Woodhead Publishing Limited, 2013

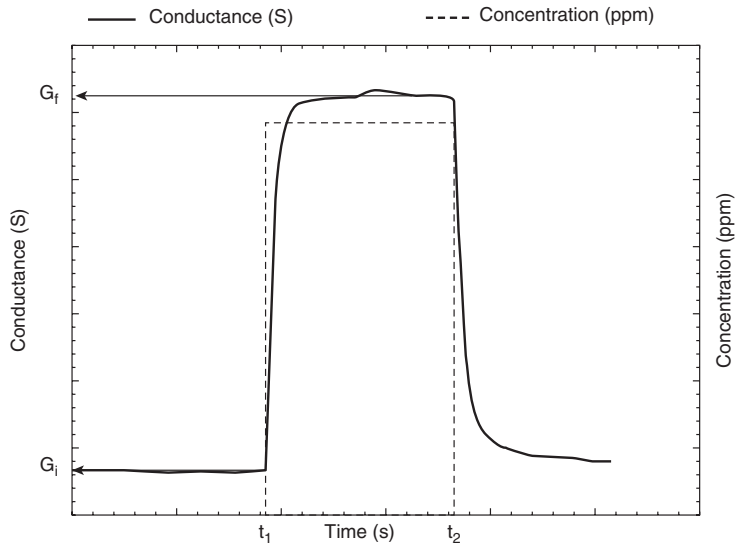

8.2 Conductance variation of the sensor produced by the introduction of a step concentration of a reducing gas.

For an oxidizing species and an n-type metal oxide, there is an increase in the resistance and the sensor response may be defined as the relative change of resistance:

$$R_f/R_i$$

The calibration curve can be obtained after measuring the response at different concentrations in the same operational conditions. The calibration curve is generally reported in a bi-logarithmic scale since the relation between concentration and conductance follows a power law (Fig. 8.3).

Impedance is another possible transduced signal, and it can be measured by a spectroscopic analyzer or by LCR (L = inductance, C = capacitance, R = resistance) bridges. It may be useful to identify the different contributions to the sensor response (grain, bulk and contact) but, due to higher costs, there are no commercial devices based on this transduction.

Most of the sensing performances reported in the literature are based on measurements of individual devices in artificial environments that do not reproduce field conditions. In many studies, the carrier gas is nitrogen; no air, humidity or interfering gases are introduced. That is why it is very difficult, and sometimes impossible, to make a comparison of all the results reported, or to speculate on sensing performances in a real environment.

© Woodhead Publishing Limited, 2013

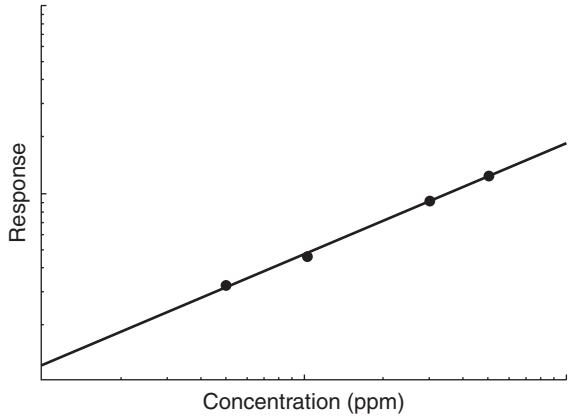

8.3 Calibration curve of the response of a chemical sensor towards a chemical species.

Few comparative studies between nanowire and polycrystalline chemical sensors have been reported.[78,79,80] Sysoev[79] reported that, even if the nanoparticles had a higher response to 2-propanol vapors at first, after some days of operation the response of the nanoparticles decreases to the stable response of nanowires. This was ascribed to the irreversible sintering process in the nanoparticles that occurs due to high temperature operation.

The research on one-dimensional nanostructures is not as advanced as that on two-dimensional nanostructures, due to the difficulties in fabricating the device. Nevertheless, to exploit the unique possibilities of these structures, the focus has to be on peculiar properties that can lead to essential advances in functional devices. For example, the self-heating property that was recently reported can be used for the development of fully-autonomous chemical sensors.[81]

Self-heating of a single nanowire is due to the dissipated power (Joule effect) induced by the bias current applied in conductometric measurements. Nanowires, with their small mass, can be heated up to several hundreds of degrees with a few tens of microwatts. By combining low power electronics with continuous and pulsed self-heating of nanowires, it will be possible to reduce power consumption to the microwatt range, or even lower.[81]

Another most interesting approach proposed to improve chemical interactions and reduce the operating temperature is optical excitation. High temperatures limit the application of chemical sensors to nonexplosive and inflammable environments. As photons above the bandgap are absorbed by metal oxide semiconductors, free carriers are produced in the space charge area. The excess electrons are swept away from the surface, while excess holes are swept towards it due to the electrical field in the space charge

© Woodhead Publishing Limited, 2013

area, with a decrease in the surface band bending. Several years ago the effect of photoactivation on the sensing performances was demonstrated for two-dimensional nanostructures metal oxide chemical sensors.[82–85] The first report on the possibility of using optical excitation on one-dimensional nanostructures sensing devices was published by Law *et al*.[86] After several years[87–88] the response of optically excited single-nanowire devices was shown to be comparable to devices that were thermally activated, in the optimal experimental conditions.

8.5 Conclusion and future trends

Significant efforts have been made to develop and test new metal oxides. However, the application of chemical sensors still faces problems such as selectivity and long-term drift due to stoichiometry changes and coalescence of crystallites. The notion of preparing multipurpose devices has been replaced by the development of sensors tailored for specific and focused applications.

The improvement of computer systems and of imaging and spectroscopic techniques will provide powerful tools for the better understanding of chemical sensing mechanisms, and help to optimize sensor design. One-dimensional nanostructures have a greater surface-to-volume ratio, better stochiometry and a higher degree of crystallinity compared with two-dimensional nanostructures. They also have reduced instability associated with grain coalescence. These factors make one-dimensional metal oxides very promising for the better understanding and the development of a new generation of chemical sensors.

8.6 References

1. Brattain WH, Bardeen J. Surface properties of germanium. *Bell Syst. Tech. J.,* 1953; **32**: 1–41.
2. Yamazoe N. New approaches for improving semiconductor gas sensors. *Sensor. Actuat. B*, 1991; **5**: 7.
3. Kanitkar P, Kaur M, Sen S, Joshi A, Kumar V, Gupta SK, Yakhmi JV. Growth and gas-sensing studies of metal oxide semiconductor nanostructures. *Int. J. Nanotechnol.* 2010; **7**: 9–12, 883–906.
4. Yaacob MH, Yu J, Latham K, Kalantar-Zadeh K, Wlodarski W. Optical hydrogen sensing properties of nanostructured Pd/MoO(3) films. *Sensor. Lett.* 2011; **9**(1): 16–20. DOI: 10.1166/sl.2011.1410.
5. Xu YX, Tan QQ, Tang ZL, Zhang ZT, Yuan ZF. WO(3)-Based gas sensors. *Prog. Chem.* 2009; **21**(12): 2734–2743.
6. Wongchoosuk C, Wisitsoraat A, Tuantranont A, Kerdcharoen T. Portable electronic nose based on carbon nanotube-SnO(2) gas sensors and its application for detection of methanol contamination in whiskeys. *Sensor. Actuat. B-Chem.* 2010; **147**(2): 392–399. DOI: 10.1016/j.snb.2010.03.072.

© Woodhead Publishing Limited, 2013

7. Lu C, Chen Z. High-temperature resistive hydrogen sensor based on thin nanoporous rutile TiO(2) film on anodic aluminum oxide. *Sensor. Actuat. B-Chem.* 2009; **140**(1): 109–115. DOI: 10.1016/j.snb.2009.04.004.
8. Durrani SMA, AI-Kuhaili MF. Effect of biasing voltages and electrode metals and materials on the sensitivity of electron beam evaporated HfO2 thin film CO sensor. *Mater. Chem. Phys.* 2008; **109**(1): 56–60. DOI: 10.1016/j.matchemphys.2007.10.034.
9. Trucchi DM, Zanza A, Bellucci A, Marotta V, Orlando S. Photoconductive and photovoltaic evaluation of In(2)O(3)-SnO(2) multilayered thin-films deposited on silicon by reactive pulsed laser ablation. *Thin Solid Films* 2010; **518**(16): 4738–4742. DOI: 10.1016/j.tsf.2009.12.072.
10. Belysheva TV, Gerasimov GN, Gromov VF, Trakhtenberg LI. The sensor properties of Fe2O3 center dot In2O3 films: The detection of low ozone concentrations in air. *Russ. J. Phys. Chem. A* 2008; **82**(10):1721–1725. DOI: 10.1134/S0036024408100142.
11. Mitu B, MarottaV, Orlando S. Multilayered metal oxide thin film gas sensors obtained by conventional and RF plasma-assisted laser ablation. *Appl. Surf. Sci.* 2006; **252**(13):4637–4641. DOI: 10.1016/j.apsusc.2005.07.102.
12. Al-Hardan N, Abdullah MJ, Aziz AA. Impedance spectroscopy of undoped and Cr-doped ZnO gas sensors under different oxygen concentrations. *Appl. Surf. Sci.* 2011; **257**(21):8993–8997. DOI: 0.1016/j.apsusc.2011.05.078.
13. Shaalan NM, Yamazaki T, Kikuta T. Effect of micro-electrode geometry on NO(2) gas-sensing characteristics of one-dimensional tin dioxide nanostructure microsensors *Sensor. Actuat. B-Chem.* 2011; **156**(2):784–790. DOI: 10.1016/j.snb.2011.02.039.
14. Batista C, Teixeira V, Ribeiro RM. Pulsed DC reactive magnetron sputtering of vanadium dioxide thermochromic thin films. *Mater. Technol.* 2011; **26**(1):35–39. DOI: 10.1179/175355511X12941605982307.
15. Arivazhagan V, Rajesh S. Preparation of nanocrystalline Sno(2) thin films for micro gas sensors *J. Ovonic. Res.* 2010; **6**(5):221–226.
16. Beardslee JA, Mebust AK, Chaimowitz AS, Davis-VanAtta CR, Leonard H, Moersch TL, Afridi MY, Taylor CJ. Using precursor chemistry to template vanadium oxide for chemical sensing. *Chem. Vapor Depos.* 2010; **16**: 206–210. DOI: 10.1002/cvde.201004286.
17. Bekermann D, Rogalla D, Becker HW, Winter M, Fischer RA, Devi A. Volatile, monomeric, and fluorine-free precursors for the metal organic chemical vapor deposition of zinc oxide. *Eur. J. Inorg. Chem.* 2010; **9**:1366–1372. DOI: 10.1002/ejic.200901037.
18. Neri G. Non-conventional sol-gel routes to nanosized metal oxides for gas sensing: from materials to applications. *Sci. Adv. Mat.* 2010; **2**(1):3–15. DOI: 10.1166/sam.2010.1062.
19. Breedon M, Spizzirri P, Taylor M, du Plessis J, McCulloch D, Zhu JM, Yu LS, Hu Z, Rix C, Wlodarski W, Kalantar-zadeh K. Synthesis of nanostructured tungsten oxide thin films: A simple, Controllable, Inexpensive, Aqueous sol-gel method. *Cryst. Growth. Des.* 2010; **10**(1):430–439. DOI: 10.1021/cg9010295.
20. Mohammadi M, Fray DJ. Development of nanocrystalline TiO(2)-Er(2)O(3) and TiO(2)-Ta(2)O(5) thin film gas sensors: Controlling the physical and sensing properties. *Sensor. Actuat. B-Chem.* 2009; **141**(1):76–84. DOI: 10.1016/j.snb.2009.05.026.

© Woodhead Publishing Limited, 2013

21. Haghiri-Gosnet AM, Vieu C, Simon G, Mejıas M, Carcenac F, Launois H. Nanofabrication at a 10 nm length scale: Limits of lift-off and electroplating transfer processes. *J. Phys IV* 1999; **9**:133–141.
22. Marrian CRK, Tennant DM. Nanofabrication. *J. Vac. Sci. Technol. A* 2003; **21**:S207–S215.
23. Candeloro P, Comini E, Baratto C, Faglia G, Sberveglieri G, Kumar R, Carpentiero A, Di Fabrizio E. SnO2 lithographic processing for nanopatterned gas sensors. *J. Vac. Sci. Technol. B* 2005; **23**:2784–2788.
24. Candeloro P, Carpentiero A, Cabrini S, Di Fabrizio E, Comini E, Baratto C, Faglia G, Sberveglieri G, Gerardino A. SnO2 sub-micron wires for gas sensors. *Micro. Eng.* 2005; **78–79**:178–184.
25. Liu B, Zeng HC. Hydrothermal synthesis of ZnO nanorods in the diameter regime of 50 nm. *J. Am. Chem. Soc.* 2003; **125**:4430–4431.
26. Wang JSM, Gao L. Wet chemical synthesis of ultralong and straight single-crystalline ZnO nanowires and their excellent UV emission properties. *J. Mater. Chem.* 2003; **13**:2551–2554.
27. Guo M, Diao P, Cai SM. Hydrothermal growth of well-aligned ZnO nanorod arrays: dependence of morphology and alignment ordering upon preparing conditions. *J. Solid. State. Chem.* 2005; **178**:1864–1873.
28. Cao MH, Wang YH, Guo CX, Qi YJ, Hu CW, Wang EB. A simple route towards CuO nanowires and nanorods. *J. Nanosci. Nanotechnol.* 2004; **4**:824–828.
29. Zhou KB, Wang X, Sun XM, Peng Q, Li YD. Enhanced catalytic activity of ceria nanorods from well-defined reactive crystal planes. *J. Catal.* 2005; **229**:206–212.
30. Yuan ZY, Su BL. Titanium oxide nanotubes, nanofibers and nanowires, *Colloids. Surf. A. Physicochem. Eng. Aspects* 2004; **241**:173–183.
31. A. Formhals, Process and apparatus for preparing artificial threads, US patent, 1 975 504, 1934.
32. Dai H, Gong J, Kim H, Lee D. A novel method for preparing ultra-fine alumina-borate oxide fibres via an electrospinning technique. *Nanotechnology* 2002; **13**:674–677.
33. Viswanathamurthi P, Bhattarai N, Kim HY, Lee DR, Kim SR, Morris MA. Preparation and morphology of niobium oxide fibres by electrospinning. *Chem. Phys. Lett.* 2003; **374**:79–84.
34. Shao C, Kim HY, Gong J, Ding B, Lee DR, Park SJ. Fiber mats of poly(vinyl alcohol)/silica composite via electrospinning. *Mater. Lett.* 2003; **57**:1579–1584.
35. Guan H, Shao C, Chen B, Gong J, Yang X. A novel method for making CuO superfine fibres via an electrospinning technique. *Inorg. Chem. Commun.* 2003; **6**:1409–1411.
36. Guan H, Shao C, Chen B, Gong J, Yang X. Preparation and characterization of NiO nanofibres via an electrospinning technique. *Inorg. Chem. Commu.* 2003; **6**:1302–1303.
37. Yang X, Shao C, Guan H, Li X, Gong J. Preparation and characterization of ZnO nanofibers by using electrlospun PVA/zinc acetate composite fiber as precursor. *Inorg. Chem. Commun.* 2004; **7**:176–178.
38. Ding B, Kim H, Kim C, Khil M, Park S. Morphology and crystalline phase study of electrospun TiO_2-SiO_2 nanofibres. *Nanotechnol.* 2003; **14**:532–537.
39. Viswanathamurthi P, Bhattarai N, Kim HY, Lee DR. Vanadium pentoxide nanofibers by electrospinning. *Scr. Mater.* 2003; **49**:577–581.

© Woodhead Publishing Limited, 2013

40. Guan H, Shao C, Wen S, Chen B, Gong J, Yang X. Preparation and characterization of NiO nanofibres via an electrospinning technique. *Mater. Chem. Phys.* 2003; **6**:1302–1303.
41. Dharmaraj N, Park HC, Lee BM, Viswanathamurthi P, Kim HY, Lee DR. Preparation and morphology of magnesium titanate nanofibres via electrospinning. *Inorg. Chem. Commun.* 2004; **7**: 431–433.
42. Xu CK, Xu GD, Liu YK, Wang GH. A simple and novel route for the preparation of ZnO nanorods. *Solid State Commun.* 2002; **122**:175–179.
43. Xu CK, Zhao XL, Liu S, Wang GH. Large-scale synthesis of rutile SnO_2 nanorods. *Solid State Commun*. 2003; **125**:301–304.
44. Xu CK, Xu GD, Wang GH. Preparation and characterization of NiO nanorods by thermal decomposition of NiC_2O_4 precursor. *J. Mater. Sci.* 2003; **38**:779–782.
45. Gao T, Li QH, Wang TH. Sonochemical synthesis, optical properties, and electrical properties of core/shell-type ZnO nanorod/CdS nanoparticle composites. *Chem. Mater.* 2005; **17**:887–892.
46. Miao JJ, Wang H, Li YR, Zhu JM, Zhu JJ. Ultrasonic-induced synthesis of CeO2 nanotubes. *J. Cryst. Growth.* 2005; **281**:525–529.
47. Kumar RV, Koltypin Y, Xu XN, Yeshurun Y, Gedanken A, Felner I. Fabrication of magnetite nanorods by ultrasound irradiation. *J. Appl. Phys.* 2001; **89**:6324–6328.
48. Liu B, Zeng HC. Hydrothermal synthesis of ZnO nanorods in the diameter regime of 50 nm. *J. Am. Chem. Soc.* 2003; **125**:4430–4431.
49. Wang JM, Gao L. Wet chemical synthesis of ultralong and straight single-crystalline ZnO nanowires and their excellent UV emission properties. *J. Mater. Chem.* 2003; **13**:2551–2554.
50. Guo M, Diao P, Cai SM. Hydrothermal growth of well-aligned ZnO nanorod arrays: dependence of morphology and alignment ordering upon preparing conditions. *J. Solid. State. Chem.* 2005; **178**:1864–1873.
51. Sun Y, Ndifor-Angwafor NG, Riley DJ, Ashfold MNR. Synthesis and photoluminescence of ultra-thin ZnO nanowire/nanotube arrays formed by hydrothermal growth. *Chem. Phys. Lett.* 2006; **431**:352–357.
52. Cao MH, Wang YH, Guo CX, Qi YJ, Hu CW, Wang EB. A simple route towards CuO nanowires and nanorods. *J. Nanosci. Nanotechnol.* 2004; **4**:824–828.
53. Zhou KB, Wang X, Sun XM, Peng Q, Li YD. Enhanced catalytic activity of ceria nanorods from well-defined reactive crystal planes. *J. Catal.* 2005; **229**:206–212.
54. Yuan ZY, Su BL, Titanium oxide nanotubes, nanofibers and nanowires, *Colloids. Surf. A Physicochem. Eng. Aspects* 2004; **241**:173–183.
55. Yuan ZY, Ren TZ, Du G, Su BL. A facile preparation of single-crystalline a-Mn_2O_3 nanorods by ammonia-hydrothermal treatment of MnO2. *Chem. Phys. Lett.* 2004; **389**:83–86.
56. A. Formhals, Process and apparatus for preparing artificial threads, US patent, 1 975 504, 1934.
57. Dai H, Gong J, Kim H, Lee D. A novel method for preparing ultra-fine alumina-borate oxide fibres via an electrospinning technique. *Nanotechnol.* 2002; **13**:674–677.
58. Viswanathamurthi P, Bhattarai N, Kim HY, Lee DR, Kim SR, Morris MA. Preparation and morphology of niobium oxide fibres by electrospinning. *Chem. Phys. Lett.* 2003; **374**:79–84.

© Woodhead Publishing Limited, 2013

59. Shao C, Kim HY, Gong J, Ding B, Lee DR, Park SJ. Fiber mats of poly(vinyl alcohol)/silica composite via electrospinning. *Mater. Lett.* 2003; **57**:1579–1584.
60. Guan H, Shao C, Chen B, Gong J, Yang X. A novel method for making CuO superfine fibres via an electrospinning technique. *Inorg. Chem. Commun.* 2003; **6**:1409–1411.
61. Guan H, Shao C, Chen B, Gong J, Yang X. Preparation and characterization of NiO nanofibres via an electrospinning technique. *Inorg. Chem. Commun.* 2003; **6**:1302–1303.
62. Yang X, Shao C, Guan H, Li X, Gong J. Preparation and characterization of ZnO nanofibers by using electrlospun PVA/zinc acetate composite fiber as precursor. *Inorg. Chem. Commun.* 2004; **7**:176–178.
63. Ding B, Kim H, Kim C, Khil M, Park S. Morphology and crystalline phase study of electrospun TiO_2-SiO_2 nanofibres. *Nanotechnol.* 2003; **14**:532–537.
64. Viswanathamurthi P, Bhattarai N, Kim HY, Lee DR. Vanadium pentoxide nanofibers by electrospinning. *Scr. Mater.* 2003; **49**:577–581.
65. Guan H, Shao C, Wen S, Chen B, Gong J, Yang X. Preparation and characterization of NiO nanofibres via an electrospinning technique. *Mater. Chem. Phys.* 2003; **6**:1302–1303.
66. Dharmaraj N, Park HC, Lee BM, Viswanathamurthi P, Kim HY, Lee DR. Preparation and morphology of magnesium titanate nanofibres via electrospinning. *Inorg. Chem. Commun.* 2004; **7**:431–433.
67. Hulteen JC, Martin CR. A general template-based method for the preparation of nanomaterials *J. Mater. Chem.* 1997; **7**:1075–1087.
68. Freer EM, Grachev O, Duan X, Martin S, Stumbo DP. High-yield self-limiting single-nanowire assembly with dielectrophoresis. *Nat. Nanotechnol.* 2010; **5**:525–530. Doi:10.1038/nnano.2010.106.
69. Raychaudhuri S, Dayeh SA, Wang D, Yu ET. Precise Semiconductor Nanowire Placement Through Dielectrophoresis. *Nano. Lett.* 2009; **9**(6):2260–2266
70. Chang Y.-K, Hong F. C.-N. The fabrication of ZnO nanowire field-effect transistors by roll-transfer printing. *Nanotech*. 2009; **20**:195302 6pp.
71. Ramírez FH, Tarancón A, Casals O, Rodríguez J., Romano-Rodríguez A, Morante JR, Barth S, Mathur S, Choi TY, Poulikakos D, Callegari V, Nellen PM. Fabrication and electrical characterization of circuits based on individual tin oxide nanowires, *Nanotechnol.* 2006; **17**:5577–5583.
72. Kim Y.-K, Kim G. T, Ha J. S. Simple patterning via adhesion between a buffered-oxide etchant-treated PDMS stamp and a SiO_2 substrate. *Adv. Funct. Mater*. 2007; **17**:2125–32.
73. Maury P, Peter M, Mahalingam V, Reinhoudt DN, Huskens J. Patterned self-assembled monolayers on silicon oxide prepared by nanoimprint lithography and their applications in nanofabrication photolithographic route to the fabrication of micro/nanowires of III–V semiconductors. *Adv. Funct. Mater*. 2005; **15**:451–7.
74. Sun Y, Khang D.-Y, Hua F, Hurley K, Nuzzo RG, Roger JA. Photolithographic route to the fabrication of micro/nanowires of III-V semiconductors. *Adv. Funct. Mater*. 2005; **15**:30–40.
75. VomieroA, Ponzoni A, Comini E, Ferroni M, Faglia G, Sberveglieri G. Direct integration of metal oxide nanowires into an effective gas sensing device. *Nanotechnol.* 2010; **21**:145502. DOI: 10.1088/0957–4484/21/14/145502.

© Woodhead Publishing Limited, 2013

76. Griffith S, Mondol M, Kong DS, Jacobson JM. Nanostructure fabrication by direct electron beam writing of nanoparticles. *J. Vac. Sci. Technol. B* 2002; **20**:2768–2772.
77. Mårtensson T, Carlberg P, Borgstrom M, Montelius L, Seifert W, Samuelson L. Nanowire arrays defined by nanoimprinting lithography. *Nano. Lett*. 2004; **4**:699–702.
78. Sberveglieri G, Baratto C, Comini E, Faglia G, Ferroni M, Pardo M, Ponzoni A, Vomiero A. Semiconducting tin oxide nanowires and thin films for chemical warefare agents detection. *Thin Solid Films* 2009; **517**:6156.
79. Ponzoni A, Baratto C, Bianchi S, Comini E, Ferroni M, Pardo M, Vezzoli M, Vomiero A, Faglia G, Sberveglieri G. Metal oxide nanowire and thin films based gas sensors for chemical warefare simulant detection. *IEEE Sensor. J.* 2008; **8**:735.
80. Sysoev VV, Schneider T, Goschnick J, Kiselev, Habicht W, Hahn H, Strelcov E, Kolmakov A. Percolating SnO_2 nanowire network as a stable gas sensor: Direct comparison of long-term performance versus SnO_2 nanoparticle films. *Sens. Actuat. B* 2009; **139**:699.
81. Ramírez FH, Tarancón A, Casals O, Arbiol AJ, Rodríguez R, Morante JR. High response and stability in CO and humidity measures using a single SnO2 nanowire. *Appl. Phys. Lett.* 2008; **93**:123110.
82. Comini E, Cristalli A, Faglia G, Sberveglieri G. Light enhanced gas sensing properties of indium oxide and tin dioxide sensors. *Sens. Actuat. B* 2000; **65**:260.
83. Comini E, Faglia G, Sberveglieri G. UV light activation of tin oxide thin films for NO2 sensing at low temperatures. *Sens. Actuat. B* 2001; **78**:73–77.
84. Comini E, Ottini L, Faglia G, Sberveglieri G. SnO_2 RGTO UV activation for CO monitoring. *IEEE Sens. J.* 2004; **4**:17.
85. de Lacy Costello BPJ. Highly sensitive room temperature sensors based on the UV-LED activation of zinc oxide nanoparticles. *Sens. Actuat. B* 2008; **134**:945.
86. Law M. Photochemical sensing of NO_2 with SnO_2 nanoribbon nanosensors at room temperature. *Angew. Chem., Int. Ed.* 2002; **41**:2405.
87. Prades JD. Jimenez-Diaz R, Hernandez-Ramirez F, Cirera A, Romano-Rodriguez A, Morante JR. Equivalence between thermal and room temperature UV light-modulated responses of gas sensors based on individual SnO_2 nanowires. *Sens. Actuat. B* 2009; **140**:337.
88. Prades JD. A model for the response towards oxidizing gases of photoactivated sensors based on individual SnO_2 nanowires. *Phys. Chem. Chem. Phys*. 2009; **11**:10881.

© Woodhead Publishing Limited, 2013

9

Semiconductor quantum dots for photoluminescence-based gas sensing

Z. ZHAO, M. A. CARPENTER and
M. A. PETRUKHINA, University at Albany-SUNY, USA

DOI: 10.1533/9780857098665.3.316

Abstract: The photoluminescence (PL) characteristics of semiconductor quantum dots (QDs) and their intrinsic sensitivity to their surrounding environment have made them an attractive material set for sensing applications. However, their development into PL-based gas sensors requires several considerations. Specifically, the QD surface chemistry via manipulation with surface ligand engineering, rational design and control of polymer host chemistry and *in situ*/*ex situ* dispersing methods, or polymer-free QD deposition methodologies and sensible introduction of functional substrates all need to be considered, as each of these will likely affect the sensor detection limits, selectivity, and detection dynamic range. These specific choices and their corresponding effects on the QD sensing properties will be discussed in detail.

Key words: gas sensing, cadmium selenide (CdSe) quantum dots, photoluminescence, nanocomposites.

9.1 Introduction

Semiconductor nanocrystals or quantum dots (QDs) are a unique set of materials that have narrow, size tunable, and symmetric emission spectra; high quantum yields; photochemical stability; low susceptibility to photobleaching; and broad absorption profiles.[1–6] The distinctive optical and electronic properties of QDs result from the quantum confinement effect. Quantum confinement occurs when the dimensions of the nanocrystals approach the radius of the photoexcited electron–hole pairs or excitons. This gives rise to increased discrete energy levels, widened band gaps of the QDs, and a correspondent blue-shifted absorption and emission spectra at decreased sizes. QDs typically consist of a few hundreds to thousands of atoms with particle sizes ranging from 1 nm to 10 nm depending on the specific material systems. With these qualities, QDs have attracted great attention for a variety of exciting and novel applications that include biosensors, chemical sensors, and lighting, as well as *in vivo* cell imaging.[7–11] QD-enabled

© Woodhead Publishing Limited, 2013

all-optical sensors are attractive compared with electrical equivalents due to a number of advantages. These include enhanced detection limits due to the high surface-to-volume ratio of the nanostructures, selectivity via multivariate QD optical array design, safety in harsh (e.g. flammable or corrosive gas) environment applications owing to the absence of any electrical components in the sensing elements, low power and easy operation without a requirement for heating and temperature control to maintain sensitivity, and free from complicated and costly device fabrication technology.

Colloidal semiconductor QDs have a large fraction of surface atoms and are typically capped with organic ligands, which provide surface passivation and prevent their aggregation, make them dispersible in solvents for easy processibility, and can offer desired surface functionality.[10, 12–16] A prominent characteristic of these nanoparticles is that their photoluminescent (PL) properties have shown strong sensitivity to surface-bound ligands, as well as to changes in their surrounding chemical environment,[17–24] rendering them promising candidates for chemical sensing applications.[25–29] Depending on the nature of these interactions, possible causes for environmental sensitivity include changes in the surface/interface trap states, charge trapping/untrapping (surface passivation) at these states, and charge or energy transfer with the surroundings, as well as charge relaxation dynamics such as trapping duration. It has been already shown that the PL intermittency of CdSe/zinc sulfide (ZnS) core/shell QDs is correlated with the dielectric environment surrounding the QDs.[20,23,26, 29–32] It is often observed that external electrons (and holes) can transfer from the surface adsorbed or nearby redox species to the QD valence or conduction band or band gap surface states, modifying the nanocrystal PL.[31, 33–35] It is also noted that PL perturbation is dependent on the polarity of the species in the surrounding environment, like water, methanol, xylenes, and toluene.[24, 26, 36–38] This is indicative of the role of the dielectric environment change that may alter the trap states or trapping dynamics through the local electrical field introduced by the external agent molecules, causing PL enhancement or quenching.[32, 39–41]

In contrast to the progressively matured use of QDs in bio-sensing and the extensive investigation of QDs in solution phase sensing applications,[25–27, 42–44] relatively less investigation has considered the strategic use of QDs for gas sensing. Cordero *et al*. studied the luminescence dependence of CdSe quantum dot monolayers on several common environmental gases and observed reversible PL enhancement in the presence of water vapor.[36] Nazzal *et al*. tested polymer embedded CdSe QD thin films as potential gas sensors.[19] They found that the PL properties of QD/polymer films responded to exposures of triethylamine, butylamine, and benzylamine gases at saturated vapor pressures in a reversible, rapid, and species-specific fashion. Potyrailo *et al*. reported selective chemical sensing by introducing CdSe nanocrystals of two sizes into a polymer matrix.[37] Each size of the

© Woodhead Publishing Limited, 2013

nanocrystals encapsulated in the polymer host was observed to have a distinct PL response pattern upon exposure to percentage levels of methanol and toluene vapors in air at atmospheric pressure, allowing speciation with principal components analysis (PCA). Likewise, Vassiltsova *et al*. explored the surface-tailored synthesis of CdSe QDs to enhance their PL response in the detection of aromatic hydrocarbons.[10] As a result, with the use of a controlled drop-casting method to form surface rough films, the polymer embedded QDs exhibited a detection limit of 15 ppm for xylenes, which is the lowest within the QD-based hydrocarbon detection technologies.

The complication of the above approach is that the QDs/polymer-based optical systems show inconsistent or non-monotonic sensing behaviors with respect to each other, or over large analyte concentration ranges, due to the competing or multi-sensing processes involved – for example, intrinsic QD–analyte interaction enhanced PL and extrinsic wetting-effect quenched PL. The extrinsic effects are a result of a light–matter interaction change with increased analyte molecule absorption into the system and resultant refractive index change.[38,45,46] This limits the study and practical applications of these materials, and thus requires the development of advanced synthetic methods that allow one to suppress the above effects. Zhao *et al*. have found that porous and rough film structures is a preferred structural property for QD-based fluorescence sensors, allowing high sensitivity due to the surface roughness, in addition to scattering enhanced local electromagnetic fields and optical absorption and emission.[38,47,48] This inspired the authors to introduce the direct integration of QDs onto nanopore arrays. This not only greatly enhanced the resulting PL, but also enabled monotonic sensing characteristics over a large analyte concentration range. These effects were attributed to the submicron pore arrays that dictate the light–matter interaction with a limited or reduced susceptibility to analyte absorption.[11,49,50] Furthermore, a larger PL response to 10 ppm xylenes in air has been achieved from CdSe QDs dispersed on anodic aluminum oxide (AAO) supported on Au-coated Si, suggesting that a detection limit down to hundreds of ppb of xylenes is quite possible. The reliability issues have been addressed through the use of high quality CdSe/ZnS core/shell QDs assembled on AAO, which have shown the sensitive detection of hydrocarbons over an almost nine-month period, and thus are very promising for future applications.

These results are all indicative of the great potential that QDs have for use as chemical gas sensors. The rational design of QD-based sensing hybrid (or composite) materials is important in achieving functioning devices with enhanced sensitivity, selectivity, and reliability for the rapid and efficient analysis of different gas species. The remainder of this chapter will address each of these issues with topics covering QD synthesis, surface-bound ligand

© Woodhead Publishing Limited, 2013

modifications, QD encapsulation methods, as well as deposition and substrate variations, with respect to their effects on the resulting QD gas sensing characteristics.

9.2 Quantum dot synthesis, surface functionalization and polymer encapsulation

9.2.1 Quantum dot synthesis

Colloidal QDs are synthesized in a solution system containing suitable precursors, organic surfactants, and solvents.[51–55] Generally, when a reaction mixture is heated to a high temperature (e.g. 320°C), the precursors decompose into active species or monomers and, soon after a supersaturation of the monomers is reached and nucleation starts, the temperature is slightly lowered. At this point, subsequent growth of nanocrystals takes place, with a monolayer of surfactant molecules surrounding the core of nanoparticles. Choosing an optimal temperature is important for growing high-quality crystalline nanoparticles. The surfactant dynamically adhered to the growing nanocrystals in solution, thus preventing the nanoparticles from aggregation while allowing their continuous growth. The attached surfactant also chemically passivates the QD surface and permits easy post-synthesis processing, or further development of QDs into more advanced hybrid materials. A typical organic surfactant used in the growth of CdSe nanocrystals is, for example, trioctylphosphine oxide (TOPO),[51] which represents a common system within II-VI colloidal semiconductor QDs. Production of nanocrystals with a relatively narrow size distribution is a central requirement for many applications and can be obtained post synthesis from original broadly size-distributed samples by using separation techniques like size-selective precipitation.

When the inorganic core dot is coated over with larger band gap inorganic materials like ZnS, the core/shell system is able to attain higher PL quantum yields, photostability, and chemical resistance owing to improved surface passivation by the shell, and is thus preferred for most applications.[56] The overcoating of core dots with inorganic shells can be realized with several developed synthetic techniques at lower temperatures, such as ~90–250°C, allowing epitaxial growth of ZnS monolayers on the CdSe core.[56–60] As a result, highly luminescent and stable CdSe/ZnS core/shell dots have been produced with quantum yields up to 80–85%.[56,58,60]

To gain a diversity of applications, core or core/shell dots are mostly required to be modified at their surfaces with various organic functionalities, which render them compatible with the desired surroundings, such as water soluble for biological applications or sensitive to target analyte

© Woodhead Publishing Limited, 2013

variations in environment.[10,27,61] Both tailored design and practical realization using proper surface engineering strategies for surface functionalization are important to furnish QDs as building elements for development into advanced materials and devices for a variety of applications.

9.2.2 Quantum dot surface modification

For sensing applications with enhanced sensitivity and selectivity, surface modification of QDs with selected organic ligands has been explored with regard to specific targets, including bio, liquid, and vapor species detections.[10,27,44] For example, it has been proposed to surface-modify CdSe core dots for sensitive and selective detection of aromatic hydrocarbon vapors by utilizing a combination of stabilizing ligands (TOPO and stearic acid (SA)) and interaction-enhancing functional agents.[10,28,38] As for the latter, the surface-modifying group such as benzoic acid (BA) is expected to enhance the QD interaction with the aromatic hydrocarbons through electrostatic π–π interactions between the grafted group and the target analyte.

Typically, new surface groups are introduced by post-synthesis ligand exchange, as the high-temperature QD growth methods are not always compatible with these organic functional groups.[27,61] However, generally, this process leads to incomplete surface exchange and ligand coverage. More often, the PL is quenched due to aggregations of QDs or generation of surface defects during ligand exchange procedures.[62,63] PL may also oscillate due to adsorption and desorption of the newly-grafted surface groups.

In order to overcome these problems, *in situ* surface functionalization for QDs with selected surface-modifying groups was attempted not via ligand exchange but, rather, through direct ligand addition during the QDs synthesis for development of QD-based hydrocarbon-sensing materials.[10] With this technique, strong luminescent CdSe core dots that are surface modified with different functionalities (details of which are given later) have been produced, allowing for the sensitive detection of aromatic hydrocarbon vapors. The attachment of BA, for example, to CdSe core dots synthesized via *in situ* surface functionalization is confirmed by the chemical shift of BA signals in the ^{1}H NMR spectrum of QDs in $CdCl_3$ (Fig. 9.1), with an estimated coverage of about 1 molecule of BA per 12 molecules of TOPO for each quantum dot.

In this preparation technique, the surface-modifying agent is mixed with the QD growth precursors from the beginning, allowing for a one-step *in situ* synthesis. This strategy can be applied to introduce other surface ligands targeting various applications, like enhancing the QD accommodation to specific hosts for polymer encapsulation.

© Woodhead Publishing Limited, 2013

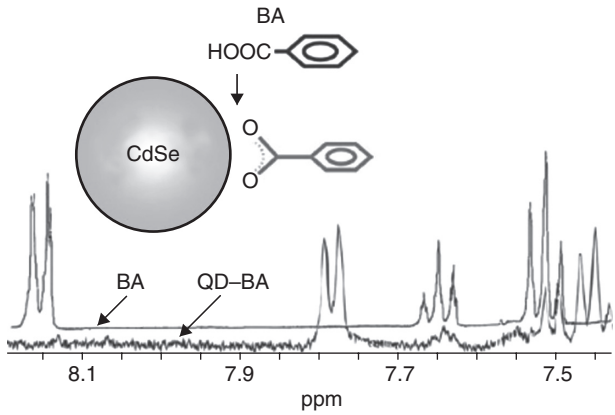

9.1 ^{1}H NMR spectra of BA and CdSe-BA in $CDCl_3$. Reprinted from *Sensors and Actuators B*, 123, 522 (2007). Copyright (2007), with permission from Elsevier.

9.2.3 Quantum dot *in-situ* polymerization

Incorporating colloidal QDs into polymers as a second level of protection is a typical attempt to construct QD-based composite materials for solid-state applications. Two methods are generally used for preparation of QD–polymer composites: (a) *in situ* synthesis of QDs in either a polymer solution[64] or within a polymer film;[65] and (b) *ex situ* synthesis of QDs followed by their subsequent incorporation into either a monomer or a polymer solution for encapsulation into a film.[68] However, it has been shown that, in many polymer matrices, nanoparticles segregate from the polymer host and agglomerate as result of their limited solubility in polymers, which is often accompanied by a simultaneous quenching of the PL.[67–70] Therefore, intimate interactions between QDs and a given macromolecular matrix through the introduction of surface-grafted functional groups as mediators are crucial for control of the particle's spatial organization. This requires tailoring the QD surfaces with versatile surface functionalities to accommodate specific hosts.[71–74] On the other hand, the choice of monomers for polymer matrices is also important. For example, Lee *et al*. suggested that a polymer matrix with longer alkyl branches such as poly(lauryl methacrylate),[68] instead of traditional polystyrene or poly(methyl methacrylate) (PMMA), is capable of preventing phase separation during polymerization.

By adapting Lee's approach, Vassiltsova *et al*. performed *in situ* polymerization for CdSe QDs using different monomers of varied hydrocarbon side chain lengths – such as hexyl, lauryl, stearyl, or behenyl methacrylate – to examine their effects on the optical and morphological properties of the

© Woodhead Publishing Limited, 2013

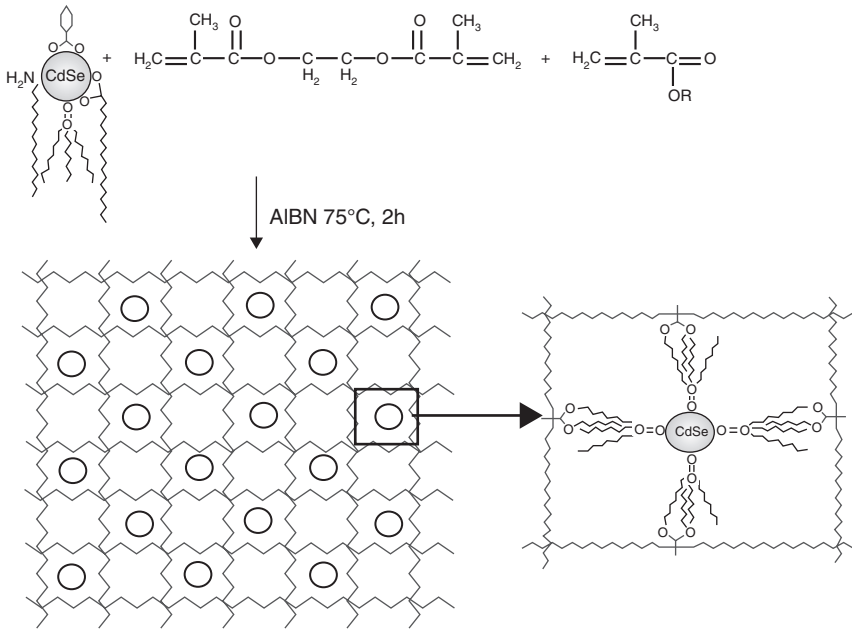

9.2 Schematic representation of CdSe QDs dispersion in poly(hexyl methacrylate) after *in situ* polymerization. Monomers: hexyl methacrylate (R = C_6H_{13}), lauryl methacrylate (R = $C_{12}H_{25}$), stearyl methacrylate (R = $C_{18}H_{37}$), and behenyl methacrylate (R = $C_{22}H_{45}$). AIBN (azobisisobutyronitrile). Reprinted from *J. Nanoscience and Nanotechnology*, **10**, 1635 (2010), with permission from American Scientific Publishers.

resulting nanocomposites.[75] In this process, the pre-synthesized CdSe QDs are fully mixed with one of the monomers and TOP, followed by the addition of a cross-linker and a radical initiator, while continuously stirring the mixture. The final solution is used for *in situ* polymerization in a glass tube or between two optical flats at 75ºC in air. This low temperature process, determined by the chosen monomers, has worked well for preserving the original optical properties of the QDs.

Figure 9.2 is a schematic representation of CdSe QDs dispersed in poly(hexyl methacrylate) by *in situ* polymerization. The polymer with long alkyl branches is expected to prevent or reduce phase separation of the QDs from the polymer matrix during polymerization. This technique resulted in the preparation of a series of QD-based nanocomposite materials for which laser scanned confocal microscopy imaging revealed a nearly uniform dispersion of nanoparticles within the polymethacrylate matrix (Fig. 9.3). Notably, the resulting macroscopic QD–polymer composites appeared to be clear and uniformly colored.

© Woodhead Publishing Limited, 2013

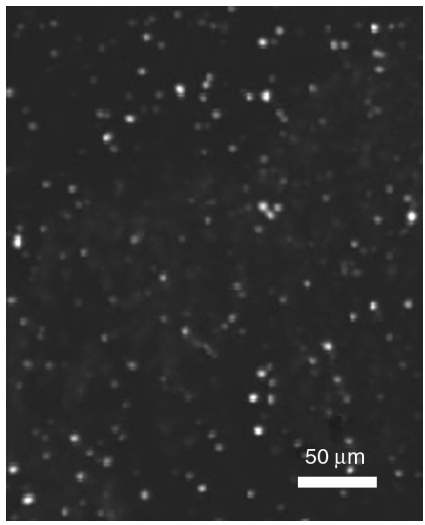

9.3 Confocal microscopic image of CdSe/polymer film C_{18}. Reprinted *from J. Nanoscience and Nanotechnology*, **10**, 1635 (2010), with permission from American Scientific Publishers.

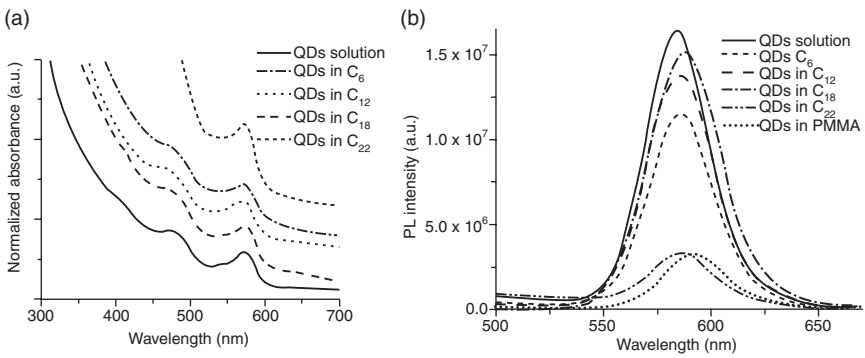

9.4 Spectra of CdSe QDs in polymers of different hydrocarbon side chain lengths: (a) UV-vis absorption and (b) PL. Reprinted from *J. Nanoscience and Nanotechnology*, 10, 1635 (2010), with permission from American Scientific Publishers.

Importantly, the polymer encapsulation did not affect the optical properties of the original highly luminescent CdSe QDs, as reflected by the nearly identical absorption and PL spectra of the composites and the initial QD solution (Fig. 9.4). The slight difference in the PL maxima is an indication of small QD size changes (due to oxidation) and particle aggregation during the *in situ* polymerization. It is noteworthy that the PL intensity and quantum

© Woodhead Publishing Limited, 2013

yield (not shown in Fig. 9.4) of the composites have strong dependencies on the monomers used, with the moderately long alkyl branch monomer lauryl methacrylate giving rise to the best effects. The other monomers with alkyl branches that are either too short or too long with regard to that of the QD surface-stabilizing TOPO ligands appear unable to allow QDs to be evenly or optimally packed in the cages during polymerization, leading to QD aggregation and PL quenching. This could be due to the well-documented understanding that disordered or amorphous media can introduce a high density of trap states to the material they contact, quenching QD PL by charge trapping effects.[76–80]

Photoactivation of the as-prepared samples of QDs embedded in the above polymers increased their quantum yields, which was attributed to photoinduced surface state passivation, in addition to system relaxation.[36] The resulting polymer-encapsulated QDs systems show an extended photochemical stability under continuous illumination in air without any observed blue shift, in contrast to the very short lifetime of the original QD solutions. While such fabricated QD–polymer composites in the initial work appear less sensitive toward hydrocarbon vapor exposures, many optimizations – for example, for the composite guest/host selection and the layer thickness – may be pursued to allow for the making of functional QD/polymer sensing materials based on the developed method. In addition, the encapsulation of QDs with selected monomers via *in situ* polymerization to make QD-based precursors is a useful technique with which to enhance QD life for, potentially, many other applications.

9.2.4 Quantum dot layer-by-layer deposition

The controlled integration of functionally distinct QDs into hybrid structures or complex systems appears to be an essential prerequisite for the realization of high-performance electronic and optical devices. Numerous attempts have been made to fabricate uniform two-dimensional and three-dimensional nanoparticle-based multilayers by using diverse approaches like self assembly,[81,82] colloid crystallization, Langmuir–Blodgett techniques,[83] and electrostatic interactions.[72,84] These approaches generally involve tailoring the QD surfaces with additional functional groups so as to engineer specific interactions with their close environment. Then, the QDs may be immobilized on substrates by means of solution-dipped self-assembly via surface modification of a substrate with functional groups that provide attractive intermolecular interactions with the deposited nanoparticles.[85–87] Vassiltsova *et al*. reported a successful *in situ* preparation of stable and highly luminescent CdSe QDs using 11-hydroxyundecanoic acid (11-HUDA) as the surface-bound functional group, followed by fabrication of

© Woodhead Publishing Limited, 2013

layered thin films on glass or silicon substrates through a covalently bonded layer-by-layer formation at ambient temperature.[88]

The monolayer formation approach is based on the covalent bond forming reactions between 11-HUDA grafted on the surface of CdSe QDs and the 1,6-hexamethylene diisocyanate (HMDIC) molecules that serve as an organic linker. These reactions facilitate the immobilization of QDs onto solid supports and allow the construction of three-dimensional networks of QDs in a layer-by-layer fashion. Figure 9.5 shows the coupling scheme for using a glass substrate. The layer-by-layer formation is performed, first, by chemically treating the substrate to be hydrophilic with hydroxyl groups grafted on the surface and successively alternating immersions of the substrates in the solutions containing QDs and HMDIC, respectively. The desired thickness of a multilayered film is obtained by repeating the steps with each layer of QDs being covalently bonded and separated by a fixed distance designated by the organic linker. This distance is adjustable through the use of hydroxycarboxylic acids of different chain lengths. Importantly, the carbamate bond formed between the CdSe QDs and the substrate prevents the QDs from being removed by, for example, repeated washing with a variety of organic solvents and water at a wide range of pH under ultrasonication. This same procedure can be applied to Si-substrates through the use of a surface pretreatment with 3-aminopropyltriethoxysilane (APTES). This treatment allows the formation of dense self-assembled monolayers on the native SiO_2 surface of Si wafers for the surface-bound aminopropyl groups, which can then be covalently bound to HMDIC.

A key step in these processes is the use of 11-HUDA as a QD surface functionalization agent grafted not via tedious ligand exchange but, rather, during the synthesis of CdSe QDs to afford stable and highly luminescent quantum dot solutions. As shown in Fig. 9.6, the narrow and strong PL of QDs confirms that the *in situ* addition of 11-HUDA does not impede the optical properties and homogeneity of size of the resulting QDs. The observed redshifts of the absorbance and PL maxima with growth time or QD size (see the inset in Fig. 9.6(a)) are a reflection of the QDs unique size-dependent electronic and optical properties. The quantum efficiency of thus prepared CdSe QDs in solution before washing is measured at 34%, and ~11% after washing. Importantly, the attachment of 11-HUDA to the QD surface before and after the cleaning process is confirmed by the characteristic O–H stretch of 11-HUDA in the Fourier Transform Infrared (FTIR) spectrum.

Optical absorbance, PL, and atomic force microscopy (AFM) characterizations clearly demonstrated the successful fabrication of the multilayered films. The resulting multilayered films preserve the stable and highly-luminescent optical properties of the *in situ* functionalized CdSe QDs. The layered deposition of QDs is uniform in each step during the film formation process as inferred from the inset in Fig. 9.7(a), indicating likely equal

© Woodhead Publishing Limited, 2013

© Woodhead Publishing Limited, 2013

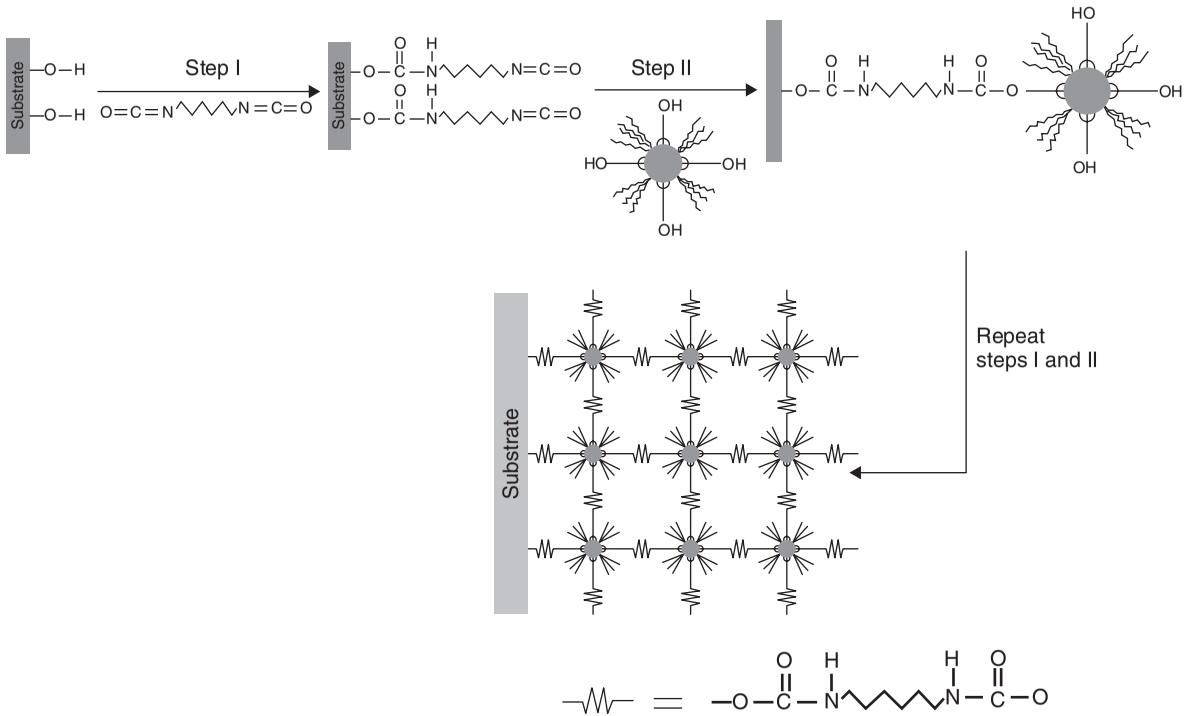

9.5 Schematic illustration of functionalization of a glass substrate by HMDIC followed by immobilization of the 11-HUDA surface-modified CdSe nanoparticles on the isocyanate-bearing substrate through the carbamate-bond forming reaction. *Dalton Transactions*, 43, 9426 (2009). Reproduced by permission of The Royal Society of Chemistry.

© Woodhead Publishing Limited, 2013

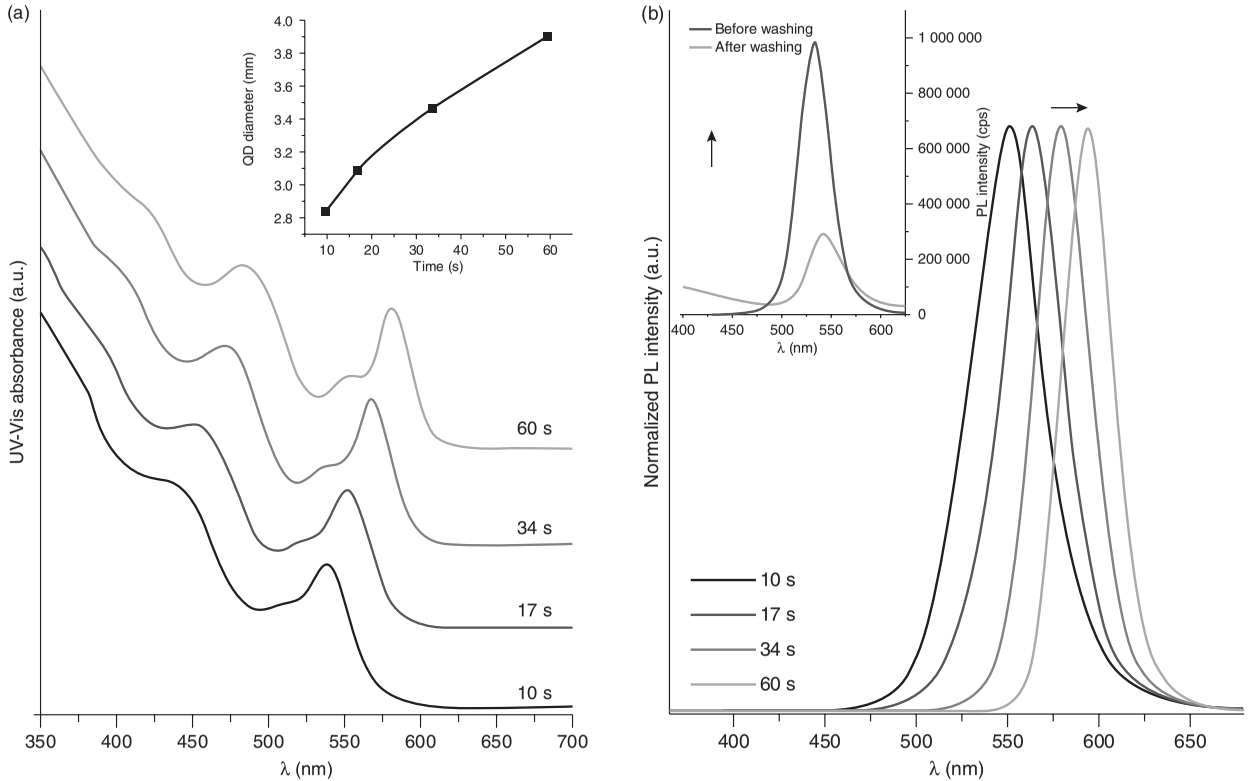

9.6 Spectra of the *in situ* functionalized CdSe QDs in solutions collected at different time intervals: (a) optical absorbance and (b) PL. The insets show (a) the calculated QDs diameter vs time of collection and (b) the PL properties of the QDs before and after washing. *Dalton Transactions*, **43**, 9426 (2009). Reproduced by permission of The Royal Society of Chemistry.

© Woodhead Publishing Limited, 2013

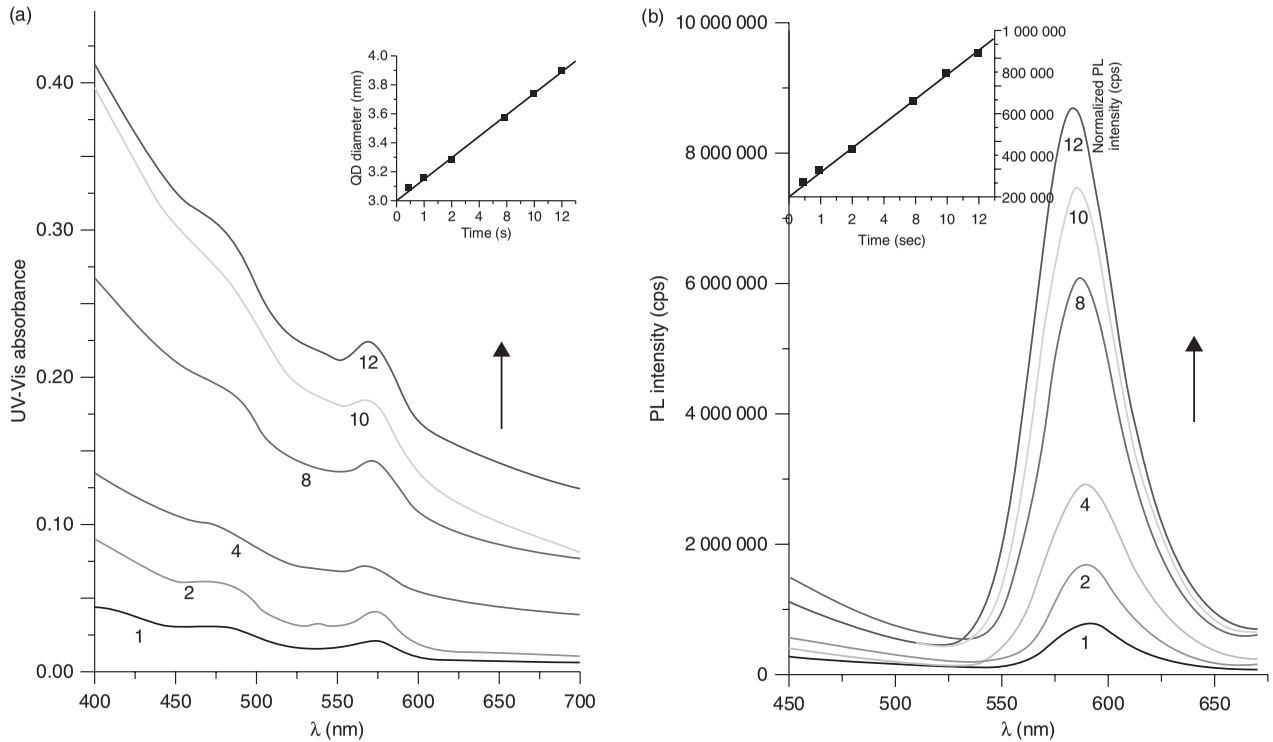

9.7 (a) Optical absorbance spectra of the multilayered films. Number of layers is shown below each trace. Inset represents the linear-fitting curve for the peak at 570 nm as a function of the number of deposited layers on a glass substrate, and (b) PL spectra of the corresponding films. Number of layers is shown below each trace. *Dalton Transactions*, 43, 9426 (2009). Reproduced by permission of The Royal Society of Chemistry.

amounts of QDs assembled in each cycle of fabrication. The PL spectra of the same films (Fig. 9.7(b)) consistently show a gradual increase in the PL intensity with the successive increase in the number of layers. The quantum efficiency of the 12-layered QDs film is estimated to be 6%. The absorption and emission intensities of the multilayers on Si support are similarly a linear function of the layer number. Note that the use of APTES as a Si-coupling agent improves QD attachment to the silicon wafer, since PL intensity in this case is substantially increased as compared with the non-APTES treated substrates.

This approach allows the formation of homogeneous and stable multilayered films with high density of QD packing. There are no visible defects, opaque areas, or color inhomogeneities within the resulting bright orange film. The films are impressively robust and environmentally stable, since there are no drastic changes in the optical absorbance and PL properties observed over a three-month period, except a small gradual blue shift in the emission peak over time due to the QD surface oxidation in ambient air.

Though the films have not demonstrated promising sensing capabilities in the reported work, the method for QD multilayer construction with the ability to introduce additional surface-bound functional groups should facilitate the use of these novel composite materials in sensing applications. This method may also be useful for preparing QD precursor materials with nanoscale to microscopic, or even macroscopic dimensions, retaining their original properties for various other applications. For example, this multilayered ordering may be very valuable for light-emitting devices, as it would allow one to attain uniform charge transport through the film, which should extend longevity and reduce the turn-on voltage of LEDs.[89] This approach can be also extended to the fabrication of multilayered semiconductor-metal nanostructured films with different chain length organic linkers to study the distance effect on the exciton–plasmon interactions. Overall, these findings are important for the development of QD-based optical and electronic devices that can harness the highly-photoluminescent properties of these ordered and stable nanocomposite materials.

9.3 Quantum dots for sensing: dependence of detection limits and selectivity on surface-modifying ligands

The strategic use of QDs for PL-based chemical sensors is examined with a focus on hydrocarbon vapor detection. Sensitivity and selectivity enhancement characteristics have been incorporated into the design of these sensing systems using a combination of stabilizing and surface-modifying groups attached to the surface of CdSe core QDs.[10, 90] Figure 9.8 shows a schematic

© Woodhead Publishing Limited, 2013

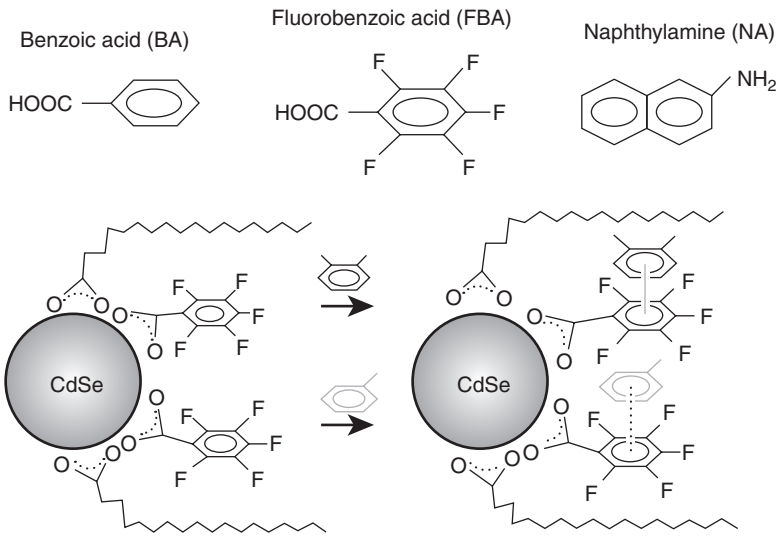

9.8 Schematic representation of the CdSe QDs modified with surface enhancing reagents (fluorobenzoic acid – FBA) and expected interactions with xylenes and toluene.

representation of CdSe core dots with the surface chemistry tuned by different agents bearing aromatic functionalities such as BA, pentafluorobenzoic acid (FBA), or naphthylamine (NA). These agents were chosen for their expected electrostatic interactions with toluene and xylenes, which can enhance the detection of the hydrocarbons (HCs). Controlled drop-casting of QD–polymer films provides an effective way to construct these nanocomposite thin films for gas sensing applications.[38] Proper integration of the QDs is crucial to determine the usefulness of QDs as a sensing probe, as detailed later, while examination of the surface-modifying agent effects on sensing is the focus of this section.

9.3.1 Ligands type dependence

Unmodified CdSe QDs having TOPO plus SA as surface-stabilizing ligands and modified QDs using additional ligands (BA, FBA or NA) as the surface functional group are respectively incorporated into PMMA to form different sensing systems, followed by photocuring or annealing for stabilization as an important step prior to sensing tests.[19] The PL spectra of the resulting systems (the QD loading variation within each of these films was kept to a minimum, and is within a factor of 3) confirm that these QDs preserve their optical properties, as they show nearly similar PL peaks positions (at wavelengths >530 nm for each) and are consistent with that of the QDs in

© Woodhead Publishing Limited, 2013

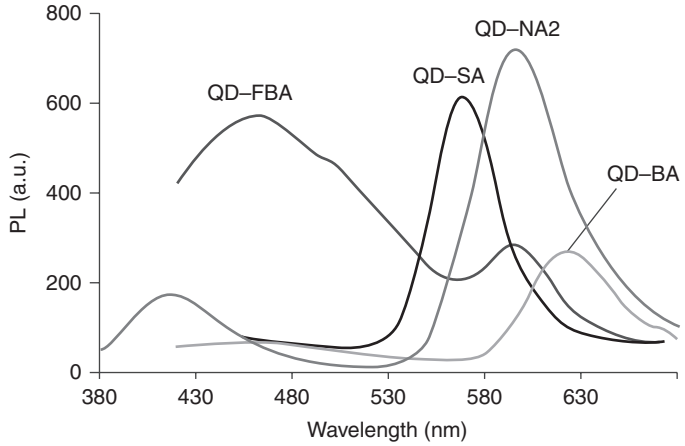

9.9 PL spectra of PMMA films imbedded with CdSe QDs of different surface chemistries: SA for unmodified QDs, BA, FBA, and NA for surface-modified QDs.

solution (Fig. 9.9). The peaks at the shorter wavelengths (<530 nm) originate from excimers of the QD surface-modifying groups and can be used as an indicator to adjust the surface group coverage, as discussed later.

The unique approach of using the surface-modified QDs has been shown to provide enhanced sensitivity and selectivity of QD-based materials for the detection of hydrocarbons. This is demonstrated in Fig. 9.10, which compares the normalized sensing capabilities of the unmodified QD films and the 'surface-modified' QD–BA, QD–FBA, and QD–NA films to exposures of 50 ppm xylenes in nitrogen.[90] The arylcarboxylate surface-modified QDs have a higher sensitivity toward xylenes over the unmodified QD films that show no measurable response at this concentration. The best performance was observed with the QD–FBA film and is likely due to the more pronounced electron-withdrawing properties of the F-substituents of FBA. The introduction of fluorine to the π-system of BA proffers its electron-deficient properties and that should enhance the surface interaction of QDs with the targeted HC molecules.

Reversible PL enhancement or quenching upon film exposures to toluene and xylene vapors are observed from these systems, as representatively illustrated in Fig. 9.11 for the QD–FBA system.[10] PL enhancement dominates at low target gas concentrations with the onset of the quenching process for each of the films being dependent on the target gas type and its concentration. The reason for the non-monotonic sensing behavior is discussed later. With a definition of signal/noise ratio (S/N) of ~2, detection limits of 15 ppm xylenes and 50 ppm toluene in a balance of nitrogen have been achieved with the QD–FBA/PMMA film. These are a factor of

© Woodhead Publishing Limited, 2013

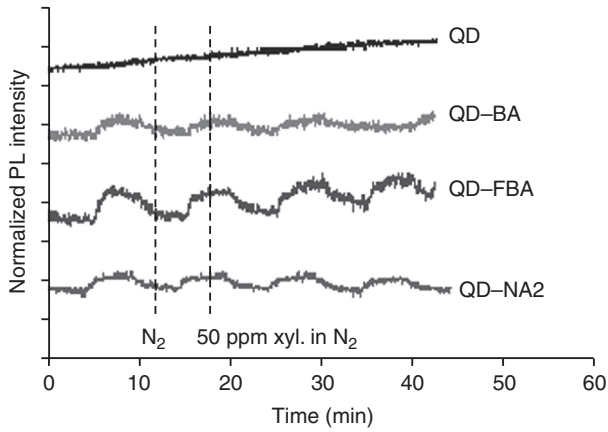

9.10 Comparison of the sensitivity of the CdSe QD films of different surface chemistries toward exposures of 50 ppm xylenes in nitrogen.

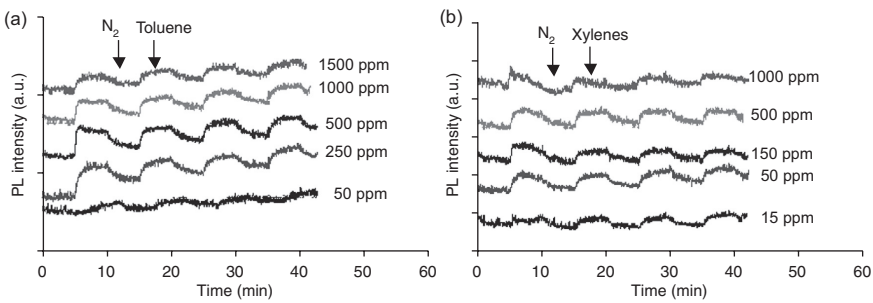

9.11 PL peak intensity of the CdSe-FBA film as a function of time for chemical vapor exposures: (a) toluene and (b) xylenes in nitrogen. Reprinted from *Sensors and Actuators B*, 123, 522 (2007). Copyright (2007), with permission from Elsevier.

16 and 10 sensing enhancement, respectively, over that of the unmodified QDs, with a selectivity factor of greater than 3 for the detection of xylenes relative to toluene.

The PL enhancement upon low level HC exposure arises from enhanced radiative recombination of photoexcited carriers within the QDs, introduced by the interacting HC molecules.[10,38] This may come from the methyl group enhanced donor property of the selected HCs, when the molecules approach to or become physisorbed onto the QD surface under photoirradiation. The sensing process in this case depends on both the polarity and the electron donation strength of the target molecules. The process therefore permits a degree of selectivity for different analytes, as evidenced here

© Woodhead Publishing Limited, 2013

from the detection limit difference between toluene and xylenes. It is clear that surface modification of QDs with selected ligands is a very useful tool with which to enhance the sensitivity and selectivity.

9.3.2 Surface-modifying group coverage dependence

The surface-modifying groups studied here tend to form excimers, depending on both the QD surface coverage and the QD loadings in polymers, which fluoresce and likely interfere with the QD optical properties and sensing capability. A study of surface ligand coverage effects on hydrocarbon sensing using the systems of PMMA embedded CdSe-NA (naphthylamine) QDs demonstrates that sensitivity is affected by not only the nature of the group, but also the degree of surface coverage.[90]

In this study, QD–NA1, QD–NA2, and QD–NA3 represent three batches of CdSe QDs synthesized with *in situ* tethering of three low levels of NA to suppress formation of an overabundance of NA excimers. Consistent with the molar content control of NA in the synthesis, the readily observed intensity difference of the excimer emissions (at wavelengths <450 nm) of the three corresponding QD–PMMA films are shown in Fig. 9.12. The QD emissions (at wavelength >550 nm) are roughly the same for the three samples, indicating the QD loadings in the films are similar to and independent of the large variation observed in the excimer emission intensities.

The sensing characteristics of three QD–NA systems tested against 15 ppm xylenes in an air carrier gas exhibits a maximum signal change from the medium surface coverage (NA2), while too little or too much NA coverage lead to weaker sensing responses (Fig. 9.13). It is understandable that for the

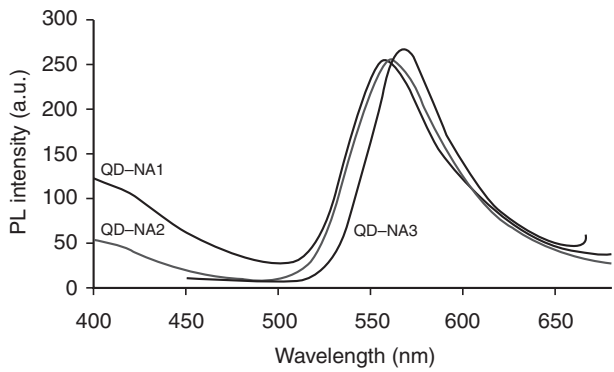

9.12 Comparison of PL of CdSe–NA films made from the QD solutions with three different NA surface coverage levels. NA1, NA2, and NA3 represent high, medium, and low surface coverage, respectively.

© Woodhead Publishing Limited, 2013

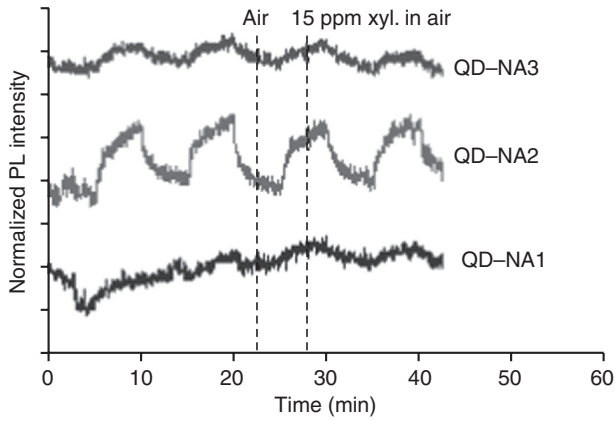

9.13 Dependence of CdSe–NA sensing characteristics on surface NA coverage. NA1, NA2, and NA3 represent high, medium, and low surface coverage, respectively.

QD–NA3 film this is most likely due to a lack of surface-modifying groups available for enhanced QD interactions with the target molecules. The reduced signal change observed at a high surface coverage (NA1) is attributed to the formation of excessive NA excimers, which affect the interaction capabilities of the surface groups with the target molecule. Thus, a balance between having sufficient NA species available for sensing interactions, while not inducing a large quantity of excimer formation can provide a sensing film with an enhanced sensitivity to hydrocarbon detection. This is further evident from the reversible and large PL enhancement responses of the CdSe–NA2 film to exposure to low concentrations of xylenes balanced in dry air (Fig. 9.14). In addition to the stable sensing performance in air, the sensing signal is large at 15 ppm xylenes exposure (PL change by ~7.5 a.u.), suggesting a possible lower detection limit at the level of hundreds of parts per billion (ppb).

9.3.3 Surface-modifying group length dependence

The π–π stacking interaction between the QD surface-modifying groups and target hydrocarbon species has been shown to enhance the QD sensing performance. Thus, it is of interest to study the dependence of hydrocarbon sensitivity on the distance of the linked phenyl group to the QD surfaces.[28] CdSe QDs of roughly the same size were synthesized with *in situ* attachment of BA, phenylacetic (PA), 4-phenylbutanoic (PBA), or 6-phenylhexanoic acids (PHA) surface agents with similar surface coverage, as determined by nuclear magnetic resonance techniques. This is important to confirm since, as noted above, different surface coverage will likely affect the degree of ligand to QD charge transfer effects.[33–35] The surface-modified QDs were

© Woodhead Publishing Limited, 2013

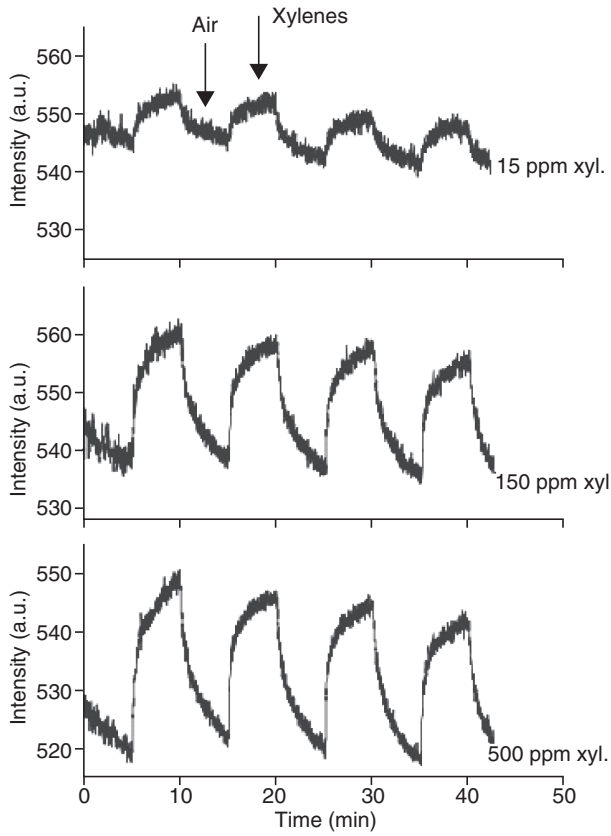

9.14 PL peak intensity of CdSe–NA/PMMA film as a function of chemical vapor exposure time, with the exposure cycled between air and air-balanced xylenes at different concentrations. The NA surface coverage on the QD is at a medium level.

drop-coated onto porous AAO substrates to form QD-based porous films for sensing tests.

The absorption spectra of the four QD solutions of nearly the same QD sizes and concentrations used in these studies show little variation with the lengths of the ligands bound to the surface of the QDs. It is interesting that the emission quantum yields increase with an increase in the distance between the phenyl ring of the surface-enhancing ligand and the QD surface, consistent with their fluorescence spectra (Fig. 9.15). The quantum yield of CdSe QDs with PHA has a higher value, 29.4%, compared with those with BA, 4.5%. This is presumably due to photogenerated charge transfer from the QDs to the surface-attached BA, PA, PBA, or PHA, resulting in partial quenching of PL, with the longest PHA having the weakest effect. The smaller degree of quenching involved with QD–PHA is consistent with

© Woodhead Publishing Limited, 2013

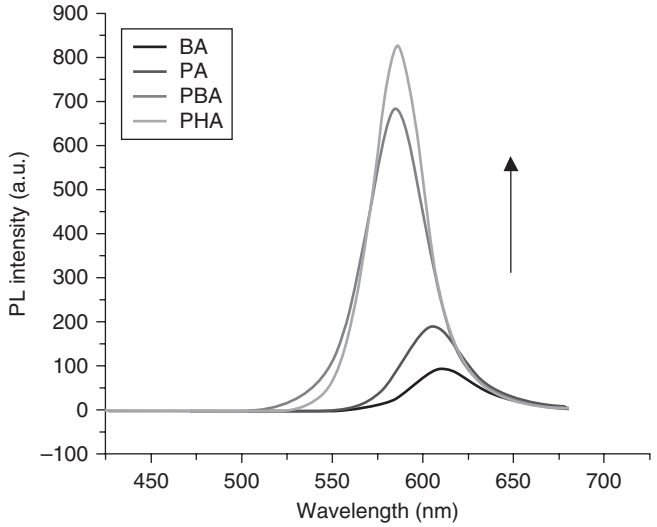

9.15 PL spectra of CdSe QD solutions in chloroform (~4.9×10^{-6} M) with average ~3.5 nm QD size and different surface-modifying ligands containing phenyl groups of varied distances from the QD surface. Reprinted with permission from *J. Phys. Chem. C*, 114, 4272 (2010). Copyright (2010) American Chemical Society.

its slightly blue-shifted PL peaks with respect to the PL peak observed for the QD–BAs and QD–PAs. A number of previous studies have shown similar phenomena[21,91] – that is, longer ligand length has less PL quenching effect for different types of ligands studied. This possibly suggests a sterically enhanced disordering of QD surface ligands, introducing interface trap states to capture photogenerated electrons or holes of QDs.[76–80]

Sensing graphs of the QDs drop-coated on AAO substrates showed monotonic PL enhancement upon film exposure to xylenes vapor over the range of 15 ppm to 9400 ppm in a balance of air (Fig. 9.16(a)). Proportional to their PL intensity, the sample with the longest surface-enhancing ligand displays a larger change in PL upon xylenes exposure. The normalized PL enhancement did not vary noticeably for QDs with longer chained phenyl groups compared with those with shorter length groups on film exposure to xylenes vapors over all the concentrations. However, it is significant to note that the PL sensitivity toward xylenes exposure for QDs with PHA versus those with BA was about 8 times greater at xylenes concentrations below 2500 ppm and 16 times greater at concentrations above 4500 ppm (Fig. 9.16(b)). The finding that the sample with the longer surface-enhancing ligand studied here showed a higher quantum yield, larger change in PL on xylenes exposure. As a result, a greater sensitivity to the target analyte may serve as a design principle for development of QD-based chemical sensing materials.

© Woodhead Publishing Limited, 2013

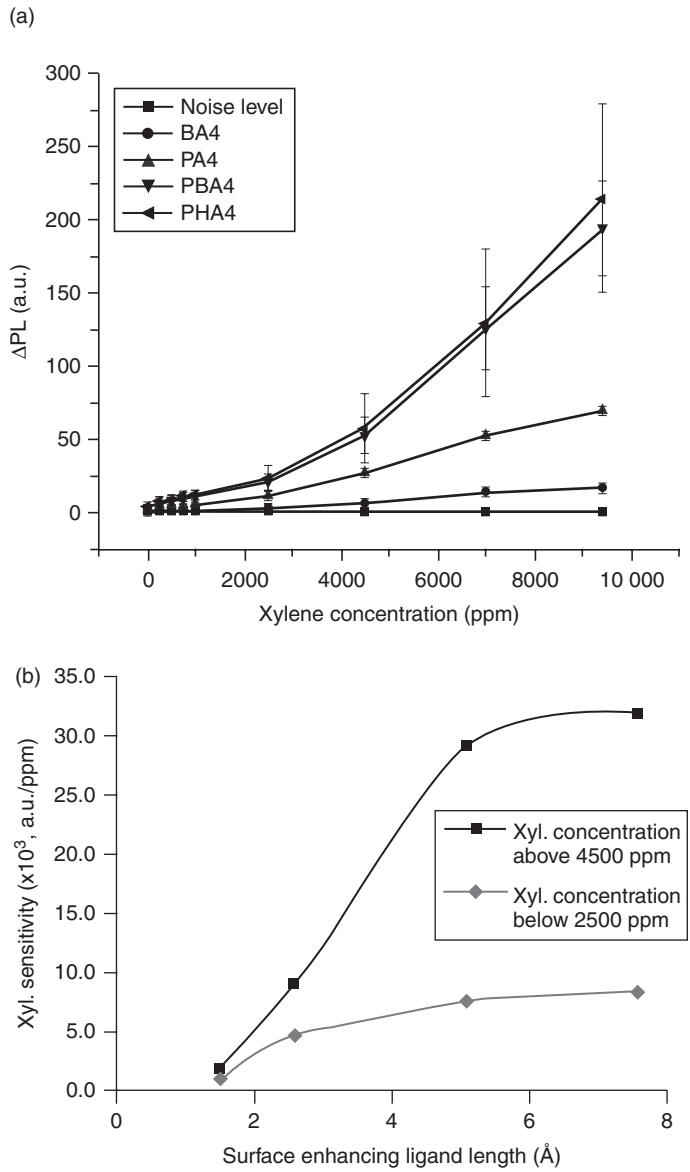

9.16 (a) Absolute change in PL peak intensity of CdSe-BA, -PA, -PBA, -PHA QD films with exposure to xylenes of varied concentrations, and (b) sensitivity of xylenes as a function of surface-enhancing ligand lengths, which are 1.5, 2.6, 5.1, and 7.6 Å for BA, PA, PBA, and PHA, respectively. Reprinted with permission from *J. Phys. Chem. C*, 114, 4272 (2010). Copyright (2010) American Chemical Society.

© Woodhead Publishing Limited, 2013

9.3.4 Quantum dot integration effects – dependence of sensing mechanisms on deposition method

When QDs are embedded into a matrix or assembled onto substrates as an optical system for chemical vapor sensing, complexities may appear as a result of the interaction of the composite material with the light source. This light–matter interaction will result in a combination of photophysical and photochemical effects with both intrinsic and extrinsic contributions. Therefore, a study of the QD/matrix sensing mechanism as a whole is important to advance the research and development of QD-based materials for sensing applications.

9.4 Quantum dot–polymer system

This section describes the enhancement of emission and sensitivity of the QD-polymer system before going on to review intrinsic and extrinsic PL responses in non-monotonic sensing.

9.4.1 Enhancement of emission and sensitivity

Incorporating QDs into polymer matrices is a typical practice used for sensing applications. Deposition methods mostly include spin- or drop-casting of QD–polymer blended solutions, copolymerization of QDs with monomers, or layer-by-layer growth using *in situ* functionalization of QDs with organic linkers. Among them, blending QD and polymer solutions is a simple way to make the composite films using spin- or drop-coating techniques. By using the spin-coating method, different researchers have demonstrated the capabilities of the resulting QD–PMMA films for detection of different organic vapors at percentage level concentrations.[19,37] However, PL quenching is often observed from QD–polymer systems. This can be ascribed to phase separation and QD agglomeration in polymer matrices. This could also stem from interfacial trap states introduced by the embedding polymers due to their disordered nature in general. For hydrocarbon-sensing study, controlled drop-casting, rather than fast spin-coating, was used to allow slow self-assembly-like deposition of CdSe QDs–PMMA composite films on silicon substrates.[38] To do so, the QD solution in chloroform (CF) was mixed with PMMA in chlorobenzene (CB) and the drop-casting was performed with control of the droplet size to avoid spreading, followed by slow-drying in a covered dish. The resulting CdSe–NA QD–PMMA film (A) has ~270% (a factor of ~3.7) higher PL intensity over the control film (B) fabricated from a mixture of QDs/CF with PMMA/CF using the same QD–PMMA loading ratio for both (Fig. 9.17). The difference observed is not associated with QD agglomeration according to the similar full width half maximum (FWHM) of

© Woodhead Publishing Limited, 2013

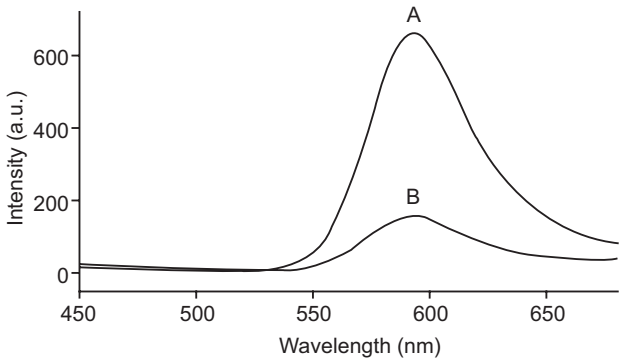

9.17 Comparison of PL spectra of CdSe QDs–PMMA thin films with different surface roughness: rougher sample A and smoother sample B. Reprinted from *Sensors and Actuators B*, 141, 26 (2009). Copyright (2009), with permission from Elsevier.

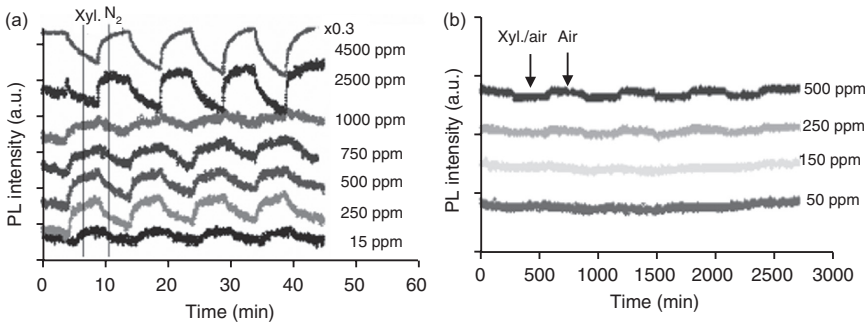

9.18 PL peak intensity responses to exposures of xylenes at different concentrations from CdSe QDs-PMMA thin films prepared with (a) method A for a cloudy and rougher sample, and (b) method B for a clearer and smoother sample. Reprinted from *Sensors and Actuators B*, 141, 26 (2009). Copyright (2009), with permission from Elsevier.

their PL spectra. Instead, the high luminescence of film A is attributed to two factors. First, is the slow and self-assembly-like packing in the presence of the high boiling point solvent CB (131°C) that evaporates much slower than the low boiling point CF (61°C). Second, slight immiscibility of CB and CF gives rise to a higher degree of roughness as film A has a 'cloudy' appearance. The rougher surface induces multiple reflections or scattering effects that redistribute and intensify the local electromagnetic field and, thus, enhance optical absorption and emission of sample A.[47,48]

Controlled drop-casting, plus manipulation of the solvents, is the key to the high emission and collection outcomes achieved for the QD–polymer system A. One direct benefit is that film A displays sensitive PL responses to hydrocarbon vapor exposures with a detection limit of ~15 ppm for xylenes,

© Woodhead Publishing Limited, 2013

while film B has unobservable PL responses at xylenes levels up to 150 ppm (Fig. 9.18). These results are reproducible and suggest that rough nanostructured QD/polymer films are preferred over smooth and clear films for QD-based gas sensing.

9.4.2 Non-monotonic sensing – intrinsic and extrinsic PL responses

While the sensitivity is promising with the 'cloudy' QD–polymer system, the PL response characteristics over a wider range of xylenes concentrations demonstrate a reversible PL enhancement, and quenching at low and high xylenes concentrations, respectively.[38] This leads to a PL response inversion, desensitization, and non-monotonic sensing behavior (Fig. 9.18), which is more clearly displayed by the derived sensing characteristics (Fig. 9.19). The PL response inversion and desensitization points have been found to occur at specific analyte concentrations depending on the nature of QD surface-bound ligands, target chemical species, QD loadings, and polymer matrices. Such a sensing behavior appears to be a general characteristic for both surface-modified and unmodified QDs dispersed in different polymers to aromatic hydrocarbons and other chemicals like methanol and water, irrespective of rough or smooth films made using different preparation methods (drop-casting, *in situ* polymerization, layer-by-layer deposition, etc.).

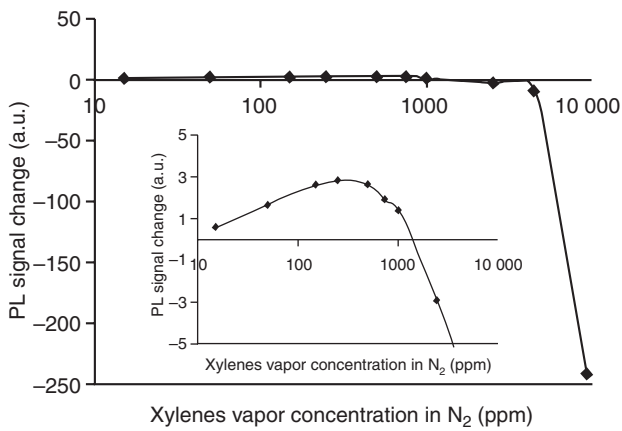

9.19 PL peak intensity as a function of xylenes concentration from a cloudy and rough CdSe QDs–PMMA thin film sample prepared with method A. Reprinted from *Sensors and Actuators B*, 141, 26 (2009). Copyright (2009), with permission from Elsevier.

© Woodhead Publishing Limited, 2013

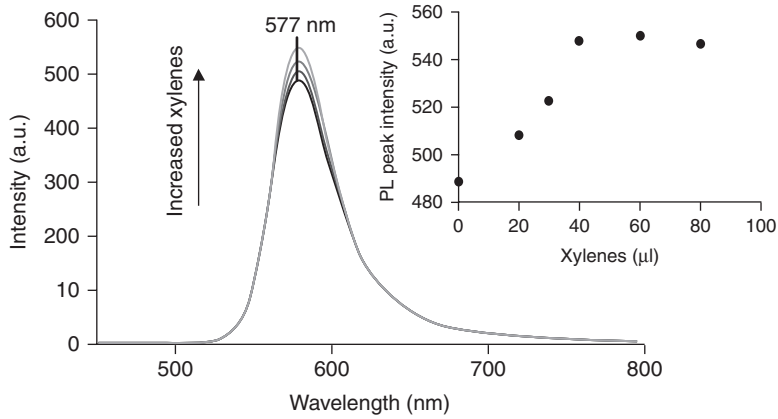

9.20 PL of solutions of CdSe–NA QDs in $CHCl_3$ balanced with different volumes of liquid xylenes, where the inset shows peak PL intensity as a function of added xylenes volume. Reprinted from *Sensors and Actuators B*, 141, 26 (2009). Copyright (2009), with permission from Elsevier.

Detailed studies revealed that the PL enhancement at low hydrocarbon levels results from the intrinsic optical property change from the QDs responding to the admitted target HCs. In strong support, or even as evidence, is the PL enhancement observed from the QD solutions when xylenes were added in both the presence and absence of PMMA in the solutions (Fig. 9.20). The result is also consistent with the data based on using toluene, as reported in the literature.[37] The interacting aromatic hydrocarbons are believed to reduce photogenerated charge trapping at QD surface/interface trap states, or perturb surface electron–hole recombination rates via introduction of their charge donating effects, leading to enhanced QD emission.[38] As described earlier, a three times greater sensitivity to xylenes over toluene has been observed, although xylenes proffer only one more methyl group than toluene. An increased sensitivity is also shown with changing the QD surface-bound groups from BA to NA, and to FBA, due to increased electrophilicities offered by these different functionalities. Methanol and water exposures have also been observed to cause PL enhancement.[24,36] For surface-unmodified QDs, these chemical sensing trends remain the same, but with weaker responses. These suggest that the QD sensing is dependent on both the polarity and the electron donation strength of the target molecules, as well as on the attracting ability of the QD surface-bound groups. However, it should be mentioned that different external species can introduce either PL enhancement or quenching depending on whether or not the species have electron donating or accepting properties. Such properties are determined by their relative molecular energy levels with respect to that of QDs or the surface/interface trap state levels.[31,32]

© Woodhead Publishing Limited, 2013

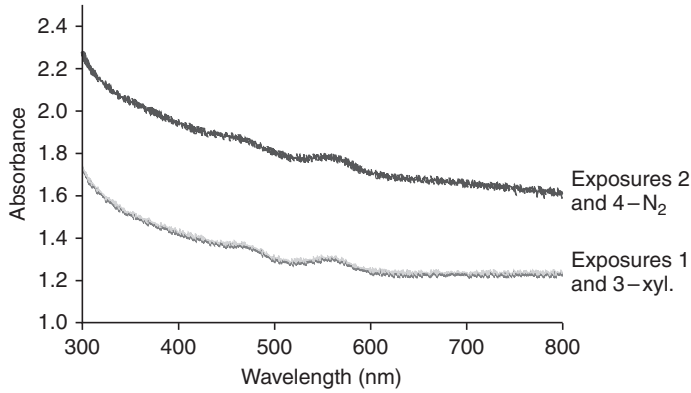

9.21 Two-cycle reversible changes in the absorbance of a CdSe-NA QDs–PMMA film on a glass substrate under exposures switched between N_2 and 9400 ppm xylenes mixed with N_2. Reprinted from *Sensors and Actuators B*, 141, 26 (2009). Copyright (2009), with permission from Elsevier.

In situ spectroscopy and fluorescence imaging studies of the films under cyclic analyte exposures pinpointed that PL quenching at increased HC exposure levels is attributed to a wetting effect, with increased analyte molecule absorption into the films.[38,45,46] The increased analyte absorption modifies the QD–polymer system refractive index and changes the light–matter interaction including absorption, scattering, transmission and reflection, leading to reduced light absorption and emission (Fig. 9.21). This explains why the PL response inversion point depends on a combination of surface chemistry and loading of QDs, polymer hosts, and target species, as all of these affect the analyte molecule absorption into the films. This wetting effect takes place regardless of the QD–polymer film structures, smooth and clear films, or rough and cloudy films. In the case of rough and cloudy films, this process may involve analyte absorption associated filling and smoothing effects on the film surface. This reduces the surface roughness-enhanced scattering or local electromagnetic field as a key contribution for enhanced emission and sensing properties, leading to more attenuated light absorption and emission of the QDs.

It is noteworthy that the wetting effect caused PL quenching, as an extrinsic sensing mechanism, is likely extendable to other QD–polymer systems used as chemical vapor sensors for detection of different molecular species. The complexity arises from solid-state optical systems for vapor detections involving a combination of nanoparticles and polymer interaction with chemical species under illumination. This is an important point to which to pay attention in the studying and development of this type of dependable QD-based chemical sensor.

© Woodhead Publishing Limited, 2013

9.5 Quantum dot–nanopore array system

This section describes the enhancement of emission efficiency and sensitivity of the QD-nanopore array system before going on to review monotonic sensing and intrinsic PL responses. A final section discusses enhanced sensing stability and the results of core vs. core-shell studies.

9.5.1 Enhancement of emission efficiency and sensitivity

The observation that porous QD–polymer films are preferred for QD-based optical systems for hydrocarbon vapor sensing inspired the introduction of a porous platform into the design of the sensor materials.[11] In this design, QDs are directly self-assembled onto AAO nanopore arrays as a platform so as to form confined optically active elements for chemical vapor detection. Controlled drop-casting and slow-drying (solvent annealing) was used to self-assemble the QD monolayers onto AAO without QD agglomerations, which allows enhanced performance to be achieved. A comparison of AFM images of AAO before and after QD assembly reveals that the QDs sit on the backbone of the AAO with minimal filling of the 200 nm size pores (Fig. 9.22), leaving the sample both porous and rough as the desired structural property. The porous structure of the unique AAO platform is found to be able to enhance both the QD PL and sensing response, while effectively suppressing the wetting effects by the pore arrays that are filled with air.

The resulting AAO/QD sample, mechanically supported on a Si support, showed PL enhancement by a factor of 8.4 relative to that of a Si–QD control sample in 350 nm light excitation (curves 3 and 1 in Fig. 9.23). The

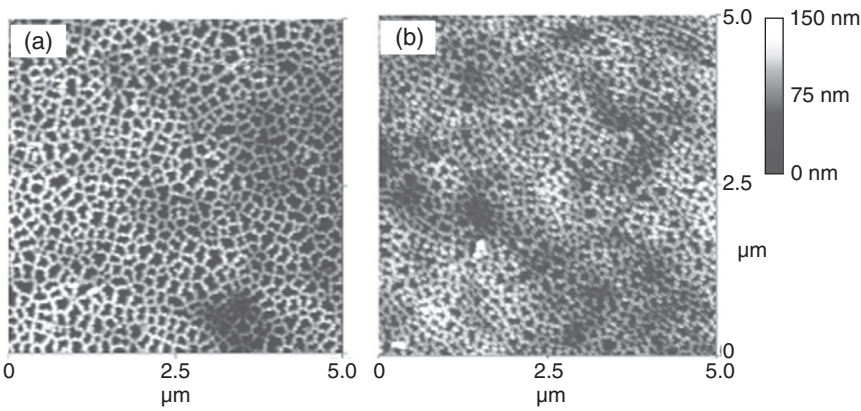

9.22 AFM images of (a) a blank AAO and (b) QD drop-cast AAO. Reprinted with permission from *Appl. Phys. Lett.*, 97, 113105 (2010). Copyright (2010), American Institute of Physics.

© Woodhead Publishing Limited, 2013

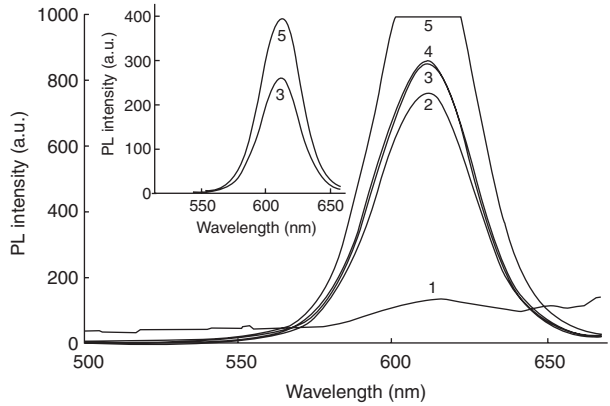

9.23 PL spectra of CdSe/ZnS QDs cast on Si (curve 1) and cast on AAO placed on Si supports of different surface layers (curve 2: Si with 920 nm SiO_2; curve 3: Si with 235 nm SiO_2, curve 4: Si with ~1–2 Å native SiO_2; curve 5: Si with 235 nm SiO_2 topped by 50 nm Au). The inset is a PL re-comparison using Si supports 3 and 5 at reduced QD excitation intensity. Reprinted with permission from *Appl. Phys. Lett.*, 97, 113105 (2010). Copyright (2010), American Institute of Physics.

intensification of QD PL by AAO is explained by the surface scattering effects of the porous AAO redistributing high intensity electromagnetic near-fields for enhanced excitation of the QDs, and likewise for promoting the enhanced collection of the QD emission.[11,49,50] The optical properties can be further improved by manipulating the surface coating on the underlying Si support via reflection and interference. For example, a Au-coated Si support further enhanced the PL by a factor of 1.5, leading to an overall enhancement by a factor of 12.6 relative to the control sample (curves 5 and 1), and owing to the high reflectivity of the noble metal at the QD emission wavelength. The PL enhancement of the QDs accordingly raises the sensitivity of the QD-based materials for analyte detection.

9.5.2 Monotonic sensing with intrinsic PL response

The most distinctive attribute of the AAO/QD system is that it enables a monotonic sensing behavior as a prerequisite of chemical sensors.[11] As shown in Fig. 9.24 inset (a), the PL of an AAO/QD sample supported on Si is reversibly enhanced on exposure to 9400 ppm xylenes in air, in contrast to the wetting-effect induced PL quenching problem associated with QD–polymer systems.[38] Thus, consistent PL enhancement resulting from the intrinsic interaction of the analyte and QDs prevails over the entire 15 ppm to 9400 ppm xylenes exposure range (Fig. 9.24), giving rise to a monotonic sensing behavior over this large analyte concentration range.

© Woodhead Publishing Limited, 2013

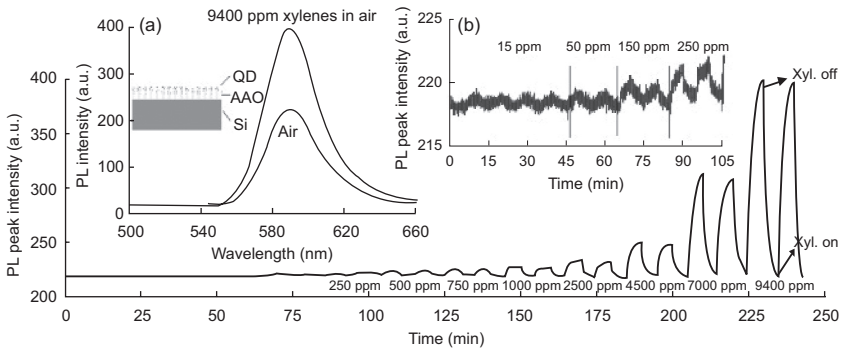

9.24 PL peak intensity responses to exposures of xylenes balanced in a dry air from an AAO/CdSe QD (core dot) sample placed on Si. The inset (a) shows two-cycle reversible PL enhancement of the sample upon exposure to a high level of xylenes vapor and the inset (b) is a zoomed-in sensing trace at low levels of xylenes. Reprinted with permission from *Appl. Phys. Lett.*, 97, 113105 (2010). Copyright (2010), American Institute of Physics.

The sensing characteristics of this nanocomposite are attributed to the introduction of submicron pore arrays, which modify the light–matter interaction. According to the Maxwell–Garnett effective medium approximation, adsorption of analyte molecules in a medium will cause the system's effective dielectric constant, and thus its optical property, to change.[45,46,92,93] The still relatively large pores (Fig. 9.22(b)), after QD dispersion on AAO, prevent the adsorbed analyte from filling the pores or forming an analyte wetting layer on the AAO/QD surface during the vapor exposure cycles. This retards a large modulation of the system refractive index and surface roughness, which would otherwise cause a consequent attenuation of QD excitation and an extrinsic PL response. Employing a nonpolarized and normal incident light source for the QD assembled on the AAO quasi photonic crystal also makes the system insensitive to analyte absorption in the light–matter interaction process. In addition, eliminating polymers as encapsulation matrices appear crucial, as polymers have characteristic chemical affinities and solubility to different chemicals and are prone to absorb analytes, introducing potential light–matter interaction changes.

The demonstrated method is readily applicable to other systems. The ability both to enhance QD PL/responses and to suppress analyte adsorption induced wetting effects through utilization of porous structures is essential for these fluorescence-based sensors. Refined design of the platform through a creation of ordered periodic dielectric structures of desired dimensions, together with optical amplifications by surface plasmon resonance of noble metal nanoparticles, may further contribute to the sensor development. Overall this would offer benefits for employing QDs in a broader range of device applications.

© Woodhead Publishing Limited, 2013

9.5.3 Enhanced sensing stability – core vs core/shell dot studies

An important specification concerning QD-based sensing materials is their sensing stability. While the CdSe-core based sensing systems have been shown to be rather sensitive and selective, they do suffer from PL instabilities caused by oxidation of the surface layers, leading to nearly complete PL quenching within ~3 weeks time, for example. Core/shell QDs are more resistant to photooxidation in the presence of the additional inorganic passivation shell[56] and are, thus, attractive for sensing studies.

To test these qualities, the PL of CdSe/ZnS core/shell QDs dispersed on an AAO platform using the method described above, supported on a Au-coated Si substrate, was monitored as a function of hydrocarbon exposure. The results showed a monotonic and sensitive PL response to xylenes exposures, with a detection limit of ~10 ppm for this analyte (Fig. 9.25(b)). The observed large signal change by ~5.5 a.u. at 10 ppm xylenes implies that there is, indeed, room to further improve the detection limit to ppb xylenes. The PL signal change is enhanced by a factor of 1.5 in the presence of Au relative to that without Au over the entire analyte concentration range (Fig. 9.25(a)). The same enhancing ratios for both PL and PL responses quantitatively indicate that high emission efficiency is beneficial for promoting sensing performances and, thus, is best to be maximized for sensor design.

Furthermore, Fig. 9.26 displays PL peak intensity evolution of a AAO/CdSe/ZnS core/shell QDs sample throughout a period of nearly nine months. The sample was tested with dry air as a carrier gas and stored in ambient air without any protection measures. Surprisingly, during such an

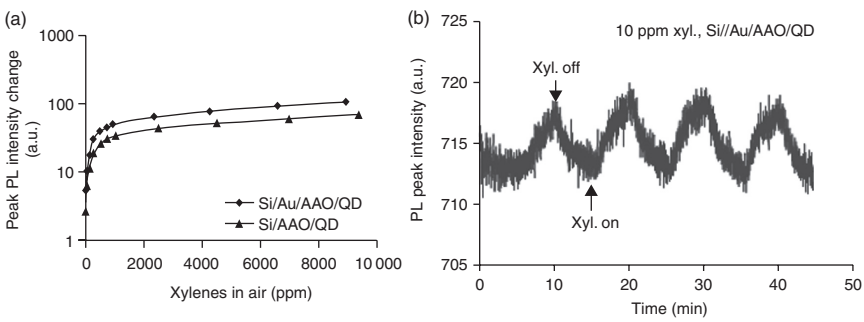

9.25 (a) Comparison of xylenes sensing characteristics of an AAO/CdSe/ZnS QD sample sitting on Si supports with/without an Au coating and (b) 10 ppm xylenes sensing trace of the sample sitting on Au-coated Si support. Reprinted with permission from *Appl. Phys. Lett.*, 97, 113105 (2010). Copyright (2010), American Institute of Physics.

© Woodhead Publishing Limited, 2013

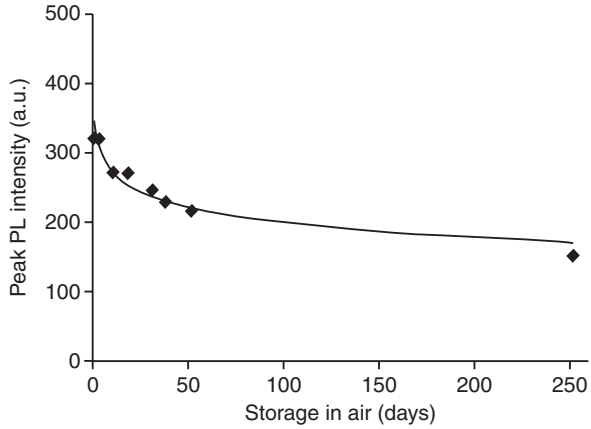

9.26 PL stability of an AAO/CdSe/ZnS QD sample stored in air over a time period of 252 days.

extended test period, the PL just showed ~10 nm blue shift in peak position and a slow decline in peak intensity, due to the photooxidation process that persists for any QDs. What was encouraging is that the sensing performance of the sample is not impacted by these slight changes. These results imply that highly-luminescent core/shell dots are more suited for sensing applications due to their high sensitivity and stability. In the future, a combination of surface-modified core/shell QDs and nanopore arrays, together with surface-coating manipulations for Si support, is expected to further improve sensor specifications for practical applications.

It is clear that the development of a detailed understanding of the sensing mechanism – and, furthermore, optimizing the QD composite film for sensing applications – will aid the design of highly-selective sensing materials. However, it is likely that the materials design will have to be utilized in combination with statistical analysis algorithms to analyze patterns within the sensing data across sensing arrays. A variety of methods are available for the statistical analysis of sensor arrays. These range from supervised learning packages – such as linear discriminant analysis (LDA) or neural networks, and unsupervised learning packages – such as PCA. The literature is rich with references to each of these algorithms and their use in electronic nose-based sensor applications, and the reader is encouraged to seek these out.[94–99] Recent work by Potyrailo *et al*. has utilized both PCA and PCA with high throughput screening experimentation to optimize QD–polymer composites for the detection of polar and nonpolar target gases.[37,100] The latter has incorporated a library of rationally selected polymer matrices to serve as the host composite material for the QDs. The library spans a range of physical and chemical properties aimed at enhancing the response of a

© Woodhead Publishing Limited, 2013

particular QD–polymer composite film to the target chemical of interest. While the library was rationally selected, it is interesting to note that the sensing characteristics of this QD–polymer library followed the expected trends toward detection of polar and nonpolar target gases in only a limited capacity. Specifically, polymers expected to perform very well toward nonpolar target gases, due to their sorbent characteristics, were not the best sensing material for the detection of toluene. Future studies which entail a broader range of polar and nonpolar targets combined with a detailed sensing/mechanistic study will likely discover interesting trends in this QD–polymer library. Such a study will lead to a broader understanding of the target gas–QD–polymer interaction driving the characteristic QD sensing response and, thus, a set of new design rules for development of rational QD–polymer libraries for the detection of chemical hydrocarbon gases.

9.6 Conclusion and future trends

Semiconductor QDs have potential for chemical sensing applications because of their unique PL properties, which are intrinsically sensitive to their surrounding environment due to their high surface area to volume ratio. The strategic use of this type of material as a sensing probe for different chemical species generally includes tailoring the surface of the QD and the controlled integration of these QDs into sensing systems with preferred attributes.

Surface-modifying groups can be introduced by post-synthesis ligand exchange; however, this may partially diminish the PL of the resulting materials due to the multiple exchanging process utilized. *In situ* surface functionalization of QDs with selected surface-modifying groups, combined with surface-stabilizing ligands – not via ligand exchange but, rather, during synthesis of the QDs – has been proposed and adapted as a method of preserving QD emission without losing PL response sensitivity. Hydrocarbon sensing experiments using such designed CdSe core dots with preselected surface functionalities have shown a detection limit and selectivity dependence on the surface-tethered modifying group chemistry, coverage ratio, and ligand length.

A critical characteristic of these sensor materials is the QD assembly into composites with design features which balance the various sensing mechanisms in order to achieve the desired sensing characteristics. Rather than a clear film structure, a porous and rough film structure has been found to be a preferred property for QD-based fluorescence sensors. These structures give rise to a high sensitivity due to the surface scattering enhanced local electromagnetic fields leading to high emission and collection outcomes. The introduction of nanopore arrays as a material for QD dispersion

© Woodhead Publishing Limited, 2013

largely enhances the PL and, more importantly, enables a monotonic sensing behavior across large dynamic ranges. Both PL intensity and the sensing responses of such a sample can be further improved by manipulating the surface-coatings of the underlying Si support. Controlled drop-casting and slow-drying (solvent annealing) is used to allow self-assembly-like deposition of monolayers of QDs without agglomeration and with their original optical properties retained.

Of specific concern is the relatively long-term PL stability of QD-based chemical sensing films. Bare high quality CdSe/ZnS core/shell QDs assembled on AAO nanopore arrays have demonstrated the sensitive detection of hydrocarbons for periods of almost nine months, in contrast to the ~3 weeks life for core dots-based films. Therefore, a combination of surface modified core/shell QDs and nanopore array platforms, together with surface-coating manipulation on Si support, is expected to further improve sensor specifications, serving as an effective method by which to produce QD-based systems for gas sensing.

The future development of smart sensor design is expected to provide an additional control with which to enhance selectivity. This will be achieved by creating optical micro-arrays of QDs that have different surface functionalities and sizes on nanopore array platforms that incorporate a temperature gradient. Pattern recognition with a multivariate data analysis tool will facilitate QD-based sensing technology for gas detection of high speciation and a sensitive manner for real-world applications.

9.7 Acknowledgments

The contribution to this work of all students, post-doctoral associates, and collaborators listed in the references cited, which pertain to the authors, is gratefully acknowledged. The authors would also like to acknowledge funding support by the NYS-DOT, US-DOT, and NYSTAR Environmental Quality Systems Research Center which made these studies possible.

9.8 References

1. Mikulec, F. V., Kuno, M., Bennati, M., Hall, D. A., Griffin, R. G. and Bawendi, M. G. (2000) Self-Assembly of CdSe-ZnS Quantum Dot Bioconjugates Using an Engineered Recombinant Protein. *J. Am. Chem. Soc.*, **122**, 2532–40.
2. Talapin, D. V., Rogach, A. L., Kornowski, A., Haase, M. and Weller, H. (2001) Highly Luminescent Monodisperse CdSe and CdSe/ZnS Nanocrystals Synthesized in a Hexadecylamine – Trioctylphosphine Oxide – Trioctylphospine Mixture. *Nano Lett*, **1**, 207–11.
3. Michalet, X., Pinaud, F. F., Bentolila, L. A., Tsay, J. M., Doose, S., Li, J. J., Sundaresan, G., Wu, A. M, Gambhir, S. S. and Weiss, S. (2005) Quantum Dots for Live Cells, in Vivo Imaging, and Diagnostics. *Science*, **307**, 538–44.

© Woodhead Publishing Limited, 2013

4. Haibing, L., Yan, Z., Wang, X., Xiong, D. and Yiqiong, B. (2007) Calixarene Capped Quantum Dots as Luminescent Probes for Hg2+ Ions. *Mater. Lett*., **61**, 1474–7.
5. Medintz, I. L., Pons, T., Trammell, S. A., Grimes, A. F., English, D. S., Blanco-Canosa, J. B., Dawson, P. E. and Mattoussi, H. (2008) Interactions Between Redox Complexes and Semiconductor Quantum Dots Coupled via a Peptide Bridge. *J. Am. Chem. Soc*., **130**, 16745–56.
6. Rogach, A. L., Talapin, D. V. and Weller, H. (2004) *Colloids and Colloid Assemblies*. ed. F. Caruso, Wiley, Weinheim, (2003), ch. 2, 52–95.
7. Mattoussi, H., Mauro, J. M., Goldman, E. R., Anderson, G. P., Sundar, V. C., Mikulec, F. V. and Bawendi, M. G. (2000) Self-Assembly of CdSe-ZnS Quantum Dot Bioconjugates Using an Engineered Recombinant Protein. *J. Am. Chem. Soc*., **122**, 12142–50.
8. Baron, T., Fernandes, A., Damlencourt, J. F., De Salvo, B., Martin, F., Mazen, F. and Haukka, S. (2003) Growth of Si Nanocrystals on Alumina and Integration in Memory Devices. *Appl. Phys. Lett*., **82**, 4151–3.
9. Coe, S., Woo, W. K., Bawendi, M. G. and Bulovic, V. (2002) Electroluminescence from Single Monolayers of Nanocrystals in Molecular Organic Devices. *Nat.*, **420**, 800–3.
10. Vassiltsova, O. V., Zhao, Z., Petrukhina, M. A. and Carpenter, M. A. (2007) Surface Functionalized CdSe Quantum Dots for the Detection of Hydrocarbons. *Sens. Actuat. B*, **123**, 522–9.
11. Zhao, Z., Dansereau, T. M., Petrukhina, M. A. and Carpenter, M. A. (2010) Nanopore-Array-Dispersed Semiconductor Quantum Dots as Nanosensors for Gas Detection. *Appl. Phys. Lett.*, **97**, 113105.
12. Mattoussi, H., Cumming, A. W., Murray, C. B., Bawendi, M. G. and Ober, R. (1998) Properties of CdSe Nanocrystal Dispersions in the Dilute Regime: Structure and Interparticle Interactions. *Phys. Rev. B*, **58**, 7850–63.
13. Murray, C. B., Kagan, C. R. and Bawendi, M. G. (2000) Synthesis and Characterization of Monodisperse Nanocrystals and Close-packed Nanocrystal Assemblies. *Annu. Rev. Mater. Sci*., **30**, 545–610.
14. Pons, T., Uyeda, H. T., Medintz, I. L. and Mattoussi, H. (2006) Hydrodynamic Dimensions, Electrophoretic Mobility, and Stability of Hydrophilic Quantum Dots. *J. Phys. Chem. B*, **110**, 20308–16.
15. Jin, W. J., Costa-Fernández, J. M., Pereiro, R. and Sanz-Medel, A. (2004) Surface-modified CdSe Quantum Dots as Luminescent Probes for Cyanide Determination. *Anal. Chim. Acta*, **522**, 1–8.
16. Shenhar, R. and Rotello, V. M. (2003) Nanoparticles: Scaffolds and Building Blocks. *Acc. Chem. Res*., **36**, 549–61.
17. Smith, A. M., Duan, H., Rhyner, M. N., Ruan, G. and Nie, S. (2006) A Systematic Examination of Surface Coatings on the Optical and Chemical Properties of Semiconductor Quantum Dots. *Phys. Chem. Chem. Phys.*, **8**, 3895–903.
18. Kalyuzhny, G. and Murray, R. (2005) Ligand Effects on Optical Properties of CdSe Nanocrystals. *J. Phys. Chem. B*,**109**, 7012–21.
19. Nazzal, A. Y., Wang X., Qu, L., Yu, W., Wang, Y., Peng, X. and Xiao, M. (2004) Environmental Effects on Photoluminescence of Highly Luminescent CdSe and CdSe/ZnS Core/Shell Nanocrystals in Polymer Thin Films. *J. Phys. Chem. B*, **108**, 5507–15.

© Woodhead Publishing Limited, 2013

20. Dorokhin, D., Tomczak, N., Reinhoudt, D. N., Velders, A. H. and Vancso, J. G. (2010) Ferrocene-coated CdSe/ZnS Quantum Dots as Electroactive Nanoparticles Hybrids. *Nanotechnol.*, **21,** 285703–8.
21. Sih, B. C. and Wolf, M. O. (2007) CdSe Nanorods Functionalized with Thiol-Anchored Oligothiophenes. *J. Phys. Chem. C*, **111**, 17184–92.
22. Liu, I.-S., Lo, H.-H., Chien, C.-T., Lin, Y.-Y., Chen, C.-W., Chen, F.-F., Su, W.-F. and Liou, S.-C. (2008) Enhancing Photoluminescence Quenching and Photoelectric Properties of CdSe Quantum Dots with Hole Accepting Ligands. *J. Mater. Chem.*, **18**, 675–82.
23. Sharma, S. N., Sharma, H., Singh, G. and Shivaprasad, S. M. (2008) Studies of Interaction of Amines with TOPO/TOP Capped CdSe Quantum Dots: Role of Crystallite Size and Oxidation Potential. *Mater. Chem. Phys.*, **110**, 471–80.
24. Jones, M., Nedeljkovic, J., Ellingson, R. J., Nozik, A. J. and Rumbles, G. (2003) Photoenhancement of Luminescence in Colloidal CdSe Quantum Dot Solutions *J. Phys. Chem. B*, **107**, 11346–52.
25. Chen, Y. F. and Rosenzweig, Z. (2002) Luminescent CdS Quantum Dots as Selective Ion Probes. *Anal. Chem.*,**74**, 5132–8.
26. Qu, F. and Li, H. (2009) Selective Molecular Recognition of Polycyclic Aromatic Hydrocarbons Using CdTe Quantum Dots with Cyclodextrin as Supramolecular Nano-sensitizers in Water. *Sens. Actuat. B*, **135**, 499–505.
27. Wang, X. Q., Wu, J. F., Li, F. Y. and Li, H. B. (2008) Synthesis of Water-soluble CdSe Quantum Dots by Ligand Exchange with P-sulfonatocalix(n)arene (n = 4, 6) as Fluorescent Probes for Amino Acids. *Nanotechnol.*, **19**, 205501–9.
28. Amiri, H., Zhao, Z., Dansereau, T. M., Petrukhina, M. A. and Carpenter, M. A. (2010) Dependence of Hydrocarbon Sensitivity on the Distance of Linked Phenyl Group to CdSe Quantum Dots Surfaces. *J. Phys. Chem. C*, **114**, 4272–8.
29. Snee, P. T., Somers, R. C., Nair, G., Zimmer, J. P., Bawendi, M. G. and Nocera, D. G. A. (2006) Ratiometric CdSe/ZnS Nanocrystal pH Sensor. *J. Am. Chem. Soc.*, **128**, 13320–1.
30. Jones, M., Lo, S. S. and Scholes, G. D. (2009) Quantitative Modeling of the Role of Surface Traps in CdSe/CdS/ZnS Nanocrystal Photoluminescence Decay Dynamic. *Proc. Natl. Acad. Sci. USA.*, **106**, 3011–16.
31. Wuister, S. F., Donega, C. D. M. and Meijerink, A. (2004) Influence of Thiol Capping on the Exciton Luminescence and Decay Kinetics of CdTe and CdSe Quantum Dots. *J. Phys. Chem. B*, **108**, 17393–7.
32. Issac, A., Borczyskowski, C. V. and Cichos, F. (2005) Correlation Between Photoluminescence Intermittency of CdSe Quantum dots and Self-trapped States in Dielectric Media. *Phys. Rev. B*, **71**, 161302(R).
33. Klimov, V. I., Mikhailovsky, A. A., McBranch, D. W., Leatherdale, C. A. and Bawendi, M. G. (2000) Quantization of Multiparticle Auger Rates in Semiconductor Quantum Dots. *Science*, **287**, 1011–13.
34. Wang, C. J., Shim, M. and Guyot-Sionnest, P. (2001) Electrochromic Nanocrystal Quantum Dots. *Science*, **291**, 2390–2.
35. Yildiz, I., Tomasulo, M. and Raymo, F. M. A. (2006) Mechanism to Signal Receptor–substrate Interactions with Luminescent Quantum Dot. *Proc. Natl. Acad. Sci. USA.*, **103**, 11457–60.
36. Cordero, S. R., Carson, P. J., Estabrook, R. A., Strouse, G. F. and Buratto, S. K. (2000) Photo-Activated Luminescence of CdSe Quantum Dot Monolayers. *J. Phys. Chem. B*, **104**, 12137–42.

© Woodhead Publishing Limited, 2013

37. Potyrailo, R. A. and Leach, A. M. (2006) Selective Gas Nanosensors with Multisize CdSe Nanocrystal/polymer Composite Films and Dynamic Pattern Recognition. *Appl. Phys. Lett.*, **88**, 134110.
38. Zhao, Z., Arrandale, M., Vassiltsova, O. V., Petrukhina, M. A. and Carpenter, M. A. (2009) Sensing Mechanism Investigation on Semiconductor Quantum Dot/polymer Thin Film Based Hydrocarbon Sensor. *Sensor. Actuat. B*, **141**, 26–33.
39. Underwood, D. F., Kippeny, T. and Rosenthal, S. J. (2001) Charge Carrier Dynamics in CdSe nanocrystals: Implications for the Use of Quantum Dots in Novel Photovoltaics. *The European Physical Journal D – Atomic, Molecular, Optical and Plasma Physics*, **16**, 241–244.
40. Zhang, J. Z. (2000) Interfacial Charge Carrier Dynamics of Colloidal Semiconductor Nanoparticles. *J. Phys. Chem. B*, **104**, 7239–53.
41. Kippeny, T. C., Bowers II, M. J., Dukes III, A. D., McBride, J. R., Orndorff, R. L., Garrett, M. D. and Rosenthal, S. J. (2008) Effects of Surface Passivation on the Exciton Dynamics of CdSe Nanocrystals as Observed by Ultrafast Fluorescence Upconversion Spectroscopy. *J. Chem. Phys*., **128**, 084713–17.
42. Medintz, I. L., Uyeda, H. T., Goldman E. R. and Mattoussi, H. (2005) Quantum Dot Bioconjugates for Imaging, Labelling and Sensing. *Nat. Mater.*, **4**, 435–46.
43. Somers, R. C., Bawendi, M. G. and Nocera, D. G. (2007) CdSe Nanocrystal Based Chem-/bio-sensors. *Chem. Soc. Rev*., **36**, 579–91.
44. Medintz, I. L., Stewart, M. H., Trammell, S. A., Susumu, K., Delehanty, J. B., Mei, B. C., Melinger, J. S., Blanco-Canosa, J. B., Dawson, P. E. and Mattoussi, H. (2010) Quantum-dot/dopamine Bioconjugates Function as Redox Coupled Assemblies for *in vitro* and Intracellular pH Sensing. *Nat. Mater.*, **9**, 676–84.
45. Guo, D. L., Fan, L. X., Wang, F. H., Huang, S. Y. and Zou, X. W. (2008) Porous Anodic Aluminum Oxide Bragg Stacks as Chemical Sensors. *J. Phys. Chem. C*, **112**, 17952–6.
46. Zhao, Y., Toyama, M., Kita, K., Kyuno, K. and Toriumi, A. (2006) Moisture-absorption-induced Permittivity Deterioration and Surface Roughness Enhancement of Lanthanum Oxide Films on Silicon. *Appl. Phys. Lett*., **88**, 072904.
47. Lee, M.-H., Chen, K.-F., Lai, C.-C., Liu, C.-W., Pai, W.-W., Chen, M.-J. and Lin, C.-F. (2002) The Roughness-Enhanced Light Emission from Metal-Oxide-Silicon Light-Emitting Diodes Using Very High Vacuum Prebake. *Jpn. J. Appl. Phys*., **41**, L326–L328.
48. Fujii, T., Gao, Y., Sharma, R., Hu, E. L., DenBaars, S. P. and Nakamura, S. (2004) Increase in the Extraction Efficiency of GaN-based Light-emitting Diodes via Surface Roughening. *Appl. Phys. Lett*., **84**, 855.
49. Gaponenko, S. V. (2010) Plasmonic Enhancement of Spontaneous Emission and Scattering of Light in Nanostructures. *J. Optoelectron. Adv. Mater.*, **12**, 39–42.
50. Chuang, L. M., Fu, H. K. and Chen, Y. F. (2005) Fabrication and Optical Properties of Two-dimensional Photonic Crystals of CdSe Pillars. *Appl. Phys. Lett*., **86**, 061902.
51. Qu, L. and Peng, X. (2002) Control of Photoluminescence Properties of CdSe Nanocrystals in Growth. *J. Am. Chem. Soc*., **124**, 2049–55.
52. Yin, Y. and Alivisatos, A. P. (2005) Colloidal Nanocrystal Synthesis and the Organic–Inorganic Interface. *Nat.*, **437**, 664–70.
53. Nordell, K. J., Boatman, E. M. and Lisensky, G. C. (2005) A Safer, Easier, Faster Synthesis W for CdSe Quantum Dot Nanocrystals. *J. Chem. Educ*., **82**, 1697–9.

© Woodhead Publishing Limited, 2013

54. Chan, E. M., Mathies, R. A. and Alivisatos, A. P. (2003) Size-Controlled Growth of CdSe Nanocrystals in Microfluidic Reactors. *Nano Lett.*, **3**, 199–201.
55. Peng, X., Wickham, J. and Alivisatos, A. P. (1998) Kinetics of II-VI and III-V Colloidal Semiconductor Nanocrystal Growth: 'Focusing' of Size Distributions. *J. Am. Chem. Soc.*, **120**, 5343–4.
56. Dabbousi, B. O., Rodriguez-Viejo, J., Mikulec, F. V., Heine, J. R., Mattoussi, H., Ober, R., Jensen, K. F. and Bawendi, M. G. (1997) (CdSe)ZnS Core-Shell Quantum Dots: Synthesis and Optical and Structural Characterization of a Size Series of Highly Luminescent Materials. *J. Phys. Chem. B*, **101**, 9463–75.
57. Li, J. J., Wang, Y. A., Guo, W., Keay, J. C., Mishima, T. D., Johnson, M. B. and Peng, X. (2003) Large-Scale Synthesis of Nearly Monodisperse CdSe/CdS Core/Shell Nanocrystals Using Air-Stable Reagents via Successive Ion Layer Adsorption and Reaction. *J. Am. Chem. Soc.*, **125**, 12567–75.
58. Reiss, P., Bleuse, J. and Pron, A. (2002) Highly Luminescent CdSe/ZnSe Core/Shell Nanocrystals of Low Size Dispersion. *Nano Lett.*, **2**, 781–4.
59. Xie, R., Kolb, U., Li, J., Basche, T. and Mews, A. (2005) Synthesis and Characterization of Highly Luminescent CdSe−Core CdS/Zn0.5Cd0.5S/ZnS Multishell Nanocrystals. *J. Am. Chem. Soc.*, **127**, 7480–8.
60. Bae, W. K., Char, K., Hur, H. and Lee, S. (2008) Single-Step Synthesis of Quantum Dots with Chemical Composition Gradients. *Chem. Mater.*, **20**, 531–9.
61. Dubois, F., Mahler, B., Dubertret, B., Doris, E. and Mioskowski, C. (2007) A Versatile Strategy for Quantum Dot Ligand Exchange. *J. Am. Chem. Soc.*, **129**, 482–3.
62. Kalyuzhny, G. and Murray, R. W. (2005) Ligand Effects on Optical Properties of CdSe Nanocrystals *J. Phys. Chem. B*, **109**, 7012–21.
63. Wang, Q., Xu, Y., Zhao, X., Chang, Y., Liu, Y., Jiang, L., Sharma, J., Seo, D.-K. and Yan, H. (2007) A facile One-step in situ Functionalization of Quantum Dots with Preserved Photoluminescence for Bioconjugation. *J. Am. Chem. Soc.*, **129**, 6380–1.
64. Skaff, H., Sill, K. and Emrick, T. (2004) Quantum Dots Tailored with Poly(para-phenylene vinylene). *J. Am. Chem. Soc.*, **126**, 11322–5.
65. Antolini, F., Di, L., Re, M. and Tapfer, L. (2005) Formation of II-VI Nanocrystals in Polymeric Matrix: Thermolytic Synthesis and Structural Characterization. *Cryst. Res. Technol.*, **40**, 948–54.
66. Zucolotto, V., Gattas-Asfura, K. M., Tumolo, T., Perinotto, A. C., Antunes, P. A., Constantino, C. J. L., Baptista, M., Leblanc, R. M. and Oliveira, O. N. (2005) Nanoscale Manipulation of CdSe Quantum Dots in Layer-by-Layer Films: Influence of the Host Polyelectrolyte on the Luminescent Properties. *Appl. Surf. Sci.*, **246**, 397–402.
67. Wang, C.-W. and Moffitt, M. G. (2004) Surface-Tunable Photoluminescence from Block-Copolymer Stabilized Cadmium Sulfide Quantum Dots. *Langm.*, **20**, 11784–96.
68. Lee, J., Sundar, V. C., Heine, J. R., Bawendi, M. G. and Jensen, K. F. (2000) Full Color Emission from II-VI Semiconductor Quantum Dot-polymer Composite, *Adv. Mater.*, **12**, 1102–5.
69. Skaff, H., Lin, Y., Tangirala, R., Breitenkamp, K., Boker, A., Russell, T. P. and Emrick, T. (2005) Crosslinked Capsules of Quantum Dots by Interfacial Assembly and Ligand Crosslinking, *Adv. Matter.*, **17**, 2082–6.

© Woodhead Publishing Limited, 2013

70. Lin, P., Shen, Y., Tetz, K. and Fainman, Y. (2005) PMMA Quantum Dots Composites Fabricated via Use of Pre-polymerization, *Opt. Express*, **13**, 44–9.
71. Caruso, F. (2001) Nanoengineering of Particle Surfaces. *Adv. Mater*., **13**, 11–22.
72. Komarala, V. K., Rakovich, Y. P., Bradley, A. L., Byrne, S. J., Corr, S. J. and Gun'ko, Y. K. (2006) Emission Properties of Colloidal Quantum Dots on Polyelectrolyte Multilayers. *Nanotechnol.*, **17**, 4117–22.
73. Shipway, A. N., Katz. E. and Willner, I. (2000) Nanoparticles Arrays on Surface for Eelectronic, Optical, and Sensor Applications. *Chem. Phys. Chem.*, **1**, 18–52.
74. Liz-Marzan, L. M. (2003) *Colloids and Colloid Assemblies*, ed. Caruso, F., *Wiley, Weinheim*, ch. 7, 216–45.
75. Vassiltsova, O. V., Jayez, D. A., Zhao, Z., Carpenter, M. A. and Petrukhina, M. A. (2010) Synthesis of Nanocomposite Materials with Controlled Structures and Optical Emissions: Application of Various Methacrylate Polymers for CdSe Quantum Dots Encapsulation. *J. Nanosci. Nanotechn*., **10**, 1635–42.
76. Bicerano, J. (1996) *Prediction of Polymer Properties*, 2nd ed. *Marcel Dekker*, New York.
77. Fabish, T. J., Saltsburg, H. M. and Hair, M. L. (1976) Charge Transfer in Metal/atactic Polystyrene Contacts. *J. Appl. Phys*., **47**, 930–40.
78. Perlman, M. M. (1972) Thermally Stimulated Currents and Voltages and Dielectric Properties. *J. Electrochem. Soc*., **119**, 892–8.
79. Lowell, J. (1977) Surface States and the Contact Electrification of Polymers. *J. Phys. D*, **10**, 65–71.
80. Duke, C. B. and Fabish, T. J. (1976) Charge-Induced Relaxation in Polymers. *Phys. Rev. Lett*., **37**, 1075–8.
81. An, M., Hong, J.-D., Cho, K.-S., Yoon, S.-M., Lee, E.-S., Kim, B.-K. and Choi, J.-Y. (2006) Spin-Coating Electrostatic Self-Assembly: Fabrication Method for CdSe Nanoparticle Monolayer. *Bull. Kor. Chem. Soc*., **27**, 1119–20.
82. Srivastava, S. and Kotov, N. A. (2008) Composite Layer-by-Layer (LBL) Assembly with Inorganic Nanoparticles and Nanowires. *Acc. Chem. Res*., **41**, 1831–41.
83. Schevchenko, E. V. and Talapin, D. V. (2008) *Semiconductor Nanocrystal Quantum Dots: Synthesis*, *Assembly*, *Spectroscopy and Applications*. ed. Rogach, A. L. *Springer*, New York, 1st edn, 119–70.
84. Neves, M. C., Pereira, A. S., Peres, M., Kholkin, A., Monteiro, T. and Trindade, T. (2006) Layer-by-Layer Deposition of Organically Capped Quantum Dots. *Mater. Sci. Forum*, 514–16, 1111–15.
85. Tsuruoka, T., Akamatsu, K. and Nawafune, H. (2004) Synthesis, Surface Modification, and Multilayer Construction of Mixed-monolayer-protected CdS Nanoparticles. *Langm.*, **20**, 11169–74.
86. Tsuruoka, T., Takahashi, R., Akamatsu, K. and Nawafune, H. (2006) Fabrication of Fluorescent Multilayers Consisting of CdTe Nanocrystals. *Trans. Mat. Res. Soc. Jpn.*, **31**, 425–8.
87. Xia, H., He, G., Peng, J., Li, W. and Fang, Y. (2010) Preparation and fluorescent sensing applications of novel CdSe-chitosan hybrid films. *Appl. Surf. Sci*., **256**, 7270–5.
88. Vassiltsova, O. V., Panda, S. K., Zhao, Z., Carpenter, M. A. and Petrukhina, M. A. (2009) Ordered Fabrication of Luminescent Multilayered Thin Films of CdSe Quantum Dots, *Dalton Trans*., 9426–32.

© Woodhead Publishing Limited, 2013

89. Rogach, A. L., Koktysh, D. S., Harrison, M. and Kotov, N. A. (2000) Layer-by-Layer Assembled Films of HgTe Nanocrystals with Strong Infrared Emission, *Chem. Mater*., **12**, 1526–8.
90. Zhao, Z., Arrandale, M., Vassiltsova, O. V., Petrukhina, M. A. and Carpenter, M. A. (2007) Quantum Dot-enabled Chemical Sensors: The Detection of Hydrocarbons with a High Degree of Sensitivity and Selectivity. *Proceedings of the Institution of Mechanical Engineers Part N Journal of Nanoengineering and Nanosystems*, **221**, 73–9.
91. Sharma, S. N., Pillai, Z. S. and Kamat, P. V. (2003) Photoinduced Charge Transfer between CdSe Quantum Dots and p-Phenylenediamine. *J. Phys. Chem. B*, **107**, 10088–93.
92. Chýlek, P. and Videen, G. (1998) Scattering by a Composite Sphere and Effective Medium Approximations. *Opt. Commun.*, **146**, 15–20.
93. Spanier, J. E. and Herman, I. P. (2000) Use of Hybrid Phenomenological and Statistical Effective-medium Theories of Dielectric Functions to Model the Infrared Reflectance of Porous SiC Flms. *Phys. Rev. B*, **61**, 10437–50.
94. Martinez, A. M. and Kak, A. C. (2001) *PCA vs. LDA*, *IEEE Trans. Patt. Analy. Mach. Intell.*, **23**, 228–33.
95. Sysoev, V. V., Goschnick, J., Schneider, T., Strelcov, E. and Kolmakov, A. (2007) A Gradient Microarray Electronic Nose Based on Percholating SnO2 Nanowire Sensing Elements, *Nanolett.*, **7**, 3182.
96. Hai, Z. and Wang, J. (2006) Electronic Nose and Data Analysis for Detection of Maize Oil Adulteration in Sesame Oil, *Sens. Actuat. B*, **119**, 449.
97. Musatov, V. Y., Sysoev, V. V., Sommer, M. and Kiselev, I. (2010) Assessment of Meat Freshness with Metal Oxide Sensor Microarray Electronic Nose: A Practical Approach, *Sens. Actuat. B*, **144**, 99.
98. Lerma-Garcia, M. J., Cerretani, L., Cevoli, C., Simo-Alfonso, E. F., Bendini, A. and Gallina Toschi, T. (2010) Use of Electronic Nose to Determine Defect Percentage in Oils. Comparison with Sensory Panel Results, *Sens. Actuators B*, **147**, 283.
99. Srivastava, J. K., Pandey, P., Jha, S. K., Mishra, V. N. and Dwivedi, R. (2011) *Chemical Vapor Identification by Plasma Treated Thick Film Tin Oxide Gas Sensor Array and Pattern Recognition*, *Sens. Transd.*, **125**, 42.
100. Potyrailo, R. A., Leach, A. M. and Surman, C. M. (2012) Multisize CdSe Nanocrystal/polymer Nanocomposites for Selective Vapor Detection Identified from High-Throughput Screening Experimentation, *ACS Comb. Sci.* dx.doi.org/10.1021/co200112s |.

© Woodhead Publishing Limited, 2013

10

Coated and functionalised single-walled carbon nanotubes (SWCNTs) as gas sensors

Y. BATTIE, Université de Lorraine, France and
O. DUCLOUX, ONERA, France

DOI: 10.1533/9780857098665.3.356

Abstract: This chapter focuses on the performances of gas sensors based on single-walled carbon nanotubes (SWCNTs). The chapter first reviews chemiresistor and field-effect transistor sensor architectures. Theoretical models based on doping effect and Schottky barrier modulation are correlated to the percolation of metallic carbon nanotubes. The functionalisation strategies of carbon nanotubes, used to acquire a gas selectivity, are discussed and offer promising application for the monitoring of air quality, or military and medical applications.

Key words: single-walled carbon nanotubes, Schottky barrier, doping, functionalisation, gas selectivity.

10.1 Introduction

Concerns about global warming, citizen protection and industrial security standards induce new needs that require the implementation of low-cost and highly-sensitive gas sensors. The reduction of the dimensions of materials to the order of several nanometers gives a higher surface-to-volume ratio than standard bulk materials. The rapid progress in the synthesis of nanomaterials and the fundamental understanding of surface chemistry has generated the emergence of ultrasensitive recognition layers based on engineered nanomaterials.

Since the landmark paper by Iijima (1991), carbon nanotubes (CNTs) have generated a great interest among researchers for their fascinating electronic, chemical and mechanical properties. CNTs are divided into two families: single-walled carbon nanotubes (SWCNTs), which can be viewed as a single graphene sheet wrapped into a cylindrical tube, and multi-walled carbon nanotubes (MWCNTs), composed of multiple layers of graphite assembled into concentric cylinders. Depending on their chirality, a SWCNT can be metallic or semiconducting, while MWCNTs are mainly metallic.

© Woodhead Publishing Limited, 2013

This one-dimensional allotropic form of carbon offers exceptional properties, such as ballistic transport over a few hundred nanometers (White and Todorov, 1998), high current-carrying capacities (10^8–10^9 A/cm^2) (Yao *et al.*, 2000) and exceptional thermal stability in a wide temperature range. SWCNTs show a hollow morphology; they consist only of surface sp^2 bonded carbon atoms. Consisting only of surface atoms, they show a large specific surface area (100–1800 m^2/g) and their electrical properties are highly influenced by their environment. Arranged into a network, SWCNTs form a porous conductive film, which is a promising candidate as a building block for new generations of high-performance gas sensors.

This chapter intends to present an overview of the current state-of-the-art of gas sensors based on SWCNTs, to provide a comparison between existing sensor technologies, and to present an outlook for future applications. It is exclusively focused on sensors based on the modification of the transport properties of SWCNTs, such as chemiresistors and carbon nanotube field-effect transistor (CNTFET) sensors (Section 10.2) because these are the only two architectures that fully exploit SWCNTs as sensitive element and transducer simultaneously. This new generation of CNT-based gas sensors completes an already large family of technologies, such as surface acoustic wave sensors (SAWs) functionalised with SWCNTs (Penza *et al.*, 2005), chemicapacitors (Snow and Keith Perkins, 2005), ionisation sensors (Modi *et al.*, 2003), impedance spectroscopy sensors (Varghese *et al.*, 2001), chemiresistors (Battie *et al.*, 2011a) and CNTFET sensors (Peng *et al.*, 2008). We will show in this chapter that SWCNT-based gas sensors are differentiated from their counterparts by their extremely low power consumption, their small size and their high sensitivity to many gases. Sensors based on SWCNTs present several benefits compared with traditional semiconducting metal oxide gas sensors: in addition to their low cost and their complementary metal oxide semiconductor (CMOS)-compatible fabrication processes, their low power consumption, room temperature compatibility with high sensitivity and their small size confers on them good potential for portable applications.

The commonly accepted physico-chemical gas sensing mechanisms of SWCNT-based gas sensors are discussed in detail by several authors (Bradley *et al.*, 2003; Peng *et al.*, 2009; Battie *et al.*, 2012b). These mechanisms, which will be described in Section 10.3, are the charge transfer between adsorbed gas molecules and SWCNTs, and the modulation of the Schottky barrier established between semiconducting SWCNTs and metallic electrodes.

Although SWCNTs show attractive features, the development of selective gas sensors based on SWCNTs remains a great challenge. Several methods exposed in Section 10.4 have been explored to overcome this problem. The most mature routes to reach gas selectivity are focused on the chemical covalent or non-covalent functionalisation of SWCNTs, the decoration of SWCNTs with metallic nanoparticles and the diversification of the metallic electrodes.

© Woodhead Publishing Limited, 2013

Due to their intrinsic characteristics, gas sensors based on SWCNTs are used to detect and identify a wide range of gases, such as atmospheric pollutants or warfare agents. These applications are detailed in Section 10.5.

The performance of gas sensors is defined by the following parameters: first, the sensitivity and response are related to the modification of the measured value when an analyte gas is submitted to the sensor. For example, in the case of resistive CNT-based gas sensors, the response is defined as the ratio between the observed resistance variation and a baseline resistance. The sensitivity is directly related to the response as being the signal change divided by the change in gas concentration. The second important characteristic for gas sensing is the detection limit, which defines the smallest value of target gas measurable. In practice, this parameter depends not only on the detection technology, but also on the associated electronics as it takes into account the experimental noise level, which explains why it is used less frequently in scientific reports. One final important characteristic: selectivity defines the ability of a sensor to detect only one species (or a reduced number of species) in often complex mixtures of gases in practical applications.

10.2 Gas sensor architecture

In this section, the performances of electrical gas sensors based on SWCNTs are reviewed. Three types of gas sensors are introduced: field-effect transistor based on individual SWCNT and chemiresistor or field-effect transistor based on SWCNT network.

10.2.1 Carbon nanotube field-effect transistor based on individual single-walled carbon nanotubes

The first report on the realisation of a gas sensor based on a CNTFET was introduced by Kong *et al.* (2000), a group at Stanford University. The sensor architecture consists in an individual SWCNT bridging two photo-lithographically patterned titanium/gold source–drain electrodes. The doped silicon substrate is used as back-gate, separated from the electrodes by an SiO_2 insulating layer. A schematic representation of this sensor is depicted in Fig. 10.1(a). The SWCNTs used as the conducting channels were synthesised by chemical vapour deposition (CVD).

Under a constant bias voltage (V_{ds}), the conductance of semiconducting SWCNTs can be modulated by applying a gate voltage (V_{gs}). The device exhibits a p-type transistor characteristic in air (Derycke *et al.*, 2002) (Fig. 10.1(b)) with a suppressed conductance at positive gate voltage. Indeed, due to the high electron affinity of oxygen, atmospheric oxygen atoms adsorbed on semiconducting SWCNTs create holes and induce an extrinsic p-doping (Collins *et al.*, 2000). The $I_{ds,on}/I_{ds,off}$ ratio, defined as

© Woodhead Publishing Limited, 2013

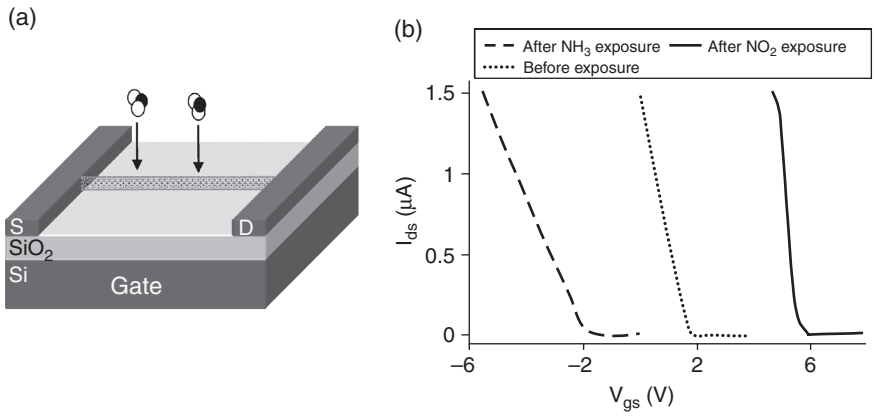

10.1 (a) Schematic representation of CNTFET based on individual SWCNT. S and D are the source and drain electrodes, respectively. (b) Effect of NH_3 or NO_2 exposure on the I_{ds} vs V_{gs} CNTFET characteristic (adapted from Kong *et al.* (2000)).

the ratio between the on-state current and the off-state current, characterises the quality of the CNTFET and is currently greater than 10^5–10^6 (Javey *et al.*, 2003). The gate voltage modifies the height of the Schottky barrier built at the semiconducting SWCNT/metal electrodes contact and, therefore, the probability for holes to travel from the electrodes to the valence band of the semiconducting SWCNT. Consequently, the $I_{ds}(V_{gs})$ characteristics depend on the nature of the electrodes. The work-functions of the metallic electrodes must be smaller than the work-function of the semiconducting SWCNT in order to observe a gate voltage effect.

To test the CNTFET as a gas sensor, Kong *et al.* (2000) exposed the device to an NH_3 or an NO_2 flow diluted in air or in argon. These gases were chosen because they exhibit two opposite electronic behaviours: NH_3 being an electron donor and NO_2 an electron acceptor. Exposure to NO_2 creates a positive shift of the $I_{ds}(V_{gs})$ characteristic of approximately 4 V, while exposure to NH_3 induces a negative shift of approximately –4 V (Fig. 10.1(b)). Consequently, at a constant gate voltage, the resistance of the device increases during NH_3 exposure and decreases during NO_2 exposure. No effect of the carrier gas was observed in these experiments because adsorbed oxygen was difficult to remove from the SWCNT under argon and generally remains on the nanotubes. For V_{gs} = 4 V, the response, defined as the relative variation of resistance during gas exposure, was approximately 100–1000 for 200 ppm NO_2 and the response time was a few seconds. On the other hand, for V_{gs} = 0 V, the response time was a few minutes and the response to 1% of NH_3 was 10–100 minutes. The authors claim that the detection limit was 2 ppm for NO_2 and 0.1% for NH_3. The detection limit could be improved by selecting a proper gate bias (Kong *et al.*, 2000). The fast response time and the high sensitivity of this sensor come from the full exposure of the chemically active

© Woodhead Publishing Limited, 2013

SWCNT surface. Sensor recovery was achieved at room temperature in 12 hours under a pure argon flow, but recovery could be accelerated by heating the sample at 200°C. This reveals a slow molecular desorption at room temperature. Similar CNTFET sensors were also successfully used to detect organic alcohol vapours with high reproducibility (Someya *et al.*, 2003). This pointed out the inability of CNTFETs to identify gases in a complex environment. On the other hand, the characterisation of sensors based on individual metallic SWCNTs showed a small gate effect (Kong *et al.*, 2000). Similar to semiconducting SWCNTs, the resistance of metallic SWCNTs increased on exposure to NH_3, while it decreased on exposure to NO_2. More quantitatively, the responses of individual metallic SWCNTs to 1% of NH_3 or to 200 ppm of NO_2 were smaller than 40%. Thus, the transport properties of metallic carbon nanotubes were affected to a lesser degree by the environment than semiconducting SWCNTs.

For comparison, metal oxide semiconductor sensors such as Cd-doped SnO_2, currently used to detect NO_2 or NH_3, operate at 250°C with a response to 300–100 ppm of NO_2 (Shimizu and Egashira, 1999). The response time is 50 seconds. These sensors can detect 1% of NH_3 at 300°C–500°C, with a response time of 1 minute. Conducting polypyrole polymer sensors, another useful gas sensor, show a response of 10% to 0.1% of NO_2 with a response time of 5–10 minutes (Miasik *et al.*, 1986). They detect 1% of NH_3 at room temperature with a response time of 10 minutes and a response to 30%. Thus, CNFETs based on individual semiconducting SWCNTs have the advantage of operating at room temperature with high sensitivity and good reproducibility.

10.2.2 Gas sensor based on single-walled carbon nanotube networks

Carbon nanotube field-effect transistors based on single-walled carbon nanotube networks

The main drawback of sensors based on individual SWCNTs is the lack of control for preparing nanotubes of the same diameter and chirality. Depending on its chirality, an SWCNT can be metallic or semiconducting. Typical as-produced SWCNT solutions comprise, theoretically, one-third of metallic SWCNTs and two-thirds of semiconducting SWCNTs. Although some progress has been made recently in sorting techniques and SWCNT production (Arnold *et al.*, 2006, Posseckardt *et al.*, 2010), the synthesis of samples containing 100% of semiconducting nanotubes remains a great challenge. Although CNTFETs based on individual SWCNTs offer high sensitivity and a rapid response time, their elaboration is time-consuming, not reproducible, and is not suitable for mass production. Indeed, it is necessary to localise and to perform a previous individual characterisation of SWCNTs with an atomic force microscope (AFM) or a scanning tunnelling

© Woodhead Publishing Limited, 2013

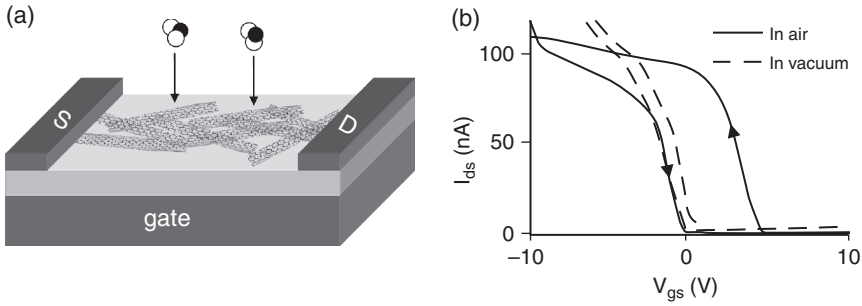

10.2 (a) Schematic representation of a CNTFET based on SWCNT network, (b) hysteresis loop in the CNTFET I_{ds} vs V_{gs} characteristic measured in air and in vacuum (adapted from Kim *et al.* (2003)).

microscope (STM). To overcome this problem, the new generation of SWCNT-based sensors take advantage of SWCNT networks where multiple nanotubes connect the source and drain electrodes. SWCNT networks can be easily elaborated by CVD, drop-coating, spray-coating, vacuum filtration-coating or spin-coating, and offer better reproducibility due to the averaging of the electrical properties of individual SWCNTs. Compared with individual SWCNTs, the description of the gas detection mechanism is more complicated due to the presence of many nanotube–nanotube contacts of varying types: metallic–metallic, metallic–semiconducting, semiconducting–semiconducting.

The typical architecture of CNTFET sensors based on SWCNT networks is illustrated in Fig. 10.2. To build this sensor with the best $I_{ds,on}/I_{ds,off}$ ratio, the density of SWCNTs needs to be sufficiently high to ensure the percolation of semiconducting SWCNTs between the electrodes without exceeding the percolation threshold of metallic SWCNTs, because these tubes cannot be tuned by gate effect. The drain–source inter-electrode distance must be greater than the SWCNT length to prevent the formation of short circuits caused by metallic nanotubes which could directly bridge the electrodes. The doped substrate is considered as the back-gate electrode.

Kong *et al.* (2000) have compared the sensitivity to NO_2 and NH_3 of (a) a CNTFET based on individual semiconducting carbon nanotubes with the sensitivity of (b) a CNTFET-based SWCNT network. The SWCNTs which composed this second device were synthesised by laser ablation. The resistance of device (a) increases and the resistance of device (b) decreases when exposed, respectively, to NH_3 and NO_2. The responses of a CNTFET based on an SWCNT network to 1% of NH_3 and 200 ppm of NO_2 were approximately 50%. Compared with a CNTFET based on individual SWCNTs, the sensitivity is dramatically reduced. In the case of SWCNT networks, the response of semiconducting SWCNTs is averaged by the small response of metallic carbon nanotubes. Furthermore, due to the van der Waals

© Woodhead Publishing Limited, 2013

interaction, SWCNTs are generally clustered into bundles, which contribute to a decrease in the active specific surface area. As proposed by Lim *et al.* (2010) and Wongwiriyapan *et al.* (2005), a selective pyrolysis of metallic SWCNTs, achieved by applying a large source–drain bias while gating off the semiconducting nanotubes, improves sensor sensitivity. Wongwiriyapan *et al.* (2005) predict an 8 ppb detection limit for NO_2. A better sensitivity can also be achieved by adjusting the gate voltage (Lucci *et al.*, 2005), or by aligning SWCNTs between interdigitated electrodes by dielectrophoresis. Indeed, as demonstrated by Lucci *et al.* (2005), the sensitivity to NH_3 of sensors based on aligned SWCNTs is twice as large as that of sensors based on random SWCNT networks because some interaction sites become more accessible in aligned SWCNTs than in the more complex structure of SWCNT networks.

The response time of CNTFETs based on randomly orientated SWCNT networks under NO_2 and NH_3 exposure is currently a few tens of minutes. The slower response time, compared with sensors based on individual SWCNTs, is attributed to the time needed by the analytes to diffuse into the SWCNT network. The response time of sensors exposed to NO_x and NH_3 was considerably improved by applying a positive or negative gate pulse voltage (Lucci *et al.*, 2006). The polarisation of the pulse depends on the redox properties of the target gas. Indeed, NH_3 is an electron donor, whereas NO_2 is an electron withdrawer. The gate pulse voltage locally modifies the surface charge of the SWCNTs and generates an attractive electrostatic force between the analyte molecules and SWCNTs. Interestingly, another pulse voltage of the opposite polarisation reduces the recovery time from several hours to a few seconds (Lucci *et al.*, 2006). This allows the gas sensor to refresh without the help of a heating element by generating a repulsive Coulomb force between the analyte molecules and SWCNTs.

Different gas molecules have been successfully detected by this type of sensor: for example, dimethyl methylphosphonate (DMMP) (a simulant for the nerve agent sarin) (Novak *et al.*, 2003), trinitrotoluene (TNT) (Roberts *et al.*, 2009), aromatic compounds (Star *et al.*, 2003), Cl_2 (Wongwiriyapan *et al.*, 2005) or water vapour. The effect of water vapour on the CNTFET sensors has been widely studied because moisture can be considered as an interfering species. CNTFETs fabricated on SiO_2/Si exhibit a large hysteresis in current–gate voltage(Fig. 10.2(b)). This hysteresis is reduced when the CNTFET is placed in a vacuum, and completely vanishes after annealing the device at 200°C (Kim *et al.*, 2003). This reveals that water molecules, always present in ambient environment, induce charge traps. Kim *et al.* (2003) assumed that two types of water-induced charge traps exist: the first involves water molecules weakly adsorbed on SWCNTs that can be removed under vacuum; the second is due to water molecules bound with the silanol groups situated on the SiO_2 substrate surface near the SWCNTs.

© Woodhead Publishing Limited, 2013

Ab initio simulations reveal a negligible affinity between H_2O molecule and pure SWCNTs, (Sung *et al.*, 2006) suggesting that the second effect is predominant.

Several groups (Kim *et al.*, 2003, McGill *et al.*, 2006) succeeded in reducing the hysteresis loop by passivating the substrate with a poly-methyl methacrylate (PMMA) or an octadecyltrichlorosilane (OTS) hydrophobic layer, confirming that silanol groups play a crucial role in the formation of trap sites. Hysteresis can introduce systematic errors, thus passivation of the substrate is an attractive way to prevent the humidity cross-sensitivity.

Chemiresistor

The simplest sensor architecture is the chemiresistor, which consists of two electrodes connected by a SWCNT film. Rather than CNTFETs, thick and dense SWCNT films can be used. Modifications of the SWCNT network resistance are monitored during gas exposure. This configuration requires fewer auxiliary electronics than CNTFETs, making it a relatively cheap device for chemical sensing applications. Different gases were detected using this architecture: for example, NO_2, NH_3, nitrotoluene, thionyl chloride ($SOCl_2$), dimethylmethylphosphonate (DMMP), methanol and acetone.

At room temperature, the resistance of SWCNT chemiresistors depends on the chemical environment and decreases under an oxidising atmosphere such as NO_2, whereas it increases under a reducing atmosphere such as NH_3 (Fig. 10.3). For this type of sensor, the sensor response often refers to the resistance variation from a base level divided by this resistance base level ($\Delta R/R_0$). Chemiresistors present a nearly linear response to a great variety of gases, such as NH_3 and NO_2, from a few ppb to several tens of ppm. Beyond, the response tends to saturate since all the absorption sites of the sensing layer become occupied at high gas concentrations. Currently, the better detection limit of a chemiresistor based on raw SWCNTs is 44 ppb for NO_2 (Li *et al.*, 2003) and 600 ppb for NH_3 (Battie *et al.*, 2011a). The response time is similar to that of CNTFETs based on SWCNT networks, since the response kinetics are essentially limited by the diffusion of gases within the porous network of nanotubes. Chemiresistors demonstrate a remarkable recovery capacity, suggesting that the sensor is reusable. Recovery takes several hours but, as for their FET counterparts, it can be accelerated by annealing the sensor in a vacuum (Battie, 2011a), or by exposing the sensor to a UV light (Li *et al.*, 2003). UV exposure decreases the desorption-energy barrier formed between adsorbed molecules and the SWCNT film. It can also influence the adsorption stage by enhancing the sensitivity of SWCNT gas sensors (Karkkanen, 2008).

An integrated chemiresistor based on an SWCNT network was reported by NASA Ames Research Centre (Li *et al.*, 2005). The device was composed

© Woodhead Publishing Limited, 2013

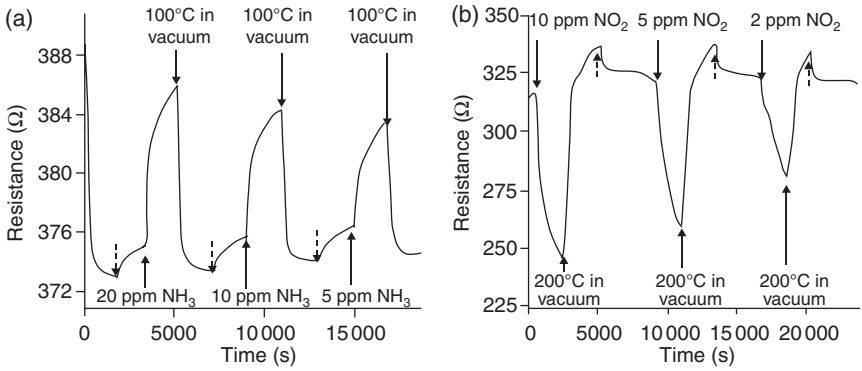

10.3 Typical response to (a) NH_3 and (b) NO_2 of a chemiresistor based on a SWCNT network (adapted from Battie *et al.* (2011a)). The dashed arrows indicate the beginning of cooling and the introduction of carrier gas.

of 12 chemiresistors consisting of SWCNT films located between interdigitated Pt electrodes. An integrated heating layer situated between the substrate and the Si_3N_4 dielectric layer was used to reset the sensor. This lab-on-a-chip sensor is particularly interesting because it constitutes a step towards the final packaging of chemiresistors for real life applications.

10.3 Gas sensing mechanisms

Gas sensing mechanism must be highlighted to improve the sensor performances. Two sensing mechanisms are considered in this section: the charge transfer between adsorbed molecules and SWCNTs, and the Schottky barrier modulation at the contacts.

10.3.1 Doping effect generated by the adsorption of gas molecules on single-walled carbon nanotubes

In order to exploit SWCNT sensors, we need to explore the physics of its response to gas. Depositing a thick SWCNT film on a transmission line method (TLM) platform, the SWCNT film resistance and the contact resistance were monitored separately during gas exposures, revealing that the sensing mechanism of chemiresistors mainly relies on a modification of the tube conductivity during gas exposure (Battie *et al.*, 2011a). In other words, gas molecules are adsorbed on SWCNTs and modify the transport properties of the SWCNT film. To correlate more quantitatively the stationary response, S_{st}, and the response time, τ, to the temperature or to the gas concentration, several authors (Lee and Strano, 2005; Battie *et al.*, 2011a) have proposed modelling the sensor response in accordance with the Langmuir

© Woodhead Publishing Limited, 2013

model. This phenomenological model is based on the equilibrium state between adsorption and desorption of a gas molecule A on an SWCNT adsorption site θ:

$$A + \theta \leftrightarrow A\theta \qquad [10.1]$$

When a gas interacts with SWCNTs, the adsorbed molecules act as dopants, which possibly influences the SWCNT transport properties. These dopants can shift the Fermi level of SWCNTs or can modify the SWCNT band structure due to the orbital hybridisations between the analytes and the electron cloud of SWCNTs. If the response is assumed to be proportional to the fractional monolayer coverage of molecules adsorbed on the SWCNTs, then the stationary response is given by Equation [10.2] and the response time is given by Equation [10.3]:

$$S_{st} = \frac{S_0 C e^{E_a/kT}}{1 + C e^{E_a/kT}} \qquad [10.2]$$

$$\tau = \frac{\alpha e^{(E_a - E_{ad})/kT}}{1 + C e^{E_a/kT}} \qquad [10.3]$$

S_0 represents the maximal sensor response, α a constant, k the Boltzmann constant, C the reduced gas concentration, T the temperature, E_a the binding energy and E_{ad} the activation energy of adsorption. These laws successfully describe the sensor performance–temperature dependence (Fig. 10.4). At low temperatures, the chemiresistor sensitivity to NO_2 and NH_3 is enhanced, while the response time is dramatically increased. When the temperature increases, both the response time and the sensitivity decrease.

An increase in temperature displaces the equilibrium state towards desorption and consequently decreases sensitivity, because fewer analytes are immobilised on the nanotube surface and decreases the response time, because the adsorption and desorption reaction kinetics are more rapid at higher temperatures (at a very low concentration, the response may be limited by convection of the molecules towards the sensor). The faster recovery observed when the sensor is annealed is simply explained by this equilibrium state displacement.

To address the problem from a microscopic point of view, the binding energy, the SWCNT-molecule distance, and the charge transfer between SWCNT and the absorbed molecule were evaluated by Density Functional Theory (DFT) to quantify the SWCNT/gas molecules interaction (Zhao *et al.*, 2002). These parameters are essential to understand the nature of the sensor response. High binding energy represents the chemisorption of analytes, whereas low binding energy suggests a physisorption mechanism. Physisorption through van der Waals interaction or hydrogen bonds allows

© Woodhead Publishing Limited, 2013

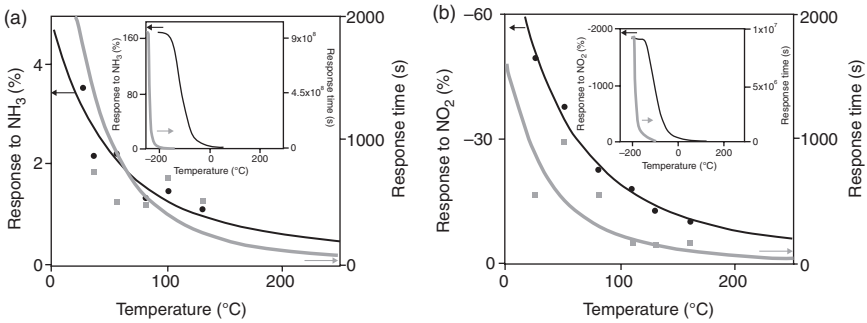

10.4 Sensor response (in black) and response time (in grey) of a chemiresistor exposed to 200 ppm of (a) NH_3 and (b) NO_2. The experimental results (black dots and grey squares) are compared with the Langmuir model. Inset, Langmuir modelling from –250°C to 300°C. The figure was reproduced from Battie *et al.* (2011a).

the sensor to be easily reset. The charge transfer is used in the qualitative estimation of sensor sensitivity to the gas under consideration. Chemisorption induces a larger charge transfer than physisorption. In other words, molecular sensing requires a strong interaction between the sensing material and the target gas. Thus, a trade-off must be found between chemisorption and physisorption to obtain a refreshable sensor with adequate sensitivity.

These parameters calculated for various gases adsorbed on a (10,0), (17,0) or (5,5) individual SWCNT are summarised in Table 10.1 (Zhao *et al.*, 2002). Charge donors – for example, NH_3 – interact weakly with SWCNTs and can be considered as physisorbed. Note that the responses to N_2, H_2 and CO_2 are negligible. On the contrary, charge acceptor gas molecules present high adsorption energy and significant charge transfer. No clear dependence of adsorption on the tube size and chirality were observed. These theoretical predictions are consistent with several experimental results (Battie *et al.*, 2011a). Indeed, NO_2 bears an unpaired electron and is considered as a strong oxidiser. The electron charge transfer is likely to occur from p-type SWCNTs to NO_2. The concentration of the hole charge carriers increases in the SWCNTs, causing a decrease in resistance. The opposite effect is obtained with NH_3 which is an electron donor. Note that, as-prepared or purified SWCNTs are not defect-free and contain oxide groups or missing carbon atoms forming Stone–Wales defects. These defects could induce a strong interaction between the gas molecules and SWCNTs, which can be used to enhance the sensitivity of SWCNT gas sensors (Feng *et al.*, 2005).

10.3.2 Modulation of the Schottky barrier

The doping effect induced by the adsorption of gas molecules on the surface of SWCNTs is controversial. When the contacts of a CNTFET are

© Woodhead Publishing Limited, 2013

© Woodhead Publishing Limited, 2013

Table 10.1 Equilibrium tube–molecule distance (d), adsorption energy (E_a), and the amount of transferred charge (Q) for several analytes adsorbed on (10,0), (17,0) and (5,5) individual SWCNTs calculated from DFT (adapted from Zhao *et al.* (2002))

		NO_2	O_2	H_2O	NH_3	CH_4	CO_2	H_2	N_2	Ar
(10,0) SWNT	d (Å)	1.93	2.32	2.69	2.99	3.17	3.20	2.81	3.23	3.32
	E_a (meV)	797	509	143	149	190	97	113	164	57
	Q (e)	–0.061	–0.128	0.035	0.031	0.027	0.016	0.014	0.008	0.01
(5,5) SWNT	d (Å)	2.16	2.46	2.68	2.99	3.33	3.54	3.19	3.23	3.58
	E_a (meV)	427	306	128	162	122	109	84	123	82
	Q (e)	–0.071	–0.142	–0.033	0.033	0.022	0.014	0.016	0.011	0.011
(17,0) SWNT	d (Å)	2.07	2.50	2.69	3.00	3.19	3.23	2.55	3.13	3.34
	E_a (meV)	687	487	127	133	72	89	49	157	82
	Q (e)	–0.089	–0.096	0.033	0.027	0.025	0.015	0.012	0.006	0.01

covered with a Si_3N_4 layer, the device becomes insensitive to NH_3 at room temperature. For comparison, if the Si_3N_4 layer passivates the CNTFET channel without covering the contacts, the sensor shows a high sensitivity to NH_3 (Peng *et al.*, 2009). Moreover, as reported by Suehiro *et al.* (2006), the CNTFET response to NO_2 depends on the nature of the electrode material. These behaviours cannot be interpreted as a direct chemical doping induced by molecular adsorption on SWCNTs, and suggest that electrical contacts play a crucial role in sensor response. An important contribution to understanding the mechanism of gas detection was introduced by the IBM group (Derycke *et al.*, 2002; Heinze *et al.*, 2002) and concerns the effect of atmospheric O_2 on a CNTFET with gold electrodes. A CNTFET, which exhibits p-type behaviour in air, could be converted into an n-type transistor by annealing in a vacuum at 300°C. Annealing is supposed to desorb oxygen. The IBM group has demonstrated that the effect of O_2 on a CNTFET is not consistent with the oxygen doping of SWCNTs but, rather, with a modification of the Schottky barrier generated at the contact between semiconducting SWCNTs and metallic electrodes. They claim that CNTFETs operate as non-conventional Schottky barrier transistors. Indeed, considering the traditional Schottky barrier theory, the adsorption of electronegative oxygen molecules at the surface of gold electrodes acts as negative charges which increase the SWCNT electron affinity. This should generate the opposite effect to that observed by the IBM group. To overcome these discrepancies, electrostatic phenomena at electrode–SWCNT junctions must be taken into account (Fig. 10.5) (Yamada, 2006). A potential drop, ΔU, is associated with the transition region between the electrode and SWCNTs. The adsorption of gases in the transition region tunes the potential drop ΔU and the Schottky barrier height ϕ_{Bh} as shown in Equation [10.4]:

$$\phi_{Bh} = E_g + \phi_s - \chi_m - |\Delta U| \qquad [10.4]$$

where E_g is the energy bandgap of the SWCNT, χ_m the metal work-function and ϕ_s the SWCNT electron affinity. By analogy with the model developed for organic compounds (Crispin *et al.*, 2002; Crispin, 2004) and metal junctions, gas molecules introduce electric dipoles close to the electrodes which tunes the metal electrode work-function and the Fermi level alignment, resulting in a modulation of the Schottky barrier height. Based on this assumption, sensor sensitivity depends on the number of adsorbed gas molecules at the SC–SWCNT/electrodes interface, but also on their dipole moment. If this dipole is orientated towards the metals, the metal work-function of the electrodes is reduced and, consequently, the Schottky barrier increases. Consistent with the increase of resistance under exposure to NH_3, NH_3 molecules are inherently polarised and have a preferred dipole orientation with respect to the metallic surfaces (Bilic *et al.*, 2002).

© Woodhead Publishing Limited, 2013

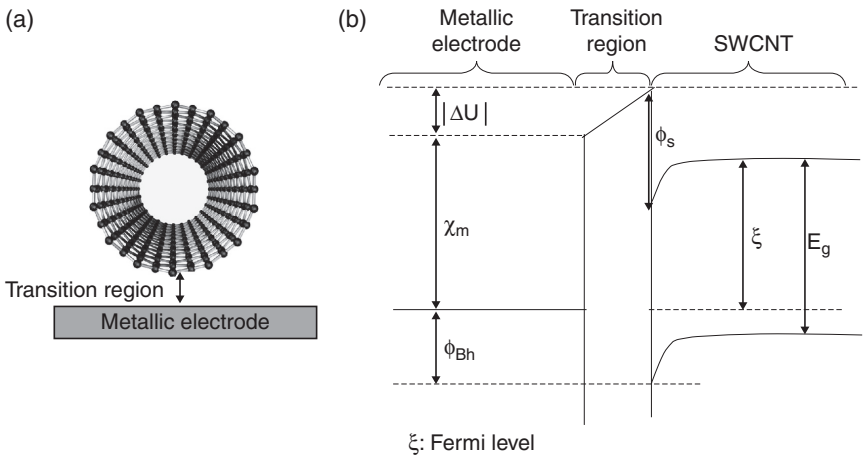

10.5 (a) Illustration of the transition region between the electrode and SWCNT, (b) band diagram at metallic electrode–semiconducting SWCNT junction using the modified Schottky barrier model (adapted from Yamada (2006)). The quantities in the band diagram are explained in the text; ξ is the difference between the valence band minimum and Fermi level.

10.3.3 Effect of the metallic single-walled carbon nanotube percolation

Due to the complexity of the transport properties of an SWCNT network, the physical mechanisms at stake during exposure to gas constitute an important source of debate. The percolation theory is invoked to account for the influence of SWCNT density on the percolation threshold of metallic SWCNTs and on the transport properties of SWCNT networks (Topinka *et al.*, 2009). As a result, the SWCNT network exhibits a metallic or a semiconducting character.

In the absence of a gate voltage, the hole carrier injection through the Schottky barrier formed at the interface between metallic electrodes and semiconducting SWCNTs is dominated by thermal emission at room temperature. Considering this effect, the I_{ds} vs V_{ds} characteristics are described by the analytical Equation [10.5]:

$$V_{ds} = R_f I_{ds} + \frac{mkT}{q} \ln\left(\frac{I_{ds}}{AA^{*}T^{2}} e^{\frac{\phi_{Bh}}{kT}} + 1\right) \qquad [10.5]$$

where R_f is the intrinsic SWCNT network resistance, q the elementary charge, T the temperature (300 K), k the Boltzmann constant, A* the Richardson constant, A the average area cross-section of the network, m a constant and

© Woodhead Publishing Limited, 2013

ϕ_{Bh} the effective Schottky barrier height formed at the contact between the electrodes and the SWCNT film. ϕ_{Bh} depends on the work-function of the electrode material. The first term of Equation [10.5] describes the linear part of the I_{ds} vs V_{ds} curve due to the resistance of the SWCNT film; the second term of the equation characterises the non-linear part attributed to the Schottky barrier.

Using this model to describe experimental measurements, Battie *et al.* (2012b) have compared the responses of sensors based on SWCNT networks presenting different degrees of percolation. They conclude that the sensing mechanism (i.e. the doping effect or the Schottky barrier modulation) depends on the percolation of metallic SWCNTs. Below the percolation threshold of metallic SWCNTs, sensing is dominated by the modulation of the Schottky barrier; above this threshold, the device shows a metallic character and the sensing mechanism is only attributed to a charge transfer between the SWCNTs and adsorbed gas molecules. In other words, the response of CNTFETs and chemiresistors is dominated, respectively, by Schottky barrier modulation and an adsorption-induced doping effect. Although CNTFETs generally show better sensitivity than chemiresistors, they present a noisier signal due to their low SWCNT density and high channel resistance, which is needed to guarantee a semiconducting behaviour. As a consequence, the detection limit of CNTFETs is altered, arguing in favour of chemiresistors based on thick and dense SWCNT films for ultrasensitive resistive gas sensing applications.

10.4 Routes towards sensor selectivity

Although SWCNT gas sensors exhibit a high sensitivity, these devices have a poor selectivity. Several mature routes to acquire gas selectivity are explored in this section.

10.4.1 Functionalisation of single-walled carbon nanotubes

As has been pointed out by Cantalini *et al.* (2003), the cross-sensitivity of SWCNT gas sensors can lead to false alarms in a complex atmosphere. To exploit CNT-based devices, it is crucial to find ways to give them selectivity. To modify the chemical activity of SWCNTs and enhance their sensitivity to a specific gas, the common approach is to functionalise the nanotube sidewall. There are two types of functionalisation depending on the binding of the functional group onto the nanotube sidewall: covalent functionalisation and non-covalent functionalisation. Covalent functionalisation of SWCNTs is often obtained from the esterification of carboxylic acid groups formed on

© Woodhead Publishing Limited, 2013

the SWCNT surface during an acid treatment. This operation creates defect sites which can be viewed as charge scattering centres leading to a loss of conductivity. On the other hand, non-covalent functionalisation, mainly based on π-stacking and Van der Waals interactions, preserves the structure and the intrinsic physical properties of SWCNTs.

Chemiresistors based on SWCNTs functionalised with covalently attached poly-(m-aminobenzene sulfonic acid) (PABS) demonstrate better sensing performances towards NH_3 and NO_2 than standard chemiresistors based on pristine SWCNTs (Bekyarova *et al.*, 2004; Zhang *et al.*, 2007). The functionalisation is based on the acyl chloride-activated amidation of nanotube-bound carboxylic acids with the amine-rich PABS. This sensor shows ppb level detection limits, a rapid response at room temperature and good reversibility. The improved sensing performance was attributed to the protonation–deprotonation of the PABS acid group which changed the charge carrier density in the SWCNTs. For example, the deprotonation of PABS during NH_3 exposure depletes the valence band in holes and reduces the conductance of the SWCNT–PABS material.

The CNT functionalisation strategy adopted at Stanford University is to cover the CNTFET channel with a specific recognition layer composed of a conducting polymer such as Nafion or polyethyleneimine (PEI) (Qi *et al.*, 2003). After PEI non-covalent functionalisation, the CNTFET electrical character switches from p-type to n-type due to a doping effect. This device is able to detect 100 ppt of NO_2 and presents good linearity from 100 ppt to 3 ppb without interference by weakly electron-donating molecules such as NH_3, H_2, CO_2, CO and CH_4. This detection limit constitutes the lowest NO_2 concentration ever detected by a CNTFET gas sensor, suggesting that electron enrichment in SWCNTs due to PEI functionalisation improves the chemical affinity between NO_2 and SWCNTs. In contrast, the p-type CNTFET channel coated with Nafion guarantees the selective recognition of NH_3. CO_2 molecules usually have a low affinity with pristine SWCNTs (Table 10.1). CNTFETs coated with a mixture of PEI and starch exhibit n-type characteristics and a high sensitivity to CO_2 (Star *et al.*, 2004). This device demonstrates a rapid response time and complete reversibility for CO_2 concentrations ranging from 500 ppm to 10% in air. CO_2 molecules are dissolved by water trapped near the hygroscopic starch and react with the amine groups of the PEI to form carbamates. This introduces charge scattering centres that decrease the CNTFET channel conductivity. As a result, arrays of functionalised SWCNT sensors are a promising solution for the detection of specific analytes in a complex mixture of interfering gases.

Gas sensors based on bio-functionalised SWCNTs with DNA strands were explored by the University of Pennsylvania group (Staii *et al.*, 2005). DNA preferentially wraps around SWCNTs via π-stacking interaction. Compared with CNTFET based on pristine SWCNTs, DNA functionalised CNTFETs

© Woodhead Publishing Limited, 2013

show an enhanced sensitivity to different vapours, such as methanol, trimethylamine (TMA), dinitrotoluene (DNT), propionic acid and DMMP. Interestingly, the response of DNA functionalised CNTFET to a specific gas depends on the base sequence of the DNA strand. Until now, the physicochemical mechanism at the basis of this chemical selectivity has not been completely understood. By varying the DNA sequence, DNA functionalisation offers the opportunity to achieve multiplexed sensor arrays able to discriminate several varieties of odours.

10.4.2 Selective diffusion barrier

In the effort to improve the selectivity of SWCNTs to gas, an original route consists in covering the SWCNT channel with a selective diffusion barrier layer which blocks interfering molecules. As an example: a SWCNT-based chemiresistor covered with a 2 μm thick polyisobutylene polymer film is able to achieve the selective detective of an organophosphorous nerve agent (Cattanach *et al.*, 2006). Interferent vapours are filtered out by the chemoselective polymer layer. However, the sensitivity to the considered nerve agent was also reduced, indicating that a certain amount of the targeted analyte was also blocked by the polymer layer.

An important issue consists in the development of new strategies to suppress the influence of atmospheric humidity on sensor response. As reported in Section 10.3.2, moisture has a dramatic effect on the CNTFET $I_{ds}(V_{gs})$ characteristic, which can lead to erroneous measurements.

A hybrid sensor architecture proposed by Battie *et al.* (2012a) combines an SWCNT network with a mesoporous silica layer elaborated by the sol-gel process. These mesoporous silica films offer a highly-specific surface area and open pores that can be easily filled with atmospheric species such as moisture. Compared with an uncoated SWCNT film, the hybrid sensor is insensitive to water vapour and its sensitivity to NH_3 is reduced. This device is highly sensitive to NO_2 and has a response time comparable to the uncoated device. The silanol groups situated on the silica wall limit the diffusion of highly polarised molecules. At the same time, micropores and mesopores present in the silica film allow the diffusion of weakly polarised vapour species to the SWCNTs film. Considering the dipole moment of H_2O, NH_3 and NO_2, the amplitude of the dipolar interactions between the silica walls and H_2O molecules is higher than those of NH_3, while the interaction with NO_2 is relatively small. In other words, mesoporous silica films act as a selective membrane which captures water molecules before their interaction with SWCNTs. This behaviour suggests that mesoporous silica layers can be used to eliminate other polar-interfering species, making this sensor architecture highly-selective and sensitive to NO_2 molecules.

© Woodhead Publishing Limited, 2013

10.4.3 Doping with heteroatoms

Poor thermal and mechanical stability, combined with the low chemical inertness of organic molecules and DNA, prohibit the use of the functionalisation introduced in Section 10.4.1 for sensors operating under harsh conditions. Carbon atoms, which constitute the nanotube wall, can be substituted with other heteroatoms such as boron, nitrogen or aluminium atoms (Wang *et al.*, 2007). This type of functionalisation offers a high degree of stability, and modulates chemical affinity, as well as the electrical properties of SWCNTs. SWCNTs doped with electron acceptor atoms such as boron or aluminium exhibit p-type behaviour (Bai and Zhou, 2007; Wang *et al.*, 2007). These dopants introduce electronic states in the band gap of semiconducting SWCNTs and shift their Fermi level. On the other hand, substituting a carbon atom with an electron donor leads to n-type SWCNTs. However, contrary to B doping, N atoms do not only simply replace C atoms but generate energetically-favoured pyridinic-like defects. SWCNTs with pyridinic-like N-defects are p-type. Since B and N show approximately the same atomic radius as C, both dopants barely alter the SWCNT shape. Due to their larger atomic diameter compared with the carbon atom, the incorporation of Al atoms in the nanotube wall locally enlarges the diameter of the SWCNT (Wang *et al.*, 2007).

Toxic gases, such as carbon monoxide (CO) or nitrogen monoxide (NO), are not detected by sensors based on pristine SWCNTs. Simulations based on the DFT formalism reveal that these gases have a high chemical affinity with doped SWCNTs. This offers a promising way to extend the range of detectable molecules. In particular, boron integrated as a dopant forms highly-active sites where the gas is favourably chemisorbed. It has been attractive for the detection of CO (Peng and Cho, 2003), formaldehyde (HCOH) (Wang *et al.*, 2006) and cyanide vapour (Zhang *et al.*, 2006). However, as pointed out by Bai and Zhou (2007), the strong binding energy between NO_2 and B dopant, which is estimated at 1.05 eV, may generate an irreversible sensor response.

The adsorption of gas molecules near the dopant induces a large charge transfer which shifts the Fermi level of the SWCNT and modifies the doped-SWCNT conductivity to a considerable degree. Increasing the dopant concentration increases the number of active sites and the sensor becomes progressively more sensitive (Hamadanian *et al.*, 2011).

Chemiresistors composed of N-doped SWCNT (1.2% at), elaborated by the floating catalyst chemical deposition method, show a sensitivity to NH_3 twice as large as that of standard sensors based on pristine SWCNTs (Battie *et al.*, 2011b). These sensors were reset by annealing treatment at 150°C–200°C with good reproducibility of the base resistance level. As predicted theoretically (Villalpando-Paez *et al.*, 2004), the NH_3 molecule, which interacts with

© Woodhead Publishing Limited, 2013

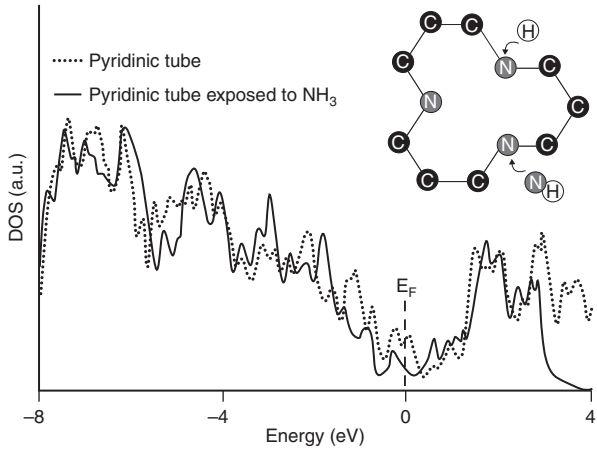

10.6 Density of state (DOS), given in arbitrary units, of a (5,5) carbon nanotube doped with an N-pyridinic-like defect before and after the adsorption of NH_3 molecules. The most stable configuration corresponds to an amino (NH_2) group bonded to an N atom and the H atom adsorbed on another N atom present in the pyridinic site (adapted from Villalpando-Paez *et al.* (2004)).

the N-pyridinic site of the SWCNTs, is fragmented into an NH_2 amino group. This group is adsorbed on a nitrogen atom within the pyridinic site, whereas the other hydrogen atom bonds to another N-pyridinic defect. This induces an important charge transfer from the adsorbed molecule to the SWCNTs, which decreases the electronic density of states at the Fermi level – that is, the nanotube conductivity (Fig. 10.6). Although N doping improved the sensitivity of the SWCNT sensor to NH_3, it was shown to have no significant effect on sensitivity to NO_2 or H_2O (Battie *et al.*, 2011b). This unique property can be used for the realisation of a differential gas sensor selective for NH_3.

10.4.4 Decoration by metallic nanoparticles

Kong *et al.* (2001) exploited the idea to decorate the sidewall of SWCNTs with metallic nanoparticles to tune the chemical activity of CNTFETs. Dihydrogen, used as clean energy source in fuel cells, is not detected by conventional sensors based on pristine SWCNTs (Table 10.1). Nevertheless, CNTFETs based on SWCNTs decorated with palladium nanoparticles demonstrate an important sensitivity to H_2. Palladium was chosen because it is a standard metal catalyst for the activation of small molecules such as H_2. Nanoparticles show a high surface area, which is ideal for sensing applications. Sensor sensitivity depends neither on the size nor on the geometry of the nanoparticle, but only on its metal work-function (Kauffman and Star, 2007). The presence of metallic particles grafted on the nanotube sidewall

© Woodhead Publishing Limited, 2013

induces interfacial potential barriers. The height of this barrier depends on the work-function of the metallic nanoparticles. When the sensor is exposed to H_2, this molecule is dissociated at the nanoparticle surface. Hydrogen atoms are dissolved in the Pd nanoparticles, and occupy octahedral interstitial sites within the cubic face centred lattice of Pd. This reduces the Pd work-function and facilitates the electron transfer from the nanoparticles to the p-type SWCNTs. Thus, the concentration of holes decreases and the SWCNT network conductivity decreases. This sensor is self-regenerated in air because adsorbed H atoms react with oxygen to form water molecules (Mubeen *et al.*, 2007).

The detection of mercury vapour (Hg) (McNicholas *et al.*, 2011) or hydrogen sulfide (H_2S) (Mubeen *et al.*, 2010) was also performed using a CNTFET decorated with gold nanoparticles. Hg is easily dissolved in gold, forming an amalgam without any chemical reaction with this metal. On the other hand, H_2S is known to absorb strongly onto gold because of the strong chemical affinity between gold and sulfur. By a process similar to the adsorption of H_2 into Pd nanoparticles, this alters the work-functions of gold nanoparticles and the conductivity of the SWCNT network. The detection limit of Hg vapour, estimated at 2 ppb, is slightly lower than the personal exposure limit fixed by the United States Occupation Safety and Health Administration at 11 ppb. The detection limit of H_2S was 3 ppb, which is about the same as the odour threshold level for humans.

Star *et al.* (2006) suggested fabricating an array of 18 CNTFETs (Fig. 10.7) decorated with different metallic nanoparticles (Mg, Al, Ti, V, Cr, Mn, Fe, Co, Ni, Zn, Mo, Rh, Ph, Sn, W, Pt, Au and Pb). Electrodeposition was used to localise the growth of metallic particles on the chip. Although each decorated CNTFET, taken separately, is cross-sensitive to multiple gases, the sensor array demonstrates selective responses. Employing principal component analysis and partial least squares regression to analyse the array response, it was possible to identify the target gas (Fig. 10.7). Thus, this multiplexed array can be considered as an on-chip ultrasensitive electronic noise which unambiguously discriminates target gas species in a complex environment.

10.4.5 Electrode metal diversification

The Thales group has patented an original sensor architecture based on an array of CNTFETs with various metals for the electrodes (Bondavalli *et al.*, 2008, 2010). As described in Section 10.3.3, the sensing mechanism of CNTFETs is mainly attributed to the modulation of the Schottky barrier built at the contacts between metallic electrodes and semiconducting SWCNTs. Assuming that the adsorption of gas at the contacts depends on its chemical affinity with the electrodes, each gas–metal couple should induce different modulation of the Schottky barrier.

© Woodhead Publishing Limited, 2013

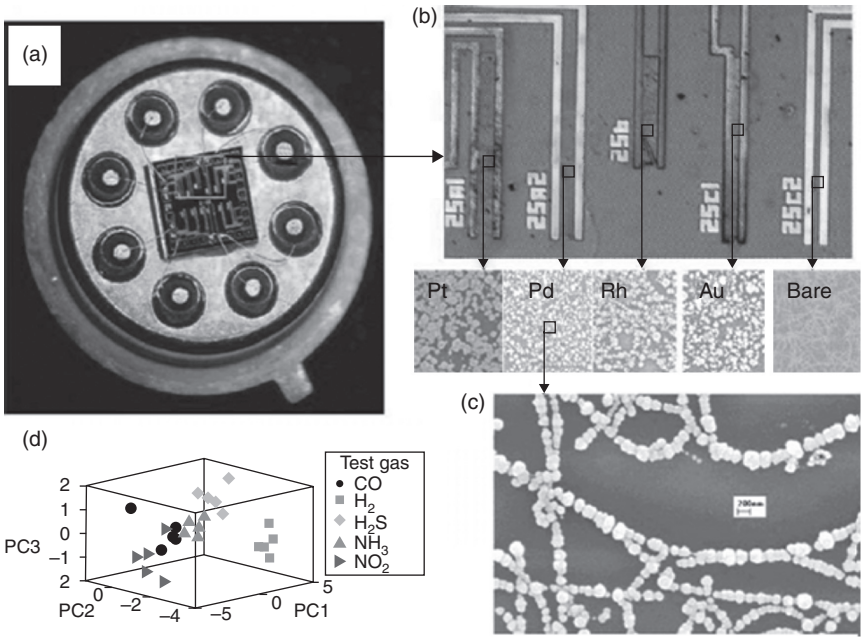

10.7 (a) Multiplexed sensor array composed of ((b)–(c)) CNFETs decorated with several metallic nanoparticles, (d) representation of the first three components analyses (adapted from Star *et al.* (2006)).

Table 10.2 Metal work-function and relative change of I_{ds} as a function of the metal electrodes after a 1 ppm DMMP or a 10 ppm NH_3 gas exposure

	Ti/Mo	Ti/Au	Ti/Pd	Ti/Pt
Work-function (eV)	4.60	5.10	5.12	5.60
1 ppm of DMMP (%)	65.00	80.00	90.00	20.00
10 ppm of NH_3 (%)	50.00	45.00	65.00	–

As reported in Table 10.2, the responses to 1 ppm of DMMP or 10 ppm of NH_3 of four CNTFETs with Pd, Pt, Au and Ti metal contacts, differ from each other, confirming that different metals interact in a different way with the gases. Although Pd and Au show similar work-functions, their responses are different, revealing that CNTFET sensor characteristics are not only related to the initial metal work-function of the electrodes, but also to a specific chemical interaction between the metal and the gas. Therefore, this peculiar sensor architecture is attractive for the recognition of gas from its electronic fingerprint in complex environment (Table 10.2).

© Woodhead Publishing Limited, 2013

10.5 Applications

Gas sensors based on SWCNTs present great potentials for several applications. Three potential applications are introduced in this section: the air quality monitoring, the warfare and explosive gas detection, and the medical diagnostics.

10.5.1 Air quality monitoring

The *in situ* control of air quality is a major concern at the time of writing. The United States Environmental Protection Agency (EPA) has defined National Ambient Air Quality Standard (NAAQS) for pollutants considered as harmful for public health and the environment. Among the major air pollutants, we can mention SO_2, CO and NO_x (NO/NO_2).

NO_x is a prominent air pollutant produced from the combustion of fuel. The amount of NO_x emitted into the atmosphere is significant in cities with dense traffic. NO_x reacts with water vapour and oxygen to form nitric acid, which contributes to acid rain. Moreover, associated with volatile organic compounds (VOCs) in the presence of sunlight, NO_x generates ground-level smog. It plays a central role in the formation of tropospheric ozone which can damage lung tissue, create oedema and cause respiratory diseases in susceptible populations. For NO_2, the threshold limit value (TLV), defined as the level of exposure without risk of injury, has been set to 3 ppm over a 10-hour day. Since NO_2 is harmful to human health and damages the environment, its concentration must be monitored accurately and the hazardous level must be determined rapidly. Standard current methods used to analyse air quality need bulky equipment, such as photoluminescence spectrophotometers or mass spectrometers. On the other hand, the detection limit of typical commercial solid state metal oxide sensors ranges from 1 to 1000 ppm at an operating temperature of a few hundred degrees Celsius. The detection of air pollutants generates a growing demand in ultrasensitive compact gas sensors with low power consumption. A promised application of SWCNTs as NO_2 gas sensor is mentioned in the initial report of the Standford group (Kong *et al.*, 2000). SWCNT gas sensors show a high sensitivity to NO_2, attributed to their considerable chemical affinity. The detection limit of pristine SWCNT gas sensors was 20 ppb to 40 ppb, which is less than the TLV. This sensor is easily refreshable at room temperature by using a pulse gate voltage (Lucci *et al.*, 2006) or an UV exposure (Li *et al.*, 2003), suggesting that it can be reusable for subsequent gas exposure. Using one of the procedures presented in Section 10.4, it was possible to recognise other pollutants, such as SO_2 or CO, and to extract their concentration, suggesting that an SWCNT sensor is able to perform a complete chemical analysis of the atmosphere.

© Woodhead Publishing Limited, 2013

10.5.2 Military applications

Increasing terrorist activity creates new needs for the detection of malicious chemical gas species. Two types of gases can be distinguished: explosives and nerve agents. Military specifications differ from those of the mass market: sensors can be more expensive but need to be highly-sensitive (typically, in the ppb range) and highly-selective in order to avoid false alarms. Nevertheless, CNT-based sensors are still interesting for the military market, in particular for the surveillance of public places and the equipment of soldiers.

The resistance of an SWCNT chemiresistor, made by drop-casting SWCNTs onto interdigitated gold electrodes, shows a fast and reversible decrease upon exposure to nitrotoluene (Li *et al.*, 2003). Nitrotoluene is an organic molecule composed of a nitrogen oxide group bound to benzene, used as tag for detecting explosives such as 2,4,6- (TNT). This device has a linear behaviour with respect to gas concentrations from 262 ppb to 162 ppm. The detection limit, estimated at 262 ppb, is similar to that of commercial gas chromatography–mass spectrometric sensors, suggesting that SWCNT-based gas sensors would have great potential as portable electronic noses for the detection of explosive devices such as land mines. Moreover, thanks to their small size and light weight, these devices can be easily integrated into portable units, facilitating their handling and making them compatible for security control in airports, for example.

DMMP is a commonly-used simulant for sarin, a lethal organophosphorous nerve agent used in the terrorist attack perpetrated in the Tokyo subway in 1995. This gas was successfully detected at a sub-ppb level by SWCNT chemiresistors or CNTFETs (Novak *et al.*, 2003). Thus, SWCNT sensors have the potential to provide chemical agent detection with better performances than conventional electronic transducers. The gas adsorption is fully reversible by applying a positive gate voltage pulse of a few hundred seconds. An interesting device architecture proposed by Cattanach *et al.* (2006) was composed of SWCNT bundles deposited onto plastic polyethylene terephthalate (PET) polymer substrates. This device detects DMMP and diisopropyl methylphosphonate (DIMP) even under flexural strain. DIMP is a stimulant for soman, a nerve agent constituted with a strong electrophilic phosphorus centre. To avoid false alarms due to interfering species, gas selectivity was achieved by covering the SWCNT channel with a chemoselective polyisobutylene polymer. This device demonstrates a robust response, even under high concentrations (30 000 ppm) of interfering gases.

10.5.3 Medical applications

CNT-based sensors also find applications in the medical market. Contrary to mass-production markets, the medical market is adapted to highly-selective

© Woodhead Publishing Limited, 2013

gas sensors, with a sensitivity highly-dependent of the application (ppb to %), and a compatibility with the targeted light equipment of medical staff and laboratories.

Exhaled breath is composed of a complex mixture of nitrogen, oxygen, carbon dioxide, water and organic vapour species. Therefore, medical diagnosis from the exhaled breath requires gas sensors with a high degree of selectivity.

The monitoring of the CO_2 concentration in the human breath, called capnography, is important for the diagnosis of lung diseases and is currently undertaken with non-dispersive infrared (NDIR) sensors. SWCNTs are poorly sensitive to weak Lewis acid or bases such as CO_2. As reported, by Nanomix Inc. (a Berkeley University spin-out specialised in nanotube-based medical analytical detection devices), sensitivity can be achieved by functionalising an SWCNT with an organic recognition layer composed of a mixture of PEI and starch (Star *et al.*, 2004). The conductance of this sensor scales linearly with a CO_2 concentration from 500 ppm to 10%. Some efforts must be made to improve the selectivity of this capnography sensor.

Traces of VOCs in human breath can be a symptom of diabetes, kidney failure, asthma or breast cancer. VOCs were mainly detected by mass spectroscopy with a ppb detection limit. The most advanced VOC sensor based on SWCNTs for medical application was introduced by Peng *et al.* (2008a, 2008b). This device is designed as an array of ten SWCNT chemiresistors coated with different non-polymeric organic layers. Since the responses of each chemiresistor are different, a principal component analysis of the measurement allows the direct discrimination between a healthy patient and a patient with cancer or renal diseases. The same authors have also highlighted the dramatic effect of humidity on the sensor response and have proposed coupling the device with a water extractor (Fig. 10.8).

The detection of NO in the breath of medical patients is crucial, because changes in NO levels can indicate heart failure, asthma or neuron death induced by degenerative diseases such as Alzheimer's. Chemiluminescence is the common method used to evaluate the amount of NO in the exhaled breath. Although this technique can detect a few hundred ppt of NO, drawbacks are its large size and high cost. Gas sensors based on pristine SWCNTs generally show a small response to NO. Their sensitivity can be enhanced by decorating the SWCNT channel with metal nanoparticles (Pt, Pd, Au, Ag). Nanomix Inc. develops and commercialises a selective CNTFET-based NO sensor based on an original approach (Kuzmych *et al.*, 2007). This sensor combined a CNTFET based on PEI-functionalised SWCNT, a chromium trioxide (CrO_3) converter and an ascarite scrubber. The CrO_3 converter is used as an oxidising layer to transform nitric oxide NO into NO_2 with a relative efficiency of approximately 90%. As reported in Section 10.4.1, PEI-

© Woodhead Publishing Limited, 2013

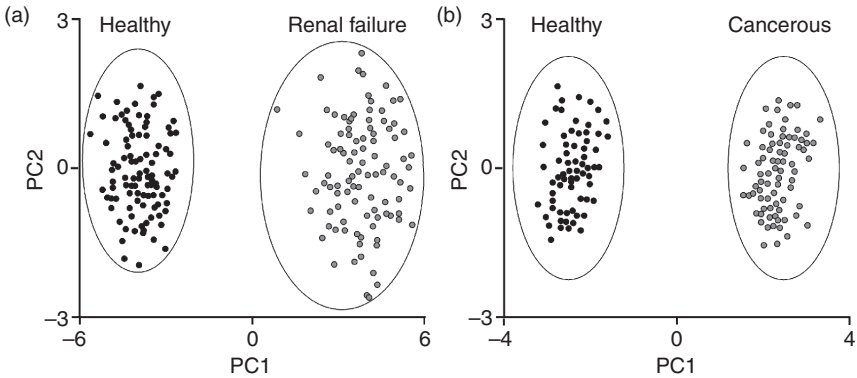

10.8 Principal components score plots of an array of ten sensors upon exposure to (a) renal failure and (b) cancerous patterns (adapted from Peng *et al.* (2008a, 2008b)).

functionalised SWCNT sensors are highly-sensitive and selective to NO_2. Moreover, the ascarite scrubber, placed before the CrO_3 converter, is used to prevent interference from exhaled CO_2 by removing it. This sensor is able to detect 5 ppb NO in a breath environment, which is comparable to that of standard NO detection techniques.

10.6 Conclusion

The recent development of SWCNT-based materials offers huge potential for the development of highly-sensitive devices. The one-dimensional shape of SWCNTs makes their intrinsic properties highly-sensitive to very small external perturbations. Compared with conventional sensors, SWCNT-based gas sensors allow low cost, low weight, ultrasensitivity and low power consumption. Although they are less sensitive than sensors based on individual SWCNTs, sensors based on SWCNTs assembled into networks are preferred for mass production. The gas sensing mechanism can be explained as a combination of a doping effect and Schottky barrier modulation, each mechanism being dependent on the sensor type and layout. The main drawback of gas sensors based on pristine SWCNTs is their lack of selectivity. Different solutions were successfully developed to overcome this technical challenge, such as chemical functionalisation, metal nanoparticle decoration or electrode diversification. As a result, carbon nanotube-based sensors attract tremendous interest for practical applications because of their potential for environmental monitoring, public security and medical diagnosis.

© Woodhead Publishing Limited, 2013

10.7 References

Arnold, M. S., Green, A. A., Hulvat, J. F., Stupp, S. I. and Hersam, M. C. (2006), 'Sorting carbon nanotubes by electronic structure using density differentiation', *Nature Nanotechnology*, **1**, 60–5.

Bai, L. and Zhou, Z. (2007), 'Computational study of B- or N-doped single-walled carbon nanotubes as NH3 and NO2 sensors', *Carbon*, **45**, 2105–10.

Battie, Y., Ducloux, O., Thobois, P., Dorval, N., Lauret, J. S., Attal-Trétout, B. and Loiseau, A. (2011a), 'Gas sensors based on thick films of semi-conducting single walled carbon nanotubes', *Carbon*, **49**, 3544–52.

Battie, Y., Ducloux, O., Thobois, P., Susi, T., Kauppinen, E. I. and Loiseau, A. (2011b), 'Selective differential ammonia gas sensor based on N-doped SWCNT films', *Physica Status Solidi B*, **248**, 2462–6.

Battie, Y., Ducloux, O., Patout, L., Thobois, P. and Loiseau, A. (2012a);Selectivity enhancement using mesoporous silica thin films for single walled carbon nanotube based vapour sensors', *Sensors and Actuators B*, **163**, 121–7.

Battie, Y., Gorintin, L., Ducloux, O., Thobois, P., Bondavalli, P., Feugnet, G. and Loiseau, A. (2012b), 'Thickness dependent sensing mechanism in sorted semiconducting single walled nanotube based sensors', *Analyst*, **137**, 2151–7.

Bekyarova, E., Davis, M., Burch, T., Itkis, M. E., Zhao, B., Sunshine, S. and Haddon, R. C. (2004), 'Chemically functionalized single-walled carbon nanotubes as ammonia sensors', *Journal of Physical Chemistry B*, **108**, 19717–20.

Bilić, A., Reimers, J. R., Hush, N. S. and Hafner, J. (2002), 'Adsorption of ammonia on the gold (111) surface', *Journal of Chemical Physics*, **116**, 8981–7.

Bondavalli, P., Legagneux, P. and Pribat, D. (2008), 'Gas fingerprinting using carbon nanotubes transistors arrays', *Journal Experimental Nanoscien*ce, **3**, 347–56.

Bondavalli, P., Legagneux, P., Pribat, D., Lebarny, P and Naigle, J. (Thales) 2010. *Conductive nanotube or nanowires FET transistor network and corresponding device*, *for detecting analytes.* European Patent WO2006128828. 2010, October 27.

Bradley, K., Gabriel, J. C. P, Briman, M., Star, A. and Grüner, G. (2003), 'Charge Transfer from Ammonia Physisorbed on Nanotubes', *Physical Review Letters*, **91**, 218301.1–218301.4.

Cantalini, C., Valentini, L., Armentano, I., Lozzi, L., Kenny, J. M. and Santucci, S. (2003), 'Sensitivity to NO2 and cross-sensitivity analysis to NH3, ethanol and humidity of carbon nanotubes thin film prepared by PECVD', *Sensors and Actuators B*, **95**, 195–202.

Cattanach, K., Kulkarni, R. D., Kozlov, M. and Manohar, S. K. (2006), 'Flexible carbon nanotube sensors for nerve agent simulants', *Nanotechnology*, **17**, 4123–8.

Collins, P. G., Bradley, K., Ishigami, M. and Zettl, A. (2000), 'Extreme oxygen sensitivity, of electronic properties of carbon nanotubes', *Science*, **287**, 1801–4.

Crispin, X., Geskin, V., Crispin, A., Cornil, J., Lazzaroni, R., Salaneck, W. R. and Brédas, J. L. (2002), 'Characterization of the interface dipole at organic/ metal interfaces', *JACS*, **124**, 8131–41.

Crispin, X. (2004) 'Interface dipole at organic/metal interfaces and organic solar cells', *Solar Energy Materials and Solar Cells*, **83**, 147–68.

© Woodhead Publishing Limited, 2013

Derycke, V., Martel, R., Appenzeller, J. and Avouris, P. (2002), 'Controlling doping and carrier injection in carbon nanotube transistors', *Applied Physics Letters*, **80**, 2773–5.

Feng, X., Irle, S., Witek, H., Morokuma, K., Vidic, R. and Borguet, E. (2005), 'Sensitivity of ammonia interaction with single-walled carbon nanotube bundles to the presence of defect sites and functionalities', *JACS*, **127**, 10533–8.

Hamadanian, M., Khoshnevisan, B. and Fotooh, F. K. (2011), 'Single-walled carbon nanotubes as CO sensor', *Structural Chemistry*, **22**, 1205–11.

Heinze, S., Tersoff, J., Martel, R., Derycke, V., Appenzeller, J. and Avouris, P. (2002), 'Carbon nanotubes as Schottky barrier transistors', *Physical Review Letters*, **89**, 106801.1–106801.4.

Iijima S (1991), 'Helical microtubules of graphitic carbon', *Nature*, **354**, 56–8.

Javey, A., Guo, J., Wang, Q., Lundstrom, M. and Dai, H. (2003), 'Ballistic carbon nanotube field-effect transistors', *Nature*, **424**, 654–7.

Karkkanen, A. (2008), 'Gas Sensing Properties of SWCNT and Teflon AF Composites', *Proceedings of the 6th IEE Conference on Sensors*, 547–9.

Kauffman, D. R. and Star, A. (2007), 'Chemically induced potential barriers at the carbon nanotube-metal nanoparticle interface', *Nano Letters*, **7**, 1863–8.

Kim, W., Javey, A., Vermesh, O., Wang, Q., Li, Y. and Dai, H. (2003),' Hysteresis caused by water molecules in carbon nanotube field-effect transistors', *Nano Letters*, **3**, 193–8.

Kong, J., Franklin, N. R., Zhou, C., Chapline, M. G., Peng, S., Cho, K. and Dai, H. (2000), 'Nanotube molecular wires as chemical sensors', *Nature*, **287**, 622–5.

Kong, J., Chapline, M. G. and Dai, H. (2001), 'Functionalized carbon nanotubes for molecular hydrogen sensors', *Advanced Materials*, **13**, 1384–6.

Kuzmych, O., Allen, B. L. and Star, A. (2007), 'Carbon nanotube sensors for exhaled breath components', *Nanotechnology*, **18**, 375502.1–375502.7.

Lee, C. Y. and Strano, M. S. (2005), 'Understanding the dynamics of signal transduction for adsorption of gases and vapors on carbon nanotube sensors', *Langmuir*, **21**, 5192–6.

Li, J., Lu, Y., Ye, Q., Cinke, M., Han, J. and Meyyappan, M. (2003),'Carbon nanotube sensors for gas and organic vapor detection', *Nano Letters*, **3**, 929–33.

Li, J., Lu, Y., Ye, Q., Delzeit, L. and Meyyappan, M. (2005), 'Gas Sensor Array Using Carbon Nanotubes and Microfabrication Technology', *Electrochemical and Solid-State Letters*, **8**, 100–2.

Lim, J. H., Phiboolsirichit, N., Mubeen, S., Rheem, Y., Deshusses, M. A., Mulchandani, A. and Myung, N. V. (2010), ' Electrical and sensing properties of single-walled carbon nanotubes network: effect of alignment and selective breakdown', *Electroanalysis*, **22**, 99–105.

Lucci, M., Reale, A., Di Carlo, A., Orlanducci, S., Tamburri, E., Terranova, M. L., Davoli, I., Di Natale, C., D'Amico, A. and Paolesse, R. (2006), 'Optimization of a NOx gas sensor based on single walled carbon nanotubes', *Sensors and Actuators B: Chemical*, **118**, 226–31.

Lucci, M., Regoliosi, P., Reale, A., Di Carlo, A., Orlanducci, S., Tamburri, E.,. Terranova, M. L., Lugli, P., Di Natale, C., D'Amicoa, A. and Paolesse, R. (2005), 'Gas sensing using single wall carbon nanotubes ordered with dielectrophoresis', *Sensors and Actuators B: Chemical*, 111–12, 181–6.

© Woodhead Publishing Limited, 2013

McGill, S. A., Rao, S. G., Manandhar, P., Xiong, P. and Hong, S. (2006), 'High-performance, hysteresis-free carbon nanotube field-effect transistors via directed assembly', *Applied Physics Letters*, **89**, 163123.1–163123.3.

McNicholas, T. P., Zhao, K., Yang, C., Hernandez, S. C., Mulchandani, A., Myung, N. V. and Deshusses, M. A. (2011), 'Sensitive Detection of Elemental Mercury Vapor by Gold-Nanoparticle-Decorated Carbon Nanotube Sensors', *Journal of Physical Chemistry C*, **115**, 13927–31.

Miasik, J., Hooper, A. and Tofield, B. (1986), 'Conducting polymer gas sensor', *Journal of Chemistry Society Faraday Transactions*, **82**, 1117–26.

Modi, A., Koratkar, N., Lass, E., Wel, B. and Ajayan, P. M. (2003), 'Miniaturized gas ionization sensors using carbon nanotubes', *Nature*, **424**, 171–4.

Mubeen, S., Zhang, T., Chartuprayoon, N., Rheem, Y., Mulchandani, A., Myung, N. V. and Deshusses, M. A. (2010), 'Sensitive detection of H2S using gold nanoparticle decorated single-walled carbon nanotubes', *Analytical Chemistry*, **82**, 250–7.

Mubeen, S., Zhang, T., Yoo, B., Deshusses, M. A. and Myung, N. V. (2007), 'Palladium nanoparticles decorated single-walled carbon nanotube hydrogen sensor', *Journal of Physical Chemistry C*, **111**, 6321–7.

Novak, J. P., Snow, E. S., Houser, E. J., Park, D., Stepnowski, J. L. and McGill, R. A. (2003), 'Nerve agent detection using networks of single-walled carbon nanotubes', *Applied Physics Letters*, **83**, 4026–8.

Peng, S. and Cho, K. (2003), 'Ab initio study of doped carbon nanotube sensors', *Nano Letters*, **3**, 513–17.

Peng ,G., Trock, E. and Haick, H. (2008a), 'Detecting simulated patterns of lung cancer biomarkers by random network of single-walled carbon nanotubes coated with nonpolymeric organic materials', *Nano Letters*, **8**, 3631–5.

Peng, G., Tisch, U. and Haick, H. (2008b), 'Detection of Nonpolar Molecules by Means of Carrier Scattering in Random Networks of Carbon Nanotubes: Toward Diagnosis of Diseases via Breath Samples', *Nano Letters*, **9**, 1362–8.

Peng, N., Zhang, Q., Chow, C. L., Tan, O. K. and Marzari, N. (2009),'Sensing Mechanisms for Carbon Nanotube Based NH3 Gas Detection', *Nano Letters*, **9**, 1626–30.

Peng, N., Zhang, Q., Lee, Y. C., Tan, O. K. and Marzari, N. (2008), 'Gate modulation in carbon nanotube field effect transistors-based NH3 gas sensors', *Sensors And Actuators B*, **132**, 191–5.

Penza, M., Antolini, F. and Vittori-Antisari, M. (2005), 'Carbon nanotubes-based surface acoustic waves oscillating sensor for vapour detection', *Thin Solid Films*, **472**, 246–52.

Posseckardt, J., Battie, Y., Fleurier, R., Lauret, J. S., Loiseau, A., Jost, O. and Mertig, M. (2010), 'Improved sorting of carbon nanotubes according to electronic type by density gradient ultracentrifugation', *Physica Status Solidi B*, **247**, 2687–90.

Qi, P., Vermesh, O., Grecu, M., Javey, A., Wang, Q., Dai, H., Peng, S. and Cho, K. J. (2003),' Toward large arrays of multiplex functionalized carbon nanotube sensors for highly sensitive and selective molecular detection', *Nano Letters*, **3**, 347–51.

Roberts, M. E., LeMieux, M. C. and Bao, Z. (2009), 'Sorted and aligned single-walled carbon nanotube networks for transistor-based aqueous chemical sensors', *ACS Nano*, **3**, 3287–93.

Shimizu, Y. and Egashira, M. (1999),'Basic aspects and challenges of semiconductor gas sensors', *Material Research Society Bulletin* **24**, 18–24.

© Woodhead Publishing Limited, 2013

Suehiro, J., Imakiire, H., Hidaka, S., Ding, W., Zhou, G., Imasaka, K. and Hara, M. (2006), 'Schottky-type response of carbon nanotube NO2 gas sensor fabricated onto aluminium electrodes by dielectrophoresis', *Sensors and Actuators B*, **114**, 943–9.

Someya, T., Small, J., Kim, P., Nuckolls, C. and Yardley, J. T. (2003) 'Alcohol vapor sensors based on single-walled carbon nanotube field effect transistors', *Nano Letters*, **3**, 877–81.

Snow, E. S. and Keith Perkins, F. (2005), 'Capacitance and Conductance of Single-Walled Carbon Nanotubes in the Presence of Chemical Vapors', *Nano Letters*, **5**, 2414–7.

Staii, C., Johnson, A. T., Chen, M. and Gelperin, A. (2005), 'DNA-decorated carbon nanotubes for chemical sensing', *Nano Letters*, **5**, 1774–8.

Star, A., Han, T. R., Gabriel, J. C. P., Bradley, K. and Grüner, G. (2003), 'Interaction of aromatic compounds with carbon nanotubes: correlation to the Hammett parameter of the substituent and measured carbon nanotube FET response', *Nano Letters*, **3**, 1421–3.

Star, A., Han, T. R., Joshi, V., Gabriel, J. C. P. and Grüner, G. (2004), 'Nanoelectronic carbon dioxide sensors', *Advanced Materials*, **16**, 2049–52.

Star, A., Joshi, V., Skarupo, S., Thomas, D. and Gabriel, J. P. C. (2006), 'Gas sensor array based on metal-decorated carbon nanotubes', *Journal of Physical Chemistry B*, **110**, 21014–20

Sung, D., Hong, S., Kim, Y. H., Park, N., Kim, S., Maeng, S. L. and Kim, K. C. (2006), 'Ab initio study of the effect of water adsorption on the carbon nanotube field-effect transistor', *Applied Physics Letters*, **89**, 243110.1–243110.3.

Topinka, M. A., Rowell, M. W., Goldhaber-Gordon, D., McGehee, M. D., Hecht, D. S. and Gruner, G. (2009), 'Charge transport in interpenetrating networks of semiconducting and metallic carbon nanotubes', *Nano Letters*, **9**, 1866–71.

Varghese, O. K., Kichambre, P. D., Gong, D., Ong, K. G., Dickey, E. C. and Grime, C. A. (2001), 'Gas sensing characteristics of multi-wall carbon nanotubes', *Sensors And Actuators B*, **81**, 32–41.

Villalpando-Paez, F., Romero, A. H., Munoz-Sandoval, E., Martınez, L. M., Terrones, H. and Terrones, M. (2004), 'Fabrication of vapor and gas sensors using films of aligned CNx nanotubes', *Chemical Physics Letters*, **386**, 137–43.

Wang, R., Zhang, D., Sun, W., Han, Z. and Liu, C. (2007), 'A novel aluminum-doped carbon nanotubes sensor for carbon monoxide', *Journal of Molecular Structure: THEOCHEM*, **806**, 93–7.

Wang, R., Zhang, D., Zhang, Y. and Liu, C. (2006), 'Boron-doped carbon nanotubes serving as a novel chemical sensor for formaldehyde', *Journal of Physical Chemistry B*, **110**, 18267–71.

White, C. T. and Todorov, T. N. (1998), 'Carbon nanotubes as long ballistic conductors', *Nature,* **393**, 240–2.

Wongwiriyapan, W., Honda, S., Konishi, H., Mizuka, T., Ikuno, T., Ito, T., Maekawa, T., Suzuki, K., Ishikawa, H., Oura, K. and Katayama, M. (2005), 'Single-walled carbon nanotube thin-film sensor for ultrasensitive gas detection', *Japanese Journal of Applied Physics*, **44**, 482–4.

Yamada, T. (2006), 'Equivalent circuit model for carbon nanotube Schottky barrier: Influence of neutral polarized gas molecules', *Applied Physics Letters*, **88**, 083106.1–083106.3.

© Woodhead Publishing Limited, 2013

Yao, Z., Kane, C. L. and Dekker, C. (2000), 'High-Field Electrical Transport in Single-Wall Carbon Nanotubes', *Physical Review Letters*, **84**, 2941–4.

Zhang, T., Mubeen, S., Bekyarova, E., Yoo, B. Y., Haddon, R. C., Myung, N. V. and Deshusses, M. A. (2007), 'Poly(m-aminobenzene sulfonic acid) functionalized single-walled carbon nanotubes based gas sensor', *Nanotechnology,* **18**, 165504.1–165504.1.

Zhang, Y., Zhang, D. and Liu, C. (2006), 'Novel chemical sensor for cyanides: boron-doped carbon nanotubes', *Journal of Physical Chemistry B*, **110**, 4671–4.

Zhao, J., Buldum, A., Han, J. and Lu, J. P. (2002), 'Gas molecule adsorption in carbon nanotubes and nanotube bundles', *Nanotechnology*, **13**, 195–200.

© Woodhead Publishing Limited, 2013

11

Carbon nanotube and metal oxide hybrid materials for gas sensing

T. KERDCHAROEN, Mahidol University, Thailand and
C. WONGCHOOSUK, Kasetsart University, Thailand

DOI: 10.1533/9780857098665.3.386

Abstract: This chapter discusses nanocomposites based on carbon nanotubes (CNTs) and metal oxides (MOX) for gas sensing applications. The chapter first reviews the historical background of the MOX and the hybridized MOX/CNT composite gas sensors. It then describes several popular methods for preparation of MOX/CNT sensing films such as spin-coating, drop-coating, screen-printing, dip-coating, and electron beam evaporation techniques. The ways to characterize MOX/CNT materials with their basic theories including raman spectroscopy, X-ray diffraction, scanning electron microscopy, and transmission electron microscopy have been presented. Finally, the sensing mechanism of a MOX/CNT gas sensor based on p–n heterojunctions has been highlighted.

Key words: carbon nanotubes/metal oxides gas sensor, MOX/CNT composites, p–n heterojunctions, hybrid sensor, sensing part for e-nose.

11.1 Introduction

Until recently, classical methods such as human sensory evaluation,[1] gas chromatography,[2] and mass spectrometry[3] have been the only available techniques for assessing the odors of objects, products, and the environment. Although the methods are reliable and accurate, practical utilization of these instruments is time-consuming, complicated, and costly. The advent of chemical gas sensors and the electronic nose (e-nose) in the 1990s[4, 5] has opened new opportunities for applications in many areas never seen before, especially for real-time, on-site, and rapid measurements. Since then, chemical gas sensors and the e-nose have been adopted as standard tools with which to complement, or even replace, traditional analytical instruments in many areas ranging from quality control of foods[6, 7] and beverages,[8, 9] environment protection[10] to public safety.[11] In general, chemical gas sensors can be classified into four types[12] based on their transduction principles: optical, thermal, electrochemical, and gravimetric. Among these techniques, electrochemical transduction has so far dominated applications of chemical gas

© Woodhead Publishing Limited, 2013

sensors in the measurement systems, because the interface setup is more straightforward than other transduction methods.[13–16]

At present, most commercial chemical gas sensors adopt this technology, and metal oxide (MOX) semiconductors offer the most favored sensor architecture due to their low-cost, high sensitivity, and simplicity in function.[17] One could easily combine several functional elements in the same device, such as the sensitive layer, signal converter, and control electronics. Despite the simple working principles of MOX gas sensors, the gas-sensing mechanism at the microscopic level is very complex and is still not adequately understood.[18, 19] Gas sensors made of the same MOX materials can have different properties depending on the fabrication techniques and preparation conditions. It is firmly believed that catalytic reduction/oxidation at the microscopic surface, underlies the chemo-resistive property of MOXs.[20] These reactions are governed by the electronic structure, chemical composition, crystal structure, and relative orientation of the oxide surface to the analyte molecules, thereby allowing their gas-sensing properties to be tuned by modifying such parameters. The most successful approach to optimizing the gas-sensing properties of MOXs is to modify the microscopic structure by reducing grain size and modifying various crystallite parameters.[21]

Among MOX materials, tin oxides have been the most frequently used in solid-state gas sensors. The sensitivity and selectivity of these materials can be tuned on the basis of structural engineering. Tin oxides have a rich set of structural parameters that can be modified. For example, tin oxide nanocrystals obtained from a spray pyrolysis experiment can have many crystallographic planes such as (110), (111), (200), (101), (011), (–1,–1,2), etc.[22] Such crystallographic parameters are sensitive to the change in grain size responsible for the different gas-sensing properties of films prepared using different conditions.[23] MOXs can be doped by a small amount of metals, such as Sn, Pd, Cu, Nb, etc., in order to modify structural and electronic properties. It was found that doping tin oxide with Sn, In, and Nb leads to a decrease in the grain size down to the nanometer range.[24] Kawamura *et al*. found that the inter-play between different crystal growth directions can be controlled by the addition of impurities.[25] Besides pure metals, MOXs can be doped or mixed with organic materials, leading to so-called 'hybrid' chemical gas sensors. The field of hybrid chemical gas sensors is still in the infant stage.[26] Combining both hard and soft materials into a single film is quite challenging due to complications both in the preparation and fabrication processes.[27] In this chapter, we are specifically interested in the hybridized MOX gas sensors based on MOX and carbon nanotube (CNT) composites.[28, 29] For more information about the modification of the MOXs with other additives, other chapters in this book or the current reference section should be consulted.[30]

© Woodhead Publishing Limited, 2013

MOXs are a very robust technology mostly adopted commercially for semiconductor gas sensors. The stability and durability (an average life of five years) have been gladly welcomed by industries, including the environment, security, petrochemicals, and agriculture. However, MOXs have certain disadvantages that limit their applicability in many areas, such as in mobile devices where energy consumption is a major concern. Reducing the operating temperature (around 250°C–400°C for most MOXs) to room temperature has become a topic of research interest worldwide. Since the sensing mechanism of MOXs is based on the surface reactivity of the materials to incoming analyte gases where electron transfer will play a major role,[31] engineering the conductivity of the surface can lead to desirable sensing properties. Doping with impurities has been a successful technique for the modification of MOX surfaces. Apart from metal dopants as mentioned in the previous section, CNTs have several advantages over other composite materials.[29] The carbon nanotube is very conductive and the gas sensing can be performed at room temperature. Consequently, mixing CNT with MOXs would result in increasing surface conductivity and reducing the operating temperature. The highly-specific area of CNTs will also enhance the active surface of MOXs, leading to enhanced sensitivity and selectivity. MOX and CNT composite materials can be classified into two groups, depending on which material is the greater in the composition: MOX-decorated carbon nanotubes, and CNT-doped metal oxides.

1. *MOX-decorated carbon nanotubes.* In this case, the CNT is functionalized by attaching MOX nanoparticles, either by bonded or non-bonded interaction, onto the sidewall of the carbon nanotube.[32,33] The most common method for achieving strong interaction of MOX nanoparticles on the CNT is to oxidize CNTs by strong acids to introduce carboxyl or hydroxyl groups on the CNT surface. Such functional groups can directly interact with the oxygen of the MOX nanoparticles via hydrogen bonding. The bonded interactions between such functional groups with metal atoms through the pair of electrons on the oxygen are also possible. Various MOX nanocrystals coated onto CNTs have been investigated for their functionality, such as ZnO,[34] TiO_2,[35] SiO_2,[36] SnO_2,[37] MnO_2,[38] and Fe_2O_3.[39] Such functionalization creates novel properties which extend the applicability of CNT into many new areas, such as capacitors, photocatalysts, and batteries. In gas-sensing applications, MOX-decorated CNTs have shown enhanced sensitivity, improved response and recovery times, and a dramatic reduction in operating temperature. Several ambient gases have been reported – for example, CO, NO_2, NH_3, and ethanol (see reference 29 and comprehensive reference list therein).

© Woodhead Publishing Limited, 2013

2. *CNT-doped metal oxides.* In this case, CNTs are embedded within the MOX matrix. This chapter will focus on this type of CNT and MOX hybrid material. The MOX/CNT thin films can be prepared using various techniques, such as spin-coating, drop-coating, dip-coating, and electron beam evaporation, details of which will be given in the following sections.

11.2 Fabrication and synthesis of carbon nanotube–metal oxide sensing devices

CNTs are generally produced using three main techniques: arc discharge, laser ablation, and chemical vapor deposition. Each technique can be modified to suit the specific research purpose.

11.2.1 Arc discharge

Arc discharge was the first technique recognized for producing multi-walled carbon nanotubes (MWNTs)[40] and single-walled carbon nanotubes (SWNTs).[41,42] The arc discharge technique generally involves the use of two high-purity graphite electrodes as anode and cathode. The electrodes are vaporized by the passage of a DC current (~100 A) through the two high-purity graphite electrodes separated (~1–2 mm) in 400 mbar of helium atmosphere. After arc discharging for a period of time, a carbon rod is built up at the cathode. The native method will mainly produce MWNTs, rather than SWNTs. However, with the addition of a metal catalyst, such as Fe, Co, Ni, Y, or Mo, on either the anode or the cathode, SWNTs can also be produced. The quantity and quality (such as length, diameter, purity, etc.) of the nanotubes obtained depend on various parameters, such as the surface density of the metal catalysts, inert gas pressure, type of gas, plasma arc, temperature, current, and system geometry.

11.2.2 Laser ablation

Smalley and colleagues produced CNTs using the laser ablation technique in 1995.[43] For the laser ablation technique, a high-power laser is used to vaporize carbon from a graphite target at high temperature. Both MWNTs and SWNTs can be produced with this technique. In order to generate SWNTs, metal particles must be added as catalysts to the graphite targets, similar to the arc discharge technique. The quantity and quality of CNTs produced depend on several factors, such as the amount and type of catalysts, laser power and wavelength, temperature, pressure, type of inert gas, and the fluid

© Woodhead Publishing Limited, 2013

dynamics near the carbon target. The laser was focused onto a carbon target containing 1.2% of cobalt/nickel with 98.8% of graphite composite that was placed in a 1200°C quartz tube furnace under an argon atmosphere (~500 Torr). These conditions were achieved for production of SWNTs in 1996 by Smalley's group.[44] In such a technique, argon gas carries the vapors from the high temperature chamber into a cooled collector positioned downstream. The nanotubes will self-assemble from carbon vapors and condense on the walls of the flow tube. The diameter distribution of SWNTs that result from this method vary by about 1.0–1.6 nm. CNTs produced by laser ablation were purer (up to 90% purity) than those produced by the arc discharge process and have a very narrow distribution of diameters.

11.2.3 Chemical vapor deposition

The use of the chemical vapor deposition (CVD) technique to produce MWNTs was first reported by Endo and his research group in 1993.[45] Three years later, Dai in Smalley's group successfully adapted CO-based CVD to produce SWNTs.[46] The CVD technique can be achieved by taking a carbon source in the gas phase and using an energy source, such as plasma or a resistively heated coil, to transfer energy to a gaseous carbon molecule. The CVD process employs hydrocarbons as the carbon sources, including methane, carbon monoxide, and acetylene. The hydrocarbons flow through the quartz tube placed inside an oven at a high temperature (~720°C). At high temperature, the hydrocarbons are broken down to hydrogen and carbon radicals, producing pure carbon clusters. The carbon then diffuses to the substrate, which is heated and coated with a catalyst (usually a first-row transition metal such as Ni, Fe, or Co) where CNTs will be formed if the proper parameters are maintained. The advantages of the CVD process are low power input, lower temperature range, relatively high purity and, most importantly, the possibility of scaling up the process. This method can produce both MWNTs and SWNTs depending on the temperature – production of SWNTs will occur at a higher temperature than MWNTs.

11.3 Preparation of carbon nanotube–metal oxide sensing films

Sensing film is the heart of a gas sensor device. The key to success in developing a gas sensor device is a technique capable of preparing a sensing film that exhibits high selectivity and sensitivity to a desired target gas, long-term stability, good repeatability, rapid response, small size, and low power consumption. Until now, it has been widely known that most commercially available gas sensors are still based on pure MOX gas sensors (i.e. SnO_2

© Woodhead Publishing Limited, 2013

Table 11.1 List of hybrid CNT/MOX gas sensors

Target gas	Detection range	Operating temperature	Sensing material	Fabrication technique	Ref.
NO_2	25–1000 ppm	25°C	SWNTs-SnO_2	Spin-coating	47
NO_2	100–500 ppb	25°C	MWNTs-SnO_2	Drop-coating	48
CO	10–50 ppm	150°C	MWNTs-WO_3	Drop-coating	48
CH_2O	0.03–10 ppm	250°C	MWNTs-SnO_2	Screen-printing	49
NH_3	60–800 ppm	25°C	MWNTs-SnO_2	Spin-coating	50
EtOH/MeOH	100–1000 ppm	250°C	MWNTs-SnO_2	E-beam evaporation	51
H_2	5000–50 000 ppm	250°C	MWNTs-WO_3	E-beam evaporation	52
NO_2	100–1000 ppb	25°C	MWNTs-WO_3	Drop-coating	53
NH_3	20 ppm	25°C	CNTs-ZnO	Spin-coating	54
CH_3COCH_3	1 vol.%	25°C	MWNTs-TiO_2	Screen-printing	55
NH_3	1 vol.%	25°C	MWNTs-TiO_2	Dip-coating	56
O_2	10 ppm	350°C	CNTs-TiO_2	Drop-coating	57
H_2	4% in air	25°C	SWNTs-Co_3O_4	Spin-coating	58

and WO_3). Such gas sensors have been successfully used in many applications, but they still suffer from poor selectivity and high power consumption. These disadvantages can be crucial obstacles for the development of future advanced technology, such as wearable sensing devices. Recently, doping of CNTs into MOX has attracted considerable attention since hybrid SWNTs/SnO_2 sensors exhibit high sensitivity and a good recovery property in detecting NO_2 at room temperature.[47] The hybrid CNT/MOX gas sensors based on thin-film nanostructures are summarized in Table 11.1.

As shown in Table 11.1, there are five methods by which to deposit hybrid CNTs/MOXs onto electrodes.

11.3.1 Spin-coating

Spin-coating is a method for applying liquid-based coatings onto a rotating substrate. A typical spin-coating process consists of four basic stages,[59] as shown in Fig. 11.1. The coating liquid material is applied to the top of substrate in the deposition stage. The amount of applied liquid depends on the viscosity of the liquid and the size of the substrate to be coated. In the acceleration stage, liquid is spread across the wafer by centrifugal force. The spinning speed is set at a specific value depending on the desired film thickness. The coated substrate is then spun at a higher speed. The liquid flows radially outward, whereas excess liquid flows to the perimeter and leaves

© Woodhead Publishing Limited, 2013

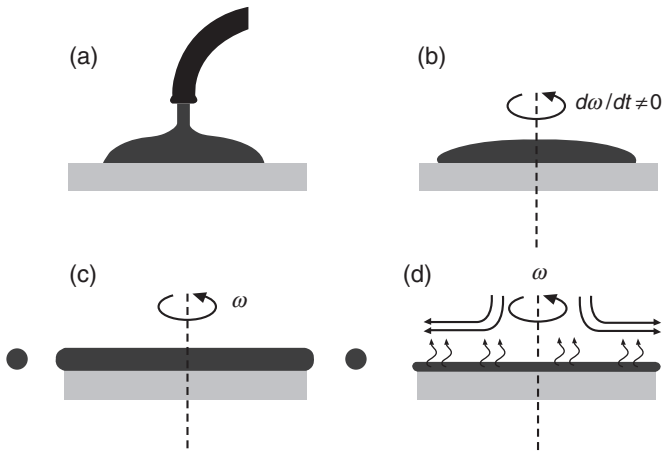

11.1 The four basic stages of spin coating: (a) deposition, (b) acceleration, (c) flow domination, and (d) evaporation. ω is spin speed.

as droplets. In the final stage, evaporation of the solvent takes over as the primary mechanism of thinning. The thickness of the dry film (L_{film}) with an approximation of constant evaporation and no liquid remaining at the end of the process can be written as:[60, 61]

$$L_{\text{film}} = \left[\frac{3\beta_0(x_{\text{A}}^0 - x_{\text{A}}^{\text{I}})\tilde{k}}{2}\right]^{1/3} e^{i\theta}\omega^{-1/2} \qquad [11.1]$$

$$\tilde{k} = \frac{cD_{\text{g}}p_{\text{A}}M_{\text{A}}}{RT\rho\beta_{\text{g}}^{1/2}} \qquad [11.2]$$

where β_0 is kinematic viscosity; x_{A}^0 represents the initial concentration of solvent in the coating liquid; x_{A}^{I} represents the mass fraction of solvent in the coating liquid that would be in equilibrium with the mass fraction of solvent in the bulk gas; ω is the spin speed; c denotes the ratio of kinematic viscosity and mass diffusivity of the ambient gas; D_{g} is the binary diffusivity of the solvent in the ambient gas; p_{A} is the vapor pressure of the pure solvent at temperature (T); M_{A} is the molecular weight of the solvent; and R, ρ, and β_{g} denote the universal gas constant, liquid density, and kinematic viscosity of the ambient gas, respectively.

To prepare the CNT/MOX liquids for spin-coating, the SWCNT bundles were dispersed in the organometallic solutions (Sn $[OOCCH(C_2H_5)$-$C_4H_9]_{2,\text{aq.}}$; tin (II) 2-ethylhexanoate ~90% in 2-ethylhexanoic acid)[47] by ultrasonic vibration. Alternatively, MWCNTs bundles with SnO_2 nanoparticles and cetyltrimethyl ammonium bromide can be dispersed in water.[50] In

© Woodhead Publishing Limited, 2013

the case of synthesis of CNT-ZnO,[54] CNT in a mixture of ethanol and water was dropped into triethanolamine and $ZnCl_2$ solution at a specific temperature. For SWNT/Co_3O_4 thin films,[58] these can be formed by spin-coating a metal–polymer complex ($Co_x(C_2H_5N)_n$), as a product of the reaction of $CoSO_4 \cdot 7H_2O$ and polyethylenimine in water, onto an SWNT thin film. After deposition, the Co_3O_4 and SWNTs thin films were annealed at a high temperature in order to form Co_3O_4/SWCNT composite.

11.3.2 Drop-coating

Drop-coating is a simple method for preparing films and employs a precision pipette to put solution onto the substrate. The film thickness is controlled by the amount and concentration of solution deposited on the substrate. This technique is closely related to spin-coating. Therefore, it can be used as an alternative when spin-coating is not possible – for example, when the solvents are not sufficiently volatile to evaporate during a spin-coating process or not sufficiently viscous to produce a thick film.[62] Preparation of some CNT/MOX sensors[48, 53, 57] successfully uses this method for depositing films. Before a drop-coating process, hybrid CNT/MOX solution is usually prepared using an adapted sol–gel method for obtaining well-dispersed CNT in the MOX matrix. For example, CNT/TiO_2 was obtained by adding CNTs to TiO_2 prepared from titanium isopropoxide(IV) $Ti[OCH(CH_3)_2]_3$ precursors in a dry nitrogen atmosphere. An adequate mixture of the two components was obtained by dissolving them in glycerol (employed as an organic vehicle) and stirring the resulted solution in an ultrasonic bath at a specific temperature.[48]

11.3.3 Screen-printing

Screen-printing is a commonly used industrial technique for fast and inexpensive deposition of films over large areas. The principle of screen-printing[63] is shown in Fig. 11.2.

A pattern is photographically defined on a stainless steel screen by means of an emulsion layer. A paste of the material to be screen-printed is pressed through the screen using a foam applicator (squeegee). After leveling, the printed wet film is dried at a specific temperature. The thickness of the screen-printed film depends on the viscosity of the paste, the pressure and speed of the squeegee, the snap-off distance between the screen and the substrate, and the mesh number of the screen. In a roller squeegee system, Fox and his colleague employed a numerical model to estimate deposition thickness at different half-tone coverage (more detail can be found in ref. 64). Preparation of a paste to fabricate an MWCNT/TiO_2 gas sensor was reported by Sanchez *et al*.[55] The MWCNT/TiO_2 composites were prepared

© Woodhead Publishing Limited, 2013

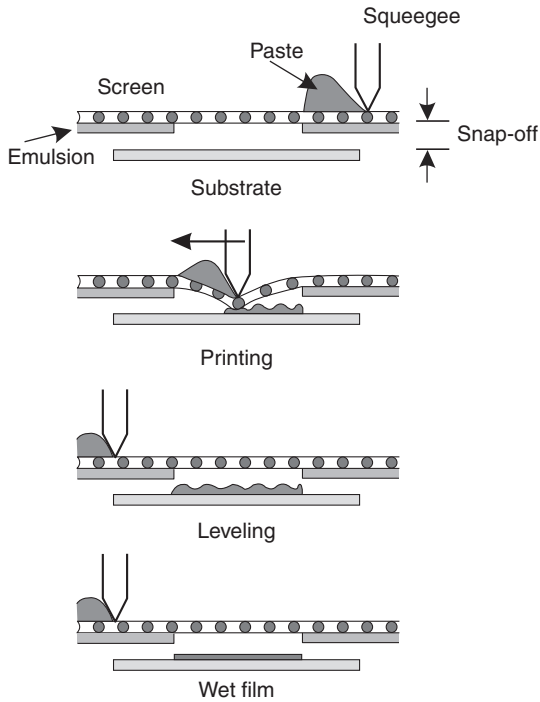

11.2 The screen-printing process.

by sol–gel techniques using titanium tetraisopropoxide [$Ti(C_3H_6OH)_4$] as the precursor, and 2-propanol as the solvent. The mixture was added in HCl and heated at a specific temperature. The solid output was mixed with few drops of Triton-X and propylene glycol to prepare a paste for the screen-printing method.

11.3.4 Dip-coating

Dip-coating can be described as a process where a substrate is dipped into a solution. It is then withdrawn from the solution at a controlled speed under controlled temperature and atmospheric conditions. The coating thickness is primarily affected by the withdrawal speed, fluid viscosity, fluid density, and surface tension. If the withdrawal speed is chosen such that the sheer rates keep the system in the Newtonian regime, the coating thickness (L_{Dip}) can be calculated by the Landau–Levich equation:[65, 66]

$$L_{Dip} = 0.94 \frac{(\eta v)^{2/3}}{\gamma_{LV}^{1/6} (\rho g)^{1/2}} \qquad [11.3]$$

© Woodhead Publishing Limited, 2013

where η denotes fluid viscosity, v represents the withdrawal speed, γ_{LV} is the liquid–vapor surface tension, ρ is fluid density, and g is gravity.

In the case of MWCNT/TiO_2 gas sensors, Sánchez and Rincón[56] employed dip-coating based on a sol–gel solution. The sol–gel solution containing Ti-isopropoxide and acid treated MWCNTs was either precipitated or kept as a sol by adjusting the pH and surfactant concentration.

11.3.5 Electron beam (E-beam) evaporation

The electron beam (E-beam) evaporation process is a physical vapor deposition that yields a high deposition rate from 0.1 μm/min to 100 μm/min at relatively low substrate temperatures. The E-beam process offers extensive possibilities for controlling film structure and morphology, with desired properties such as dense coating, high thermal efficiency, low contamination, high reliability and high productivity. The deposition chamber is evacuated to a pressure of 10^{-5} Torr or lower. The material to be evaporated is in the form of ingots or a compressed solid. The E-beam can be generated from electron guns by thermionic emission, field electron emission or the anodic arc method. The electron beam is accelerated to a high kinetic energy and focused towards the starting material. The kinetic energy of the electrons is converted into thermal energy that will increase the surface temperature of the materials, leading to evaporation and deposition onto the substrate. The deposition rate depends on the starting material and E-beam power. The deposited film thickness can be measured in situ by a quartz crystal monitor. The evaporation of CNTs with MOXs (i.e. SnO_2 and WO_3) is a relatively new concept. A plausible mechanism for CNT/MOX co-evaporation can be drawn as follows:[51,52] the E-beam is used to bombard the surface of the starting materials (i.e. CNT/SnO_2 or CNT/WO_3). The MOXs (such as SnO_2 or WO_3) are evaporated at a temperature of ~1500°C in a high vacuum, while CNT fragments that are small and very light are carried into the vapor by surrounding SnO_2 or WO_3 molecules. It should be noted that CNTs themselves are not decomposed during evaporation because this temperature is well below CNT sublimation point (> 3000°C) in a high vacuum condition. When CNT molecular fragments arrive at the substrate, SnO_2 or WO_3 vapor is condensed and coated around them. As the substrate cools down, CNTs remain in the lattice of MOXs due to physicochemical binding between the MOXs and CNTs.

11.4 Sensor assembly

A typical sensor structure is displayed in Fig. 11.3. The sensing film is deposited on top of a substrate between the electrodes. The heater is

© Woodhead Publishing Limited, 2013

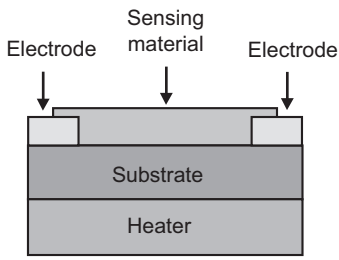

11.3 A simple sensor structure.

also integrated on the reverse of the substrate. It should be noted that a heater unit may not be necessary if the sensor will be operating at room temperature.

Apart from the sensing film, the electrodes also play an important role in gas-sensing response. For instance, the electrode material, gap sizes, and electrode structure can affect the sensor response.[67–69] Mishra and Agarwal[67] reported that the sensitivity of the thick-film SnO_2 sensor for H_2 and CO is much higher when silver electrodes are used instead of gold electrodes (about 65.5% and 42.6%, respectively). Tamaki *et al*. found that sensitivity was increased with decreasing gap size.[68] The performance of the sensor was improved by using interlacing electrodes.[69] Therefore, the design of a gas sensor structure is necessary for fabricating a high-performance hybrid CNT/MOX sensing device.

11.5 Characterization of carbon nanotube–metal oxide materials

To confirm the structure and quality of produced carbon nanotube and metal oxide hybrid materials, there are four characterization techniques that are normally used. These techniques are described in the following subsections.

11.5.1 Raman spectroscopy

Raman spectroscopy is a spectral measurement based on inelastic scattering of monochromatic radiation. When a molecule is irradiated with an intense monochromatic light (usually a laser source), photons excite the molecule from the ground state to a virtual energy state. The photons are re-emitted when the molecule relaxes. The frequency of the re-emitted photons shifts in comparison with the original monochromatic light frequency. This shift provides information about vibrational, rotational, and other low frequency transitions in molecules. Information from Raman spectroscopy is summarized in Fig. 11.4.

Raman spectroscopy was used to confirm the existence of CNTs in a MOX film. Raman spectra of an SWNT/Co_3O_4 film[58] are displayed in Fig. 11.5. The

© Woodhead Publishing Limited, 2013

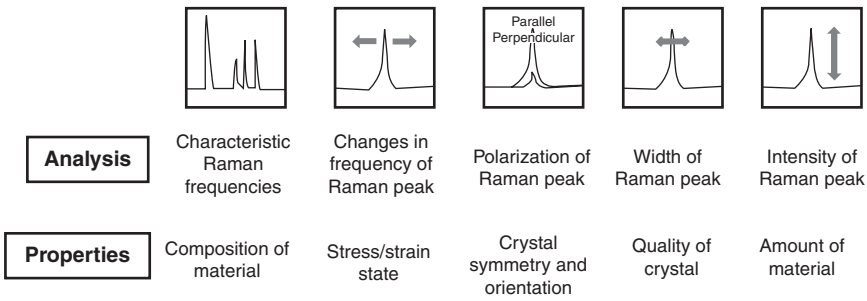

11.4 Information from Raman spectroscopy.

peak of crystalline Co_3O_4 can be clearly observed at 694 cm^{-1} for the A_{1g} mode, while it appears as two significant peaks for SWNTs – namely D-band and G-band at 1350 and 1590 cm^{-1}, respectively. It should be noted that the intensity of the D-band (~1300–1500 cm^{-1}) is a qualitative metric of SWNT defects holding significant information on the crystalline quality, while the G-band (~1500–1605 cm^{-1}) is derived from the in-plane vibration usually existing in graphite and useful for measuring SWNT graphene sheet folding. For analysis of a CNT/MOX sensing film, the minimum Raman shift for the MOXs (i.e. SnO_2, WO_3, TiO_2, etc.), D-band, and G-band should be observed.

11.5.2 X-ray diffraction

X-ray is a high-energy electromagnetic radiation having energies ranging from ~200 eV to 1 MeV. The X-ray diffraction (XRD) is based on the elastic scattering of monochromatic X-rays. It is usually used to characterize the chemical composition and crystallographic structure of materials by plotting the angular positions and intensities of the resultant diffracted peaks of radiation satisfied with Bragg's Law conditions. The diffraction intensity can be written as:[70]

$$I_{(hkl)\alpha} = \frac{I_0 \lambda^3}{64\pi r}\left(\frac{e^2}{m_e c^2}\right)^2 \frac{M_{(hkl)}}{V_\alpha^2}\left|F_{(hkl)\alpha}\right|^2 \left(\frac{1+\cos^2(2\theta)\cos^2(2\theta_m)}{\sin^2\theta\cos\theta}\right)_{hkl} \frac{v_\alpha}{\mu_s} \qquad [11.4]$$

where $I_{(hkl)\alpha}$ is the intensity of the reflection of *hkl* in phase α, I_0 is the incident beam intensity, λ denotes the X-ray wavelength, r denotes the distance from the specimen to the detector, $\left(e^2/m_e c^2\right)^2$ represents the square of the classical electron radius, $M_{(hkl)\alpha}$ is the multiplicity of reflection of *hkl* in phase α, V_α is the volume fraction of phase α, $F_{(hkl)\alpha}$ is the structure factor for reflection *hkl* of phase α (i.e. the vector sum of scattering intensities of all atoms contributing to that reflection), $2\theta_m$ represents

© Woodhead Publishing Limited, 2013

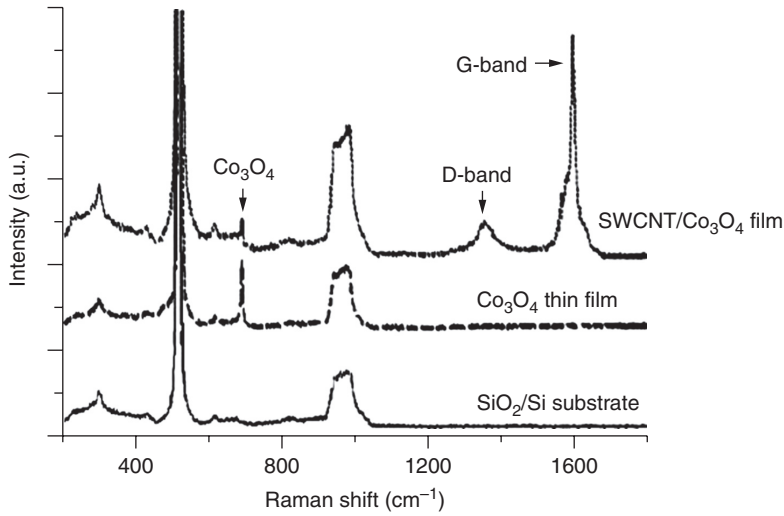

11.5 Raman spectra of SWCNT/Co_3O_4 film (upper line), Co_3O_4 thin film (middle line), and the SiO_2/Si substrate (lower line).[58]

the diffraction angle of the monochromator, v_α is the volume of the unit cell of phase α and μ_s is the linear absorption coefficient of the specimen.

The XRD patterns of MWNT/SnO_2[50] are shown in Fig. 11.6. In general, an XRD pattern of CNT locates near the (002), (100), (110), and (112) reflections of graphite. The prominent peak ($2\theta \approx 26^\circ$) can be attributed to the (002) reflection of carbon. In this case, the most intense two peaks of MWNTs correspond to (002) and (100), while only SnO_2 in the crystalline phase can be indexed from the patterns for SnO_2. It can be observed that the characteristic peaks of MWNT/SnO_2 composites are quite similar to the patterns of SnO_2. From this observation it may be hypothesized that the MWNTs are well-embedded in the SnO_2 matrix. However, almost CNT/MOX films from other studies have a similar pattern. Peaks of CNT are usually absent for the CNT/MOX composite films in the XRD analysis.

11.5.3 Scanning electron microscope

The scanning electron microscope (SEM) employs a focused beam of high-energy electrons to generate a variety of signals at the surface of sample. The types of signals produced from the interaction of the high-energy electrons with the sample include secondary electrons, back-scattered electrons, characteristic X-rays, and other photons of various energies. These signals can be used to examine many characteristics of the samples, such as surface

© Woodhead Publishing Limited, 2013

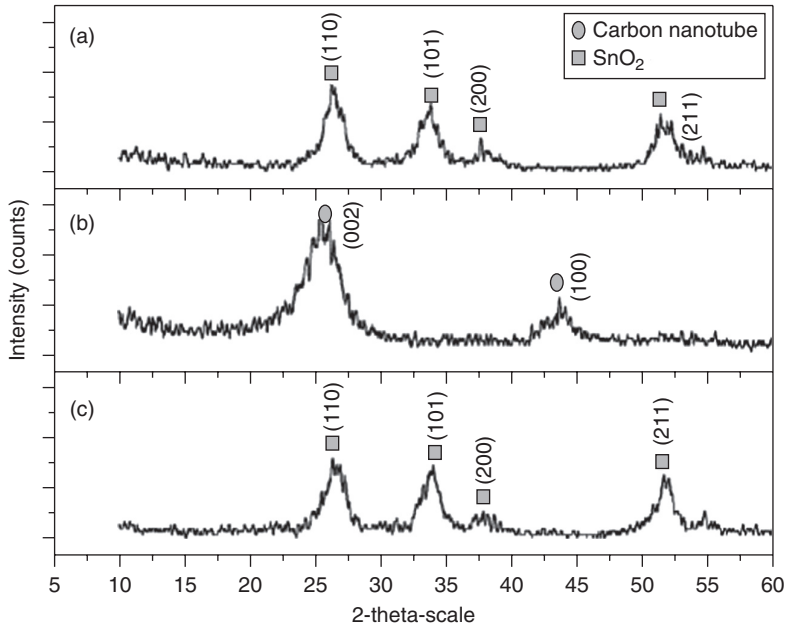

11.6 XRD patterns of: (a) SnO_2, (b) MWNTs, and (c) SnO_2/MWNT composites.[50]

topography and morphology, crystallographic information and composition. The basic principle of SEM is shown in Fig. 11.7.

The SEM surface morphology of a CNT/WO_3 film prepared by E-beam evaporation is displayed in Fig. 11.8. One can see that the sensing film prepared by this technique is highly homogeneous, with grain sizes ranging from 40 to 80 nm. It should be noted that the surface morphology of other films (including pure SnO_2, pure WO_3, and CNT/SnO_2) prepared by E-beam evaporation[51,52] is in accordance with observations on the nanocrystalline CNT/WO_3 film. With SEM resolution, a CNT structure cannot be observed on the thin film surface. In cases of CNT/MOX films prepared by other methods (i.e. spin-coating)[47] the morphologies of the pure and hybrid CNT/MOX are also very similar. Thus, it is quite difficult to observe the CNTs on the surface. In the previous studies, it was suggested that CNTs are most embedded in the MOX-based matrix.

11.5.4 Transmission electron microscopy

Transmission electron microscopy (TEM) provides a much higher spatial resolution than SEM. TEM can facilitate study of the inner structure and analysis of the features on an atomic scale (in the range of a few nanometers).

© Woodhead Publishing Limited, 2013

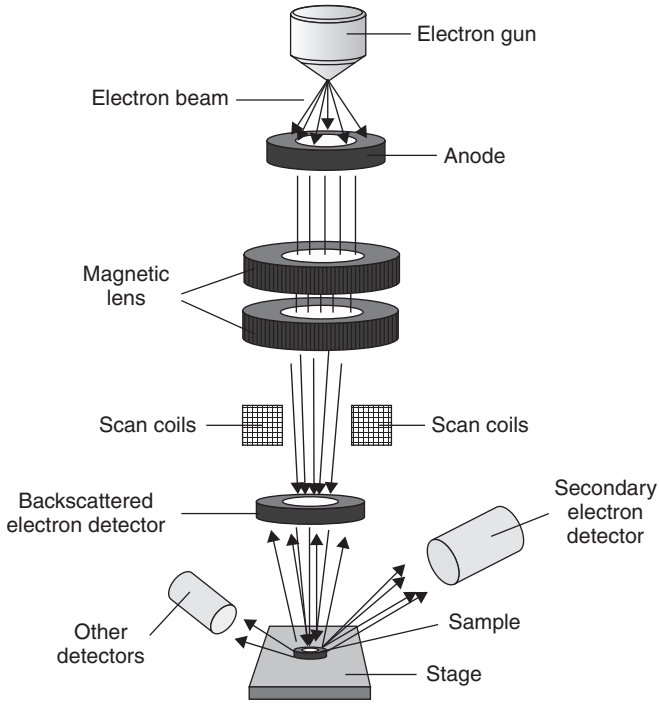

11.7 Principle of scanning electron microscope.

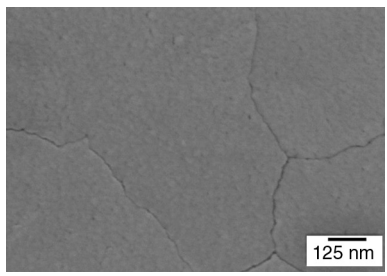

11.8 SEM image of MWCNT-WO_3 thin film on Si substrate.

Although the TEM technique involves electrons to produce enlarged images similar to the SEM technique, the working principle of TEM is somewhat different from SEM. In general, TEM uses high E-beam energies in the range of 60 to 350 keV to pass through a thin sample in order to project an image onto a fluorescent screen. The sample for TEM is usually required to be sliced into an extremely thin section (< 100 nm) and pre-treated with heavy metals (staining) before visualization. The image resolution of TEM

© Woodhead Publishing Limited, 2013

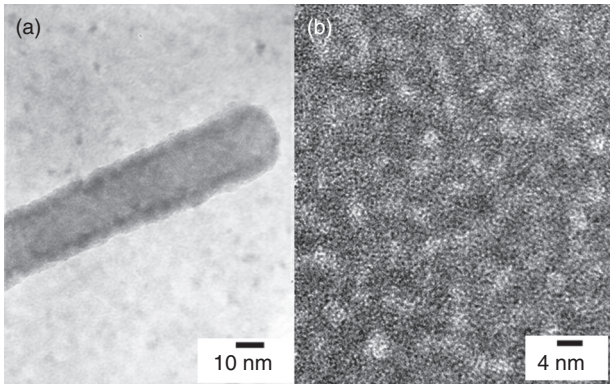

11.9 Typical HRTEM image of: (a) CNT/WO_3 film and (b) nanocrystalline WO_3 prepared by the E-beam evaporation technique.

(δ) in terms of the classic Rayleigh criterion for the visible-light microscope can be given approximately by Equation [11.5]:

$$\delta = \frac{0.61\lambda}{\mu \sin \beta} \qquad [11.5]$$

where λ denotes the wavelength of the radiation, μ represents the refractive index of the viewing medium, and β is the semi-angle of collection of the magnifying lens.

TEM characterization can be used to confirm CNT inclusion in MOX films. A typical high-resolution TEM (HRTEM) image of a CNT/WO_3 composite prepared by E-beam evaporation is shown in Fig. 11.9. It should be noted that HRTEM uses both transmitted and scattered beams to create an interference image. HRTEM observation clearly shows that a single multi-walled CNT fragment is, indeed, embedded into the nanocrystalline WO_3 layer (see Fig. 11.9(a)). The diameter of CNTs and the crystal size of WO_3 were estimated to be in the range of ~20–50 nm (see Fig. 11.9(a)) and 3–10 nm (see Fig. 11.9(b)), respectively. By comparison with pure WO_3, the doping of CNT does not change the phase or surface morphology of the film, but it may help form nanochannels in the MOX films, leading to the enhancement of the sensitivity and reduction of the operating temperature.

11.6 Sensing mechanism of carbon nanotube–metal oxide gas sensors

It is widely known that many MOXs (such as WO_3, SnO_2, and TiO_2) are n-type semiconductors, while CNT is a p-type semiconductor. CNT/MOX

© Woodhead Publishing Limited, 2013

gas sensors can be either p-type or n-type semiconductors, depending on the quantity of CNTs and the operating temperature. The CNT/MOX gas sensor behaves as an n-type semiconductor if the electrical conductivity of the gas sensor increases when reducing gases (i.e. H_2, CO, or NH_3) are absorbed by its surface. In the case of the p-type semiconductor, the electrical conductivity of the sensor decreases in the presence of an oxidizing gas (O_3, NO_X, etc.). Various oxygen species chemisorbed at the surface (such as O^{2-}, O_2^-, and O^-) are available for catalytic reactions with gas, depending on the temperature at the MOX surface. Of the oxygen species, O^- is commonly chemisorbed at the operating temperature range of 200°C–400°C while O^{2-} and O_2^- are mostly contributed at low temperature. The main sensing mechanism of CNT/MOX gas sensors can be described by using the model of a potential barrier to electronic conduction at the grain boundary, as shown in Fig. 11.10.

From many studies, it was found that CNTs are embedded in the MOX layer leading to the formation of p–n heterojunctions. Therefore, there are

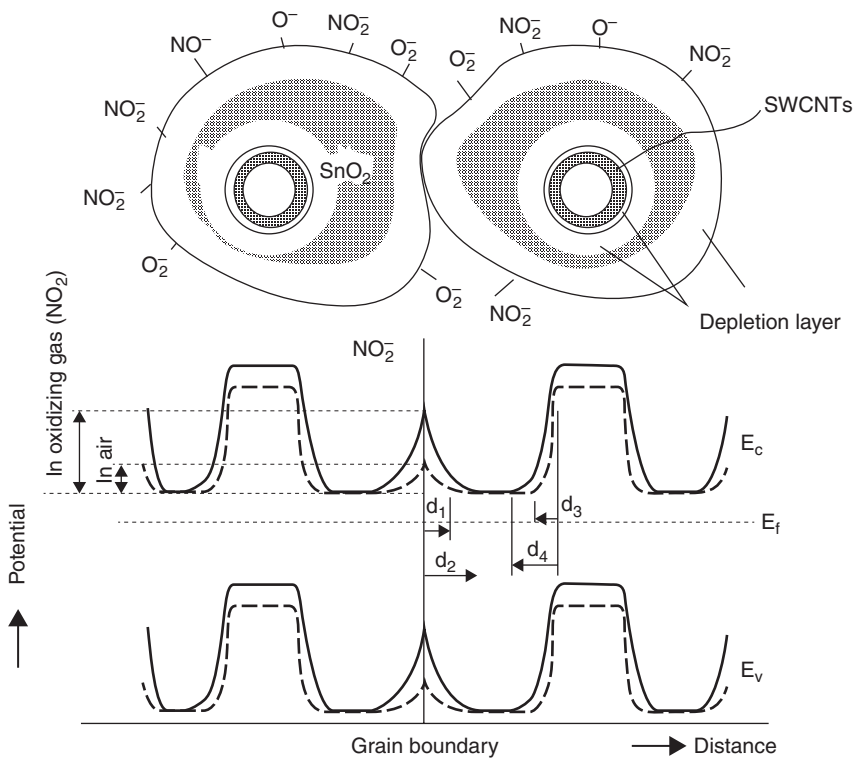

11.10 Model of a potential barrier to electronic conduction at grain boundary for hybrid SWNT/SnO_2 sensors.[47] The dashed and continuous lines show the potential barriers of hybrid SWNT/SnO_2 in environment of air and environment of oxidizing gas (i.e. NO_2), respectively.

© Woodhead Publishing Limited, 2013

two depletion layers to interact with gas, as shown in Fig. 11.10. Two depletion layers are the region on the surface of the MOX and the interface between the CNTs and MOX. The depletion layers at the p–n heterojunctions can be modulated. The potential barriers at the interfaces or inside the MOX may be changed. This change of the depletion layer in the p–n heterojunctions of CNT/MOX was used to explain the enhanced response of the film at low operating temperatures due to the amplification effects of junction structure combined with the gas reaction. Moreover, the formation of CNTs in the MOX matrix can also introduce nanochannels. These nanochannels play an important role in gas diffusion. The gas molecules can easily transport into the gas-sensing layers, leading to increasing sensitivity.[51,52]

11.7 Conclusion

The unique structure and electronic properties of CNTs provide a tremendous potential for construction of CNTs and MOX hybrid materials in the field of gas-sensing applications. Advantages for mixing CNTs in metal oxides for gas sensors are the reduction of operating temperature and enhancement of sensitivity and selectivity due to the amplification effects of p–n heterojunctions with the gas reaction, formation of nanochannels for gas diffusion, high specific surface area, and increase of charge carrier on the surface. As a result of these advantages, the hybrid CNT/metal oxide gas sensor may be used instead of the popular commercial metal oxide gas sensors (such as TGS gas sensors) in the near future.

11.8 References

1. Granitto, P. M., Biasioli, F., Endrizzi, I. and Gasperi, F. (2008) 'Discriminant models based on sensory evaluations: single assessors versus panel average', *Food Qual. Prefer.*, **19**, 589–95.
2. Fitzgerald, G., James, K. J., MacNamara, K. and Stack, M. A. (2000) 'Characterisation of whiskeys using solid-phase microextraction with gas chromatography–mass spectrometry', *J. Chrom A*, **896**, 351–9.
3. Vinaixa, M., Vergara, A., Duran, C., Llobet, E., Badia, C., Brezmes, J., Vilanova, X. and Correig X. (2005) 'Fast detection of rancidity in potato crisps using e-noses based on mass spectrometry or gas sensors', *Sens. Actuat. B*, **106**, 67–75.
4. Shurmer, H. V., Gardner, J. W. and Corcoran, P. (1990) 'Intelligent vapour discrimination using a composite 12-element sensor array', *Sens. Actuat. B*, **1**, 256–60.
5. Shurmer, H. V. and Gardner, J. W. (1992) 'Odour discrimination with an electronic nose', *Sens. Actuat. B*, **8**, 1–11.
6. Tikk, K., Haugen, J.-E., Andersen, H. J. and Aaslyng, M. D. (2008) 'Monitoring of warmed-over flavour in pork using the electronic nose – correlation to sensory attributes and secondary lipid oxidation products', *Meat Science*, **80**, 1254–63.

© Woodhead Publishing Limited, 2013

7. Santonico, M., Pittia, P., Pennazza, G., Martinelli, E., Bernabei, M., Paolesse, R., D'Amico, A., Compagnone, D. and Natale, C. D. (2008) 'Study of the aroma of artificially flavoured custards by chemical sensor array fingerprinting', *Sens. Actuat. B*, **133**, 345–51.
8. Ragazzo-Sanchez, J. A., Chalier, P., Chevalier, D., Calderon-Santoyo, M. and Ghommidh, C. (2008) 'Identification of different alcoholic beverages by electronic nose coupled to GC', *Sens. Actuat. B*, **134**, 43–8.
9. Yu, H. and Wang, J. (2007) 'Discrimination of LongJing green-tea grade by electronic nose', *Sens. Actuat. B*, **122**, 134–40.
10. Kuske, M., Romain, A. C. and Nicolas, J. (2005) 'Microbial volatile organic compounds as indicators of fungi. Can an electronic nose detect fungi in indoor environments?', *Build Environ.*, **40**, 824–31.
11. Zhang, S., Xie, C., Zeng, D., Zhang, Q., Li, H. and Bi, Z. (2007) 'A feature extraction method and a sampling system for fast recognition of flammable liquids with a portable E-nose', *Sens. Actuat. B.*, **124**, 437–43.
12. James, D., Scott, S. M., Ali, Z. and O'Hare, W. T. (2005) 'Chemical sensors for electronic nose systems', *Microchim. Acta.*, **149**, 1–17.
13. Choopun, S., Hongsith, N., Mangkorntong, P. and Mangkorntong, N. (2007) 'Zinc oxide nanobelts by RF sputtering for ethanol sensor', *Physica E*, **39**, 53–6.
14. Sriyudthsak, M. and Supothina, S. (2006) 'Humidity-insensitive and low oxygen dependence tungsten oxide gas sensors', *Sens. Actuat. B*, **113**, 265–71.
15. Anukunprasert, T., Saiwan, C. and Traversa, E. (2005) 'The development of gas sensor for carbon monoxide monitoring using nanostructure of Nb–TiO_2', *Sci. Technol. Adv. Mater.*, **6**, 359–63.
16. Watcharaphalakorn, S., Ruangchuay, L., Chotpattananont, D., Sirivat, A. and Schwank, J. (2005) 'Polyaniline/polyimide blends as gas sensors and electrical conductivity response to CO-N_2 mixtures', *Poly Inter.*, **54**, 1126–33.
17. Korotcenkov, G. (2007) 'Metal oxides for solid-state gas sensors: What determines our choice?', *Mater. Sci. Eng. B*, **139**, 1–23.
18. Korotcenkov, G. (2005) 'Gas response control through structural and chemical modification of metal oxide films: state of the art and approaches', *Sens. Actuat. B*, **107**, 209–32.
19. Surnev, S., Ramsey, M. G. and Netzer, F. P. (2003) 'Vanadium oxide surface studies', *Prog. Surf. Sci.*, **73**, 117–65.
20. Batzill, M. and Diebold, U. (2005) 'The surface and materials science of tin oxide', *Prog. Surf. Sci.*, **79**, 47–154.
21. Brinzari, V., Korotcenkov, G., Schwank, J., Lantto, V., Saukko, S. and Golovanov, V. (2002) 'Morphological rank of nano-scale tin dioxide films deposited by spray pyrolysis from $SnCl_4$•$5H_2O$ water solution', *Thin Solid Films*, **408**, 51–8.
22. Korotcenkov, G., Cornet, A., Rossinyol, E., Arbiol, J., Brinzari, V. and Blinov, Y. (2004) 'Faceting characterization of SnO2 nanocrystals deposited by spray pyrolysis from $SnCl_4$–$5H_2O$ water solution', *Thin Solid Films*, **471**, 310–19.
23. Korotcenkov, G., Macsanov, V., Tolstoy, V., Brinzari, V., Schwank, J. and Faglia, G. (2003) 'Structural and gas response characterization of nano-size SnO_2 films deposited by SILD method', *Sens. Actuat. B*, **96**, 602–9.
24. Szezuka, D., Werner, J., Oswald, S., Behr, G. and Wetzing, K. (2001) 'XPS investigations of surface segregation of doping elements in SnO_2', *Appl. Surf. Sci.*, **179**, 301–6.

© Woodhead Publishing Limited, 2013

25. Kawamura, F., Takahashi, T., Yasui, I. and Sunagawa, I. (2001) 'Impurity effect on [1 1 1] and [1 1 0] directions of growing SnO2 single crystals in SnO_2–Cu_2O flux system', *J. Cryst. Growth*, **233**, 259–68.
26. Judeinstein, P. and Sanchez, C. (1996) 'Hybrid organic–inorganic materials: a land of multi-disciplinarity', *J. Mater. Chem.*, **6**, 511–25.
27. Matsubara, I., Hosono, K., Murayama, N., Shin, W. and Izu, N. (2005) 'Organically hybridized SnO_2 gas sensors', *Sens. Actuat. B*, **108**, 143–7.
28. Wisitsoraat, A., Tuantranont, A., Thanachayanont, C., Patthanasettakul, V. and Singjai, P. (2006) 'Electron beam evaporated carbon nanotube dispersed SnO_2 thin film gas sensor', *J. Electroceramics*, **17**, 45–9.
29. Eder, D. (2010) 'Carbon nanotube – inorganic hybrids', *Chem. Rev.*, **110**, 1348–85.
30. Wang, C., Yin, L., Zhang, L., Xiang, D. and Gao, R. (2010) 'Metal oxide gas sensors: sensitivity and influencing factors', *Sensors*, **10**, 2088–106.
31. Schierbaum, K. D., Weimar, U., Göpel, W. and Kowalkowski, R. (1991) 'Conductance, work function and catalytic activity of SnO_2-based gas sensors', *Sens. Actuat. B*, **3**, 205–14.
32. Zhang, W.-D., Xu, B. and Jiang, L.-C. (2010) 'Functional hybrid materials based on carbon nanotubes and metal oxides', *J. Mater. Chem*, **20**, 6383–91.
33. Goldoni, A., Petaccia, L., Lizzit, S. and Larciprete, R. (2010) 'Sensing gases with carbon nanotubes: a review of the actual situation', *J. Phys: Condensed Matter*, **22**, 013001.
34. Khanderi, J., Hoffmann, R. C., Gurlo, A. and Schneider J. J. (2009) 'Synthesis and sensoric response of ZnO decorated carbon nanotubes', *J. Mater. Chem.*, **19**, 5039–46.
35. Moriguchi, I., Hidaka, R., Yamada, H., Kudo, T., Murakami, H. and Nakashima, N. (2006) 'A Mesoporous nanocomposite of TiO_2 and carbon nanotubes as a high-rate Li-intercalation electrode material', *Adv. Mater.*, **18**, 69–73.
36. Whitsitt, E. A., Moore, V. C., Smalley, R. E. and Barron, A. R. (2005) 'LPD silica coating of individual single walled carbon nanotubes, *J. Mater. Chem.*, **15**, 4678–87.
37. Chen, Y., Zhu, C. and Wang, T. (2006) 'The enhanced ethanol sensing properties of multi-walled carbon nanotubes/SnO_2 core/shell nanostructures', *Nanotechnology*, **17**, 3012–17.
38. Chen, J., Zhang, W.-D. and Ye, J.-S. (2008) 'Nonenzymatic electrochemical glucose sensor based on MnO2/MWNTs nanocomposite', *Electrochem. Comm.*, **9**, 1268–71.
39. Zhao, X., Johnston, C. and Grant, P. S. (2009) 'A novel hybrid supercapacitor with a carbon nanotube cathode and an iron oxide/carbon nanotube composite anode', *J. Mater. Chem.*, **19**, 8755–60.
40. Iijima, S. (1991) 'Helical microtubules of graphitic carbon', *Nature (London)*, **354**, 56–8.
41. Iijima, S. and Ichihashi, T. (1993) 'Single-shell carbon nanotubes of 1-nm diameter', *Nature (London)*, **363**, 603–5.
42. Bethune, D. S., Kiang, C. H., De Vries, M. S., Gorman, G., Savoy, R., Vazquez, J. and Beyers, R. (1993) 'Cobalt-catalysed growth of carbon nanotubes with single-atomic-layer walls', *Nature (London)*, **363**, 605–7.

© Woodhead Publishing Limited, 2013

43. Guo, T., Nikolaev, P., Thess, A., Colbert, D. T. and Smalley, R. E. (1995) 'Catalytic growth of single-walled nanotubes by laser vaporization', *Chem. Phys. Lett.*, **243**, 49–54.
44. Thess, A., Lee, R., Nikolaev, P., Dai, H., Petit, P., Robert, J., Xu, C., Lee, Y. H., Kim, S. G., Rinzler, A. G., Colbert, D. T., Scuseria, G. E., Tománek, D., Fischer, J. E. and Smalley, R. E. (1996) 'Crystalline ropes of metallic carbon nanotubes', *Science*, **273**, 483–7.
45. Endo, M., Takeuchi, K., Igarashi, S., Kobori, K., Shiraishi, M. and Kroto, H. W. (1993) 'The production and structure of pyrolytic carbon nanotubes', *J. Phys. Chem. Solids*, **54**, 1841–8.
46. Dai, H., Rinzler, A. G., Nikolaev, P., Thess, A., Colbert, D. T. and Smalley, R. E. (1996) 'Single-wall nanotubes produced by metal-catalyzed disproportionation of carbon monoxide', *Chem. Phys. Lett.,* **260**, 471–5.
47. Wei, B. Y., Hsu, M. C., Su, P. G., Lin, H. M., Wu, R. J. and Lai, H. J. (2004) 'A novel SnO_2 gas sensor doped with carbon nanotubes operating at room temperature', *Sens. Actuat. B*, **101**, 81–9.
48. Espinosa, E. H., Ionescu, R., Chambon, B., Bedis, G., Sotter, E., Bittencourt, C., Felten, A., Pireaux, J. J., Correig, X. and Llobet, E. (2007) 'Hybrid metal oxide and multiwall carbon nanotube films for low temperature gas sensing', *Sens. Actuat. B*, **127** 137–42.
49. Wang, J., Liu, L., Cong, S. Y., Qi, J. Q. and Xu, B. K. (2008) 'An enrichment method to detect low concentration formaldehyde', *Sens Actuat B*, **134**, 1010–15.
50. Hieu, N. V., Thuya, L. T. B. and Chien, N. D. (2008) 'Highly sensitive thin film NH3 gas sensor operating at room temperature based on SnO_2/MWCNTs composite', *Sens. Actuat. B*, **129**, 888–95.
51. Wongchoosuk, C., Wisitsoraat, A., Tuantranont, A. and Kerdcharoen, T. (2010) 'Portable electronic nose based on carbon nanotube-SnO_2 gas sensors and its application for detection of methanol contamination in whiskeys', *Sens. Actuat. B*, **147**, 392–9.
52. Wongchoosuk, C., Wisitsoraat, A., Phokharatkul, D., Tuantranont, A. and Kerdcharoen, T. (2010) 'Multi-walled carbon nanotube-doped tungsten oxide thin films for hydrogen gas sensing', *Sensors*, **10**, 7705–15.
53. Sedlackova, K., Ionescu, R. and Balazsi, C. (2008) 'TEM investigations on CNT added hexagonal WO_3 films for sensing applications', *Nano.*, **3**, 223–7.
54. Zhang, H., Du, N., Chen, B., Li, D. and Yang, D. (2009) 'Carbon nanotube-ZnO nanosphere heterostructures: low-temperature chemical reaction synthesis, photoluminescence, and their application for room temperature NH3 gas sensor', *Sci. Adv. Mater.*, **1**, 13–7.
55. Sanchez, M., Guirado, R. and Rincon, M. E. (2007) 'Multiwalled carbon nanotubes embedded in sol–gel derived TiO_2 matrices and their use as room temperature gas sensors', *J. Mater. Sci: Mater. Electron*, **18**, 1131–6.
56. Sánchez, M. and Rincón, M. E. (2009) 'Sensor response of sol–gel multiwalled carbon nanotubes-TiO2 composites deposited by screen-printing and dip-coating techniques', *Sens. Actuat. B*, **140**, 17–23.
57. Llobet, E., Espinosa, E. H., Sotter, E., Ionescu, R., Vilanova, X., Torres, J., Felten, A., Pireaux, J. J., Ke, X., Tendeloo, G. V., Renaux, F., Paint, Y., Hecq, M. and Bittencourt, C. (2008) 'Carbon nanotube–TiO_2 hybrid films for detecting traces of O_2', *Nanotechnology*, **19**, 375501.

© Woodhead Publishing Limited, 2013

58. Li, W., Jung, H., Hoa, N. D., Kim, D., Hong, S.-K. and Kim, H. (2010) Nanocomposite of cobalt oxide nanocrystals and single-walled carbon nanotubes for a gas sensor application, *Sens. Actuat. B*, **150**, 160–6.
59. Stern, K. H. (1996) *'Metallurgical and ceramic protective coatings'*, Chapman & Hall, Springer Publisher, ISBN-10: 041-254-4407; ISBN-13: 978-041-254-440-8.
60. Hellstrom, S. L. (2007) *'Basic Models of Spin Coating'*, Lecture note, Stanford University.
61. Bornside, D. E., Macosko, C. W. and Scriven, L. E. (1991) 'Spin coating of a PMMA/chlorobenzene solution', *J. Electrochem. Soc.*, **138**, 317–20; Bornside, D. E., Macosko, C. W. and Scriven, L. E. (1989) 'Spin coating: one-dimensional model', *J. Appl. Phys.*, **66**, 5185.
62. Zhang, L., Fang, X. and Ye, C. (2007) *'Controlled growth of nanomaterials'*, World Scientific Publishing, ISBN-10: 981-256-7283; ISBN-13: 978-981-256-728-4
63. Burgelman, M. (1998) 'Thin film solar cells by screen printing technology', *Proc. Workshop Microtech. Therm. Prob. Electron*, 129–35.
64. Fox, I. J., Bohan, M. F. J., Claypole, T. C. and Gethin, D. T. (2003) 'Film thickness prediction in halftone screen-printing', *J P Mech Eng.*, **217**, 345–9.
65. Landau, L. D. and Levich, B. G. (1942) 'Acta physiochim', *U R S S*, **17**, 42–54.
66. Schmidt, H. and Mennig, M. (2000) 'Wet coating technologies for glass, Institut für Neue Materialien', Tutorial.
67. Mishra, V. N. and Agarwal, R. P. (1994) 'Effect of electrode material on sensor response', *Sens. Actuat. B*, **22**, 121–5.
68. Tamaki, J., Miyaji, A., Makinodan, J., Ogura, S. and Konishi, S. (2005) 'Effect of micro-gap electrode on detection of dilute NO_2 using WO_3 thin film microsensors', *Sens. Actuat. B*, **108**, 202–6.
69. Jain, U., Harkera, A. H., Stoneham, A. M. and Williams, D. E. (1990) Effect of electrode geometry on sensor response', *Sens. Actuat. B*, **2**, 111–14.
70. Connolly, J. R. (2010) *'Introduction quantitative X-ray diffraction methods'*, Spring; Chung, F. H. (1974) 'Quantitative interpretation of X-ray diffraction patterns. I. Matrix-flushing method of quantitative multicomponent analysis', *J. Appl. Crystallography*, **7**, 519–525.

© Woodhead Publishing Limited, 2013

12

Porous silicon gas sensors

V. M. AROUTIOUNIAN, Yerevan State University, Armenia

DOI: 10.1533/9780857098665.3.408

Abstract: This chapter discusses the use of porous silicon (PSi) for gas sensors. It is of great importance to develop efficient and economically viable gas sensors for different applications. PSi can be used as an alternative material for gas sensors, operating at a relatively low temperature, including room temperature. The interest in this material is mainly due to its extremely high surface-to-volume ratio, the ease of its formation and its compatibility with modern silicon microelectronics fabrication technologies. A large variety of different sensors made of PSi have been manufactured in recent years, and achievements in this field are reported in this chapter.

Key words: porous silicon, gas sensor, photoluminescence quenching, noise.

12.1 Introduction

There is a growing interest in developing efficient and economically viable gas sensors for detecting the leakage of different gases into the atmosphere. Environment air quality has improved considerably in the last few decades due to modern air pollution legislation. However, there is strong evidence suggesting that exposure to air pollution, even at the levels commonly achieved nowadays in developed countries, leads to adverse health effects. In particular, the content of ozone, hydrogen and nitrogen dioxide has been found to be too high in many cities in the USA, Europe and Asia. Many semiconductor gas sensors have been developed in 30 years, mainly based on metal oxide semiconductors such as SnO_2, ZnO, TiO_2, etc (see, for example, the review paper by Aroutiounian (2007)). A high operating temperature (sometimes up to several hundred degrees Celsius) and high electric power consumption are limitations of the majority of such hydrogen gas sensors (Boon-Bret *et al.*, 2009, 2010). Although hydrogen sensors working at nearly room temperature have been developed recently (Adamyan *et al.*, 2007; Aroutiounian, 2012), the temperature and power limitations remain for other important gases.

PSi can be used as an alternative material for gas sensors, as it requires a relatively low level of preheating in order to operate (up to room

© Woodhead Publishing Limited, 2013

temperature). The interest in this material is mainly due to its extremely high surface-to-volume ratio, the ease of its formation and its compatibility with modern silicon microelectronics fabrication technologies. Usually, PSi is electrochemically formed by anodic dissolution of silicon in a hydrofluoric solution. Passing an electric current between the acid electrolyte and the Si sample leads to the formation of an array of deep narrow pores. Pores with diameters from nanometers up to micrometers deep have been achieved. PSi exhibited strong visible luminescence at room temperature (Canham, 1990; 1997). Canham's discovery opened up the possibility of developing silicon-based optoelectronic devices, fabricating Si quantum wires and pillars of crystalline Si only a few nanometers wide etc. (Pavesi *et al*., 2004). Depending on the electrolysis conditions and the illumination level, a porous texture with pore diameters varying from 2 nm to 15 nm and with a density varying from 20% to 80% of that of the original substrate can be realized (Foucaran, 1997). Many theoretical works were carried out in order to understand the processes of such a porous texture (for example, a simple model based on dangling bonds was proposed to explain quantitatively observed phenomena (Stievenard and Deresmes, 1995)).

PSi attracted the attention of specialists in photovoltaics for the manufacture of antireflection coatings (ARC) for silicon solar cells (Yerokhov, 1999; Adamyan *et al*., 2000; Aouida *et al*., 2004). Calculations of the reflectance of such PSi coatings have been carried out (Aroutiounian *et al*., 2004; 2006a; 2006b; 2007; 2008; Martirosyan *et al*., 2007) using the optical matrix approach method. Dramatically lower reflectance within a larger energy range that includes the ultraviolet, visible and infrared regions of the solar spectrum can be realized in the case of diamond-like carbon (DLC)/PSi and silicon oxynitride/PSi double layers, as proposed by the authors, during comparison with the spectra obtained that are usually used in SiO_2/TiO_2 ARC solar cells. Investigations of the influence of different gases on the properties of coatings will be carried out.

A large variety of different sensors made of PSi has been fabricated over recent years. The detection and quantification of bacterium, viruses and other organic materials, including DNA, measured by PSi sensors have been reported (Saha, 2008; Miller, 2012). The properties of gas sensors will be discussed below.

12.2 Conductivity and capacitance sensors

The capacitance and the conductance of a porous layer depend on its porosity (i.e. the size and distribution of pores, which can vary from mesopores to micro- and nano-pores). Capacitance and conductance are also affected by controlling the etching current density, etching time, the concentration of the electrolyte, and the intensity and wavelength of the illumination (Baratto

© Woodhead Publishing Limited, 2013

et al., 2002). Gas molecules in a PSi-based gas sensor are adsorbed on the surface of the PSi layer and diffuse into the porous bulk. Condensation of the diffused gas may occur inside pores that have radii less than a critical value called the 'Kelvin radius' (Saha, 2008).

The differences in permittivity are directly related to the gas concentration level in the environment. A theoretical model was proposed by Saha (2008) in order to explain the change in the dielectric constant of the PSi layer and to provide a theoretical basis for optimizing the porosity and pore morphology of the PSi layer. This model considers PSi as a three-phase mixture of dispersed spherical particles consisting of silicon nano-particles, silicon oxides and voids. The sensitivity of the PSi layer to a particular gas is due to the adsorption of the gas molecules on its surface, as well as the condensation inside the pores. A change in the dielectric constant of the matrix can affect the channel conductivity in a metal oxide semiconductor field effect transistor (MOSFET) and in *p*–*n* junction gas sensors. An interaction with dangling bond states may also lead to adsorbate-induced conductance changes. Peculiarities of the conductivity in PSi have been studied theoretically, for example by Aroutiounian and Ghulinyan (2003). An analytical study of the dependence of PSi conductivity on porosity has been made. It was found that, for porosities much lower than the percolation threshold of 57%, conductivity is mainly crystalline, while fractal behavior is observed at porosities near the percolation threshold. Quazi-one-dimensional hopping is expected at higher values of porosity.

In certain papers (Aroutiounian and Ghulinyan, 2000; Aroutiounian *et al*., 2000), a fractal model of a porous layer formation was proposed. The consideration of the time-dependent pore growth process has allowed us to calculate important parameters of the porous matrix, such as the formed surface area, and the surface and volume porosity values. We have theoretically shown that the formed surface area is strongly dependent on the difference between the pore size growth velocities parallel and perpendicular to the surface (i.e. the crystallographic orientation of the silicon surface). The volume and surface porosity values and the formed porous surface area are linear functions of the density of the anodization current. These results are in agreement with other theoretical and experimental data.

The condensation of vapors inside nanometric PSi structures has been investigated (Moretti *et al*., 2007). The liquid phase covers the pore surface as a thin film and fills a volume fraction in the sponge-like structure depending on the physical and chemical properties of each compound. The filling factor of different substances can be measured as a function of fractal-like PSi film porosity by means of an interferometric technique. The capillary condensation exhibits a nonlinear behavior at high porosities (greater than 0.8).

© Woodhead Publishing Limited, 2013

A simple nondestructive capacitance method is proposed (Adamyan *et al*., 2006) for the determination of basic PSi parameters such as layer thickness, porosity and dielectric permittivity. The method is based on two comparative measurements of the capacitance of the metal/PSi/single crystalline silicon/metal structure: one measurement is taken when there are air-filled pores, while the other measurement involves pores filled by an organic compound with a high value of dielectric permittivity. Comparison of results obtained in Adamyan *et al*. (2006) by the ball lap and the gravimetric techniques before and after anodization, with the data of capacitance measurements carried out with the same samples prior to their destruction, shows sufficiently good agreement.

12.3 Luminescence from PSi

In 1990, Canham observed intense visible photoluminescence (PL) from PSi at room temperature. Visible luminescence ranging from green to red in color was soon reported for other PSi samples and ascribed to quantum size effects in wires of width ~3 nm (Ossicini *et al*., 2003). Several models of the origin of PL have been developed, from which we chose two. In the first (the defect model), the luminescence originates from carriers localized at extrinsic centers that are defects in the silicon or silicon oxide that covers the surface (Prokes, 1993). In the second model (Koch *et al*., 1996), absorption occurs in quantum-confined structures, but radiative recombination involves localized surface states. Either the electron, the hole, both or neither can be localized. Hence, a hierarchy of transitions is possible that explains the various emission bands of PSi. The energy difference between absorption and emission peaks is explained well in this model, because photoexcited carriers relax into surface states. The dependence of the luminescence on external factors or on the variation of the PSi chemistry is naturally accounted for by surface state changes.

The most widely-studied PL occurs in the far-red to orange-yellow wavelengths. Red PL is the only wavelength that can be electrically excited. This PL shows a blue shift with an increase in anodization current density. We noted that the porosity of PSi increases with an increase in anodization current density, which leads to a decrease in the dimensions of Si nanocrystals within the PSi. The blue shift of the PL and optical absorption with increasing porosity are the first important signs that quantum confinement plays a significant role in PSi. The splitting of the luminescent states, the polarization of the PL and the phonon replicas seen in the PL under resonant excitation can be observed. The PL peak wavelength and intensity are sensitive to the PSi surface, which makes the PL phenomena very responsive to different gases.

© Woodhead Publishing Limited, 2013

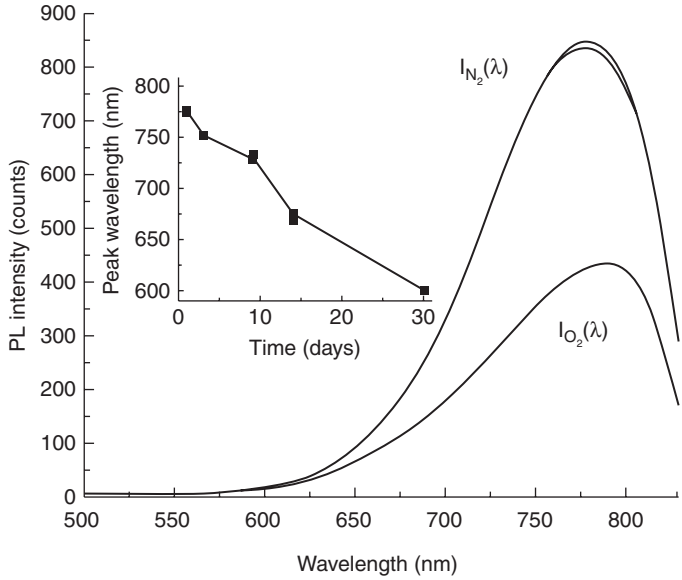

12.1 PL emission from the electrochemically prepared PSi layer on wafer in gas phase and different atmospheres: nitrogen ($I_{N_2}(\lambda)$) and oxygen ($I_{O_2}(\lambda)$). Inset: evolution of the PL maximum peak position with ageing time. After Ballaguer and Matveeva (2010) with the permission of the authors.

Balaguer and Matveeva (2010) have considered the phenomenon of PSi photoluminescence by molecular oxygen. Figure 12.1 shows the PL spectra of a freshly prepared PSi layer in N_2 and O_2 gases. The decrease of PL in oxygen is due to an interaction between excited PSi and the molecule that received a part of an emitted optical energy, transforming it into excited specie. This phenomenon is reversible and, after placing the layer in a N_2 atmosphere, the PL is completely recovered (see second PL curve in N_2 atmosphere in Fig. 12.1). Thus, energy transfer inside the system takes place without any chemical transformation of PSi. In other words, physicosorbed chemicals can quench PL without effecting any net chemical reaction at the surface (Lauerhass and Sailor, 1993), and such interactions are mainly reversible. There are many mechanisms that explain the quenching phenomenon. Changes in both spectral distribution and spectral intensity offer promising methods for the detection of gases. PSi-based sensors that use PL quenching technology allow the detection, for example, of gaseous NO_x, Cl_2, Br_2, I_2, O_2, ethanol, methanol, benzene, toluene, xylene, freons, ethers and chlorinated carbons (Canham, 1997, p. 364). PSi sensors were fabricated and tested, using the PL quenching technique, in the presence of various linear aliphatic alcohols (methanol to n-hexanol) and water in the range

© Woodhead Publishing Limited, 2013

of 10–100 ppm. The phenomenon of the PL quenching effect in the presence of target analytes is used in optical sensing. An increase in the degree of quenching was observed with the chain length of alcohols, while minimum response was given to water. Responses as high as 80–90% and an almost instant response time have proven the sensors to be highly efficient. Sensitivity, response and recovery time increased with the chain length of alcohols. Exceptional improvements in sensor response and recovery time were observed for methanol. From methanol to butane, the sensitivity was dependent on the effective concentration of analytes in the PSi matrix. For pentane and hexane, which have high boiling points, sensitivity was linked to the dielectric quenching mechanism, due to the condensation of vapors inside the pores.

There are irreversible quenchers. Their molecules react with the inner surface of PSi by introducing efficient non-radiative charge carrier traps. Some chemical reactions lead to the generation of surface species that produce electronically passive interfaces. Other species are very efficient electron–hole recombination traps. For example, the reaction of PSi with chlorine, bromine or iodine gas leads to the introduction of Si–Cl, Si–Br or Si–J surface traps and complete quenching of PL (Canham, 1997, p. 364). PL is recovered upon air hydrolysis. Irreversible quenching was demonstrated in the case of the halogens, NO_x and amines. Reversible quenching of PL had been detected following the reaction of the vapors of benzene, hexane, or dichloromethane, as well as gaseous molecules such as SO_2 with PSi.

The PL quenching measurements of sensor elements based on prepared PSi, oxidized PSi and methyl-10-undecenoate functionalized PSi are reported by Dian *et al*. (2010). It was demonstrated that relatively simple functionalization of the PSi surface via oxidation and hydrosilylation with methyl-10-undecenoate substantially modifies the PL quenching response in the presence of polar analytes, as compared with H-terminated PSi surface.

PSi and porous polymer substrates for optical chemical sensors are discussed by Hajj-Hassan *et al*. (2010). They were used as substrates to encapsulate gaseous oxygen (O_2) responsive luminophores in their nanostructured pores. These substrate materials behave as optical interference filters that allow efficient and selective detection of the wavelengths of interest in optical sensors.

A PSi microcavity was exposed to the saturated vapor of ethanol. The ethanol substitutes the air inside the pores and leads to a rise in a progressive monotonic red shift of the interference pattern of the PL spectrum. Moreover, the PL intensity of the cavity peak oscillates over time. Both effects are sequences in the progressive change of the refractive index of air and ethanol. Large, repeatable and selective red-shifts in the reflectivity spectra of PSi microcavities have been registered following exposure to

© Woodhead Publishing Limited, 2013

vapors of aliphatic hydrocarbons with different molecular weights. The shift in the resonant peak of the optical microcavity is due to average refractive index changes. Vapors of HCl, NH_3 and NO at the 10 ppm level, as well as isopropyl alcohol and aliphatic molecules, were detected by a PSi gas PL sensor (Vrkoslav *et al*., 2007; Acquaroli *et al*., 2010; Dian *et al*., 2010; Ong *et al*., 2010; Huang *et al*., 2011). The reflectivity spectrum and Fourier-transform data analysis was applied (Hutter and Ruschin, 2010) in order to enable simple discrimination between different ammonia and water vapor concentrations.

A distributed PSi Bragg reflector was used for optical interferometric sensing of organic vapor (Kim *et al*., 2011). A fully-integrable optical PSi-based Bragg grating waveguide sensor for chemical monitoring has been reported; the PSi had nanometric pores. PSi filters and preconcentrators have recently been realized since 2008, which opens new possibilities in the detection of chemical vapor (Salem *et al*., 2008; Camara *et al*., 2010; Jalkanen *et al*., 2011).

A theory for semiconductor nanostructure reactivity to a gas environment has been developed (Ninno *et al*., 2000) to link the nanostructure geometry of PSi to its optical properties. Light emission and absorption energies have been calculated within a variational scheme, which includes a position-dependent boundary condition. The results of measurements of both PL quenching and peak position shift in the presence of oxygen can be accounted for by the theory. The model can be considered as one of the first attempts to create a general theory governing the functioning of semiconductor nanostructure-based gas sensors.

12.4 Optical and photo properties of PSi sensors

The absorption and transmission spectra of PSi (Fig. 12.2) were considered (von Behren *et al*., 1998; Pavesi, 2004). Measurements of transmission spectra of several 20 μm thick, freestanding PSi films (made on 5–7 Ωcm *p*-type Si substrates of various porosities) and a 20 μm thick c-Si film have shown that the increase in porosity leads to an increase in transmission. Its shift in photon energy ranges from 2 eV up to 3.5 eV. The absorption spectra of bulk single-crystalline silicon and PSi with grains of different sizes (from 240 nm up to 410 nm) were measured. The absorption coefficient was 10^2 cm^{-1} at photon energy 1.3 eV for single-crystalline grains and 2 eV for PSi grains of 240 nm. As expected, a further decrease in the size of PSi grains led to the transmission of photons having greater energies.

The features of optical absorption and emission in PSi have been discussed by Alexanyan *et al*. (2003). An allowance for the finite nature of the potential well depth when calculating the shift of the absorption edge of the quantum wire, as well as the probability of transition between states in

© Woodhead Publishing Limited, 2013

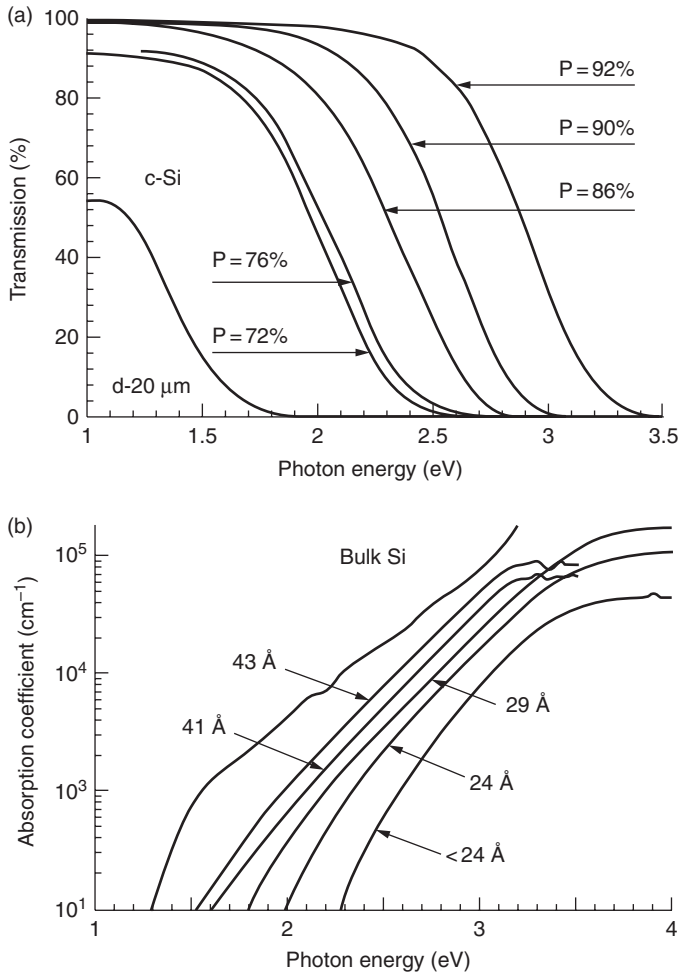

12.2 (a) Transmission spectra of several 20 μm thick freestanding PSi films (5–7 Ωcm *p*-type Si substrate) of various porosities (P) and a 20 μm thick c-Si (crystalline silicon) film. (b) Absorption spectra for Si nanocrystals with sizes from 4.3 nm to 2.4 nm deduced from the transmission spectra of (a). The absorption of c-Si is shown for comparison. The saturation beyond 3 eV is an artifact of the measurement procedure. After von Behren *et al.* (1998) with the permission of the authors.

conduction and valence bands, along with the radiation lifetime, is shown to introduce significant amendments into the dependences of these parameters on the size of quantum wire in PSi.

It has been shown that the refractive index of a material is proportional to its porosity (Pavesi, 2004). Therefore, complex structures can be realized using PSi etched layers. Moreover, the refractive index of PSi can be changed

© Woodhead Publishing Limited, 2013

by the current density during the etching. A current profile is reflected in a correlated in-depth refractive index profile. This allows the formation of microcavities, Bragg reflectors, an optical delay line etc. If a crystal has uniaxial symmetry, a crystal possessing such as anisotropic dielectric properties is said to be 'birefringent'. The optical anisotropy in PSi is due to the anisotropic geometry of the pores and depends on the crystalline orientation of the silicon substrate. Birefringence has been reported in (100), (111) and (110) oriented PSi. The optical form of the birefringence property of PSi is used in a compact polarization interferometer to demonstrate a novel optical transduction mechanism for vapor- or gas-sensing applications. This technique uses high interferometric sensitivity of the polarization interference intensity when the PSi sample is exposed to solvent vapors. Heptane and ethanol vapors were detected (Liu *et al*., 2002).

Anisotropically nanostructured silicon layers exhibit a strong in-plane birefringence. Their optical anisotropy parameters are found to be extremely sensitive to the presence of dielectric substances inside the pores. Polarization-resolved transmittance measurements provide an extremely sensitive tool with which to analyze the adsorption of various gases in negligible quantities; this makes these layers a good candidate for sensor applications. A highly-sensitive recognition element based on birefringent PSi layers has been realized.

In multiparametric PSi optical microcavities, developed by Baratto *et al*. (2002), three independent quantities can be measured: the electrical conductance, the PL intensity and the wavelength of the optical resonance. The change of these parameters as a function of NO_2 (0.5–5 ppm), ethanol (300–15 000 ppm) and relative humidity (0–100%) has been investigated.

A gas sensor for simultaneous monitoring of the electrical and optical properties developed by Jalkanen *et al*. (2010) is based on a PSi optical interference filter layer. This was produced with an electrochemical etching process. Sensors with differing hygroscopic properties were produced, and their response to atmospheric variations was tested. This sensor had a rapid response and an increased level of selectivity between different gases. In tests, the sensor response changed according to humidity. The sensors were sensitive to ethanol and dimethylformamide vapors. The size of such sensing elements was reduced.

A new method for using photo-electromotive force (Photo-EMF) in the detection of gas and for controlling sensitivity is proposed (Vashpanov *et al*., 2011). Photo-EMF on the heterojunction between the PSi thin layer and the crystalline silicon wafer depends on the concentration of ammonia in the measurement chamber. A light-transparent contact to the porous Si was formed. Photo-EMF sensitivity corresponding to the ammonia concentration in the range from 10 ppm to 1000 ppm can be controlled by the intensity of the source of illumination.

© Woodhead Publishing Limited, 2013

12.5 PSi noise sensors

The sensitivity of gas sensors is mainly measured by the classical method of a comparison of the ohmic resistance of the sensors in gas media and air. However, excellent results have been obtained by studying and comparing the low-frequency noise characteristics of sensors to determine their sensitivity.

In Paremuzyan and Aroutiounian (2012a, 2012b), the phenomenon of a reduction in the heat of adsorption was taken into account using the results of Langmuir's theory. The noise for oxygen and other type of gases was calculated.

We studied experimental samples of PSi-layered structures Au/PSi/SCS/Al (SCS being single crystal silicon) (Mkhitaryan *et al*., 2007a, 2007b; Aroutiounian *et al*., 2008). The PSi layer was formed by electrochemical etching on a substrate made of heavily doped p+–type silicon with orientation (100) and resistivity of 0.01 Ωcm. The samples were ~2 μm thick. The reverse of the wafer was coated with an Al film 20–30 nm thick. The top contact was of gold sprayed on the surface of PSi and had a diameter of 1.5 mm. Conductive glue based on silver 'conductive epoxy' was used for the top contact. The porosity of PSi films was 50% and 73%.

Measurements of current–voltage characteristics (CVCs) of the above-mentioned structures were carried out at room temperature in air and in mixtures of air with different concentrations of carbon monoxide. The typical CVCs of samples with a porosity of 73% in all environments have a nonlinear behavior. The CVC is nonlinear for low back bias, but becomes linear with an increase in low back bias. The CVCs for PSi of 73% porosity, both in air and in air + 0.4% CO, have rectifying characteristics, but, as compared with the corresponding characteristics of samples with 50%-PSi, a sharp decrease in conductivity and an absence of current saturation took place. The factor of ideality m was estimated from the initial part of the direct branch. The barrier height was determined from the linear part of the backward branch of the CVC.

A model where the resistance R_S of the heterojunction interface PSi/Si-single crystal is connected in series with the base resistance of the PSi layer was applied for the study of CVCs. As in the field of small direct bias, the voltage drop is insufficient and displacement on the base resistance may be ignored; the initial part of the direct branch is approximated by the exponential dependence of current J on voltage U with a large factor of ideality m:

$$J \sim \exp(qU/mkT) \qquad [12.1]$$

Here q is electron charge, k is the Boltzmann constant and T is temperature. The factor m can be estimated from Equation [12.1].

© Woodhead Publishing Limited, 2013

We observed that a change in the structure of the experimental environment resulted in the change of CVCs both in the direct displacement region and in the region of backward displacement. Essentially, the current grows in both regions at the same displacement with the introduction of CO into the air.

A reduction of the height of a heterojunction barrier took place because of the migration of CO molecules into pores of the heterojunction interface. This is one of the reasons for the high gas response of the heterostructure containing a nanosize porous film. However, the mechanism of the high gas-sensitivity of porous structures is not yet completely understood. Analysis of experimental data has shown that the gas adsorption of CO molecules leads to a decrease in the height of the heterojunction barrier. It is accompanied by the reduction of the PSi layer base resistance, which is connected in series with the heterojunction. The degree of decrease in the barrier height V_B depends on the amount of CO in the air. Numerical estimations of the R_S, m and V_B values were carried out. Depending on content, the value of m for PS-73%, is changed from 21 to 9.5 for air and air + CO.

A sharp drop, by several orders of magnitude, of $S_U(f)/U^2$ with the change in concentration of CO in the air suggests the possibility of making a precise estimation of the gas content in air – that is, we can offer a new method of estimation of the concentration of gases in an environment and the noise spectroscopy (Figs 12.3 and 12.4). S_U is the spectral density of the noise voltage.

It is known that the parameter α_{H} is determined for the frequency 10 Hz from the empirical Hooge's formula:

$$\alpha_{\text{H}} = S_U N f^{\gamma} / U^{\delta} \qquad [12.2]$$

Here, N is the number of free carriers in a sample, α_{H} is the dimensionless Hooge parameter, U is the voltage applied to the studied structure, γ is the frequency index (which is usually approximately equal to unity) and $\delta \approx 2$. The values of S_U, U^{δ} and γ were determined experimentally from the spectra obtained. Parameter γ (in air) was equal to 0.5; γ (in air + 0.4% CO) = 1, γ (in air + 2% CO) = 1.3. Comparison of α_{H} values shows that, for crystal materials, α_{H} are several orders of magnitude higher than for noncrystalline structures: α_{H} can take values from 1 up to 10^4. One of the reasons for this is the low mobility of charge carriers in disordered materials, to which category PSi also belongs. The nonuniformity of the current density in the sample may also cause a large value of α_{H}. In our case, this can probably be caused by the nano-crystalline structure of the PSi layer. The nonuniform density of the current in the nano-crystallite arises for several reasons: (a) the coral-like systems of variable cross-section silicon strings, (b) the presence of the depletion region around each pore, and (c) inhomogeneity of the density

© Woodhead Publishing Limited, 2013

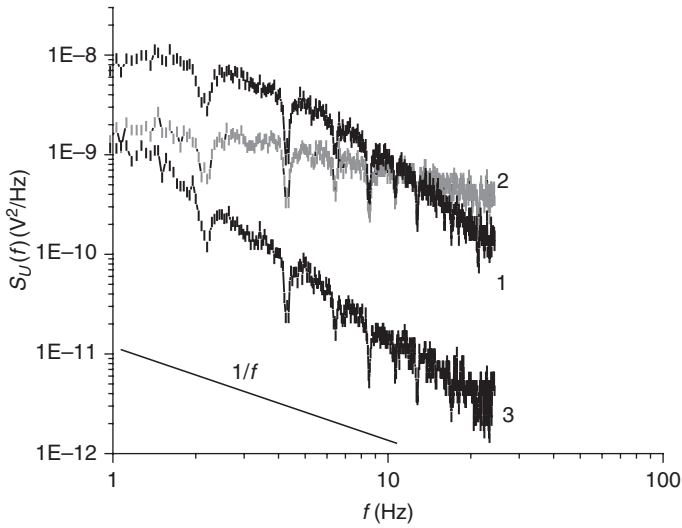

12.3 Noise spectra for samples with the 50%-porosity PSi layers exposed to the indicated gases at a current of 0.1 mA. The straight line refers to 'classical' 1/*f* noise. Samples were placed in air (1), air + ethyl alcohol vapor (2) and air + 1.7% CO (3).

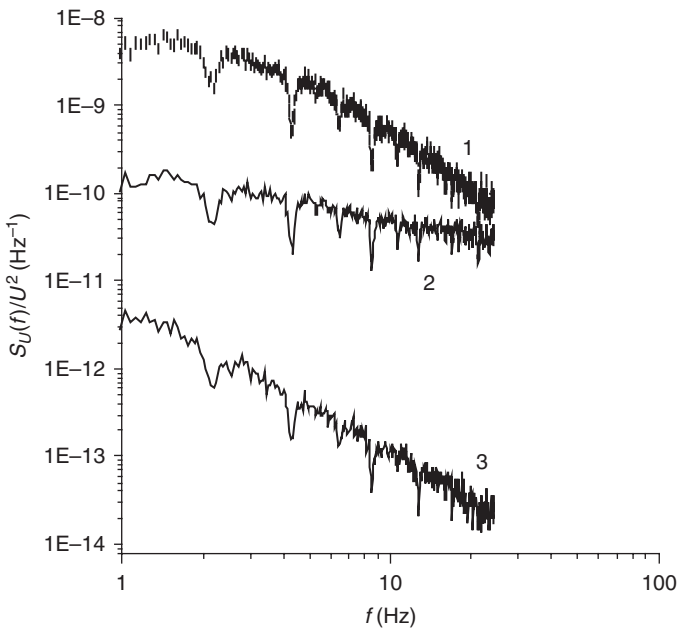

12.4 Normalized noise spectra for samples with the 50%-porosity PSi layers exposed to the indicated gases at a current of 0.1 mA. Samples were placed in air (1), air + 0.4% CO (2) and air + 1.7% CO (3).

© Woodhead Publishing Limited, 2013

and mobility of free charge carriers. It was observed that the value of α_H varies after the introduction of carbon oxide (CO) into the air; namely α_H increases with the increase in the concentration of CO in air. We explain this as follows: with an increase in the concentration of gas molecules, the number of molecules (ions) adsorbed on a surface increases and therefore the density of traps located at the PSi/SCS interface increases. The hetero-barrier height at gas adsorption decreases with an increase in the adsorbate concentration. Therefore, the effect of a potential barrier, in comparison with increasing concentration of surface traps, becomes less important.

So, the $S_U(f)$ value grows with the increase in porosity of silicon and in the concentration of polar CO molecules in air. Correspondingly, the noise parameter α_H varies also. Noise spectra of the structures investigated in various gas media in the low-frequency range were quantitatively different and displayed different characteristics. The physics of the noise phenomena in a system containing a gas-semiconductor structure is rather complicated. The possible reasons for large values of γ and α_H for PSi samples in air and their increase in the gas chamber are discussed below.

As seen from our measurements, the values of the spectral density of the noise voltage change to a significant degree when samples are placed in different gas media and air. Therefore, we have compared the gas response of sensors made using different technologies. We compared data for Figaro TGS 2443, 2511, 3870 and 821 sensors, as well as our sol–gel H_2 and PSi sensors (Paremuzyan and Aroutiounian, 2012b). The response of this range of sensors was earlier measured by the classical method of comparison of the resistance of sensors in gas media and air. Here, we reported results of the study of low-frequency noise characteristics of the metal–PSi–silicon single crystal–metal structure with differing porosities of PSi. The study was performed in dry air and in a mix of dry air with CO, hydrogen and alcohol at different concentrations. A calculation of the response of the porous structures under investigation was carried out using results obtained during an experiment for changes in target gas media and air of resistance $G_{dc} = R_{sa} / R_{tg}$ (in the ohmic element of CVCs) and of the spectral density of noise (SND) due to voltage fluctuations:

$$G_{noise} = \frac{S(f)_{SA} / U_{sa}{}^2}{S(f)_{tg} / U_{tg}{}^2} \qquad [12.3]$$

We introduced the results of measurements of the response of the Figaro sensors and our samples made of SnO_2 and PSi (Figs 12.5 and 12.6) (Aroutiounian *et al.*, 2009). We see from Figs 12.5 and 12.6, the dc resistance response G_{dc}, measured by the classical method, led to smaller values of the

© Woodhead Publishing Limited, 2013

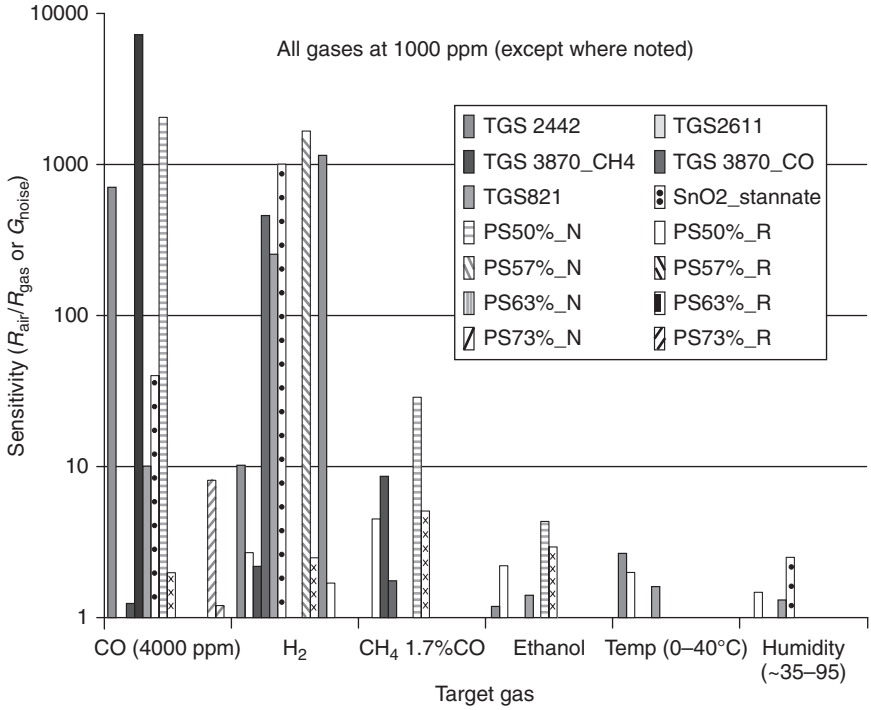

12.5 Sensitivity of different sensors to gases. We compare data for Figaro sensors TGS 2442, 2611, 3870 and 821, as well as our sol–gel H_2 and PSi sensors.

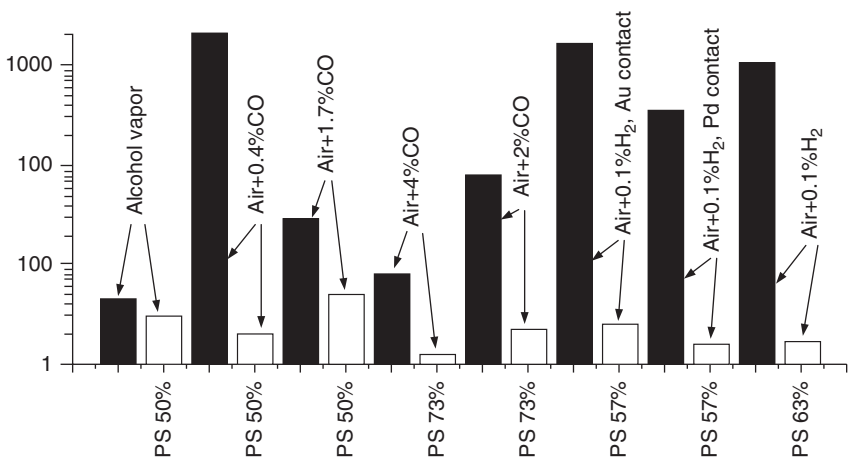

12.6 Comparison of the sensitivity of different sensors obtained by measurements using classical resistivity (G_R) and noise (G_{noise}) methods. G_R, open bars; G_{noise}, black bars. The values of sensitivity (response) are compared for measurements by the noise (black) and resistance (white) methods.

© Woodhead Publishing Limited, 2013

sensitivity (response) in comparison with the SND sensitivity. It allows the carrying out of fluctuation-enhanced measuring of sensor response.

A discussion of changes of parameter α_H in Hooge's formula in gas media suggests that α_H increased with the increase in concentration of CO in air. The explanation for this is that, with the increase in the concentration of CO, the number of molecules (ions) adsorbed on a surface increases; therefore, the density of traps located at the PSi/SCS interface increases. The heterojunction barrier height at gas adsorption decreases with the increase in the adsorbate concentration. Therefore, the effect of a potential barrier, in comparison with increasing concentration of surface traps, becomes less important. Nonuniform density of the current in the nano-crystallite arises for several reasons: (a) the coral-like systems of variable cross-section silicon strings, (b) the presence of the depletion region around each pore, and (c) inhomogeneity of the density and mobility of free charge carriers.

12.6 Different PSi gas sensors

Barillaro *et al*. (2010, 2009) have presented PSi junction field effect (JFET) transistor gas sensors. They are an integrated *p*-channel JFET device modified with a PSi layer which acts as a sensing element to both synthetic air and NO_2 with concentrations of 100, 300 and 500 ppb at room temperature. The quantitative information on the effect of the NO_2 adsorption/desorption at the PSi surface on conductance and surface charge density of PSi was obtained.

In Barillaro *et al*. (2008), nitrogen dioxide detection by using *p*+–*n* silicon diodes surrounded by a PSi layer was demonstrated. Adsorption of NO_2 in the PSi layer modifies the electrical properties of the PSi/crystalline silicon interface and, in turn, the *p*+–*n* diode current. The device shows a higher selectivity to NO_2 in comparison with ethanol, at any polarization voltage and relative humidity level.

A novel PSi sensor for the detection of 0.1–10 ppm of NO_2 was sensitive simultaneously to 200 ppb of O_3, 1000 ppm of CO, 20 ppm of benzene, organic vapors and humidity. At low concentration (100 ppb) of NO_2, the interference from ozone benzene, CO and organic vapors was not detected (Baratto *et al*., 2001).

Pancheri *et al*. (2003) have reported sensitivity to 12–50 ppb NO_2 at room temperature in the sensor, based on the change in conductivity of a single meso-porous Si layer with about 80% porosity. Meso-porous Si shows higher sensitivity and better selectivity for NO_2, while macro-porous Si shows better selectivity for NH_3 (Sun *et al*., 2012). The light-enhanced NO_2 sensing properties of PSi at room temperature have been demonstrated (Chen *et al*., 2012).

© Woodhead Publishing Limited, 2013

The Pd-sensitized PSi H_2 sensor with a thin zinc oxide (ZnO) over-layer demonstrated improved gas response behavior at higher temperatures (Kanungo *et al*., 2010a). PSi was produced during a gas sensor study with the Pd–Ag/Pd:ZnO/Pd:PSi/Si/Al structure indicating that the Pd-sensitized ZnO on Pd-modified PSi exhibits consistent H_2-sensing performance, including improvements in gas response, the response time and long-term stability. However, recovery took considerable time.

Effects of surface passivation in PSi as a H_2 gas sensor were also investigated (Ali *et al*., 2008). A peroxide-based PSi sample fabricated as a H_2 gas sensor showed better electrical (I–V) sensitivity compared with those without peroxide, which has been associated with good surface passivation. Surface passivation in peroxide-based PSi is also maintained at higher temperatures (100°C).

PSi samples coated with a continuous palladium layer in an electro less process were reported in Razi *et al*. (2010). I–V curves of Schottky-like Pd/PSi samples were measured in air and in hydrogen. The samples can sense H_2 in a wide range of concentrations (100–40 000 ppm) without any saturation behavior. Hydrogen-sensing properties of these samples were investigated at room temperature for a duration of nine months. Sample sensitivity (response time) decreased to a saturated value after 45 days. The effect of different porosities on the performance of the Pd-Ag modified PSi H_2 sensor in a metal-insulator-semiconductor (MIS) configuration was studied at room temperature and for long-term performance (Kanungo *et al*., 2009c, 2010b). Improved sensing was reported for 55% porosity. Ni-PSi-Ni H_2-sensitive diodes with Schottky contacts (Naderi *et al*., 2012).

Pd and WO_3/Pd MIS gas-sensitive structures based on PSi layers have been studied by Solntsev *et al*. (2009) using the high frequency C (V) method. The WO_3/Pd structures are more sensitive and selective to the adsorption of hydrogen sulphide (H_2S) compared with Pd gates. Mechanisms of enhanced sensitivity and selectivity to H_2S adsorption of MIS gas sensors with WO_3/Pd composite gate electrodes compared with pure Pd have been analyzed. The effect of H_2S on the CVCs of MIS structures based on nanoPSi under copper doping has been investigated in Gorbanyuk *et al*. (2007). It was also shown that the doping of nanoPSi by Cu led to enhanced H_2S sensitivity in MIS structures even without catalytic active top electrodes (e.g. Pd) at room temperature.

Coulomb blockade sensors based on nanostructured mesoPSi (i.e. a nanosponge where Si nanocrystals are interconnected forming a disordered three-dimensional array) have been investigated (Borini *et al*., 2007; Boarino *et al.*, 2009). The electronic characteristics of this material are particularly interesting due to some intriguing effects, such as a huge increase in conductivity, reversible insulator-to-metal transition and *n*- or *p*-type doping of the nanocrystals, exhibited in the presence of donor or acceptor

© Woodhead Publishing Limited, 2013

molecules such as NH_3 and NO_2. A sharp conductance gap, which can be ascribed to Coulomb blockade phenomena, was reported. Borini *et al.* (2006), have shown that the width of the gap can be tuned by NO_2 molecules, meaning that the fabrication of highly-sensitive threshold sensors is possible. PSi nanowires demonstrated a fast response and excellent reversibility to subparts per million of NO concentrations at room temperature (Peng *et al.*, 2009).

The hydrocarbon thin-film coating of PSi led to enhancement of one and two orders of magnitude in current under CO_2 gas exposure (Prabakaran *et al.*, 2008). Changes in the resistance of PSi material, of about MOhm, in the presence of CO, observed by Martinez *et al.* (2008), have shown that PSi is also suitable as a CO sensor. The potential of PSi gas sensors is also reviewed by Ozdemir *et al.* (2007), where the authors reported on the sensitivity of PSi sensors to isopropanol, O_2, HCl and SO_2. Ozdemir *et al.* (2010) have also reported on phosphine detection by modified PSi. The effect of ethanol vapor adsorption on optical and electrical parameters of PSi has been investigated (Baratto *et al.*, 2000; Bolotov *et al.*, 2009; Kim *et al.*, 2010). Aluminum-mesoporous Si coplanar type structure was suggested for methanol gas sensing (Khardani *et al.*, 2010). The influence of molecular kinetics during organic vapor sensing by PSi has been discussed by Dhanekar *et al.* (2010).

The corresponding functionalization of PSi allows the proposal of amine and organophosphorus vapor detectors (Bjourqvist *et al.*, 2009; Badilla *et al.*, 2011; Tudisco *et al.*, 2012). The detection of toxins, volatile organic compounds, polycyclic aromatic hydrocarbons, and explosives on the level of at least a few ppb was demonstrated using stacked PSi photonic crystals, multilayer structures, and distributed Bragg reflector structured PSi (Ruminski *et al.*, 2008; Park *et al.*, 2010; Kelly *et al.*, 2011; Kim *et al.*, 2011). PSi layers with embedded metal oxides, as well as PSi-polymer hybrid structures, have recently been proposed for gas-sensing applications (Belhousse *et al.*, 2010; Bolotov *et al.*, 2011; Moshnikov *et al.*, 2012).

Gas sensors based on field ionization from multiwall carbon nanotube arrays grown on PSi templates have been developed (Nikfarjam *et al.*, 2010). Such sensors showed good sensitivity, selectivity and short response times, as well as higher discharge current and good mechanical stability in comparison with those which were fabricated on polished silicon substrates. Validation of the compatibility between PSi-based gas sensor technology and standard microelectronic processes has been demonstrated (Barillaro *et al.*, 2010).

12.7 Conclusion

Various types of PSi-based gas sensor have been developed. Using such sensors, the detection of a wide range of gases and vapors is now possible,

© Woodhead Publishing Limited, 2013

including H_2, CO, CO_2, Cl_2, Br_2, J_2, O_2, NH_3, H_2S, HCl, halogens, amines, ethanol, butanol, methanol, isopropanol, benzene, toluene, xylene, freons, ethers, chlorinated carbons, linear aliphatic alcohols, organic vapors, etc.

12.8 References

Adamian, Z. N., Hakhoyan, A. P., Aroutiounian, V. M., Barseghian, R.S. and Touryan, K. J. 'Investigations of solar cells with porous silicon as antireflection layer', (2000) *Sol. Energy Mater. Sol. Cells,* **64**, 347–51.

Adamyan, A. Z., Adamian, Z. N. and Aroutiounian, V. M. 'Determination of basic parameters of porous silicon', (2006) *J. Phys. D: Appl. Phys.* **39**, 3543–6.

Adamyan, A. Z., Adamyan, Z. N., Aroutiounian, V. M., Arakelyan, A. H., Touryan, K. J. and Turner, J. A. 'Sol–gel derived thin-film semiconductor hydrogen gas sensor', (2007) *Int. J. Hydrogen Energy*, **32**, 4101–8.

Acquaroli, L. N., Urteaga, R. and Koropecki R. R. 'Innovative design for optical porous silicon gas sensor', (2010) *Sensor. Actuat. B.* **149**, 189–93.

Alexanian, A. G., Yeremyan, A. S. and Aroutiounian, V. M. 'Features of optical absorption and photoluminescence of porous silicon', (2003) *Phys. Stat. Solidi a* **197**, 425–31.

Ali, N. K., Hashim, M. R. and Abdul, A. A. 'Effects of surface passivation in porous silicon as H2 gas sensor', (2008) *Solid-State Electron.* **52**, 1071–4.

Aouida, S., Saadoun, M. and Boujmil, M. F. 'Effect of UV irradiation on the structural and optical features of porous silicon: Application in silicon solar cells', (2004) *Appl. Surf. Sci.* **238**, 193–8.

Aroutiounian, V. M., Ghoolinian, M. Zh. and Tributsch, H. 'Fractal model of a porous semiconductor', (2000) *Appl. Surf. Sci.* **162–3**, 122–32.

Aroutiounian, V. M. and Ghulinyan, M. Zh. 'On the fractal model of the porous layer formation', (2000) *Mod. Phys. Lett. B*. **14**, 39–46.

Aroutiounian, V. M. and Ghulinyan, M. Zh. 'Electrical conductivity mechanisms in porous silicon', (2003) *Phys. Stat.Sol. (a)*. **197**, 462–5.

Aroutiounian, V. M. 'Hydrogen detectors', (2005) *Int. J. Alternative Energy Ecol.* **3**, 21–31.

Aroutiounian, V. M., Martirosyan, Kh. and Soukiassian, P. 'Low reflectance of diamond-like carbon/porous silicon double layer antireflection coating for silicon solar cells', (2004) *J. Phys. D: Appl. Phys.* **37**, L25–L28.

Aroutionian, V. 'Metal oxide hydrogen, oxygen, and carbon monoxide sensors for hydrogen setups and cells', (2007) *Int. J. Hydrogen Energy*, **32**, 1145–58.

Aroutiounian, V. (2012) *Encyclopedia of Nanoscience and Nanotechnology*. CRC Press (10 pages).

Aroutiounian, V. M., Martirosyan, Kh. and Soukiassian, P. 'Almost zero reflectance of a silicon oxynitride/porous silicon double layer antireflection coating for silicon photovoltaic cells', (2006a) *J. Phys. D: Appl. Phys.* **39**, 1623–5.

Aroutiounian, V. M., Martirosyan, Kh. and Soukiassian, P. 'Reflectance calculation of a diamond-like carbon/porous Si thin films in silicon-based photovoltaic cells', (2006b) *J. Phys. IV France*, **132**, 325–8.

Aroutiounian, V. M., Martirosyan, Kh. and Soukiassian, P. 'Reflectance spectrum of diamond-like carbon/porous silicon double-layer antireflection coatings designed for silicon solar cells', (2007) *Phys. Stat. Sol. (C)*. 42107–10.

© Woodhead Publishing Limited, 2013

Aroutiounian, V. M., Martirosyan, Kh. S., Hovhannisyan, A. S. and Soukiassian, P. G. 'Use of porous silicon for two-or three layer antireflection coating for silicon solar cells', (2008) *J. Contemp. Phys*. **43**, 111–19.

Aroutiounian, V. M., Mkhitaryan, Z., Adamian, A., Granqvist, C.-G. and Kish L. B. 'Fluctuation-enhanced gas sensing', (2009) *Procedia Chemistry*, **1**, 216–19.

Aroutiounian, V. M., Mkhitaryan, Z. H., Shatveryan, A. A., Gasparyan, F. V., Ghulinyan, M. Zh., Pavesi, L., Kish, L. B. and Granqvist, C.-G. 'Noise spectroscopy of gas sensors', (2008) *IEEE Sensors J.* 786–90

Badilla, J. P., Rojas, D. C., Lopez, V., Fahlman, B. D. and Ramırez-Porras, 'Development of an organic vapor sensor based on functionalized porous silicon', (2011) *Phys. Stat. Solidi A*. **208**, 1458–61.

Balaguer, M. and Matveeva. E. 'Quenching of porous silicon photoluminescence by molecular oxygen and dependence of this phenomenon on storing media and method of preparation of pSi photosensitizer', (2010) *J. Nanopart. Res*. **12**, 2907–17.

Baratto, C., Comini, E., Faglia, G., Sberveglieri, G., Di Francia, G., De Filippo, F., La Ferrara, V., Quercia, L. and Lancellotti, L. 'Effects of surface passivation in porous silicon as H2 gas sensor', (2000) *Sensor. Actuat. B.* **65**, 257–9.

Baratto, C., Faglia, G., Comini, E., Sberveglieri, G., Taroni, A., F. La Ferrara, V., Quercia, L. and Di Francia, G. 'A novel porous silicon sensor for detection of sub-ppm NO_2 concentrations', (2001) *Sensor. Actuat. B.* **77**, 62–6.

Baratto, C., Faglia, G., Sberveglieri, G., Gaburro, Z., Pancheri, L., Oton, C. and Pavesi, L. 'Multiparametric porous silicon sensors', (2002) *Sensors*, **2**, 121–6.

Barillaro, G., Bruschi, P., Lazzerini, G. M. and Strambini, L. M. 'Validation of the compatibility between a porous silicon-based gas sensor technology and standard microelectronic process', (2010) *IEEE Sens. J.* **10**, 893–9.

Barillaro, G., Diligentia, A., Strambini, L.M., Comini, E. and Fagli, G. 'NO_2 adsorption effects on p^+-n silicon junctions surrounded by a porous layer', (2008) *Sensor. Actuat. B*. **134**, 922–7.

Barillaro, G., Lazzerini, G. M. and Strambini, L. M. 'A novel power-controlling approach for integrated, conductometric gas sensors', (2009) *Procedia Chemistry* **1**, 188–91.

Barillaro, G., Lazzerini, G. M. and Strambini L. M. 'Modeling of porous silicon junction field effect transistor gas sensors: Insight into NO_2 interaction', (2010) *Appl. Phys. Lett.* **96**, 162105.

von Behren, J., van Buuren, T., Zacharias, M., Chimowitz, E. H. and Fauchet, P. M. 'Quantum Confinement In Nanoscale Silicon: The Correlation Of Size With Bandgap And Luminescence', (1998) *Solid State Commun.* **105**, 317–22.

Belhousse, S., Boukherroub, R., Szuneris, S., Gabouze, N., Keffous, A., Sam S. and Benaboura A. 'Electrochemical grafting of poly(3-hexylthiophene) on porous silicon for gas sensing', (2010) *Surf. Interface Anal.* **42**, 1041–5.

Bolotov, V. V., Korusenko, P. M., Nesov, S. N., Povoroznyuk, S. N., Roslikov, V. E., Kurdyukova, E. A., Sten'kin Yu, A., Shelyagin, R. V., Knyazev, E. V., Kan, V. E. and Ponomareva, I. V. 'Fabrication of poor-Si/SnO*x* nanocomposite layers for gas microsensors and nanosensors', (2011) *Semiconductors*, **45**, 693–8.

Bolotov, V. V., Sten'kin Yu, A., Roslikov V. E., Kang, V. E., Ponomareva, I. V. and Nesov, S. N. 'Effect of Ethanol on Optical and Electrical Parameters of Porous Silicon', (2009) *Semiconductors*, **43**, 925–8.

© Woodhead Publishing Limited, 2013

Boon-Brett, L., Bousek, J., Black, G., Moretto, P. *et al*. 'Identifying performance gaps in hydrogen safety sensor technology for automotive and stationary applications', (2010) *Int. J. Hydrogen Energy*, **35**, 373–84.

Boon-Brett, L., Bousek, J. and Moretto, P. 'Reliability of commercially available hydrogen sensors for detection of hydrogen at critical concentrations: Part II – selected sensor test results', (2009) *Int. J. Hydrogen Energy*, **34**, 562–71.

Boarino, L., Borini, S. and Amato G. 'Electrical Properties of Mesoporous Silicon: From a Surface Effect to Coulomb Blockade and More', (2009) *L. Elecrochemical Soc.* **156**, K223–K226.

Borini, S., Boarino, L. and Amato G. (2006) *Adv. Mater.* **18**, 2422–5.

Borini, S., Boarino, L. and Amato G. 'Coulomb blockade sensors based on nanostructured mesoporous silicon', (2007) *Physica E*. **38**, 197–9.

Bjourkvist, M., Salonen, J., Tuura, T. Jalkanen Tero, and Lehto Vesa-Pekka. 'Detecting amine vapours with thermally carbonized porous silicon gas sensor', (2009) *Phys. Stat. Solidi C*. **6**, 1769–72.

Camara, E. H. M., Breuil, P., Briand, D., Cuillot, L., Pijolat, C. and de Rooij, N. F. 'Micro gas preconcentrator in porous silicon filled with a carbon absorber', (2010) *Sensor. Actuat. B.* **148**, 610–19.

Canham, L.T. 'Silicon quantum wire array fabrication by electrochemical and chemical dissolution of wafers', (1990) *Appl. Phys. Lett*. **57**, 1046–8.

Canham, L. (1997) (Editor) Properties of Porous silicon INSPEC IEE London.

Chen, H., Hu, M., Zeng, J. and Wang, W. 'Porous silicon First-principles calculation Gas sensor: Hydrogen adsorption', (2012) *Chin. Phys.B.* **21**, 058201 (5 pages).

Dian, J., Vrkoslav, V. and Jelínek, I. 'Recognition enhancement of oxidized and methyl-10-undecenoate functionalized porous silicon in gas phase photoluminescence sensing', (2010) *Sensor. Actuat. B*. **147**, 406–10.

Dhanekar, S., Islam, S. S., Islam, T. Shukla, A. K. and Harsh, T. 'Organic vapour sensing byporous silicon: Influence of molecular kinetics in selectivity studies', (2010) *Physica E*. **42**, 1648–52.

Foucaran, A., Pascal-Delannoy, F., Giani, A., Sackda, A., Combette, P. and Boyer, A. 'Porous silicon layers used for gas sensor applications', (1997) *Thin Solid Films*, **297**, 317–20.

Gorbanyuk, T. I., Evtukh, A. A., Litovchenko, V. G. and Solntsev, V. S. 'Nanoporous silicon doped by Cu for gas-sensing applications', (2007) *Physica E*. **38**, 211–14.

Hajj-Hassan, M., Kim, S. J., Cheung, M. C., Lei, Y., Chodavarapu, V. and Cartwright, A. 'Porous silicon and porous polymer substrates for optical chemical sensors', (2010) *J. Nanophotonics*, **4**, 043513 (18 pages).

Huang, J. F., Sha, L. I., Chen, Q. W. and Cai, L. T. 'Optical characteristics and environmental pollutants detection of porous silicon microcavities', (2011) *Science China Chemistry*, **54**, 1348–56.

Hutter, T. and Ruschin, Sh. 'Non-Imaging Optical Method for Multi-Sensing of Gases Based on Porous Silicon', (2010) *IEEE Sensors J.* **10**, 97–103.

Jalkanen, T., Tuura, J., Mäkilä, E. and Salonen, J. 'Electro-optical porous silicon gas sensor with enhanced selectivity', (2010) *Sensor. Actuat. B*. **147**, 100–4.

Jalkanen, T., Salonen, J., Torres-Costa, V., Kazuhiro Fukami, K., Sakka, T. and Ogata, Y. 'Structural considerations on multistopband mesoporous silicon rugate filters prepared for gas sensing purposes', (2011) *Opt. Express*, **19**, 13291–305.

© Woodhead Publishing Limited, 2013

Kanungo, J., Saha, H. and Basu, S. 'Room temperature metal–insulator–semiconductor (MIS) hydrogen sensors based on chemically surface modified porous silicon', (2009) *Sensor. Actuat. B.* **140**, 65–72.

Kanungo, J., Saha, H. and Basu, S. 'Pd sensitized porous silicon hydrogen sensor—Influence of ZnO thin film', (2010a) *Sensor.Actuat. B* **147**, 128–36.

Kanungo, J., Saha. H. and Basu S. 'Effect of porosity on the performance of surface modified porous silicon hydrogen sensors', (2010b) *Sensor. Actuat.B.* **147**, 145–51.

Kelly, T. L., Sega, A. G. and Sailor M. J. 'Identification and Quantification of Organic Vapors by Time-Resolved Diffusion in Stacked Mesoporous Photonic Crystals', (2011) *NANO Lett.* **11**, 3169–73.

Khardani, M., Bouaicha, M., Boujmil, M. F. and Bessaïs, B. 'Aluminum-mesoporous silicon coplanar type structure for methanol gas sensing', (2010) *Microporous and Mesoporous Mater.* **135**, 9–12.

Kim, H., Kim, Y. and Lee, K. 'Multiparametric sensor based on DBR porous silicon for detection of ethanol gas', (2010) *Current Appl. Phys.* **10**, 181–3.

Kim, H., Kim, Y. and Lee K. 'Sensing characteristics of the organic vapors according to the reflectance spectrum in the porous silicon multilayer structure', (2011) *Sensor. Actuat. A.* **165**, 276–9.

Koch, F., Kovalev, D. and Averbouck, B. 'Luminescence in porous silicon', (1996). *J. Luminescence* **70**, 320–8

Lauerhass, J. M. and Sailor, M. J. 'Chemical Modification of the Photoluminescence Quenching of Porous Silicon', (1993) *Science*, **26**, 11567–68.

Liu, R., Schmedake, T. A., Li, Y.Y., Sailor, M. J. and Fainman, Y. 'Novel porous silicon vapor sensor based on polarization interferometry', (2002) *Sensor Actuat. B.* **87**, 58–62.

Martirosyan, Kh. S., Hovhannisyan, A. S. and Aroutiounian, V. M. 'Calculation of reflectance of porous silicon double-layer antireflection coating for silicon solar cells', (2007) *Phys. Stat. Sol.* (*C*) **42**, 103–6.

Martinez, H. M., Rinson, N. E., Torres, J. and Alfonso, J. E. 'Porous silicon thin film as CO sensor', (2008) *Microelectr. J.* **39**, 1354–5.

Miller, B. L., Fauchet, P. M., Horner, S. R. and Chan, S. (2012) *Dekker Encyclopedia for Nanoscience and Nanotechnology*, CRC Press, 408–5.

Mkhitaryan, Z. H., Shatveryan, A. A., Aroutiounian, V. M., Ghulinyan, M., Pavesi, L.,Kish, L. B. and Granqvist, C. G. 'Current–voltage and low-frequency noise characteristics of structures with porous silicon layers exposed to different gases', (2007a) *Physica E*. **38**, 160–3.

Mkhitaryan, Z. H., Shatveryan, A. A., Aroutiounian, V. M., Ghulinyan, M. and Pavesi, L. 'Low-frequency noise in structures with porous silicon in different gas media', (2007b) *Phys. stat. sol.* (c). **4**, 2063–7.

Moretti, L., De Stefano, L. and Rendina, I. J. 'Quantitative analysis of capillary condensation in fractal-like porous silicon nanostructures', (2007) *Appl. Phys.* **101**, 024309.

Moshnikov, V. A., Gracheva, I., Lenshin, A. S., Spivak, Y. M., Anchkov, M. G., Kuznetsov, V. V. and Olchowik, J. M. 'Porous silicon with embedded metal oxides for gas sensing applications', (2012) *J. Non-Cryst. Solids*, **358**, 590–5.

Naderi, N., Hashim, M. R. and Amran, T. S. T. 'Enhanced physical properties of porous silicon for improved hydrogen gas sensing', (2012) *Superlattice. Microst.* **51**, 626–636.

© Woodhead Publishing Limited, 2013

Nikfarjam, A., Iraji Zad, A., Razi, F. and Mortazavi, S. 'Mortazavi Fabrication of gas ionization sensor using carbon nanotube arrays grown on porous silicon substrate', (2010) *Sensor. Actuat. A.* **162**, 24–8.

Ninno, D., Iadonisia, G., Buonocore, F., Cantele, G., Di Francia, G. 'A theory for semiconductor nanostructure reactivity to gas environment', (2000) *Sensor. Actuat. B.* **68**, 17–21.

Ong, P. and Levitsky, I. A. 'Fluorescent gas sensors based on nanoporous optical resonators (microcavities) infiltrated with sensory emissive polymers', (2010) *IEEE Sensor. Conf.* 75–8.

Ossicini, S., Pavesi, L. and Priolo, F. 'Light Emitting Silicon for Microphotonics, STMP 194', (2003) *Light Emitting Silicon for Microphotonics, STMP*. **194**, 75–122, Springer-Verlag Berlin Heidelberg.

Ozdemir, S. and Cole, J. L. 'The potential of porous silicon gas sensors', (2007) *Curr. Opin. Solid State Mater. Sci.* **11**, 92–100.

Ozdemir, S. and Cole, J. L. 'A phosphine detection matrix using nanostructure modified porous silicon gas sensors', (2010) *Sensor. Actuat. B.* **151**, 274–80.

Pancheri, L., Oton, C. J., Gabbuzo, Z., Soncini, G. and Pavesi, L. 'Very sensitive porous silicon NO_2 sensor', (2003) *Sensor. Actuat. B.* **89**, 237–9.

Park, S., Seo, D., Kim, Y. and Lee, K. 'Organic vapor detection using a color-difference image technique for distributed Bragg reflector structured porous silicon', (2010) *Sensor. Actuat. B.* **147**, 775–9.

Peng, K., Wang, X. and Lee, Sh. 'Gas sensing properties of single crystalline porous silicon nanowires', (2009) *Appl. Phys. Lett.* **95**, 243112 (3 pages).

Paremuzyan, V. G. and Aroutiounian, V. M. 'Power density of noise spectrum in gas sensors', (2012a) *Proc. State Engng. Univ. Armenia*, **15**, 62–69.

Paremuzyan, V. G. and Aroutiounian, V. M. 'Influence of reduction in the heat of adsorption on noise characteristics of sensors', (2012b) *Sensor. Trans. J.* **137**, 95–103.

Pavesi, L. and Lockwood, D. J. (eds.). (2004) 'Silicon photonics', *Topics Appl. Phys*. **94**, 1–52.

Prabakaran, R., Silva, L., Fortunato, E., Martins, R. and Ferreira, I. 'Investigation of hydrocarbon coated porous silicon using PECVD technique to detect CO2 gas', (2008) *J. Non-Cryst. Solids*, **354**, 2610–14.

Prokes, S. M. (1993) *Appl. Phys. Lett.* **62**, 3244–6.

Razi, F., Iraji, Zad A. and Rahimi, F. 'Investigation of hydrogen sensing properties and aging effects of Schottky like Pd/Porous Si', (2010) *Sensor. Actuat. B*. **146**, 53–60.

Ruminski, A. M., Moore, M. M. and Sailor, M. J. (2008) *Adv. Funct. Mater.* **18**, 3418–26.

Saha, H. 'Porous Silicon Sensors- Elusive and Erudite', (2008) *Int. J. of Smart Sensing and Intelligent Systems*, **1**, 34–56.

Salem, M. S., Sailor, M. J., Fukami, K., Sakka, T. and Ogata, Y. H. 'Sensitivity of porous silicon rugate filters for chemical vapor detection', (2008) *J. Appl. Phys.* 083516 (7 pages).

Sailor, M. J. and Lee, E. J. 'Surface chemistry of luminescent silicon nanocrystals', (1997) *Adv. Mater*. **9**, 783–793.

Solntsev, V. S., Gorbanyuk, T. I., Litovchenko, V. G. and Evtukh, A. A. (2009) *Thin Solid Films*, **517**, 6202–5.

© Woodhead Publishing Limited, 2013

Stievenard, D. and Deresmes, D. 'Identification of a defect in porous silicon', (1995) *Appl. Phys. Lett.* **67**, 1570–2.

Sun, P., Hu, M., Li, M. and Ma, Sh. 'Microstructure, electrical and gas sensing properties of meso-porous silicon and macro-porous silicon', (2012) *Acta Phys.-Chim. Sin.* **28**, 489–93.

Tudisco, C., Betti, P., Motta, A., Roberta Pinalli, R., Bombaci, L., Enrico Dalcanale, E., Guglielmo, G and Condorelli, G. G. 'Cavitand-functionalized porous silicon as an active surface for organophosphorus vapor detection', (2012) *Langmuir* **28**, 1782–9.

Vashpanov, Y., Jung, J. and Kwack, K. 'Photo-EMF sensitivity of porous silicon thin layer–crystalline silicon heterojunction to ammonia adsorption sensors', (2011) *Sensors* **11**, 1321–7.

von Behren, J., van Buuren, T., Zacharias, M., Chinowitz, E. H. and Fauchet, P. M. 'Quantum conement in nanoscale Si for correlation of size with band gap and luminescence', (1998) *Solid State Commun.* **105**, 317–20.

Vrkoslav, V., Jelinek, J., Trojan, T., Jindrich, T. J. and Dian, J. 'Porous silicon with b-cyclodextrin modified surface for photoluminescence sensing of organic molecules in gas and liquid phase', (2007) *Physica E*. **38**, 200–4.

Yerokhov, V. Yu. and Melnyk I. I. 'Porous silicon in solar cell structures', (1999) *Renew. Sust. Energ. Rev.* **3**, 291–322.

© Woodhead Publishing Limited, 2013

13

Metal oxide semiconductor gas sensors in environmental monitoring

R. BINIONS, Queen Mary, University of London, UK and
A. J. T. NAIK, University College London, UK

DOI: 10.1533/9780857098665.4.433

Abstract: Environmental sustainability is a pressing and growing problem due to issues such as climate change, pollution and disturbances associated with biodiversity. A major cause of these environmental threats is pollutants in the atmosphere. In this chapter, we give a general outline of how metal oxide gas sensors can be prepared and how they have been used to monitor levels of environmentally important gases. We include a section on future trends which discusses some of the new approaches being used to improve the selectivity and sensitivity of metal oxide semiconductor gas sensors. Finally, we conclude with some remarks on the outlook for metal oxide semiconductor gas sensors in environmental monitoring.

Key words: metal oxide semiconductors, gas sensors, environmental monitoring, air pollution.

13.1 Introduction

Environmental sustainability is a pressing problem at the current time due to issues such as climate change, pollution and disturbances associated with biodiversity. A wide variety of organisations, such as governments, universities and industry, are working at the forefront of scientific and technological research to find solutions to these problems.

A major cause of these environmental threats are pollutants in the atmosphere, such as: carbon monoxide (CO), carbon dioxide (CO_2), nitrous oxides (NO_x), sulphurous oxides (SO_x), hydrocarbons and volatile organic compounds (VOCs), among a list of other atmospheric toxins (Akbar *et al.*, 2006; Becker *et al.*, 1999; Bourgeois *et al.*, 2003; De Wit *et al.*, 1998; Dejous *et al.*, 1995; Rapp *et al.*, 1995; Rock *et al.*, 2008; Zellers *et al.*, 1998). These gases are generated from various activities, locations and other factors which can be grouped into two categories : natural sources, and man-made or anthropogenic sources (Olivier *et al.*, 1998). Natural sources of air pollutants are lightning, soils, fires and volcanoes; anthropogenic sources incorporate

© Woodhead Publishing Limited, 2013

emissions from human activity – for example, transportation and industrial action such as power plants and landfill sites. Once the primary pollutants are in the air, they are either chemically transformed (Fay and Rosenzweig, 1980; Jenkin and Clemitshaw, 2002) (e.g. by photochemistry, oxidation, etc.) into secondary pollutants (e.g. ozone (O_3), various oxidised products and other compounds based on nitrogen and sulphur, etc.) and/or transported over larger areas by prevailing winds, vertical mixing and dispersion into the outer atmosphere. Some percentage of the pollutants are subsequently removed underground by wet or dry deposition; however, a substantial amount stays in the atmosphere adversely affecting not only human health but also natural and aquatic ecosystems.

The monitoring of the emissions of various gaseous pollutants can assist in the control, reduction or even elimination of such gases. This is imperative and will contribute significantly to environmental protection, the development of a sustainable environment and lead to a healthier well-being of the natural world. Further, monitoring may potentially enhance the efficiency of the predominant anthropogenic processes that emit, or are an indirect cause of, production of these gases.

The use of analytical instruments to detect, analyze and rate the emissions has been a convention in this field (Rock *et al.*, 2008; Yamazoe and Miura, 1995); examples include instruments such as infra-red (IR) spectroscopy, ultraviolet (UV) absorption, chemiluminescence (Yamazoe and Miura, 1995) and gas chromatography/mass spectrometry (GC/MS) (James *et al.*, 2005). These analytical techniques are associated with good limits of detection and fast response times (Akbar *et al.*, 2006; Szabo *et al.*, 2003); however, they do suffer from various disadvantages – such as maintenance requirements, as well as weight and portability issues (Akbar *et al.*, 2006). They tend to be expensive and therefore are unsuited for *in-situ* analysis or continuous operation (Rock *et al.*, 2008). Data gathering may also be time-consuming with these methods (Yamazoe and Miura, 1995), and the requirement for trained personnel to utilise the instruments and conduct analysis also limits their effectiveness (James *et al.*, 2005).

As such, the use of sensors is desirable to overcome the disadvantages of these various analytical techniques. Although sensing technology does pose various challenges in terms of implementation in an environmental monitoring context, it is a preferred choice of monitoring medium, possibly due to ease of utilisation and flexibility, low mass, cost-effective operation and, therefore, ease of *in-situ* analysis (Bourgeois *et al.*, 2003; Capone *et al.*, 2003; Rock *et al.*, 2008).

Sensors are instruments that are able to convert one form of energy to another, and are alternatively called 'transducers'. In the particular case of environmental monitoring, chemical sensors are utilised because they constitute an active chemical sensing material that is able to convert a

© Woodhead Publishing Limited, 2013

chemical interaction between itself and a target gas into an output electrical signal (James *et al.*, 2005), examples being changes in resistance, voltage, current and frequency, among others (Rock *et al.*, 2008; Wilson and Baietto, 2009).

An array of sensors is called an 'electronic nose' (e-nose) which is an electronic device associated with the ability to 'smell' (Rock *et al.*, 2008) target gases or volatiles in the atmosphere and therefore its function can be compared with that of the human nose. Electronic noses have been commercially available since the mid-1990s and have been used for the purposes of detection, discrimination and recognition of simple and complex gaseous mixtures (Bourgeois *et al.*, 2003).

There are a number of industries that currently are employing or potentially could use sensors for monitoring purposes, such as in scientific, technological and environmental industries (Bourgeois *et al.*, 2003). Research and development and utilisation of sensor technology has become an area of booming interest.

The three main elements of a sensor device constitute (Rock *et al.*, 2008): (1) a system for delivery of the sample which carries out the sampling, filtering and preconditioning of the target gas; (2) a system for the detection of the sample, consisting of the sensor array which converts the chemical interaction into an electrical signal; and (3) a computing system which is able to evaluate the data and convert it into an interpretable format. The most important element to be discussed here is the detection system, which is the use of metal oxide semiconductor gas sensors. This type of sensor has specific advantages over others, being robust and resilient, cheap and easily mass-produced.

The past 40 years have seen an incredible research initiative in the development of metal oxide semiconductor gas sensors (Rickerby and Serventi, 2010), which includes production of innovative materials and associated deposition technologies, studies into the mechanistic principles of gas sensing and improved efficiency of sensors through changes to the overall architecture of the device. This initiative has been driven by several fundamental requirements for good quality and efficient gas-sensing devices, which are: excellent sensitivities and selectivity; fast and efficient response and recovery times; low temperatures of operation, or even the ability to function independent of temperature which would lead to efficient power utilisation; stability in the performance of the sensor; and a low consumption of the chemically sensitive layer which would allow the sensor to be utilised a multiple number of times for measurements (Wang and Yeow, 2009). Sensitivity, in particular, is very important, as many of the pollutants to be detected are present in the surrounding environment in minimal concentrations (Yamazoe *et al.*, 2003). Other factors that need to be taken into account when designing a sensor are its size, and its resilience and robust nature in

© Woodhead Publishing Limited, 2013

the various environmental conditions in which it may be used (Bourgeois *et al.*, 2003).

This chapter will report on aspects of the current state of research on metal oxide semiconductor gas sensors and explore various applications of these devices in environmental monitoring. Manufacturing and synthesis methods will initially be discussed, followed by a more in-depth look at the use of metal oxide gas sensors for environmental monitoring purposes, with a particular focus on CO, CO_2 and NOx gases. The chapter will then discuss future trends, including new synthetic methods, the use of transformation layers and next generation sensors for use in e-nose technology (Rock *et al.*, 2008). To conclude, a discussion on the future research and development of chemical gas sensors, especially in terms of novel materials and sensor fabrication, will be presented, together with a section containing further sources of information.

13.2 Sensor synthesis methods

In this section we examine the factors that influence sensor design and explore some of the sensor fabrication methods that are widely employed in sensor synthesis making a critical comparison between them.

13.2.1 Factors influencing sensor design

Many factors must be considered when designing new metal oxide semiconductor gas sensors: such as whether the sensor material is sensitive and specific to the analyte gas in question, and whether the sensitivity of the proposed sensor material is appropriate for the desired application. The same gas sensor may not be appropriate for use in two different environments. For example, a CO_2 sensor for the inside of a car exhaust should be designed for high concentrations, whereas one to be used at the roadside should be far more sensitive to CO_2 in lower concentrations. Such a CO_2 sensor would not be sufficiently accurate to register concentration changes of 10 ppm if its sensitive range were 1000–10 000 ppm. Other gases present in the surrounding environment may also affect the sensor gas response. It is well-known that certain gases, such as water or ozone (Fine *et al.*, 2010), can change the charge carrier concentration of the metal oxide semiconductor sensor despite not being the target analyte. A sensor in a photocopying room, for example, might give anomalous results because the concentration of ozone is elevated in such an environment. The ozone gas may interact with the film, nullifying or increasing the sensor response. In this case, it would be necessary either to select a material that has no (or little) response to ozone, or to alter the design of the sensor to stop ozone interacting with the metal oxide semiconductor surface.

© Woodhead Publishing Limited, 2013

13.2.2 Techniques for sensor fabrication

A wide variety of fabrication methods has been used for the production of metal oxide semiconductor sensors. Several important factors must be considered when selecting a suitable production technique, such as expense, purity, and porosity and microstructure. If the films are expensive, the demand will be lowered and will have only limited applications; small changes in the material composition may have significant affects in the sensors performance. If the material is highly porous, the surface area available to the gas for interaction will be far higher, leading to a greater magnitude of response (Seiyama *et al.*, 1962). The most common techniques for making metal oxide films for use as metal oxide semiconductor gas sensors are: chemical vapour deposition (CVD), screen-printing of ceramic powders, sol-gel techniques and physical vapour deposition (PVD).

13.2.3 Screen-printing

Screen-printing is the most widely-used technique for producing metal oxide semiconductor gas sensors commercially (Shriver, 2006; Vaishanv *et al.*, 2006). Screen-printing involves pushing an ink through a patterned layer or sheet (stencil), which has the geometry that matches the substrate. The ink is essentially the metal oxide to be used well mixed into a viscous vehicle that is then printed directly onto the surface of the substrate (in this case, the electrode). Once the ink is on the surface, the print can be heated to remove the vehicle, leaving a solid material on the specific target area. Specific heat treatments can lead to great control over the porosity and microstructure of the subsequent sensor film. Figure 13.1 indicates the general form of commercial metal oxide semiconductor gas sensors.

13.2.4 Chemical vapour deposition (CVD)

In CVD, a heated substrate is exposed to a precursor or controlled mixture of precursors in the vapour phase (Binions and Kanu, 2010). The vapour then reacts or decomposes on the heated substrate, forming a film of the desired material (Fig. 13.2).

There are many examples of CVD: those that have been used for the production of metal oxide semiconductor gas sensors include atmospheric pressure CVD (APCVD), where the film synthesis is performed at or slightly above atmospheric pressure, and aerosol-assisted CVD (AACVD), where volatile or non-volatile precursors are made into an aerosol prior to deposition (Binions *et al.*, 2004; Cross and Parkin, 2003).

© Woodhead Publishing Limited, 2013

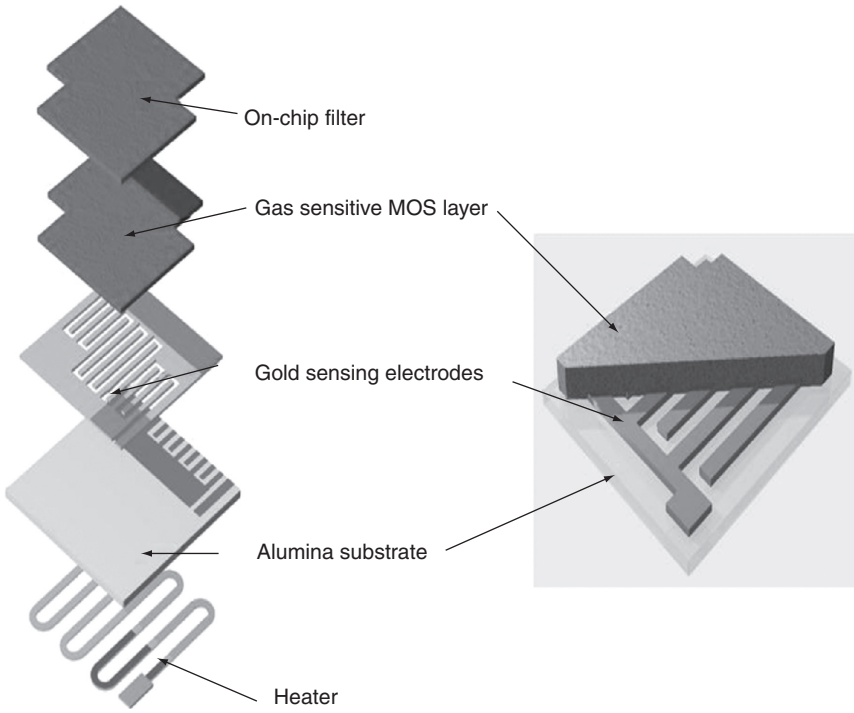

13.1 Diagram detailing the production of a gas sensitive film on a sensor substrate (diagram courtesy of Capteur Sensors and Analysers).

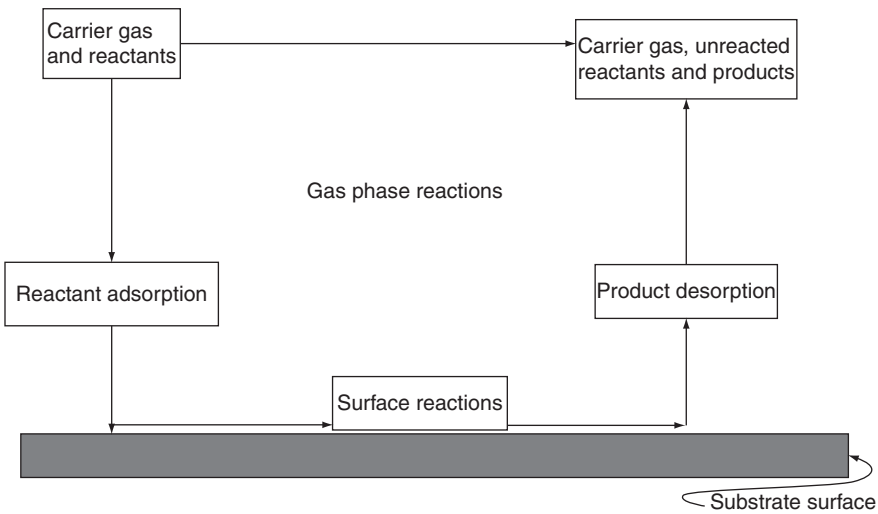

13.2 Diagram detailing the important processes in chemical vapour deposition methodologies.

© Woodhead Publishing Limited, 2013

CVD techniques can give control over important aspects of gas-sensing materials: porosity, grain size and film thickness can all be well-controlled (Guo *et al.*, 2006). The rapid speed of film growth is an advantage of the technique, with a rate of up to 1 micrometer per minute for processes that occur at atmospheric pressure.

The problem of gas phase reactions in CVD can be addressed by reducing precursor concentration – though, in doing so, the film growth rate is also reduced, or by selecting precursors that will only react with each other at the elevated temperature of the substrate surface. The selection of suitable precursors may also be an issue in CVD. Precursors must be sufficiently volatile in order to allow a significant gas phase partial pressure and sufficiently thermally stable to allow successful delivery to the heated substrate. Gas phase reactions and decomposition must be minimal, and the precursor must decompose or react on the substrate giving the desired product.

APCVD has been used to deposit films of tungsten oxide for use as gas sensors (Ashraf *et al.*, 2007a; Binions *et al.*, 2007) and the gas sensors were shown to give a good response in the presence of ethanol.

Williams and others (Shaw *et al.*, 2003, 2005) have used CVD methodologies to produce films of WO_3 and chromium titanium oxide. This work demonstrated that the desirable high porosity of the gas sensitive film is obtainable via CVD routes. The suitability for the material as a gas sensor was not tested, but the author suggested the properties might be suitable for gas-sensing.

Blackman *et al.* (Ashraf *et al.*, 2007b, 2008; Blackman and Parkin 2005) have used AACVD to produce high surface area, nano-structured tungsten oxide films with various precursors, and investigated their gas-sensing properties. Choy (2003) observes that AACVD is a useful technique when forming oxides and the aerosol is readily surrounded by oxygen, for larger-scale applications, it could be favoured as it is low cost. The area of AACVD is promising, but in industry it is proving difficult to produce a repeatable and controlled aerosol on a large scale. A suitable solution is yet to be found to tackle this problem. So, whilst the capabilities of this process in producing good films has been demonstrated in the lab, the process has not yet been adapted by industry.

13.2.5 Spray pyrolysis

Spray pyrolysis (Fig. 13.3) is a technique similar to AACVD, where the precursors for the metal oxide film are aerosolized and sprayed on to the target substrate. The deposited droplets then react on the surface when the substrate is heated, forming the desired film.

© Woodhead Publishing Limited, 2013

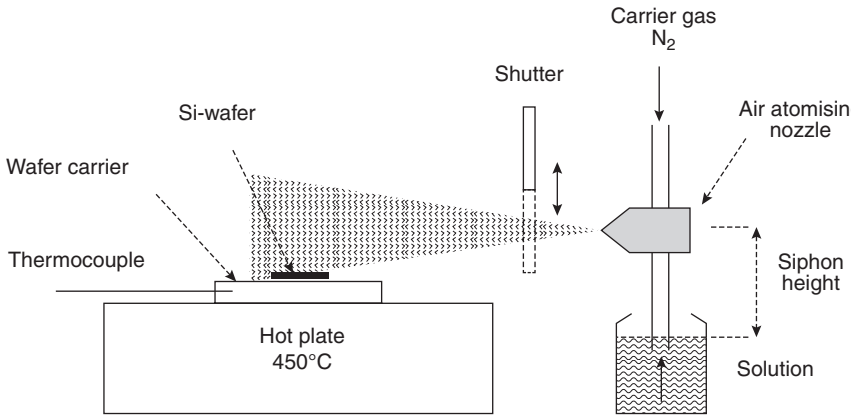

13.3 Diagram of the spray pyrolysis technique for depositing thin films.

13.2.6 Sol-gel techniques

Sol-gel has been utilised for the production of gas sensitive metal oxide semiconductor films (Goldberg *et al.*, 1994; Vincenzi *et al.*, 2000; Yadava *et al.*, 2010). A report by Khun *et al.*, uses the sol-gel method to synthesise tin dioxide particles, which then demonstrated a good response in the presence of trace amounts of ammonia gas. The sol-gel process involves the formation of a sol – a colloidal suspension of precursor species. The sol then undergoes gelation where cross-linking between the precursor species occurs. This technique can lead to new materials with unusual and unexpected properties. In the case of ceramic film formation, the sol then undergoes evaporation, giving a highly porous xerogel film. Upon heating, the film then forms a dense ceramic material upon the substrate surface.

13.2.7 Physical vapour deposition (PVD)

The material to be deposited is put into the gas phase either by sputtering (bombardment of the material by ions) or by evaporation through heating (Alhomoudi and Newaz, 2009; Boulmani *et al.*, 2007). A reactive gas may be introduced – for example, where oxygen gas reacts with sputtered metal atoms – forming a metal oxide, which is then deposited on the substrate, giving a process where there is control over the overall property of the coating. The resultant film is only bound to the substrate through physisorption.

PVD has been used to fabricate metal oxide semiconductor gas sensors widely – for example, Michel *et al.* (1995) used magnetron sputtering to produce SnO_2 films. The films were shown to have a level of conductivity and, upon exposure to hydrogen, the conductivity was shown to increase. Gupta

© Woodhead Publishing Limited, 2013

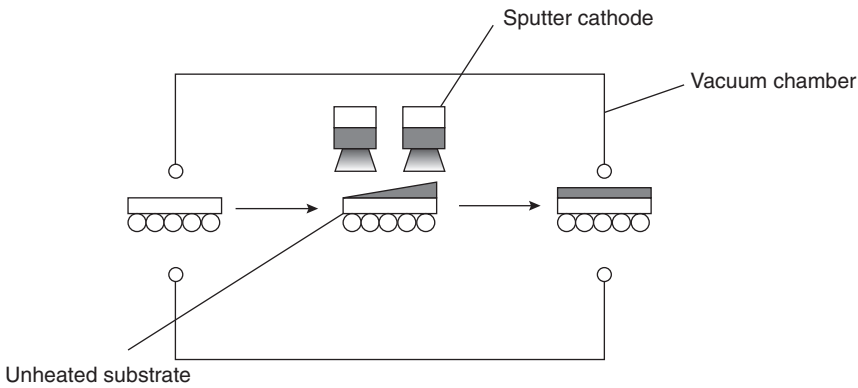

13.4 Diagram of the PVD process.

et al. (2004) produced a film of tin oxide by magnetron sputtering that demonstrated sensitivity to liquid petroleum gas. PVD is performed under vacuum and, on a large scale, this can quickly become a very expensive technique. Growth rates tend to be slow, around 10 nm an hour, making these techniques less suitable for high throughput for industrial applications. A schematic of the PVD process is presented in Fig. 13.4.

13.2.8 Comparison of synthetic techniques

There are various advantages and disadvantages for each of the synthetic techniques for the production of metal oxide semiconductor gas sensors mentioned above. PVD techniques require a vacuum or reduced pressure conditions, which are time-consuming to achieve and maintain, and require expensive equipment, which leads to an increase in production costs. Therefore, economic factors restrict the wide-scale commercial applications of PVD. The slow film growth rates associated with PVD methods make the system unsuitable for incorporation into flow manufacturing processes. However, PVD techniques allow for the more efficient use of precursors and the production of ultra-thin films with relative ease – at least, in comparison to CVD. PVD may also operate at lower temperatures; hence, it is compatible with a wide variety of substrates. Given that no chemical reaction takes place in PVD, as opposed to CVD, careful precursor selection is not a main concern; however, purity of the target is required in order to deposit non-contaminated thin films. Also, a variety of targets can be incorporated into the system without difficulty, developing multi-layer arrays.

Sol-gel methods are straightforward to perform, but time is required to establish the sol and is important for obtaining the desired product; thus, sol-gel can be a slow multi-step process. Complete and even-thickness coverage

© Woodhead Publishing Limited, 2013

of the substrate can be achieved (although this may be tricky to control over larger substrates), by using spin- or dip-coating techniques. Sol-gel also uses readily available metal alkoxide precursors, and dopants may be easily introduced by the simple addition of another precursor compound. Sol-gel processes have low processing temperatures, although the process tends to have high levels of wastage, hence reducing process efficiency.

CVD is a non-line-of-sight process (unlike PVD) with high deposition rates at relatively high temperatures. Deposited films tend to be pure and uniform with good conformal coverage, and generally exhibit good adhesion to the substrate surface. CVD tends to produce dense films which is a disadvantage for gas sensors, as the surface area of the film is reduced and the contribution from the bulk resistance is substantially increased. However, a wide variety of growth modes are achievable, including nanowires and nanoparticles, which may lower the bulk resistive contribution and increase surface area.

Binions *et al.* (2007) have compared CVD and screen-printing using gallium, antimony and tin oxides. It was found that sensors produced using CVD responded best to reducing gases at lower temperatures (450°C); screen-printed films showed a larger response at higher temperatures (500°C). Screen-printing is the simplest and most widely-used of the techniques mentioned. It allows for the production of porous films and, by modifying post-printing heat treatments, good control over grain boundaries can be achieved.

13.3 Metal oxide semiconductors in detecting environmentally important gases

In this section we review the use of metal oxide semiconductor gas sensors for the detection of environmentally important gases such as carbon monoxide, carbon dioxide, ammonia and nitrous oxides.

13.3.1 Carbon monoxide

Carbon monoxide (CO) is a colourless gas which is undetectable by the human olfactory system. It is the leading cause of poisoning in the United States and might account for more than half of fatal poisonings reported in industrialised countries (Cobb and Cetzel, 1991; Meredith, 1988; Runyan *et al.*, 2005; Varon *et al.*, 1999). CO has been shown to irreversibly bind to the iron centre of haemoglobin. This irreversible binding means that oxygen can no longer be absorbed and, at elevated levels of exposure, results in death. The source of the gas is mainly as a by-product of poorly combusted organic materials, such as petrol, oil or methane gas. CO is notorious in the

© Woodhead Publishing Limited, 2013

Table 13.1 The effects of different concentrations and exposure times of carbon monoxide on human health

Carbon monoxide concentration (ppm)	CO_{Hb} level (%)	Signs and symptoms
35	<10	Headache and dizziness within 6 to 8 hours of exposure
100	>10	Slight headache in 2 to 3 hours
200	20	Slight headache within 2 to 3 hours; loss of judgement
400	25	Frontal headache within 1 to 2 hours
800	30	Dizziness, nausea and convulsions within 45 minutes, insensible within 2 hours
1600	40	Headache, tachycardia, dizziness and nausea within 20 minutes; death within 30 minutes
3200	50	Headache dizziness and nausea in 5 to 10 minutes; death within 30 minutes
6400	60	Headache and dizziness in 1 to 2 minutes; convulsions, respiratory arrest, and death in less than 20 minutes
12800	>70	Death in less than 3 minutes

CO_{Hb}, percentage of carbon monoxide in the blood.

public eye because the home is such a susceptible place for CO poisoning to occur (Table 13.1), usually from faulty gas-powered boilers, leading to a number of deaths every year. CO concentrations are especially high in areas containing industry, where fossil fuels are combusted for energy purposes, and in cities where traffic levels are high. Existing sensors are used in homes to warn of otherwise undetectable CO. Such sensors fall in to two main categories: 'blob' sensors and electrical sensors. 'Blob' sensors are essentially a patch of a metal oxide salt that is reduced upon interaction with CO, forming carbon dioxide. The salt turns black when it is reduced, the colour change being the feature alerting the observer. Although cheap, the alerting system requires the vigilance of the observer in order to recognise the change in concentration and, given that at high concentration CO causes dizziness and confusion, the occupant may be in no condition to observe this change, particularly if the concentration of CO increases rapidly. Electronic CO sensors come in two main types: thermistor-type metal oxide detectors that detect a change in temperature when CO lands on the oxide and reacts, and an electrolytic detector that works by sensing the change in charge carriers in an electrolyte solution when CO interacts with an electrode in the device.

© Woodhead Publishing Limited, 2013

CO gas sensors have a myriad of applications, not only for home safety, but also in measuring atmospheric concentrations, in the exhaust of cars, and for process monitoring in industrial plants.

13.3.2 Carbon dioxide

Carbon dioxide (CO_2) is present in air at concentrations of 388 ppm in the Earth's atmosphere (as of January 2010, Fig. 13.1) (ESRL, 2010). CO_2 has a wide range of applications including carbonating drinks, pneumatics, fire extinguishers, lasers and refrigerants and, of course, photosynthesis; it is an essential ingredient for these processes to take place.

Most significantly, CO_2 is a well-known greenhouse gas. In the atmosphere, it absorbs blackbody infra-red radiation, causing the molecule to vibrate, a process which passes heat to its surroundings, increasing the ambient temperature. As such, if the concentration of CO_2 increases in the atmosphere, the temperature also increases. Thus, accurate and reliable sensors need to be employed to measure CO_2 concentrations. The recent increase in the concentration of CO_2 through human activity (the combustion of hydrocarbons and other carbon-containing fuels such as petrol, coal, oil, methane and kerosene with an appropriate amount of oxygen yields CO_2 and water) is helping to increase anthropogenic global warming. Sensors can measure the output of CO_2 during combustion, thus giving important real-time information as to the amount of CO_2 being produced by the activity.

Atmospheric CO_2 concentrations have risen steadily since 1958, and are expected to carry on rising as long as mankind satisfies its thirst for combusting fossil fuels (Fig. 13.5).

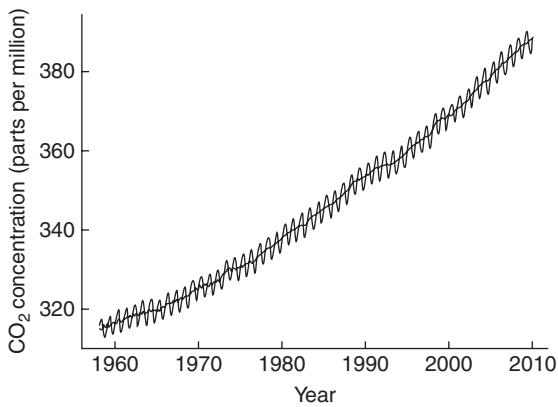

13.5 A graph depicting the steady increase in CO_2 concentrations since 1958 at the Mauna Loa Observatory (ESRL, 2010).

© Woodhead Publishing Limited, 2013

Table 13.2 The effects of different concentrations and exposure times of carbon dioxide on human health

CO_2 concentration (ppm) and exposure time	Effect on health (symptoms)
0.035%	Approximate atmospheric concentration, no noticeable effect
3.3–5.4% for 15 mins	Increased depth of breathing
7.5% for 15 mins	Feeling of an inability to breathe, increased pulse rate, headache, dizziness, sweating, restlessness, disorientation and visual distortion
3%, for over 15 hours for 6 days	Decreased night vision, colour sensitivity
10%, 1.5 mins	Eye flickering, increased muscle activity, twitching
10+%	Difficulty in breathing, impaired hearing, nausea, vomiting, a strangling sensation, sweating, loss of consciousness after 15 minutes
30%	Unconsciousness, convulsions; several deaths attributed to CO_2 at concentrations of more than 20%

Source: Tans (2010).

CO_2 can cause substantial negative health effects for humans (Table 13.2), including drowsiness and, at sufficiently high concentrations, suffocation. As such, it is highly desirable to be able to measure CO_2 in order to control indoor air quality.

13.3.3 Nitrous oxides

Nitrous oxides (NO_x) comprise a varied group of gases, the simplest form being nitric oxide (NO), then nitrogen dioxide (NO_2), nitrous oxide (N_2O), dinitrogen trioxide (N_2O_3), dinitrogen tetroxide (N_2O_4) and dinitrogen pentoxide (N_2O_5). The gases are principally formed from the combustion of fossil fuels in internal combustion engines, where the energy of the combustion reaction helps combine oxygen gas (O_2) and nitrogen gas (N_2). Nitric oxide is a well-known component of photochemical smog, combining with hydrocarbons and oxygen to form a thick cloud, typically over heavily industrialised areas. Photochemical smog, as well as the haze it produces, is extremely irritating to the eyes and can also damage plant life in the affected areas. The monitoring of the concentrations of NO in the air can be particularly useful to help environmental agencies to predict how likely smog is to form and for how long it may last.

Nitrogen dioxide is toxic upon inhalation but, unlike CO, it is easily detected by smell. However, one complicating factor of this is that exposure to a concentration of 4 ppm NO_2 gas anaesthetises the nose. This increases the possibility

© Woodhead Publishing Limited, 2013

that raised concentrations in an environment may go unnoticed, leading to potential health risks. The main risk of NO_2 is the effect on the lungs and respiratory tract. People with bronchitis or asthma are particularly sensitive to the gas, and exposure can lead to inflammation and breathing difficulties. Animals subjected to long-term exposure of NO_2 have been found to have damaged lungs (Barth *et al.*, 1995; Wegmann *et al.*, 2005), and other studies have linked the concentration of NO_2 and SO_2 to the exacerbation of conditions such as chronic bronchitis and emphysema (Ponka and Virtanen, 1994). The monitoring of the gas in environments where NO_2 is at particularly high concentrations is desirable so as to reduce the risks to human health as much as possible.

13.4 Advances in carbon monoxide sensors

Metal oxide semiconductor gas sensors have been extensively used to measure the concentration of CO in the environment. Approaches have almost exclusively focused on tin dioxide-based materials, with the focus on a variety of different scenarios.

Wiegleb and Heitbaum (1994) reported the use of metal oxide semiconductor gas sensors for monitoring NO and CO gas concentrations in automobiles. They studied the variation in CO gas concentration over an extensive period of time. SnO_2 was used to detect the change in concentration of CO (Fig. 13.6) and In_2O_3 to detect the concentration of NO. It was found that the SnO_2 sensor gave results comparable to a near infra-red (NIR) optical sensor but with a faster response time.

Barbi *et al.* (1995) developed an SnO_2-based metal oxide semiconductor gas sensor that gave a response to the presence of CO gas in concentrations as low as 10 ppm. The ideal operating temperature was found to be relatively low, at 250°C, with a measured response (R_0/R) (where R_0 is the resistance in air and R or R_g is the resistance in the test gas) of 2.2 to 20 ppm CO, and 4.1 to 100 ppm CO, giving a steady increase with concentration, indicating excellent responsivity and a useful dynamic range. Doping the material with platinum in order to improve the selectivity of the sensor led to a change in the structure. In general, the addition of platinum reduced the sensitivity of the material and also led to a slower response time compared with the original tin oxide material. The authors also demonstrated the importance of control over grain size (Fig. 13.9), in line with previous work by Yamazoe (1991). The largest responses to CO gas were found with small grain sizes, typically 20 angstroms. At such a scale length, the electrical behaviour of the grain is dominated by contributions from the surface, as the Debye length is comparable to the scale length of the material and the whole grain behaves as if it were 100% from surface. The response is also found to be large at 80 angstroms, and this is attributed to grain dominating the response behaviour, as demonstrated by the equivalent circuit model (Naisbitt *et al.*, 2006).

© Woodhead Publishing Limited, 2013

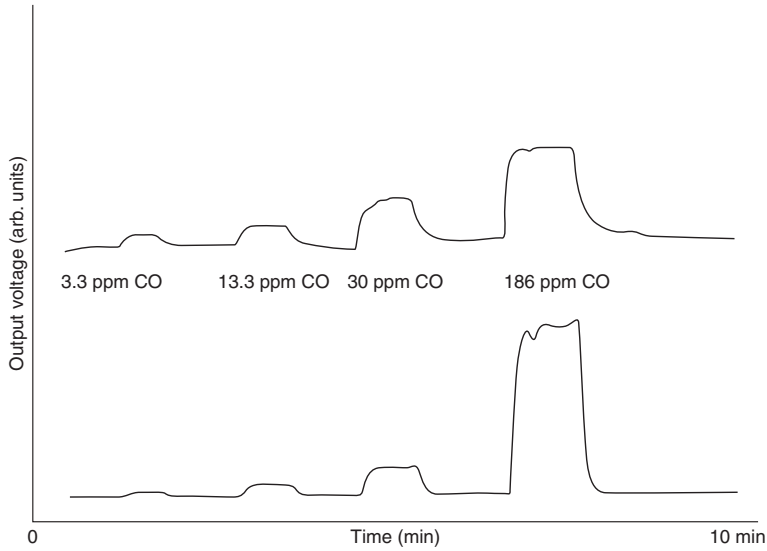

13.6 Comparison of sensor response to varying concentrations of carbon monoxide for both a SnO_2 sensor (top) and an infrared gas sensor (bottom). Reproduced with permission (Wiegleb and Heitbaum, 1994).

Various methods have been used to fabricate tin dioxide metal oxide semiconductor gas sensors. Riviere *et al.* (2003) used screen-printing to produce a tin dioxide film. The composition of the printed ink was varied. The materials showed a significant response to CO gas – typically, a resistance change of 1 log (Ohm^{-1}) to a CO concentration of 300 ppm, at an operating temperature of 500°C. Tischner *et al.* (2008) fabricated sensors using a spray pyrolysis method. The SnO_2 sensor films were between 50 and 100 nm thick and showed good gas responses between 250–400°C, detecting CO gas at concentrations as low as 5 ppm – a typical concentration found in a residential scenario. The gas response of the films was found to be dependent on the operating temperature of the sensor. At 250°C, the film showed excellent responses between 0 and 40 ppm CO gas. At higher concentrations, the response began to plateau. At an operating temperature of 400°C, the sensors response range increased to between 0 and 100 ppm CO gas. However, the sensor film was also found to be extremely sensitive to changes in levels of relative humidity (Fig. 13.7), a significant problem for real-world applications.

Various other materials have been examined for their gas-sensing properties to CO. Li *et al.* (2009) compared different phases of titanium oxide (TiO_2) films. Anatase TiO_2 was found to show an *n*-type response to the presence of CO gas. Films of the rutile material, however, exhibit *n*- and *p*-type responses depending on the operating temperature. The magnitude

© Woodhead Publishing Limited, 2013

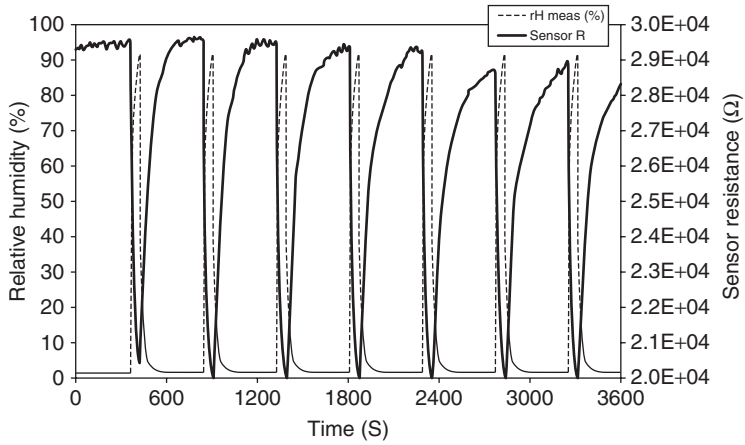

13.7 The response of the sensor to humidity (rH). Note the decrease in baseline response over time and successive introductions. Reproduced with permission (Tischner *et al.,* 2008).

of the gas responses were also found to be poor. These problems makes the use of TiO_2 an unlikely solution for sensing CO gas as the conversion temperature from anatase form to the rutile form is low, around 600°C and higher responses are desirable.

Cerium dioxide has also been investigated by Izu *et al.* (2009), They performed various sintering surveys and gas response studies, but always found that the response to low concentrations was poor and high operating temperatures were required, typically 450°C or higher. Cerium dioxide films have also been fabricated using electron beam evaporation (Durrani *et al.*, 2008). The optimum operating temperature of the films was found to be 390°C; however, gas responses were also lower than desirable and response times were unacceptably slow. Tin dioxide remains the leading material for CO sensing.

13.5 Advances in carbon dioxide sensors

Various materials and fabrication methods have been investigated to produce metal oxide semiconductor CO_2 gas sensors. The most widely-used materials based on tin dioxide have largely been found to be insufficient for the task. Typically, poor response behaviour to CO_2 and high cross-sensitivity are major problems for tin dioxide-based materials. Examples are work conducted by Patel *et al.* (1994) and Hoefer *et al.* (1994). The sensors in the study by Hoefer *et al.* showed a marked response in the concentration range of 1000–10 000 ppm CO_2 at an operating temperature of 270°C. The most significant responses were above CO_2 concentrations of 5000 ppm but,

© Woodhead Publishing Limited, 2013

overall, the response behaviour is poor and the sensor can only effectively differentiate between large concentrations (thousands of parts per million), limiting its real-world application.

The best results for CO_2 detection have been obtained with materials based on lanthanum or barium, both of which have significant natural affinities for CO_2 and are often found as carbonates in nature. Kim *et al.* (2000) studied the precursor $LaCl_3.7H_2O$. They performed various heat treatments, heating the material within a range of temperatures (400–1200°C), and as such created different compositions. They found that the material adopted a composition of LaOCl when heated to around 400°C. Above this temperature, La_2O_3–LaOCl mixtures were found; above 800°C, La_2O_3 alone was found. The material was subsequently deposited on top of an SnO_2 thick film and the gas response behaviour investigated. The highest sensitivity to CO_2 was found to be a response value of 1.37 (R/R_0). The gas response was found to be linear between CO_2 concentrations of 0–2500 ppm (Fig. 13.8). Significant investigations into the cross sensitivity of the material have yet to be performed. It was found that the sensor film needed to be heat-treated at 1000°C in order to achieve optimum response behaviour; such high

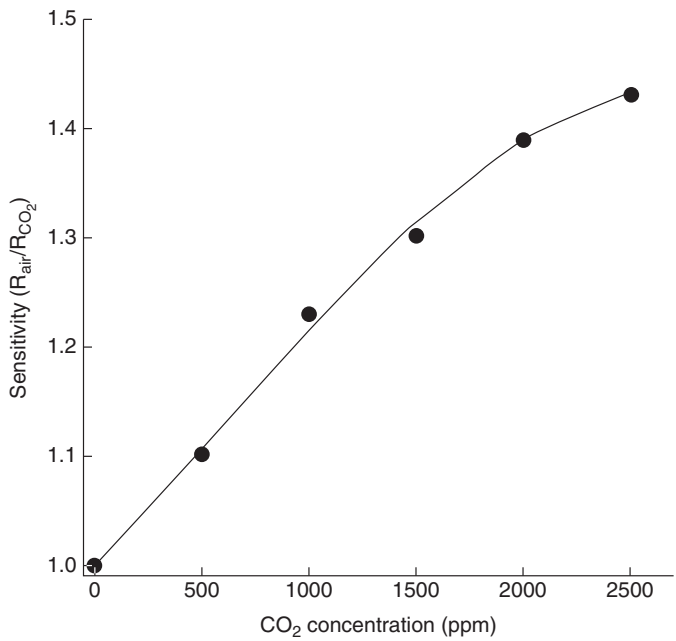

13.8 The gas response change of the lanthanum based film to CO_2 on increasing concentration (temperature unreported). Reproduced with permission (Kim *et al.,* 2000).

© Woodhead Publishing Limited, 2013

temperatures are undesirable, as few sensor substrates can withstand such temperatures.

Marsal *et al.* (2003a) also reported on the fabrication of a CO_2 sensor based on LaOCl. The films were made by screen-printing. The resulting sensor showed a gas response of 3.4 to 2 500 ppm CO_2 at an operating temperature of 260°C. The authors also tested the response to CO and found that their sensor was more responsive to CO_2 than to CO by a factor of 3.

Lee and Meyer (2000) produced microcrystalline films with thicknesses of 2–5 μm made from $LaCl_3$ doped $BaTiO_3$ that showed a good response to CO_2 gas. A paste was screen-printed onto a sensor substrate surface and then dried at 80°C. The substrate was subsequently heated at 750°C for 20 minutes. Materials with a range of compositions were tested in air with 1% CO_2 content. The greatest response was obtained with $BaTiO_3$- with 10 weight percent $LaCl_3$ at an operating temperature of 550°C. Sensor responses were also found to be rapid under these conditions (Fig. 13.9).

Composite materials containing $BaTiO_3$, SnO_2 and La_2O_3 have also been investigated by Marsal *et al.* (2003b). Undoped tin dioxide showed a good response to CO_2 at 100°C (all be it with high cross-sensitivity); other doped materials showed better responses, but required higher operating temperatures – typically in the region of 400°C. The highest response was obtained with $BaTiO_3$–CuO–La_2O_3, which performed best at 550°C. The percentage

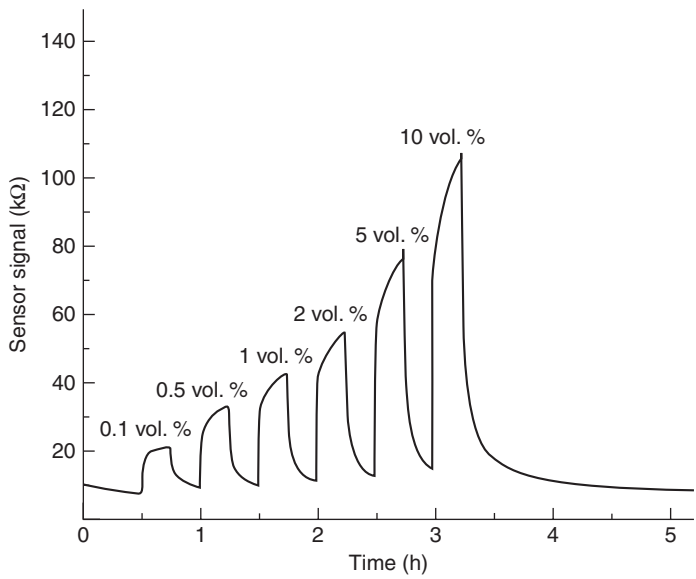

13.9 The effect of varying CO_2 concentration on the signal of the $BaTiO_3$ sensing material (note the baseline increase over time). Operating temperature is 550°C. Reproduced with permission (Lee and Meyer, 2000).

© Woodhead Publishing Limited, 2013

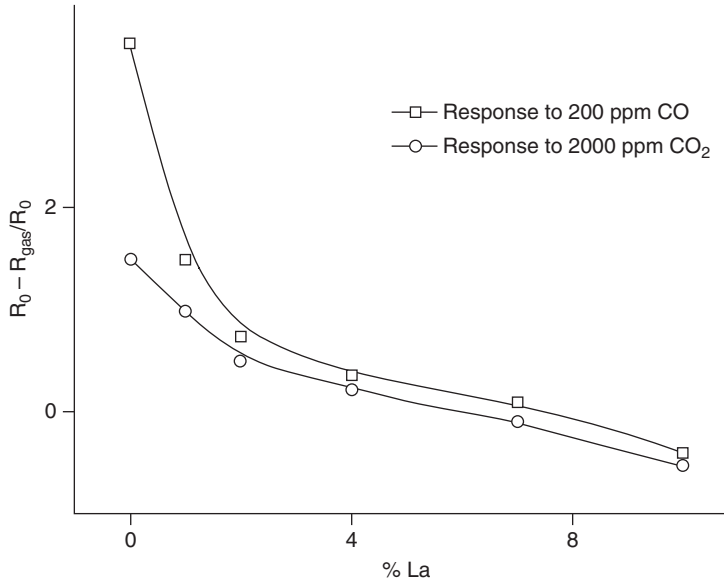

13.10 Results demonstrating the effect of changing the lanthanum content on the gas response of the SnO_2 film, also showing poor discrimination between carbon monoxide and carbon dioxide. Reproduced with permission (Marsal *et al.,* 2003b).

of lanthanum in the films was found to be critical in maximising the gas response (Fig. 13.10.).

The good sensitivity and lower operating temperature needed for LaOCl make this the most likely candidate for use in detecting CO_2 gas. However, the material is fairly unstable, converting to La_2O_3 at temperatures of 400°C and higher. The material is also difficult to prepare in large quantities and has various air sensitive intermediaries.

$Nd_2O_2CO_3$ (a metal oxide carbonate) has also been reported as a strong candidate for a CO_2 sensor (Djerdj *et al.*, 2009) and gives an impressive response of 7.5 to 3000 ppm CO_2 at an operating temperature of 350°C in 50% relative humidity air. The material also displays an impressive dynamic with sub-100 ppm concentrations of CO_2 being readily detectable. However, the authors do not comment on the long-term stability of the material; although it is well-known that oxides of the lanthanide metals are the most thermodynamically stable.

Recently, Binions *et al.* (Cavanagh and Binions, 2011; Cavanagh *et al.*, 2012) have developed two new barium-based materials for CO_2 detection. $BaSnO_3$ was screen-printed directly onto a sensor substrate and found to give a large response to 2000 ppm pulses of CO_2 at an operating temperature of 500°C. The cross-sensitivity of the sensors was tested

© Woodhead Publishing Limited, 2013

against CO and ethanol, and it was found that a preferential response to CO_2 was obtained. The same group also investigated a barium tungstate material (Cavanagh and Binions, 2011) which gave a response of 5.8 to a 2500 ppm pulse of CO_2 at an operating temperature of 450°C. The authors noted that increased values of relative humidity enhanced the gas response to CO_2 in contrast to previous work (Lee and Meyer, 2000; Mizuno, *et al.*, 1993).

13.6 Advances in nitrogen oxides sensors

Tungsten trioxide has been repeatedly demonstrated to be the most sensitive material to a variety of nitrogen oxides – NO_2 and NO, in particular. The vast bulk of the literature focuses on investigating WO_3-based materials using a variety of fabrication techniques.

Akiyama (1991) produced a sintered film of WO_3 which was found to be very sensitive to both NO and NO_2 gases. The sensor was most responsive to the presence of 200 ppm NO gas at an operating temperature of 200°C. But when sensing NO_2 gas, the sensor showed the greatest response at an operating temperature of 300°C. It was noted that in both cases the sensors had a very rapid recovery rate. When cross-sensitivity tested against gases such as CO, hydrogen and methane, the sensor showed extremely low responses, indicating that these sensors were able to discriminate between gases.

Tamaki *et al.* (1994) investigated the effects of grain size on the response of a WO_3 sensor. The crystallite sizes ranged between 16 and 57 nm. Varying the size of the grains caused the response of the material to the target gases to vary (Fig. 13.11). A large increase in the gas response to both NO and NO_2 was noted where the grain size was 25 nm or less.

Cross-sensitivity experiments conducted by Cantalini *et al.* (1996) indicated that, whilst poor gas responses were observed in the presence of CO or methane, ethanol and water did cause a gas response. It was found that different material-annealing temperatures affected the susceptibility of the films to cross-contaminates.

Chung *et al.* (1999) fabricated thick-film sensors based on WO_3 using screen-printing. The ink was formed from ball milling WO_3 powder with ethanol for 24 hours. The sensors were dried and fired in a furnace for one hour at 600°C, 700°C and 800°C. The resulting films were found to be 30 μm in thickness. The gas-sensing properties of the films were investigated at an operating temperature of 100°C. Those sensors fired at 700°C showed rapid response times, good sensitivity and good recovery times. The sensors fired at 800°C, had an increased film resistance, interaction with the analyte gas was poor and the signal-to-noise ratio was found to be bad; the authors attributed this to a change of phase in the material (Fig. 13.12).

© Woodhead Publishing Limited, 2013

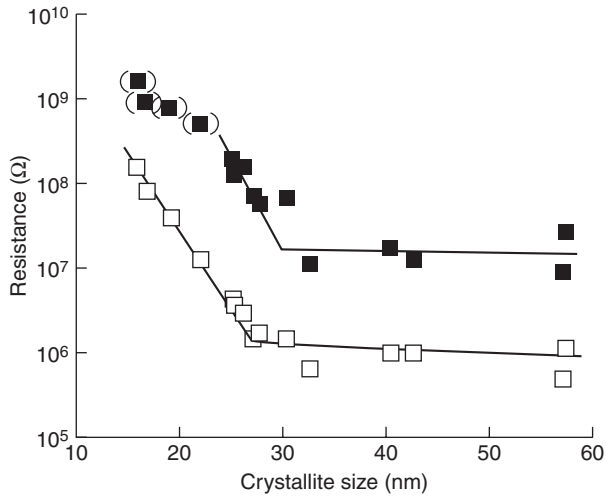

13.11 The variation in resistance according to WO_3 crystallite size. Reprinted with permission from *J. Electrochem. Soc.*, **141**, 2207 (1994). Copyright 1994, The Electrochemical Society (Tamaki *et al.,* 1994).

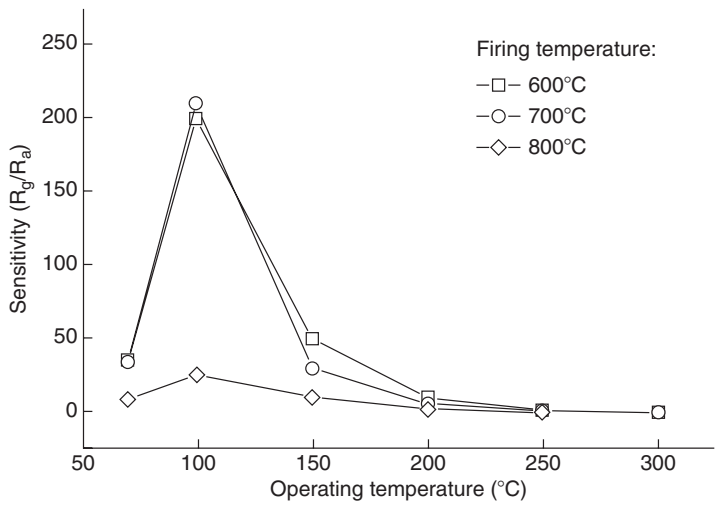

13.12 Demonstrating the effect of firing temperature on the responsivity of the material. Reproduced with permission (Chung *et al.,* 1999).

Heat treatment in 40–50% oxygen atmospheres gave the highest sensitivity; control of oxygen content in the film was shown to be important in optimising the response behaviour of WO_3 and reducing the required operating temperature.

© Woodhead Publishing Limited, 2013

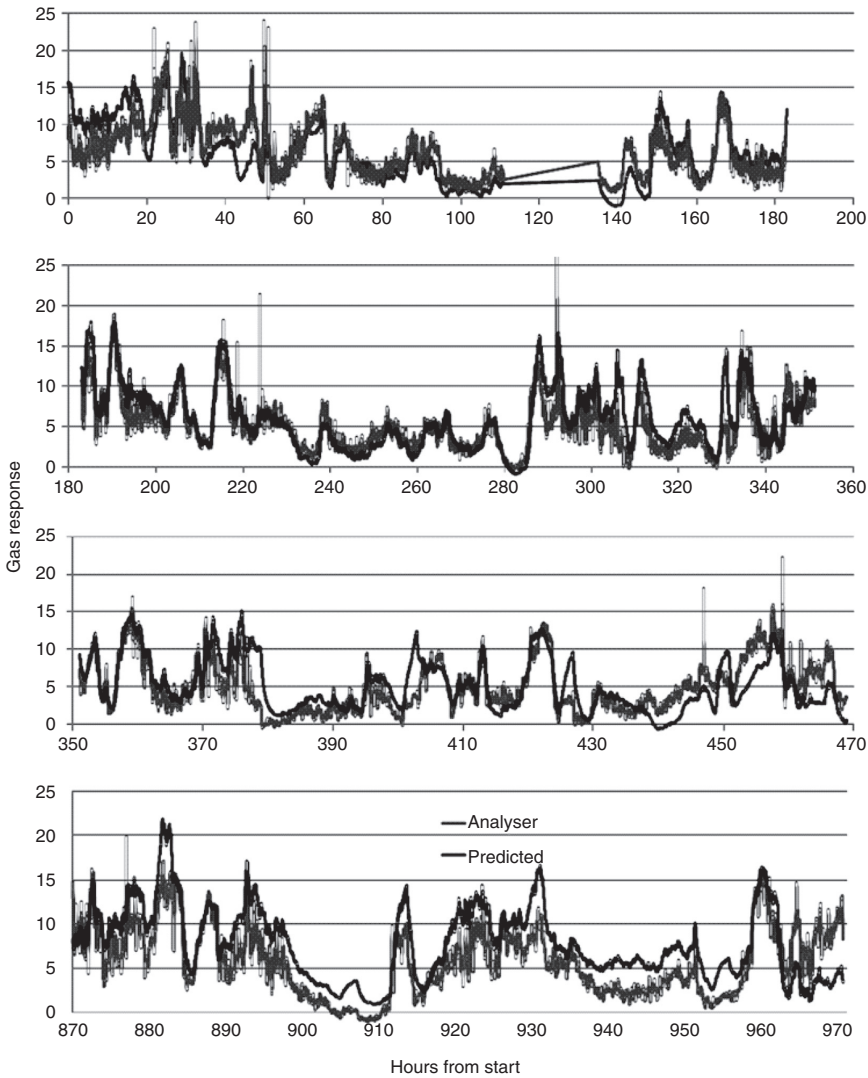

13.13 Data plots comparing the responses of chemiluminescence and semiconductor sensors. Adapted from Williams (2009).

The development of a sensor for ozone (O_3) and NO_2 with measurable responses to less than 10 ppb was reported by Williams (2009). The sensor is based on a film of tungsten oxide (WO_3) of ~90 μm thickness screen-printed on inter-digitated gold electrodes. The author reported that the sensitivity and selectivity of the sensor is strongly related to maintaining a consistent

© Woodhead Publishing Limited, 2013

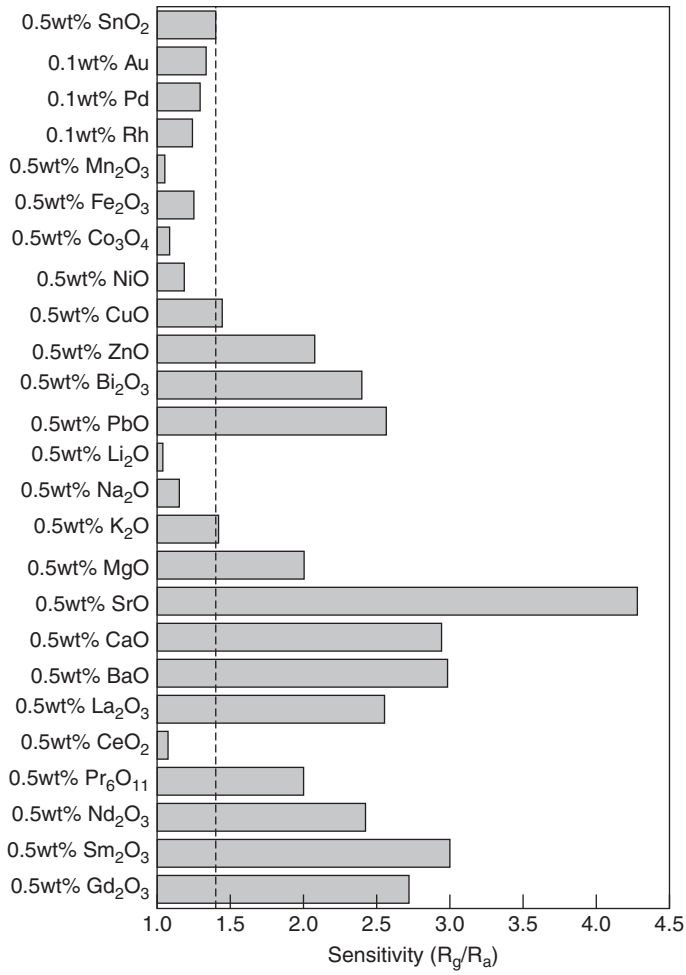

13.14 The effect of doping the material with various oxides on the responsivity of SnO_2 to N_2O gas. Reproduced with permission (Kanazawa *et al.,* 2001).

operating temperature. The response times of the sensors were found to be rapid, and the sensors exhibited a linear response between gas concentration and sensor resistance, with an error of ±2 ppb when compared with a chemiluminescence instrument. The gas response of the tungsten trioxide sensor was tracked along with the reference system over monthly periods, and showed good agreement with the reference system. Williams then compared the results between the chemiluminescence sensor and the tungsten sensor, finding the two systems to be virtually equal in response. The equality suggests that metal oxide sensors could be preferable, as the sensors are

© Woodhead Publishing Limited, 2013

far cheaper than their chemiluminescence analogues with similar response patterns (Fig. 13.13).

Much less attention has been paid to other nitrogen oxides – particularly N_2O, which has been implicated as a greenhouse gas. Kanazawa *et al.* (2001) conducted a survey of metal oxide semiconductor sensors to investigate the detection of N_2O, principally for medical purposes (Fig. 13.14). The authors first examined pure oxides on their own, with most oxides showing little or no gas response, although SnO_2, WO_3 and ZnO all gave responses at an operating temperature of 450°C. The authors then doped SnO_2, the best material with varying other metal oxides, and found that the material doped with 0.5 (by mass) SrO gave a sensor with an increased response (R/R_0) of 4.25, compared with the original 1.66. This material shows promise as an N_2O sensor.

13.7 Future trends

In this section we explore some of the latest trends in gas sensor synthesis and modification. We consider how these innovations may help improve sensor sensitivity, selectivity and speed of response.

13.7.1 Electric fields and chemical vapour deposition

The gas sensor substrates to be used have inter-digitated electrodes, which allow CVD reactions with an electric field parallel to the substrate to be set up. The electrode array comprises of gold electrode 'fingers' 100 microns wide and 10 microns thick. Typically, the electrode gap is 40 microns, though a variety of substrates with different electrode gaps have been used (40, 80 and 150 microns).

The effect of an electric field in chemical vapour deposition reactions of any kind is largely unknown; Williams (1991) noted, whilst trying to follow WO_3 film growth from an aerosol-assisted chemical vapour deposition (AACVD) using impedance measurements, that the bias of the measuring circuit led to a change in film microstructure (Shaw *et al.*, 2005). We have previously reported how electric fields in the deposition of vanadium oxides can substantially alter microstructure (Crane *et al.*, 2011; Warwick and Binions, 2011; Warwick *et al.*, 2011), including a dramatic reduction in crystallite size.

The sensor substrates can easily be incorporated into pre-existing deposition equipment (Fig. 13.15a). This technique has led to the production of fibrous growth and high surface area morphologies (Fig. 13.15b). This

© Woodhead Publishing Limited, 2013

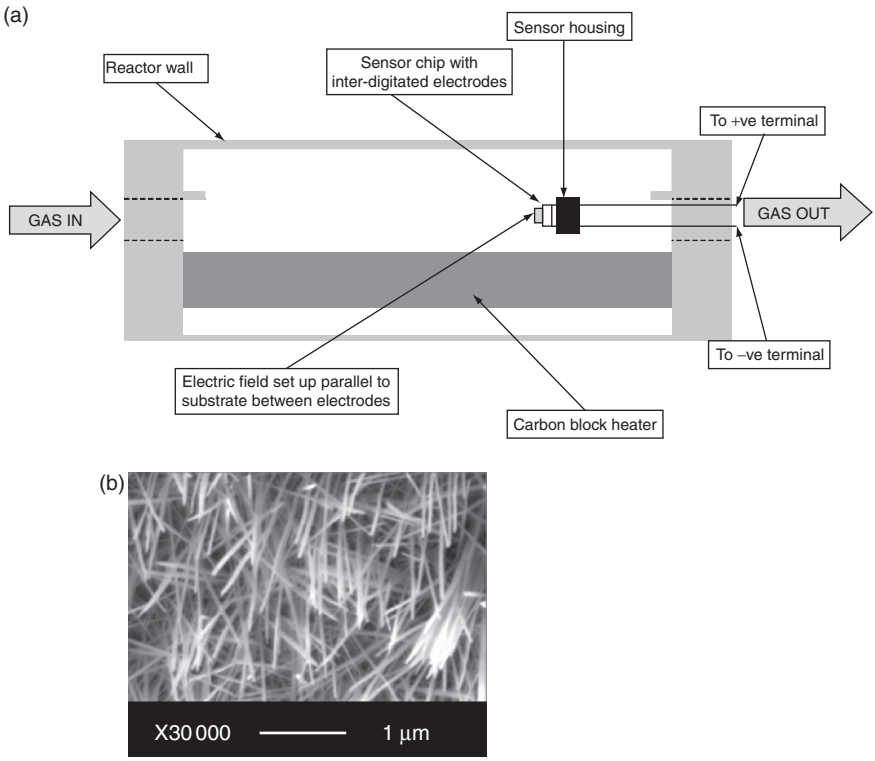

13.15 (a) Diagram illustrating the CVD reactor design used in the production of sensors using electric field CVD; (b) example morphology of tungsten trioxide thin films grown on sensor substrates from the electric field CVD reaction of tungsten hexaphenoxide at 600°C with an applied electric field.

indicates the suitability of this method for the preparation of next generation metal oxide semiconductor devices.

Titanium dioxide sensors have also been grown using this method. The sensors grown without an applied electric field (Fig. 13.16A) responded quickly to ethanol and rapidly saturated, achieving a steady state (Naisbitt *et al.*, 2006; Williams, 1999). When the ethanol flow was stopped, the response dropped to near baseline level and then tailed off more slowly to the baseline. Sample B (Fig. 13.16B), grown with an applied field of 1.11×10^4 Vm^{-1}, also displayed similar gas response characteristics, although the magnitude of response was almost double that of the sensor grown without an electric field (Fig. 13.16A).

© Woodhead Publishing Limited, 2013

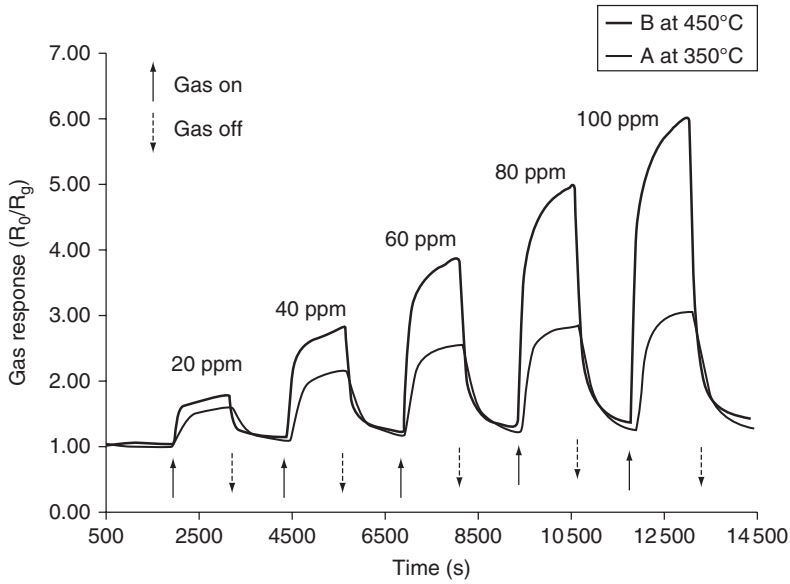

13.16 Gas response (R_0/R_g) of TiO_2 sensors (samples A and B) on exposure to differing concentrations of ethanol in flowing air over time at the optimum sensor operating temperature.

13.7.2 Zeolite modified sensors

Zeolites are porous aluminosilicate cage-like structures that are able to accommodate cations such as Na^+, Mg^+, Mg^{2+} and small molecules such as ethanol etc. These species are typically contained within a large three-dimensional framework, with external pore sizes usually ranging from 4–12Å. The oxygen atoms in the structure may be negatively charged due to substitution of silicon with aluminium; this charge can be used to counterbalance other species, most commonly cations such as Na^+ or H^+. Due to the pore structure and ability to host metal ions, zeolites can behave as selective catalysts and have been demonstrated to be capable of discriminating between small gaseous molecules on the basis of size and shape, allowing some gases into their structure, whilst preventing others from entering. Further to this, zeolites can also behave in a chromatographic manner as each zeolite framework has specific diffusion characteristics. Therefore, a mixture of gases may enter the zeolite pore but, because the zeolite framework has different binding strengths to the gaseous molecules, this leads to a difference in diffusion speed of the molecules through the zeolites. The zeolite may also be able to perform a catalytic transformation involving the target gas, which may lead to the production of one or more molecules to which the sensor layer may be more or less sensitive. In the ideal case, any catalytic reaction is specific to

© Woodhead Publishing Limited, 2013

a particular target analyte and leads to the production of multiple species to which the sensor element is more sensitive, leading to a large enhancement in response signal for a given analyte with no chance of cross-sensitivity.

Recent work (Azad *et al.*, 1992; Binions *et al.*, 2009, 2011; Dubbe *et al.*, 2006; Fischerauer *et al.*, 2011; Fong *et al.*, 2007; Mann *et al.*, 2005, 2007; Morrison, 1987; Naisbitt *et al.*, 2006; Sahana *et al.*, 2008; Sahner *et al.*, 2008; Satsuma *et al.*, 2011) demonstrates that it is possible to use zeolites as transformation layers to improve both the gas response characteristics and selectivity of metal oxide semiconductor gas sensors. Figure 13.17 gives an example of gas response to NO_2 for a standard screen-printed tungsten oxide sensor and other sensors that have been modified with an over-layer of various other zeolites. As can be seen from Figure 13.17, only one of the modified sensors gives a considerably larger gas response than the unmodified sensor; this is attributed to a catalytic reaction taking place within the zeolites pores. This sensor also proves to be more selective as the zeolite

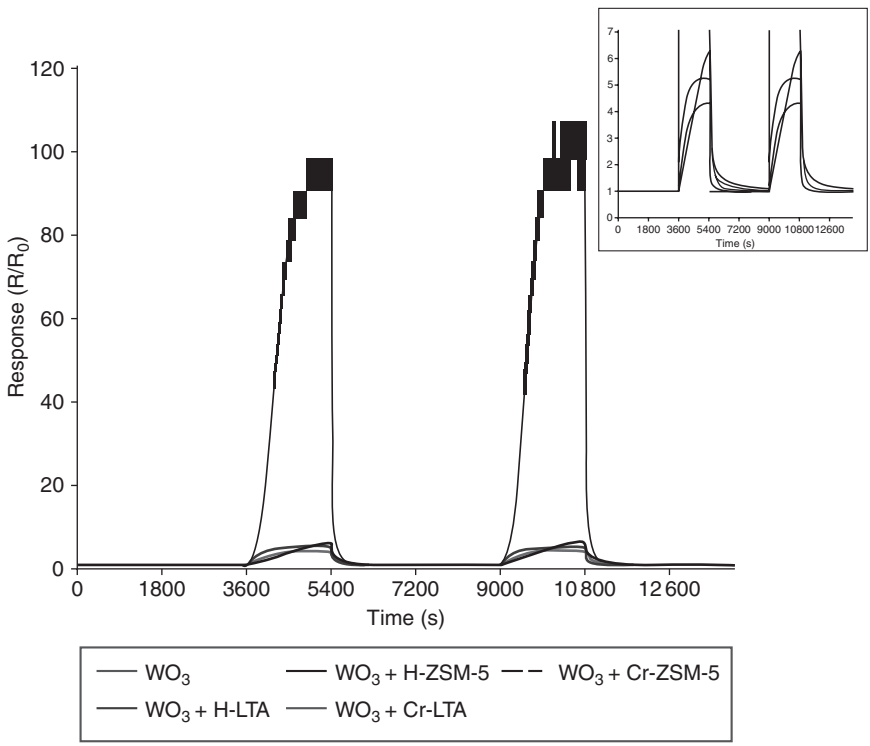

13.17 Resistive response of WO_3 sensors to 400 ppb NO_2 in dry air at an operating temperature of 350°C. Inset shows magnified data of sensor response excluding the WO_3 + H-ZSM-5 sensor. Reproduced with permission (Varsani *et al.,* 2011).

© Woodhead Publishing Limited, 2013

layer also acts as a size and shape selective filter for the sensing element. Essentially, this excludes potential interferents such as larger hydrocarbon molecules, branched alcohols etc., from reaching the sensor element and disrupting the NO_2 response (Varsani *et al.*, 2011).

13.8 Conclusion

The development of semiconducting metal oxides as gas sensors has accelerated dramatically over the past 20 years. We have tried to show that these sensors are increasingly being applied to the monitoring of environmentally important gases. Metal oxide semiconductor sensors have been shown to be sensitive to a large range of gases, with excellent responses varying with both target gas concentration and device operating temperature. These properties can be tailored in the specific environment in which the sensor is to be used by understanding the material science involved. Advances have been made in the understanding of materials chemistry and processing for sensors such as doping, deposition temperatures and annealing temperatures. These have been shown to have a profound effect on the material structure and subsequent gas-sensing properties of the sensors. Modification of the surface by selective and catalytic materials such as zeolites is an important development, and shows a further way in which materials science can be used to further improve the specificity and response to a target gas, whilst making sure the response of the film is not disrupted by a competing gas, or humidity. New materials and techniques continue to be developed to push the abilities and properties of gas sensors. Currently, metal oxide semiconductor sensors find limited commercial use; other types of sensor are still favoured for many applications. However, with recent advances, their properties, coupled with their relative low cost, will lead to them becoming ever more important tools in environmental monitoring.

13.9 Sources of further information and advice

The Gas Analysis and Sensors Group (www.gasg.org.uk) is an excellent organisation, bringing together a wide variety of industry, academic and consultant groups. Consultants, in particular, are a useful source of information; for example, Robert Bogue & Partners have produced a number of publications and directories summarising the important contributions groups have made to the field of gas-sensing in the UK and Europe. Various other societies are focused, or have divisions focused, on sensors and their applications – for example, the Electrochemical Society, the Institute for Electronic and Electrical Engineers and the International Society for Chemical Sensing. There are also a number of trade associations such as the AMA Association for Sensor Technology that are useful sources of information.

© Woodhead Publishing Limited, 2013

13.10 References

Akbar, S., Dutta, P. and Lee, C. H. (2006) High-temperature ceramic gas sensors: A review. *International Journal of Applied Ceramic Technology* **3**, 302–11.

Akiyama, M. (1991) Tungsten Oxide-Based Semiconductor Sensor Highly Sensitive to NO and NO_2. *Chemistry Letters* **20**, 1611.

Alhomoudi, I. A. and Newaz, G. (2009) Residual stresses and Raman shift relation in anatase TiO2 thin film. *Thin Solid Films* **517**, 4372–8.

Ashraf, S., Binions, R., Blackman, C. S. and Parkin, I. P. (2007a) The APCVD of tungsten oxide thin films from reaction of WCl6 with ethanol and results on their gas-sensing properties. *Polyhedron* **26**, 1493–8.

Ashraf, S., Blackman, C. S., Naisbitt, S. C. and Parkin, I. P. (2008) The gas-sensing properties of WO3-x thin films deposited via the atmospheric pressure chemical vapour deposition (APCVD) of WCl6 with ethanol. *Measurement Science and Technology* **19**, 025203.

Ashraf, S., Blackman, C. S., Palgrave, R. G., Naisbitt, S. C. and Parkin, I. P. (2007b) Aerosol assisted chemical vapour deposition of WO3 thin films from tungsten hexacarbonyl and their gas sensing properties. *Journal of Materials Chemistry* **17**, 3708.

Azad, A. M., Akbar, S. A., Mhaisalkar, S. G., Birkefeld, L. D. and Goto, K. S. (1992) Solid-state gas sensors. A review. *Journal of The Electrochemical Society* **139**, 3690–704.

Barbi, G. B., Santos, J. P., Serrini, P., Gibson, P. N., Horrillo, M. C. and Manes, L. (1995) Ultrafine grain-size tin-oxide films for carbon monoxide monitoring in urban environments. *Sensors and Actuators B: Chemical* **25**, 559–63.

Barth, P. J., Muller, B., Wagner, U. and Bittinger, A. (1995) Quantitative analysis of parenchymal and vascular alterations in NO2 induced lung injury in rats. *European Respiratory Journal* **8**, 1115–21.

Becker, T., Tomasi, L., Bosch-von Braunmuhl, C., Muller, G., Fagli, G. and Comini, E. (1999) Ozone detection using low-power-consumption metal-oxide gas sensors. *Sensors and Actuators a-Physical* **74**, 229–32.

Binions, R. (2007) A comparison of the gas sensing properties of solid state metal oxide semiconductor gas sensors produced by atmospheric pressure chemical vapour deposition and screen printing. *Measurement Science and Technology* **18**.

Binions, R., Afonja, A., Dungey, S., Lewis, D. E., Parkin, I. P. and Williams, D. E. (2011) Discrimination Effects in Zeolite Modified Metal Oxide Semiconductor Gas Sensors. *IEEE Sensors Journal* **11**, 1145–51.

Binions, R., Carmalt, C. J. and Parkin, I. P. (2004) Aerosol-assisted chemical vapour deposition of sodium fluoride thin films. *Thin Solid Films* **416**, 469–70.

Binions, R., Davies, H., Afonja, A., Dungey, S., Lewis, D., Williams, D. E. and Parkin, I. P. (2009) Zeolite-Modified Discriminating Gas Sensors. *Journal of the Electrochemical Society* **156**, J46–J51.

Binions, R. and Kanu, S. S. (2010) Thin films for solar control applications. *Proceedings of the Royal Society of London. Series A. Mathematical and Physical Sciences* **466**, 19–44.

Blackman, C. S. and Parkin, I. P. (2005) Atmospheric Pressure Chemical Vapor Deposition of Crystalline Monoclinic WO3 and WO3-x Thin Films from Reaction of WCl6 with O-Containing Solvents and Their Photochromic and Electrochromic Properties. *Chemistry of Materials* **17**, 1583–90.

© Woodhead Publishing Limited, 2013

Boulmani, R., Bendahan, M., Lambert-Mauriat, C., Gillet, M. and Aguir, K. (2007) Correlation between rf-sputtering parameters and WO3 sensor response towards ozone. *Sensors and Actuators B-Chemical* **125**, 622–7.

Bourgeois, W., Romain, A. C., Nicolas, J. and Stuetz, R. M. (2003) The use of sensor arrays for environmental monitoring: interests and limitations. *Journal of Environmental Monitoring* **5**, 852–60.

Cantalini, C., Pelino, M., Sun, H. T., Faccio, M., Santucci, S., Lozzi, L. and Passacantando, M. (1996) Cross sensitivity and stability of NO2 sensors from WO3 thin film. *Sensors and Actuators B: Chemical* **35**, 112–18.

Capone, S., Forleo, A., Francioso, L., Rella, R., Siciliano, P., Spadavecchia, J., Presicce, D. S. and Taurino, A. M. (2003) Solid state gas sensors: State of the art and future activities. *Journal of Optoelectronics and Advanced Materials* **5**, 1335–48.

Cavanagh, L. M. and Binions, R. (2011) BaxWOy Thick Film as a Carbon Dioxide Sensor. *Proceedings of the IEEE Sensors Conference* **2011**, 1006–9.

Cavanagh, L. M., Smith, P. and Binions, R. (2012) BaSnO3 Thick Film as a Carbon Dioxide Sensor. *Journal of The Electrochemical Society* **159**, J67–J71.

Choy, K. L. (2003) Chemical vapour deposition of coatings. *Progress in Materials Science* **48**, 57–170.

Chung, Y.-K., Kim, M.-H., Um, W.-S., Lee, H.-S., Song, J.-K., Choi, S.-C., Yi, K.-M., Lee, M.-J. and Chung, K.-W. (1999) Gas sensing properties of WO3 thick film for NO2 gas dependent on process condition. *Sensors and Actuators B: Chemical* **60**, 49–56.

Cobb, C. N. and Cetzel, C. R. (1991) Unintentional carbon monoxide related deaths in the United States 1979 through 1988. *JAMA* **266**, 659–63.

Crane, J., Warwick, M., Smith, R., Furlan, N. and Binions, R. (2011) The Application of Electric Fields to Aerosol Assisted Chemical Vapor Deposition Reactions. *Journal of The Electrochemical Society* **158**, D62–D67.

Cross, W. B. and Parkin, I. P. (2003) Aerosol assisted chemical vapour deposition of tungsten oxide films from polyoxotungstate precursors: active photocatalysts. *Chemical Communications*, 1696–7.

De Wit, M., Vanneste, E., Geise, H. J. and Nagels, L. J. (1998) Chemiresistive sensors of electrically conducting poly(2,5-thienylene vinylene) and copolymers: their responses to nine organic vapours. *Sensors and Actuators B-Chemical* **50**, 164–72.

Dejous, C., Rebiere, D., Pistre, J., Tiret, C. and Planade, R. (1995) A surface-acoustic-wave gas sensor – detection of organophosphorus compounds. *Sensors and Actuators B-Chemical* **24**, 58–61.

Djerdj, I., Haensch, A., Koziej, D., Pokhrel, S., Barsan, N., Weimar, U. and Niederberger, M. (2009) Neodymium Dioxide Carbonate as a Sensing Layer for Chemoresistive CO2 Sensing. *Chemistry of Materials* **21**, 5375–81.

Dubbe, A., Hagen, G. and Moos, R. (2006) Impedance spectroscopy of Na^+ conducting zeolite ZSM-5. *Solid State Ionics* **177**, 2321–3.

Durrani, S. M. A., Al-Kuhaili, M. F. and Bakhtiari, I. A. (2008) Carbon monoxide gas-sensing properties of electron-beam deposited cerium oxide thin films. *Sensors and Actuators B: Chemical* **134**, 934–9.

ESRL. 2010 ftp://ftp.cmdl.noaa.gov/ccg/co2/trends/co2_mm_mlo.txt.

Fay, J. A. and Rosenzweig, J. J. (1980) An analytical diffusion model for long distance transport of air pollutants. *Atmospheric Environment* (1967) **14**, 355–65.

© Woodhead Publishing Limited, 2013

Fine, G. F., Cavanagh, L. M., Afonja, A. and Binions, R. (2010) Metal Oxide Semi-Conductor Gas Sensors in Environmental Monitoring. *Sensors* **10**, 5468–502.

Fischerauer, A., Fischerauer, G., Hagen, G. and Moos, R. (2011) Integrated impedance based hydro-carbon gas sensors with Na-zeolite/Cr_2O_3 thin-film interfaces: From physical modeling to devices. *Physica Status Solidi (A) Applications and Materials* **208**, 404–15.

Fong, Y. Y., Abdullah, A. Z., Ahmad, A. L. and Bhatia, S. (2007) Zeolite membrane based selective gas sensors for monitoring and control of gas emissions. *Sensor Letters* **5**, 485–99.

Goldberg, H. D., Brown, R. B., Liu, D. P. and Meyerhoff, M. E. (1994) Screen printing: a technology for the batch fabrication of integrated chemical-sensor arrays. *Sensors and Actuators B: Chemical* **21**, 171–83.

Guo, Y., Zhang, X.-W. and Han, G.-R. (2006) Investigation of structure and properties of N-doped TiO2 thin films grown by APCVD. *Materials Science and Engineering: B* **135**, 83–7.

Gupta, S., Roy, R. K., Chowdhury, M. P. and Pal, A. K. (2004) Synthesis of SnO_2/Pd composite films by PVD route for a liquid petroleum gas sensor. *Vacuum* **75**, 111–19.

Hoefer, U., Kühner, G., Schweizer, W., Sulz, G. and Steiner, K. (1994) CO and CO_2 thin-film SnO_2 gas sensors on Si substrates. *Sensors and Actuators B: Chemical* **22**, 115–19.

Izu, N., Nishizaki, S., Itoh, T., Nishibori, M., Shin, W. and Matsubara, I. (2009) Gas response, response time and selectivity of a resistive CO sensor based on two connected CeO2 thick films with various particle sizes. *Sensors and Actuators B: Chemical* **136**, 364–70.

James, D., Scott, S. M., Ali, Z. and O'Hare, W. T. (2005) Chemical sensors for electronic nose systems. *Microchimica Acta* **149**, 1–17.

Jenkin, M. E. and Clemitshaw, K. C. (2002) Ozone and other secondary photochemical pollutants: chemical processes governing their formation in the planetary boundary layer, in *Developments in Environmental Sciences*, Volume **1** (ed. P. B. Jill Austin and S. William), pp. 285–338: Elsevier, Amsterdam, Netherlands.

Kanazawa, E., Sakai, G., Shimanoe, K., Kanmura, Y., Teraoka, Y., Miura, N. and Yamazoe, N. (2001) Metal oxide semiconductor N_2O sensor for medical use. *Sensors and Actuators B: Chemical* **77**, 72–7.

Khun Khun, K., Mahajan, A. and Bedi, R. K. (2009) SnO_2 thick films for room temperature gas sensing applications. *J. Appl. Phys.* **106**, 124509.

Kim, D. H., Yoon, J. Y., Park, H. C. and Kim, K. H. (2000) CO_2-sensing characteristics of SnO_2 thick film by coating lanthanum oxide. *Sensors and Actuators B: Chemical* **62**, 61–6.

Lee, M.-S. and Meyer, J.-U. (2000) A new process for fabricating CO_2-sensing layers based on BaTiO3 and additives. *Sensors and Actuators B: Chemical* **68**, 293–9.

Li, X., Ramasamy, R. and Dutta, P. K. (2009) Study of the resistance behavior of anatase and rutile thick films towards carbon monoxide and oxygen at high temperatures and possibilities for sensing applications. *Sensors and Actuators B: Chemical* **143**, 308–15.

Mann, D. P., Paraskeva, T., Pratt, K. F. E., Parkin, I. P. and Williams, D. E. (2005) Metal oxide semiconductor gas sensors utilizing a Cr-zeolite catalytic

© Woodhead Publishing Limited, 2013

layer for improved selectivity. *Measurement Science and Technology* **16**, 1193–200.

Mann, D. P., Pratt, K. F. E., Paraskeva, T., Parkin, I. P. and Williams, D. E. (2007) Transition Metal Exchanged Zeolite Layers for Selectivity Enhancement of Metal-Oxide Semiconductor Gas Sensors. *Sensors Journal*, *IEEE* **7**, 551–6.

Marsal, A., Cornet, A. and Morante, J. R. (2003a) Study of the CO and humidity interference in La doped tin oxide CO_2 gas sensor. *Sensors and Actuators B: Chemical* **94**, 324–9.

Marsal, A., Dezanneau, G., Cornet, A. and Morante, J. R. (2003b) A new CO_2 gas sensing material. *Sensors and Actuators B: Chemical* **95**, 266–70.

Meredith, C. T. (1988) Carbon monoxide poisoning. *BMJ. British medical journal (Clinical research ed.)* **296**, 77–9.

Michel, H. J., Leiste, H. and Halbritter, J. (1995) Structural and electrical characterization of PVD-deposited SnO_2 films for gas-sensor application. *Sensors and Actuators B: Chemical* **25**, 568–72.

Mizuno, N., Yoshioka, T., Kato, K. and Iwamoto, M. (1993) CO_2-sensing characteristics of SnO_2 element modified by La_2O_3. *Sensors and Actuators B: Chemical* **13**, 473–5.

Morrison, S. R. (1987) Selectivity in semiconductor gas sensors. *Sensors and Actuators* **12**, 425–40.

Naisbitt, S. C., Pratt, K. F. E., Williams, D. E. and Parkin, I. P. (2006) A microstructural model of semiconducting gas sensor response: The effects of sintering temperature on the response of chromium titanate (CTO) to carbon monoxide. *Sensors and Actuators B-Chemical* **114**, 969–77.

Olivier, J. G. J., Bouwman, A. F., Van der Hoek, K. W. and Berdowski, J. J. M. (1998) Global air emission inventories for anthropogenic sources of NOx, NH_3 and N2O in 1990. *Environmental Pollution* **102**, 135–48.

Patel, N. G., Makhija, K. K. and Panchal, C. J. (1994) Fabrication of carbon dioxide gas sensor and its alarm system using indium tin oxide (ITO) thin films. *Sensors and Actuators B: Chemical* **21**, 193–7.

Ponka, A. and Virtanen, M. (1994) Chronic bronchitis, emphysema and low level air pollution in Helsinki, 1987–1989. *Environmental Research* **65**, 207–17.

Rapp, M., Boss, B., Voigt, A., Gemmeke, H. and Ache, H. J. (1995) Development of an analytical microsystem for organic gas-detection based on surface-acoustic-wave resonators. *Fresenius Journal of Analytical Chemistry* **352**, 699–704.

Rickerby, D. G. and Serventi, A. M. (2010) Nanostructured Metal Oxide Gas Sensors for Air-Quality Monitoring, in *Enviro-nanotechnology*, pp. 99–136: Elsevier, Amsterdam, Netherlands.

Riviere, B., Viricelle, J. P. and Pijolat, C. (2003) Development of tin oxide material by screen-printing technology for micro-machined gas sensors. *Sensors and Actuators B: Chemical* **93**, 531–7.

Rock, F., Barsan, N. and Weimar, U. (2008) Electronic nose: Current status and future trends. *Chemical Reviews* **108**, 705–25.

Runyan, C. C., Johnson, C., Yang, C. J., Waller, C. A., Perkis, C. D. and Marshall, C. S. (2005) Risk and protective factors for fires burns and carbon monoxide poisoning in US households. *American journal of preventive medicine* **28**, 102–8.

Sahana, M. B., Sudakar, C., Setzler, G., Dixit, A., Thakur, J. S., Lawes, G., Naik, R., Naik, V. M. and Vaishnava, P. P. (2008) Bandgap engineering by tuning parti-

© Woodhead Publishing Limited, 2013

cle size and crystallinity of SnO_2 Fe_2O_3 nanocrystalline composite thin films. *Applied Physics Letters* **93**, 231909.

Sahner, K., Hagen, G., Schönauer, D., Reiß, S. and Moos, R. (2008) Zeolites – Versatile materials for gas sensors. *Solid State Ionics* **179**, 2416–23.

Satsuma, A., Yang, D. and Shimizu, K. I. (2011) Effect of acidity and pore diameter of zeolites on detection of base molecules by zeolite thick film sensor. *Microporous and Mesoporous Materials* **141**, 20–5.

Seiyama, T., Kato, A., Fujiishi, K. and Nagatani, M. (1962) A new detector for gaseous components using semiconductive thin films. *Analytical Chemistry* **34**, 1502–3.

Shaw, G., Parkin, I. P., Pratt, K. F. E. and Williams, D. E. (2005) Control of semiconducting oxide gas-sensor microstructure by application of an electric field during aerosol-assisted chemical vapour deposition. *Journal of Materials Chemistry* **15**, 149–54.

Shaw, G. A., Parkin, I. P. and Williams, D. E. (2003) Atmospheric pressure chemical vapour deposition of Cr_2-x$TixO_3$ (CTO) thin films on to gas sensing substrates. *Journal of Materials Chemistry* **13**, 2957–62.

Shriver, A. (2006) *Inorganic Chemistry*: Oxford, United Kingdom.

Szabo, N., Lee, C., Trimboli, J., Figueroa, O., Ramamoorthy, R., Midlam-Mohler, S., Soliman, A., Verweij, H., Dutta, P. and Akbar, S. (2003) Ceramic-based chemical sensors, probes and field-tests in automobile engines. *Journal of Materials Science* **38**, 4239–45.

Tamaki, J., Zhang, Z., Fujimori, K., Akiyama, M., Harada, T., Miura, N. and Yamazoe, N. (1994) Grain-Size Effects in Tungsten Oxide-Based Sensor for Nitrogen Oxides. *Journal of the Electrochemical Society* **141**, 2207–10.

Tans, P. (2010) http://www.esrl.noaa.gov/gmd/ccgg/trends/.

Tischner, A., Maier, T., Stepper, C. and Köck, A. (2008) Ultrathin SnO2 gas sensors fabricated by spray pyrolysis for the detection of humidity and carbon monoxide. *Sensors and Actuators B: Chemical* **134**, 796–802.

Vaishanv, V. S., Patel, P. D. and Patel, N. G. (2006) Indium tin oxide thin-film sensor for detection of volatile organic compounds (VOCs). *Materials and Manufacturing Processes* **21**, 257–61.

Varon, J., Marik, P. E., Fromm Jr, R. E. and Gueler, A. (1999) Carbon monoxide poisoning: a review for clinicians. *Journal of Emergency Medicine* **17**, 87–93.

Varsani, P., Afonja, A., Williams, D. E., Parkin, I. P. and Binions, R. (2011) Zeolite-modified WO_3 gas sensors , Enhanced detection of NO2. *Sensors and Actuators B: Chemical* **160**, 475–82.

Vincenzi, D., Butturi, M. A., Guidi, V., Carotta, M. C., Martinelli, G., Guarnieri, V., Brida, S., Margesin, B., Giacomozzi, F., Zen, M., Giusti, D., Soncini, G., Vasiliev, A. A. and Pisliakov, A. V. (2000) Gas-sensing device implemented on a micromachined membrane: A combination of thick-film and very large scale integrated technologies. *Journal of Vacuum Science & Technology B* **18**, 2441–5.

Wang, Y. and Yeow, J. T. W. (2009) A Review of Carbon Nanotubes-Based Gas Sensors. *Journal of Sensors*, 1–24.

Warwick, M. E. A. and Binions, R. (2011) On the Effects of Electric Fields in Aerosol Assisted Chemical Vapour Deposition Reactions of Vanadyl Acetylacetonate Solutions in Ethanol. *Journal of Nanoscience and Nanotechnology* **11**, 8126–31.

Warwick, M. E. A., Ridley, I. and Binions, R. (2011) Electric Fields in the Chemical Vapour Deposition Growth of Vanadium Dioxide Thin Films. *Journal of Nanoscience and Nanotechnology* **11**, 8158–62.

© Woodhead Publishing Limited, 2013

Wegmann, M., Fehrenbach, A., Heimann, S., Fehrenbach, H., Renz, H., Garn, H. and Herz, U. (2005) NO2-induced airway inflammation is associated with progressive airflow limitation and development of emphysema-like lesions in C57BL/6 mice. *Experimental and Toxicologic Pathology* **56**, 341–50.

Wiegleb, G. and Heitbaum, J. (1994) Semiconductor gas sensor for detecting NO and CO traces in ambient air of road traffic. *Sensors and Actuators B: Chemical* **17**, 93–9.

Williams, D. E. (1999) Semiconducting oxides as gas-sensitive resistors. *Sensors and Actuators B-Chemical* **57**, 1–16.

Williams, D. E. (2009) *Proceedings of IEEE Sensors conference 2009*, pp. 1100–04, The Printing House Inc., Stoughton, Wisconsin.

Wilson, A. D. and Baietto, M. (2009) Applications and Advances in Electronic-Nose Technologies. *Sensors* **9**, 5099–148.

Yadava, L., Verma, R. and Dwivedi, R. (2010) Sensing properties of CdS-doped tin oxide thick film gas sensor. *Sensors and Actuators B: Chemical* **144**, 37–42.

Yamazoe, N. (1991) New approaches for improving semiconductor gas sensors. *Sensors and Actuators B: Chemical* **5**, 7–19.

Yamazoe, N. and Miura, N. (1995) Development of gas sensors for environmental-protection. *IEEE Transactions on Components Packaging and Manufacturing Technology Part A* **18**, 252–6.

Yamazoe, N., Sakai, G. and Shimanoe, K. (2003) Oxide semiconductor gas sensors. *Catalysis Surveys from Asia* **7**, 63–75.

Zellers, E. T., Park, J., Hsu, T. and Groves, W. A. (1998) Establishing a limit of recognition for a vapor sensor array. *Analytical Chemistry* **70**, 4191–201.

© Woodhead Publishing Limited, 2013

14

Semiconductor gas sensors for chemical warfare agents

D.-D. LEE and J.-C. KIM,
Kyungpook National University, Korea

DOI: 10.1533/9780857098665.4.467

Abstract: A brief overview is given for a variety of sensors for the detection of chemical warfare agents (CWA): semiconductor thick- or thin-film gas sensors with oxide and noble metal additives, surface acoustic wave (SAW) sensors with a polymer membrane, and an ion mobility sensor (IMS). This is followed by discussion on the preparation methods for the sensing materials employed in semiconducting devices, and SAW sensors are introduced. The chapter closes with the results and observations from the examination and study of these devices.

Key words: chemical warfare agents (CWA), polymer, semiconducting device, SAW-type sensor, principal component analysis (PCA).

14.1 Introduction

Chemical warfare agents (CWAs) are highly toxic materials which are known to cause fatal damage to human beings, animals, and plants. The agents are known as the 'nuclear weapons for poor countries', as the cost is much lower compared with nuclear weapons.[1]

Since the September 11 attacks, there has been increased concern worldwide about CWAs, as well as increased interest in developing technology for confronting this threat.

The general requirements of devices with which to monitor CWAs are:

- high sensitivity to the agents (ppb level)
- high selectivity
- high-speed sensing
- stability
- small size
- good repeatability.

© Woodhead Publishing Limited, 2013

Of these requirements, high sensitivity and selectivity are the most important, for it is vital that we protect against fatal damage caused by the diffusion of CWAs.

There are four categories of CWA: blood, blister, nerve, and choking agents.[1] To cover the greatest number of eventualities, we should undertake a wide range of experiments to investigate as many CWAs as possible.

In this chapter, we will describe and discuss the fabrication and characterization of metal oxide thick- and thin-film sensors (which are based on the conductivity modulation principle) and SAW devices (which are based on frequency modulation). The sensing properties of thick or thin semiconductor films with various components will be discussed, focusing on sensitivity and stability. In addition, SAW-type CWA sensors[2] will be introduced for different pairs of interdigitated transducer (IDT) fingers, various wave lengths, and different polymer coatings on the input and output IDTs of the device.

14.2 Chemical warfare agents

Chemical warfare agents (CWAs) are known to be highly dangerous for human health because of their fatal toxicity, colorlessness and toxicity. Therefore, fast and selective detection of CWAs is essential to protect human beings and animals. In this chapter, properties of CWAs and various detecting techniques for CWAs were introduced in detail.

14.2.1 Classification and properties

As mentioned, there are four categories of CWA: blood, choking, vesicant (blister), and nerve agents.[3–6] Each agent has a simulant which is not as toxic as the real gas but that should have nearly the same chemical reactions with the surfaces of the sensing materials (metal oxides or polymers).

Table 14.1 shows a comparison between nuclear weapons and chemical agents.[3] As shown here, the cost ($/ton) of chemical agents is about one-tenth of that of nuclear weapons. Table 14.2 shows acceptable concentrations of chemical agents in the air (mg/m^3) and the concentration required to cause lethal damage to humans.[3–7] In this table, LD_{50} means the dosage required to kill half of the people who inhale an agent. Table 14.3 shows a comparison of toxicity between real and simulant gases.[8–14] As shown here, the concentration of nerve gas is lower than that of the other three agents. Table 14.4 shows the physical properties of chemical agents. As shown in this table, the melting points of the agents are below 0°C. In addition, the boiling points of choking and blood gases are below 50°C. The LC_{t50} (lethal concentration for 50%) (human) mg min/m^3 is comparatively low for VX gas (nerve agent). Table 14.5 shows a comparison of

© Woodhead Publishing Limited, 2013

Table 14.1 Comparison of nuclear weapons and chemical agents

Contents	Nuclear weapon	Chemical weapon
Direct offset range (km^2)	190~260	260
Remaining effect period	6 months	3~36 hrs
Casualties	98% (death)	30% (injured or death)
Direct efficiency period	A few seconds	7 s~30 min
Cost ($/ton)	1 000 000	10 000
Detection method	Simple	Complex

Table 14.2 Acceptable concentration of chemical agents in air and the lethal dosage (LD)

Agents	Acceptable concentration in the air (mg/m^3)			Lethal dosage (man)		
	Worker	Stack	Citizen	Skin LD_{50} (mg/kg)	Injection LD_{50} (mg/kg)	Inhalation LD_{50} (mg·min/kg)
GA (nerve)	0.0001	0.0003	0.000003	14–21	0.014	70~100
GB (nerve)	0.00001	0.00003	0.000003	24	0.014	20~50
VX (nerve)	0.003	0.03	0.0001	0.04	0.008	10 000
HD (vesicant)	0.003	0.03	0.003	100	–	10 000
L (vesicant)	0.003	0.03	0.003	–	–	10 000

Table 14.3 Comparison of toxicity between real gases and simulant gases

Agents		GA (Tabun)	Mustard	AC	CG (Phosgene)
Type		Nerve	Vesicant	Blood	Choking
Chemical formula		$C_5H_{11}N_2O_2P$	$C_4H_8SCl_2$	HCN	$COCl_2$
Toxicity	mg/kg	0.6	0.7	1	3.2
LD_{50}	ppm	83	99	830	724
Simulants		DMMP	DPGME	Acetonitrile	Acetonitrile
Chemical formula		$C_3H_9O_3P$	$C_7H_{16}O_3$	CH_3CN	CH_2Cl_2
Exposure standard (TWA*)	mg/m^3	10	600	70	175
	ppm	2	100	40	50

*TWA (time weighted value): permissible time averaged exposure concentration.
DMMP, dimethyl methyl phosphonate; DPGME, dipropylene glycol methyl ether.

© Woodhead Publishing Limited, 2013

Table 14.4 Physical properties of chemical warfare agents

	Choking	Blood		Vesicant		Nerve		
	Phosgene	HCN	CNCl	HD	Lewisite	Tabun	Sarin	VX
Mol. weight	99	27	61	159	207	162	140	267
Melt. point (°C)	–118	–15	–6.5	14.5	–18	–49	–57	–39
Boil. point (°C)	8.2	26	15.5	217	190	240	151	298
Vapor pressure (mmHg)	1173 20°C	742 25°C	1000 25°C	0.072 20°C	0.394 20°C	0.07 25°C	2.9 2.5°C	0.0007 25°C
Vapor density	1.42	0.69	1.22	1.27	1.89	1.07	1.09	1.03
LC_{t50} (human) mg min/m^3	3200	4500	11 000	1500	1200	300	150	40
Effect	Lung, fast	Respiration	Inhibition	Eye, skin slow	Blister, fast	Miosis	Respiration, repression	Sweat

© Woodhead Publishing Limited, 2013

Table 14.5 Comparison of acute toxicity of various nerve agents

Species	Route	Term	Unit	Tabun	Sarin	Soman	VX
Man	PC	LD_{50}	mg/kg	23	28	18	–
Man	Inhalation	LD_{50}	mg/m^3	150	70	70	50
Rat	PC	LD_{50}	mg/kg	18	–	–	–
Rat	Inhalation	LC_{50}	$mg{\cdot}10\ min/m^3$	304	150	–	86
Rabbit	PC	LD_{50}	mg/kg	2.5	0.93	–	–
Rabbit	Inhalation	LC_{50}	$mg{\cdot}10\ min/m^3$	840	120	–	–

toxicity for different kinds of nerve agents.[14] Here, PC means 'skin path'. In this table, among humans, rats, and rabbits, the rabbit is the most sensitive to tabun and sarin for the PC route.

14.3 Chemical warfare agent detecting techniques

Various techniques have been developed for the detection of CWAs (see Table 14.6, which shows the most important detection techniques).[10] Among the various detection techniques, the methods most highly recommended are: the use of an ion mobility spectrometer (IMS), semiconductors, and SAW-type devices.

14.3.1 Ion mobility spectrometry

The ion mobility spectrometry detection technique was first developed in 1965 by the Franklin GNO Corporation. It has become a representative tool for the detection of CWA. Using this instrument, the types and concentrations of agents can be checked in real time.

Ion separation and recognition can be accomplished by analyzing the ion mobility difference of various materials. Figure 14.1 shows the structure of the IMS.[10] The sample constituents enter the reaction area and are ionized (A+, B+) via reaction ion R+ and gated into the drift region, where they are separated based on the mobilities of their sample constituents. IMS is very sensitive to organic compounds (picogram level).

14.3.2 Semiconducting device technique

One of most recommended methods for the detection of CWAs is the semiconducting device. There are two main types of semiconducting devices: SnO_2 and ZnO. Among SnO_2 devices, there are several different types which can be differentiated according to the thickness and size, such as: thick-film, thin-film, and micro. Although different, these types of sensor actually have

© Woodhead Publishing Limited, 2013

Table 14.6 CWA detecting techniques

Techniques	Advantages	Disadvantages
Photoionization	Rapid response, Sensitive to organics	Poor specificity
Paper tape	Very specific to certain compounds	Requires frequent replacement
Fourier transform infrared (IR)	More sensitive than standard IR, rapid response	High cost
Gas chromatography	Applicable to a wide variety of gases, good sensitivity	Slow response, requires frequent calibration
IMS	Very good sensitivity, very specific to certain compounds	Slower than IR
Semiconductor	Low cost, fast response	Low selectivity
SAW type	Portability, high sensitivity, low cost	Sensitive to environmental factors

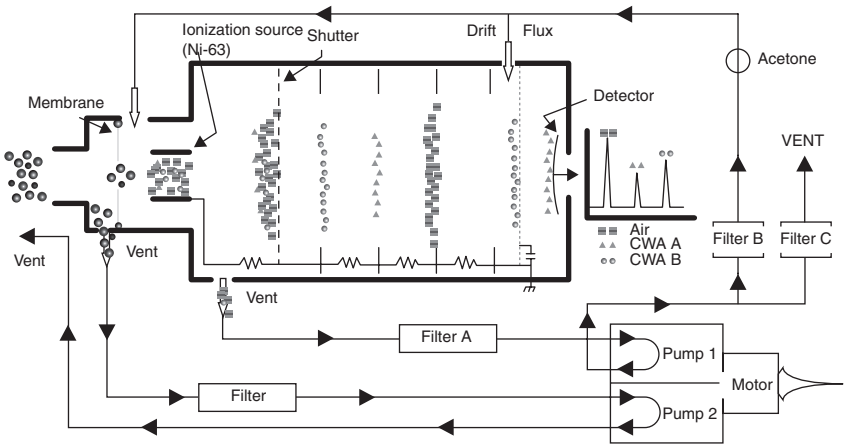

14.1 Structure of IMS. The sample constituents (A,B) enter the reaction region and they are ionized (A+, B+) with reactant ion R+ and gated into the drift region, where they separated based on mobilities.

similar aspects in terms of the arrangement of the sensing electrode. In addition, the thickness of micro-type sensors is, in general, almost the same as that of thin-film devices.

ZnO devices can also be classified into three types: thick-film, thin-film, and microsensor (array). In addition, the additives to the films serve to make the sensors sensitive, selective, stable, etc.

© Woodhead Publishing Limited, 2013

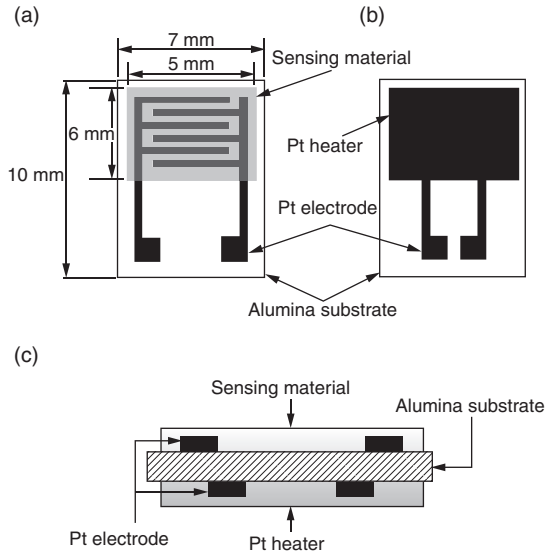

14.2 Device structure: (a) front; (b) back; (c) cross section.

Figure 14.2 shows the structure of a semiconducting sensing device. Here, the sensing film can be formed with SnO_2-based or ZnO-based thick films. Various additives to the thick-film can be used to obtain highly-sensitive and selective devices – for example In_2O_3, Al_2O_3, ZrO_2, Pt, and Pd.

14.3.3 Surface acoustic wave (SAW) sensor technique

As a third method of CWA detection, the surface acoustic wave (SAW) sensor attracts a great deal of attention. In principle, CWA-sensing using SAW devices is based on the shift in frequency of the surface acoustic wave in gas ambience upon exposure to chemical agents. Figure 14.3 shows the structure of a SAW device.[3] When the surface acoustic waves pass through the sensing membrane of a SAW device, the velocity of the transmitting wave is supposed to alter due to the reaction of the wave with gas molecules.

14.4 Device preparation

Among the instruments and devices used to detect the agents, the IMS, the semiconducting sensor, and the SAW-type sensor have drawn particular interest, as they exhibit high sensitivity and provide comparatively stable and reliable responses.

© Woodhead Publishing Limited, 2013

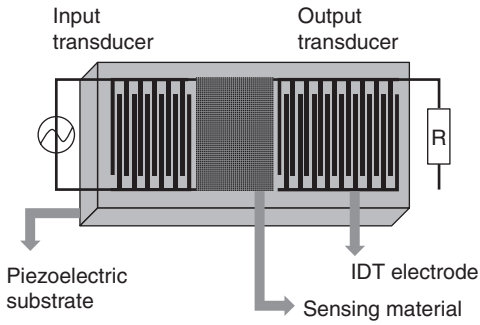

14.3 Schematic diagram of SAW device.

Table 14.7 Synthesis method of sensing materials and their amount of addition (base material:SnO_2)

Added material	Added amounts (wt.%)	Synthesis method
ZnO	1, 2, 3, 4, 5	Co-precipitation
ZrO_2	1, 3, 5	Co-precipitation
Pt	1, 3, 5	Impregnation
Pd	–	–
Al_2O_3	0, 4, 12, 20	Ball-milling
In_2O_3	1, 2, 3	Ball-milling
WO_3	–	–
SiO_2	3, 5, 10	Ball-milling
TiO_2	–	–

The following description of the preparation of a CWA detection device will focus on semiconductors.

14.4.1 Semiconducting device

The process starts with the preparation of materials. Table 14.7 shows the synthesis method of sensing materials with various additives.[3] As shown in this table, the synthesis of ZnO or ZrO_2 with SnO_2 additives is carried out by using the co-precipitation method. Also, Al_2O_3, In_2O_3, WO_3, SiO_2, TiO_2, etc., with SnO_2 additives could be synthesized using the ball-milling method. Methods such as Pt and Pd addition are carried out by impregnation. The synthesis methods introduced above will now be described in more detail.

Figure 14.4 shows the synthesis sequence for SnO_2 using the co-precipitation method.[3] As shown in this figure, to prepare ZnO with SnO_2 additives, $SnCl_4{\cdot}H_2O$ and $(CH_3CO_2)_2{\cdot}H_2O$ were co-precipitated. Finally, to

© Woodhead Publishing Limited, 2013

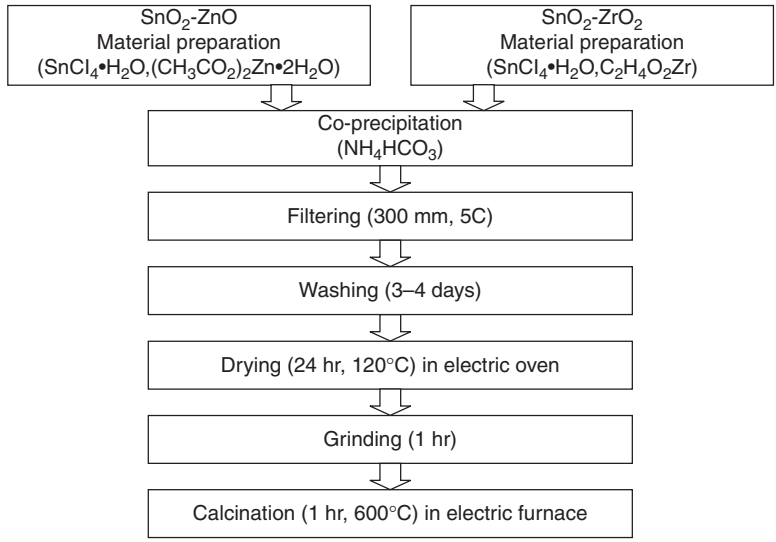

14.4 Synthesis sequence for SnO_2 by co-precipitation method.

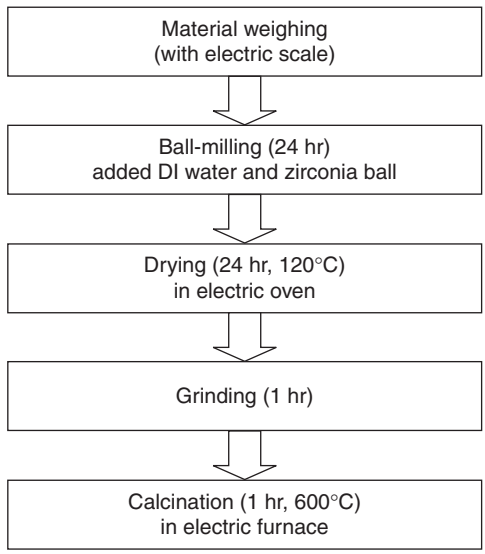

14.5 Synthesis sequence of ball-milling method for SnO_2-based device materials. DI, deionized.

make ZrO_2 with SnO_2 additives, $SnCl_4 \cdot H_2O$ and $C_2H_4O_2Zr$ were used for co-precipitation.

Figure 14.5 shows the synthesis process of sensing materials using the ball-milling method.[3] The ball-milling method is known to be an efficient

© Woodhead Publishing Limited, 2013

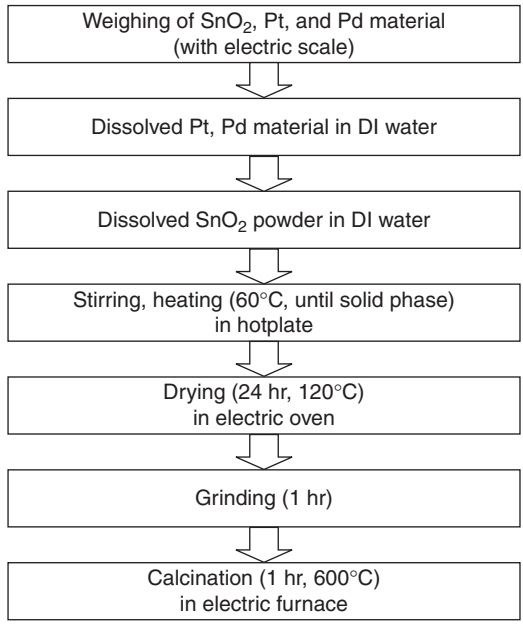
Weighing of SnO_2, Pt, and Pd material (with electric scale)
Dissolved Pt, Pd material in DI water
Dissolved SnO_2 powder in DI water
Stirring, heating (60°C, until solid phase) in hotplate
Drying (24 hr, 120°C) in electric oven
Grinding (1 hr)
Calcination (1 hr, 600°C) in electric furnace

14.6 Synthesis process of sensing material using impregnation method.

and effective technique with which to prepare In_2O_3, TiO_2, WO_3, SiO_2, Al_2O_3, etc., with SnO_2 additives. The obtained calcined powder was coated on the substrate, which comprised electrodes (Si or Al_2O_3). In this case, thick- or thin-film single or multiple sensors were formed on the substrate for the purpose of these experiments. The noble metal with SnO_2 additive materials can be obtained by using impregnation.

Figure 14.6 shows the synthesis sequence of impregnation techniques.[3] First, $PdO{\cdot}xH_2O$ and $PtO_2{\cdot}xH_2O$ are weighed and put in deionized (DI) water to achieve a fully-dissolved solution of Pd and Pt mixture. Also, SnO_2 powder is mixed with the noble metal dissolved in DI water.

14.4.2 Microsensor array device

Microsensor arrays can be obtained by applying a combination of the integrated circuit process and microelectromechanical (MEMS) techniques. Using this array, we can enhance the selectivity and reliability of the system, employing statistical techniques.

Figure 14.7 shows the preparation process of a microsensor.[3] SiNx thin-film (2 μm) is grown on a *p*-type silicon wafer using the low-pressure CVD (LPCVD) method. Next, a Ta/Pt thin-film is sputtered and patterned. An

© Woodhead Publishing Limited, 2013

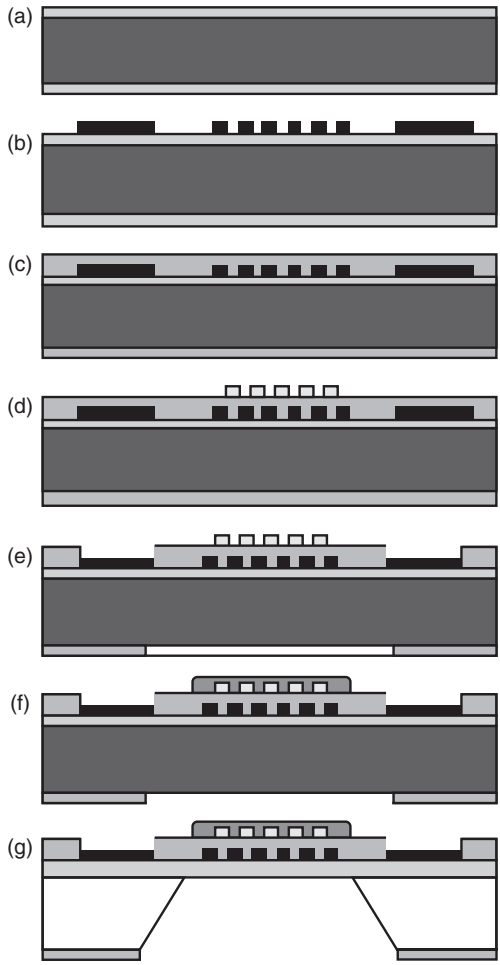

14.7 Preparation process of microsensor. (a) Depositing of Si_3N_4 layer (LPCVD 2 μm). (b) Patterning of heaters (mask#1) (DC sputter, Ta (300 Å), Pt (2000 Å)). (c) Depositing of insulation layer (PECVD (plasma-enhanced chemical vapor deposition) SiO_2, 2000 Å). (d) Patterning of electrodes (mask#2) (DC sputter, Ta (300 Å), Pt (2000 Å)). (e) Patterning of insulation layer (mask# 3, 4) (RIE (reactive ion etching)). (f) Depositing of sensing material (thick-film 20 μm). (g) Backside etching of Si by KOH (circulator 85°C, etch rate 1.4 μm/min, DI water:KOH=100:24).

insulation layer of about 2000 Å is deposited on the patterned heater. It is important that the deposition of sensing material is carried out with care in order not to compromise the efficiency of the device.

Figure 14.8 shows the arrangement of the microsensor array. The sensing membrane area was undercut so that the part can be heated with a comparatively low level of power.

© Woodhead Publishing Limited, 2013

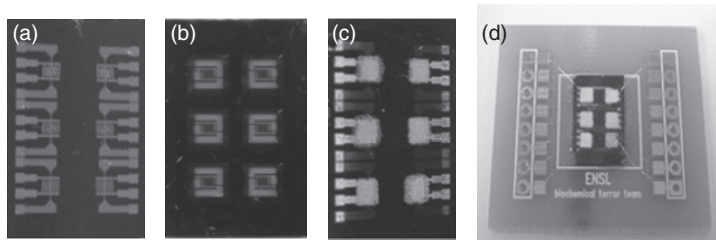

14.8 Microsensor array arrangements: (a) sensing electrode heater (front), (b) etching figure on reverse (back heater), (c) device for sensing thick-film formation, (d) mounted on PCB.

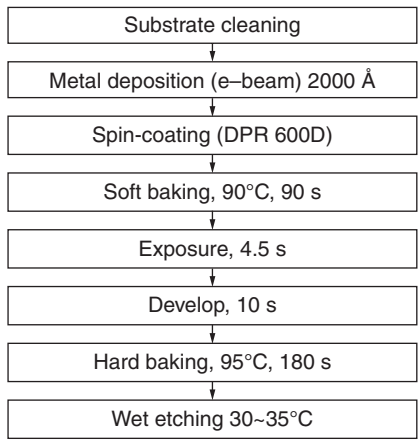

14.9 Preparation sequence of SAW sensor.

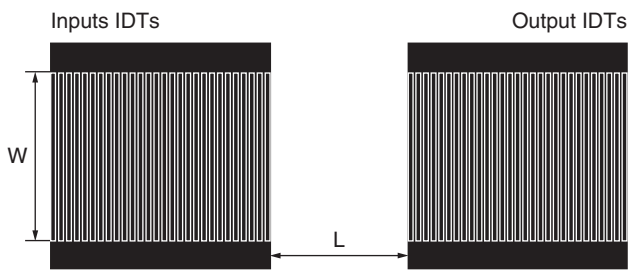

14.10 Schematic diagram of the SAW delay line for CWA sensor.

14.4.3 Surface acoustic wave (SAW) sensor

Figure 14.9 shows the fabrication sequence of SAW sensors.[14] The piezoelectric materials used as SAW sensor substrate materials are quartz, $LiNbO_3$, $LiTaO_3$, ZnO, AlN, etc. Among these materials, quartz has attracted strong

© Woodhead Publishing Limited, 2013

interest because it has a low temperature coefficient of frequency (TCF (temperature coefficient of frequency): ppm/°C). SAW sensors are comprised of an input IDT, a mass loading area, and an output IDT, as shown in Fig. 14.10.[14]

The conventional λ/4 IDT-width design rule has been adopted (reference 13, p. 48). The number of finger pairs formed on the input and output IDTs can be selected according to the design of the device.

14.5 Sensing properties

The 4S and 2R conditions are considered to be requirements of gas sensor properties.[15] 4S means sensitivity, selectivity, stability, and speed; 2R means reversibility and repeatability. To realize the above conditions, we try to prepare devices according to optimal device design, fabrication process, and operational conditions. The sensing properties of metal oxide and SAW-type devices will now be described in brief.

14.5.1 SnO_2-based single device

In previous sections, various oxides and noble metals with SnO_2 additive materials were introduced.[3] Figure 14.11 shows the sensing response curve of the semiconducting device to dimethyl methyl phosphonate (DMMP) (a simulant of nerve gas) at different operating temperatures. The results in Fig. 14.10 are the sensing curves of SnO_2 additives with 4 wt% Al_2O_3. Figure 14.12 shows the dynamic response of the SnO_2 sensor with Al_2O_3 additives.[3] As shown here, the response time is relatively long. Thus, further study is needed to shorten the response time in the case of the oxide semiconductor.

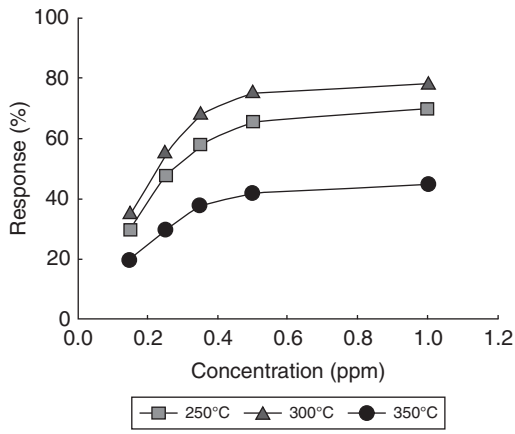

14.11 Sensitivity change with DMMP gas concentration for SnO_2 with 4% Al_2O_3 added.

© Woodhead Publishing Limited, 2013

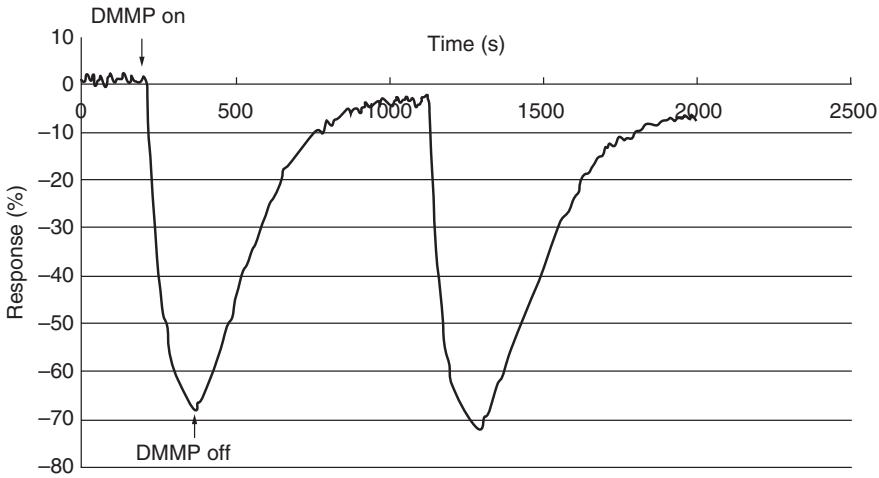

14.12 Dynamic response curve.

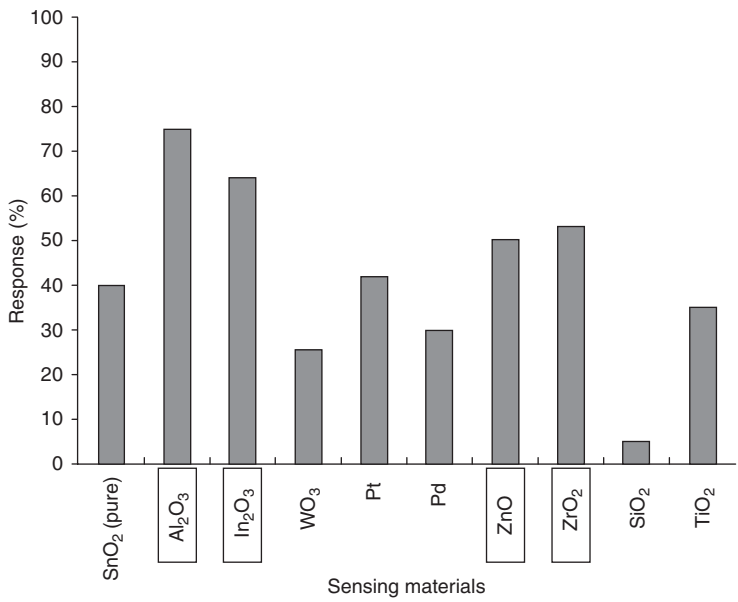

14.13 Sensing properties of various additives for DMMP. Amount of addition: 3%.

Figure 14.13 shows the sensing properties of various additives incorporated into the device.[3,10,15,16] These results are for DMMP (ppb level). As shown here, the additives Al_2O_3, In_2O_3, Pt, ZnO, and ZrO_2 exhibit enhanced sensitivity to DMMP. Figure 14.14 shows the sensitivities of sensing materials with different additives to dipropylene glycol methyl ether (DPGME),

© Woodhead Publishing Limited, 2013

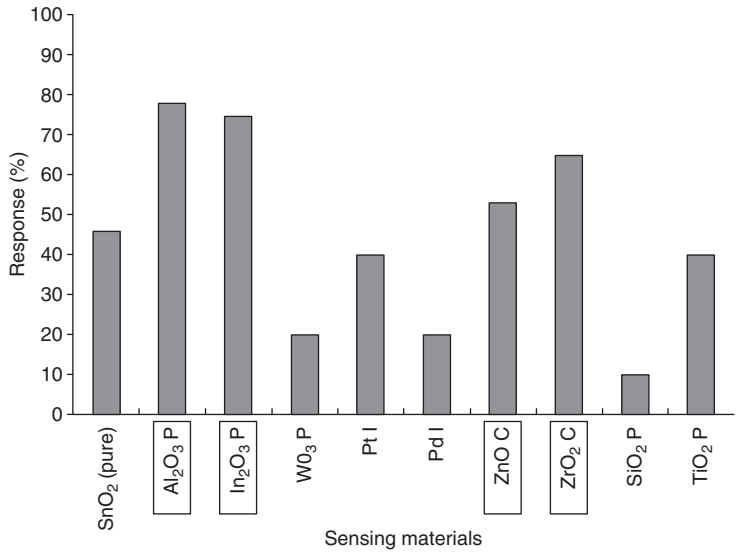

14.14 Sensing properties for DPGME, vesicant simulant. Amount of addition: 3%.

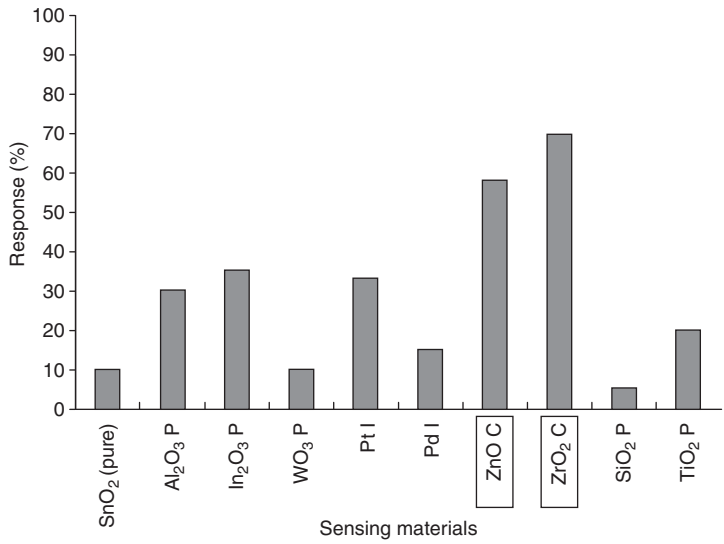

14.15 Sensing properties for CH_3CN, simulant of blood agent. Amount of addition: 3%.

a vesicant agent.[9] As in the case of DMMP, devices with Al_2O_3, In_2O_3, ZnO, and ZrO_2 additives show high sensitivity to DPGME. Figure 14.15 shows the sensitivities of acetonitrile (CH_3CN), a simulant blood agent;[9] SnO_2 devices with ZnO and ZrO_2 additives exhibit high sensitivity to acetonitrile.

© Woodhead Publishing Limited, 2013

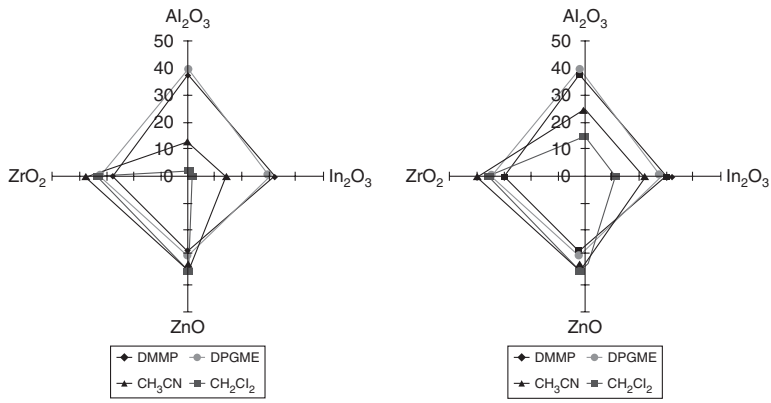

14.16 Response of sensor arrays with four devices at different operating temperatures (2.5 ppm). Left figure shows the response of sensor array at 250°C. Right figure shows the response of sensor array at 300°C.

14.5.2 Microsensor array device

A sensor area with two or more sensors can be obtained using a combination of silicon integrated circuit technology and the MEMS technique. Using sensor arrays, a highly-selective device can be realized. Figure 14.16 shows sensitivities of sensor arrays with four devices at different operating temperatures.[15, 17, 18, 19]

14.5.3 Surface acoustic wave (SAW) type sensor

As described earlier, the sensing films were formed on the area between the input IDTs and output IDTs (Fig. 14.10).[14] The wavelengths of SAW devices are decided by the width of the fingers and the spacing between fingers.

The sensing films can be formed by spin-coating. Chemical agents (DMMP, acetonitrile, DCM (dichloromethane), and DCP (dichloropanthane)) are injected onto the sensing film area. As a result of the mass loading effect, this causes a change of the SAW propagation velocity and a shift of the center frequency.

The sensing materials used are polyisobutylene (PIB), polyepichlorohydrin (PECH), polydimethylsiloxane (PDMS), polyisoprene (PIP), and polybutadiene (PBD):[14]

- PIB has a high bulk density for an amorphous elastomer, which leads to low gas permeability and high hysteresis at a given temperature.
- PDMS has thermal stability, a temperature effect, and good resistance to UV radiation.

© Woodhead Publishing Limited, 2013

- PBD also has good low-temperature properties and adhesion to metals.
- PIP has high resistance, excellent dynamic properties, and general fatigue resistance.[15, 17, 18, 19]

To form the viscous sensing films, the polymers are mixed with the appropriate solvent. The solvent for a PIB film is ethyl acetate; as PDMS is a liquid polymer with a strong viscosity, to get thin-film and to achieve weak viscosity ethyl acetate is used.

A mixture of PIB and cyclohexane is obtained by heating it at 44°C for 4 hours. The solution is coated on the fabricated SAW device by spin-coating at 5000 rpm. The response characteristics of the SAW sensor depend on the

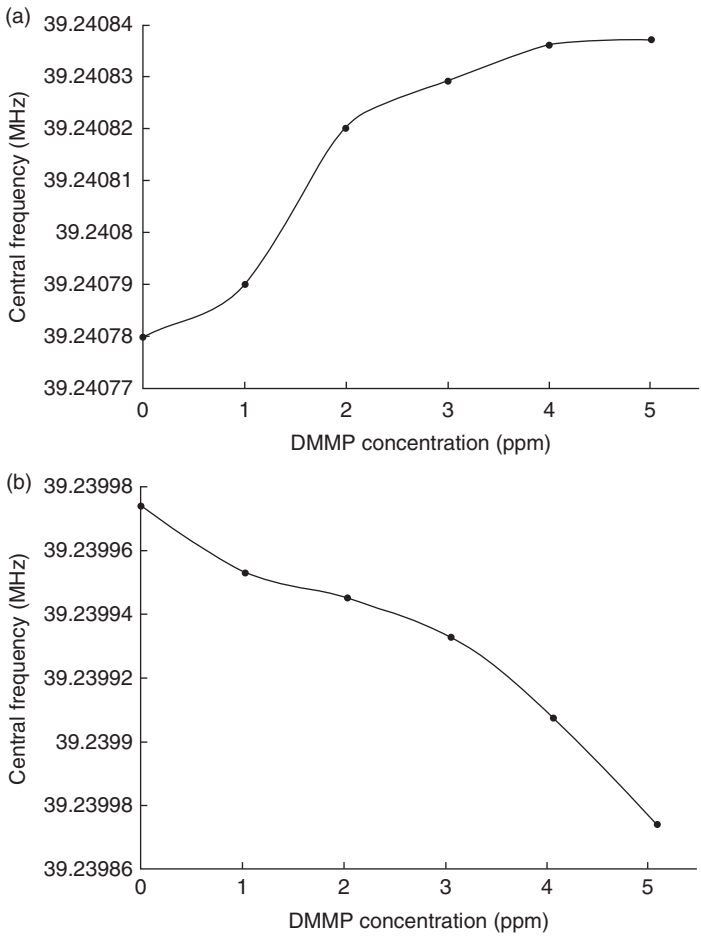

14.17 Sensing characteristics to DMMP of the 39.6 MHz SAW device coated with PIB films: (a) with heat treatment and (b) without heat treatment.

© Woodhead Publishing Limited, 2013

thickness of the sensing material. To investigate this relationship, a mixture of PIB and solvent are used to coat the SAW device at several different mixture ratios. The optimal mixing ratios of PIB, PECH, PDMS, PBD, and PIP to solvents are 1:30, 1:40, 1:10, 1:30, and 1:30, respectively, when 264 MHz quartz substrate is used.

The polymer films coated onto sensing areas are heat-treated to remove solvent and to achieve a stable response. The achieved treatment conditions of PECH and PDMS are 65°C for 1 hour and 70°C for 2 hours, respectively, in N_2 ambient, while PBD and PIP are heat-treated at 60°C for 1 hour in N_2 ambient.

Sensitivity to chemical agents is defined as the frequency shift of the SAW device – that is, the difference between the frequency in pure air and the frequency in a target gas. Figure 14.17 shows the sensing characterization of DMMP by a 39.6 MHz SAW device coated with PIB films (a) with and (b) without heat treatment.[13–14] From these figures, the effect of solvent on the frequency response of the device can be confirmed. Figure 14.18 shows the frequency shift characterization for DMMP depending on polymer thickness and DMMP concentration.[13] Figure 14.19 shows the frequency shift of various sensing films for different simulant gases: (a) DMMP, (b) acetonitrile.[13–14] It was found that the PIB-coated device showed an excellent selectivity of DMMP. Figure 14.20 shows the frequency shifts of various sensing films for different gases:[13] (a) DCM, (b) DCP.[10] In this figure, the frequency shift for the PIP-coated device showed a high sensitivity to CH_2Cl_2. The PECH device is

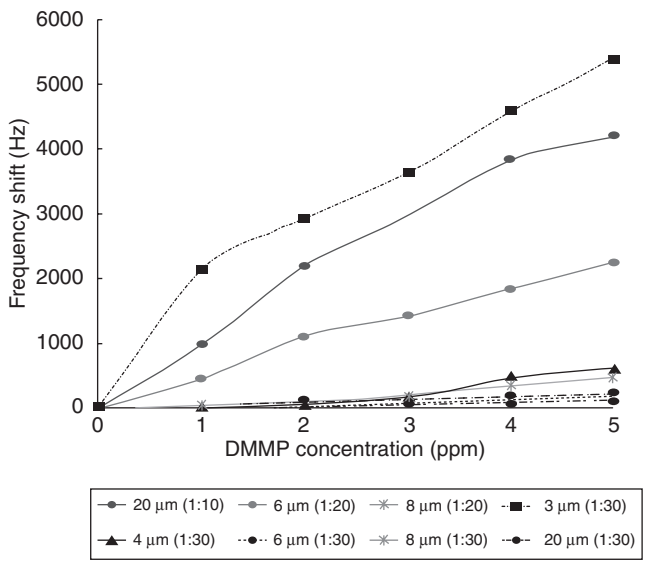

14.18 Variation of center frequency with changes in polymer thickness and DMMP concentration.

© Woodhead Publishing Limited, 2013

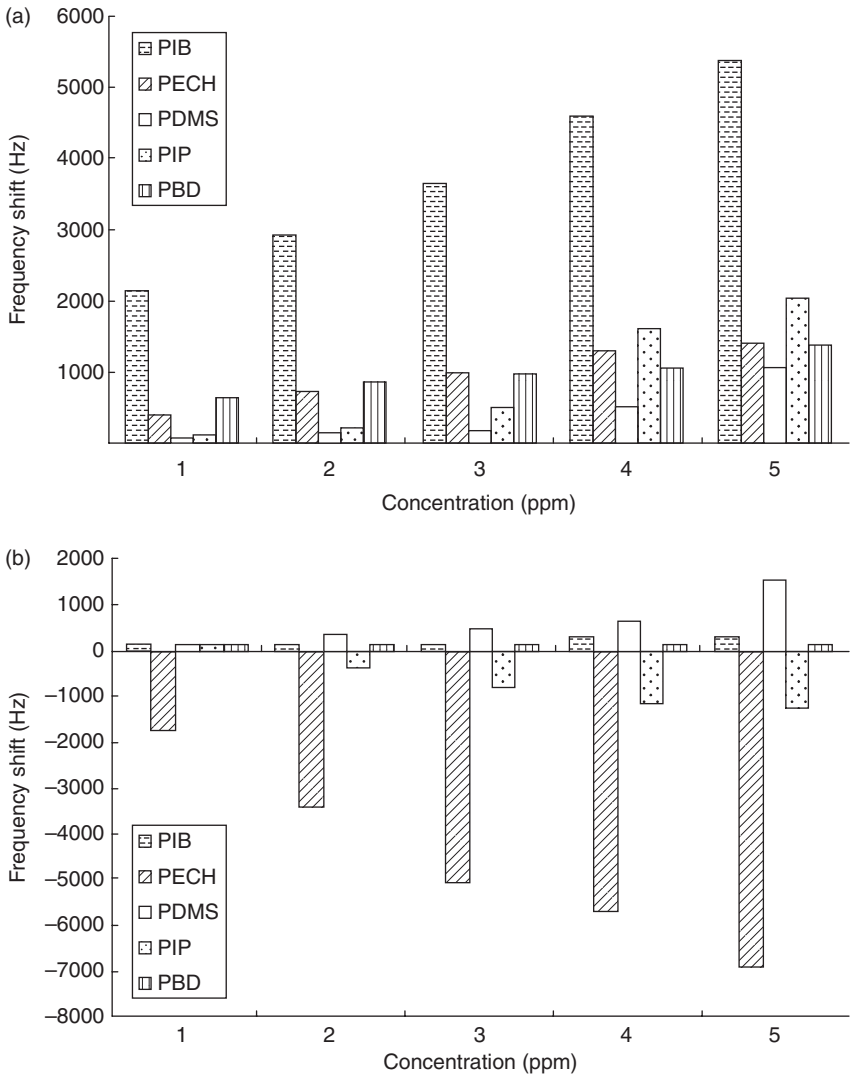

14.19 Frequency shift of various sensing films for different simulant gases: (a) DMMP, (b) CH_3CN.

highly selective to CH_3CN; however, the frequency shift to 5 ppm gas concentration is 5.369 kHz, even though it showed a negative frequency shift to it.

Almost every solid state gas sensor exhibits a sensing effect for humidity. Figure 14.21 shows the humidity dependence of a frequency shift of a polymer-type SAW sensor for different sensing films.[14] As shown in this figure, the SAW sensor shows comparatively high sensitivity to humidity. Thus, there needs to be an improvement in this regard in order to ameliorate this drawback before SAW sensors can be used in practical applications.[19–21]

© Woodhead Publishing Limited, 2013

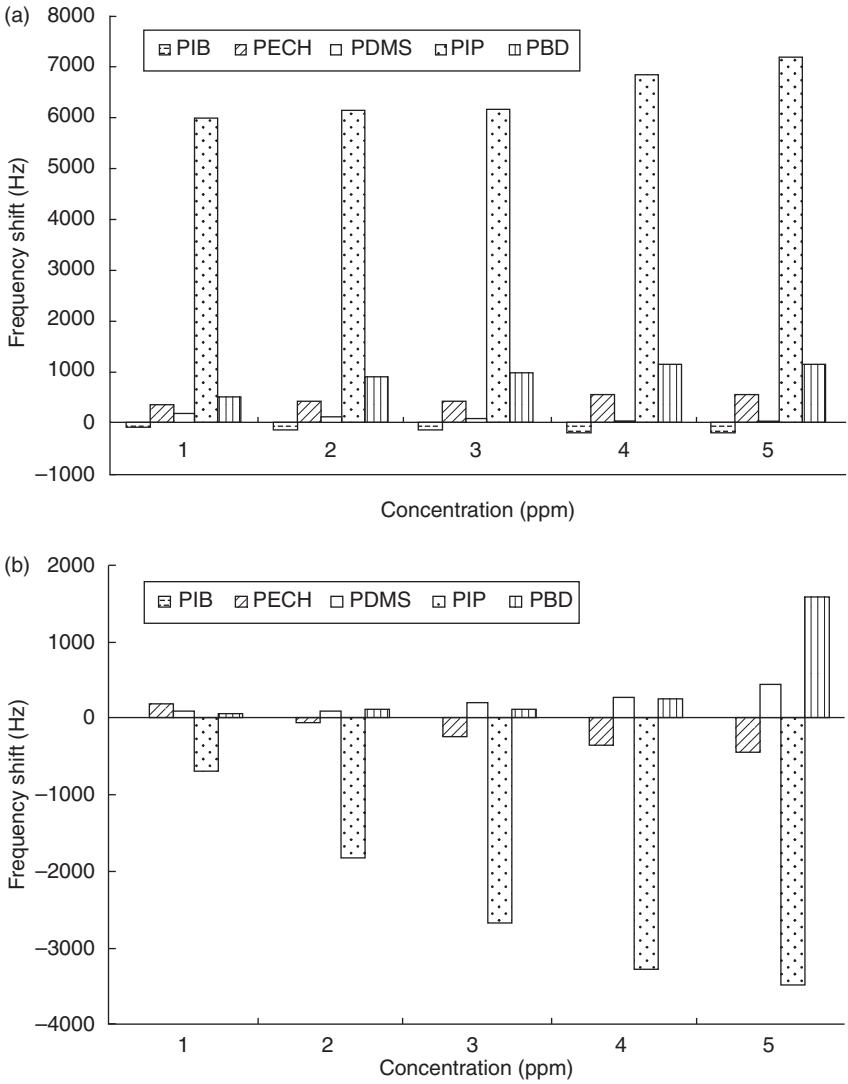

14.20 Frequency shift of various sensing films for different simulant gases: (a) CH_2Cl_2, (b) DCP.

Principal component analysis (PCA) is known as a statistical distribution method. For example, if we assume four parameters, these can be shown on a four-dimensional graph. However, doing so is very difficult and complicated. However, the PCA method can reduce the parameters to two dimensions by extracting significant data from various parameters.[20–29] Sensor arrays can be used to check for CWAs of different concentrations. The PCA method has been adapted here to classify chemical agents. Figure 14.22 shows the PCA

© Woodhead Publishing Limited, 2013

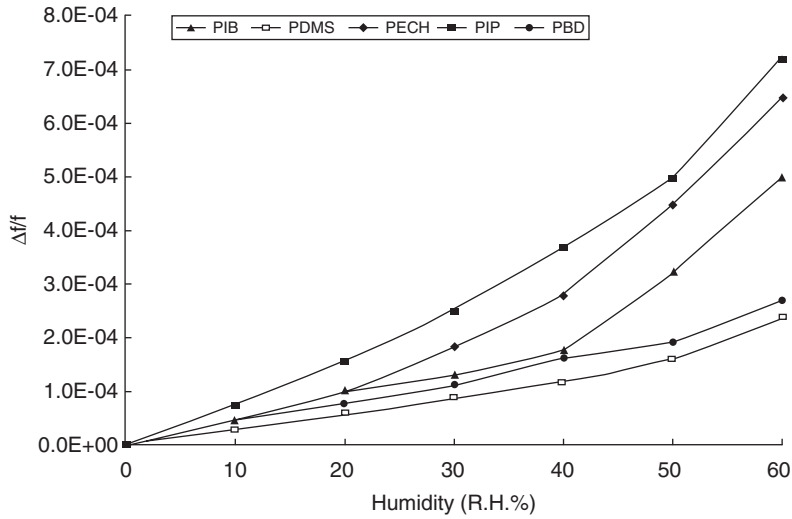

14.21 Sensing properties of SAW sensors for various levels of humidity.

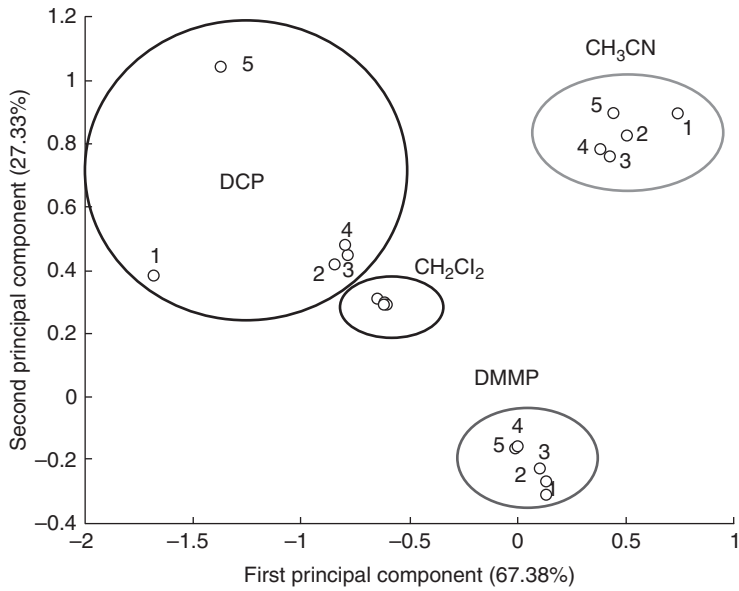

14.22 PCA results for the concentration change of each gas.

© Woodhead Publishing Limited, 2013

results for each chemical agent at different concentrations and with various simulant gases, using the SAW sensor array.[21]

Considering the merits and demerits of both semiconducting devices and SAW-type devices, an array with both a semiconductor and a SAW device might be designed as a useful means of detecting odors, including those of CWAs.

14.6 Conclusion

This chapter has presented a brief overview of sensing devices for CWAs. Three detecting methods were introduced (ion mobility spectrometers, semiconducting devices, and SAW-type devices), and their fabrication and sensing properties were described.

The sensing properties of semiconductor devices and sensor arrays were presented for four different simulants: dimethyl methyl phosphonate (DMMP) as a simulant of tabun (nerve agent), dipropylene glycol methyl ether (DPGME) as a simulant of mustard (blister agent), and dichloromethane (DCM) as a simulant of phosgene (choking agent).

Semiconductor device arrays were examined to classify the agents at different operating temperatures. In addition, the sensing properties of an array could include different sensing membrane SAW sensors (polyisobuthylene (PIB), polyepichlorohydrin(PECH), polydimethysiloxane (PDMS), polybutadiene (PBD), and polyisoprene (PIP)).

The sensing principle of SAW-type devices is based on a frequency shift during wave transmission over the sensing area between the input IDT and output IDT. It is also well-known that semiconductor devices are based on conductivity modulation due to the adsorption of gas molecules on the sensing membrane.

The simulants (DMMP, DCP, acetonitrile, and DCM) can be classified employing the PCA technique, which is acknowledged as a statistical distribution method. The polymer membrane SAW sensor arrays show fair selectivity to simulant gases by adapting the PCA method.

14.7 References

1. S. Yasuo, K.-K. Mieko, T. Kouichiro, O. Isaac, M. Koji, S. Hiroyuki, L. Teruo, L. Kazumitsu and S. Yasuhiro (2004) *Sensing technology for chemical warfare agents and its evaluation using real agents*, 10th IMCS, Japan, July, 886–7.
2. M. J. Vellekoop (1998) 'Acoustic wave sensors and their technology', *Ultrasonics*, **36**,7–14.
3. N.-j. Choi (2004) *Fabrication and its characteristics of micro gas sensor array for detection of chemical warfare agents*, Ph.D. Thesis, Kyungpook National University, Korea, December.
4. F. R. Sidell (1974) 'Soman and sarin: clinical manifestations and treatment of accidental poisoning', *Clinical Toxicology*, **7**, 1–7.

© Woodhead Publishing Limited, 2013

5. H. H. Rengatorff (1985) 'Accidental exposure to sarin; vision effects', *Architecture Toxicology*, **56**, 201–3.
6. D. Grob and A. M. Harvey (1953) 'The effects and treatments of nerve gas poisoning', *American Journal of Medicine*, **14**, 52–63.
7. C. J. West (1920) 'The history of mustard gas', *Chemical Metallurgy Engineering*, **22**, 541–54.
8. Program manager for chemical demilitarization (1997) Fact sheet, PMCD, US Army.
9. T. C. Marrs, R. L. Maynard and F. R. Sidell (1996) *Chemical warfare agents: toxicity and treatment*, John Wiley & Sons, New York.
10. D. D. Lee and J. C. Kim (2011) *Sensing technology for detection of chemical warfare agents*, 9th ACCS, Taiwan, November.
11. J. D. Ferry (1980) *Viscoelastic properties of polymer*, 3rd edn, John Wiley & Sons, New York.
12. J. E. Mark (1996) *Polymer Data Handbook*, Oxford University Press Inc., Lavoisier.
13. B. S. Joo, J. S. Huh and D. D. Lee (2007) 'Fabrication of polymer SAW sensor array to classify chemical warfare agents', *Sensors and Actuators B*, **121**, 47–53.
14. B. S. Joo (2006) *Polymer sensing film SAW sensor array for detection of chemical warfare agents*, Ph.D. Thesis, Kyungpook National University, Korea, December.
15. B. K.Sohn and D. D. Lee (2009) *Sensor Engineering*, Iljinsa, Korea.
16. S. C. Lee, H. Y. Choi, S. J. Lee, W. S. Lee, J. S. Huh, D. D. Lee and J. C. Kim (2009) 'The development of SnO_2-based recoverable gas sensors for the detection of DMMP', *Sensors and Actuators B*, **137**, 239–45,
17. M. Tochigi, T. Umekage, T. Otani, T. Kato, A. Iwanami , N. Asukai, T. Sasaki and N. Kato (2002) 'Serum cholesterol, uric acid and cholinesterase in victims of the Tokyo subway sarin poisoning: A relation with post-traumatic stress disorder', *Neuroscience Research*, **44**, 267–72.
18. A. Iwanami, O. Toshiyuki, T. Mamoru, K. Tadafumi, S. Tsukasa and K. Nobumasa (2002) 'Mental symptoms in victims of sarin poisoning 5 years after the Tokyo subway attack', *European Psychiatry*, **17**(1), 199.
19. J. A. F. Compton (1988) *Military chemical and biological agents*, Telford Press Caldwell, NJ, USA.
20. R. L. Maynard (1995) 'Toxicology of chemical warfare agents', *General & Applied Toxicology*, Macmillan, USA, 1123–53.
21. Y. S, Lee, B. S. Choi, B. H. Kang and D. D. Lee (2000) Pattern recognition of a gas sensor array using impedance, *Journal of the Korean Physical Society*, **37**, 862–5.
22. J. W. Strutt and Lord Rayleigh (1885) 'On waves propagated along the plane surface of an elastic solid', *Proceedings of the London Mathematical Society*, **17**, 4–11.
23. R. M. White and F. W. Voltmen (1965) 'Direct piezoelectric coupling to surface electric waves', *Applied Physics Letters*, **7**, 314–16.
24. H. Wohljen (1984) 'Mechanism of operation and design considerations for surface acoustic device vapor sensors', *Sensors and Actuators B*, **5**, 307–25.
25. H. Wohljen and R. Dessy (1979) 'Surface acoustic wave probe for chemical analysis, II Gas chromatography detector', *Analytical Chemistry*, **51**, 1465–70.

© Woodhead Publishing Limited, 2013

26. H. Wohljen and R. Dessy (1979) 'Surface acoustic wave probe for chemical analysis, III. Thermomechanical polymer analyzer', *Analytical Chemistry*, **51**, 1470–5.
27. J. W. Gardner and P. N. Bartlett (1994), 'A brief history of electronic nose', *Sensors and Actuators B*, **18**, 210–211.
28. T. Nakamoto, H. Takagi, S. Utumi and T. Moriizumi (1992) 'Gas/odor identification by semiconductor gas sensor array and an analog artificial neural network circuit', *Sensors and Actuators B*, **8**,181–6.
29. D. S. Lee, J. K. Jung, J. W. Lim. J. S. Huh and D. D. Lee (2001), 'Recognition of volatile organic compounds using SnO2 sensor array and pattern recognition analysis', *Sensors and Actuators B*, **77**, 228–36.
30. A. Guadarrama, M. L. Rodriguez-Mendez and J. A. de Saja (2002) 'Conducting polymer-based array for the discrimination of odours from trim plastic materials used in automobiles', *Analytica Chimica Acta*, **455**, 41–7.
31. A. Guadarrama, M. L. Rodriguez-Mendez and J. A. de Saja (2000) 'Array of sensors based on conducting polymers for quality control of the aroma of the virgin olive oil', *Sensors and Actuators*, **69**, 276–82.

© Woodhead Publishing Limited, 2013

15

Integrated complementary metal oxide semiconductor-based sensors for gas and odour detection

P. K. GUHA and S. SANTRA, Indian Institute of Technology, Kharagpur, India and J. W. GARDNER, University of Warwick, UK

DOI: 10.1533/9780857098665.4.491

Abstract: This chapter addresses both the challenges and benefits of fabricating gas sensors using complementary metal oxide semiconductor (CMOS) technology and the integration of associated circuitry onto a single silicon chip. The main objective described here is, specifically, the development of ultra-low power (~mW) resistive and calorimetric gas sensors that can operate at high temperatures (up to 600°C) on a CMOS platform. This compatibility with the standard CMOS manufacturing process will permit high volumes of production (>100k per annum) at low unit cost (<$1). The chapter describes in turn the design of interface electronics for these high-temperature gas sensors, the necessity of having arrays when employing non-selective gas-sensing materials, and the exploitation of a new generation of nano-materials as the gas sensing layer on CMOS devices. Finally, the outlook of smart CMOS-based gas (or odour) sensors is considered, with particular emphasis on the possibility of new domains of application.

Key words: smart sensors, complementary metal oxide semiconductor (CMOS) gas sensors, nano-materials on CMOS.

15.1 Introduction

The modern gas sensor is increasingly becoming an important part of our everyday lives. It can be found in our homes (e.g. monitoring the level of CO in air from gas-fired boilers), in our workplace (e.g. checking the levels of toxic gases and odours) and in hospitals (e.g. monitoring anaesthetic and respiratory gases). There has been a continual demand for improved workplace safety for certain industries (e.g. working in coal mines) through tougher government legislation – even in developing countries such as China and India. Moreover, there are also some emerging niche markets (e.g. sensors for notebooks, tablets and mobile phones) which require low-cost (<$5) and low-power (mW or less) gas (or odour) sensors in high volumes

© Woodhead Publishing Limited, 2013

(millions of units per year). However, the average cost of a gas sensor available today is in excess of $25. This is because the production of discrete gas sensors tends to be semi-automated and in batches of relatively small volumes. In addition, these sensors require associated interface electronics using discrete components to monitor the sensor output and drive heaters. This increases the cost even further (well in excess of $100).

The current gas sensor market has been estimated to be around $500 million per year and growing at a rate of 10% per annum (MNT Gas Sensor Roadmap, n.d.). However, the growth in the market in recent years has been achieved by lowering the unit cost of sensors through the development of smaller gas sensors. Further growth will be generated for semiconductor-based gas sensors (as opposed to electrochemical or optical sensors) if solid-state gas sensors can be developed on a complementary metal oxide semiconductor (CMOS) chip combined with the associated circuitry using standard microelectronic and microelectromechanical (MEMS) processes. Success in this endeavour should reduce the volume cost of sensors to below $1 and, hence, access new high volume markets.

One of the most common types of gas sensor sold is the electrochemical gas sensor; however, although these are low power, it is not possible to integrate this type of sensor and the necessary circuits on the same chip. This is because it requires significant volumes of liquid electrolytes and non-CMOS catalytic materials, such as platinum or silver electrodes. Another common gas sensor is based on infrared absorption but these require high power for the source and non-CMOS optical band-pass filters. They are also even more expensive than electrochemical sensors at $50 or more.

In this chapter, we will discuss two types of semiconductor gas micro-sensors employing (i) resistive and (ii) calorimetric sensing materials. Recent research shows that it is possible to integrate these types of gas sensor on a CMOS chip and, hence, they have the potential to open up mass markets in the near future. The chapter addresses the key issues associated with the integration of these gas sensors onto a standard CMOS wafer – the main challenges being to deposit/grow sensing materials (CMOS, in particular, imposes many constraints on material integration) and the nature of the electronic circuits required to interface the sensors. We also briefly discuss the potential for low-cost arrays of gas sensors, such as those required for e-nose applications. Finally, we consider the future of smart CMOS gas sensors.

15.2 Micro-resistive complementary metal oxide semiconductor gas sensors

Resistive gas sensors are based upon monitoring a change in the electrical conductivity of a sensing material (primarily, non-stoichiometric semiconducting metal oxides like SnO_2, WO_3, ZnO and TiO_2) at high temperature

© Woodhead Publishing Limited, 2013

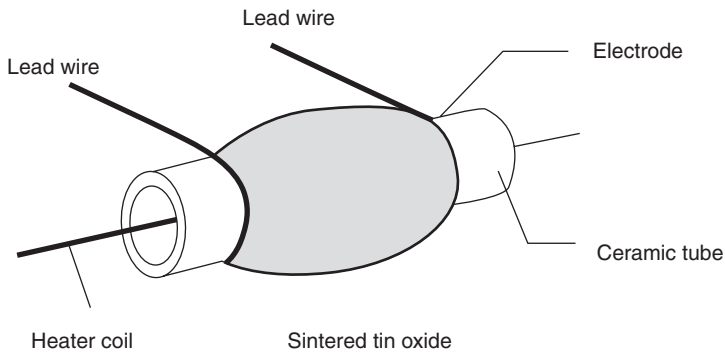

15.1 Basic structure of a Taguchi-type tin oxide gas sensor (Figaro Engineering, Japan).

(typically, 200–500°C) in the presence of the gas. They are perhaps the earliest form of available gas sensor on the market. For example, Taguchi gas sensors (TGS) were commercialised in the early 1970s and are still produced today by Figaro Inc., Japan. The Taguchi gas sensor comprises a platinum heater coil inside a ceramic tube. A manually painted thick layer of porous tin oxide film is deposited over platinum electrodes on a ceramic cylinder and sintered at a high temperature (e.g. 650°C) to achieve the appropriate crystalline structure. Figure 15.1 shows the structure of a Taguchi-type tin oxide gas sensor. The resistance of the tin oxide coating changes in the presence of a gas that reacts with chemisorbed oxygen at high temperature (typically 400°C), and this is measured via the electrodes and a basic potential divider circuit. The reasons for the high-temperature operation of metal oxide gas sensors are: (i) the reaction with chemisorbed oxygen sites (and catalytic dopants) is more specific at higher temperatures, (ii) the reaction kinetics are much faster, and (iii) the interference from water vapour is reduced (Gardner *et al.*, 2001). Platinum wire resistive heaters are used to heat up the gas-sensing material to high operating temperatures in order for the reaction to be efficient, but require several hundred milliwatts of power. The key challenges associated with resistive CMOS sensor design are to reduce the power consumption significantly, and to achieve a stable and uniform temperature over the sensing area.

New-generation micro-resistive sensors are usually formed on a thin thermally-insulated silicon membrane so as to reduce the power loss; this thin membrane-like structure is often referred to as a 'micro-hotplate'. Researchers have studied different materials for designing micro-heaters, such as doped polysilicon, aluminium and platinum (Cavicchi *et al.*, 1995; Houlet *et al.*, 2006; Udrea *et al.*, 2001). Platinum heaters are probably the most stable material at 400°C, but this material is not available in a CMOS foundry; hence, post-CMOS deposition is necessary. Within the CMOS

© Woodhead Publishing Limited, 2013

process, polysilicon has a poor long-term stability at high temperature due to electro-migration, grain boundary movement and crack propagation, whilst aluminium shows electro-migration at high temperatures. Metal oxide semiconductor field effect transistor (MOSFET) heaters can be controlled by applying varying bias voltage at the gate; however, very high temperature operation is not reliable in silicon on insulator (SOI) CMOS because of the triggering of a parasitic bipolar transistor (Guha *et al.*, 2007).

In the literature, many researchers have claimed that their design is 'CMOS compatible', where in most of the cases 'CMOS compatible' means that either the sensor design can be made using a modified CMOS process, or CMOS materials have been used in the fabrication. However, no standard CMOS process has been used to produce their respective devices or components (Graf *et al.*, 2004). Recent work from Prof. Gardner's group at Warwick University (using industrial CMOS foundry) shows that heaters made from *p*+ silicon performs better than *n*+ silicon and much better than doped polysilicon in long-term operation (Iwaki *et al.*, 2006). Some commercial foundries now support high-temperature metals along with aluminium metallisation in the same wafer; so, high-temperature metal (e.g. tungsten) can be used for the heater and aluminium (lower resistivity compared with tungsten) for circuit metallisation. Work led by a group from Cambridge University using SOI CMOS wafer reported the superiority and reliability of a tungsten heater (Ali *et al.*, 2008). Here, the heater is embedded in a oxide/nitride membrane; hence, thermally isolated from the rest of the chip, which ensures reliable on-chip circuit operation. The membranes were formed at a wafer level (from MEMS foundry) using a deep reactive ion etch (i.e. a

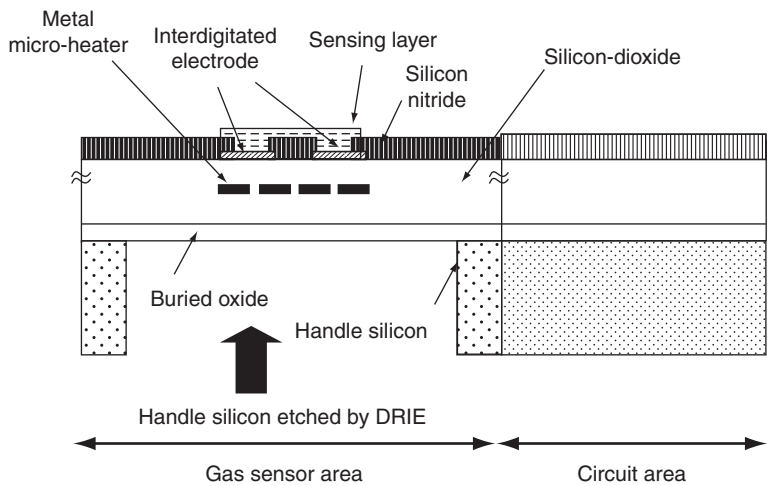

15.2 (a) Cross-sectional view of CMOS micro-hotplate-based gas sensor (drawing not to scale).

© Woodhead Publishing Limited, 2013

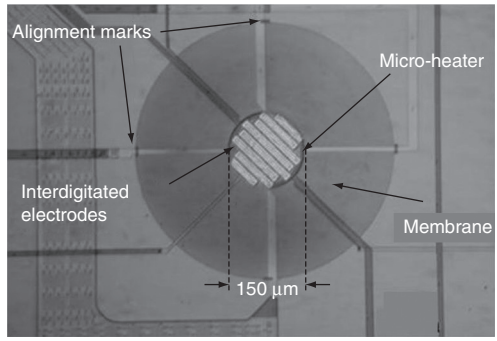

15.2 An optical microscope image of the fabricated micro-hotplate device (adapted from Santra *et al.*, 2010a).

post-CMOS MEMS process). The heaters can heat up the membrane and at, say, 300°C only require 6 mW of power. The interdigitated electrode (for resistance measurement of the sensing material), formed by the top metal layer was exposed at the same step of bond pad opening. The cross-sectional view of the sensor and a top view of a fabricated device are shown in Figs 15.2(a) and 15.2(b). At the same time, other research groups – such as Baltes (ETH, Zurich) and de Rooij (IMT, Neuchatel) – reported equally power-efficient non-SOI micro-heaters fabricated inside silicon plugs (Barrettino *et al.*, 2004b; Briand *et al.*, 2000).

15.3 Micro-calorimetric complementary metal oxide semiconductor gas sensor

Micro-calorimetric sensors detect heat, or the change in enthalpy generated from the chemical reaction that takes place between the sensing material and the gas molecules. This kind of sensor functions at higher temperatures than resistive gas sensors (around 500°C or more), and there is a need to integrate the micro-heater under the catalytic sensing area, as in the case of micro-resistors. One of the popular micro-calorimeters is called the 'pellet resistor' or 'pellistor', which was designed and patented by English Electric Valve (EEV) Ltd in the early 1970s (www.e2v.com). Conventional pellistors (shown in Fig. 15.3) are made of a platinum coil in a porous alumina bead along with an embedded metal catalyst (e.g. palladium). The platinum coil not only heats up the bead to enable the reaction, but also acts as a resistance thermometer to measure the change in temperature of the catalytic surface relative to a second non-catalytic bead. The latest designs of micro-calorimeters usually use membrane technology like micro-resistive sensors (except these do not have electrodes). Two identical sensors (one having an active sensing material and the other playing the role of a reference) and

© Woodhead Publishing Limited, 2013

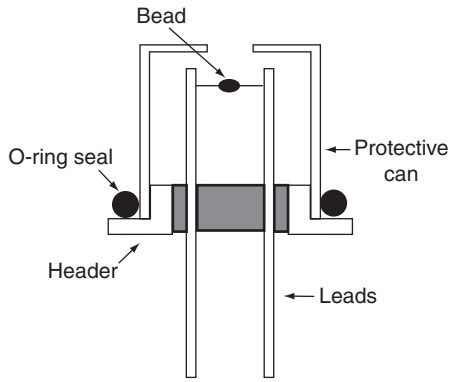

15.3 A conventional commercial pellistor (City Technology Ltd, UK, now part of Honeywell).

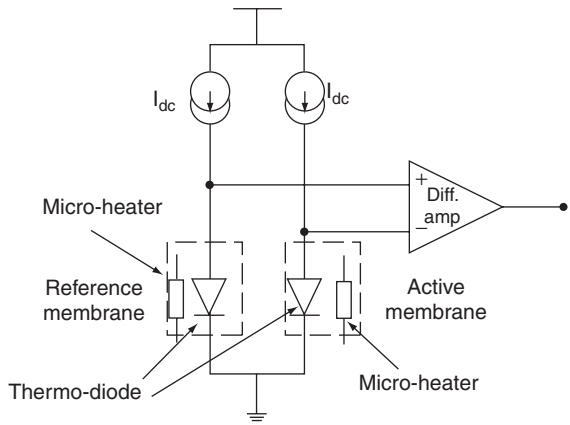

15.4 A differential transducing circuit for micro-calorimeter (adapted from Udrea *et al.*, 2001).

a differential amplifier are used to measure the difference in temperature caused by the chemical reaction, as shown in Fig. 15.4. Two accurate temperature sensors placed within the membranes are used to detect the temperature in the respective micro-calorimetric sensors (Udrea *et al.*, 2001).

15.4 Sensing materials and their deposition on complementary metal oxide semiconductor gas sensors

Modern solid-state (resistive) gas sensors are generally based on wide-band-gap semiconducting metal oxide sensing materials. Resistive gas sensors available in the market (e.g. TGS 812, Figaro Engineering) generally use

© Woodhead Publishing Limited, 2013

doped tin oxide as the sensing material. Solid thin film metal oxides are not effective for micro-sensors (the smaller surface area causes lower sensitivity). Thus, nano-materials are suitable candidates for gas detection, because of their exceptionally high surface area and dimension compared with the depletion region. So, there is a possible increase in sensitivity even for a miniaturised sensor area using new nano-materials with even smaller grain sizes or dimensions. However, growing nano-materials on CMOS wafer is very challenging; the CMOS substrate cannot sustain prolonged high temperature heating (because of aluminium electro-migration), which is often necessary during the growth process and annealing of the nano-materials. Again, it is recommended not to use any harsh chemicals and environments (e.g. long plasma exposure might damage fragile micro-hotplate structure) for nano-material synthesis on CMOS. Therefore, a low temperature growth process (<500°C) with CMOS-friendly chemicals is desirable for sensing material synthesis. One such method has been reported by Santra *et al.* (2010b) for growing zinc oxide nanowires on a fully-processed CMOS micro-hotplate. A scanning electron microscopy (SEM) picture of grown nanowires on an SOI device is shown in Fig. 15.5. Recently, a local growth technique has also been reported for carbon nanotubes (CNTs) – again, on micro-hotplate area (Santra *et al.*, 2010a). Here, micro-heaters are used to form catalytic islands and, hence, CNTs are grown only on the heater areas without exposing the whole CMOS chip to problematic high temperatures. This idea has been extended to grow CNTs at the wafer level in specified areas of multiple chips simultaneously (scheme shown in Fig. 15.6), which later can be diced and thus serve the purpose of post-CMOS batch fabrication of sensing material.

There are many possible ways of depositing nano-materials onto a CMOS substrate – for example, chemical vapour deposition (CVD) is possible

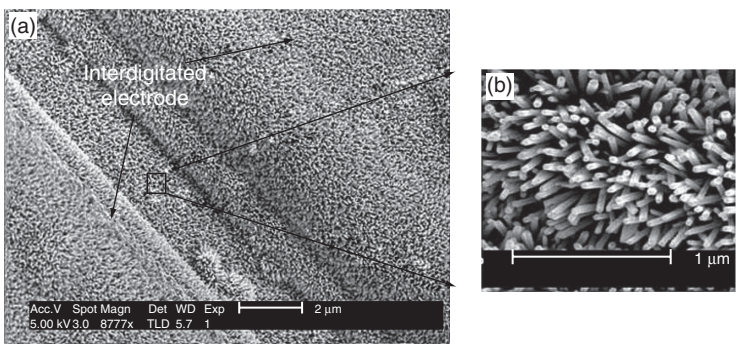

15.5 (a) SEM image of the zinc oxide nanowires on a CMOS micro-hotplate (adapted from Santra *et al.*, 2010b). (b) Higher magnification view of nanowires (adapted from Santra *et al.*, 2010b).

© Woodhead Publishing Limited, 2013

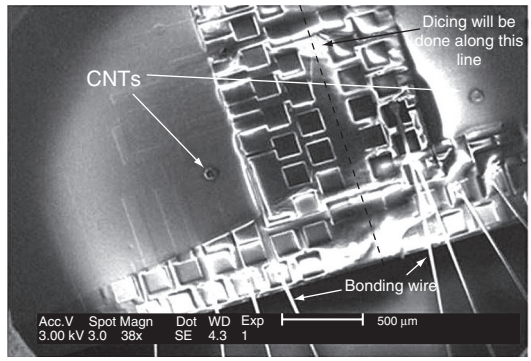

15.6 SEM image of CNTs which were locally grown simultaneously using micro-heaters placed at adjacent chips (adapted from Santra *et al.,* 2010a).

provided the process temperature can be reduced to below 600°C. One type of CVD is aerosol assisted chemical vapour deposition (AACVD); in this process, precursors are transported to the substrate by means of a liquid/gas aerosol, which can be generated ultrasonically. This technique is suitable for use with non-volatile precursors. Alternatively, very thin layers of metal oxides can be grown by using an atomic layer deposition (ALD) process. Another promising recent approach is flame spray pyrolysis (FSP), because it enables the control of the size of the metal oxide nano-crystals on the wafer level. Most of the materials mentioned above show a response to different gases (i.e. the response is non-specific); however, it is possible to increase the sensitivity/selectivity to a particular gas by functionalizing them. This functionalization can be performed in different ways – for example, the inclusion of nano-clusters of metal or metal complex doping etc. Instead of employing a single metal oxide (e.g. SnO_2), mixed metal oxides (e.g. $CuO:SnO_2$) can also be developed to improve the response to a particular gas.

Techniques like spray-coating and even inkjet-printing can be very useful for depositing materials (like metal oxides, CNTs, graphene, nanocomposites) on specified areas; particularly, printers with high precision are already available in the market (Altatech, Tesscorn). The advantage of this approach is that one can avoid several steps of conventional lithography and that use of very high temperatures and harsh chemicals is not required. However, sometimes, nano-materials are not easy to dissolve or form suspensions in a liquid; in this case, it may be necessary to use a high-speed sonicator for hours in order to avoid the nozzle clogging up in the printer or spray-coater.

© Woodhead Publishing Limited, 2013

15.5 Interface circuitry and its integration

There are two possible ways of interfacing gas sensors with their associated interface circuitry: the hybrid approach and the monolithic approach.

- *Hybrid approach*: this method employs separate chips for the sensors and the circuits. So, one can reuse the same circuit chip, even if there is a problem with the sensor device (e.g. breaking of the membrane) and enhance manufacturing yield through screening. The other main advantage is that there is no restriction on the type of material used and the process steps for the fabrication of the sensors; hence, both the material and the fabrication process can be adjusted to optimise the overall performance of the sensor devices. However, parasitic capacitances or inductances associated with long interconnects and bonding wires are undesirable and can cause higher levels of signal degradation/noise. In addition, the hybrid approach is more expensive than a single-chip implementation when considering high volumes.
- *Monolithic approach*: in this method, the sensor and the circuits are on the same silicon chip. The monolithic approach is cost-effective in high unit volumes, making it commercially attractive. From the performance point of view, this system offers advantages such as a significant reduction in the noise and cross-talk levels as the number (and length) of wires and bonds is substantially reduced and there should be much better matching between different sensors. However, a fault in a sensor will result in the failure of the complete chip, even if the circuitry is working properly.

A common problem with any micro-sensor is that they tend to generate small electrical signals at the sensor output, so the front-end circuitry needs to be of very low noise (i.e. a good analogue design). Present submicron CMOS processes offer very low rail-to-rail supply (say, 0 to 1.1 V); this is good for low power, but makes front-end design much harder because of sensor drift (due to ageing and incomplete release of analyte at the end of a measurement etc.).

As chemo-resistive sensors are based on a change in conductivity at high operating temperatures, so main circuit blocks required for interfacing these sensors are: driving circuits for micro-heaters, temperature control units and sensing material interface circuits.

- *Driving circuits for micro-heaters*: this generally requires a stable, accurate current or voltage source circuit with large current (tens of milliamps) driving capability.

© Woodhead Publishing Limited, 2013

- *Temperature control unit*: the temperature of the gas-sensing material plays a vital role in improving the selectivity of almost all sensing materials; hence, accurate control of the temperature of the gas-sensing material is extremely important. In most commercial gas sensors, the change in heater resistance with temperature is used to set or control the operating temperature of the heater itself. In one such reported work, Bota *et al.* (2004) used the same resistor element as the heater and temperature sensor. They used a pulse width modulation (PWM) technique where, during the off mode of the heater, a small current was driven through the heater to measure its temperature (as shown in Fig. 15.7). However, a separate temperature sensor (in the form of silicon/polysilicon resistor or silicon diode) can increase the flexibility in circuit design and, hence, the reading and control of the precise temperature of the sensing area. There are several ways to control the heater temperature – for example, the heating can be controlled in on–off mode (sometimes called a 'bang-bang' controller), proportional mode, or proportional integral derivative (PID) mode. The on–off controller is the simplest form: if the micro-hotplate is cooler than a set-point temperature, the heater is turned on at maximum power; once it is hotter than the set-point temperature, the heater is switched off completely. However, bang-bang control can give rise to instability and might, unless controlled carefully, damage the heater due to very rapid changes in voltage (hence, temperature). The on-chip digital PID controller using an 0.8 μm commercial CMOS process for controlling heater temperature was reported in Barrettino *et al.* (2004a); a PID controller has many advantages, such as a rapid respond time without over-swing and steady state error; hence, smooth temperature control of the heater.
- *Sensing material interface circuit*: the design of this interfacing circuit is one of the main challenging components of a resistive gas sensor. This is because:

  (a) The circuit must handle the precision and dynamic range that is demanded by the gas-sensing element. The baseline resistance varies enormously depending on the sensing material used, e.g., sensing materials like metal oxides can have sheet resistances from 1 kΩ per square up to even 10 GΩ per square.
  (b) Often, there is drift in the baseline resistance of the sensing material; this can be due to a variety of reasons (e.g. material is not thermodynamically stable, material has been polluted by sulphur-based compounds, electro-migration). The circuits should be able to compensate for this drift to give accurate changes in resistance in the presence of the target gas.

© Woodhead Publishing Limited, 2013

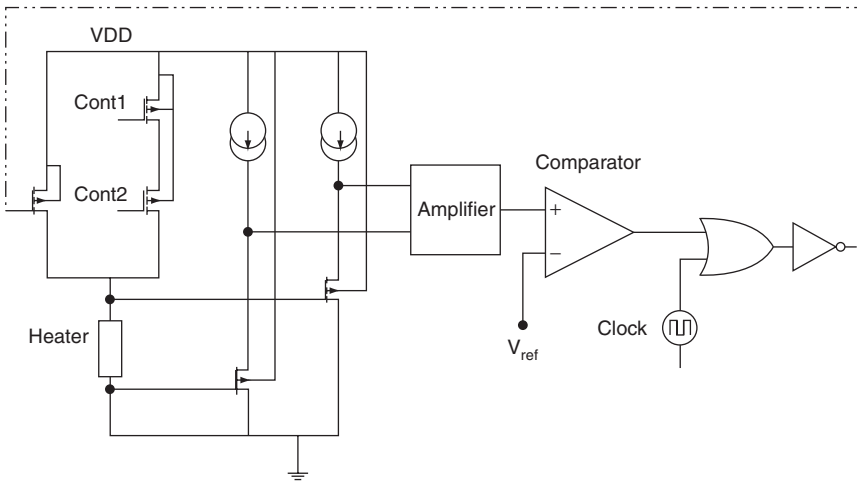

15.7 Diagram of a temperature control circuit, in which the same heater is used for measuring the temperature (adapted from Bota *et al.*, 2004). (VDD, supply voltage. V_{ref}, reference voltage.)

The literature reports many different solutions to the challenges mentioned briefly above. A very simple scheme is simply a resistor divider circuit or Wheatstone bridge technique. But these are not ideal when seeking full integration, as they need either trimming or variable resistors from outside the chip. One of the popular approaches found in the literature is the resistance-to-frequency conversion. The challenge with such a scheme is to retrieve/isolate parasitic capacitances associated with the sensing material, because this is a high-frequency process and, hence, resistance measurement will be contaminated with sensing material capacitance. Two such schemes have been reported by De Marcellis *et al.* (2008) and Grassi *et al.* (2006, 2007). In the scheme reported by De Marcellis *et al*., the generated pulse provides both sensing resistance values and also parasitic capacitances associated with the sensing material. In the scheme reported by Grassi *et al*. (shown in Fig. 15.8), the parasitic capacitor role can be avoided by isolating the sensor resistor from the oscillator portion of the circuit. This was achieved by using a sensing material resistor at the reference arm of a current mirror, and then using the mirror current to charge and discharge a capacitor. The capacitor voltage is then fed into comparators to compare with high (VH) and low voltage (VL) levels to generate a digital pulse. This resultant square wave time period has the information of the sensing material resistor. The scheme achieved (simulation result) a worst-case precision of about 0.5% over the range of 5 decades (1 kΩ–100 MΩ), as shown in Table 15.1.

A relatively simple scheme has been reported by Barrettino *et al.* (2002). A large dynamic range of sensing material was compressed by using two

© Woodhead Publishing Limited, 2013

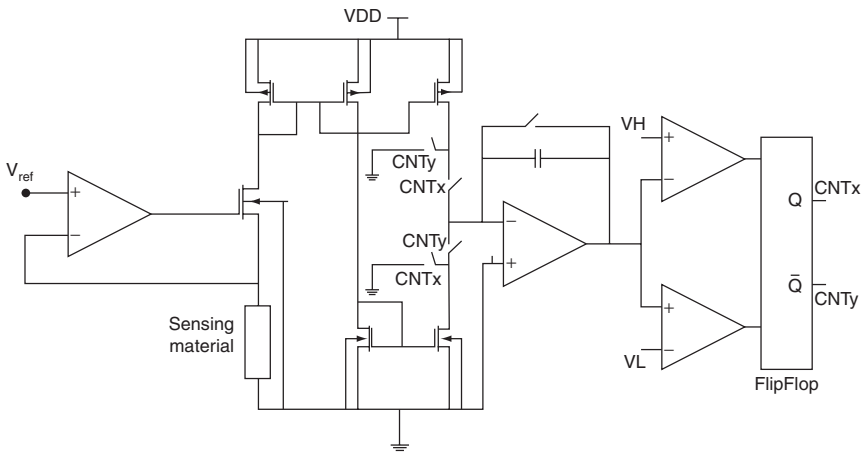

15.8 Resistance controlled oscillator circuit for gas-sensing material interface (adapted from Grassi *et al.,* 2007). Q and $\bar{Q}$ are two complementary signals at the output of the flip flop.

Table 15.1 Simulation precision results for sensors resistance materials

$R_{nominal,applied}$	$R_{measured,simulated}$	Linear error (%)
1 kΩ	1.0183 kΩ	–0.30881
100 kΩ	102.27 kΩ	+0.13148
1 MΩ	1.0212 MΩ	–0.01593
100 MΩ	101.90 MΩ	–0.04878

diodes (log converter approach); however, the scheme generated losses of only 8-bit resolution (the circuit is shown in Fig. 15.9). One popular baseline drift removal approach has been reported by Koickal *et al.* (2005, 2007) and is shown in Fig. 15.10. In this scheme, during the set-up phase, each sensor is driven by a small value current source and the voltage across the sensor is digitally stored using a simple counting analogue-to-digital converter. This stored value is converted back to an analogue signal (using a digital-to-analogue converter) and then subtracted from the sensor signal, thus removing the baseline resistance. The scheme achieved good sensor stability, and the drift of base line resistance found to be less than 5 mV.

More advanced signal-processing circuitry is best performed using digital blocks and micro-controllers. These components can be integrated with standard CMOS processes, they are very low-cost and permit the conversion of time-varying analogue signals to filtered digital signals for standard digital communication ports. Moreover, the relatively slow response times (seconds) of these sensors would require very large analogue CMOS

© Woodhead Publishing Limited, 2013

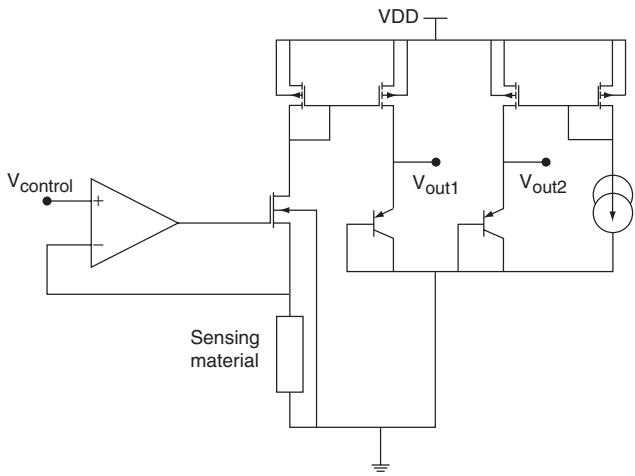

15.9 Logarithmic compression circuit for gas-sensing material interface (adapted from Barrettino *et al.*, 2002). ($V_{control}$ is a voltage applied from outside which will fix the voltage across the sensing material and thus fix the current at the reference arm of the current source. V_{out1} and V_{out2} are two output terminals of the circuit.)

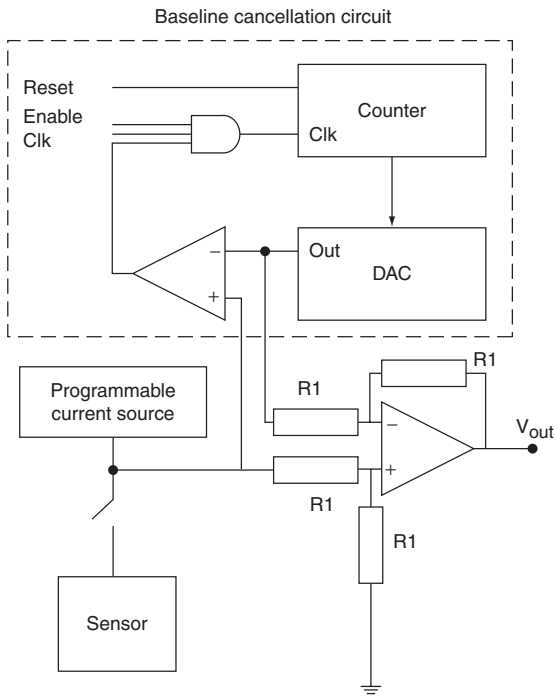

15.10 Diagram for baseline cancellation circuit (adapted from Koickal *et al.*, 2007). (Clk, clock; DAC, digital to analogue converter; R1, resistance; V_{out}, output voltage of the circuit.)

© Woodhead Publishing Limited, 2013

components (resistors and capacitors) that would be problematic in terms of cost and accuracy.

15.6 Integrated multi-sensor and sensor array systems

There is an increasing desire to measure more than one gas simultaneously. For example, in a boiler combustion process there could be a requirement to measure hydrogen or methane, as well as CO, CO_2 and even oxygen. Alternatively, in the case of automotive gases there is a desire to measure CO, NO_2 and unburnt hydrocarbons. In other words, there is an increasing demand to have multi-gas sensing systems with perhaps between four and eight sensors (including humidity and ambient temperature).

In some ways, this is the same requirement faced when developing electronic nose technology. Sensor-based electronic noses are based upon an array of non-specific gas sensors coupled with a pattern recognition technique (Gardner and Bartlett, 1999; Pearce *et al.*, 2003). Electronic noses tend to be large, expensive instruments. For example, the Fox 4000 electronic nose (Alpha MOS, France) comprises 18 power-hungry Taguchi-like metal oxide resistive gas sensors (see Fig. 15.11).

Consequently, there is a significant market pull for sensor arrays containing selective gas-sensing materials (multi-gas devices) and partially-selective gas-sensing materials (electronic noses). The two main challenges in sensor array-based technology is cost and power consumption. First, the

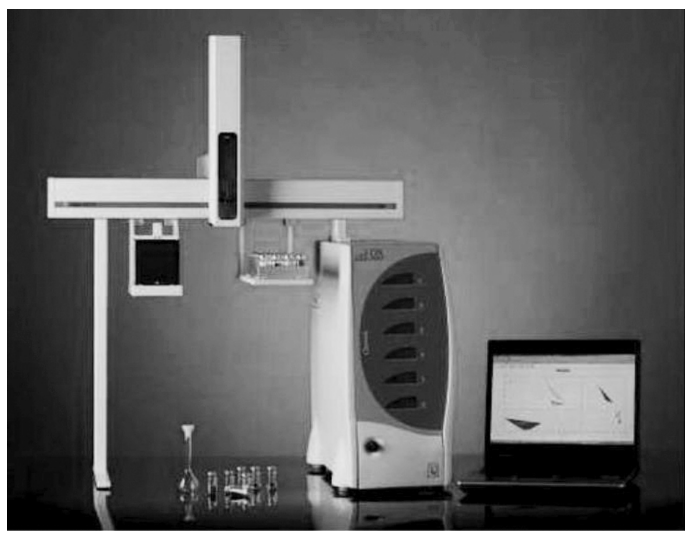

15.11 Fox 4000 electronic nose (Alpha MOS, France).

© Woodhead Publishing Limited, 2013

cost of sensor arrays will be significant; a set of four gas sensors will probably cost $100. This, with the addition of discrete circuitry, display, packaging etc., leads to prices of $500 to $1000 and, so, a limited market take-up. Second, the power consumption of a set of six metal oxide gas sensors will be 1–2 W. This is not compatible with their implementation of battery-operated devices (such as mobile phones and tablets), neither would it be suitable for automotive applications, where power is still a major issue.

The power consumption of SOI-based gas sensing is much lower than other technologies and enables individual devices to operate at below 10 mW DC (Ali *et al.*, 2008); through the pulsing of the heater, it is possible to obtain a power consumption of less than 1 mW per device. In addition, the use of deep reactive ion etching permits the integration of at least four micro-hotplates on a single 1 mm by 1 mm die. For example, Fig. 15.12 shows 1 mm square silicon dies with two and four separate micro-hotplates on them. The four-element chip can run four gas sensors at different temperatures with low-power consumption (power consumption of less than 25 mW at 400°C). The small thin SOI membranes provide a thermal response time of about 5 ms and so these devices can be operated in a pulsed mode and, hence, reduce the power consumption by a factor of 10 whilst still sampling every second.

The utilisation of SOI CMOS technology enables on-chip annealing at 650°C and operating temperatures of up to 600°C, thus allowing the use of not only metal oxide resistive materials (e.g. SnO_2 or WO_3), but also catalytic metals (e.g. palladium or platinum). With a CMOS or BiCMOS process comprising analogue components, it is now possible to combine a set of four sensors with analogue sensing/drive circuitry and a digital controller in a die of only 1 mm by 2 mm, thus permitting the production of smart gas sensors in high volumes for only $1–2. In practice, the cost of mounting and wire-bonding the chip onto, say, a TO-5 package is likely to cost more than the silicon die itself!

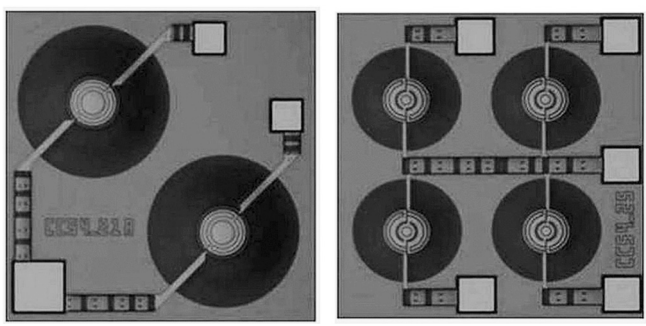

15.12 Multiple micro-hotplate-based gas sensors on a single silicon die (Cambridge CMOS Sensors, UK).

© Woodhead Publishing Limited, 2013

15.7 Conclusion and future trends

In this chapter, we have discussed technological developments towards the reduction in the size, power and – most importantly – cost of both resistive and calorimetric gas (and odour) sensors. A recent Cambridge-Warwick University spin-out Cambridge CMOS Sensors Ltd in the UK (www.ccmoss.com) believes that it is possible to fabricate a set of gas sensors and associated circuitry on a single silicon die at a cost of $1–2 in volume production and with a power consumption of a few milliwatts. This can be achieved through the use of high-temperature tungsten interconnects in a SOI CMOS process and deep reactive ion etching on the reverse of the silicon wafers. The low thermal mass of the SOI membrane results in a thermal response time of just a few milliseconds. This, in turn, makes the technology suitable for using more advanced signal-processing methods that modulate the device temperature. For example, it has been shown that switching the operating temperature between set points and measuring the time-series signals can result in a single micro-sensor measuring more than one gas (Iwaki *et al.*, 2009)! The method is based upon the principle that different gases react at different rates and so the dynamical information can be used not only to identify different gases, but also simple mixtures of gases.

The future of smart gas sensors may also be based upon new sensing materials. The SOI CMOS technology permits the on-chip deposition of new, exciting materials using chemical vapour deposition at 600°C to 750°C. For example, it is now possible to grow zinc oxide nanowires and carbon nanotubes (CNTs) directly onto the gas sensors (Santra *et al.*, 2010a, 2010b). Similarly, it is also possible to grow a single layer of graphene directly on the chip at 650°C with a nickel rather than copper catalyst. Although, the response of CNTs and graphene to gases has been shown recently to suffer from poor selectivity and response times, it may be that future developments in functionalisation will overcome these problems and open up a clear route to successful commercialisation.

Such low-power, smart and selective chemical sensors will be appropriate in many applications – safety, security, environmental monitoring, health care to name a few. In the case of biomedical detection, a non-invasive breath test approach looks very promising, since it is easy to repeat the detection process and also it does not cause the discomfort associated with blood tests. The breath test method is inexpensive and also point-of-care detection can be undertaken. It has been found that specific gases/vapours correspond to specific diseases – for example, acetone (for diabetes), nitric oxide (for asthma), carbon dioxide (for monitoring respiratory patients to evaluate their lung and pulmonary function), etc. In such health care applications, the cost of the sensor will be a major factor, because one requires simple plug-and-play low-cost sensors. We envisage smart sensor modules that cost less than €5 each and are 1 mm by 1 mm, and so could be packaged

© Woodhead Publishing Limited, 2013

in a micro-SD card and inserted into tablets, and even mobile phones. This means that they can be used in home automation; for example, users would be able to monitor many types of environmental gases, such as combustible CH_4 and toxic CO levels from domestic boilers. More challenging will be addressing health care for an ageing population – again, in homes. With more advanced circuitry and signal-processing techniques, it should be possible to measure the breath gases mentioned above with results wired straight to doctors' surgeries or hospitals.

We believe that the next generation of tablets, smart phones and other portable electronic devices will contain integrated gas sensors and, thus, CMOS gas sensors will find their way into everyday use in the next five years. As about 600 million smart phones are expected to be sold in 2013 alone, this is an exciting prospect for sensor manufacturers.

15.8 Useful web addresses

http://www.alpha-mos.com/
http://www.altatech-sc.com/en/index.php
http://www.ccmoss.com/
http://www.customsensorsolutions.com
http://www.detcon.com/electrochemical01.htm
http://www.e2v.com
http://www.figarosensor.com/
http://www.tesscorn.com/nanotechnology.htm

15.9 References

Ali, S. Z., Udrea, F., Milne, W. I. and Gardner, J. W. (2008) Tungsten-Based SOI Microhotplates for Smart Gas Sensors. *Journal of Microelectromechanical Systems*, **17**, 1408–1417.

Barrettino, D., Graf, M., Hafizovic, S., Taschini, S., Hagleitner, C., Hierlemann, A. and Baltes, H. (2004a) A single-chip CMOS micro-hotplate array for hazardous-gas detection and material characterization. *International Solid-State Circuit Conference*. San Francisco, CA.

Barrettino, D., Graf, M., Song, W. H., Kirstein, K., Hierlemann, A. and Baltes, H. (2004b) Hotplate-based monolithic CMOS microsystems for gas detection and material characterization for operating temperatures up to 500°C. *J. Solid-State Circuits*, **39**, 1202–1207.

Barrettino, D., Graf, M., Zimmermann, M., Hierlemann, A., Baltes, H., Hahn, S., Barsan, N. and Weimar, U. (2002) A smart single-chip micro-hotplate-based chemical sensor system in CMOS-technology. *International Symposium on Circuits and Systems*, **2**, 157–160.

Bota, S. A., Dieguez, A., Merino, J. L., Casanova, R., Samitier, J. and Cane, C. (2004) A monolithic interface circuit for gas sensor arrays: Control and measurement. *Analog Integrated Circuits and Signal Processing*, **40**, 175–184.

© Woodhead Publishing Limited, 2013

Briand, D., Schoot, B. V. D., Rooij, N. F. D., Sundgren, H. and Lundstrom, I. (2000) A low-power micromachined MOSFET gas sensor. *J. Microelectromech. Syst.*, **9**, 303–307.

Cavicchi, R. E., Suehle, J. S., Kreider, K. G., Shomaker, B. L., Small, J. A., Chaparala, P. and Gaitan, M. (1995) Growth of SnO2 films on micromachined hotplates. *Applied Physics Letters*, **66**, 812–814.

De Marcellis, A., Depari, A., Ferri, G., Flammini, A., Marioli, D., Stornelli, V. and Taroni, A. (2008) Uncalibrated integrable wide-range single-supply portable interface for resistance and parasitic capacitance determination. *Sensors and Actuators B: Chemical*, **132**, 477–484.

Gardner, J. W. and Bartlett, P. N. (1999) *Electronic noses: principles and application*, Oxford, Oxford University Press.

Gardner, J. W., Varadan, V. K. and Awadelkarim, O. O. (2001) *Microsensors MEMS and Smart Devices*, Wiley, West Sussex, England.

Graf, M., Barrettino, D., Zimmermann, M., Hierlemann, A., Baltes, H., Hahn, S., Barsan, N. and Weimar, U. (2004) CMOS monolithic metal-oxide sensor system comprising a micro-hotplate and associated circuitry. *IEEE Sensors Journal*, **4**, 9–16.

Grassi, M., Malcovati, P. and Baschirotto, A. (2006) Wide-range integrated gas sensor interface based on a resistance-to-number converter technique with the oscillator decoupled from the input device. *Proceedings of IEEE Symposium on Circuits and Systems*. Kos Isl, Greece.

Grassi, M., Malcovati, P. and Baschirotto, A. (2007) A 141-dB Dynamic Range CMOS Gas-Sensor Interface Circuit Without Calibration With 16-Bit Digital Output Word. *IEEE Journal of Solid-State Circuits*, **42**, 1543–1554.

Guha, P. K., Ali, S. Z., Lee, C. C. C., Udrea, F., Milne, W. I., Iwaki, T., Covington, J. A. and Gardner, J. W. (2007) Novel design and characterisation of SOI CMOS micro-hotplates for high temperature gas sensors. *Sensors and Actuators B: Chemical*, **127**, 260–266.

Houlet, L. F., Tajima, K., Shin, W., Itoh, T., Izu, N. and Matsubara, I. (2006) Platinum micro-hotplates on thermal insulated structure for micro-thermoelectric gas sensor. *IEEJ Transactions on Sensors and Micromachines*, **126**, 568–572.

Iwaki, T., Covington, J. A. and Gardner, J. W. (2009) Identification of different vapors using a single temperature modulated polymer sensor with a novel signal processing technique. *IEEE Sensors Journal*, **9**, 314–328.

Iwaki, T., Covington, J. A., Gardner, J. W., Udrea, F., Blackman, C. S. and Parkin, I. P. (2006) SOI-CMOS based single crystal silicon micro-heaters for gas sensors. *Proceedings of IEEE Sensors Conference*. Korea.

Koickal, T. J., Hamilton, A., Tan, S. L., Covington, J., Gardner, J. W. and Pearce, T. (2005) Smart interface circuit to ameliorate loss of measurement range in chemical microsensor arrays. *Proceedings of the IEEE Instrumentation and Measurement Technology Conference*. Ottawa, Ont., Canada.

Koickal, T. J., Hamilton, A., Tan, S. L., Covington, J. A., Gardner, J. W. and Pearce, T. C. (2007) Analog VLSI Circuit Implementation of an Adaptive Neuromorphic Olfaction Chip. *Circuits and Systems I: Regular Papers, IEEE Transactions on*, **54**, 60–73.

MNT Gas Sensor Roadmap. Available at https://connect.innovateuk.org/c/document_library/get_file?folderId=124339&name=DLFE-2150.pdf

© Woodhead Publishing Limited, 2013

Pearce, T., Schiffman, S. S., Nagle, H. T. and Gardner, J. W. (2003) *Handbook of Machine Olfaction: Electronic Nose Technology*, Weinheim, Wiley VCH.

Santra, S., Ali, S. Z., Guha, P. K., Covington, J. A., Zhong, G., Robertson, J., Milne, W. I., Gardner, J. W. and Udrea, F. (2010a) Post-CMOS wafer level growth of carbon nanotubes for low-cost microsensors—a proof of concept. *Nanotechnology*, **21**, 485301 (7 pp).

Santra, S., Guha, P. K., Ali, S. Z., Hiralal, P., Unalan, H. E., Covington, J. A., Amaratunga, G. A. J., Milne, W. I., Gardner, J. W. and Udrea, F. (2010b) ZnO nanowires grown on SOI CMOS substrate for ethanol sensing. *Sensors and Actuators B*, **146**, 559–565.

Udrea, F., Gardner, J. W., Setiadi, D., Covington, J. A., Dogaru, T., Lu, C. C. and Milne, W. I. (2001) Design and simulations of SOI CMOS micro-hotplate gas sensors. *Sensors and Actuators B*, **78**, 180–190.

© Woodhead Publishing Limited, 2013

16

Solid-state sensors for carbon dioxide detection

G. G. MANDAYO, CEIT-IK4 and Tecnun, Spain and
J. HERRÁN, CIDETEC-IK4, Spain

DOI: 10.1533/9780857098665.4.510

Abstract: Sensors for carbon dioxide are required in diverse fields, from air quality control to intelligent food-packaging. The requirements for those sensors in terms of performance, detection range and price vary greatly, depending on the field under consideration. Although infrared technology detectors are very widespread and are accurate, they are still expensive for some applications; thus, a considerable research effort is focusing on the improvement of the characteristics of solid-state devices. This chapter reviews electrochemical, impedimetric (conductometric) and field-effect devices for carbon dioxide detection. Throughout the chapter, the role of semiconductor materials in different devices is analyzed.

Key words: carbon dioxide (CO_2), mixed metal oxide, solid-state sensor.

16.1 Introduction

This section reviews the fields of application for carbon dioxide (CO_2) sensors as well as the existing regulations regarding CO_2 detection. It also gives an overview of the detectors currently available on the market and their price range.

16.1.1 Application fields for carbon dioxide sensors: where are carbon dioxide sensors necessary and/or useful?

Carbon dioxide (CO_2) sensors are widely required in many industrial and environmental fields. As an example, the food industry is using intelligent packaging techniques that involve the reduction of the oxygen content up to levels below 1% and the use of high levels of nitrogen and CO_2. While the oxygen reduction decreases the oxidation processes of the product, nitrogen avoids the collapse of the package when the product absorbs CO_2. CO_2 delays the growth of aerobic fungi and bacteria, so it prolongs the

© Woodhead Publishing Limited, 2013

shelf life of the vegetables. In this application, the quantity of CO_2 must usually be controlled within a range between 20% and 60% (Mullan, 2010; Nanotechnology, 2010; Nofima n.d.).

Looking at the gas industry, another application is the monitoring of gas quality. In the case of biogas generation, there is a need to analyze the composition of the gas in order to know its quality when it is mixed with natural gas from different sources. In particular. it is necessary to check the percentage of CO_2 in the gas mixture. This content can change depending on the origin of the biogas, going from 25% to 55% (Renewable Energy Concepts). If natural gas is considered, the majority of European standards currently in force require that the content of inert gases such as N_2 and CO_2 in natural gas is below 2.5%. Natural gas distributors measure gas quality with bulky equipment at various points on the pipelines (OFGEM, 2007). One possible idea in relation to this issue could be to charge the consumer according to the quality of the gas supplied. In this case, each consumer point would require a CO_2 sensor.

Air pollution is also a worldwide concern, and CO_2 is considered one of the causes of the greenhouse effect. The average CO_2 content outdoors is about 400 ppm, but in some cities – such as Los Angeles or Mexico City – that average increases up to 600 ppm. In order to decrease CO_2 emissions, it is essential to reduce energy consumption in buildings – for example, in Europe it accounts for 40% of the total energy consumption. Regarding indoor air quality (IAQ), according to the American Society of Heating, Refrigerating and Air-Conditioning Engineers (ASHRAE, 2011) good indoor ventilation means less than 850 ppm of CO_2. CO_2 levels above 20000 ppm (2%) can lead to symptoms associated with the respiratory system and the central nervous system. Even without reaching such levels, 4000–5000 ppm of CO_2 may impair concentration and cause tiredness. Taking all those facts into account, the efficient management of IAQ can be based on keeping a safe and healthy level of CO_2 inside buildings. This principle can be a fundamental source of energy savings.

In other cases, CO_2 detection is related to workers' safety – for example, in the brewing industry, where the fermentation process generates this gas. For short-term exposure (under 10 minutes), the US National Institute for Occupational Safety and Health (NIOSH) and the American Conference of Government Industrial Hygienists (ACIGH, 2011) limit is 30000 ppm (3%). NIOSH also states that CO_2 concentrations exceeding 4% are immediately dangerous to life and health.

16.1.2 Carbon dioxide sensors currently available on the market

After reviewing some of the possible uses of CO_2 detectors, it can be said that there is a wide market for this kind of device. Nevertheless, in the

© Woodhead Publishing Limited, 2013

applications mentioned, the detection ranges were very different. While in the case of pollution control it was in the order of 100–1000 ppm, in the case of gas quality control or modified atmospheres for intelligent packaging, the ranges increased even over 50%. Some of the applications mentioned can stand higher prices, while others require low-cost devices in order for them to be affordable and widespread. Therefore, there is a great interest in low-cost CO_2 detectors. In all the sensing devices that will be evaluated in this review, semiconductor materials (particularly semiconductor oxides) have a key role.

Analyzing the devices on the market (Table 16.1), we can find two main groups of sensors for CO_2 detection: electrochemical sensors, such as the

Table 16.1 Some of the sensors available on the market for the detection of carbon dioxide

Detection principle	Company	Model	Detection range	Photograph
Electro-chemical	Figaro	TGS4161 TGS4160	350–10 000 ppm 350–50 000 ppm	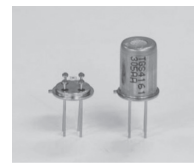
	Alphasense	CO2-D1	0.2–95%	
	Hanwei Electronics	MG811	350–10 000 ppm	
NDIR	Alphasense	IRC-A1	0–5000 ppm (min) 0–100% (max)	
	Dynament	TDS003	0–1000 ppm (min) 0–50% (max)	
		TDS0048	0–500 ppm (min) 0–100% (max)	

NDIR, non-dispersive infrared.

© Woodhead Publishing Limited, 2013

Figaro or Alphasense (Alphasense, 2009; Figaro, 2011), which cost between €15 and €30; and non-dispersive infrared (NDIR) sensors, such as the Dynament (Dynament, 2011), which are more expensive (between €70 and €130). These prices are always dependent on the quantity of sensors bought.

Looking at the great interest of such devices, several research groups are working to realize low-cost CO_2 sensors. This chapter reviews the current investigation into electrochemical, impedimetric (conductometric) and field-effect solid-state sensors.

16.2 Electrochemical sensors

This section analyzes electrochemical sensors for CO_2 detection. The two main categories of electrochemical sensing principles are reviewed (amperometric and potentiometric) and among potentiometric sensors, special attention is given to mixed potential sensors, because carbon monoxide sensors belong to this group. The influence of the materials and fabrication processes in the sensor performance is also evaluated.

16.2.1 Classification of electrochemical sensors according to the sensing principle

The common element in all the electrochemical solid-state CO_2 sensors is the solid electrolyte as an ionic conductor. According to the way the measurement is performed, they can be classified into two groups: amperimetric and potentiometric. Electrochemical sensors for CO_2 detection are usually mixed potential sensors, a subcategory of potentiometric sensors to detect other gases than oxygen. The mixed potential sensors generally involve oxide semiconductors as electrode materials.

Amperimetric sensors

These sensors usually have four different components: a diffusion barrier, a cathode, an anode and the electrolyte. The diffusion barrier is a key element in the sensor because it limits the gas flow to the cathode. The electrolyte is an oxygen ionic conductor. The most common material used as an ionic conductor is Yttria-stabilized zirconia (YSZ), always employed at temperatures over 300°C. Electrodes (anode and cathode) are usually made of conductive materials. The electrodes provide the necessary electrons for the reduction–oxidation reaction. In this reaction, ambient oxygen is incorporated in a vacancy in the electrolyte and forms an O^{2-} ion. Platinum is one of the most widely-used materials for electrodes because it shows good performance at

© Woodhead Publishing Limited, 2013

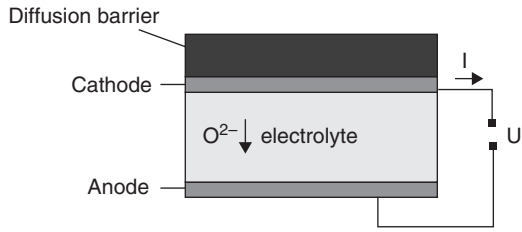

16.1 Scheme of a basic amperimetric sensor: anode, cathode, electrolyte and diffusion barrier. The applied voltage U and the diffusion barrier control the O^{2-} ion flow and thus the current (I).

high temperatures. Reactions in the anode and the cathode in this kind of sensor would be as follows:

$$O_2 + 4e^- \rightarrow 2O^{2-} \text{ cathode} \qquad [16.1]$$

$$2O^{2-} \rightarrow O_2 + 4e^- \text{ anode} \qquad [16.2]$$

This kind of sensor works in the following way: oxygen ions that enter the cathode go through the electrolyte and reach the anode. The voltage applied between anode and cathode is controlled so that the gas flow going through the diffusion barrier is not able to carry all the ions the electrolyte is able to transfer. This way, all the O_2 molecules that reach the cathode immediately react, and the current takes a constant value that only depends on the diffusion barrier and is a linear function of the oxygen concentration (see Fig. 16.1).

Potentiometric sensors

In potentiometric devices, an open-circuit voltage is measured. They also consist of an electrolyte (that is also typically made of YSZ) and two electrodes (also typically made of platinum). One of the electrodes is the working electrode (WE) – also called the sensing electrode (SE) – and the other is the reference electrode (RE). Both YSZ and Pt are suitable for high-temperature applications such as exhaust gas detection. They work as follows: the electrolyte is an ionic conductor and there is a thermodynamic equilibrium between ambient oxygen, electrons in the electrodes and mobile oxygen ions. In the simplest case, the following reaction takes place in the electrodes:

$$O_2(\text{gas}) + 2V_{o^{\cdot\cdot}} + 4e^- \leftrightarrow 2O^{2-} \qquad [16.3]$$

© Woodhead Publishing Limited, 2013

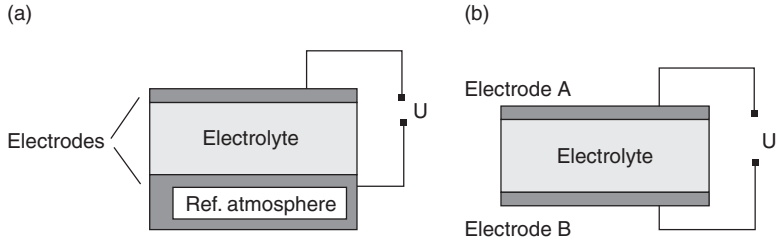

16.2 Scheme of a basic potentiometric sensor: electrodes and electrolyte: (a) with reference atmosphere chamber and (b) without reference. The electrochemical U potential is measured between electrodes.

where $V_{o^{..}}$ is an oxygen vacancy with a double positive charge in the electrolyte.

This working principle is the one in the lambda probes used to control combustion in engines. If the two electrodes are under different oxygen partial pressures, then an electromotive force is produced following the Nernst law (Equation [16.4]). In practical devices, one of the electrodes is in permanent contact with a reference atmosphere (see Fig. 16.2).

$$E_{emf} = \frac{RT}{nF} \ln \frac{p_{O_2}(1)}{p_{O_2}(2)} \qquad [16.4]$$

where R is the universal gas constant, T the temperature in Kelvin, n the number of moles of electrons taking part in the reaction, F is the Faraday constant, and $p_{O_2}(1)$ and $p_{O_2}(2)$ are the oxygen concentrations in each electrode.

There is a subcategory of potentiometric sensor known as a 'mixed potential' sensor, which is used to detect other gases than oxygen. This type of principle is used to detect gases such as NO_x, CO or CO_2. In this case, the sensor consists of two different electrodes (electrode A and electrode B) and the solid electrolyte (as seen in Fig. 16.3). Both electrodes are exposed to the same gas, which is usually a small percentage of the oxidizing or reducing target gas in oxygen. As electrodes are different, the redox reaction kinetics lead to different potentials in each electrode. This is the reason why they are referred to as 'mixed potential', because there is a competition between two different reduction–oxidation reactions in each electrode. In those cases, the form of the Nernst equation given in Equation [16.4] is no longer valid. A simple example of this type of sensor could use YSZ as the electrolyte, and gold and platinum for the electrodes. The most important advantage of these sensors is that they can be fabricated in a planar configuration, so the manufacturing process can take advantage of microfabrication techniques.

© Woodhead Publishing Limited, 2013

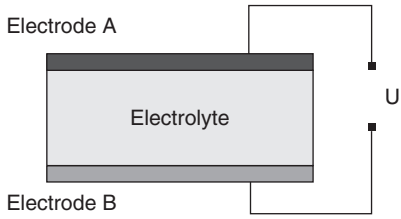

16.3 Scheme of a basic configuration of a mixed potential sensor: two different electrodes and an electrolyte. The mixed potential U is measured between electrodes.

16.2.2 Mixed potential electrochemical sensors for carbon dioxide detection

The first attempts to realize devices for low-cost electrochemical CO_2 sensors took place more than two decades ago (Hötzel and Weppner, 1987; Weppner, 1987). There is a classical categorisation of electrochemical sensors (Weppner, 1987) into types I, II and III. In type I, an ionic conductor for A_i ions is used and, thus, the partial pressure of component A_i is determined. Examples of this group are lambda probes. Type II sensors have an ionic conductor for A_i ions to determine the partial pressure of a different component, A_j. An example could be the detection of SO_x gas sensors made of Ag sulphate that reacts to the partial pressure of SO_3. Finally, in type III, an ionic conductor for A_i ions helps determine the partial pressure of another component A_j by the application of auxiliary phases. In the case of electrochemical detection of CO_2, as it is difficult to find an ionic conductor for CO_3^{2-} ions, it is typical to use an auxiliary phase that will be in thermodynamic equilibrium with the solid electrolyte, the electrons in the electrode and the gaseous phase. CO_2 electrochemical sensors generally belong to type III, according to this classification. As an example, Fergus (2008) says that the simplest electrochemical sensor to measure CO_2 uses a carbonate electrolyte, where the electrochemical potential is calculated by the ratio of the carbonate ion concentrations at the sensing electrode and at the reference electrode, according to the Nernst equation:

$$E = \frac{RT}{nF} \ln\left(\frac{[CO_3^{2-}]^{SE}}{[CO_3^{2-}]^{RE}}\right)$$

where R is the universal gas constant, T the temperature in degrees Kelvin, F is the Faraday constant and n is the number of electrons (n = 2 for CO_3^{2-}).

A further classification can be made in type III sensors according to the relationship between the auxiliary phase, the species to be detected and

© Woodhead Publishing Limited, 2013

the solid electrolyte (Yamazoe and Miura, 1998). Generally, those sensors are based on electrolytes of ionic conductors of sodium ions (Na+) such as NaSICON or β-alumina, or also of lithium ions (Li^+) such as LiSICON, together with sensing electrodes with auxiliary phases of lithium or sodium carbonates and reference electrodes of several materials. As an example, if a LiSICON electrolyte is used at 500°C, the reactions in the sensing electrode and in the reference electrode will be, respectively:

$$2Li^+ + CO_2 + \frac{1}{2}O_2 + 2e^- \leftrightarrow Li_2CO_3\,(SE)$$

$$2Li^+ + \frac{1}{2}O_2 + 2e^- \leftrightarrow Li_2O\,(RE)$$

The reduction–oxidation reactions create a Nernst potential (E) between the sensing electrode and the reference electrode that is related to the CO_2 concentration and given by Equation [16.5].

$$E = E_0 + \frac{RT}{2F}\ln(p_{CO_2}) \qquad [16.5]$$

where R is the universal gas constant, T the temperature in degrees Kelvin, F is the Faraday constant, p_{CO_2} is the CO_2 partial pressure and E_0 can be experimentally calculated if T and the activity of the electrolyte are fixed. By means of this equation, p_{CO_2} and E can be uniquely interrelated.

According to the results in the bibliography, although the majority of the works use NaSICON for the electrolyte, LiSICON is an option to take into account because its cross-sensitivity to water can be better lowered. Moreover, this electrolyte material shows a greater detection range, as shown in Fig. 16.4 (Fergus, 2008).

16.2.3 Relevance of the material and fabrication techniques in electrochemical sensor performance

A key point regarding electrochemical sensors is the fabrication process. These devices are usually obtained by means of sintering techniques to achieve pellet structures (Kida *et al.*, 2000), and some authors even combine thin- or thick-film techniques to fabricate some elements such as electrodes (Salam *et al.*, 1998). But the great potential of the use of planar configurations has made them more usual in the literature (Ramírez-Salgado and Fabry, 2003, Fergus, 2008). Planar devices ease the fabrication process so

© Woodhead Publishing Limited, 2013

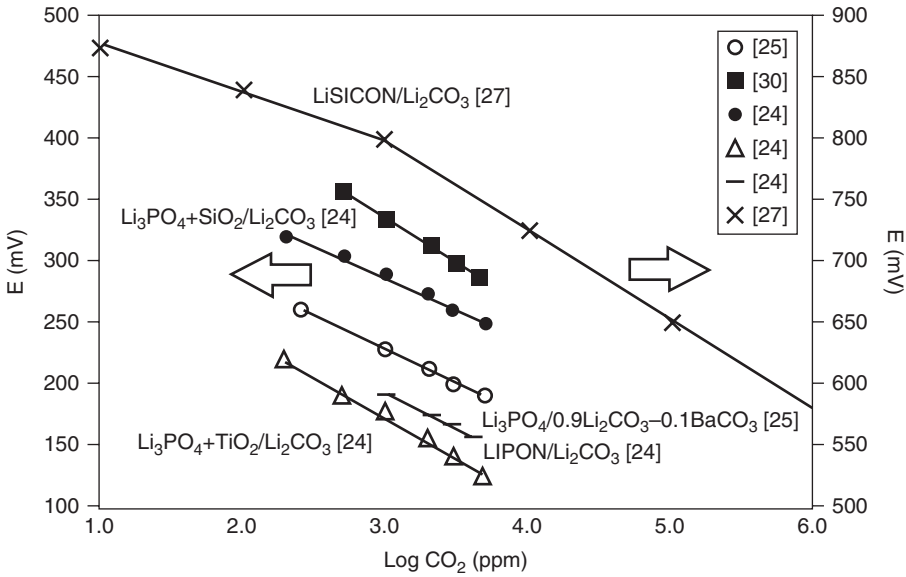

16.4 Electrochemical sensor potentials with lithium-ion conducting electrolytes and Li_2CO_3-$BaCO_3$ auxiliary electrodes at 500°C as a function of the carbon dioxide concentration (Fergus, 2008). Numbers [24], [25], [27] and [30] refer to the following references: 24, Park *et al.* (2003); 25, Noh *et al.* (2005); 27, Ménil *et al.* (2005); 30, Satyanarayana *et al.* (2007).

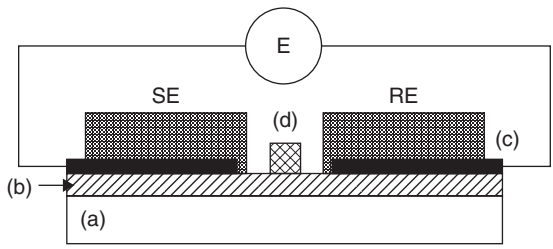

16.5 Planar structure of a potentiometric sensor from Belda *et al.* (2009): (a) substrate, (b) Na-β-aluminate (NBA) electrolyte, (c) Au electrodes, (d) inert barrier; SE (sensing electrode), RE (reference electrode).

that advantage can be taken of the wide range of thin- and thick-film fabrication technologies, making them suitable for mass production. Figure 16.5 (from Belda *et al.*, 2009) shows a planar CO_2 sensor configuration.

A promising approach is the use of thin films for the electrodes and the electrolyte. The optimization of the material microstructure, both in the sensing electrode and in the electrolyte, leads to good detection. The superficial nature of the chemical reactions involved in CO_2 detection suggests that a higher velocity of response can be reached if the electrodes and electrolyte

© Woodhead Publishing Limited, 2013

are thin films. The reason is that the gas will have a shorter path to the electrode–electrolyte barrier, facilitating the formation of the phase boundary, defined as the contact between the gaseous phase, the auxiliary phase, the electrode and the ionic conductor. Some authors report results using thin films, but they still are a minority. As an example, Chu *et al.* (1992) compared the fabrication of sintered, thick- and thin-film devices and reach the conclusion that the lowest drift is shown by the sensor fabricated using thin-film techniques. Leonhard *et al.* (1993) compared thin and thick films preparation methods for the electrodes and state that the thin-film method gives the best results, both in terms of the value and the slope of the measured electromotive force. The micromachined prototype presented by Lang *et al.* (1996) and further developed by Currie *et al.* (1999) shows a good sensing capability, as well as better response times than its bulky counterparts.

Regarding the influence of humidity on sensor performance, some authors suggest the addition of alkaline or alkaline-earth metal carbonates (such as $BaCO_3$ or $CaCO_3$) to the sensing electrodes in order to reduce cross-sensitivity to water (Miura *et al.*, 1992; Pasierb *et al.*, 2003). Other research groups also use this approach to reduce cross-sensitivity to water but go even further and mix the metallic component with the auxiliary phase in order to improve the recovery of the baseline of the sensors (Ménil *et al.*, 2005). The same authors state that the use of the metal mixed with the sensing electrode instead of a layer of the same metal improves the contact phase boundary, thus improving the electrochemical equilibrium in the sensor and also reducing the recovery time of the sensors.

Another drawback in electrochemical sensors is the long-term drift, which is sometimes related to the instability of the materials working at high temperatures. Some recent works propose the use of dispersed nanoparticles on the surface, such as platinum or gold, in order to act as a catalyst in the reduction–oxidation reaction, leading to both an increase in sensitivity and a reduction in the operating temperature (Plashnitsa *et al.*, 2009).

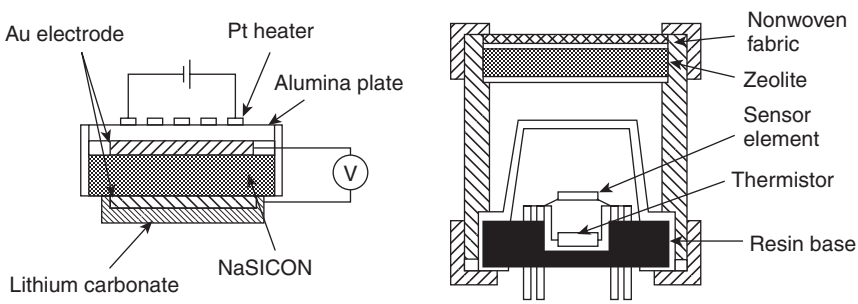

16.6 Detail of sensor elements (left) and packaged electrochemical sensor with zeolite filter (right) (Kaneyasu *et al.* 2000).

© Woodhead Publishing Limited, 2013

An example of a practical device is shown in Fig. 16.6 (Kaneyasu *et al.*, 2000), where a filter of zeolite is used to avoid cross-sensitivity to interfering gases.

16.3 Impedimetric, capacitive and resistive sensors

Impedimetric, capacitive or resistive sensors measure electrical changes due to the chemical interaction between the gas target and the sensing material. The chemical reaction is usually activated at high temperature. While impedimetric sensors measure complex impedance variations, and capacitive sensors give capacitance variations (in both cases, an AC signal is applied), resistive sensors (also called 'conductometric' sensors) evaluate resistance (or conductance) variations in the samples when a DC signal is applied, so they usually require simpler circuits to perform the measurement. The classical materials used for those sensors are based on the interaction of different oxygen specimens with oxidant or reducing gases, so they are no longer useful in the case of gas molecules such as CO_2 that do not react to oxygen. Therefore, in the case of inert molecules, alternative materials that involve other chemical reactions must be chosen. As in the chemical sensors, not only the material, but also the fabrication process and the working conditions – mainly temperature and humidity – are the key factors for the gas detection.

16.3.1 Influence of the fabrication processes in the performance of impedimetric CO_2 gas sensors

Table 16.2 shows a comparison of the response to CO_2 of different materials and material combinations, indicating the working temperature and the kind of fabrication process that was used to obtain the material. As different authors use different gas concentrations to perform the measurements, the base gas concentration and the final gas concentration are also indicated in brackets in Table 16.2.

Sintering is the most widely-used technique for CO_2 impedimetric devices and the most reported material is the $BaTiO_3$-CuO mixed oxide. Some examples of $BaTiO_3$-CuO sintered devices can be found in the bibliography, such as those by Ishihara *et al.* (1992, 1995). It was their original suggestion that the sensing mechanism in this mixed oxide involves the adsorption of CO_2 in the heterojunction between the n-type $BaTiO_3$ and the p-type CuO, which supposes p–n junction barrier energy decrease that leads to a capacitance variation in the material. They prepared $BaTiO_3$ pellets by the calcination of an equimolar mixture of $BaCO_3$ and TiO_2 at 1200°C. The $BaTiO_3$ was mechanically mixed with a commercial metal oxide (CuO) without further

© Woodhead Publishing Limited, 2013

Table 16.2 Comparison of the working temperature (T), electrical response, sensing material and method employed in different works related to impedimetric CO_2 gas sensors

Reference	T (°C)	Response[a]	Material (method[b])
Yoshioka, Mizuno and Iwamoto, 1991	300	R (2000/0 ppm) = 1.57 DC	SnO_2+La_2O_3 (Thick)
Ishihara *et al.,* 1991	356	C (2/0%) = 2.89 AC f = 50 kHz	$BaTiO_3$-CuO (Sint)
Ishihara *et al.,* 1992 Ishihara *et al.,* 1995	370	C (2/0%) = 7.74 AC f = 50 kHz	$BaTiO_3$-CuO+Ag (Sint)
Haeusler and Meyer, 1996	600	R (5000/0 ppm) = 0.3 AC f = 1 kHz	$BaTiO_3$-CuO-$CaCO_3$-La_2O_3 (Thick)
Keller *et al.,* 1999	550	R (5000/0 ppm) = 0.5 AC f = 1 kHz	$BaTiO_3$-CuO-$CaCO_3$-La_2O_3 (Thick)
Wei *et al.,* 2000	312	C (2/0%) = 7 AC f = 20 Hz–100 kHz	$BaTiO_3$-CuO (Sint)
Kim *et al.,* 2000	1000	R (2500/0 ppm) = 1.45 DC	SnO_2+La_2O_3 (Thick)
Matsubara *et al.,* 2000	550	C (2/0%) = 0.56 AC f = 50 kHz	CeO_2/$BaCO_3$/CuO (Sint)
Diagne and Lumbreras, 2001	425	R (2000/0 ppm) = 1.37 AC f = 500 Hz–13 MHz	SnO_2+LaOCl (Thick)
Liao *et al.,* 2001	302	C (2/0%) = 2.3 AC f = 20 Hz–100 kHz	$BaTiO_3$-CuO (Sint)
Jiao *et al.,* 2002	425	R (5000/0 ppm) = 1.5 DC	$BaTiO_3$-CuO+Ag (Sint)
Marsal *et al.,* 2003	260	R (2000/0 ppm) = 3.4 DC	SnO_2+LaOCl (Thick)
Desai *et al.,* 2005	25	R (1000/0 ppm) = 0.11 DC	In_2Te_3 (Thin)
Prim *et al.,* 2007	235–315	R (2000/0 ppm) = 1.8 DC	CaO/In_2O_3 (Thick)
Haensch, 2010	250	R (5000/0 ppm) = 20 DC	$La_2O_2CO_3$ (Thick)
Chapelle, 2010	250	R (5000/0 ppm) = 1.9 AC f = 700 Hz	CuO-Cu_xFe_3-xO_4 (Thin)

[a] Response value is indicated as the ratio of the capacitance (C) or resistance (R) measured under the CO_2 concentrations in brackets.

[b] Abbreviations used for the fabrication methods (in brackets): Sint, sintered ceramics; Thin, thin films; Thick, thick films.

purification and the oxide powders thus obtained were pressed into disks. After calcinations, an Ag paste was applied on both faces of the disks to make electrodes. Then Pt lead wires were connected to the electrodes with Ag paste.

© Woodhead Publishing Limited, 2013

Wei *et al.* (2000) obtained the $BaTiO_3$-CuO equimolar mixture by means of CuO powders of around 50 nm and $BaTiO_3$ powders of around 50–100 nm. In the next step, the material was pressed and annealed at 500°C for five hours, and a Pt wire was inserted as the contact.

Liao *et al.* (2001) reported the use of $BaTiO_3$ powders prepared by co-precipitation. After filtration, drying, washing and calcination, high-purity $BaTiO_3$ powders were obtained. As one of the problems in these devices is low conductivity, Nb_2O_5 was added to $BaTiO_3$, and then the mixture of $BaTiO_3$ and Nb_2O_5 was sintered at 1150°C in air. The phase analyses by X-ray diffraction confirmed that $BaTiO_3$ was a single phase, with Nb atoms substituting some of the Ti atoms. With the impurity atoms Nb replacing part of the Ti atoms, the Ti-O bond became weak, thus favouring the production of the oxygen holes. The obtained $BaTiO_3$ powders were mechanically pressed into disks. After calcination, an Ag paste was applied on both faces of the disks to make the electrodes.

Another example of sintered resistive device is reported by Jiao *et al.* (2002), who mixed $BaCO_3$ and TiO_2 and heated the mixture up to 1300°C to obtain the powder of $BaTiO_3$, which was then thoroughly mixed with CuO. The mixture was made into pellets and sintered in air.

As seen in Table 16.2, the highest response to a level of 2% of CO_2 was achieved by Ishihara when Ag was added to the $BaTiO_3$-CuO pellet. Two different authors (Ishihara *et al.*, 1995; Jiao *et al.*, 2002) gave an extensive report of different additives (metals and oxides) that can improve the response of the sensing layers. Ag was found to be the additive that lead to the highest improvement (Jiao *et al.*, 2002), but those authors do not give any theoretical explanation for this behaviour, while Ishihara *et al.* (1995) found the best results for La_2O_3, but at a higher temperature.

Some examples of thick-film impedimetric sensors can also be found in the bibliography. In Haeusler and Meyer (1996) interdigitated gold electrodes were used and $BaTiO_3$-CuO was obtained from pulverized powders of both materials. The sensing device was printed onto an alumina substrate provided with a heater on its reverse. They found the response strongly dependent on the firing parameters and on the metal oxide additives added to the base material, such as $CaCO_3$ and La_2O_3.

Keller *et al.* (1999) reported the same material with improved response and low cross-sensitivity to other gases. If thick-film $BaTiO_3$-CuO performance is compared with the previously described sintered devices, the performance is improved in terms of response, as can be seen in Table 16.2.

Another reported material for thick-film sensors is SnO_2 with La compounds (Yoshioka *et al.*, 1991; Kim *et al.*, 2000; Diagne and Lumbreras, 2001; Marsal *et al.*, 2003). In particular, Kim *et al.* (2000) used alumina substrates with platinum electrodes and a heater printed on the same side of the sensing device, as seen in Fig. 16.7. The sensing material was tin dioxide with a

© Woodhead Publishing Limited, 2013

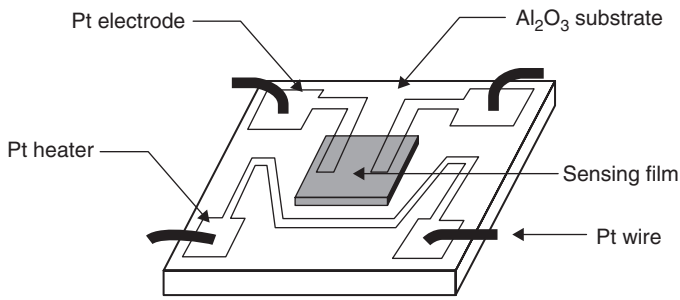

16.7 Scheme of a thick-film impedimetric gas sensor fabricated on alumina (Al_2O_3) substrate, with the sensing film of La impregnated SnO_2 on Pt electrodes, and a heating element of Pt to reach the operating temperature (Kim *et al.,* 2000).

coating of lanthanum oxide. The coating method, the amount of lanthanum and the firing temperature are the key parameters in this case, and the best results were achieved for samples annealed at 1000°C for 5 minutes. In the case of Diagne and Lumbreras (2001), the tin dioxide–lanthanum (SnO_2-La) mixture was also the sensing material, but was fabricated by spray pyrolysis. The same material and technique were also used by Marsal *et al.* (2003) and, between all the lanthanum compounds added, they found that the LaOCl offers the best results for selective and humidity-insensitive CO_2 detection. This group obtained the best performance for CO_2 detection in terms of sensor response using tin dioxide.

Only few examples of CO_2 impedimetric gas sensors can be found that are fabricated by means of thin-film techniques and they use $BaTiO_3$-CuO thin films. For example, Tunney *et al.* (2006) obtained $BaTiO_3$-CuO thin films by pulsed laser deposition (PLD) at substrate temperatures between 400°C and 650°C. The target was 1% of CuO and 99% of $BaTiO_3$. They reported some preliminary work but further results cannot subsequently be found in the literature.

Regarding thin films for CO_2 detection, there are several reports from the Mandayo *et al.* (2006), who deposited $BaTiO_3$-CuO thin films by radio frequency (RF) magnetron sputtering from a $BaTiO_3$-CuO equimolar target onto alumina substrates. The samples were annealed in O_2 at 700°C, in order to obtain a stable film. They report studies on the influence of the layer thickness on the sensor response, observing that the thickness only influenced the speed of the response: the thinnest reported film (150 nm) had the fastest response of all. They found the optimum working temperature to be 300°C, because at that temperature the speed of response is higher, although at lower temperatures the magnitude of the response increased (Herrán *et al.*, 2008). They also reported the influence of Ag as an additive.

© Woodhead Publishing Limited, 2013

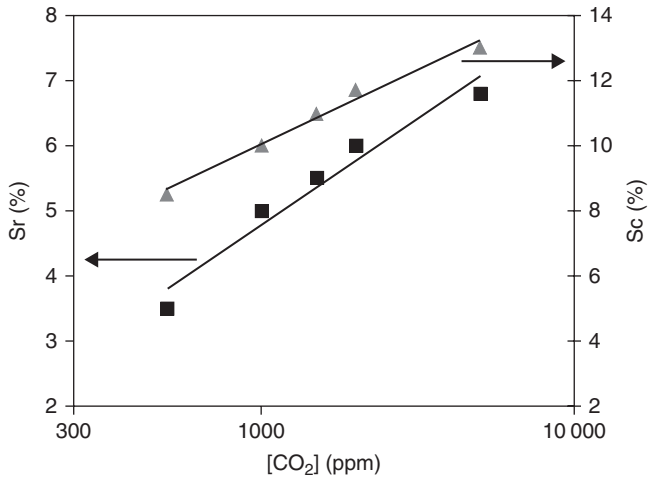

16.8 Sensitivity of a carbon dioxide $BaTiO_3$-CuO thin film impedimetric sensor at 300°C and frequency of 100 Hz as the resistance change (Sr) and as the capacitance change (Sc) (Mandayo *et al.,* 2011).

The results show that the silver enhanced the magnitude of the response but did not decrease the response time (Herrán *et al.*, 2008a). The presence of the carbonate specimens responsible for the sensing reaction was verified by DRIFT analysis (Herrán *et al.*, 2008b), and a theoretical model that related the sensing reaction to the changes in the p–n heterojunctions of the $BaTiO_3$-CuO was also proposed by the authors and qualitatively corroborated by their results (Herrán *et al.*, 2007). A prototype fabricated onto an alumina substrate with a Pt heater on the reverse was reported and its stability and repeatability tested, showing good results in the range from 0 to 5000 ppm of CO_2 (Mandayo *et al.*, 2011), as seen in Fig. 16.8.

A similar approach based on a p–n junction formed by CuO (p-type) and spinel oxide Cu_xFe_3-xO_4 (n-Type) is proposed in Chapelle *et al.* (2010), where the thin-film sensing material is obtained by sputtering techniques. Although they are able to work at reasonable temperatures (250°C), their main problem is the long response time.

Finally, a group of rare earth oxycarbonates (such as $Nd_2O_2CO_3$ or $Nd_2O_2CO_3$) synthesized from the corresponding $X(OH)_3$ (X refers to the rare earth) and then screen-printed are being researched by Haensch *et al.* (2010). Although interesting sensitivity increments in the sensor signal up to 20 times over the baseline were measured (see Table 16.2), further research work must be carried out in order to improve critical and important sensing properties such as kinetics and selectivity. The large sensor resistance and high cost of the precursors used are also a drawback for practical devices.

© Woodhead Publishing Limited, 2013

16.3.2 Relevance of the working conditions in solid-state CO_2 sensor operation

Temperature

The working temperature in a solid-state gas sensor is a critical factor in the detection process. The properties of the semiconducting materials depend on the temperature, so the voltage or current needed to determine the impedance or the conductance is usually measured at different temperatures. Then, the working temperature is fixed as a compromise between the magnitude and the speed of the sensor response. The speed of the response is directly related to the activation energy of the chemical reactions involved in the sensing mechanism, because the chemisorption processes involved in the sensing mechanism are thermally activated and temperature determines the number and type of chemisorbed specimens. Also, physical parameters such as the work-function or the carrier concentration are functions of the temperature. It is also important to take into account that, in polycrystalline films at high temperatures, gas diffusion through grain boundaries has considerable influence on the detection process.

In this context, Fig. 16.9 reported by Jiao *et al.* (2002) shows the typical experimental curve to determine the optimal working temperature at which to detect CO_2 by means of $BaTiO_3$-CuO sintered ceramics. The test is carried out at 5000 ppm of CO_2 and the sensor sensitivity is defined by the author as R_{gas}/R_{air}.

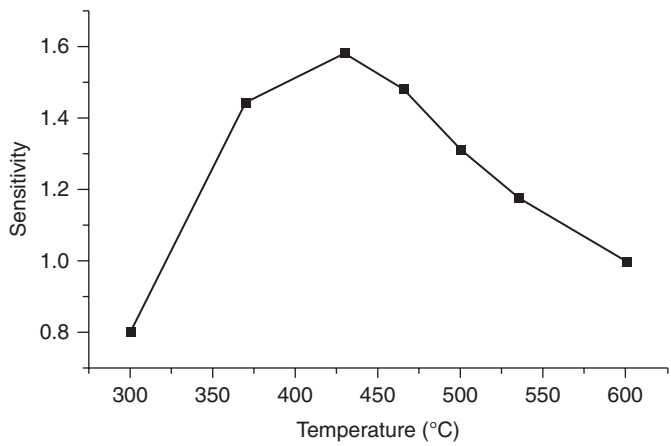

16.9 Experimental graph of the temperature of the maximum sensitivity in an impedimetric $BaTiO_3$-CuO sensor with Ag as an additive (Jiao *et al.,* 2002). CO_2 concentration = 5000 ppm.

© Woodhead Publishing Limited, 2013

Relative humidity

In solid-state gas sensors, the humidity effect in the sensing mechanism is a function of the target gas, the sensing material and the working temperature. As an example, in the work of Ostrick *et al.* (1999, 2000), the relation between the relative humidity, the working temperature and the sensing material was studied in relation to the target gas (CO_2). The author studied the reactions involved in the interaction of $BaCO_3$ with CO_2 at low and high temperatures. At high temperatures, around 200°C, the sensing mechanism is governed by the following two reactions:

$$CO_2\ (gas) + \tfrac{1}{2}O_2\ (gas) + 2e^-\ (Ba\ (metal)) \leftrightarrow CO_3^{2-}\ (material)$$

$$CO_3^{2-}\ (material) + CO_2\ (gas) + H_2O\ (gas) \leftrightarrow 2HCO_3^-\ (surface)$$

However, at working temperatures around 50°C, the sensing reactions are:

$$OH^-\ (surface) + CO_2 \leftrightarrow HCO_3^-\ (surface)$$

$$HCO_3^-\ (surface) + OH^-\ (surface) \leftrightarrow H_2O\ (gas/surface) + CO_3^{2-}\ (material)$$

These chemical reactions corroborate the hypothesis that, at low working temperatures, the sensing mechanism is activated by water vapour; at high working temperatures, the sensing mechanism is activated by the oxygen. At high temperatures, the reactions are activated by the oxygen interaction with the metallic barium, while at low temperatures the reaction between the hydroxyl groups adsorbed on the surface and CO_2 are the key to the sensing reaction. One of the conclusions of this work was that the baseline of the sensor signal is also dependent on the relative humidity.

Those results were obtained for $BaCO_3$ but Mandayo *et al.* (2011) also relate the influence of humidity in a $BaTiO_3$-CuO layer to the same reaction. In their case, sensitivity of $BaTiO_3$-CuO to CO_2 is enhanced in the presence of water. According to the high-temperature reactions, CO_2 detection needs carbonate specimens, whose presence was demonstrated by the authors in their $BaTiO_3$-CuO thin films. The sensitivity enhancement measured in humid air can be explained because the presence of water makes the second of the two high-temperature reactions to take place, so an extra amount of carbonate specimens increases the sensor response. When tests are carried out in humid air, both reactions take place, so sensitivity is higher than in dry air, where only one reaction happens.

© Woodhead Publishing Limited, 2013

16.4 Field effect transistor sensors

Field effect transistors gas sensors (gas-FET) are sensors integrated onto field effect transistors. These systems detect work-function and/or current drain variations at different target gas concentrations. The operation principle is based on the chemical changes of the different gas-sensing materials, which are used as the gate of the transistor. The chemical sensors group at Siemens has been developing this kind of configuration for CO_2 monitoring. They measure the work-function changes via a hybrid suspended gate FET. The chosen sensing film must undergo a reversible work-function change associated to the sensing reaction that creates a potential on the surface. This change is transduced by means of a FET structure. Those structures show the advantage of being good candidates for cheap manufacturing, like the one shown in Fig. 16.10 (Fleischer *et al.*, 2001). This particular structure, with an air gap between the sensor film and the channel isolation structure, can be implemented by flip-chip techniques. This way, the sensing element can be fabricated with a heater on the reverse and the use of any deposition technique (sputtering, spraying) for the sensing material. Then, an ion selective FET (sometimes called 'ISFET') is linked to this structure by flip-chip techniques, placing the FET structure right onto the sensing film in order to achieve the sensing structure with the air gap. The transistor structure is expected to reduce the working temperature of the sensors and thus obtain lower power consumption. As an example, the devices with a similar flip-chip design and screen-printed $BaTiO_3$-CuO gates have power consumption under 1 mW (Simon *et al.*, 2003; Pohle *et al.*, 2007).

A further step in gas-FET structures is the use of heteropolysiloxanes as the gas-sensitive materials in order to be able to work at room temperature. The precursors of polymer films are made by spin-coating of hydrolyzed monomers; different rotation speeds are used to get layers of different

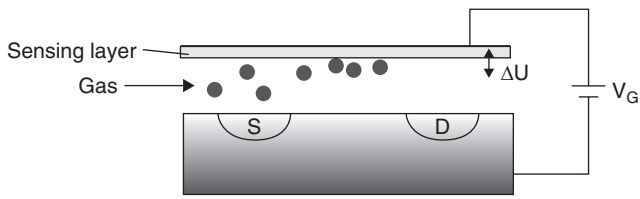

16.10 Floating gate field-effect transistor gas sensor configuration, where there is an air gap separating the sensing film from the conduction channel, as opposed to the classical arrangement in which the sensing layer lays directly on the channel. ΔU is the gas induced additional voltage; S and D are, respectively, the source and the drain of the transistor; and V_G is the gate voltage (Fleischer *et al.,* 2001).

© Woodhead Publishing Limited, 2013

thickness. The final coating is carried out via a sol–gel process. The sensitive materials reported by Stegmeier *et al.* (2009) and Stegmeier *et al.* (2010) are 3-aminopropyltrimethoxysilane (AMO) and a mixture of AMO with propyltrimethoxysilane (PTMS). The addition of PTMS causes a hydrophobization of the hydrophilic AMO due to an increase of non-polar groups in the material system. After the spin-coating process, the sensitive layers are stored in ambient air for 2 hours, to allow a removal of solvents and, therefore, to reach a gel state. During the following 16 hours, the polymerization is completed in an N_2 atmosphere at 120°C. Both materials have amino groups, which act as receptors for CO_2 detection, because they are able to perform reversible acid-based reactions at ambient temperature. The sensing reactions present in other materials that work at higher temperatures involve the formation of carbonates and also the presence of water, while the reactions in these polymers at room temperature do not require humidity, and have been demonstrated to be related to the formation of carbamates (Stegmeier *et al.*, 2011a). The chemical nature of the films is one of the key points of these materials, which have been tested at room temperature and for concentrations of CO_2 between 400 and 4000 ppm and could potentially be useful for air quality control applications once they are fully optimized and implemented in a FET platform (Stegmeier *et al.*, 2011b).

16.5 New approaches to enhance sensor performance

In the following section novel approaches to improve the performance of carbon monoxide sensors are reviewed. Firstly, photoactivation in metal oxide semiconductors is analyzed and secondly, the new possibilities open the use of nanostructured materials in this field is studied.

16.5.1 Photoactivation

There are several works where ultra-violet (UV) light is used to activate gas detection in metal oxide semiconductors. Illuminating sensing layers with UV light is becoming an alternative to the use of a heating element, because it reduces power consumption in these sensors, which is one of the main disadvantages of metal oxide conductometric sensors. The reduction of the working temperature also increases the sensor lifetime, reduces the risks of possible explosion in some applications and permits the implementation of these sensors in fields such as portable or wireless devices.

UV light stimulates carrier generation and, as a consequence, the density of free electron–hole pairs increases. It also affects intergrain potential barriers and decreases the depletion layers among them. Moreover, it can promote the photodissociation of the gas targets and of the chemical surface adsorbed species (Saura, 1994; Comini *et al.*, 2000, 2001). All of the

© Woodhead Publishing Limited, 2013

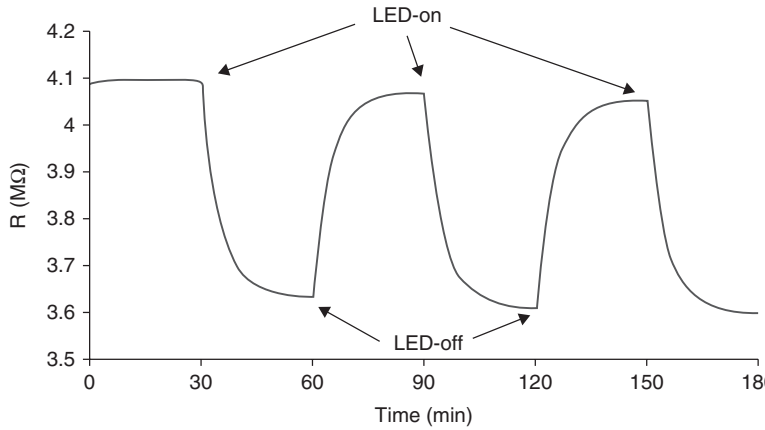

16.11 Resistance change of $BaTiO_3$-CuO film to photostimulation pulses of 30 minutes at room temperature under a blue LED with a dominant wavelength of 465 nm and a luminous intensity of 3800 mcd.

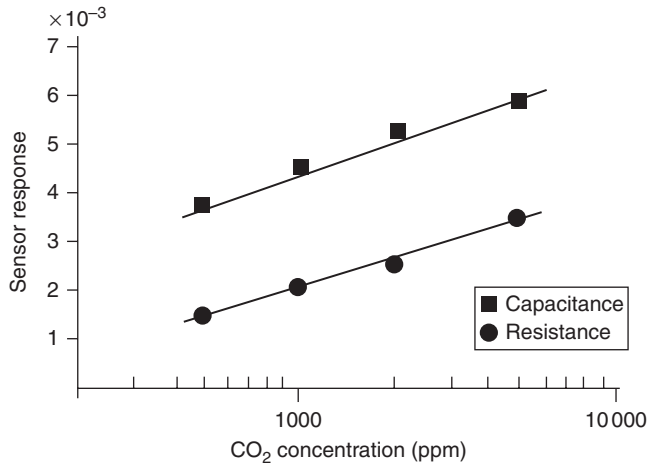

16.12 Response (measured as capacitance change and as resistance change) of $BaTiO_3$-CuO film to photostimulation pulses at room temperature (Herrán *et al.,* 2010) and at a frequency of 100 Hz. The light source is a blue LED with a dominant wavelength of 465 nm and a luminous intensity of 3800 mcd.

described physical and chemical phenomena open the option of gas-sensing at room temperature.

The response of well-established sensing materials under photoactivation has recently been proposed by several research groups. Materials such as SnO_2 (Saura, 1994; Camagni *et al.*, 1996; Comini *et al.*, 2000, 2001, 2004; Law *et al.*, 2002; Anothainart *et al.*, 2003; Prades *et al.*, 2009), In_2O_3 (Comini *et al.*,

© Woodhead Publishing Limited, 2013

2000; Wang *et al.*, 2007), or ZnO (Ge *et al.*, 2007; de Lacy Costello *et al.*, 2008), have been tested under different gas atmospheres, such as CO, NO_2, O_3 and H_2. There is also one report on photoactivated $BaTiO_3$-CuO thin films as a CO_2 sensor at room temperature (Herrán *et al.*, 2010), in which the optical semiconductor properties of $BaTiO_3$-CuO coatings are first presented and discussed. Second, the ability of the material to detect CO_2 by photoactivation is shown. Finally, a comparison between the sensing mechanism in thermo- and photo-activated sensing films is discussed. Figure 16.11 shows the resistance changes of the $BaTiO_3$-CuO thin films under LED illumination, and Fig. 16.12 demonstrates the photoactivated sensor response at different CO_2 concentrations.

16.5.2 Nanostructured materials

In recent years, nanotechnology has opened a new window on the physical-chemical properties of semiconductor materials: nanostructuration. The development of nanostructured materials (nanowires, nanotubes, nanoparticles etc.) enables improvements in the response and recovery times of the sensor signal, due to the reduction of gas diffusion effects in the bulk of the material. Additionally, the sensitivity and the sensor response are also improved by the changes in the conduction mechanisms at the nanoscale and, finally, the reduction of the dimensions of the device allows the reduction of the power consumption by the system.

Although there are many references to nanostructured semiconductors, only a few results on nanostructuration for CO_2 detection can be found in the literature.

In Ong and Grimes (2001), a thin layer of a multiwall carbon nanotube (MWNT)–silicon dioxide (SiO_2) composite upon a planar inductor–capacitor resonant circuit is used as a CO_2 sensing material. The resonant frequency of the sensor is related to the complex permittivity of the coating material as a function of the CO_2 concentration. It is shown that the permittivity of MWNTs changes linearly in response to CO_2 concentration, enabling the monitoring of ambient CO_2 levels. Experimental results show that the response of the sensor is linear and reversible, with no hysteresis between increasing and decreasing CO_2 concentrations. The response time is approximately 45 seconds.

In Anderson *et al.* (2009), gas sensor materials for CO_2 monitoring are developed using various device structures, including ZnO nanowires and GaN high electron mobility transistors (HEMTs). ZnO nanowires are particularly interesting because they have a large surface area-to-volume ratio – which improves sensitivity, and, because they operate at low current levels, they require low power. GaN-based devices offer the advantage of

© Woodhead Publishing Limited, 2013

the HEMT structure, high-temperature operation, and simple integration with existing fabrication technology and sensing systems. Improvements in sensitivity, recoverability and reliability are also presented by the authors.

16.6 Conclusion and future trends

This chapter has presented the current status of electrochemical, impedimetric and field-effect solid-state gas sensors for CO_2 detection. As can be inferred from the works reviewed, although there are already some electrochemical devices for CO_2 detection in the market, there is significant room for improvement and new detection principles to investigate in order to realize cheaper and more reliable low-cost CO_2 solid-state sensors. Researchers try to improve sensitivity, selectivity and long-term stability of the devices by exploring new fabrication methods that are cheap and reliable. As presented in Section 16.5.2, nanostructured materials are becoming more popular because of their improved sensing properties. Other approaches, such as the UV stimulation of metal oxide materials (also of nanostructured oxides), open new possibilities for room-temperature detection.

Nevertheless, there is a lack of understanding of the basic physical-chemical mechanisms, so research efforts are needed to improve the comprehension of the sensing phenomena using characterization techniques – such as diffuse reflectance infrared Fourier transform (DRIFT) spectra – that permit the checking of chemical reactions during sensor operation, not only over the sensing material. This kind of measurement will help understand the underlying chemical processes and their relation with other electrical and physical parameters, and will help in the development of theoretical detection models.

16.7 References

ACIGH (2011), *American Conference of Governmental Industrial Hygienists*. Available: http://www.acgih.org/home.htm [2011, 07/15].

Alphasense (2009), *Alphasense – The sensor technology company*. Available: http://www.alphasense.com/index.html [07/2011].

Anderson, T., Ren, F., Pearton, S., Kang, B.S., Wang, H.-, Chang, C.-Y. and Lin, J. (2009), 'Advances in hydrogen, carbon dioxide and hydrocarbon gas sensor technology using GaN and ZnO-based devices', *Sensors*, **9**, 4669–94.

Anothainart, K., Burgmair, M., Karthigeyan, A., Zimmer, M. and Eisele, I. (2003), 'Light enhanced NO_2 gas sensing with tin oxide at room temperature: conductance and work function measurements', *Sensors and Actuators B: Chemical*, **93**, 1–3, 580–4.

ASHRAE (2011), *American Society of Heating, Refrigerating and Air-Conditioning Engineers*. Available: http://www.ashrae.org/ [2011, 07/15].

© Woodhead Publishing Limited, 2013

Belda, C., Fritsch, M., Feller, C., Westphal, D. and Jung, G. (2009), 'Stability of solid electrolyte based thick-film CO_2 sensors', *Microelectronics Reliability*, **49**, 6, 614–20.

Camagni, P., Faglia, G., Galinetto, P., Perego, C., Samoggia, G. and Sberveglieri, G. (1996), 'Photosensitivity activation of SnO_2 thin film gas sensors at room temperature', *Sensors and Actuators B: Chemical*, **31**, 1–2, 99–103.

Comini, E., Cristalli, A., Faglia, G. and Sberveglieri, G. (2000), 'Light enhanced gas sensing properties of indium oxide and tin dioxide sensors', *Sensors and Actuators B: Chemical*, **65**, 1–3, 260–3.

Comini, E., Faglia, G. and Sberveglieri, G. (2001), 'UV light activation of tin oxide thin films for NO_2 sensing at low temperatures', *Sensors and Actuators B: Chemical*, **78**, 1–3, 73–7.

Comini, E., Ottini, L., Faglia, G. and Sberveglieri, G. (2004), 'SnO_2 RGTO UV activation for CO monitoring', *Sensors Journal*, *IEEE*, **4**, 1, 17–20.

Chapelle, A., Oudrhiri-Hassani, F., Presmanes, L., Barnabé, A. and Tailhades, P. (2010), 'CO2 sensing properties of semiconducting copper oxide and spinel ferrite nanocomposite thin film', *Applied Surface Science*, **256**, 14, 4715–19.

Chu, W.F., Fischer, D., Erdmann, H., Ilgenstein, M., Köppen, H. and Leonhard, V. (1992), 'Thin and thick film electrochemical CO_2 sensors', *Solid State Ionics*, **53–56**, part 1, 80–4.

Currie, J.F., Essalik, A. and Marusic, J. (1999), 'Micromachined thin film solid state electrochemical CO_2, NO_2 and SO_2 gas sensors', *Sensors and Actuators B: Chemical*, **59**, 2–3, 235–41.

de Lacy Costello, B.P.J., Ewen, R.J., Ratcliffe, N.M. and Richards, M. (2008), 'Highly sensitive room temperature sensors based on the UV-LED activation of zinc oxide nanoparticles', *Sensors and Actuators B: Chemical*, **134**, 2, 945–52.

Desai, R.R., Lakshminarayana, D., Patel, P.B. and Panchal, C.J. (2005), 'Indium sesquitelluride (In_2Te_3) thin film gas sensor for detection of carbon dioxide', *Sensors and Actuators B: Chemical*, **107**, 2, 523–7.

Diagne, E.H.A. and Lumbreras, M. (2001), 'Elaboration and characterization of tin oxide–lanthanum oxide mixed layers prepared by the electrostatic spray pyrolysis technique', *Sensors and Actuators B: Chemical*, **78**, 1–3, 98–105.

Dynament, *Dynament*, *infrared gas sensor technology*. Available: http://www.dynament.com/ [2011, 07/21].

Fergus, J.W. (2008), 'A review of electrolyte and electrode materials for high temperature electrochemical CO_2 and SO_2 gas sensors', *Sensors and Actuators B: Chemical*, **134**, 2, 1034–41.

Figaro (2011), *Figaro*, *an ISO 9001 and 14001 company*. Available: http://www.figarosensor.com/index.html [2011, 07/21].

Fleischer, M., Ostrick, B., Pohle, R., Simon, E., Meixner, H., Bilger, C. and Daeche, F. (2001), 'Low-power gas sensors based on work-function measurement in low-cost hybrid flip–chip technology', *Sensors and Actuators B: Chemical*, **80**, 3, 169–73.

Ge, C., Xie, C., Hu, M., Gui, Y., Bai, Z. and Zeng, D. (2007), 'Structural characteristics and UV-light enhanced gas sensitivity of La-doped ZnO nanoparticles', *Materials Science and Engineering: B*, **141**, 1–2, 43–8.

Haensch, A., Koziej, D., Niederberger, M., Barsan, N. and Weimar, U. (2010), 'Rare earth oxycarbonates as a material class for chemoresistive CO_2 gas sensors', *Procedia Engineering*, **5**, 139–42.

© Woodhead Publishing Limited, 2013

Haeusler, A. and Meyer, J. (1996), 'A novel thick film conductive type CO_2 sensor', *Sensors and Actuators B: Chemical*, **34**, 1–3, 388–95.

Herrán, J., Mandayo, G. G., Ayerdi, I. and Castaño, E. (2008a), 'Influence of silver as an additive on $BaTiO_3$–CuO thin film for CO_2 monitoring', *Sensors and Actuators B: Chemical*, **129**, 1, 386–90.

Herrán, J., Mandayo, G. G., Pérez, N., Castaño, E., Prim, A., Pellicer, E., Andreu, T., Peiró, F., Cornet, A. and Morante, J.R. (2008b), 'On the structural characterization of $BaTiO_3$–CuO as CO_2 sensing material', *Sensors and Actuators B: Chemical*, **133**, 1, 315–20.

Herrán, J., Mandayo, G.G. and Castaño, E. (2008), 'Solid state gas sensor for fast carbon dioxide detection', *Sensors and Actuators B: Chemical*, **129**, 2, 705–9.

Herrán, J., Mandayo, G.G. and Castaño, E. (2007), 'Physical behaviour of $BaTiO_3$–CuO thin-film under carbon dioxide atmospheres', *Sensors and Actuators B: Chemical*, **127**, 2, 370–5.

Herrán, J., Fernández-González, O., Castro-Hurtado, I., Romero, T., Mandayo, G. G. and Castaño, E. (2010), 'Photoactivated solid-state gas sensor for carbon dioxide detection at room temperature', *Sensors and Actuators B: Chemical*, **149**, 2, 368–72.

Hötzel, G. and Weppner, W. (1987), 'Potentiometric gas sensors based on fast solid electrolytes', *Sensors and Actuators*, **12**, 4, 449–53.

Ishihara, T., Kometani, K., Hashida, M. and Takita, Y. (1991), 'Application of Mixed Oxide Capacitor to the Selective Carbon Dioxide Sensor. Part 1. Measurement of Carbon Dioxide Sensing Characteristics', *Journal of the Electrochemical Society*, **138**, 1, 173–6.

Ishihara, T., Kometani, K., Mizuhara, Y. and Takita, Y. (1992), 'Mixed Oxide Capacitor of CuO-$BaTiO_3$ as a New Type CO_2 Gas Sensor', *Journal of the American Ceramic Society*, **75**, 3, 613–18.

Ishihara, T., Kometani, K., Nishi, Y. and Takita, Y. (1995), 'Improved sensitivity of CuO-$BaTiO_3$ capacitive-type CO_2 sensor by additives', *Sensors and Actuators B: Chemical*, **28**, 1, 49–54.

Jiao, Z., Chen, F., 2, S., R., Huang, X., Liu, W. and Liu, J. (2002), 'Study on the Characteristics of Ag Doped CuO-$BaTiO_3$ CO_2 Sensors', *Sensors*, **2**, 9, 366–73.

Kaneyasu, K., Otsuka, K., Setoguchi, Y., Sonoda, S., Nakahara, T., Aso, I. and Nakagaichi, N. (2000), 'A carbon dioxide gas sensor based on solid electrolyte for air quality control', *Sensors and Actuators B: Chemical*, **66**, 1–3, 56–8.

Keller, P., Ferkel, H., Zweiacker, K., Naser, J., Meyer, J.-. and Riehemann, W. (1999), 'The application of nanocrystalline $BaTiO_3$-composite films as CO_2-sensing layers', *Sensors and Actuators B: Chemical*, **57**, 1–3, 39–46.

Kida, T., Kawate, H., Shimanoe, K., Miura, N. and Yamazoe, N. (2000), 'Interfacial structure of NASICON-based sensor attached with $Li2CO_3$–$CaCO_3$ auxiliary phase for detection of CO_2', *Solid State Ionics*, **136**, 137, 647–53.

Kim, D.H., Yoon, J.Y., Park, H.C. and Kim, K.H. (2000), 'CO_2-sensing characteristics of SnO_2 thick film by coating lanthanum oxide', *Sensors and Actuators B: Chemical*, **62**, 1, 61–6.

Law, M., Kind, H., Messer, B., Kim, F. and Yang, P. (2002), 'Photochemical Sensing of NO_2 with SnO_2 Nanoribbon Nanosensors at Room Temperature', *Angewandte Chemie International Edition*, **41**, 13, 2405–8.

© Woodhead Publishing Limited, 2013

Lang, T., Caron, M., Izquierdo, R., Ivanov, D., Currie, J.F. and Yelon, A. (1996), 'Material characterization of sputtered sodium-ion conductive ceramics for a prototype CO_2 micro-sensor', *Sensors and Actuators B: Chemical*, **31**, 1–2, 9–12.

Leonhard, V., Fischer, D., Erdmann, H., Ilgenstein, M. and Köppen, H. (1993), 'Comparison of thin- and thick-film CO_2 sensors', *Sensors and Actuators B: Chemical*, **14**, 1–3, 530–1.

Liao, B., Wei, Q., Wang, K. and Liu, Y. (2001), 'Study on CuO–BaTiO3 semiconductor CO_2 sensor', *Sensors and Actuators B: Chemical*, **80**, 3, 208–14.

Mandayo, G.G., Herrán, J., Castro-Hurtado, I. and Castaño, E. (2011), 'Performance of a CO_2 Impedimetric Sensor Prototype for Air Quality Monitoring', *Sensors*, **11**, 5047–57.

Mandayo, G.G., González, F., Rivas, I., Ayerdi, I. and Herrán, J. (2006), '$BaTiO_3$–CuO sputtered thin film for carbon dioxide detection', *Sensors and Actuators B: Chemical*, **118**, 1–2, 305–10.

Marsal, A., Cornet, A. and Morante, J.R. (2003), 'Study of the CO and humidity interference in La doped tin oxide CO_2 gas sensor', *Sensors and Actuators B: Chemical*, **94**, 3, 324–9.

Marsal, A., Dezanneau, G., Cornet, A. and Morante, J.R. (2003), 'A new CO_2 gas sensing material', *Sensors and Actuators B: Chemical*, **95**, 1–3, 266–70.

Matsubara, S., Kaneko, S., Morimoto, S., Shimizu, S., Ishihara, T. and Takita, Y. (2000), 'A practical capacitive type CO_2 sensor using CeO_2/$BaCO_3$/CuO ceramics', *Sensors and Actuators B: Chemical*, **65**, 1–3, 128–32.

Ménil, F., Daddah, B.O., Tardy, P., Debéda, H. and Lucat, C. (2005), 'Planar LiSICON-based potentiometric CO_2 sensors: influence of the working and reference electrodes relative size on the sensing properties', *Sensors and Actuators B: Chemical*, **107**, 2, 695–707.

Miura, N., Yao, S., Shimizu, Y. and Yamazoe, N. (1992), 'Carbon Dioxide Sensor Using Sodium Ion Conductor and Binary Carbonate Auxiliary Electrode', *Journal of the Electrochemical Society*, **139**, 5, 1384–8.

Mullan, W.M.A. (2010), *Effect of modified atmosphere packaging on major foods*. Available: http://www.dairyscience.info/packaging-/118-map-major-foods.html [2011, 07/15].

Nanotechnology (2010), *Modified atmosphere packaging technology in the food industry – A modified atmosphere packaging technology*, *food packaging – Food Industry*. Available: http://www.nanotechnology.org.in/modified-atmosphere-packaging-technology-in-the-food-industry-a-modified-atmosphere-packaging-technology-food-packaging-food-industry [2011, 07/15].

NIOSH, *National Institute of Occupational Safety and Health*. Available: http://www.cdc.gov/niosh/ [2011, 07/15].

Nofima, *Active and Intelligent Packaging*. Available: http://www.nofima.no/mat/en/researcharea/active-and-intelligent-packaging [2011, 07/15].

Noh W.S., Satyanarayana L. and Park J.S. (2005), 'Potentiometric CO_2 sensor using Li^+ ion conducting Li_3PO_4 thin film electrolyte', *Sensors* **5** (11), 465–472.

OFGEM (2007), *Office of the Gas and Electricity Markets- Markets- Wholesale Markets- Working to promote competition and efficiency- Gas Quality*. Available: http://www.ofgem.gov.uk/Markets/WhlMkts/CompandEff/GasQual/Pages/GasQual.aspx [2011, 07/15].

Ong, K.G. and Grimes, C.A. (2001), 'A Carbon Nanotube-based Sensor for CO_2 Monitoring', *Sensors*, **1**, 6, 193–205.

© Woodhead Publishing Limited, 2013

Ostrick, B., Fleischer, M., Meixner, H. and Kohl, C. (2000), 'Investigation of the reaction mechanisms in work function type sensors at room temperature by studies of the cross-sensitivity to oxygen and water: the carbonate–carbon dioxide system', *Sensors and Actuators B: Chemical*, **68**, 1–3, 197–202.

Ostrick, B., Mühlsteff, J., Fleischer, M., Meixner, H., Doll, T. and Kohl, C. (1999), 'Adsorbed water as key to room temperature gas-sensitive reactions in work function type sensors: the carbonate–carbon dioxide system', *Sensors and Actuators B: Chemical*, **57**, 1–3, 115–19.

Park C.O., Lee C., Akbar S.A. and Hwang J. (2003), 'The origin of oxygen dependence in a potentiometric CO_2 sensor with Li- ion conducting electrolytes', *Sensors and Actuators B: Chemical*, **88**, 53–59.

Pasierb, P., Komornicki, S., Gajerski, R., Kozinski, S. and Rekas, M. (2003), 'The performance and long-time stability of potentiometric CO_2 gas sensors based on the (Li–Ba)CO3/NASICON/(Na–Ti–O) electrochemical cells', *Solid State Ionics*, **157**, 1–4, 357–63.

Plashnitsa, V.V., Elumalai, P., Fujio, Y. and Miura, N. (2009), 'Zirconia-based electrochemical gas sensors using nano-structured sensing materials aiming at detection of automotive exhausts', *Electrochimica Acta*, **54**, 25, 6099–106.

Pohle, R., Simon, E., Schneider, R., Fleischer, M., Sollacher, R., Gao, H., Müller, K., Jauch, P., Loepfe, M., Frerichs, H.-. and Wilbertz, C. (2007), 'Fire detection with low power fet gas sensors', *Sensors and Actuators B: Chemical*, **120**, 2, 669–72.

Prades, J.D., Jimenez-Diaz, R., Hernandez-Ramirez, F., Barth, S., Cirera, A., Romano-Rodriguez, A., Mathur, S. and Morante, J.R. (2009), 'Equivalence between thermal and room temperature UV light-modulated responses of gas sensors based on individual SnO_2 nanowires', *Sensors and Actuators B: Chemical*, **140**, 2, 337–41.

Prim, A., Pellicer, E., Rossinyol, E., Peiró, F., Cornet, A. and Morante, J.R. (2007), 'A Novel Mesoporous CaO-Loaded In_2O_3 Material for CO_2 Sensing', *Advanced Functional Materials*, **17**, 15, 2957–63.

Ramírez-Salgado, J. and Fabry, P. (2003), 'Study of CO_2 electrodes in open devices of potentiometric sensors', *Solid State Ionics*, **158**, 3–4, 297–308.

Renewable Energy Concepts, *Biogas Basics- Biogas Composition*. Available: http://www.renewable-energy-concepts.com/biomass-bioenergy/biogas-basics/gas-composition.html [2011, 07/15].

Salam, F., Bredikhin, S., Birke, P. and Weppner, W. (1998), 'Effect of the thickness of the gas-sensitive layer on the response of solid state electrochemical CO_2 sensors', *Solid State Ionics*, **110**, 3–4, 319–25.

Satyanarayana L., Choi G.P., Noh W.S., Lee W.Y. and Park J.S. (2007), 'Characteristics and performance of binary carbonate auxiliary phase CO_2 sensor based on Li_3PO_4 solid electrolyte', *Solid State Ionics,* **177** (39-40), 3485–3490.

Saura, J. (1994), 'Gas-sensing properties of SnO_2 pyrolytic films subjected to ultraviolet radiation', *Sensors and Actuators B: Chemical*, **17**, 3, 211–14.

Simon, E., Lampe, U., Pohle, R., Fleischer, M., Meixner, H., Frerichs, H.-., Lehmann, M. and Verhoeven, H. (2003), 'Novel carbon dioxide gas sensors based on field effect transistors', *Proceedings of Eurosensors 2003*, *Guimaraes*, *Portugal*, 21–24 September.

Stegmeier, S., Fleischer, M., Tawil, A. and Hauptmann, P. (2010), 'Stepwise improvement of (hetero-) polysiloxane sensing layers for CO_2 detection operated at room temperature by modification of the polymeric network', *Sensors and Actuators B: Chemical*, **148**, 2, 450–8.

© Woodhead Publishing Limited, 2013

Stegmeier, S., Fleischer, M., Tawil, A., Hauptmann, P., Egly, K. and Rose, K. (2011a), 'Sensing mechanism of room temperature CO_2 sensors based on primary amino groups', *Sensors and Actuators B: Chemical*, **154**, 2, 270–6.

Stegmeier, S., Fleischer, M., Tawil, A., Hauptmann, P., Egly, K. and Rose, K. (2009), 'Mechanism of the interaction of CO_2 and humidity with primary amino group systems for room temperature CO_2 sensors', *Procedia Chemistry*, **1**, 1, 236–9.

Stegmeier, S., Fleischer, M., Tawil, A., Hauptmann, P. and Endres, H.-. (2011b), 'Sensing of CO_2 at room temperature using work function readout of (hetero-)polysiloxanes sensing layers', *Sensors and Actuators B: Chemical*, **154**, 2, 206–12.

Tunney, J., Kunkel, M., Post, M., Srinivasan, R., Marcotte, D. and Segall, D. (2006), 'Conductometric CO_2 Sensing Using $BaTiO_3$-CuO Composite Thin Films Grown by Pulsed Laser Deposition', *ECS Meeting Abstracts*, **501**, 45, 1742.

Wang, C.Y., Cimalla, V., Kups, T., Röhlig, C.C., Stauden, T., Ambacher, O., Kunzer, M., Passow, T., Schirmacher, W., Pletschen, W., Köhler, K. and Wagner, J. (2007), 'Integration of In_2O_3 nanoparticle based ozone sensors with GaIn N/GaN light emitting diodes', *Applied Physics Letters*, **91**, 103509.

Wei, Q., Luo, W.D., Liao, B., Liu, Y. and Wang, G. (2000), 'Giant capacitance effect and physical model of nano crystalline CuO-$BaTiO_3$ semiconductor as a CO_2 gas sensor', *Journal of Applied Physics*, **88**, 8, 4818–24.

Weppner, W. (1987), 'Solid-state electrochemical gas sensors', *Sensors and Actuators*, **12**, 2, 107–19.

Yamazoe, N. and Miura, N. (1998), *Potentiometric Gas Sensors for Oxidic Gases*, Springer Netherlands.

Yoshioka, T., Mizuno, N. and Iwamoto, M. (1991), 'La_2O_3-loaded SnO_2 Element as a CO_2 Gas Sensor', *Chemistry Letters*, **20**, 7, 1249–52.

© Woodhead Publishing Limited, 2013

Index

adsorption equilibrium, 17
aerosol assisted chemical vapour deposition (AACVD), 437, 456, 498
AlGaN/GaN HEMT Schottky diode-based hydrogen sensor, 169
Alphasense, 513
aluminium, 373
American Society of Heating, Refrigerating and Air-Conditioning Engineers (ASHRAE), 511
3-aminopropyltriethoxysilane (APTES), 325
3-aminopropyltrimethoxysilane (AMO), 528
ammonia (NH_3), 127
anodic aluminium oxide (AAO), 318
antireflection coatings (ARC), 409
ascarite scrubber, 380
atmospheric pressure chemical vapour deposition (APCVD), 302, 437
atomic force microscopy (AFM), 360
atomic layer deposition (ALD), 498

β-alumina, 517
ball-milling method, 475
'bang-bang' controller, 500
barrier height, 87
base air resistance, 17–18
  reduced resistance for device using oxide grains, 18
baseline conductance, 73, 74
$BaTiO_3$, 522
benzoic acid (BA), 320
bias cycling, 138
'blob' sensors, 443
boron, 373

Cambridge CMOS Sensors Ltd, 506
capacitive sensors, 520–6
capnography, 379
carbon, 373
carbon dioxide (CO_2), 134
carbon dioxide sensing, 163–6
  AlGaN/GaN HEMT-based O_2 sensor, 164
  drain current changes of an HEMT sensor, 165
  drain current of a PEI/starch functionalised HEMT sensor, 165
carbon dioxide sensors, 510–31
  application fields for carbon dioxide sensors, 510–11
  available on the market, 511–13
  electrochemical sensors, 513–20
    classification according to sensing principle, 513–16
    mixed potential for carbon dioxide detection, 516–17
    relevance of material and fabrication techniques in sensor performance, 517–20
  field-effect transistor sensors, 527–8
    floating gate field-effect transistor gas sensor configuration, 527
  future trends, 531
  impedimetric, capacitive and resistive sensors, 520–6

© Woodhead Publishing Limited, 2013

carbon dioxide sensors (*cont.*)
influence of fabrication processes on the performance of impedimetric CO_2 gas sensors, 520–4
relevance of working conditions in solid-state CO_2 sensors operation, 525
sensitivity of carbon dioxide $BaTiO_3$-CuO thin film impedimetric sensor, 524
temperature of the maximum sensitivity in an impedimetric $BaTiO_3$-CuO sensor, 525
thick film impedimetric gas sensor, 523
working temperature, electrical response, sensing material and obtention method, 521
performance enhancement, 528–31
nanostructured materials, 530–1
photactivation, 528–9
resistance change of $BaTiO_3$-CuO film to photostimulation pulses, 529
response of $BaTiO_3$-CuO film to photostimulation pulses, 529
sensors on the market for carbon dioxide detection, 512
carbon monoxide (CO), 128–30, 373
carbon nanotube field effect transistor (CNTFT), 357
carbon nanotube/metal oxides gas sensor
characterisation, 396–401
HRTEM image of CNT/WO_3 film and nanocrystalline WO_3, 401
information from Raman spectroscopy, 397
principles of scanning electron microscope, 400
Raman spectra of SWCNT/Co_3O_4 film, Co_3O_4 thin film and the SiO_2/Si substrate, 398
Raman spectroscopy, 396–7
scanning electron microscopy, 398–9
SEM image of MWCNT-WO_3 thin film on Si substrate, 400
transmission electron microscopy, 399–401
X-ray diffraction, 397–8
XRD patterns of SnO_2, MWNTs and SnO_2/MWNTs composites, 399
classification, 388–9
CNT-doped metal oxides, 389
MOX-decorated carbon nanotubes, 388
fabrication and synthesis of devices, 389–90
arc discharge, 389
chemical vapour deposition, 390
laser ablation, 389–90
hybrid materials for gas sensing, 386–403
preparation of sensing films, 390–5
dip-coating, 394–5
drop-coating, 393
electron beam (E-beam) evaporation, 395
screen-printing, 393–4
spin-coating, 391–3
sensing mechanism, 401–3
model of a potential barrier to electronic conduction at grain boundary, 402
sensor assembly, 395–6
carbon nanotube (CNT), 143
cerium dioxide, 448
charge carrier transport
electrode-oxide semiconductor interfaces, 89–103
electric field and capacitance in metal-semiconductor interface, 90–5
interfacial layer structure, 100–3
transport mechanism across the junction barrier, 95–8
tunnelling through barrier, 98–100
chemical sensing
one- and two-dimensional metal oxide nanostructures, 299–310
conductometric sensor, 306–7
deposition techniques, 300–6
future trends, 310
transduction and novel devices, 307–10

© Woodhead Publishing Limited, 2013

chemical vapour deposition (CVD), 300, 358, 437–9, 442
chemical warfare agents (CWA), 467–88
  acceptable concentration in air and the lethal dosage, 469
  classification and properties, 468–71
    acute toxicity of various nerve agents, 471
    comparison of nuclear weapons and chemical agents, 469
    physical properties, 470
    toxicity of real gases and simulant gases, 469
  detecting techniques, 471–3, 474
    CWA detecting techniques, 472
    IMS structure, 472
    ion mobility spectrometer (IMS), 471
    SAW device schematic diagram, 474
    semiconducting device technique, 471–3
    semiconducting sensing device structure, 473
    surface acoustic wave (SAW) sensor technique, 473
  device preparation, 473–9
    microsensor array arrangements, 478
    microsensor array device, 476
    preparation process of microsensor, 477
    SAW sensor preparation sequence, 478
    schematic diagram of SAW delay line for CWA sensor, 478
    semiconducting device, 474–6
    surface acoustic wave (SAW) sensor, 478–9
    synthesis method of sensing materials and their amount of addition, 474
    synthesis process of sensing material using impregnation method, 476
    synthesis sequence for SnO_2 by co-precipitation method, 475
    synthesis sequence of ball-milling method for SnO_2-based device materials, 475
  frequency shift of various sensing films for different simulant gases
    CH_2C_{l2} and DCP, 486
    DMMP and CH_3CN, 485
  sensing properties, 479–88
    CH_3CN, 481
    DPGME, 481
    dynamic response curve, 480
    microsensor array device, 482
    PCA results for concentration change of each gas, 487
    SAW sensors for various levels of humidity, 487
    sensing characteristics to DMMP of 39.6 MHz SAW device coated with PIB films, 483
    sensitivity change with DMMP gas concentration for SnO_2 added with Al_2O_3 4%, 479
    sensitivity of sensor array with four devices, 482
    SnO_2-based single device, 479–82
    surface acoustic wave (SAW) type sensor, 482–8
    variation of centre frequency with polymer thickness and DMMP concentration, 484
    various additives for DMMP, 480
chemisorption, 266, 278
chemo-resistive sensors, 499
chemresistor, 107
complementary metal oxide semiconductor-based sensors (CMOS-based sensors)
  future trends, 506–7
  gas and odour detection, 491–507
  integrated multi-sensor and sensor array systems, 504–5
    FOX 4000 electronic nose, 504
    multiple micro-hotplate-based gas sensors on a single silicon die, 505
  interface circuitry and its integration, 499–504
    diagram for baseline removal circuit, 503
    hybrid approach, 499
    logarithmic compression circuit for gas-sensing material interface, 503

© Woodhead Publishing Limited, 2013

complementary metal oxide semiconductor-based sensors (*cont.*)
monolithic approach, 499
resistance controlled oscillator circuit for gas-sensing material interface, 502
simulation precision results for sensors resistance materials, 502
temperature control circuit, 501
micro-calorimetric CMOS gas sensors, 495–6
commercial pellistor, 496
differential transducing circuit for micro-calorimeter, 496
micro-resistive CMOS gas sensors, 492–5
CMOS micro-hotplate based gas sensor, 494
fabricated micro-hotplate device, 495
sensing materials and their deposition on CMOS gas sensors, 496–9
CNTs locally grown simultaneously using micro-heaters, 498
zinc oxide nanowires on a CMOS microhotplate, 497
complementary metal-oxide semiconductor (CMOS)
compatible metal-oxide sensors, 242–6
monolithic metal-oxide-based gas sensor system, 245
tungsten SOI chip, 245
conduction mechanism
future trends, 61
semiconducting metal oxide sensing films, 35–61
semiconducting metal oxide sensing layers, 51–61
n-type SnO_2, 56–61
p-type Cuo, 52–6
sample preparation and experimental conditions, 51–2
sensing and transduction for *p*- and *n* -type semiconducting metal oxides, 42–51
sensing with semiconducting metal oxide gas sensors, 36–42
conductometric sensor, 306–7, 520
contact potential difference, 82
Coulomb blockade sensors, 423
covalent functionalisation, 370
CrO_3 converter, 379
current–voltage characteristics (CVC), 94, 417

D-band, 397
dangling bonds, 85
Debye length, 17, 275, 278, 446
Density Function Theory (DFT), 361
device fabrication, 9
device integration, 306–7
dielectric material-gate field effect transistor, 28
differential sensor, 180–2
absolute and differential current of HEMT diodes measured at 25°C, 181
absolute and differential current of HEMT diodes measured at 50°C, 182
diffuse reflectance infrared Fourier transform (DRIFT), 531
dihydrogen, 374
diisopropyl methylphosphonate (DIMP), 378
dimethyl methylphosphonate (DMMP), 362, 372, 378, 479
dinitrotoluene (DNT), 372
diode type sensors, 30–1
dipropylene glycol methyl ether (DPGME), 480–1
direct thermoelectric gas sensors (DTEGs), 264–6, 267–91
ionic direct thermoelectric gas (iDTEG) sensors, 290–1
measurement techniques, 267–71
measured and analysed signals, 270
set-up, 268
modelling and simulation, 271–80
calculated electron and hole concentration, 277
effective thermopower, 279
obtained simulation data for the reduced potential, 276

© Woodhead Publishing Limited, 2013

results of thermal modelling, 273
rotational symmetry model, 274
set-up for the one-dimensional model, 272
motivation for research, 261–3
principle of set-up, 265
results, 280–90
DTEGs with Fe_2O_3 as the gas sensitive material, 288
DTEGs with SnO_2 as the gas sensitive layer, 283
DTEGs with $SrTi_{0.6}Fe_{0.4}O_{3-\delta}$ as the gas sensitive material, 285
experimental results of DTEG with Fe_2O_3 as an oxygen sensitive layer, 289
measurement results of DTEG with SnO_2 as gas sensitive material, 282
resistance and thermopower of porous STF specimen, 280
results obtained from a DTEG with SnO_2, 284
SnO_2 -based DTEG, 281
thermopower results of a DTEG, 286
discriminant functions (DF), 136
double Schottky barrier model, 15
DRIFT analysis, 524
drift velocity, 67
driving circuits for micro-heaters, 499
drop-coating, 233–5
Dynament, 513

electrical CO sensors, 443
electrochemical sensors, 513–20
classification according to sensing principle, 513–16
amperimetric sensors, 513–14
basic amperimetric sensor, 514
basic configuration of mixed potential sensor, 516
basic potentiometric sensor, 515
potentiometric sensors, 514–15
mixed potential for carbon dioxide detection, 516–17
relevance of material and fabrication techniques in performance, 517–20
electrochemical sensor potentials with lithium-ion conducting electrolytes, 518
packaged electrochemical sensor with zeolite filter, 519
planar structure of potentiometric sensor, 518
electrode–oxide interfaces
charge carrier transport in electrode–oxide semiconductor interfaces, 89–103
gas/solid interactions in electrode–oxide semiconductor interfaces, 103–9
semiconductor gas sensors, 64–109
electrode–oxide semiconductor interfaces, 80–9
charge carrier transport, 89–103
electric field and capacitance in metal–semiconductor interface, 90–5
interfacial layer structure, 100–3
transport mechanism across the junction barrier, 95–8
tunnelling through barrier, 98–100
contact with surface states and interfacial layer, 84–8
electron energy-band diagram, 87
energy-band diagram of the band bending interface, 86
gas/solid interactions, 103–9
ideal contact of metal and oxide semiconductor, 80–4
energy-band diagram of metal contact, 81, 84
work functions of some metals and semiconductors, 84
image force effects on the barrier height, 88–9
image charge, electric field lines and electron energy diagram, 89
electrode width–electrode gap ratio, 72
electrodes
geometry, 71–7
ceramics type one-electrode semiconductor gas sensors, 76
gas profile in the active film, 75

© Woodhead Publishing Limited, 2013

electrodes (*cont.*)
planar constructions of standard and one electrode semiconductor sensors, 76
sensitivity *vs.* electrode gap, 72
structures used with gas sensors, 71
thin film type one-electrode semiconductor gas sensors and circuits, 76
material influence, 68–71
comparison of hydrogen sensitivity in AlGaN/GaN Schottky diodes, 70
sensitivity influence of three electrodes on a SnO_2 –Mn_2O_3 sensor, 68
metals and conduction, 65–8
drift of electrons in a conductor, 67
room temperature conductivity, 66
paste materials properties, 77–80
semiconductor gas sensors, 64–109
electrolyte metal oxide oxygen sensor, 161
electron beam evaporation (EBE), 301
'electronic nose' (e-nose), 435
English Electric Valve (EEV) Ltd, 495
epitaxial graphene
SiC as gas sensors, 145–8
highly selective NO_2 detection using epitaxial graphene, 146
single-layer graphene sensor response, 147
SiC field effect transistor as gas sensors, 148
solution-gated epitaxial graphene FET, 149
transistor device, 150
ethylene sensing, 166–7
AlGaN/GaN MOS diode, 167

field-effect transistor sensors, 527–8
floating gate field-effect transistor gas sensor configuration, 527
field-effect transistor type gas sensors, 24–8
principles, 24–5
structure of Pd-gate FET, 24
field-emission (FE), 99
field test, 204–5
improved results, 204–5
Figaro, 513
flame spray pyrolysis (FSP), 236, 498
Fourier transform infrared (FTIR) spectrum, 325

G-band, 397
gallium nitride (GaN), 168
nanowires, 195
schematic diagram, 196
GaN Schottky diode sensor, 182–8
N-face and Ga-face comparison, 182–6
device structure and fabrication, 183–4
experimental results, 184–6
Ga-polar and N-polar, 184
I-V characteristics from the three types of diodes, 185
I-V characteristics of the N-polar diodes, 187
time dependence of current change in three sensors, 186
W/Pt contacted GaN Schottky diodes, 186–8
gas response, 10
disturbances, 12
gas sensing, 10–12, 160–7
disturbances to gas response, 12
operating temperature, 11–12
response and response transients, 10–11
response and recovery transients, 10
gold, 78
good indoor ventilation, 511
graphene
gas-sensitive material, 141
production, 141–3
isolated graphene oxide, 142
production on SiC, 143–5
reconstruction of SiC(0001) and monolayer graphene, 145
single monolayer of graphene on SiC, 144
properties, 139–40
band structure, 139
field effect in few-layer graphene (FLG), 140

© Woodhead Publishing Limited, 2013

graphene-based gas sensor, 117–50
dynamic sensor operation, 134–7
estimation of NO_x levels in typical exhaust and flue gases, 137
material development, 130–4
gas-sensing abilities of field effect sensors, 132
materials combinations, 131–4
MISiC field effect-based CO_2 sensor, 135
tailor-made sensing layers for oxygen, 131–2
tailoring layers for CO_2 and NO_x, 132–4
novel devices, 137–48
transducting and sensing mechanism, 119–30
graphene nanoribbons, 143

1,6-hexamethylene diisocyanate (HMDIC), 325
high electron mobility transistors (HEMTs), 530
high-resolution TEM (HRTEM), 401
Hooge's formula, 418, 422
'hybrid' chemical gas sensors, 387
hydrogen sensing, 167–82
AlGaN/GaN HEMT Schottky diode-based hydrogen sensor, 169
differential sensor, 180–2
effect of humidity on hydrogen sensors, 177–80
Schottky diode hydrogen sensor, 169–76
TiB_2 ohmic contacts, 176–7
hydrogen sensors
based on ZnO nanorods, 189–95
effect of humidity, 177–80
hydrogen sensitivity as a function of humidity, 178
time dependence of recovery time of AlGaN/GaN HEMT diode, 179
time dependence of the absolute value of the AlGaN/GaN HEMT diode, 178
hydrogen sulfide, 375
11-hydroxyundecanoic acid (11-HUDA), 324

impedimetric sensors, 520–6
indirect thermoelectric gas sensors, 264–6
principle of set-up, 265
inflammable gases, 11, 18–19
correlations between gas response and partial pressure of hydrogen, 20
InN nanobelts, 195–7
MOCVD-grown InN nanobelts, 197
interfacial layer
dipole formation
energy band diagram of Schottky junction, 104
structure, 100–3
addition monolayers and interdiffusion, 103
clean semiconductor surface, 101–2
dilute limit, 102–3
metal-semiconductor interfacial zones, 102
monolayer formation, 103
Schottky barrier formation, 101
internal voltage drop, 125
ion mobility spectrometer (IMS), 471
ion selective FET (ISFET), 527
ionic direct thermoelectric gas (iDTEG) sensors, 290–1
YSZ as an oxygen sensitive layer, 291
ionosorption, 14
IZO films, 161–2

junction field effect (JFET), 422

Kelvin radius, 410

Landau-Levich equation, 394
Langmuir model, 364–5
laser chemical vapour deposition (LCVD), 302
layer deposition, 300–6
one-dimensional nanostructures, 303–6
two-dimensional nanostructures, 300–3
'lifetime' semiconductors, 278
linear discriminant analysis (LDA), 136, 137, 347
liquid phase growth, 305

© Woodhead Publishing Limited, 2013

LiSICON, 517
lithium ions, 517
low pressure chemical vapour deposition (LPCVD), 302

Maxwell–Garnett effective medium approximation, 345
mercury vapour, 375
metal-insulator-semiconductor capacitor type sensors, 29–30
  MIS capacitor, 30
metal insulator semiconductor field effect transistor (MISFET), 3, 4–5, 108–9, 119
metal insulator semiconductor (MIS), 3, 4–5, 119, 423
metal oxide nanostructures
  conductometric sensor, 306–7
  deposition techniques, 300–6
  future trends, 310
  one- and two-dimensional for chemical sensing, 299–310
  transduction and novel devices, 307–10
    calibration curve, 309
    conductance variation, 308
metal oxide semiconductor
  advances in carbon dioxide sensors, 448–52
    effect in changing the lanthanum content on the gas response of SnO_2 film, 451
    effect of varying CO_2 concentration on $BaTiO_3$ sensing material, 450
    gas response change of lanthanum based film to CO_2, 449
  advances in carbon monoxide sensors, 446–8
    comparison of sensor response to varying CO concentrations, 447
    response of sensor to humidity, 448
  advances in nitrogen oxide sensors, 452–6
    effect of doping material with various oxides on SnO_2 responsivity to N_2O gas, 455
    effect of firing temperature on the material responsivity, 453
    responses of chemiluminescence and semiconductor sensors, 454
    variation in resistance according to WO_3 crystallite size, 453
  detecting environmentally important gases, 442–6
    carbon dioxide, 444–5
    carbon dioxide effects on human health, 445
    carbon monoxide, 442–4
    effects of carbon monoxide on human health, 443
    increase in CO_2 concentration since 1958, 444
    nitrous oxides, 445–6
  future trends, 456–60
    CVD reactor design used in production of sensors using ElFi CVD, 457
    electric fields and chemical vapour deposition, 456–8
    gas response of TiO_2 sensors, 458
    resistive response of WO_3 sensors, 459
    zeolite modified sensors, 458–60
  gas sensors in environmental monitoring, 433–60
  sensor synthesis methods, 436–42
    chemical vapour deposition, 437–9
    comparison of synthetic techniques, 441–2
    factors influencing sensor design, 436
    gas sensitive film production on sensor substrate, 438
    important processes in chemical vapour deposition methodologies, 438
    physical vapour deposition, 440–1
    PVD process diagram, 441
    screen-printing, 437
    sol-gel techniques, 440
    spray pyrolysis, 439–40
    spray pyrolysis technique for depositing thin films, 440
    techniques for sensor fabrication, 437

© Woodhead Publishing Limited, 2013

metal oxide semiconductor field effect transistor (MOSFET), 410, 494
metal-oxide sensors
  complementary metal oxide semiconductor (CMOS) compatible, 242–6
    monolithic metal-oxide-based gas sensor system, 245
    tungsten SOI chip design, 245
metal semiconductor
  ideal contact, 80–4
  interface, electric field and capacitance, 90–5
    electrical field and potential distribution, 92
metalorganic chemical vapour deposition (MOCVD), 302
micro electro-mechanical system (MEMS), 9
micro-hotplate, 222–30, 493
  concept and thermal design, 223–4
    heat losses in a micro-heating device, 224
    micromachined metal-oxide gas sensor, 223
  nanostructured gas sensing layers, 250–2
    nanowires, 250
    SNAP nanowire sensors, 251
  realisation and performance, 224–7
    CMOS silicon micromachined hotplate, 226
    comparison of various designs, 228–9
    suspended-membrane-type gas sensor, 225
  reliability, 227, 230
micromachined field-effect gas sensors, 247–9
  Ir-MOSFET voltage, 249
  low-power MOSFET array gas sensor, 248
micromachined metal-oxide gas sensors, 230–42
  packaging, 240–2
  temperature modulation, 237–40
  thick gas sensitive films, 233–7
  thin gas sensitive films, 231–3
micromachined semiconductor gas sensors, 220–55
  complementary metal oxide semiconductor (CMOS)-compatible metal-oxide sensors, 242–6
  micro-hotplate concept and technologies, 222–30
  micromachined field-effect gas sensors, 247–9
  micromachined metal-oxide gas sensors, 230–42
  semiconductors as gas sensitive device, 221–2
  trends and perspectives, 249–55
'mixed potential' sensor, 515
Mott barrier, 83
moving-boundary gas profile type II, 74
multi-walled carbon nanotube (MWCNT), 356, 389

n-type oxide, 6
n-type semiconducting metal oxides
  sensing and transduction, 42–51
    conduction processes and energy bands, 46
    conduction processes for *n* -type SnO_2, 49
    extension to low oxygen concentration, 48–51
    modelling of conduction in normal conditions, 44–8
    p -type $Cr_2 O_3$ *vs. n* -type SnO_2, 43
n-type SnO_2, 56–61
  CPD and electrical resistance changes of SnO_2 sensor
    during exposure to five pulses of H_2, 59
    during exposure to four pulses of CO, 58
    stepwise increasing amounts of oxygen, 57
  dependence of the resistance and the corresponding band bending changes, 60
Naflon, 371
Nanomix Inc., 379

© Woodhead Publishing Limited, 2013

nanostructured gas sensing layers
micro-hotplates
nanowires, 250
SNAP nanowire sensors, 251
nanostructured wide bandgap materials, 188–99
GaN nanowires, 195
hydrogen sensors based on ZnO nanorods, 189–95
InN nanobelts, 195–7
single ZnO nanowire, 197–9
nanotube field effect transistor (NTFET) sensor, 163
narrow-gap sensor, 73
NaSICON, 517
National Ambient Air Quality Standard (NAAQS), 377
Nernst equation, 516
Nernst law, 515
Nernst potential, 517
Nernst relation, 133
nitric oxide, 445
nitrogen, 373
nitrogen dioxide (NO_2), 134, 445
nitrogen monoxide, 373
nitrotoluene, 378
noise sensors, 417–22
non-covalent functionalisation, 370, 371
non-dispersive infrared (NDIR) sensors, 163, 379, 513
non-resistive sensors, 23–31
normalised conductance, 10
normalised resistance, 10
NO_x, 377

Ohm's Law, 66
on-off controller, 500
one-dimensional nanostructures, 303–6
morphologies, 304
one-electrode sensors, 75
operating temperature, 11–12
oxide semiconductor, 13
ideal contact, 80–4
oxide semiconductor-gate field effect transistor, 27–8
NO_2 sensing characteristics, 27
oxidising gas sensors, 77
oxidising gases, 11, 19–22
correlations between gas response and partial pressure of nitrogen dioxide, 21
oxygen concentration cell type sensors, 28–9
attached with oxide semiconductors, 29
oxygen sensing, 161–3
AlGaN/GaN HEMT-based O_2 sensor and IZO functionalised HEMT sensor, 162

p-type CuO, 52–6
dry air condition, 54
operational temperature, 56
CPD and electrical resistance changes of CuO sensor, 53
fitting curve, 54
p-type semiconducting metal oxides
sensing and transduction, 42–51
energy bands representation, 45
modelling of conduction in normal conditions, 44–8
p-type Cr_2O_3 *vs. n* -type SnO_2, 43
packaging, 240–2
chip on board wafer-level packaged metal-oxide gas sensors, 242
wafer-level packaged and individual sensor area of metal-oxide sensor, 241
wafer-level packaged semiconductor gas sensors, 243
palladium, 374
palladium–gold, 80
palladium–silver, 79
partial differential equation, 271–2
pellet resistor, 495
pellistor, 495
penetration depth, 273
phase boundary, 519
photo-electromotive force (Photo-EMF), 416
photochemical vapour deposition (PCVD), 302
photoluminescence-based gas sensing
future trends, 348–9
quantum dot *in-situ* polymerisation, 321–4
CdSe/polymer film C_{18}, 323

© Woodhead Publishing Limited, 2013

CdSe QDs dispersion in poly(hexyl methacrylate) after *in situ* polymerisation, 322
spectra of CdSe QDs in polymers of different hydrocarbon side chain lengths, 323
quantum dot layer-by-layer deposition, 324–9
glass substrate functionalisation by HMDIC, 326
optical absorbance spectra of multilayered films, 328
spectra of the *in situ* functionalised CdSe QDs, 327
quantum dot modification, 320–1
BA and CdSe-BA in CDC_{13}, 321
quantum dot-nanopore array system, 343–8
blank AAO and QD drop-cast-AAO AFM images, 343
CdSe/ZnS QDs cast on Si, 344
enhanced sensibility stability, 346
enhancement of emission efficiency and sensitivity, 343–4
monotonomic sensing with intrinsic PL response, 344–5
PL peak intensity responses to exposures of xylenes balanced in dry air, 345
PL stability of an AAO/CdSe/ZnS QD sample, 347
xylenes sensing characteristics of an AAO/CdSe/ZnS, 346
quantum dot-polymer system, 338–42
emission and sensitivity enhancement, 338–40
non-motonic sensing, 340–2
PL of solutions of CdSe-NA QDs in CHC_{13}, 341
PL peak intensity as function of xylene concentration, 340
PL spectra of CdSe QDs/PMMA thin films, 339
two-cycle reversible changes in the CdSe-NA QDs/PMMM film, 342
quantum dot synthesis, surface functionalisation and polymer encapsulation, 319–29
quantum dots for sensing, 329–38
absolute change in PL peak intensity, 337
CdSe QD films of different surface chemistries, 332
CdSe QDs modified with surface enhancing reagents, 330
dependence of CdSe-NA sensing characteristics on surface NA coverage, 334
ligands type dependence, 330–3
PL intensity of the CdSe-FBA films, 332
PL of CdSe-NA films made from QD solutions, 333
PL peak intensity of CdSe-NA/PMMA film, 335
PL spectra of CdSe QD solutions in chloroform, 336
PL spectra of PMMA films, 331
surface modifying group coverage dependence, 333–4
surface modifying group length dependence, 334–8
semiconductor quantum dots, 316–49
physical vapour deposition (PVD), 300, 440–1
plasma enhanced chemical vapour deposition (PECVD), 302
platinum, 78, 513
platinum–gold, 79
platinum–silver, 79
Poisson-Boltzmann equation, 274–5
poly-(m-aminobenzene sulfonic acid) (PABS), 371
polybutadiene (PBD), 482
polydimethylsiloxane (PDMS), 482
polyepichlorohydrin (PECH), 482
polyethylene terephthalate (PET), 378
polyethyleneimine (PEI), 371
polyisobuthylene (PIB), 482
polyisoprene (PIP), 482
poly(lauryl methacrylate), 321
polymeric foil, 253
poly(methyl methacrylate) (PMMA), 321
polystyrene, 321

© Woodhead Publishing Limited, 2013

porous silicon gas sensors, 408–25
conductivity and capacitance sensors, 409–11
different gas sensors, 422–4
luminescence from PSi, 411–14
PL emission from the electrochemically prepared layer on wafer, 412
noise sensors, 417–22
noise spectra for samples with 50% porosity PS layers, 419
normalised noise spectra for samples with 50% porosity PS layers, 419
sensitivity of different sensors, 421
optical and photo properties, 414–16
transmission spectra of thick freestanding PS films, 415
principal component analysis (PCA), 136, 486
propionic acid, 372
proportional integral derivative (PID) controller, 500
propyltrimethoxysilane (PTMS), 528
pulse width modulation (PWM), 500
pulsed laser deposition (PLD), 301

quantum confinement, 316

Raman spectroscopy, 396–7
rare earth oxycarbonates, 524
reduced resistance, 16
reducing gas sensors, 77
reference electrode (RE), 514
Renewable Energy Concepts, 511
resistive sensors, 520–6
resistor divider circuit, 501
resistor type sensors
empirical aspects, 5–13
gas sensing characteristics, 10–12
semiconductor oxygen sensors, 12–13
sensing materials and devices, 5–9
theoretical aspects, 13–23
electron depletion for oxide grains, 15
energy band diagrams, 16
energy band diagrams of oxide grain and metal electrode, 23
extensions, 22–3
receptor and transducer function, 13–16
response to inflammable gases, 18–19
response to oxidising gases, 19–22
response to oxygen, 17–18

sarin, 378
scanning electron microscopy (SEM), 398–9
scanning tunnelling microscope (STM), 360–1
Schottky barrier, 83, 85, 91, 94
adsorption of other gases, 107–9
conductometric gas sensor, 108
hydrogen absorption, 105–7
surface reactions, diffusion and trapping, 106
transport mechanism across, 95–8
energy-band diagram, 96
tunnelling, 98–100
field emission and thermionic field emission tunnelling, 99
Schottky diode hydrogen sensor, 169–76
device structure and fabrication, 170–1
Schottky diode on an AlGaN/GaN HEMT layer structure, 171
experimental results, 171–6
forward and reverse bias plot of a diode, 174
hydrogen sensing system, 172
I-V characteristics in linear or log form, 173
percentage change in current as a function of bias, 175
percentage change in current as a function of hydrogen, 176
time response at 25°C of a MOS-HEMT-based diode, 174
testing procedure, 171
screen-printing, 235–6, 437
Seebeck coefficient, 276
semiconducting device, 474–6
semiconducting direct thermoelectric gas sensors, 261–93
direct thermoelectric gas sensors, 267–91

© Woodhead Publishing Limited, 2013

future trends, 291–3
overview, 261–7
early research activities, 266–7
semiconducting metal oxide, 35–6
semiconducting metal oxide based gas sensors
sensing, 36–42
difference between a porous and a compact layer, 39
energy band representation of SnO_2, 42
gas interactions in porous layer, 41
sensor substrate design, 37
surface reactions transduced into measurable signal, 38
semiconducting metal oxide sensing films
conduction mechanism, 35–61
future trends, 61
sensing and transduction for *p*- and *n*-type semiconducting metal oxides, 42–51
sensing with semiconducting metal oxide gas sensors, 36–42
studies in working conditions, 51–61
semiconductor gas sensors, 3–33
chemical warfare agents, 467–88
classification and properties, 468–71
detecting techniques, 471–3
device preparation, 473–9
sensing properties, 479–88
classification, 4–5
according to the types of transducers and receptors used, 6
constituted of a receptor and a transducer, 5
electrode materials and electrode-oxide interfaces, 64–109
charge carrier transport in electrode-oxide semiconductor interfaces, 89–103
electrode-oxide semiconductor interfaces, 80–9
gas/solid interactions in electrode-oxide semiconductor interfaces, 103–9
future trends, 31–3
basic approaches, 32–3
challenges, 33
MEMS gas sensor, 32
non-resistive sensors, 23–31
polymeric foil, 252–5
metal-oxide gas sensor, 253
resistor type sensors, 5–13, 13–23
semiconductor oxygen sensors, 12–13
semiconductor quantum dots, 316–49
semiconductors
as gas sensitive device, 221–2
MGS 1100 sensor, 222
sensing, 123–30
detection of hydrogen containing gases, 124–8
role of oxygen as adsorption sites for the hydrogen, 126
detection of non-hydrogen containing gases, 128–30
CO/O_2 and temperature-dependent binary switch, 129
general, 123–4
p- and *n*-type semiconducting metal oxides, 42–51
extension to low oxygen concentration, 48–51
modelling of conduction in normal conditions, 44–8
p-type Cr_2O_3 *vs.* *n*-type SnO_2, 43
semiconducting metal oxide (SMOX) based gas sensors, 36–42
difference between a porous and a compact layer, 39
energy band representation of SnO_2, 42
gas interactions in porous layer, 41
sensor substrate design, 37
surface reactions transduced into measurable signal, 38
sensing device, 7–9
structures adopted for resistor type sensor, 8
sensing electrode (SE), 514
sensing film, 390
sensing material, 5–6
interface circuit, 500–1
sensitisers, 7
sensor module, 201–4
sensor system, 202

© Woodhead Publishing Limited, 2013

sensor–electrode interface, 72
silicon carbide (SiC), 168
  Schottky diode hydrogen sensor, 199–201
    low bias forward I-V characteristics from SiC sensor, 200
    time response of SiC sensor, 200
silicon carbide (SiC)-based gas sensor, 117–50
  dynamic sensor operation, 134–7
    estimation of NO_x levels in typical exhaust and flue gases, 137
  material development, 130–4
    gas-sensing abilities of field effect sensors, 132
    materials combinations, 131–4
    MISiC field effect-based CO_2 sensor, 135
    tailor-made sensing layers for oxygen, 131–2
    tailoring layers for CO_2 and NO_x, 132–4
  novel devices, 137–48
  transducting and sensing mechanism, 119–30
silicon micromachined thin-film metal-oxide gas sensor, 231
silver, 78
single-walled carbon nanotube (SWCNT), 356, 389
  applications, 377–80
    air quality monitoring, 377
    medical applications, 378–80
    military applications, 378
    score plots of sensors upon exposure to renal failure and cancerous patterns, 380
  as gas sensors, 356–80
  gas sensing mechanisms, 364–70
    doping effect generated by adsorption of gas molecules, 364–6
    effect of metallic single-walled carbon nanotube percolation, 369–70
    equilibrium tube-molecule distance, adsorption energy and amount of transferred charge, 367
    Schottky barrier modulation, 366–9
    transition region between the electrode and SWCNT, 369
  gas sensor architecture, 358–64
    carbon nanotube field-effect transistor based on individual SWCNTs, 358–60
    schematic representation of CNTFET based on individual SWCNT, 359
  gas sensor based on single-walled carbon nanotube networks, 360–4
    chemiresistor, 363–4
    chemiresistor based on SWCNT network, 364
    CNFET based on single-walled carbon nanotube networks, 360–3
  routes toward sensor selectivity, 370–6
    decoration by metallic nanoparticles, 374–5
    density of state of a 5,5 carbon nanotube doped with N-pyridinic-like defect, 374
    doping with heteroatoms, 373–4
    electrode metal diversification, 375–6
    functionalisation of single-walled carbon nanotubes, 370–2
    metal work-function and relative change of I_{ds}, 376
    multiplexed sensor array, 376
    selective diffusion barrier, 372
sol, 440
sol-gel methods, 441–2
solid electrolyte-gate field effect transistor, 25–7
  $NaNO_2$-gate FET sensor, 26
solid-state sensors, 71
  carbon dioxide detection, 510–31
    application fields for carbon dioxide sensors, 510–11

© Woodhead Publishing Limited, 2013

carbon dioxide sensors currently available on the market, 511–13
electrochemical sensors, 513–20
field effect transistor sensors, 527–8
future trends, 531
impedimetric, capacitive and resistive sensors, 520–6
new approaches to enhance sensor performance, 528–31
spectral density of noise (SND), 420
spin-coating method, 338
spray pyrolysis, 439–40
steady-state conductance, 73
steady-state response, 73
stearic acid (SA), 320
Stone-Wales defects, 366
surface acoustic wave (SAW) sensor, 357, 478–9
technique, 473
suspended gate FET (SGFET), 123

Taguchi gas sensors (TGS), 493
temperature control unit, 500
temperature modulation, 237–40
conductance response of an SnO_2 gas, 239
sensor temperature *vs.* conductance, 240
template-assisted methods, 305–6
thermal evaporation (TE), 300
thermal time constant, 271
thermionic field emission (TFE), 99–100
thermoelectric power, 263–4
thermoelectricity, 263
thermovoltages, 268
thick-film-based metal-oxide sensors, 233
thick gas sensitive films, 233–7
drop-coated metal-oxide gas sensor, 234
gas response of 3% Pd-, 0.2% Pt-doped and undoped SnO_2, 235
Pt-doped SnO_2 film deposited by flame spray pyrolysis, 238
thin gas sensitive films, 231–3
gas measurement obtained from the sensors array, 233
threshold limit value (TLV), 377
TiB_2 ohmic contacts, 176–7
variation in forward current at fixed bias for diodes, 177
tin oxides, 387
titanium dioxide sensors, 457
titanium-doped chromium oxide, 232, 254
transducer platform, 119–22
n-channel enhancement-type MISFET, 120
reactions on the catalytic metal gates, 121
transducers, 434
transduction, 122–3, 307–10
p- and *n*-type semiconducting metal oxides, 42–51
extension to low oxygen concentration, 48–51
modelling of conduction in normal conditions, 44–8
p-type Cr_2O_3 *vs.* *n*-type SnO_2, 43
transmission electron microscopy (TEM), 399–401
transmission line method (TLM), 364
trimethylamine (TMA), 372
trinitrotoluene (TNT), 362
trioctylphosphine oxide (TOPO), 319
tungsten trioxide, 452
tunnelling
Schottky barrier, 98–100
field emission and thermionic field emission tunnelling, 99
two-dimensional nanostructures, 300–3

vapour phase growth, 304–5
volatile organic compounds (VOC), 379

W/Pt contacted GaN Schottky diodes, 186–8
change in current in W/Pt GaN and AlGaN/GaN diodes, 188
web server, 203–4
interface of online hydrogen level monitoring, 204
Wheatstone bridge technique, 501

© Woodhead Publishing Limited, 2013

wide bandgap semiconductor-based gas sensors, 159–206
GaN Schottky diode sensor, 182–8
gas sensing, 160–7
hydrogen sensing, 167–82
nanostructured wide bandgap materials, 188–99
silicon carbide Schottky diode hydrogen sensor, 199–201
wireless sensor network development, 201–5
wide-gap sensor, 74
wireless sensor
network development, 201–5
field test, 204–5
sensor module, 201–4
wireless transceiver, 202–3
sensor module and wireless network server, 202
system timing of a wireless sensor node, 203
working electrode (WE), 514

X-ray diffraction, 397–8

yttria-stabilised zirconia (YSZ), 513

Zigbee-compliant wireless network, 203
ZnO nanorods
hydrogen sensors based, 189–95
contact geometry for multiple nanorod gas sensor, 191
device structure and fabrication, 190–1
experimental results, 191–5
I-V characteristic of Pt-coated nanowires, 194
relative response of Pd-coated nanorods, 193
schematic diagram, 190
time dependence of resistance change of metal-coated ZnO nanorods, 194
time dependence of resistance change of Pd-coated ZnO nanorods, 193
time dependence of resistance of Pd-coated or uncoated ZnO nanorods, 192
ZnO nanowire, 197–9, 530
change in resistance as a function of time, 198
sensor, 198

© Woodhead Publishing Limited, 2013